

*NASA Conference Publication 3178
Part 2*

Third NASA Advanced Composites Technology Conference

Volume I

*Compiled by
John G. Davis, Jr.
Langley Research Center
Hampton, Virginia*

*Herman L. Bohon
Lockheed Engineering & Sciences Company
Hampton, Virginia*

Proceedings of a workshop sponsored by the
National Aeronautics and Space Administration,
Washington, D.C., and the Department of
Defense, Washington, D.C., and held in
Long Beach, California
June 8-11, 1992

NASA

National Aeronautics and
Space Administration
Office of Management
Scientific and Technical
Information Program

1992

PREFACE

This document is a compilation of papers presented at the Third NASA Advanced Composites Technology (ACT) Conference held at Long Beach, California, June 8-11, 1992.

The ACT Program is a major multi-year research initiative to achieve a national goal of technology readiness to introduce composite materials into primary structure of production aircraft before the end of the decade. This initiative is carried out through a cooperative program between industry, universities, and the government conducting research in materials processing, analysis development, innovative designs, and manufacturing methodology. Conference papers recorded results of research in the ACT Program in the specific areas of automated fiber placement, resin transfer molding, textile preforms, and stitching as these processes influence design, performance, and cost of composites in aircraft structures. These papers are published as Volume I in this document.

Conference papers were also presented on the new initiative Design and Manufacturing of Low Cost Composites (DMLCC) sponsored by the Department of Defense. These papers are published in Volume II of this document.

The use of trademarks or manufacturers' names in this publication does not constitute endorsement, either expressed or implied, by the National Aeronautics and Space Administration.

John G. Davis, Jr.
Herman L. Bohon

CONFERENCE ORGANIZATION

Sponsor: Structures Technology Program Office
Structures Directorate
NASA Langley Research Center
Hampton, Virginia 23665-5225

General Chairman

John G. Davis, Jr.
NASA Langley Research Center

Technical Chairman

Herman L. Bohon
Lockheed Engineering
and Science Company

Administrative Assistant

Stuart E. Pendleton
Lockheed Engineering
and Science Company

Session Organizers

John G. Davis, Jr.
James H. Starnes, Jr.
Norman J. Johnston
David Beeler

NASA Langley Research Center
NASA Langley Research Center
NASA Langley Research Center
Wright Laboratory

SESSION OUTLINE

THIRD NASA ADVANCED COMPOSITES TECHNOLOGY CONFERENCE

SESSION I (Volume I, Part 1)

Composites in Transport Aircraft

Chairman: John G. Davis, Jr., NASA Langley Research Center

SESSION II (Volume I, Part 1)

Advanced Composites Technology Overview

Chairman: John G. Davis, Jr., NASA Langley Research Center

SESSION III (Volume I, Part 1)

Textile Technology

Chairman: Charles E. Harris, NASA Langley Research Center

SESSION IV (Volume II)

Design and Manufacturing of Low Cost Composites

Chairmen: Paul Pirrung and Richard Holzwarth, Wright Laboratory

SESSION V (Volume I, Part 1)

RTM/Stitched Technology

Chairman: Norman J. Johnston, NASA Langley Research Center

SESSION VI (Volume I, Part 2)

Materials Technology

Chairman: H. Benson Dexter, NASA Langley Research Center

SESSION VII (Volume I, Part 2)

Automated Fiber Placement Technology

Chairman: William T. Freeman, Jr., NASA Langley Research Center

SESSION VIII (Volume I, Part 2)

Design/Analysis Technology

Chairman: James H. Starnes, Jr., NASA Langley Research Center

CONTENTS

Preface	iii
Conference Organization	iv
Session Outline	v

Volume I, Part 1*

SESSION I

COMPOSITES IN TRANSPORT AIRCRAFT

Session Chairman: Charles P. Blankenship
NASA Langley Research Center

Impact of Composites on Future Transport Aircraft	3
Robert H. Kinder	
Challenges and Payoff of Composites in Transport Aircraft: 777 Empennage and Future Applications	25
John Quinlivan	

SESSION II

ADVANCED COMPOSITES TECHNOLOGY OVERVIEW

Session Chairman: John G. Davis, Jr.
NASA Langley Research Center

Advanced Composites Technology Program	49
John G. Davis, Jr.	
Textile Composite Fuselage Structures Development	79
Anthony C. Jackson, Ronald E. Barrie, and Robert L. Chu	
Application of Composites to Primary Transport Aircraft Structure	†
Max Klotzsche	
Advanced Composite Fuselage Technology	97
Larry B. Ilcewicz, Peter J. Smith, and Ray E. Horton	

SESSION III

TEXTILE TECHNOLOGY

Session Chairman: Charles E. Harris
NASA Langley Research Center

Advanced Resin Systems and 3-D Textile Preforms for Low Cost Composite Structures	159
J. G. Shukla and T. D. Bayha	
Weavability of Dry Polymer Powder Towpreg	175
Maylene K. Hugh, Joseph M. Marchello, Janice R. Maiden, and Norman J. Johnston	

*These papers are presented in NASA CP-3178, Volume I, Part 1.

†Presented but not included in this publication.

Effects of Temperature and Humidity Cycling on the Strengths of Textile Reinforced Carbon/Epoxy Composite Materials	191
Roberto J. Cano and Keith W. Furrow	
Mechanical Characterization of 2-D, 2-D Stitched, and 3-D Braided/RTM Materials	209
Jerry W. Deaton, Susan M. Kullerd, and Marc A. Portanova	
Performance of Resin Transfer Molded Multiaxial Warp Knit Composites	231
H. Benson Dexter and Gregory H. Hasko	
Experimental and Analytical Characterization of Triaxially Braided Textile Composites	263
John E. Masters, Mark J. Fedro, and Peter G. Ifju	
Cross-Stiffened Continuous Fiber Structures	287
John R. Ewen and Jim A. Suarez	
An Engineering Model of Woven Composites Based on Micromechanics	309
W. C. Carter, B. N. Cox, M. S. Dadkhah, and W. L. Morris	
Cost Model Relationships Between Textile Manufacturing Processes and Design Details for Transport Fuselage Elements	323
Stephen L. Metschan, Kurtis S. Wilden, Garrett C. Sharpless, and Rich M. Andelman	

SESSION IV

DESIGN AND MANUFACTURING OF LOW COST COMPOSITES*

Session Chairmen: Paul Pirrung and Richard Holzwarth
Wright Laboratory

SESSION V

RTM/STITCHED TECHNOLOGY

Session Chairman: Norman J. Johnston
NASA Langley Research Center

Development of RTM and Powder Prepreg Resins for Subsonic Aircraft Primary Structures	345
Edmund P. Woo, Michael R. Groleau, James L. Bertram, Paul M. Puckett, and Shawn J. Maynard	
Analytical Modeling and Sensor Monitoring for Optimal Processing of Advanced Textile Structural Composites by Resin Transfer Molding	361
Alfred C. Loos, John D. MacRae, Vincent H. Hammond, David E. Kranbuehl, Sean M. Hart, Gregory H. Hasko, and Alan M. Markus	
A Designed Experiment in Stitched/RTM Composites	381
Larry C. Dickinson	

*Appears in Volume II.

The Effects of Aircraft Fuel and Fluids on the Strength Properties of Resin Transfer Molded (RTM) Composites	399
Anthony Falcone and Marvin B. Dow	
Effects of Thermal and Moisture Cycling on the Internal Structure of Stitched RTM Laminates	415
Jeff Walker, Lance Roundy, and Jon Goering	
The Combined Effect of Glass Buffer Strips and Stitching on the Damage Tolerance of Composites	433
Susan M. Kullerd	
Progress in Manufacturing Large Primary Aircraft Structures Using the Stitching/RTM Process	453
Alan Markus, Patrick Thrash, and Kim Rohwer	
Test Results From Large Wing and Fuselage Panels	481
Ram C. Madan and Mike Voldman	

Volume I, Part 2

SESSION VI

MATERIALS TECHNOLOGY

Session Chairman: H. Benson Dexter

NASA Langley Research Center

Characterization and Development of Materials for Advanced Textile Composites	505
J. Timothy Hartness, Timothy L. Greene, and Leo E. Taske	
The Effects of Specimen Width on Tensile Properties of Triaxially Braided Textile Composites	523
John E. Masters, Peter G. Ifju, Christopher M. Pastore, and Alexander E. Bogdanovich	
In Situ Processing Methods for Composite Fuselage Sandwich Structures	537
Hossein Saatchi, Bill Durako, Dick Reynolds, Ernest Dost, and Kurtis Willden	
The Effect of Mixed Mode Precracking on the Mode I Fracture Toughness of Composite Laminates	547
Prashanth Shankar, Williard D. Bascom, and John A. Nairn	
Master Plot Analysis of Microcracking in Graphite/Epoxy and Graphite/Peek Laminates	557
John A. Nairn, Shoufeng Hu, and Jong Song Bark	
Establishing the Relationship Between Manufacturing and Component Performance in Stretch Formed Thermoplastic Composites	571
Michael H. Santare, R. Byron Pipes, A. J. Beaussart, D. W. Coffin, B. J. O'Toole, and S. F. Shuler	
Novel Cost Controlled Materials and Processing for Primary Structures	591
S. J. Dastin	

The Effects of Design Details on Cost and Weight of Fuselage Structures	601
G. D. Swanson, S. L. Metschan, M. R. Morris, and C. Kassapoglou	

SESSION VII

AUTOMATED FIBER PLACEMENT TECHNOLOGY

Session Chairman: William T. Freeman, Jr.
NASA Langley Research Center

Automated Fiber Placement—Evolution and Current Demonstrations	625
Carroll G. Grant and Vernon M. Benson	
Response of Automated Tow Placed Laminates to Stress Concentrations	649
Douglas S. Cairns, Larry B. Ilcewicz, and Tom Walker	
Mechanical Characterization of Two Thermoplastic Composites Fabricated by Automated Tow Placement	665
Larry C. Dickinson and Jerry W. Deaton	
Manufacturing Scale-up of Composite Fuselage Crown Panels	689
K. Willden, M. Gessel, C. Grant, and T. Brown	
Dimensional Stability of Curved Panels With Cocured Stiffeners and Cobonded Frames	705
G. E. Mabson, B. W. Flynn, G. D. Swanson, R. C. Lundquist, and P. L. Rupp	
Tension Fracture of Laminates for Transport Fuselage Part II: Large Notches	727
T. H. Walker, L. B. Ilcewicz, D. R. Polland, and C. C. Poe, Jr.	
Impact Damage Resistance of Composite Fuselage Structure, Part 2	759
Ernest F. Dost, Scott R. Finn, Daniel P. Murphy, and Amy B. Huisken	
Design, Analysis, and Fabrication of a Pressure Box Test Fixture for Tension Damage Tolerance Testing of Curved Fuselage Panels	789
P. J. Smith, J. B. Bodine, C. H. Preuss, and W. J. Koch	
Global Cost and Weight Evaluation of Fuselage Keel Design Concepts	807
B. W. Flynn, M. R. Morris, S. L. Metschan, G. D. Swanson, P. J. Smith, K. H. Griess, M. R. Schramm, and R. J. Humphrey	

SESSION VIII

DESIGN/ANALYSIS TECHNOLOGY

Session Chairman: James H. Starnes, Jr.
NASA Langley Research Center

Design and Evaluation of a Foam-Filled Hat-Stiffened Panel Concept for Aircraft Primary Structural Applications	839
Damodar R. Ambur	
A Study of Structurally Efficient Graphite-Thermoplastic Trapezoidal-Corrugation Sandwich and Semi-Sandwich Panels	859
Dawn C. Jegley	

A Weight-Efficient Design Strategy for Cutouts in Composite Transport Structures	879
S. G. Russell, J. Hangen, and T. E. Palm	
Effects of Cutouts on the Behavior of Symmetric Composite Laminates Subjected to Bending and Twisting Loads	899
C. B. Prasad, M. J. Shuart, N. J. Bains, and M. Rouse	
Buckling Analysis of Curved Composite Sandwich Panels Subjected to Inplane Loadings	919
Juan R. Cruz	
ISPAN—Interactive Stiffened Panel Analysis—A Tool for Quick Concept Evaluation and Design Trade Studies	933
John W. Hairr, William J. Dorris, J. Edward Ingram, and Bharat M. Shah	
Technology Integration Box Beam Failure Study	951
M. J. Shuart, D. R. Ambur, D. D. Davis, Jr., R. C. Davis, G. L. Farley, C. G. Lotts, and J. T. Wang	
A Global/Local Analysis Method for Treating Details in Structural Design	967
Mohammad A. Aminpour, Susan L. McCleary, and Jonathan B. Ransom	
IPACS—Integrated Probabilistic Assessment of Composite Structures: Code Development and Applications	987
C. C. Chamis and Michael C. Shiao	

Session VI

MATERIALS TECHNOLOGY

Session Chairman: H. Benson Dexter
NASA Langley Research Center

CHARACTERIZATION AND DEVELOPMENT
OF MATERIALS FOR ADVANCED TEXTILE
COMPOSITES

J. Timothy Hartness
Timothy L. Greene
Leo E. Taske
BASF Structural Materials, Inc.
Charlotte, NC

51-24
51401

INTRODUCTION

Work ongoing under the NASA Langley - Advanced Composite Technology (ACT) program is discussed. The primary emphasis of the work centers around the development and characterization of graphite fiber that has been impregnated with an epoxy powder. Four epoxies have been characterized in towpreg form as to their weaveability and braidability. Initial mechanical properties have been generated on each resin system. These include unidirectional as well as 8-harness satin cloth. Initial 2D and 3D weaving and braiding trials will be reported on as well as initial efforts to develop towpreg suitable for advanced tow placement.

EPOXY POWDER CANDIDATES

Epoxy powders thought to be suitable for the BASF powder impregnation process were submitted for evaluation. All of the resins are considered developmental and are proprietary to the resin suppliers. Consideration has been given to acceptable neat resin properties, low moisture pick-up, and processability as well as unreacted glass transition (T_g). A room temperature solid is required that can be ground and delivered in an acceptable particle size. Shown in Table I below are those resin candidates being evaluated along with their neat resin properties.

Table I. Candidate Matrix Resins Physical Properties

	PR-500	RSS-1952	CET-3	High T _g
Tensile Strength (Ksi)	8.3	-	13	-
Modulus (Msi)	507	-	410	-
% Elongation	1.9	-	5	-
Flexural Strength (Ksi)	18.4	16.9	21	19.5
Modulus (Msi)	504	426	450	512
% Elongation	4.2	5.1	7	5.3
Density gm/cc	1.24	1.15	1.27	1.25
Moisture Absorption (%)	1.56	1.2	1.35	1.46
Glass transition cured °C (°F)	205(402)	219(425)	164(326)	243(470)

FUSED EPOXY TOWPREG

Epoxy resin powders are fused on to the unsized graphite fiber using a proprietary technique developed by BASF. The towpreg has been designed with handling and loss of resin the major considerations in a secondary operation. Fused epoxy towpreg examined by SEM after impregnation and then again after weaving into 8-harness satin cloth is shown in Figures 1 and 2. All towpreg must be rewound by most weaving and braiding operations with no significant resin loss or fiber damage. Composite resin contents indicate that no significant resin loss is occurring from initial towpreg manufacture through laminate consolidation.

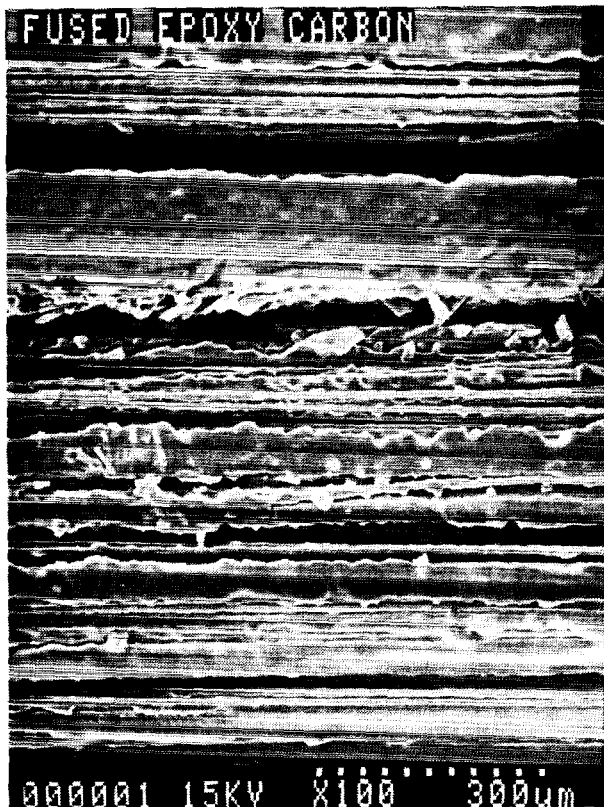


Figure 1. Initial fused epoxy towpreg before weaving.



Figure 2. Towpreg after weaving showing good wet-out.

TOWPREG HANDLING STUDY

A test was developed by Atlantic Research Corporation (ARC) to evaluate the handleability of the fused epoxy towpreg. A test was designed to simulate the rubbing or friction behavior that occurs during the braiding operation. One tow is held stationary under tension loads equivalent to the actual braid conditions while another tow is repeatedly passed over it and back similar to a bow passing over violin strings. Acid digestion of the resin was performed by BASF to determine resin loss. The results are shown in Table II below. Results indicate that no significant resin loss should be anticipated due to braiding. It is thought that the 80 rub abrasion condition is a worst case condition.

Table II. Tow Preg Assessment Matrix Digestion Results

<u>SAMPLE</u>	<u>NO.</u>	<u>RESIN CONTENT</u> (WT.%)	<u>MATRIX LOSS</u> (WT.%)
Virgin Tow Preg (RSS-1952/AS-4)	1	35.9	
	2	35.4	
	3	<u>36.3</u>	
	Avg.	35.9	---
Bobbin Wound Only	1	35.5	
	2	35.1	
	3	<u>36.1</u>	
	Avg.	35.6	0.3
40 Rub Abrasion	1	36.2	
	2	<u>35.2</u>	
	Avg.	35.7	0.2
80 Rub Abrasion (Worst Case Level)	1	34.3	
	2	<u>33.9</u>	
	Avg.	34.1	1.8

INITIAL UNIDIRECTIONAL PROPERTIES

Each candidate material was initially characterized using an unsized Hercules AS-4 (6K) fiber. Fiber bundles were impregnated with a resin content of $35 \pm 2\%$ by weight. The higher resin content was chosen with cloth in mind in which a higher resin content is normally chosen to more easily wetout the more complex fiber architecture. Shown in Table III are the initial unidirectional properties generated.

Table III. Unidirectional Mechanical Properties

	<u>PR-500/AS-4</u>	<u>RSS-1952/AS-4</u>	<u>CET-3/AS-4</u>	<u>High Tg/AS-4</u>
3 Pt. Flexural Strength (Ksi)				
RT - Dry	233	234	206	250
180°F - Dry	248	207	-	-
180°F - Wet*	175	187	-	-
3 Pt. Flexural Modulus (Msi)				
RT - Dry	15.8	15.9	19.1	17.1
180°F - Dry	16.0	16.3	-	-
180°F - Wet	17.1	16.7	-	-
4 Pt. Shear Strength (Ksi) (16:1)	12.8	10.1	-	10.2
90° - 3 Pt. Flexural Strength (Ksi)	-	7	-	-
Fiber Volume %	56.4	52.0	61.9	60.3
Void Content %	<1	<1	<1	<1
Equilibrium Moisture Gain % *	0.65	0.55	-	-

*Underwater @ 160°F

FRACTURE TOUGHNESS

Fracture toughness using double cantilever beam (DCB) and end-notch flexure (ENF) was determined for the PR-500 and RSS-1952 matrix resins combined with AS-4 unsized fiber. After tow impregnation, the unidirectional composites were manufactured by winding over a removeable frame after being placed in a graphite molding tool. Teflon film was inserted at the mid-plane as a crack starter. Piano hinges were bonded on the DCB specimens. The DCB specimens were .5" x 8" x .125" while the ENF were 1" x 8" x .125". The DCB data was reduced using ASTM compliance with the ENF data being reduced by Beam Theory. Both systems fall into the brittle resin family which was not surprising. Shown in Table IV is the generated data. Evaluation of the other two resins is ongoing.

Table IV. Fracture Toughness of Unidirectional Composites

	<u>PR-500/G30-500</u>	<u>RSS-1952/AS-4</u>
Mode I (DCB)		
Avg G_{1C} (in lbs/in ²)	1.19	1.16
Std. Dev.	0.12	0.34
	(12 data points)	(48 data points)
Mode II (ENF)		
Avg G_{2C} (in lbs/in ²)	5.64	3.53
Std. Dev.	1.05	0.36
	(23 data points)	(16 data points)

THERMAL ANALYSIS

Composite samples fabricated from PR-500/AS-4 and RSS-1952/AS-4 were analyzed to determine a dry and wet glass transition (T_g) temperature. Analytical techniques consisting of Differential Scanning Calometry (DSC), Thermal Mechanical Analysis (TMA), and Dynamic Mechanical Analysis (DMA) were compared. Wet glass transition was established using the DMA with a heating rate of 50°C/minute in both the dry and wet condition. The temperature was selected to simulate the time/temperature profile of a specimen being tested hot/wet in a flexural or shear test. Shown in Table V are the results. The change in T_g after moisture aging was 16°C and 20.6°C for the PR-500 and RSS-1952 respectively.

Table V. Thermal Analysis DMA

Heat Rate °C/Min	<u>PR-500/AS-4</u> T _g °C (G' Onset)/Tan Δ Peak	<u>RSS-1952/AS-4</u> T _g °C (G' Onset)/Tan Δ Peak
2 (dry)	195/219	207/226
10 (dry)	211/228	221/233
50 (dry)	231/247	241/250
50 (wet)	215/230	220/230

(3 specimens/data point)

		<u>PR-500/AS-4</u> (T _g)°C	<u>RSS-1952/AS-4</u> (T _g)°C
DSC	2 (dry)	192	207
DSC	10 (dry)	197	211
TMA	2 (dry)	174	163
TMA	10 (dry)	-	173

2D WEAVING

Initial weaving studies were conducted using Hercules AS-4 (6K) unsized fiber. This choice was based on a compromise between fiber coverage and cost as well as the decision to use a 6K fiber in some of the 3D weaving and braiding. A rule of mixture analysis indicates a similar property translation as compared to a 3K fiber selection. In the 6K selection, a 10 x 10 construction is used versus a 20 x 20 or 24 x 24 picks per inch. Hot/wet properties seem to be lower than expected with a percent of RT-dry being 49% and 69% for the PR-500 and RSS-1952 respectively. Percent translation with the unidirectional composite was 75% and 80% respectively. The difference may be explained in terms of edge effect where twice as many edges are exposed to moisture and the moisture profile and diffusion rates vary versus the unidirectional condition. Further study will be conducted on this issue.

Shown in Table VI are 8-harness satin cloth properties generated to date.

Table VI. Mechanical Properties 8-Harness Satin Cloth

	<u>PR-500/AS-4</u>	<u>RSS-1952/AS-4</u>
3 Pt. Flexural Strength/Modulus		
RT - Dry (Ksi/Msi)	107/7.3	99/7.5
180°F - Dry	103/7.3	90/7.5
180°F - Wet	53/6.7	68/7.4
325°D - Dry	71/7.2	-
325°F - Wet	36/6.3	-
4 Pt. Shear Strength (16:1)		
RT - Dry (Ksi)	6.0	5.6
180°F - Dry (Ksi)	3.0	-
Fiber Volume %	56	52
Void Content %	<1	<1

TENSILE & COMPRESSION MECHANICAL PROPERTIES 8-HARNESS SATIN CLOTH

Tensile and compression properties were generated for 8-harness satin cloth using 6K towpreg. A quasi-isotropic layup consisting of 20 plies with a shorthand nomenclature of $[45, 0]_5$ was used. This resulted in a panel thickness of approximately 0.25". Panels C-scanned clear and were cut according to NASA specifications (1" x 9" x 1/4" Tensile, 1.5" x 1.75" x 1/4" Compression). Five specimens were tested per data point. Data is shown in Figure 3. Tensile specimens were tested without tabs in hydraulic grips. The effect of the 6K crimp needs to be considered when examining this data. The 180°F wet property is surprisingly low as compared to unidirectional properties.

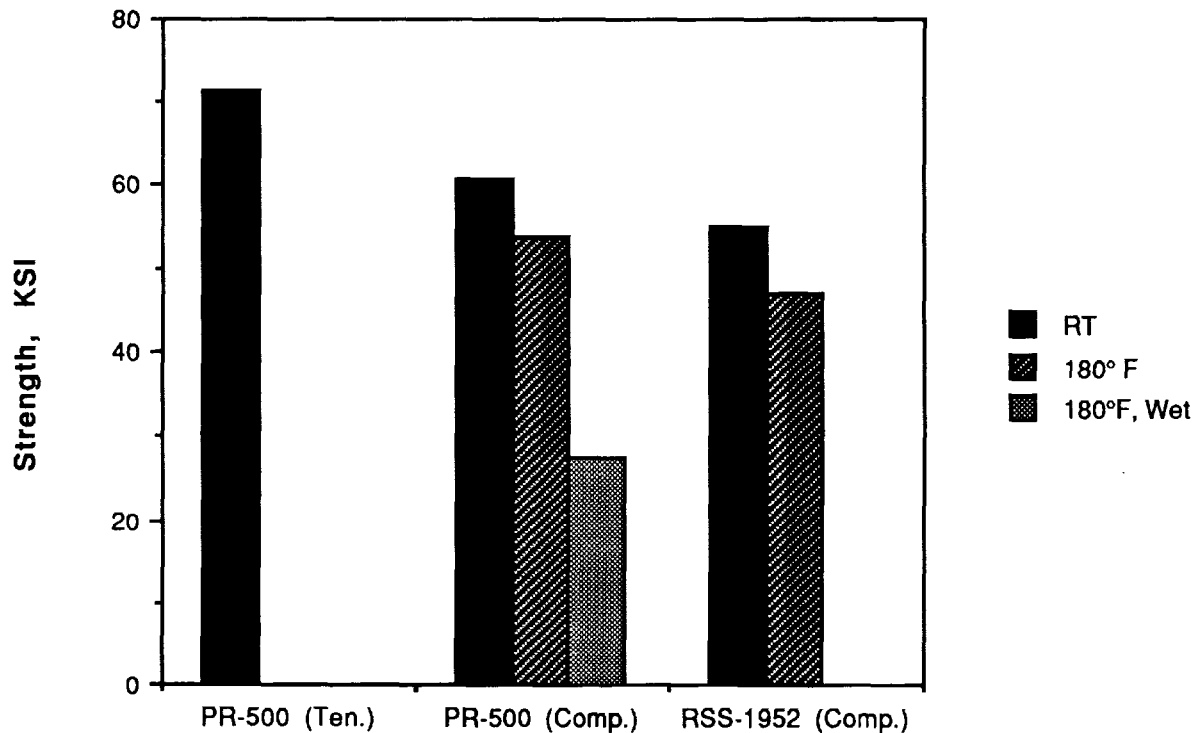


Figure 3. Tensile and short block compression properties on 8-harness satin cloth quasi-isotropic lay-up.

ADVANCED TEXTILE PREFORM EVALUATIONS

A study was initiated for evaluating the use of powder epoxy towpreg in more advanced and rigorous textile processes such as braiding and 3-D weaving. The following areas were seen as key issues for each preforming method:

- Tow Handling Characteristics
- Powder Loss Potential
- Preform Consolidation Process Development

3-D woven preforms produced by Textile Technologies, Inc. and braided preforms produced by Fiber Innovations were used for this initial evaluation work.

3-D WOVEN PREFORM CONSTRUCTION

A three inch width multilayer 3-D construction was chosen for preliminary feasibility evaluations. The particular architecture chosen utilized both 3K and 6K powder epoxy towpreg with a nominal 39% (by weight) resin content. Shell RSS-1952 powder epoxy was the resin used. Preform construction was as follows: (See Figure 4).

- 6K tow for both warp and fill, with a 14 x 14 tows/inch construction
- 3K tow for "Z" direction fiber, 7 tows/inch construction
- Nominal (cured) thickness calculated at .040"

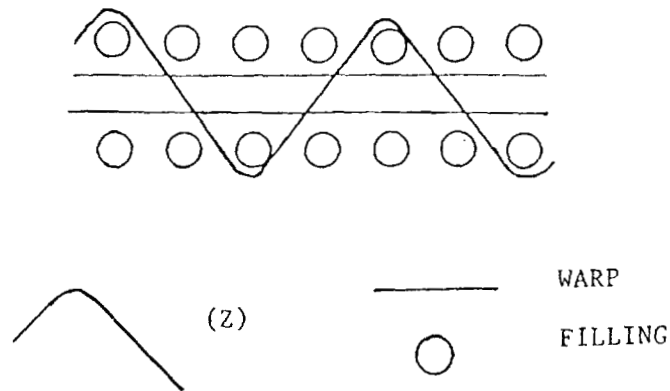


Figure 4. Multilayer 3-D preform fiber architecture.

BRAIDED PREFORM CONSTRUCTION

Powder epoxy tow was evaluated in both biaxial and triaxial braid constructions to determine suitability for use in a braiding process. The tow was braided on a 1" diameter mandrel, with the resulting braided sleeving slit open and laid flat for consolidation. Initial preform specifics were as follows:

- 24 carrier machine, 1" diameter mandrel
- 24 ends at +/- 68° used for biaxial sleeving
- 24 ends at +/- 68° plus 12 ends at 0° used for triaxial sleeving
- 6K towpreg, 39% (weight) resin content used for both constructions

Shown below in Figure 5 is a picture of a braided epoxy preform prior to cure.



Figure 5. Braided powder epoxy preform prior to cure.

PREFORMING RESULTS

Handling characteristics of the powder epoxy tow were evaluated through the use of the braiding and 3-D weaving processes. Issues such as powder loss and fiber damage as a result of “working” of the towpreg in the process as well as basic feasibility concerns were addressed.

- 3-D multilayer fabric and biaxial/triaxial braids were successfully produced
- Minimal fiber damage and powder loss (< 1%) noted
- High friction noted in braiding process due to powder fused to filament surfaces
- Bulk factor of unconsolidated preforms can be as much as 2.5 x cured thickness

CONSOLIDATION PROCESS DEVELOPMENT (3-D FABRIC)

A cure cycle developed in previous work for manufacture of void-free 8-harness powder epoxy laminates was used for initial 3-D multilayer preform cure evaluations. Resulting 3-D laminates had unacceptable void content. A major difference in cured laminate quality as a result of the more complex fiber architecture was shown.

- Standard 8-harness cure cycle unsuccessful with 3-D material
- Voids consistently located at intersection of “Z” direction tows and fill-direction tows
- Buckling of “Z” direction tows noted due to initial bulk factor and resulting compaction during cycle

Shown below in Figure 6 is a cross-section of a 3-D multilayer preform cured with a “standard” powder epoxy cure cycle.

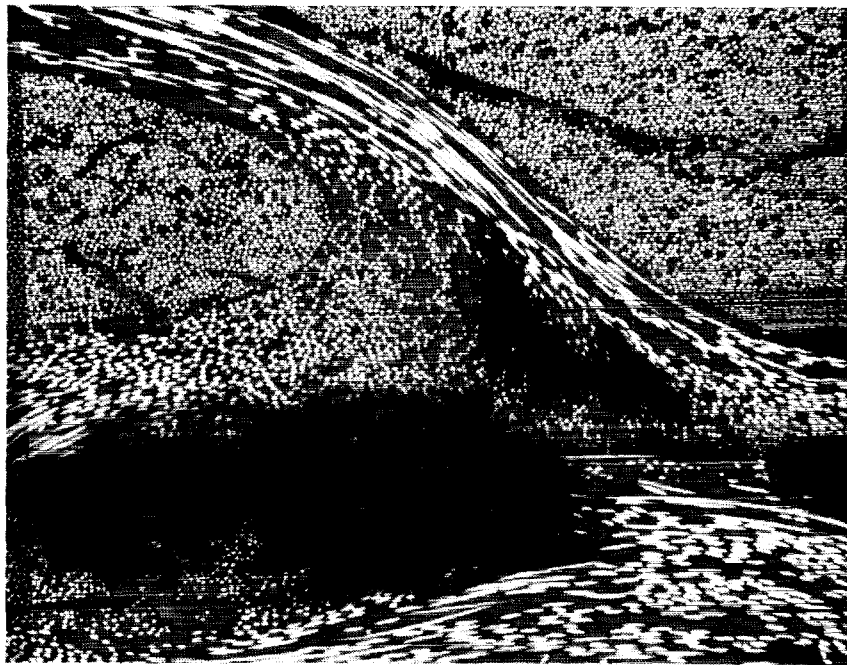


Figure 6. Initial 3-D multilayer preform cross section showing voids at “Z” fiber and fill fiber intersections.

CONSOLIDATION PROCESS DEVELOPMENT (CONTINUED)

Several processing trials were run to develop parameters for producing void-free 3-D laminates. Higher pressure and the addition of narrow (1") 120-style fiberglass cloth strips on two sides of a laminate to act as a breather/bleeder for removal of air from the preform were found to be necessary for good autoclave consolidation. Although the optimized process produced void-free panels in an autoclave, panels cured in a platen press under identical processing conditions (with the exception of vacuum) still had poor surface wet-out and areas of large voids. Apparently evacuation of air from the preform prior to resin flow is necessary for void-free consolidation with this particular fiber architecture, although this was unnecessary with 8-harness fabric. Work to understand the processing/preform architecture relationship continues.

- Autoclave processing/bagging procedures optimized for high quality 3-D laminates preform consolidation (pressure increased to 150 psi, breather strips added)
- Successful process not achieved to date in platen press
- Apparent requirement for evacuation of air from preform prior to resin flow for this architecture

Shown in Figure 7 is a 3-D panel cross-section using an optimized autoclave cycle.

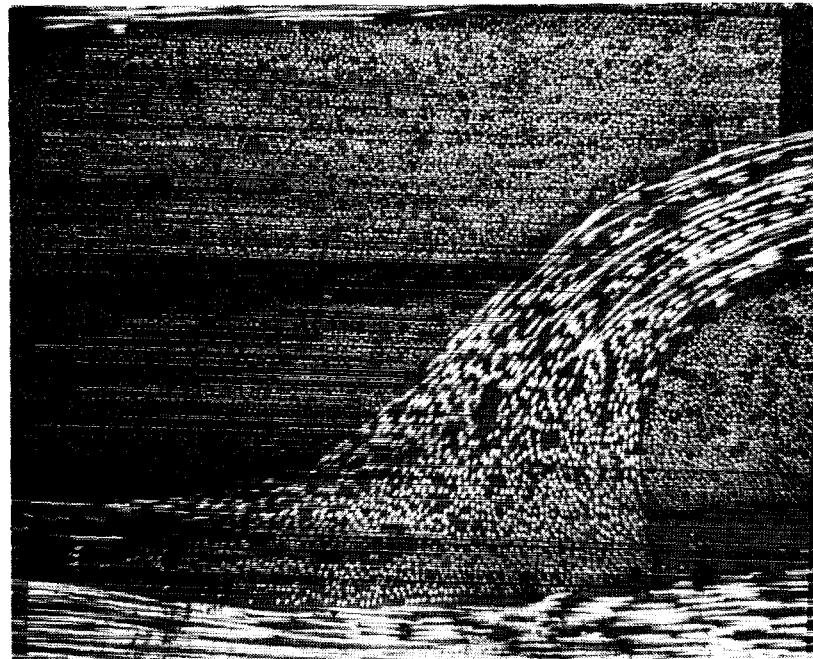


Figure 7. Cross-section 3-D woven panel cured using optimized autoclave process.

MANUFACTURING PROCESS DEVELOPMENT

Development and evaluation of part-manufacturing methods using the powder epoxy towpreg materials are underway. Due to the high bulk factor inherent in this material form, debulking methods were initially addressed. Through a series of analytical and empirical experiments, a vacuum debulking process has been established for the three materials currently under evaluation (PR-500, RSS-1952, CET-3). Vacuum debulking has been performed primarily by means of a silicone rubber diaphragm bonded to a picture frame, with the diaphragm allowed to elongate and deform around a male debulking mold after heating to the required temperature range. Work to date suggests multiple debulking cycles may be performed before the resin advances to a point that flow is inhibited during final cure.

- Debulk at 200°F under vacuum
- Multiple debulk cycles

Shown in Figure 8 is an integrally stiffened preform after vacuum debulking, prior to cure.

ORIGINAL PAGE
BLACK AND WHITE PHOTOGRAPH

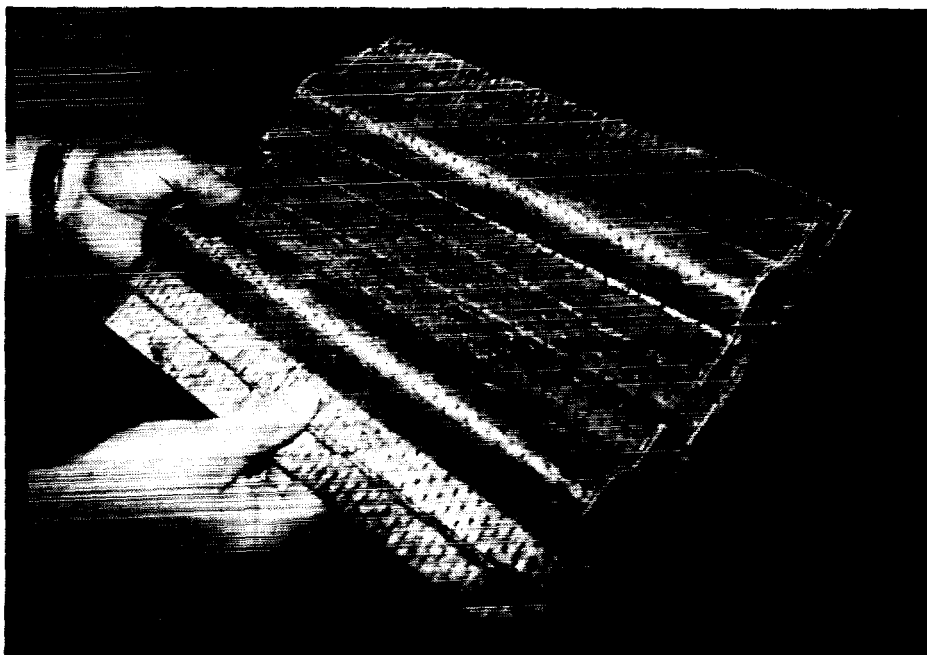


Figure 8. Vacuum debulked preform prior to cure.

DEMONSTRATION PARTS

Press and autoclave part fabrication evaluations are also underway using established processing techniques as well as relatively new approaches including diaphragm forming and stamping. Shown below in Figure 9 are typical epoxy powder parts produced using textile approaches.

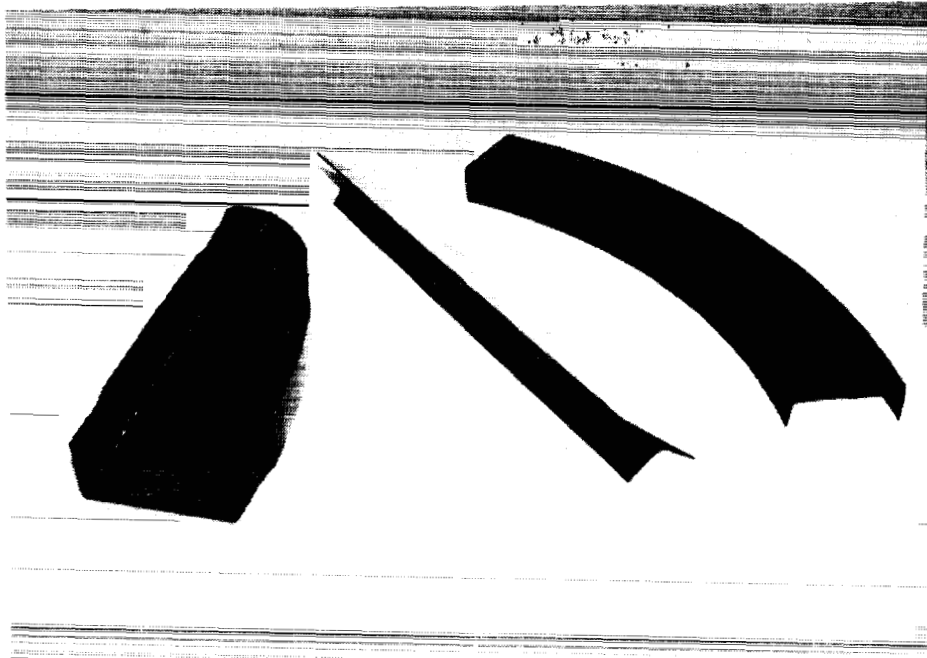


Figure 9. Typical parts fabricated using powder epoxy materials.

ORIGINAL PAGE
BLACK AND WHITE PHOTOGRAPH

STATUS

- A viable process has been developed to manufacture a towpreg suitable for textile composites.
- Ongoing evaluation of initial candidate epoxy powders for composites.
- Ongoing effort to demonstrate manufacturing technology using woven, braided, and stitched powder preforms.
- Initial work started to develop a suitable product for advanced tow placement and filament winding.

FUTURE PLANS

- Ongoing project to increase towpreg production 3x over present process.

The Effects of Specimen Width on
Tensile Properties of
Triaxially Braided Textile Composites

John E. Masters
Lockheed Engineering and Science

Peter G. Ifju
Virginia Polytechnic Institute and State University

Christopher M. Pastore
and
Alexander E. Bogdanovich
North Carolina State University

52-24

51402

OUTLINE

- INTRODUCTION -
 - DEFINITION OF MATERIAL
 - STATEMENT OF PROBLEM

- EXPERIMENTAL RESULTS -
 - MOIRE INTERFEROMETRY
 - STRENGTH & MODULUS

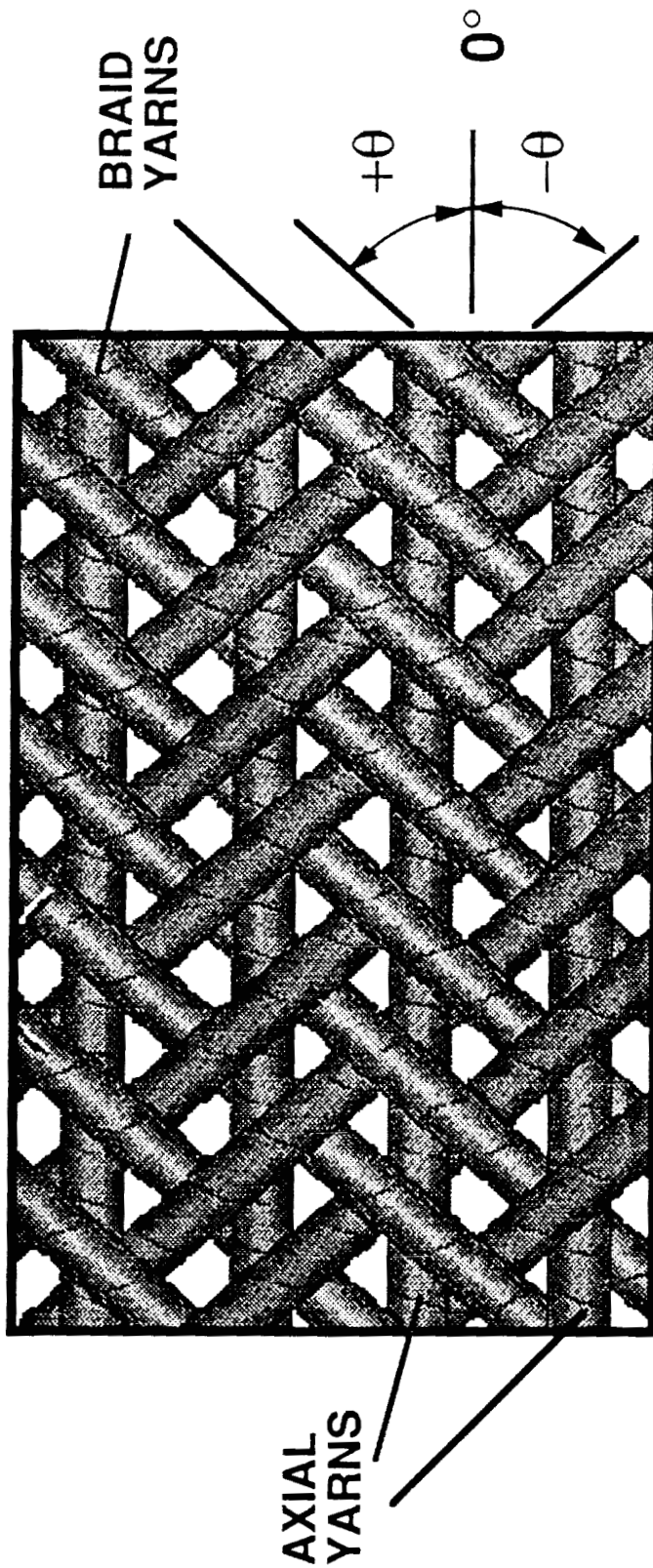
- SUMMARY

- FUTURE WORK

The objective of this study was to examine the effect of the unit cell architecture on the mechanical response of textile reinforced composite materials. Specifically, the study investigated the effect of unit cell size on the tensile properties of 2-D triaxially braided graphite epoxy laminates.

The figures contained in this paper reflect the presentation given at the conference. They may be divided into four sections as the outline listed above illustrates. A short definition of the material system tested is contained in the next figure. This is followed by a statement of the problem and a review of the experimental results. The experimental results consist of a Moire interferometry study of the strain distribution in the material plus modulus and strength measurements. Finally, a short summary and a description of future work will close the paper.

TRIAXIAL BRAID PATTERN



The specimens studied in this investigation featured 2-D triaxially braided AS4 graphite fiber preform impregnated with Shell 1895 epoxy resin. In a triaxially braided preform, three yarns are intertwined to form a single layer of $0/\pm\theta$ material. In this case, the braided yarns are intertwined in a 2X2 pattern. Each $+\theta$ yarn crosses alternatively over and under two $-\theta$ yarns and vice versa. The 0° yarns were inserted between the braided yarns. This yields a two dimensional material; there are no through-the-thickness fibers.

The yarns were braided over a cylindrical mandrel to a nominal thickness of .125 in. The desired preform thickness was achieved by overbraiding layers. After braiding, the preforms were removed from the mandrel, slit along the 0° fiber direction, flattened and border stitched to minimize fiber shifting. The resin was introduced via a resin transfer molding process.

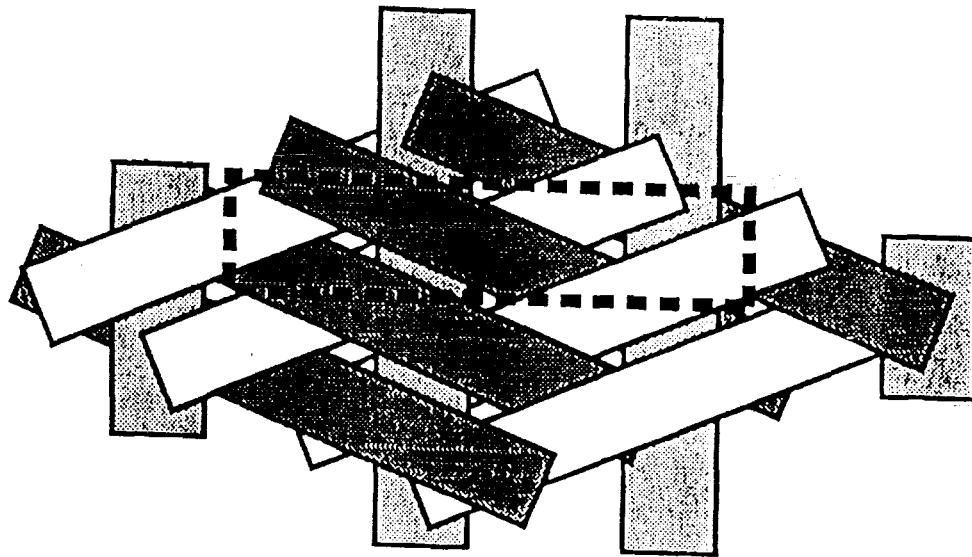
TRIAxIAL BRAID CONFIGURATIONS

MATERIAL	BRAID PATTERN	BRAIDER YARN SIZE (K)	0° YARN SIZE (K)	PERCENT 0° YARNS (%)	0° YARN SPACING (YARN/IN.)	BRAID YARN SPACING (YARN/IN.)
A1	0/± 63°	12K	24K	31.5	4.17	9.16
B1	0/±66.5°	6K	18K	37.6	4.77	11.98
B2	0/±70°	6K	18K	34.0	4.37	12.74

Three preform parameters, braid angle, yarn size, and 0° yarn content, were varied in this study. The last parameter listed is typically expressed as a percentage of 0° yarns. It is the volumetric proportion of longitudinal yarns to total yarn content and is a function of braid angle and yarn size. Yarn size is expressed in terms of the number of filaments per yarn. The AS4 yarns used in these materials have a nominal diameter of 7 microns. The longitudinal yarns were larger than the braided yarns in all cases. The B1 and B2 architectures had the same yarn sizes; they differed in braid angle and 0° yarn content. The preform parameters are listed in the table.

The fabrics were formed with a 144 carrier New England Butt triaxial braider, incorporating 72 longitudinal yarns. The mandrel diameters varied for each architecture. Since the number of carriers was constant, this had the effect of changing the yarn spacing. These parameters are also listed in the table.

The increased 0° yarn content, increased 0° yarn spacing, and decreased braid angle of the B1 architecture compared to the B2 architecture are of note. These factors, cumulatively, may aid in interpreting the experimental results.



SMALLEST UNIT CELL

UNIT CELL DIMENSIONS

MATERIAL	WIDTH (in.)	HEIGHT (in.)
A 1	0.48	0.12
B 1	0.42	0.09
B 2	0.46	0.08

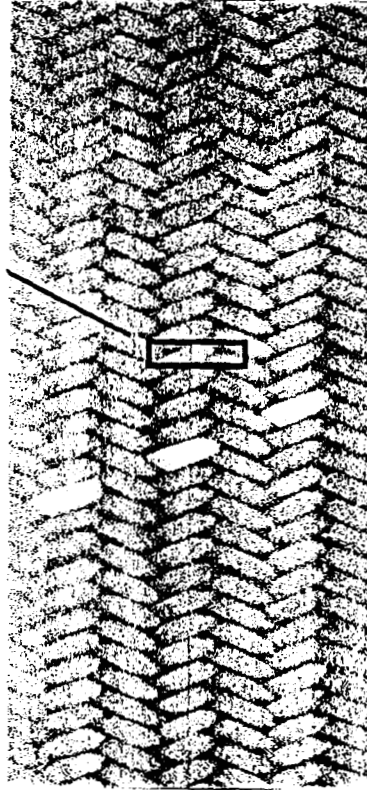
A convenient way to describe textile preforms is to identify a unit cell of material - a repeatable unit of fabric geometry. The unit cell represents the complete yarn intertwinement pattern. The unit cell approach has become the foundation of textile analysis and serves as a convenient framework in which to interpret experimental data.

The rhombic frame shown in the figure defines a unit cell for the 2-D triaxially braided material studied in this program. For computational purposes, it is desirable to define the smallest unit cell possible. In some analyses, rectangular unit cells are also required. The rectangular section shown in the figure represents the smallest unit cell identified.

The table shown above contains the dimensions of the unit cells for the three architectures tested. The unit cell width is dependent on the mandrel diameter and the number of yarns braided. The height of the unit cell is dependent on cell width and the braid angle.

Although three architectures are being investigated by NASA and Boeing, this study featured specimens made from the B2 architecture only.

MATERIAL ARCHITECTURE AND TEST COUPON GEOMETRY



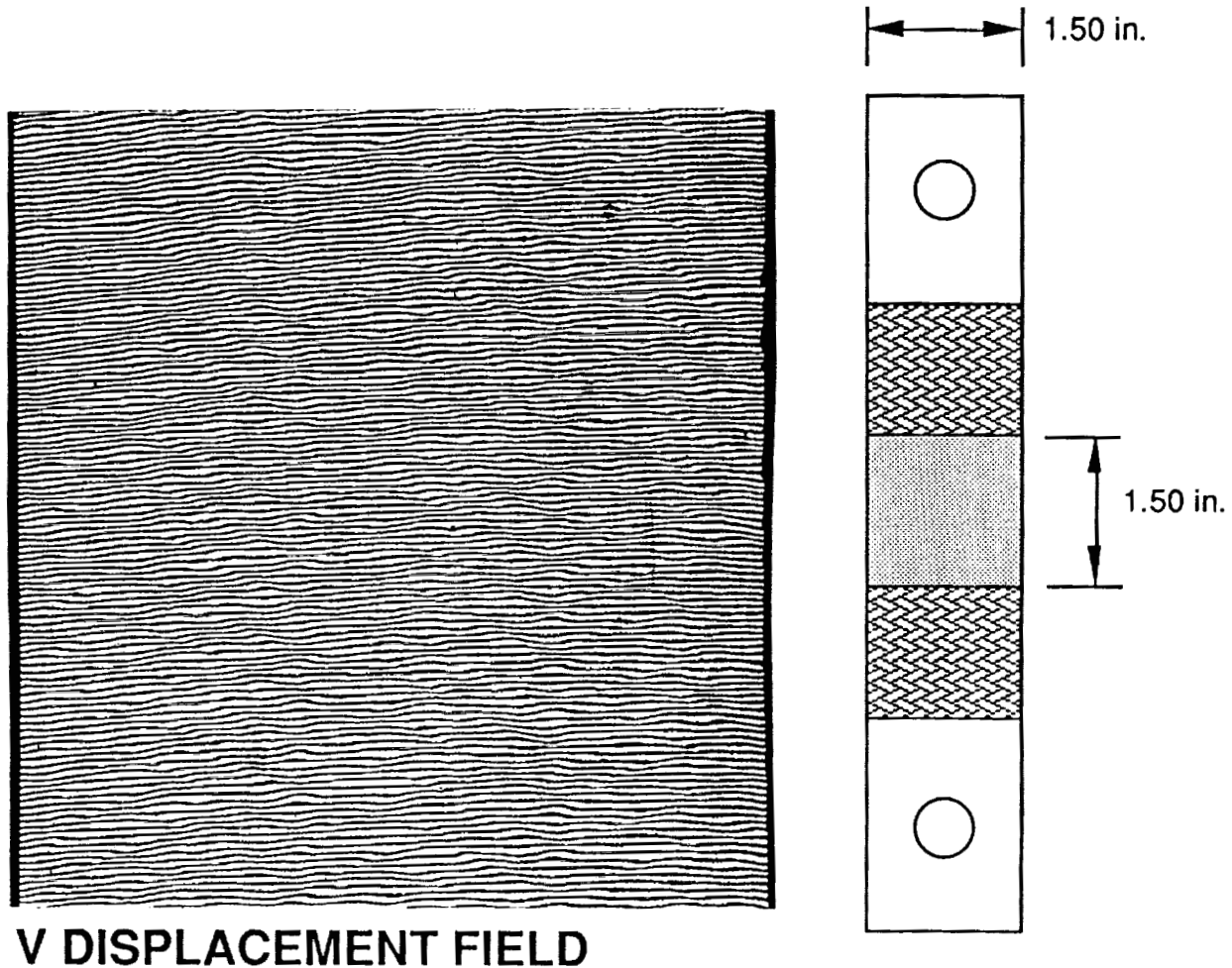
Having defined the unit cell, the question then becomes one of defining degree of heterogeneity within the unit cell. Moire interferometry provided insight into the magnitude of the strain variation in these braided materials. The next three figures summarize the results of the Moire investigation. These slides were also reported in a previous study presented at the conference (Experimental and Analytical Characterization of Triaxially Braided Textile Composites by Masters et. al.).

The strain field inhomogeneity will define the specimen design and the instrumentation used. Determining the effect of this inhomogeneity on experimental results was the subject of this paper.

As an example, consider the tensile coupons used to measure the strength and modulus. The specimen, which is shown in the figure, is 9.5 in. long and 1.5 in. wide. The rectangular section shown in the figure represents the unit cell of the B2 material. As the figure illustrates, the specimen is three unit cells wide. The specific objective of the study was to determine if the specimen width affected the tensile property measurements.

MOIRE INTERFEROMETRY

2-D Triaxial Braid - 1200 Microstrain

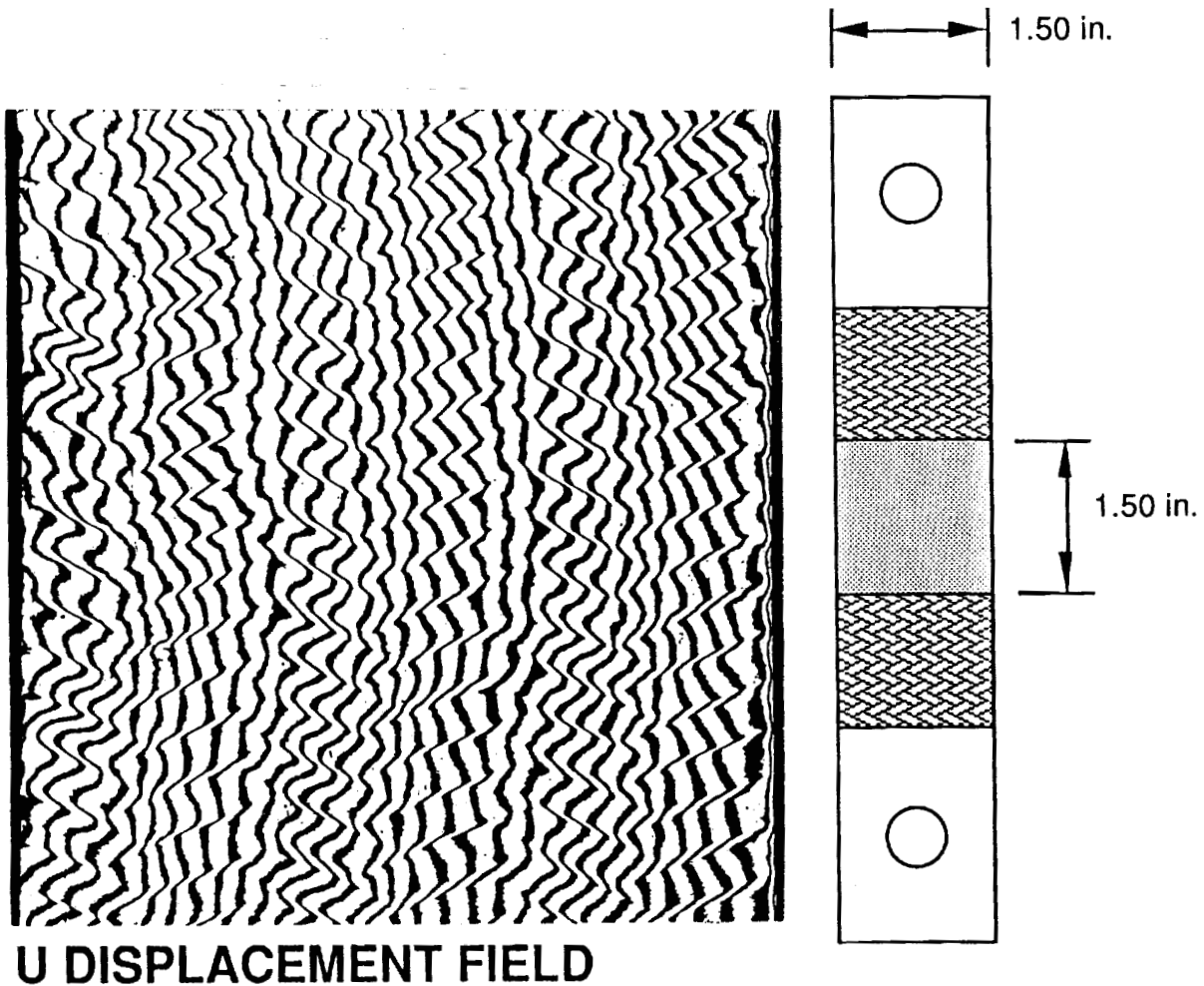


As indicated earlier, Moire interferometry was used to define the full field strain distribution in these braided specimens. The technique defines deformation patterns in both the vertical and horizontal directions. These results are shown in this and the following figure.

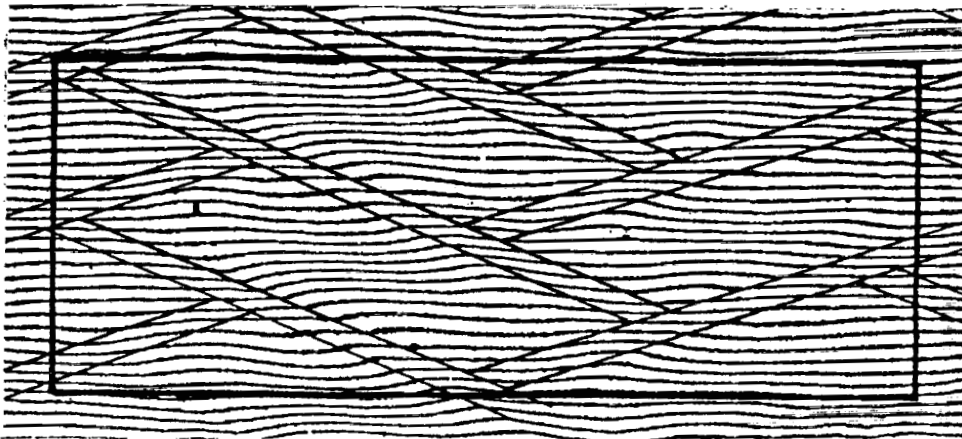
The vertical displacement fields (V fields) consist of basically horizontal fringes; this indicates specimen extension where points along one fringe have been displaced vertically with respect to points along a neighboring fringe. For a uniform extension the fringes should be evenly spaced and straight. The fringes for the specimens tested, however, are wavy and the spacing between them varies. The variation is cyclic and coincides with the repeated unit of the textile architecture.

MOIRE INTERFEROMETRY

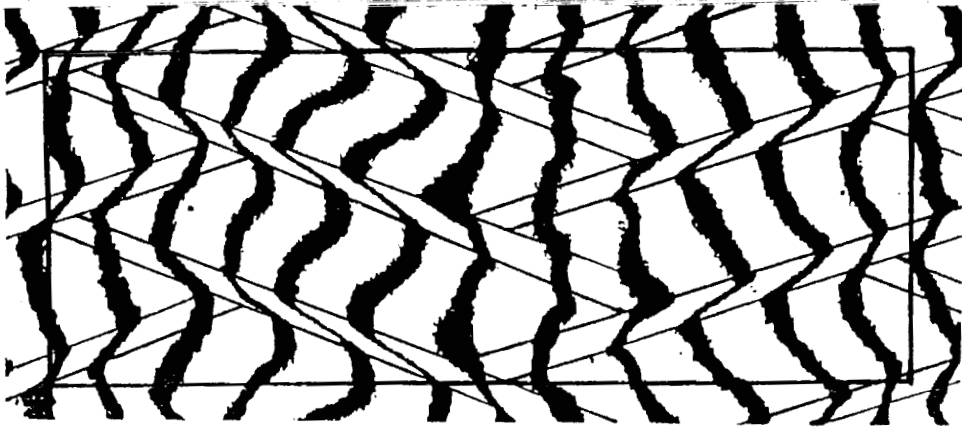
2-D Triaxial Braid - 2400 Microstrain



The horizontal displacement patterns (U fields) consist of zigzag vertical fringes that display the Poisson effect. For uniform contraction the fringes should be straight and the spacing constant. The fringes however display a variation which is cyclic, and matches that of the weave geometry. The sharp kinks in the U field fringes reveal the presence of shear strains between the fiber bundles.



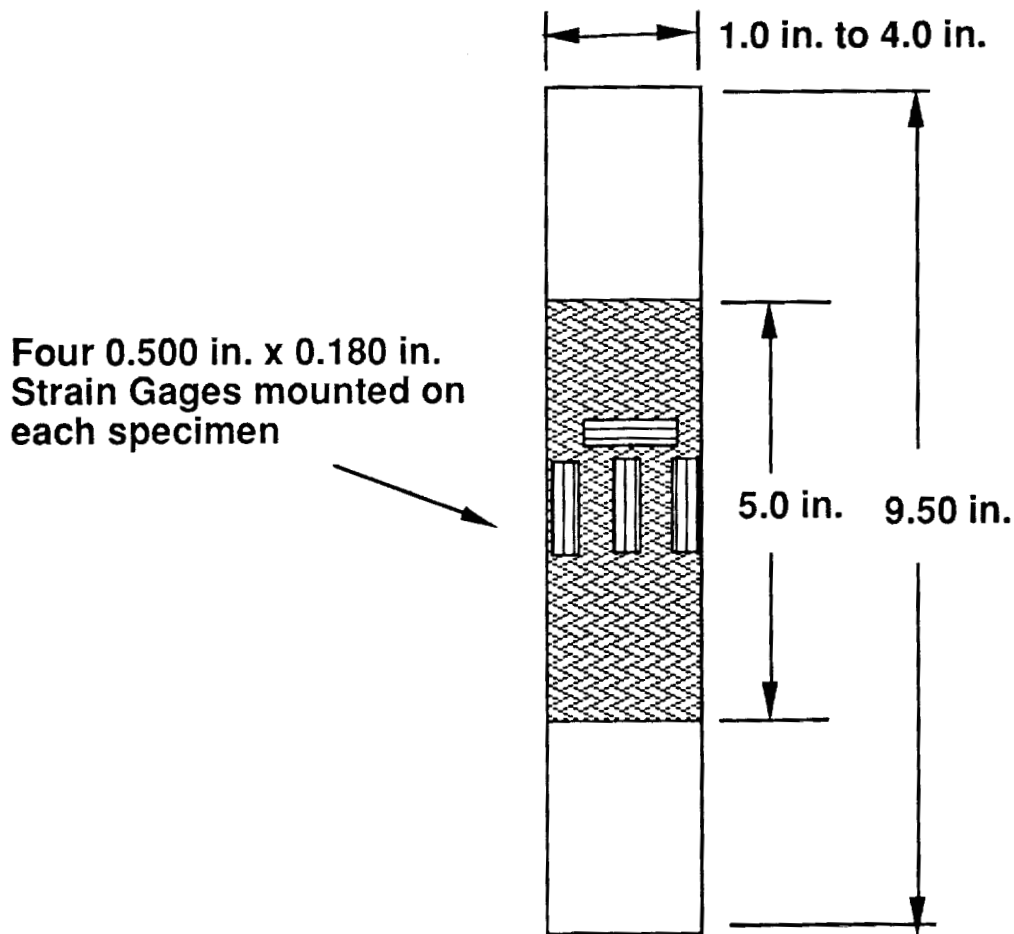
ENLARGED VIEW OF TWO UNIT CELLS - V FIELD



ENLARGED VIEW OF TWO UNIT CELLS - U FIELD

The figure shows the V and U fields of a highly magnified region of specimen that consists of two unit cells. The boundaries between adjacent fiber bundles and the outline of the cells are marked. It was revealed that the shear deformation at interfaces between the fiber bundles occurred over a finite width. This width is illustrated in the patterns as the distance between the closely spaced lines. This is consistent with the presence of the resin rich areas between the fiber bundles, which was on the order of one fifth of the width of the fiber bundle itself. The U field shows that the shear strain γ_{xy} in the resin rich zones was on the order of 0.5 times that of the average applied normal strain ϵ_y . Additionally, the U field shows that the Poisson effect was nearly constant across the unit cell. The V displacement pattern clearly shows that the strain ϵ_y varies significantly within each unit cell as can be seen by the nonuniform fringe spacing. The ratio of maximum strain ϵ_y to minimum strain was about 2.1. The normal strain varies on top of the fiber bundles and is nearly constant throughout all of the resin rich zones.

Test Specimen Configuration



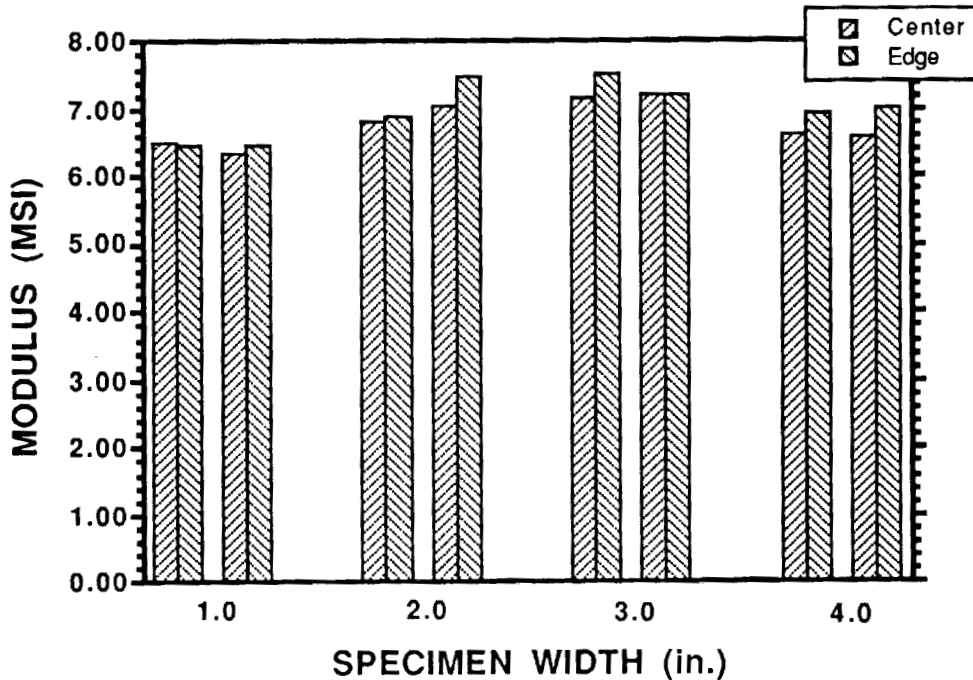
A series of tensile tests were conducted to experimentally determine the effect of specimen width of modulus and strength. The coupons used in this study are shown in the figure. Specimen width was fixed at 9.5 in. Length, however, varied from 1.0 in. to 4.0 in. in one inch increments. All specimens featured the B2 triaxial braid described in the previous table. They were loaded in the 0°, or longitudinal direction.

Each specimen was instrumented with five 0.500 in. long strain gages as shown in the figure. The strain gages effectively spanned five unit cells in this direction.

WIDTH EFFECTS ON TENSILE PROPERTY MEASUREMENT (Strength and Modulus)

SPECIMEN NUMBER	WIDTH (In.)	THICK. (In.)	FIBER		MODULI (MSI)	Left		Center		Right	
			WIDTH (In.)	VOLUME (%)		MAX STRESS (KSI)	Center	Center	Center	Center	Center
B2-13-1	1.01	.125		55.2	58.3	6.87	6.50	6.97	6.06		
B2-13-2	1.01	.124		55.2	66.0	6.39	6.34	6.77	6.58		
B2-13-4	2.01	.121		54.4	63.1	6.48	6.73	6.78	7.15		
B2-13-6	2.00	.141		46.1	54.8	5.87	5.90	5.94	6.62		
B2-13-7	3.01	.140		46.1	55.7	6.26	5.99	6.24	6.33		
B2-13-8	3.01	.141		46.1	53.9	6.14	6.02	5.98	5.92		
B2-13-10	4.01	.124		55.2	61.3	6.98	6.65	6.60	6.91		
B2-13-12	4.01	.141		46.1	54.0	5.90	5.53	5.89	5.73		

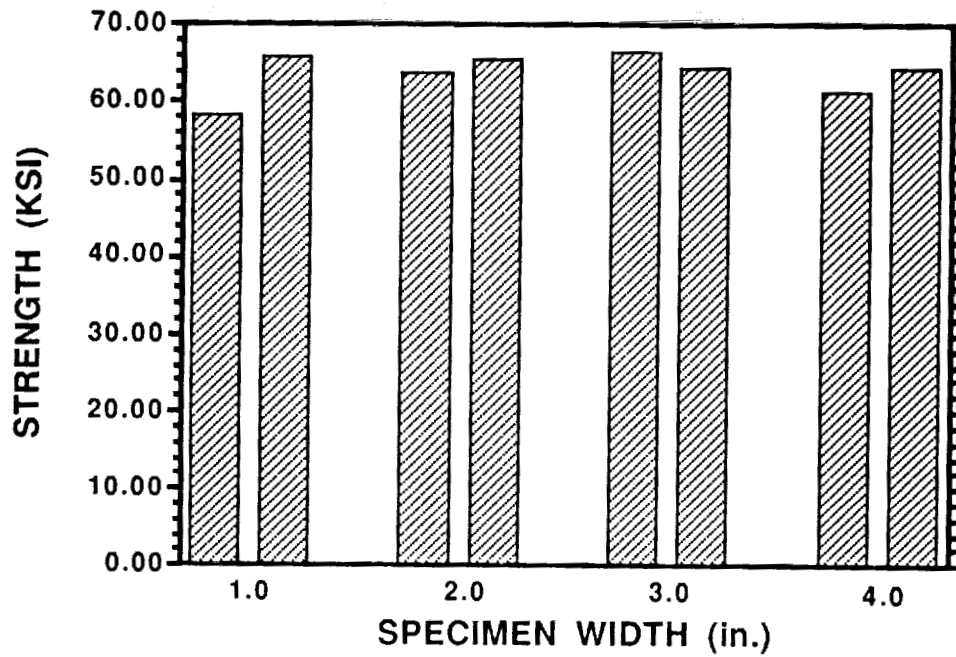
EFFECT OF SPECIMEN WIDTH OF MODULUS (Normalized to 55% Fiber Volume)



The results of the longitudinal modulus measurements are shown in the figure. A total of eight specimens, two at each width, were tested. The moduli measured at the specimen edges were averaged and are compared to the average moduli measured at the center of the specimen. Specimens were machined from several different panels whose fiber volume content varied. The data, which was shown in tabular form in the previous slide, was normalized to 55% fiber volume to isolate width effects.

The data indicate little edge to center variation in modulus. They also demonstrate no significant variation with specimen width.

**EFFECT OF SPECIMEN WIDTH OF STRENGTH
(Normalized to 55% Fiber Volume)**



The tensile strength results are shown in this figure. Like the moduli data, they too have been normalized to 55% fiber volume to isolate the effect of specimen width. The results, again, reflect no effect of width on mechanical response.

SUMMARY

- **EXPERIMENTAL RESULTS INDICATE NO WIDTH EFFECT ON TENSILE PROPERTIES**
- FOR THIS ARCHITECTURE**
- **MOIRE INTERFEROMETRY IDENTIFIED LARGE STRAIN GRADIENT WITHIN THE UNIT CELL**

The results of this short experimental investigation demonstrate that the specimen width did not affect the tensile response of the the 2-D triaxial braids tested. It must be noted, however, that these results are relevant to these architectures only. These results cannot be extended to other textile preform types. We are developing the analytical and experimental data base required to make these assessments.

The Moire interferometry results succeeded in identifying the nature of the inhomogeneity in the strain field. The technique will be applied to additional textile architectures to guide our instrumentation and analysis.

FUTURE WORK

- **INVESTIGATE SIZE EFFECTS IN OTHER TEXTILE COMPOSITES**

- **DEVELOP ANALYSES TO PREDICT MATERIAL RESPONSE**

NASA is in the process of initiating an analytical and experimental program to develop standard test methods for textile composites. This program will develop tension, open-hole tension, compression, open-hole compression, and shear test methods for woven, braided, and stitched textiles. The results of this investigation will be applied to that program.

Specifically, this study has identified the magnitude of the strain inhomogeneities within the unit cell and has demonstrated the effectiveness of Moire interferometry in defining the full field strain distribution in these textile composites. Interferometry will be applied to all material forms investigated in the test methods development program to guide specimen design and instrumentation. One objective of the program is to develop sets of criteria to be applied to all textiles.

This study also identified that width effects did not exist for these particular architectures. An experimental data base will be developed to determine if this is true for other architectures.

IN SITU PROCESSING METHODS FOR COMPOSITE FUSELAGE SANDWICH STRUCTURES

Hossein Saatchi
Bill Durako
Dick Reynolds
Sundstrand Aerospace
Rockford, IL

Ernest Dost
Kurtis Willden
The Boeing Company
Seattle, WA

53-24
51403

ABSTRACT

Conventional sandwich structure fabrication methods are labor intensive and high in cost. A low cost method is needed to produce lightweight sandwich structures. Sundstrand has developed a series of in-situ composite fabrication methods in which the raw materials (skin and core materials) are placed in a closed mold, and the component is produced in one heating cycle. Internal pressure is generated by chemical agents during the thermal cycles, which consolidates the skins and produces the foam core. The finished part is a net-shape composite sandwich structure with skins and a foamed core. The in-situ process reduces cost by eliminating several secondary operations that are used in conventional fabrication methods. Further, a strong molecular bond is produced between the core and skin, which eliminates adhesive bonding and prevents a weak bond section in the sandwich structure.

In this investigation, we evaluated the feasibility of the in-situ process using thermoset materials currently under consideration for commercial airplane fuselage applications, such as keel sections.

The materials used were Hercules 8553-40 toughened epoxy resin in both liquid and powder forms, and 3M Scotchply PR500 resin, manufactured by 3M Corporation, in powder form. We successfully foamed these resins and produced experimental panels with AS-4/8553-40 Hercules prepreg skins. Chopped fibers were added to the core to increase performance of the foam. Mechanical property testing on these panels showed properties competitive with other foams. Additional experiments are required to optimize the in-situ foam core sandwiches for specific properties and applications.

INTRODUCTION

The use of sandwich construction for a composite fuselage structure has the potential for cost and weight savings. Sandwich construction increases the plate-bending stiffness for a given axial stiffness by dividing the load-carrying material into two parts separated with a relatively low-density core. The additional bending stiffness increases the compressive load the structure will bear before buckling, reducing or eliminating the need for stiffening elements.

The basic cost and weight efficiencies of sandwich structural concepts are generally lost when considering design details associated with aircraft structural components. Design details associated with the NASA/Boeing Advanced Technology Composite Aircraft Structures (ATCAS) keel design include tapering the core to accommodate changes in facesheet thickness, while keeping constant sandwich thickness and core ramping at the panel edges to allow for attachment to the adjacent fuselage quadrants [1].

The manufacturing steps for fabrication of the NASA/Boeing ATCAS keel structure using traditional methods include:

1. Layup the outer facesheet.
2. Apply a layer of adhesive.
3. Machine the various core sections to thickness.
4. Piece the core sections together on this facesheet.
5. Finish machine all core splice locations to eliminate steps created by thickness machining tolerances.
6. Apply another layer of adhesive.
7. Apply the appropriate core section splice material.
8. Layup the outer facesheet.
9. Bag.
10. Autoclave cure.
11. Debag and do final trim.

Sundstrand has developed a family of proprietary polymer composite fabrication techniques in which a single thermal cycle is used to create the core and cure the facesheets to form sandwich structure [2-21]. These in-situ fabrication methods offer a significant cost reduction potential over conventional polymer processing by eliminating steps 2 through 7 above. In-situ composite processing also creates a molecular bond between the core and the skins, creating a strong interface, which may be a weak link in typical sandwich structures. The molecular bond coupled with the closed cell foam structure leads to improved strength, ballistic resistance, and environmental performance.

To date four in-situ processes have been developed as follows:

1. Foam Expansion Fabrication (FEF)
2. Powder Compaction Vacuum Bagging (PCVB)
3. Isostatic Pressure Processing (IPP)
4. Isoclave Processing

Each of these processes has different practical aspects, but all have the same basic processing concept: the thermal decomposition of a chemical agent creates pressure to consolidate the skins and produce gas, which creates a foam core.

In these in-situ processes, the skins and core materials are placed in a closed, matched-metal mold. The core materials consist of a resin (typically in powder form), a chemical foaming agent and fillers. The fillers are usually small-aspect ratio fibers, which improve the strength of the core and provide a better coefficient of thermal expansion match with the skins. The skin materials can be prepreg, commingle/cowoven fabrics, or a dry braided preform. The filled mold is taken through a controlled thermal cycle during which the foaming agent decomposes, consolidating the skins and producing the foam core. The result is a net-shape, foam-cored sandwich panel (Figure 1).

These in-situ processes have been developed focusing on thermoplastic resins. Several thermoplastics have been successfully processed, including polyetheretherketone (PEEK), polyphenylene sulfide (PPS), and nylon. Panels have been produced with foam core densities ranging from 20 to 40 lb/ft³. Lower

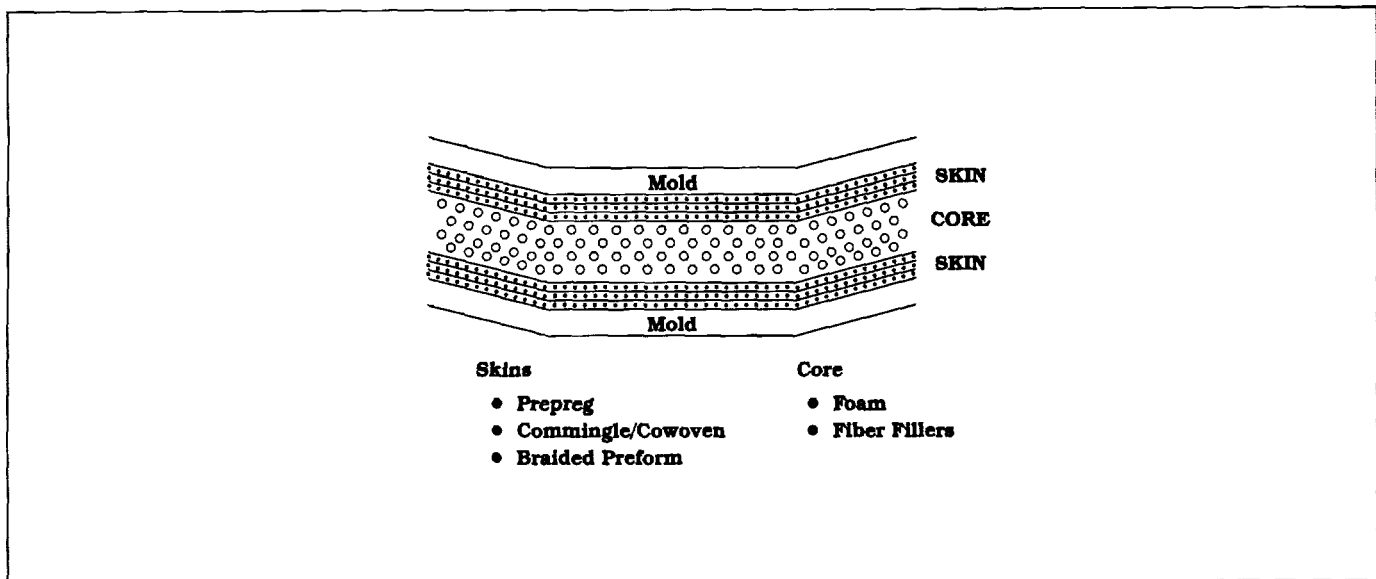


Figure 1. Sketch of in-situ sandwich structure fabrication.

densities have been achieved for in-situ produced, free-standing foam. Testing on PEEK core panels confirmed a strong molecular bond between the core and skin, which contributes to excellent mechanical properties. Testing performed by the Air Force showed that in-situ foam core panels offer ballistic resistance superior to conventionally processed composite core panels and solid panels of equal thickness.

The work performed in this study focuses on the application of Sundstrand's in-situ foam processing technology to the NASA/ATCAS fuselage keel designs. The steps involved in the study are as follows:

1. Identifying potential thermoset polymers compatible with carbon fiber/epoxy facesheets.
2. Performing foaming experiments with various fillers such as foaming agents, microspheres, and fibers.
3. Fabricating small panels.
4. Evaluating core material properties.

Processing

The processing of thermosets using in-situ technology offers both advantages and disadvantages compared to the processing of thermoplastics. The lower processing temperature of thermosets leads to simplified mold materials and processing equipment. However, the dimension of time is now added to the chemical reactions that occur during the processing. Unlike thermoplastics with their immediate solidification behavior, the solidification/curing of thermosets is also time dependent. The foaming agents must be active at the correct processing temperature for the length of time that the thermoset resin is gelling, to create the proper foam structure.

Fabrication

The development of in-situ forming foams that are compatible with thermosetting epoxy resins starts with selecting potential resin systems, which are compatible with the selected facesheet material. The NASA/Boeing ATCAS team chose Hercules' X8553 resin for use in the aircraft keel. Hercules

X8553 is among a family of resins which have varying composite properties, but the same chemical constituents. Thus, facesheet properties (compression strength vs. increased toughness) may be chosen to best suit the keel as mechanical property requirements evolve. The AS4 fiber was chosen following a cost/weight evaluation of available fibers.

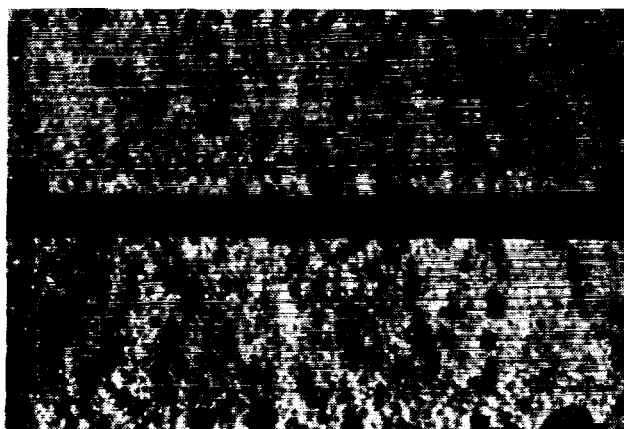
The core material chemistry and cure kinetics (resin T_g, gelation, and flow as a function of time and temperature) are needed to be compatible with AS4/8553-40 facesheets. TMA and TGA analysis was used to determine cure kinetics.

Foaming trials were performed with the 8553-40 neat resin. The initial foaming experiments were done in small crucibles to determine appropriate foaming additives and verify processing cycles. These trials yielded an excellent foam structure. However, the trials also revealed potential mixing problems associated with the liquid form of the 8553-40 resin, which might contribute to practical problems if this material were used to produce large-scale components. The majority of previous experience with in-situ processing was with resins in powder form.

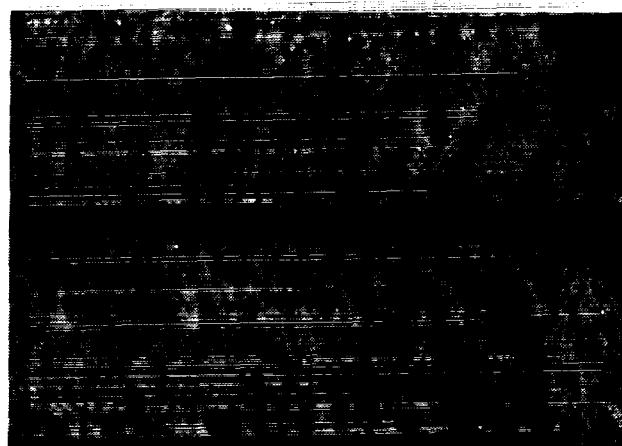
Hercules was able to produce the 8553-40 resin in a coarse powder form by chipping the solid. However, the material required modification of the catalyst to produce a powder. The need for a finer, readily-available powder resulted in the addition of 3M's PR500 toughened epoxy resin in powder form to the foaming trials. Both the PR500 and 8553-40 powder resins mixed easily and each produced foam structures in open crucible experiments.

The Foam Expansion Fabrication (FEF) in-situ process was selected for closed mold trials because of the simple geometry and relatively small size of the required panels. Panels with dimensions of 4-in. x 4-in. x 1/2-in. and 9-in. x 9-in. x 1/2-in. were successfully produced using each of the two resins. Fabrication of sandwich specimens in a 4-in. x 4-in. closed mold used 3-ply facesheets, while 9-in. x 9-in. panels used 8-ply facesheets of (45/90/-45/0/0/-45/90/45) orientation. Figure 2 shows a relatively uniform foam microstructure with some larger cells near the skin/core interface. Some evidence of porosity was noted in the facesheets. Density measurements revealed that our density goal of 20 lb/ft³ was met for both the Hercules and 3M foams.

Previous work with PEEK showed that the addition of chopped fibers to the core is an effective method to increase the strength of the core. The fibers also increase the difficulty of mixing. A trade-off must be made on the exact volume, type, and length of fiber that can be added to the core. The fibers must also be of a size that allows a good bond between the fiber and resin. Trials were conducted to assess sizing characteristics. Many of the fibers with which we have experience are sized



3M PR500 RESIN



HERCULES 8553-40 RESIN

Figure 2. Foams with no fibers.

for thermoplastics and were found to be incompatible with the thermoset resins. Mixing trials with a variety of short fibers proved that chopped Kevlar, manufactured by DuPont, and IM7/AS4 fibers, manufactured by Hercules, were difficult to blend into the powder.

Two fibers of different lengths were compatible with the PR500 resin. Amoco P55 is a high-performance, continuous fiber which we chopped to a length of 10 to 140 mils, with an average size of about 75 mils. Mill graphite produced by AKZO is a finely chopped fiber ranging from 3 to 50 mils in length, with an average of about 18 mils. These two fibers offer two very different combinations of benefits. The long Amoco fibers are difficult to mix but are a high performance fiber. In contrast, the mill graphite poses no mixing difficulties but is a lower modulus fiber.

A second series of 9-in. x 9-in. panels were produced with fibers added to the core mixture. Figure 3 shows the structure of the foam panels produced with the two different fibers.

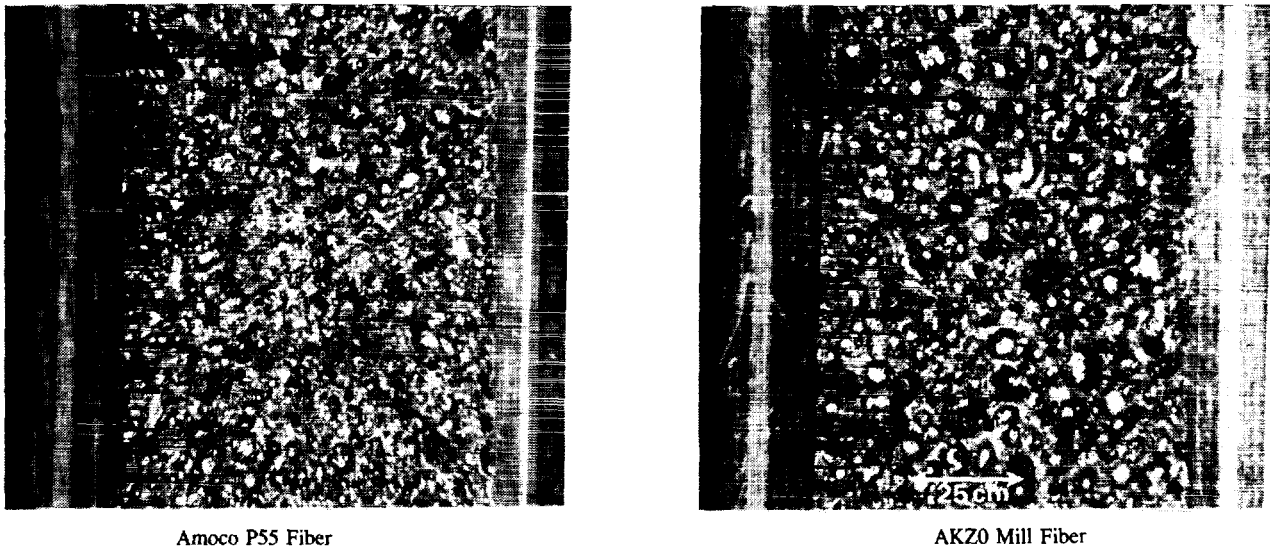


Figure 3. Foam (3 M) with two types of fibers.

Testing

Sandwich core materials are usually judged by the suitability of their mechanical and physical properties for particular applications. The use of sandwich construction in aircraft keel applications requires their ability to withstand high axial compressive loads, out-of-plane pressure loads, and local combined loads from attachments, such as bonded frames. These structural requirements place stiffness and strength requirements on the core. Coupons were cut from the small in-situ foam sandwich trials and tested to determine their suitability.

Structural sandwich core screening tests to evaluate basic mechanical properties such as compression, tension, and shear moduli and strengths were examined. ASTM standard test methods [22] were consulted to determine test procedures currently used to evaluate core materials. Because of the small sample size, foam cored sandwich specimen dimensions were held to a minimum to conserve material.

Compression properties were studied using ASTM Standard Test Methods for Flatwise Compressive Strength of Sandwich Cores, Designation C 365-57. "Stabilized" 1-in. x 1-in. compression coupons were chosen to evaluate the compression behavior. The ASTM standard requires a minimum cross-sectional area of 1-in.². This test provides a comparative compression stiffness and strength assuming Poisson's ratio is the same for all samples.

Tension performance was evaluated using ASTM Standard Test Method for Tensile Strength of Flat Sandwich Constructions in Flatwise Plane, Designation C297-61 (88). Coupons 1-in. x 1-in. sq. were machined from each panel and steel loading blocks were adhesively bonded to each facesheet. The coupons were then tested in tension to failure.

Three- and four-point flexure tests outlined in ASTM Standard Test Method for Flexural Properties of Flat Sandwich Constructions, Designation C 393-62, were chosen to qualitatively assess the shear stiffness and strength of the various samples. The width of foam core flexural coupons was 1-in. while the length was approximately 3-in. for 3-point and 8-in. for the 4-point. The 3-point test configuration used a support span of 1.88-in. while the 4-point test had a support span of 6-in.

Discussion

The performance of sandwich structures under compression loading is severely affected by non-visible internal core damage. Core materials must be damage-resistant to make sandwich construction viable in aircraft primary structure applications. A damage resistant core is one that will restrict the planar damage area when subjected to transverse impact, keeping the facesheets connected. Impact damage resistance is generally determined by examining impacted coupons and comparing impact-event metrics with damage metrics [23-24]. Damage size has been correlated to the Mode II interlaminar toughness, with increasing toughness having decreased damage size [25].

The impact damage resistance of the various in-situ foam samples was estimated by evaluating the area under the 3-point bend load-deflection curves, because of the small amount of material fabricated. This area, defined as the "work-to-fracture" for crack propagation in the core, is believed to be related to the core impact damage resistance, because crack propagation paths observed in the 3-point bend tests were found to be similar to those found in cross-sections impacted coupons.

A comparison of the work-to-fracture for the different samples is justified by the use of identical coupon geometries and test setups. Fracture energies determined by normalizing the work-to-fracture by the surface area created by crack extension could be compared with appropriate analysis. Tests of similar types to determine fracture properties of sandwich core materials were found in [26].

Figure 4 compares the load deflection curves for PR500 sandwich panels without and with short fibers. The occurrence of specific fracture events is labeled on the curves. The extension of crack "B1" from the end of crack "A1" to the coupon edge occurred at the point labeled crack "B1" on the load/deflection curves. Analysis of this data found the fracture energy for the panel with fibers, 31 in.-lb/in.², to be significantly higher than that for the panel without fibers, 9 in.-lb/in.², even though the panel with fibers had a 30 percent higher shear strength.

Sandwich panels with the same configuration as the in-situ samples were fabricated with a Rohacell foam core. These were mechanically tested in a manner similar to that of the in-situ foam sandwich panels for a one-to-one comparison. Table I shows the results from the various tests performed. Stiffnesses and strengths are presented in terms of the loading directions. Measured properties are seen to vary widely depending on the sample being examined. The results indicate that high shear strength does not necessarily mean high fracture toughness. The strength/toughness tradeoff was discussed [27].

Differences in resin properties and foam microstructure relate to foam performance. Gibson and Ashby [28] derived equations relating cell wall stiffness properties and cell geometry to the foam performance. It was shown that the foam axial and shear stiffnesses generally relate to the resin modulus and the square of the density ratio, while the fracture toughness was related to cell size.

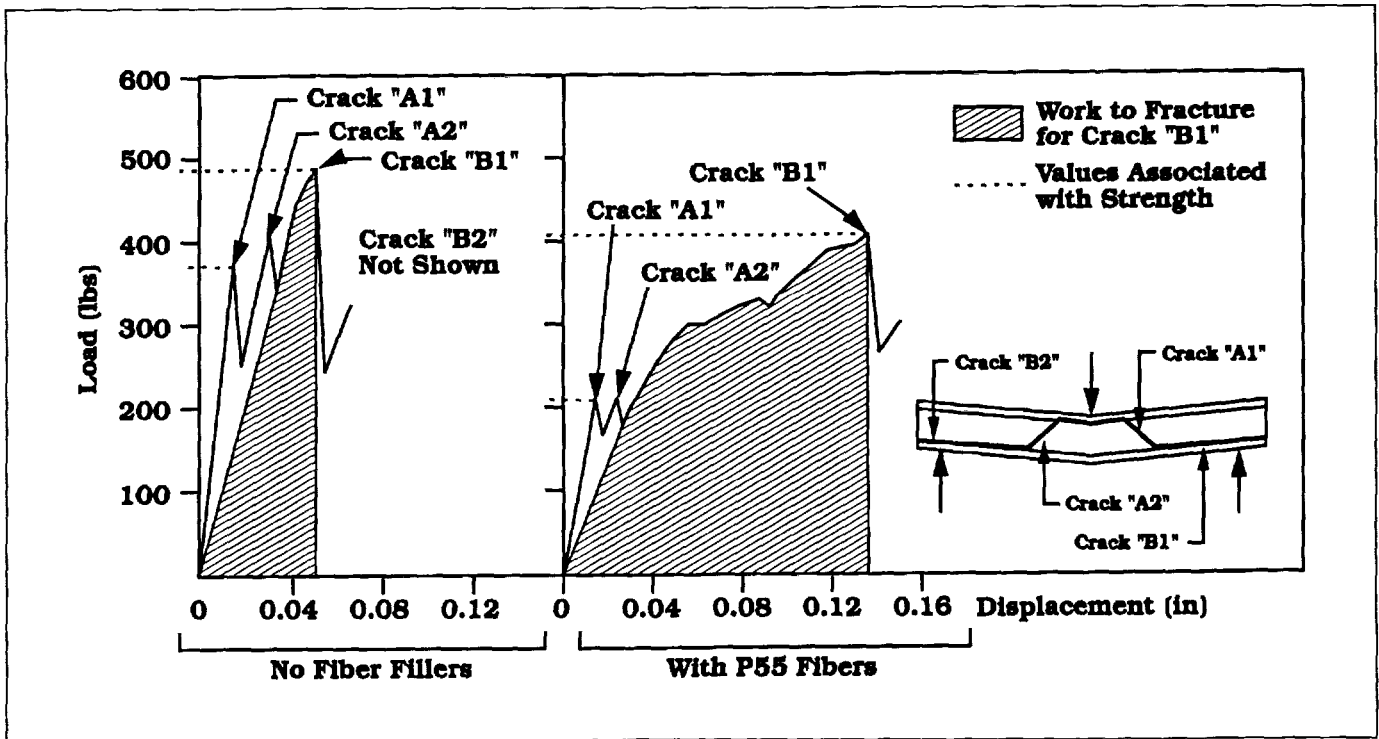


Figure 4. Two-load deflection curves.

Table I. Mechanical Properties

Panel Description	Tensile Strength (psi)	Tensile Modulus (ksi)	Compressive Strength (psi)	Compressive Modulus (ksi)	Shear Strength (psi)	Shear Modulus (ksi)	100 in.-lb Damage Area (in. ²)	Work in Fracture (in.-lb)
8553 foam	96.2*	2.3*	590	16.3				
PR500 foam	345	9.1	1,450	35.7	374	27.3		10.2
PR500/P55 fibers	234	8.9	754	29.3	236	13.5		40.1
PR500/mill fibers	374	12.9	1,360	43.1	482	22.0	14.3	2.2
Rohacell 110	399	8.5	408	12.6	334	9.9	12.1	6.5
Rohacell 200	798	19.1	1,320	39.1	693	17.8	7.8	3.6

*Failed in compression while bonding blocks.

The material combinations in the various in-situ trial panels strongly influence the performance. Further investigation of the microstructure/performance relationship is required to fully understand the effects and interactions of the input variables such as resin type, cell geometry, and chopped fiber fillers.

CONCLUSIONS

Thermoset resins were readily processed using in-situ techniques, producing a series of sandwich panels to 9-in. x 9-in. with 8-ply faceskins. Mechanical testing was conducted on these panels, showing that some of the mechanical properties could be improved by adding fibers to the foam core. A classic strength vs. toughness tradeoff was observed in the various panels.

FUTURE WORK

This program has demonstrated technical feasibility for in-situ processing of thermoset resins, laying the groundwork for future activities. These future activities should focus on optimization of the properties of the in-situ foam core sandwich structure through modification of the fiber additives to the core. Many variables relating to the chopped fiber additives, such as length, volume fraction, and composition need to be studied to determine their effect on toughness, modulus, and strength.

While this study concentrated on two toughened epoxy systems, alternate lower-cost resin systems should be investigated. It is postulated that adding chemical agents and fillers to the resin when creating a foam may prevent the resin from achieving its optimum characteristics. A resin that has been modified to adapt to the unique in-situ processing conditions is likely to offer the optimum performance in an in-situ foam core sandwich structure. Also, using an isoclave in-situ process may resolve porosity in the skin and provide lower density for a higher performance core.

We should continue to study thermoplastics because they offer advantages, including toughness, repairability, reusability, reduced VOC, and ease of manufacturing.

REFERENCES

1. Flynn, B. W.; Morris, M. R.; Metschan, S. L.; Swanson, G. D.; Smith, P. J.; Griess, K. H.; Schramm, M. R.; and Humphrey, R. J.: Global Cost and Weight Evaluation of Fuselage Keel Design Concepts. *Proceedings of the Third NASA Advanced Composite Technology Conference*, NASA CP-3178, 1993.
2. Saatchi, H.: One-Step Advanced Composite Sandwich Structure Fabrication. Presented at the FIBER-TX 88, Greenville, South Carolina, September 1988, proceedings published as an *ITAR NASA* publication (1989).
3. "Composite/Foam Sandwich," *High-Tech Materials Alert*, 5, (7), 3 (1988).
4. "Aerospace Materials: Fibers and Foam Form Hybrid Sandwich," *Aerospace America*, a publication of the American Institute of Aeronautics and Astronautics, page 42, October (1988).
5. Saatchi, H.: In-Situ Fabrication of Advanced Composite Sandwich Structure. *SAMPE International Symposium*, 34, 839 (1989).
6. Saatchi, H.: Process Fabricates Composite Sandwich Structures in Situ. *Advanced Materials*, the Newsletter of High Performance, ISSN0734-7146, 11, (8), 1 (1989).
7. "In-Situ Fabrication of Sandwich Structure," *MRP, Materials and Processing Report*, MIT Press, ISSN 0887-1949, 4, (4) (1989).
8. Saatchi, H.: In-Situ Fabrication of Thermoplastic Composite Primary Structure. *Joint Technology Coordination Group on Aircraft Survivability*, (U.S. Air Force JTCG/AS Seminar), August 1989.
9. Saatchi, H.: Low Cost Thermoplastic Composite Materials Manufacturing. *THERMOPLASTIC V: Materials and Fabrications for Low Cost Composites Structure*, *SAMPE*, Los Angeles Chapter Seminar, August 1989.
10. "In-Situ Sandwich Fabrication," *INSIDE R&D*, the weekly report on TECHNICAL INNOVATION, ISSN 0300-757X, September (1989).

11. "Make Complex Plastic, Resin Sandwich," *ADVANCED MANUFACTURING TECHNOLOGY*, A monthly intelligent service from TECHNICAL INSIGHTS, INC., ISSN 0885-5684, 10, (10) (1989).
12. Saatchi, H.: Innovative, Low-Cost Composite Sandwich Fabrication Processes. *CoGSME, Fabricating Composites '89 Conference*, October 1989.
13. Saatchi, H.: Mechanical/Damage Tolerance Property of In-Situ Sandwich Structure. FIBER-TEX 89 Conference, 1989. Proceeding published as an *ITAR NASA* publication in 1990.
14. Saatchi, H.: Isoclave Isostatically In-Situ Fabrication of Thermoplastic Sandwich Structure. *SAMPE International Symposium and Exhibition*, 35, 245 (1990).
15. Saatchi, H.; and Augustine, D. C.: Dry Fabric Impregnation in Net-Shape In-Situ Fabrication. *Proceedings of the 6th ASM/ESD Advanced Composites Conference/Exposition*, Detroit (1990).
16. Saatchi, H.: How to Make a Better Sandwich. *SME's Composites Quarterly*, 6 (1), 1 (1990).
17. "Sundstrand's Isoclave Process Makes Thermoplastic Composite Sandwich," *ADVANCED MATERIALS*, ISSN 0734-7146, 12, (7), 1 (1990).
18. "Budding Technologies for Composites Detailed in SAMPE Papers," *Plastic Technology*, 36 (8), 29 (1990).
19. "In-Situ Composite Fabrication PEEK Foam," R&D 100 Award Winner, *R&D Magazine*, (8), 76 (1990).
20. Saatchi, H.; Czarnecki, G.; and Baron, B.: Ballistic Impact Characteristics of PEEK Foamed PEEK Panels. JTCG/AS Task TS-9-02, WRDC/FI, *Presented to the JTCG/AS Vulnerability Reduction Air Force Seminar*, Naval Postgraduate School, Monterey, CA (1990).
21. "Isoclave In-Situ Fabrication," Presented to the *FIBER-TEX '90*, a NASA/Clemson Composite Conference, (1990).
22. *ASTM Standards and Literature References for Composite Materials*, Second Edition, American Society for Testing and Materials, 1990.
23. Sun, C. T.; and Rechak, S.: Effect of Adhesive Layers on Impact Damage in Composite Laminates. *Composite Materials: Testing and Design*, Eighth Conference, ASTM STP 972, American Society for Testing and Materials, 1988.
24. Wolf, E.: Impact Damage Mechanisms in Several Laminated Material Systems. *TELAC Report 92-3*, Massachusetts Institute of Technology, March 1992.
25. Grande, D. H.; Ilcewicz, L. B.; Avery, W. B.; and Bascom, W. D.: Effects of Intra- and Inter-Laminar Resin Content on Mechanical Properties of Toughened Composite Materials. In Proc. of First NASA Advanced Composite Technology Conf. (Part 2), 1990.
26. Zenkert, D.: Strength of Sandwich Beams with Interface Debondings. *Composite Structures* 17, 1991.

27. Ilcewicz, L. B.; Smith, P. J.; and Horton, R. E.: Advanced Composite Fuselage Technology. *Proceedings of the Third NASA Advanced Composite Technology Conference*, NASA CP-3178, 1993.
28. Gibson, L. J.; and Ashby, M. F.: *Cellular Solids - Structure & Properties*, Pergamon Press, 1988.

BIBLIOGRAPHY

Hossein Saatchi earned a B.S. in Metallurgical Engineering (1973), an M.S. (1975) and a Ph.D. (1978) in Materials Engineering, Composites from Drexel University and an MBA from Lake Erie College (1987). As postdoctoral fellow at the University of Pennsylvania (1978), he worked on intercalation of carbon fibers and polymer composites.

At Martin Marietta Aerospace, he developed probes and methods for nondestructive testing and repair of composites. At Gould Defense Systems, he coordinated the efforts of the composite group in the development, fabrication, and testing of several products such as pressure vessel, missile fin, torpedo drive shaft, and ablative coating. Since 1986, he has worked for Sundstrand Aerospace in the area of advanced composite materials.

Dr. Saatchi has authored over 23 technical publications and holds several patents in the area of in-situ composites. He has received several awards, including the 1990 R&D 100 Awards, served as chairman of Electronic Materials, ASM Cleveland Chapter (1984-86), and is listed in Jane's *Who's Who in Aviation and Aerospace* and the *International Directory of Distinguished Leadership*.

THE EFFECT OF MIXED MODE PRECRACKING ON THE MODE I FRACTURE TOUGHNESS OF COMPOSITE LAMINATES*

Prashanth Shankar, Williard D. Bascom and John A. Nairn
Material Science and Engineering, University of Utah
Salt Lake City, Utah 84112, USA

54-24
51404

ABSTRACT

We subjected double cantilever beam specimens from four different composite materials to mixed-mode precracking. Three different precracking mode I to mode II ratios were used—1 to 4, 1 to 1, and 4 to 1. Following precracking the specimens were tested for mode I fracture toughness. The mixed-mode precracking often influenced the mode I toughness and its influence persisted for as much as 60 mm of mode I crack growth. We tested composites with untoughened matrices, composites with rubber-toughened matrices, and composites with interlayer toughening. Depending on material type and precracking mode ratio, the precracking could cause either a significant increase or a significant decrease in the mode I fracture toughness.

Key words: composites, interlaminar fracture toughness, fiber bridging, double cantilever beam specimen, end notch flexure specimen, energy release rate, fracture mechanics, delamination, mode I, mode II, mixed mode bending.

INTRODUCTION

Delamination or propagation of an interlaminar crack is a common mode of failure in composite laminates. The presence of delaminations may cause complete fracture, but even partial delaminations will cause at least a loss of stiffness. The most common method for studying delaminations is to use fracture mechanics where the characterization is via the critical energy per unit crack growth— G_c . Because of the extreme anisotropy of the toughness of composite laminates, delamination crack growth is almost always interlaminar. By varying loading conditions, it is possible to study different modes of propagation. Some of the propagation modes observed in composites are not commonly observed in isotropic materials. The most obvious failure mode is mode I, the opening mode, which gives G_{Ic} . In certain bending geometries, the crack may propagate by sliding or shear motion, which is characterized by G_{IIc} . A combination of opening and shear loadings can give mixed mode crack propagation which is characterized by a failure envelope of G_{II} vs. G_I .

In this paper we looked at the effect of crack history on the mode I toughness or G_{Ic} . We subjected various specimens to mixed-mode precracking prior to a standard mode I test. We tested four different material types and found that crack history can have a significant effect on mode I toughness. The implication is that delamination is a complex process that not only depends on the current loading conditions, but also depends on the delamination formation history.

*Work supported by contract NAS1-18883 from NASA Langley Research Center

NOMENCLATURE

a	delamination length
B	specimen width
c	position of the applied load on the lever
C	compliance
χ_h	crack length correction factor
δ	load point displacement
G_I	mode I strain energy release rate
G_{II}	mode II strain energy release rate
G_{Ic}	delamination fracture toughness for mode I loading
G_{IIc}	delamination fracture toughness for mode II loading
h	specimen half thickness
L	specimen half span
P	applied load

MATERIALS AND METHODS

The experiments were conducted on four different carbon fiber composite materials—AS4/3501-6, IM7/8552, IM7/XLASC, and IM7/2600. AS4/3501-6 and IM7/2600 are characterized as having homogeneous, untoughened epoxy matrices. IM7/8552 has a rubber toughened epoxy matrix. IM7/XLASC has a bismaleimide matrix with toughening interlayers between the plies. AS4/3501-6, IM7/8552, and IM7/XLASC were all made by autoclave processing according to the manufacturer's instructions. IM7/2600 was made in a hot press. All tested laminates were unidirectional laminates. The AS4/3501-6, IM7/8552, and IM7/XLASC laminates were 32-ply laminates. The IM7/2600 laminates were 24-ply laminates. All specimens were six inches long and one inch wide. An aluminium foil was inserted as a crack starter in the prepreg lay-up before autoclave curing. Hinges were glued to the ends of the specimens over the insert for mounting in the fixture described below.

There are various mixed mode testing methods available. In this study, the fixture developed by Reeder and Crews [1, 2] was used. Their mixed-mode bending (MMB) fixture combines a mode I double cantilever beam (DCB) test with a mode II end notch flexure (ENF) test. This combination is achieved by adding an opening mode load to a mid-span loaded ENF specimen as shown in Fig. 1. The additional load separates the arms of the unidirectional laminate as in a DCB test. A single applied load produces two reactionary forces, tensile and bending, at the hinge and at the lever. The loading position, c , determines the relative magnitude of the two resulting loads on the specimen and, therefore, determines the mixed-mode delamination ratio. Pure mode II loading occurs when the applied load is directly above the beam mid-span ($c = 0$). Pure mode I loading can be achieved by removing the loading beam and pulling up on the hinge. Mixed mode loading is achieved by varying c .

The Reeder and Crews [1, 2] MMB fixture was used to precrack the unidirectional delamination specimens. The initial crack length created by the aluminium foil crack starter was 20–35 mm. We precracked each specimen at a selected constant mixed-mode ratio until the delamination length was about 50 mm (15–30 mm of precrack growth). The precracking was done using three different ratios of mode I to mode II loading—4 to 4, 1 to 1, and 1 to 4. After precracking, each specimen

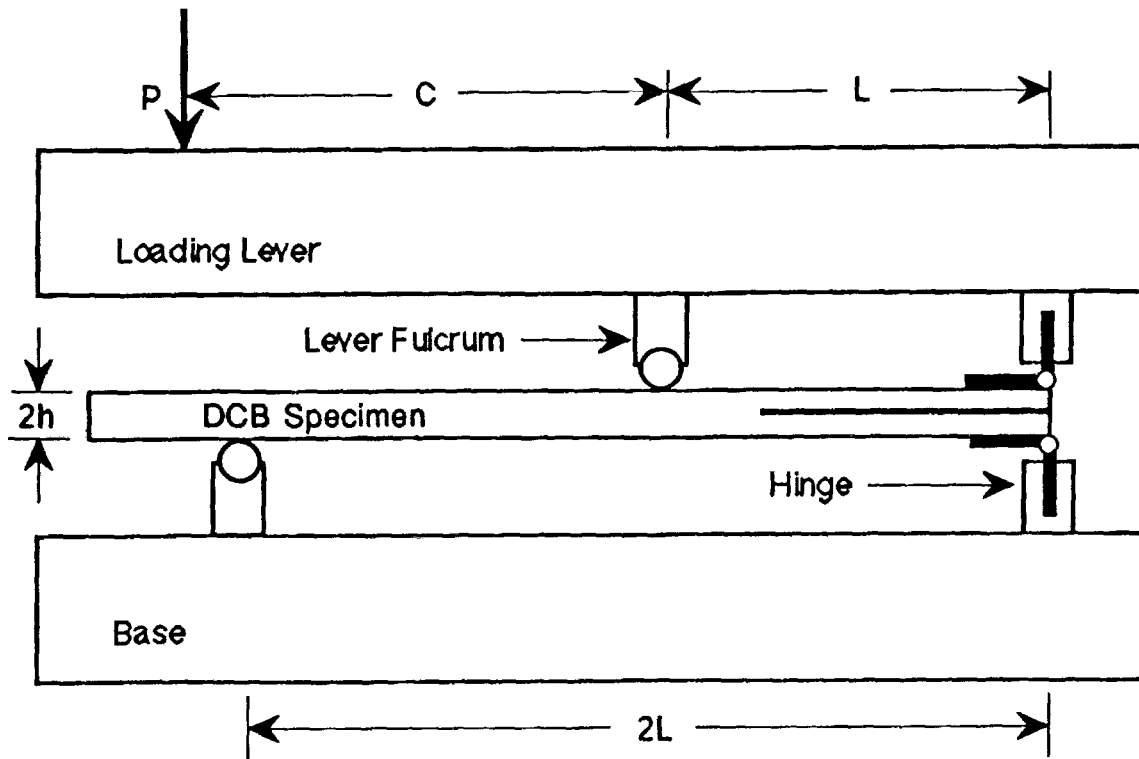


Figure 1: The mixed-mode bending fixture from Ref. [1] used to precrack DCB specimens at various mode I to mode II ratios. The mode I to mode II ratio was changed by varying c .

was subjected to a pure mode I delamination test. During the mode I delamination test, the load and displacement were noted after each 5 mm of delamination crack propagation. This data was used, as described below, to calculate fracture toughness as a function of delamination length. Both the mixed-mode precracking and the mode I test were done in a 25 kN servohydraulic Minnesota Testing Systems (MTS) testing frame under displacement control. The displacement rate was always 0.03 inches/min.

As described above, the mixed-mode precracking was followed by a mode I delamination test. According to the area method, the fracture toughness, or critical strain energy release rate in a mode I test is

$$G_{Ic} = \frac{P_1\delta_2 - P_2\delta_1}{2B(a_2 - a_1)} \quad (1)$$

where subscripts 1 and 2 refer to load, displacement, or crack length before and after a small amount of crack growth. This is an exact definition of G_{Ic} but it is imprecise because, what is in effect a derivative must be determined numerically from two experimental measurements. Area methods suffer from other disadvantages. They determine only an average value of G_{Ic} over some change in delamination length. They are influenced by hysteretic energy losses and zero offset effects as discussed by Hashemi, Kinloch, and Williams [3].

It is often desirable to use beam theory, instead of the above area method, to analyze fracture results. According to beam theory of a DCB specimen, the mode I toughness is:

$$G_{Ic} = \frac{3P\delta}{2Ba} \quad (2)$$

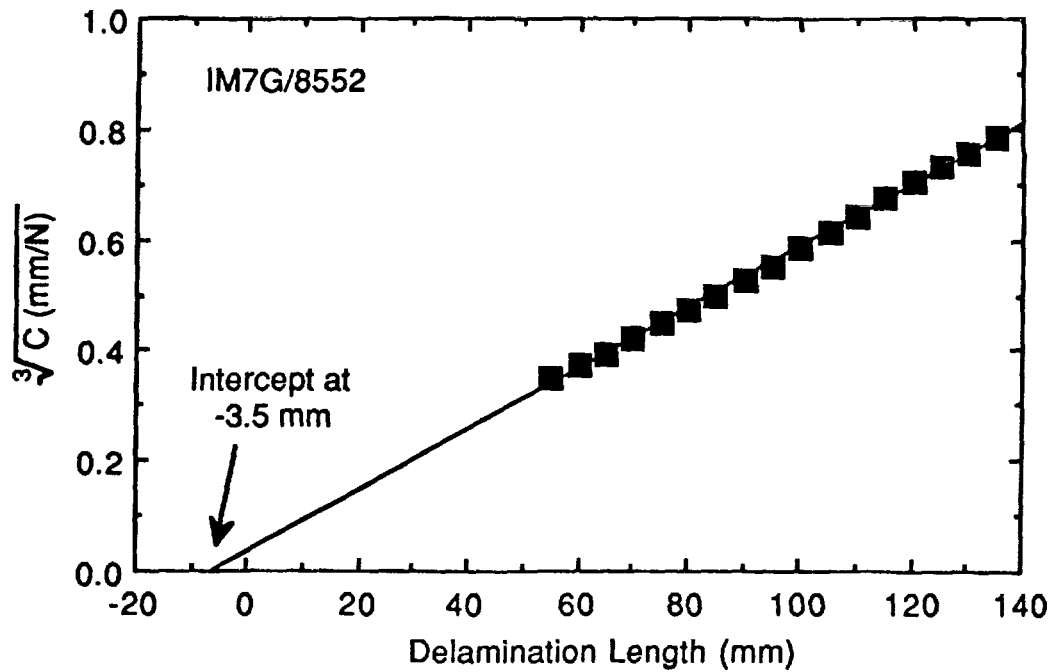


Figure 2: A plot of $C^{1/3}$ as a function of delamination length for a IM7/8552 laminate. The intercept on the x axis defines the crack length correction factor for this material.

This equation assumes that the compliance at the crack root is zero, but in reality there is some deflection and rotation at the crack tip. It has been shown experimentally by Hashemi, Kinloch, and Williams [3] that this effect can be modelled by adding a length χ_h to the real crack length where χ_h is a constant which depends on the elastic properties of the material. It can be found experimentally from the intercept of a plot of $\sqrt[3]{C}$ vs. the measured delamination length, a . The corrected value of G_{Ic} becomes

$$G_{Ic} = \frac{3P\delta}{2B(a + \chi_h)} \quad (3)$$

We used Eq. (3) to measure mode I fracture toughness as function of delamination length. For each material and each precracking condition we determined χ_h by plotting $\sqrt[3]{C}$ vs. a . A typical result for IM7/8552 is given in Fig. 2. The intercept when $C = 0$ gives $\chi_h = 3.5$ mm. For all specimens, the measured values of χ_h ranged from 0 mm to 12 mm.

EXPERIMENTAL RESULTS

For each material and for each precracking mode ratio, we measured the mode I fracture toughness as a function of delamination growth length. Some typical results at a mode I to mode II precracking ratio of 4 to 1 are given in Fig. 3. All results follow a similar pattern. They begin with some mode I toughness, which may be high or low, and eventually level off at some steady state value. The steady state value occurs after there has been enough crack growth to insure that the mode I crack *forgets* about the precracking mode ratio. Surprisingly, it can take as much as 60 mm

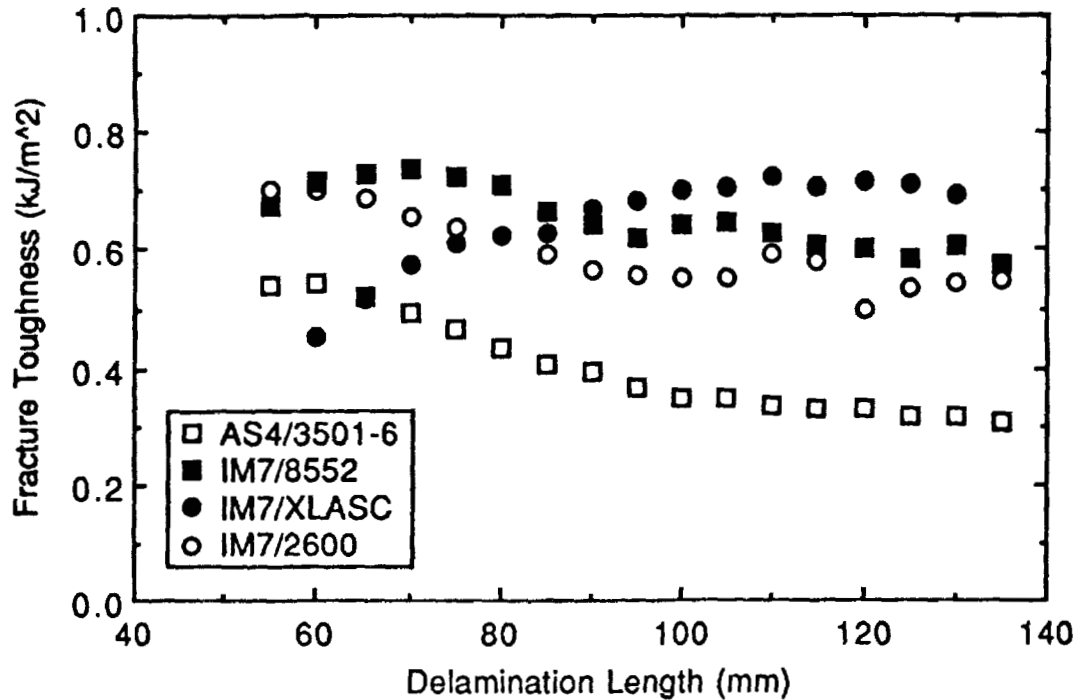


Figure 3: Mode I fracture toughness as a function a delamination length for all materials following mixed-mode precracking using a mode I to mode II ratio of 4:1.

of mode I crack growth to reach the steady state value. The steady state toughnesses of the four materials were as follows:

AS4/3501 - 6	$G_{Ic} = 0.28 \pm 0.02 \text{ kJ/m}^2$
IM7/2600	$G_{Ic} = 0.50 \pm 0.02 \text{ kJ/m}^2$
IM7/8552	$G_{Ic} = 0.60 \pm 0.10 \text{ kJ/m}^2$
IM7/XLASC	$G_{Ic} = 0.66 \pm 0.04 \text{ kJ/m}^2$

The steady state toughnesses were independent of the precracking mode ratio. The steady state results were reproducible with the most variable results coming from the IM7/8552 laminates. For the first 60 mm of crack growth, the mode I toughnesses of each material may differ significantly from its steady state toughness. The remainder of this section discusses the effect of precracking on the early mode I crack growth.

Figure 3 shows the mode I toughness of each material following a precracking mode I to mode II ratio of 4 to 1. Of the ratios we used, this ratio had the highest amount of mode I loading and should therefore be expected to produce the smallest effects. All materials, except IM7/XLASC, showed a slight increase in mode I toughness during early crack growth. For these materials the initial mode I toughnesses were 10% to 40% higher than the steady state toughnesses. As crack growth increased, the mode I toughnesses decreased towards the steady state toughnesses. For IM7/8552, the initial mode I toughness was about 35% lower than the steady state toughness. The IM7/XLASC was unique in using toughening interlayers. These results suggest that materials with toughening interlayers are susceptible to decreases in mode I toughness when they experience mixed-mode precracking.

Figure 4 shows the mode I toughness of each material following a precracking mode I to mode II

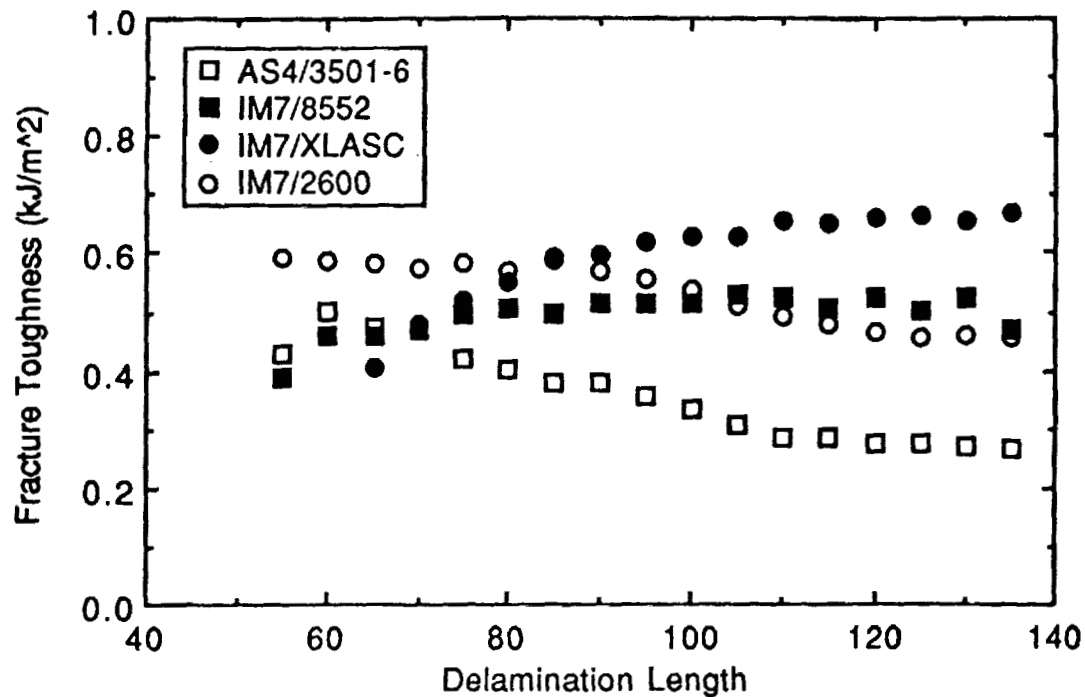


Figure 4: Mode I fracture toughness as a function a delamination length for all materials following mixed-mode precracking using a mode I to mode II ratio of 1:1.

ratio of 1 to 1. The two toughened materials (solid symbols in Fig. 4) showed a slight decrease (10% to 35%) in mode I toughness at early stages in crack growth. The two untoughened systems (open symbols in Fig. 4) showed a slight increase (15% to 50%) in mode I toughness at early stages in crack growth. An interesting observation is that both of the untoughened composite material systems have a higher mode I toughness during early stages of crack growth than either of the toughened systems. These results suggests that toughening methods that enhance pure mode I toughness may be ineffective or less effective following mixed-mode crack growth histories.

Figure 5 shows the mode I toughness of each material following a precracking mode I to mode II ratio of 1 to 4. Of the ratios we used, this ratio had the highest amount of mode II loading. The two toughened materials (solid symbols in Fig. 5) showed a significant decrease (40% to 70%) in mode I toughness at early stages in crack growth. The two untoughened systems (open symbols in Fig. 5) showed little or no effect from this predominantly mode II precracking.

It is interesting to cross-plot the results and give plots for a single material at the three different mode ratios. The results for AS4/3501-6 and for IM7/XLASC at the three different precracking mode ratios are in Figs. 6 and 7, respectively. The untoughened AS4/3501-6 laminates showed no effect of precracking or a slight increase in mode I toughness. The increase in mode I toughness got larger as the amount of mode I loading in the precracking increased. The IM7/XLASC laminates, which were toughened with an interlayer, showed only a decrease in mode I toughness with precracking. The decrease in mode I toughness got larger as the amount of mode II loading in the precracking increased. After the most extreme mode II precracking (mode I to mode II ratio of 1 to 4), the initial mode I toughness of IM7/XLASC was 70% lower than its steady state toughness. The results for the second untoughened material, IM7/2600, were similar to those of AS4/3501-6. Likewise, the results for the second toughened material, IM7/8552, were similar to those of

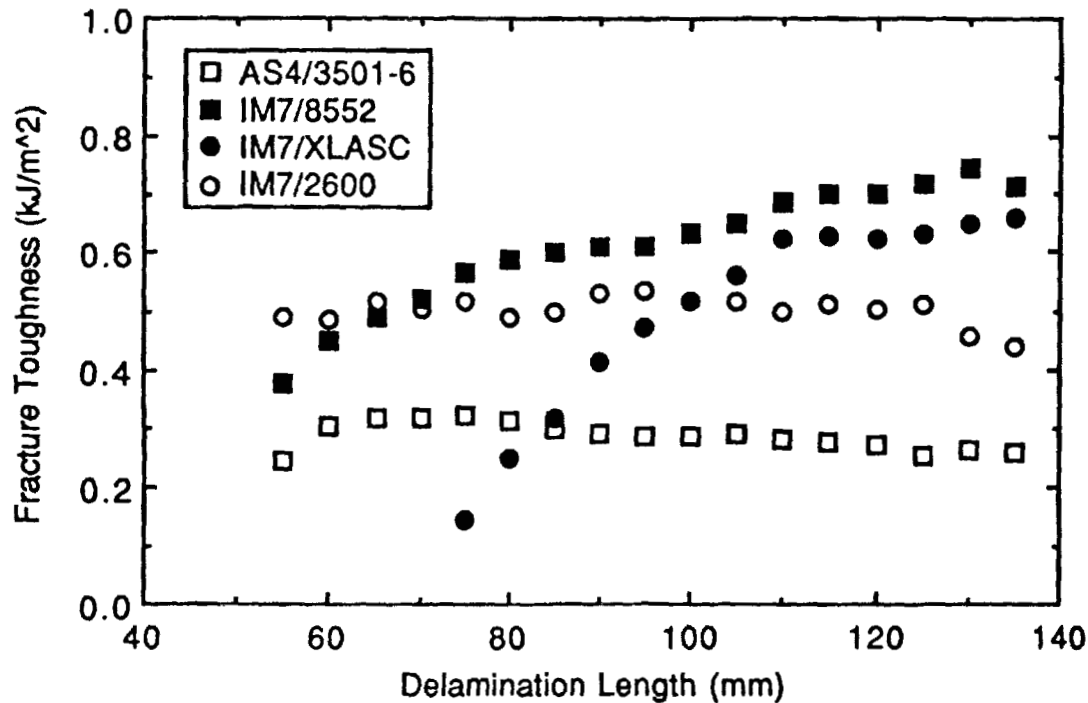


Figure 5: Mode I fracture toughness as a function a delamination length for all materials following mixed-mode precracking using a mode I to mode II ratio of 1:4.

IM7/XLASC.

To gain some insight into mechanisms, we observed the fracture surfaces of the precrack and of the mode I crack. There was a distinct contrast between the two regions showing that the delaminations grew by different growth mechanisms. As might be expected, the contrast was largest when using the mode I to mode II ratio of 1 to 4. As the amount of mode I loading in the precracking stage increased, the fracture surface contrast decreased. We attempted to assess the extent of fiber bridging. There appeared to be significantly more fiber bridging in the mode I fracture surface than in the precracking fracture surface.

DISCUSSION AND CONCLUSIONS

Our experimental results show that the mixed-mode precracking can have a profound effect on the initial mode I fracture toughness of subsequent mode I crack growth. The precracking can cause mode I toughness increases as high as 40% as well as mode I toughness decreases as high as 70%. Surprisingly, we found that the effect of the precrack persists for a macroscopic distance of about 60 mm. After 60 mm of crack growth all specimens approached a steady state mode I fracture toughness.

The two toughened materials, IM7/8552 and IM7/XLASC, tended to show decreases in mode I toughness following mixed-mode precracking. The amount of decrease increased as the mode II component of the precracking increased. We can arrive at a speculation on the effect of mode II precracking on mode I toughness by considering mode II stress states around crack tips in isotropic, homogeneous materials. When a material can yield easily, the singular stresses near the crack tip

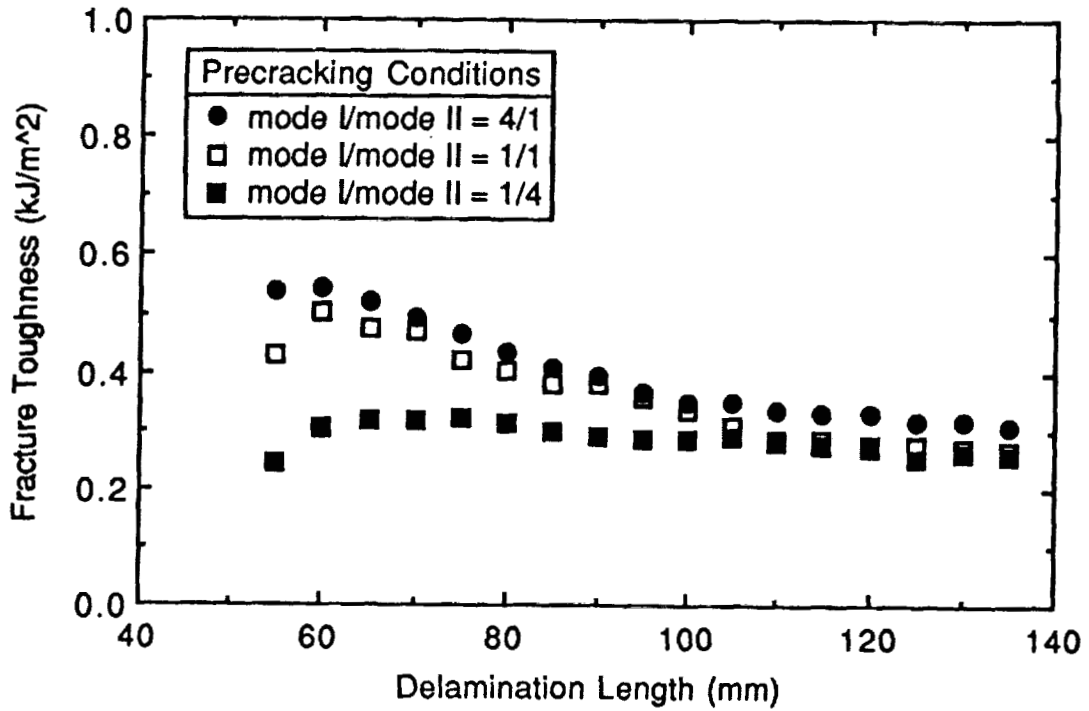


Figure 6: Mode I fracture toughness as a function of delamination length for AS4/3501-6 laminates following different mixed-mode precracking using different mode I to mode II ratios.

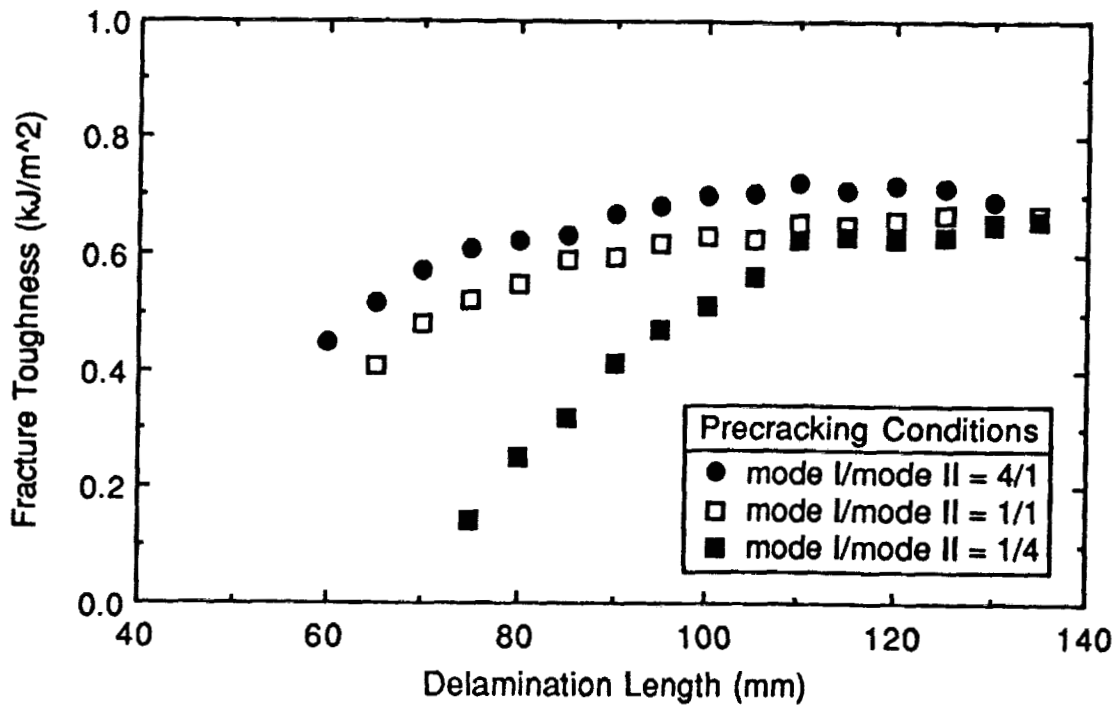


Figure 7: Mode I fracture toughness as a function of delamination length for IM7/XLASC laminates following different mixed-mode precracking using different mode I to mode II ratios.

are more realistically imagined as being limited by the yielding process. If one assumes a yield criterion (*e.g.* Von Mises or Tresca), it is possible to estimate the yield zone size for any loading condition. For delamination specimens, the most relevant dimension of the yield zone is the one directly ahead of the crack tip. For plane-strain conditions in isotropic, homogeneous materials, the extent of yielding ahead of the crack tip is profoundly affected by stress state. It is at a minimum for pure mode I loading and increases dramatically as the amount of mode II loading increases.

To interpret the results in this paper, we suggest that the rubber toughened matrix in IM7/8552 and the toughening interlayer in IM7/XLASC are prone to yielding or have a low yield strength. During the precracking stage, any mode II loading will therefore lead to a yielded damage zone ahead of the crack tip. We suggest that the mode I toughness of the damage zone is low and thus precracking causes an initial reduction in mode I toughness. This model predicts that the larger the amount of mode II loading, the larger would be the reduction in mode I toughness. This prediction agrees with the observations in Fig. 7. The AS4/3501-6 and IM7/2600 laminates are different because their untoughened matrices have higher yield strengths. The observation that mode II precracking does not decrease their subsequent mode I toughness suggests that the higher yield strength matrices did not become damaged by the mode II loading present during precracking.

When the precracking mode I to mode II ratio was 4 to 1 we observed an increased initial mode I toughness (see Fig. 3). It is difficult to imagine a precracking mechanism that would enhance the subsequent mode I toughness. The increase could possibly be related to fibers bridging from the precrack zone into the mode I crack growth. However, we have no evidence to prove or disprove this claim. For now, the apparent increase in mode I toughness remains unresolved.

In conclusion, the closer we look, the more we realize that the characterization of delamination toughness is a complex problem. It is clearly insufficient to study only mode I, mode II, or mixed-mode crack growth emanating from a crack starter. The delamination process is now seen to have *memory*. In other words, the delamination toughness is not only a function of the loading conditions but also a function of the loading conditions that gave the initial crack. A good example from this paper concerns the development of tougher composites. The IM7/8552 and IM7/XLASC composites are tougher materials by standard mode I testing. When subjected to precracking with a high component of mode II loading, however, these materials become less tough than untoughened composite systems. The design implication is that *so-called* toughened materials will not always produce tougher structures than their untoughened counterparts. We suggest there is something deficient, or rather specific, about the toughening mechanisms taking place in today's toughened composites. Their toughening mechanisms work for mode I loading but can be rendered ineffective by various precracking conditions

REFERENCES

1. Reeder, J. R.; and Crews, J. H., Jr.: Nonlinear Analysis and Redesign of the Mixed-Mode Bending Delamination Test, *NASA Technical Memorandum 102777*, 1991.
2. Reeder, J. R.; and Crews, J. H., Jr.: Mixed Mode Bending Method for Delamination Testing, *AIAA J.*, vol. 28, 1990, pp. 1270-1276.
3. Hashemi, S; Kinloch, A. J.; and Williams, J. G.: The Analysis of Interlaminar Fracture in Uniaxial Fiber-Polymer Composites, *Proc. Roy. Soc. London*, vol. A427, 1989, pp. 173-199.

MASTER PLOT ANALYSIS OF MICROCRACKING IN GRAPHITE/EPOXY AND GRAPHITE/PEEK LAMINATES*

John A. Nairn, Shoufeng Hu, and Jong Song Bark
 Material Science and Engineering, University of Utah
 Salt Lake City, Utah 84112, USA

55-24
 51405

ABSTRACT

We used a variational stress analysis and an energy release rate failure criterion to construct a master plot analysis of matrix microcracking. In the master plot, the results for all laminates of a single material are predicted to fall on a single line whose slope gives the microcracking toughness of the material. Experimental results from 18 different layups of AS4/3501-6 laminates show that the master plot analysis can explain all observations. In particular, it can explain the differences between microcracking of central 90° plies and of free-surface 90° plies. Experimental results from two different AS4/PEEK laminates tested at different temperatures can be explained by a modified master plot that accounts for changes in the residual thermal stresses. Finally, we constructed similar master plot analyses for previous literature microcracking models. All microcracking theories that ignore the thickness dependence of the stresses gave poor results.

INTRODUCTION

When the 90° plies are relatively less stiff than the supporting plies, the first form of damage in $[(S)/90_n]_s$ or $[90_n/(S)]_s$ laminates (where (S) denotes any orthotropic sublaminate) is usually microcracking or transverse cracking of the 90° ply groups [1-16]. When the 90° plies are in the middle ($[(S)/90_n]_s$ laminates), those plies crack into an array of roughly periodic microcracks. When the 90° plies are on the outside ($[90_n/(S)]_s$ laminates), the 90° ply groups also crack into an array of roughly periodic microcracks, but the two arrays are shifted from each other by half the average crack spacing [10, 17]. There are many reasons for studying microcracking. Microcracks not only change the thermal and mechanical properties of laminates [10, 18], but also present pathways through which corrosive agents may penetrate into the interior of the laminate [6]. Perhaps most importantly, microcracks act as nuclei for further damage such as delamination [1, 9], longitudinal splitting [5, 6], and curved microcracks [15]. Because microcracks are precursors to the cascade of events that leads to laminate failure, we would have little hope of understanding laminate failure or of predicting long-term durability if we did not first develop a thorough understanding of the phenomenon of microcracking.

To predict microcracking results in $[(S)/90_n]_s$ laminates under uniform axial loading of σ_0 , Nairn *et al.* [16, 19] advocated an energy release rate failure criterion. In brief, the next microcrack is assumed to form when the total energy release rate associated with the formation of that microcrack, G_m , equals or exceeds the microcracking fracture toughness of the material, G_{mc} . From a thermoelastic, variational mechanics stress state [16, 19-21], the total energy release rate due to microcracking is [16, 19-21]

$$G_m = \sigma_{x0}^{(1)2} C_3 t_1 Y(D) \quad (1)$$

*Work supported, in part, by contract NAS1-18833 from NASA Langley Research Center and, in part, by gifts from E. I. duPont deNemours & Co. and ICI Composites.

where C_3 is a constant defined in the appendix, t_1 is the semi-thickness of the 90° plies and $\sigma_{x0}^{(1)}$ is the tensile stress in the 90° plies in the absence of microcracks:†

$$\sigma_{x0}^{(1)} = k_m^{(1)} \sigma_0 + k_{th}^{(1)} T \quad (2)$$

The terms $k_m^{(1)}$ and $k_{th}^{(1)}$ are the effective thermal and mechanical stiffnesses of the 90° plies. T is the temperature difference between the specimen temperature and the stress free temperature and it is used to define the level of residual thermal stresses in the specimen. By a simple one-dimensional, constant-strain analysis the stiffness constants are

$$k_m^{(1)} = \frac{E_x^{(1)}}{E_c^0} \quad \text{and} \quad k_{th}^{(1)} = -\frac{\Delta\alpha}{C_1} \quad (3)$$

Here E_c^0 is the x -direction modulus of the laminate, $E_x^{(1)}$ is the x -direction modulus of the 90° plies, $\Delta\alpha = \alpha_x^{(1)} - \alpha_x^{(2)}$ is the difference between the x -direction thermal expansion coefficients of the 90° plies and the (S) sublaminates, and C_1 is a constant defined in the appendix.

To use Eq. (1), $Y(D)$ is needed. Following Laws and Dvorak [22], Nairn *et al.* [16, 19] evaluated $Y(D)$ for the discrete process of forming a new microcrack between two existing microcracks. The result is

$$Y(D) = \chi(\rho_k - \delta) + \chi(\delta) - \chi(\rho_k) \quad (4)$$

where $\chi(\rho)$ is a function defined in the appendix, $2\rho_k$ is the dimensionless distance between the existing microcracks, and 2δ is the dimensionless distance from the new microcrack to one of the existing microcracks [16, 19]. Normally one does not know where the next microcrack will form and therefore does not know ρ_k or δ . It is known, however, that $[(S)/90_n]_s$ laminates tend to form roughly periodic microcracks. We thus expect $\rho_k \approx \langle \rho \rangle$ and $\delta \approx \frac{\langle \rho \rangle}{2}$. Liu and Nairn [16], however, point out that these approximations are an oversimplification. From Eq. (1) it can be shown that the energy release rate is higher when the microcrack forms in a large microcrack interval than it is when it forms in a small microcrack interval. It is logical to assume that microcrack formation prefers the location that maximizes energy release rate. Thus when there is a distribution in crack spacings, the next microcrack will prefer to form in a crack interval that is larger than the average crack spacing. Liu and Nairn [16] introduced a factor f , defined as the average ratio of the crack spacing where the new microcrack forms to the average crack spacing. In this model, $Y(D)$ is approximated by

$$Y(D) \approx 2\chi(f\langle \rho \rangle/2) - \chi(f\langle \rho \rangle) \quad (5)$$

Using f values between 1.0 and 1.44, Liu and Nairn [16] get good fits to experimental results for a wide variety of laminates. Fortunately, the value of f required to get the best fit does not influence the calculated fracture toughness, G_{mc} . In this paper, we treat f as a layup independent factor that is approximately 1.2. There are tedious experimental techniques that can measure f and they show that it is usually about 1.2.

To predict microcracking results in $[90_n/(S)]_s$ laminates, Nairn and Hu [17] extended the variational analysis of $[(S)/90_n]_s$ laminates to account for the development of staggered microcracks. The analysis is more complicated due to the loss of symmetry resulting from staggered microcracks. Their results, however, can be cast in a form similar to the $[(S)/90_n]_s$ laminate results. The total strain energy release rate associated with an increase in microcracking damage is

$$G_m = \sigma_{x0}^{(1)2} C_{3a} t_1 Y_a(D) \quad (6)$$

†Note that Refs. [16, 17, 19–21] define $\sigma_{x0}^{(1)} = k_m^{(1)} \sigma_0$ or as the mechanical load in 90° plies of the undamaged laminate. As expressed in Eq. (2), we altered the definition of $\sigma_{x0}^{(1)}$ to also include the initial thermal stresses.

where C_{3a} is a constant defined in the appendix and $Y_a(D)$ can be approximated by [17]

$$Y_a(D) \approx \frac{1}{2}(3\chi_a(f(\rho)/3) - \chi_a(f(\rho))) \quad (7)$$

Here, $\chi_a(\rho)$, which is given in the appendix, is the antisymmetric damage state analog of $\chi(\rho)$.

In this paper we describe the use of the above microcracking analyses to predict microcracking in 18 different layups of AS4/3501-6 laminates at room temperature and to predict the temperature dependence of microcracking in two different layups of AS4/PEEK laminates. In brief, the variational analysis was used to develop scaling laws that permit plotting the results from all laminates of a given material on a single linear master plot. The accuracy with which the experimental data conforms to the linear master plot predictions quickly reveals the adequacy of the analysis. Our findings were that the variational stress analysis coupled with an energy release rate failure criterion can predict all experimental results. All attempts at using simpler theories based on stress analyses that ignore the z dependence of the problem gave poor results.

MATERIALS AND METHODS

Static tensile tests were run on Hercules AS4 carbon fiber/3501-6 epoxy matrix composites and on Hercules AS4 carbon fiber/ICI Polyether ether ketone (PEEK) composites. AS4/3501-6 prepreg was purchased from Hercules and cured in an autoclave at 177°C according to manufacturer's recommendations. We made eight cross-ply layups with 90° plies in the middle— $[0/90]_s$, $[0/90_2]_s$, $[0/90_4]_s$, $[0_2/90]_s$, $[0_2/90_2]_s$, $[0_2/90_4]_s$, $[\pm 15/90_2]_s$, and $[\pm 30/90_2]_s$. We made 10 cross-ply layups with surface 90° plies— $[90/0/90]_T$, $[90/0]_s$, $[90/0_2]_s$, $[90/0_4]_s$, $[90_2/0/90_2]_T$, $[90_2/0]_s$, $[90_2/0_2]_s$, $[90_2/0_4]_s$, $[90_2/\pm 15]_s$, and $[90_2/\pm 30]_s$. Two cross-ply layups of AS4/PEEK composites— $[90_4/0_2]_s$ and $[90_4/0]_s$ —were supplied by ICI Composites. Specimens, which were nominally 12 mm wide and 150 mm long with thicknesses determined by the stacking sequences (about 0.125 mm per ply), were cut from the laminate plates. Tensile tests were run in displacement control, at a rate of 0.005 mm/sec, on a Minnesota Testing Systems (MTS) 25 kN servohydraulic testing frame. While testing each specimen, the experiment was periodically stopped and the specimen was examined by optical microscopy. For $[(S)/90_n]_s$ laminates we calculated the crack density by averaging the densities of the cracks visible on the two specimen edges. For $[90_n/(S)]_s$ laminates, microcracks could be seen on the edges and on the faces of the specimen. We calculated the crack density by averaging the crack densities of the two 90° ply groups.

MASTER PLOT ANALYSIS

Assuming that microcracking occurs when $G_m = G_{mc}$, solving Eq. (1) for σ_0 , and multiplying the result by $-k_m^{(1)}/k_{th}^{(1)}$ gives

$$-\frac{k_m^{(1)}}{k_{th}^{(1)}}\sigma_0 = -\frac{1}{k_{th}^{(1)}}\sqrt{\frac{G_{mc}}{C_3 t_1 Y(D)}} + T \quad (8)$$

A similar treatment of Eq. (6) yields an identical result except that C_{3a} and $Y_a(D)$ replace C_3 and $Y(D)$. These results lead us to define a reduced stress and a reduced crack density as

$$\begin{aligned} \text{reduced stress:} & \quad \sigma_R = -\frac{k_m^{(1)}}{k_{th}^{(1)}}\sigma_0 \\ \text{reduced crack density in } [(S)/90_n]_s \text{ laminates:} & \quad D_R = -\frac{1}{k_{th}^{(1)}}\sqrt{\frac{1}{C_3 t_1 Y(D)}} \\ \text{reduced crack density in } [90_n/(S)]_s \text{ laminates:} & \quad D_R = -\frac{1}{k_{th}^{(1)}}\sqrt{\frac{1}{C_{3a} t_1 Y_a(D)}} \end{aligned} \quad (9)$$

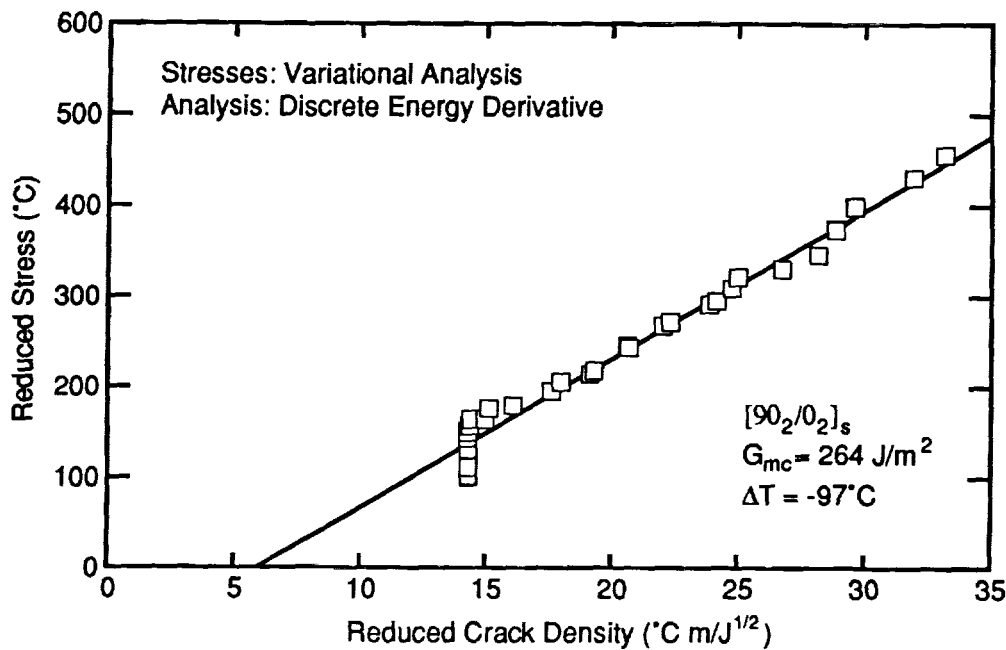


Figure 1: A master curve analysis of a $[90_2/0_2]_s$ AS4/3501-6 laminate. The energy release rate is calculated with a discrete energy derivative defined by $Y_a(D)$ in Eq. (7) using $f = 1.2$.

A plot of σ_R vs. D_R defines a master plot for microcracking experiments. If the variational analysis and energy release rate failure criterion are appropriate, a plot of σ_R vs. D_R will be linear with slope $\sqrt{G_{mc}}$ and intercept T . Because G_{mc} and T are layup independent material properties, the results from all laminates of a single material with the same processing conditions should fall on the same linear master plot.

A typical master curve analysis for a single $[90_2/0_2]_s$ AS4/3501-6 laminate is shown in Fig. 1. The master plot is linear except for a few points at the lowest crack density. The low crack density is believed to be caused by processing flaws that are not specifically included in the microcracking analysis [16]. They should be ignored when measuring G_{mc} . The straight line in Fig. 1 is the best linear fit that ignores the low crack density data. The slope gives $G_{mc} = 264 \text{ J/m}^2$ which agrees with results in other studies [16]. The intercept gives $T = -93^\circ\text{C}$. Note that a side benefit of the master curve analysis is that the value of T does not have to be assumed or measured. It can, in effect, be measured by analysis of the microcracking data.

Figure 2 gives the master plot for the 18 AS4/3501-6 laminates tested in this study. We assumed that $f = 1.2$ for all laminates and we ignored data with crack densities less than 0.3 mm^{-1} . We claim Fig. 2 verifies both the validity of an energy release rate failure criterion and the accuracy of the variational analysis calculation of G_m in Eqs. (1) and (6). There are three facts that support this claim. First, all laminates fall on a single master curve plot within a relatively narrow scatter band. The next paragraph discusses the scatter further. Second, the results for $[(S)/90_n]_s$ laminates (open symbols) agree with the results for $[90_n/(S)]_s$ laminates (solid symbols). Thus a single unified analysis can account for both the symmetric damage state in $[(S)/90_n]_s$ laminates and the antisymmetric damage state in $[90_n/(S)]_s$ laminates. Third, the slope and the intercept of the global linear fit in Fig. 2 result in $G_{mc} = 279 \text{ J/m}^2$ and $T = -93^\circ\text{C}$. Both of these results are reasonable measured values for these physical quantities.

There is an observable scatter band for the experimental points relative to the global, linear master curve. This scatter band may represent deficiencies in the analysis that need further refinement. Alternatively, we note that the scatter was caused more by a laminate to laminate variation in intercept than by a laminate to laminate variation in slope. It is thus possible that the scatter is due to real variations in T . Because all laminates were processed under identical conditions, T should be the same for all laminates. T , however, can also be interpreted as the *effective* level of residual thermal stresses. By

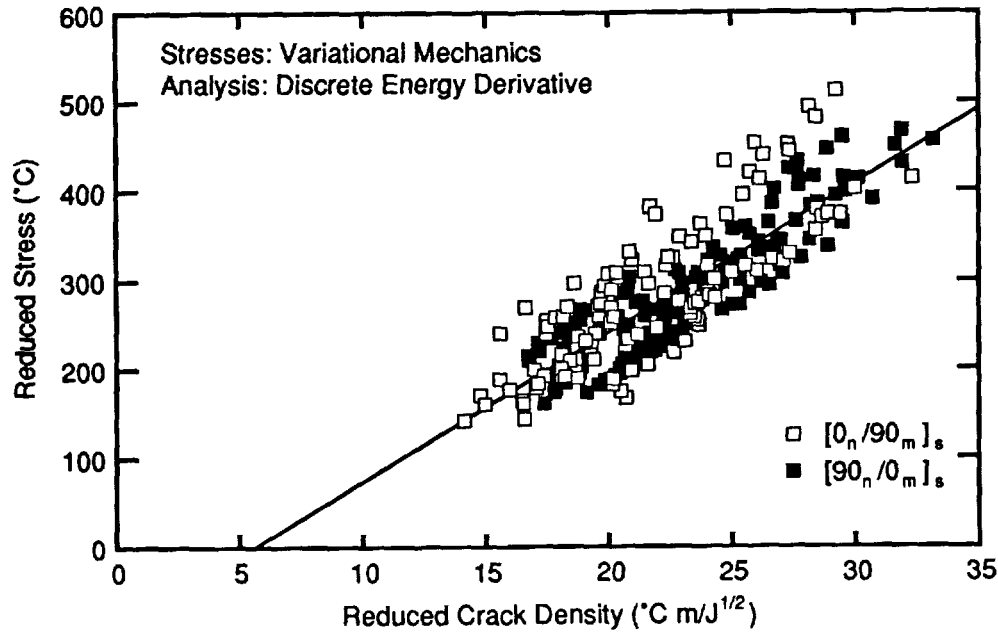


Figure 2: A master curve analysis of all AS4/3501-6 laminates. The energy release rate is calculated with a discrete energy derivative defined by $Y(D)$ or $Y_a(D)$ in Eqs. (5) and (7) using $f = 1.2$. Data for crack densities less than 0.3 mm^{-1} are not included in this plot.

Eq. (2), when $\sigma_0 = 0$ the residual stress in the 90° plies is $\sigma_{xx,th}^{(1)} = k_{th}^{(1)} T$. Although all laminates were processed under identical conditions, the laminates had different thicknesses. If the different thicknesses caused variations in thermal history, it is possible that the level of residual stresses was layup dependent. A layup dependence in T would cause the type of scatter observed in Fig. 2.

We turn next to the AS4/PEEK experiments. We tested two layups ($[90_4/0]_s$ and $[90_4/0_2]_s$) at three different temperatures (20°C , -10°C , and -50°C). Because we varied temperature, these results cannot be plotted on a single master plot. Both G_{mc} and T may be temperature dependent and thus data from different laminates would fall on lines with different slopes and intercepts. Some analyses of raw data, however, using the procedures in Refs. [16, 19] indicated that G_{mc} is independent of temperature or only weakly dependent on temperature in the range -50°C to 20°C . The major effect on the microcracking properties therefore arises from changes in the residual thermal stresses or in T . The room temperature experiments could be fit well with $T = -230^\circ\text{C}$, which is similar to the $T = -250^\circ\text{C}$ used by Liu and Nairn [16]. Assuming linear thermoelasticity from -50°C to 20°C , T at -10°C and -50°C should be -260°C and -300°C , respectively. If we accept the previous values of T as reasonable measures of the residual thermal stresses in these laminates, and we assume G_{mc} is independent of temperature, we can propose a residual stress independent master plot. We redefine the reduced stress as

$$\text{modified reduced stress: } \sigma'_R = -\frac{k_m^{(1)}}{k_{th}^{(1)}} \sigma_0 - T \quad (10)$$

A plot of σ'_R vs. D_R should be linear with a slope of $\sqrt{G_{mc}}$ and pass through the origin.

Figure 3 gives the master plot for the two AS4/PEEK laminates tested at each of the three test temperatures. We assumed that $f = 1.2$ for all laminates and we included data at all crack densities. The slope of the best fit line that is forced to pass through the origin gives $G_{mc} = 1500 \text{ J/m}^2$. The experimental results conform reasonably well to the master line and the results from the different temperatures fall on the same line. Some of the scatter may be caused by temperature variations in G_{mc} , but we do not have enough data to prove or disprove this possibility. A master plot that ignores the change in residual thermal

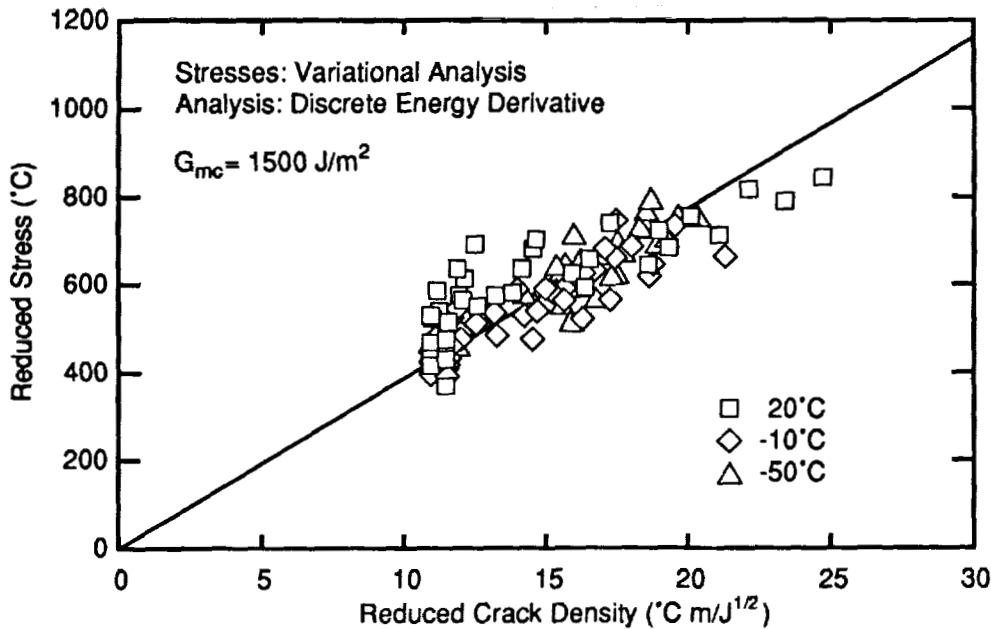


Figure 3: A master curve analysis of all AS4/PEEK laminates tested at 20°C, -10°C, and -50°C. The energy release rate is calculated with a discrete energy derivative defined by $Y(D)$ or $Y_a(D)$ in Eqs. (5) and (7) using $f = 1.2$.

stresses has two to three times the amount of scatter of the master plot in Fig. 3. These experiments thus demonstrate the real effect that residual thermal stresses have on microcracking properties of laminates. Finally, we note that previous attempts at studying microcracking in AS4/PEEK laminates used $[(S)/90_n]_s$ layups. The experiments showed only a few microcracks and yielded only a rough estimate of G_{mc} [17]. In this study the 90° plies were on the free surface instead of in the middle. The free-surface plies crack easier and we were thus able to get more experimental results and a more precise determination of G_{mc} . We recommend using $[90_n/(S)]_s$ laminates when studying microcracking in laminates with tough matrices.

OTHER MICROCRACKING THEORIES

Most previous microcracking theories are based on stress analyses that eliminate the z -dependence of the stress state by making various assumptions about the z -direction stress or displacement. The common assumptions are zero stress, zero average stress, or zero displacement. We classify any analysis using one of these assumptions as a “one-dimensional” analysis. Examples can be found in Refs. [1, 2, 5, 11, 22–30]. We note that some authors describe their analyses as “two-dimensional” analyses [25, 26, 29, 30]. In all cases, however, the second dimension is the y -dimension whose inclusion is little more than a marginal correction for Poisson’s contraction. In this section we derive master plot methods from previous literature microcracking theories and use them to analyze our AS4/3501-6 experimental results.

Garrett and Bailey [1] postulated that the next microcrack forms when the maximum stress in the 90° plies reaches the transverse strength of those plies. Using their one-dimensional, shear-lag analysis, this model yields a linear master plot defined by

$$-\frac{k_m^{(1)}}{k_{th}^{(1)}} \sigma_0 = -\frac{1}{k_{th}^{(1)}} \frac{\sigma_T}{\left(1 - \frac{1}{\cosh \Phi \rho}\right)} + T \quad (11)$$

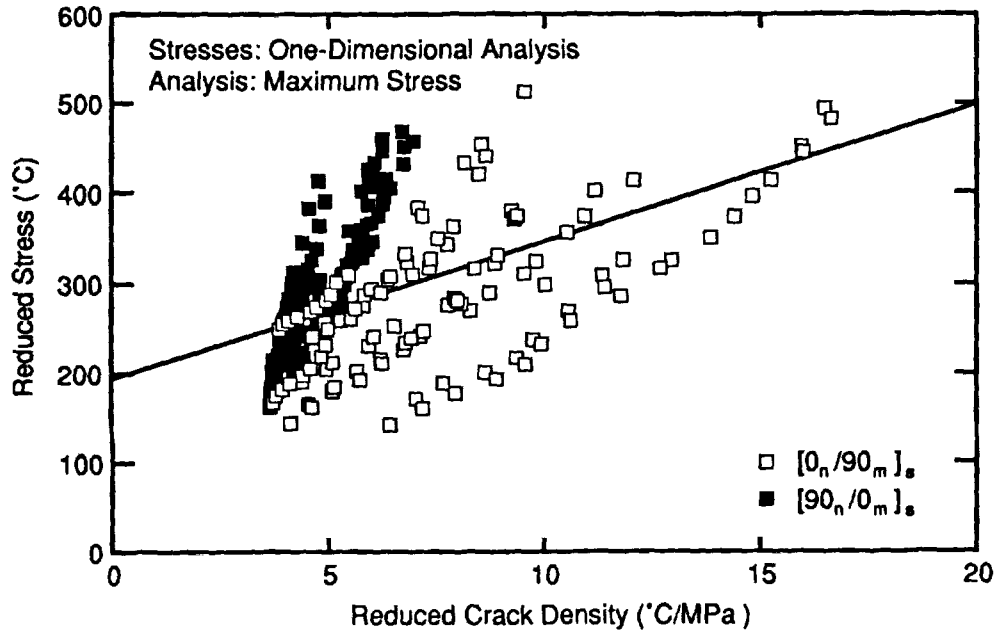


Figure 4: A master curve analysis of all AS4/3501-6 laminates using a maximum stress failure criterion and a one-dimensional stress analysis. Data for crack densities less than 0.3 mm^{-1} are not included in this plot.

where σ_T is the transverse strength of the 90° plies and $\Phi = \sqrt{G_{xz}^{(1)} C_1}$. Defining the reduced stress as in Eq. (9) and the reduced crack density as

$$\text{reduced crack density : } D_R = -\frac{1}{k_{th}^{(1)}} \frac{1}{\left(1 - \frac{1}{\cosh \Phi \rho}\right)}, \quad (12)$$

and using a master curve analysis, Eq. (11) predicts that a plot of σ_R vs. D_R should be linear with slope σ_T and intercept T .

The result of a strength theory analysis applied to our AS4/3501-6 experimental results is in Fig. 4. The master curve analysis shows the theory to be very poor. The results from individual laminates are somewhat nonlinear and they do not overlap the results from other laminates. Furthermore, the results from $[(S)/90_n]_s$ (open symbols) and $[90_n/(S)]_s$ (filled symbols) laminates segregate into two groups. This segregation is a characteristic of all one-dimensional analyses. Any analysis that ignores the z -dependence of the stress state will fail to make a distinction between inner and outer 90° ply groups. We therefore conclude that no model based on a one-dimensional stress analysis can successfully predict results for both $[(S)/90_n]_s$ and $[90_n/(S)]_s$ laminates. If we draw a least-squares linear fit through the data in Fig. 4, the slope and intercept give $\sigma_T = 15.2 \text{ MPa}$ and $T = +192^\circ\text{C}$. These results are unreasonable because the transverse tensile strength of AS4/3501-6 laminates is higher than 15.2 MPa and T must be below zero for laminates that were cooled after processing.

Because of the problems with all strength analyses, numerous authors have suggested energy failure criteria for predicting microcracking [3, 5, 13, 14, 16, 17, 19, ?, 27, 28, 30]. Caslini *et. al.* [14] used a one-dimensional stress analysis that assumes parabolic displacements in the 90° plies [23, 24] to express the structural modulus as a function of crack density. They treated crack area, $A = 2t_1 WLD$, as a continuous variable and differentiated the modulus expression to find energy release rate. Because they take an analytical derivative as a function of crack area, we refer to this approach as the "analytical derivative approach." By treating Eq. (1) as a definition of $Y(D)$, the Caslini *et. al.* [14] result for G_m can be

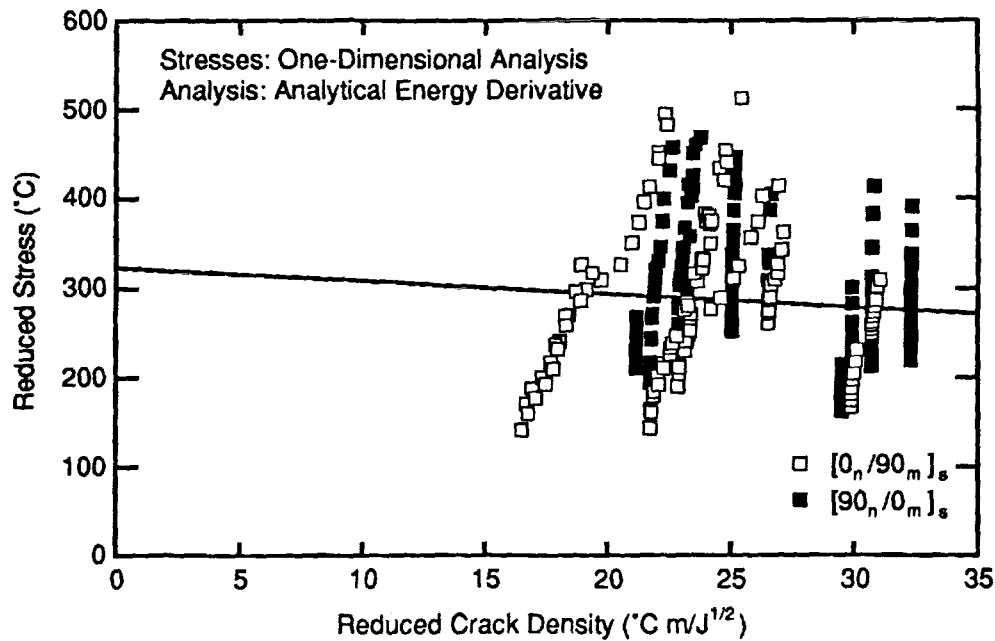


Figure 5: A master curve analysis of all AS4/3501-6 laminates using an analytical derivative energy release rate failure criterion and a one-dimensional stress analysis. Data for crack densities less than 0.3 mm^{-1} are not included in this plot.

expressed using

$$Y_{1D,a}(D) = \frac{C_1}{C_3\Phi} \left(\tanh \Phi\rho - \Phi\rho \operatorname{sech}^2 \Phi\rho \right) \quad (13)$$

where subscript “1D, a” denotes one-dimensional stress analysis and an analytical derivative approach, and $\Phi = \sqrt{3G_{zz}^{(1)} C_1}$. Han *et. al.* [27, 28] describe a similar analysis based on crack closure that gives the same G_m . Their approach is thus also an analytical derivative model.

By replacing $Y(D)$ and $Y_a(D)$ with $Y_{1D,a}(D)$ we can evaluate the microcracking models in Refs. [14, 27, 28]. The results of such an analysis applied to our AS4/3501-6 experimental results are in Fig. 5. This master curve analysis was the worst of any model we evaluated. The results from individual laminates are fairly linear but they give slopes and intercepts corresponding to toughnesses as high as 10^{12} J/m^2 and T 's that imply specimen temperatures well below absolute zero. These are clearly unreasonable results. The least-squares linear fit through the data in Fig. 5 gives $G_{mc} = 2 \text{ J/m}^2$ and $T = +323^\circ\text{C}$, both of which are unrealistic.

In the *Master Plot Analysis* section, we argued that microcracking should be analyzed using energy release rate methods. We are left with explaining why the analytical derivative approach is a complete failure. Our first attempt was to use the variational mechanics stress analysis and calculate G_m by a similar analytical derivative approach. This made slight improvements in the master curve but the overall quality and the fitting constants were still unsatisfactory. We suggest instead that the analytical derivative approach is non-physical and therefore $Y_{1D,a}(D)$ gives the *wrong* energy release rate. The analytical derivative energy release rate at a given crack density corresponds to the unlikely fracture event whereby all cracks close and then reopen again as periodic cracks with a slightly higher crack density. In real microcracking, one microcrack forms between two existing microcracks. Apparently the energy release rate for this process is dramatically different from the one calculated with an analytical derivative.

Laws and Dvorak [22] were the first to suggest modelling the actual fracture process. They calculated the change in energy associated with the formation of a new microcrack between two existing microcracks. Because they model a discrete process, we call their approach the “discrete derivative approach.” We can

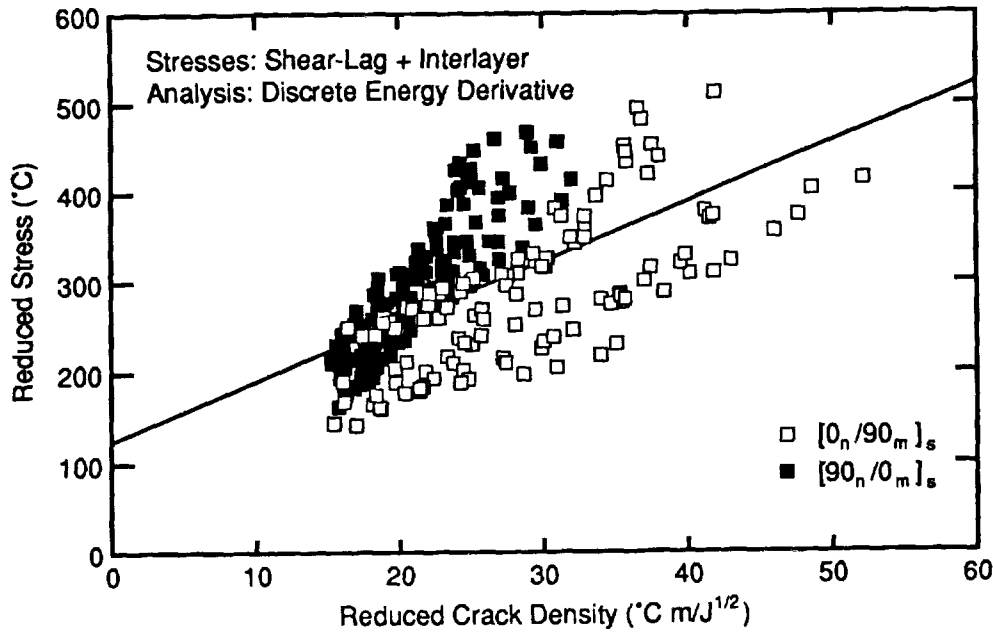


Figure 6: A master curve analysis of all AS4/3501-6 laminates using a discrete derivative energy release rate failure criterion and a one-dimensional stress analysis. Data for crack densities less than 0.3 mm^{-1} are not included in this plot.

cast Laws and Dvorak's [22] result in the form of the variational analysis by redefining $Y(D)$ to be

$$Y_{1D,d}(D) = \frac{C_1}{C_3\Phi} (2 \tanh f\Phi\rho/2 - \tanh f\Phi\rho) \quad (14)$$

where subscript "1D, d" denotes one-dimensional stress analysis and a discrete derivative approach, and f is the factor introduced earlier to account for the tendency of microcracks to prefer larger than average microcrack intervals. Following Reifsnider [2], Laws and Dvorak [22] used a shear-lag analysis that assumes an interlayer of unknown thickness and stiffness between the (S) sublaminates and the 90° plies. Their Φ can be expressed as

$$\Phi = \sqrt{\frac{Gt_1C_1}{t_0}} \quad (15)$$

where G is the shear modulus of the interlayer and t_0 is its thickness.

By replacing $Y(D)$ and $Y_a(D)$ with $Y_{1D,d}(D)$ we can evaluate the Laws and Dvorak [22] microcracking model. A drawback of their analysis is that the effective stiffness of the interlayer is an unknown parameter. Laws and Dvorak [22] suggested a circular scheme in which G/t_0 is determined by prior knowledge of G_{mc} and the stress required to form the first microcrack. Because of our concern about the sensitivity of low crack density results to laminate processing flaws, we instead used the high crack density results from the single laminate in Fig. 1 to determine G/t_0 . We varied G/t_0 until the slope of the Laws and Dvorak [22] analysis master curve gave G_{mc} equal to the variational analysis result of 280 J/m^2 . This exercise yielded $G/t_0 = 4000 \text{ N/mm}$, a linear master curve, and an intercept of $T = -73^\circ\text{C}$. These initial results were promising. The results of a master plot analysis applied to our AS4/3501-6 experimental results using $Y_{1D,d}(D)$, $G/t_0 = 4000 \text{ N/mm}$, and $f \approx 1.2$ are in Fig. 6. This master curve analysis is the most satisfactory of all previous literature models but it still has serious problems. Most importantly, the results from individual lamina do not overlap each other. As is characteristic of one-dimensional analyses, the results from $[(S)/90_n]_s$ and $[90_n/(S)]_s$ laminates segregate into two groups. The least-squares linear fit through the data in Fig. 6 gives $G_{mc} = 44 \text{ J/m}^2$ and $T = +124^\circ\text{C}$, both of which are unrealistic.

We believe the only problem with the Laws and Dvorak [22] analysis is its use of an oversimplified, one-dimensional stress analysis. If their failure criterion is implemented with the variational mechanics stress analysis, the result is equivalent to the analysis first presented by Nairn [19]. As shown in the *Master Plot Analysis* section, such an analysis gives a good master plot (see Fig. 2).

CONCLUSIONS

All analyses of composite failure can be divided into at least two separate parts. First, failure analyses must solve for the stresses in the presence of damage. These stress analyses will normally involve some simplifying assumptions. Second, to predict failure, it is necessary to assume some sort of failure criterion. The master plot analysis of microcracking shows that both the stress analysis and the failure criterion must be appropriate to be able to predict experimental results.

We considered first the stress analysis part of a failure model. Our master plot analyses in Figs. 2-3 used a two-dimensional, variational mechanics stress analysis. Such a stress analysis appears adequate for explaining microcracking. We tried numerous master plot analyses using one-dimensional stress analyses and all of them, regardless of failure criterion, gave poor results. We thus suggest that future attempts at predicting composite cracking abandon use of one-dimensional analyses and treat the variational analysis as a base-line stress analysis.

If one plots the stresses calculated by a one-dimensional analysis and those calculated by a variational analysis, the differences are marked, but hardly dramatic. We were thus initially surprised by the dramatic differences between the predictions based on the two analyses. A qualitative interpretation of the differences can follow from realizing that fracture is an instability event. When calculating instability processes, minor differences in input stresses can lead to dramatic differences in predictions. In other words, the increased accuracy in the stresses attributed to the variational analysis was crucial to the predictions of microcracking. In contrast, non-instability properties, such as plate stiffness or in-plane displacements, are much easier to predict. Researchers have been misled into believing that one-dimensional analyses are reasonably accurate due to their ability to predict such non-instability properties.

Next, we considered the failure criterion. There is a disturbing tendency of composite failure analyses to concentrate on sophisticated stress analysis or involved finite element analysis and to give too little thought to choosing the most appropriate failure criterion. As a result, one often finds complex failure models that are based on simplistic failure criteria such as maximum stress, maximum strain, average stress, point stress, or quadratic stress functions. We found that all such simplistic failure criteria gave very poor results when used to predict composite microcracking. To get a successful master plot analysis we had to use a failure criterion based on energy release rate. We further had to find the energy release rate for the actual fracture process (the discrete derivative approach). Pseudo-energy release rates, such as the analytical derivative approach, that are not derived from a realistic fracture model, give the *wrong* energy release rate, and, not surprisingly, gave poor master plot results.

We claim that microcracking, in being controlled by energy release rate, is not a unique composite failure mechanism. Instead, energy release rate is a powerful technique that should be applicable to all composite failure mechanisms. We further suggest that because energy release rate is the fundamental failure criterion, that composite failure models couched in stress-based failure criteria are doomed to inadequacy unless it can be demonstrated mathematically that the stress failure criterion is equivalent to an energy release rate criterion. A similar situation exists in the fracture of isotropic, homogeneous materials where a stress criterion or critical stress intensity factor can predict failure because it is exactly related to energy release rate. No one would consider using maximum stress, maximum strain, average stress, point stress, or quadratic stress functions to predict failure in cracked isotropic, homogeneous materials. Likewise, no one should consider using such failure criteria in composite materials.

REFERENCES

1. Garrett, K. W.; and Bailey, J. E.: Multiple Transverse Fracture in 90° Cross-Ply Laminates of a Glass Fibre-Reinforced Polyester. *J. Mat. Sci.*, vol. 12, 1977, pp. 157-168.
2. Reifsnider, K. L.: Some Fundamental Aspects of the Fatigue and Fracture Response of Composite Materials. *Proc. 14th Annual Meeting of SES, Lehigh, PA, November, 1977*, pp. 373-383.
3. Parvizi, A.; Garrett, K. W.; and Bailey, J. E.: Constrained Cracking in Glass Fiber-Reinforced Epoxy Cross-Ply Laminates. *J. Mat. Sci.*, vol. 13, 1978, pp. 195-201.
4. Parvizi, A.; and Bailey, J. E.: On Multiple Transverse Cracking in Glass-Fiber Epoxy Cross-Ply Laminates. *J. Mat. Sci.*, vol. 13, 1978, pp. 2131-2136.
5. Bailey, J. E.; Curtis, P. T.; and Parvizi, A.: On the Trans. Cracking and Long. Splitting Behavior of Glass and Carbon Fibre Epoxy X-Ply Laminates and the Effect of Poisson and Thermally Generated Strains. *Proc. R. Soc. Lond. A*, vol. 366, 1979, pp. 599-623.
6. Bader, M. G.; Bailey, J. E.; Curtis, P. T.; and Parvizi, A.: The Mechanisms of Initiation and Development of Damage in Multi-Axial Fibre-Reinforced Plastics Laminates. *Proc. 3rd Int'l Conf. on Mechanical Behavior of Materials*, vol. 3, 1979, pp. 227-239.
7. Stinchcomb, W. W.; Reifsnider, K. L.; Yeung, P.; and Masters, J.: Effect of Ply Constraint on Fatigue Damage Development in Composite Material Laminates. *ASTM STP*, vol. 723, 1981, pp. 64-84.
8. Flaggs, D. L.; and Kural, M. H.: Experimental Determination of the In Situ Transverse Lamina Strength in Graphite/Epoxy Laminates. *J. Comp. Mat.*, vol. 16, 1982, pp. 103-115.
9. Crossman, F. W.; and Wang, A. S. D.: The Dependence of Transverse Cracking and Delamination on Ply Thickness in Graphite/Epoxy Laminates. *ASTM STP*, vol. 775, 1982, pp. 118-139.
10. Highsmith, A. L.; and Reifsnider, K. L.: Stiffness-Reduction Mechanisms in Composite Laminates. *ASTM STP*, vol. 775, 1982, pp. 103-117.
11. Manders, P. W.; Chou, T. W.; Jones, F. R.; and Rock, J. W.: Statistical Analysis of Multiple Fracture in [0/90/0] Glass fiber/epoxy resin laminates. *J. Mat. Sci.*, vol. 19, 1983, pp. 2876-2889.
12. Peters, P.W.M.: The Strength Distribution of 90° Plies in 0/90/0 Graphite-Epoxy Laminates. *J. Comp. Mat.*, vol. 18, 1984, pp. 545-556.
13. Wang, A. S. D.; Kishore, N. N.; and Li, C. A.: Crack Development in Graphite-Epoxy Cross-Ply Laminates under Uniaxial Tension. *Comp. Sci. & Tech.*, vol. 24, 1985, pp. 1-31.
14. Caslini, M.; Zanotti, C.; and O'Brien, T. K.: Fracture Mechanics of Matrix Cracking and Delamination in Glass/Epoxy Laminates. *J. Comp. Tech & Research*, vol. Winter, 1987, pp. 121-132. (Also appeared as NASA TM89007, 1986).
15. Groves, S. E.; Harris, C. E.; Highsmith, A. L.; and Norvell, R. G.: An Experimental and Analytical Treatment of Matrix Cracking in Cross-Ply Laminates. *Experimental Mechanics*, vol. March, 1987, pp. 73-79.
16. Liu, S.; and Nairn, J. A.: The Formation and Propagation of Matrix Microcracks in Cross-Ply Laminates During Static Loading. *J. Reinf. Plast. & Comp.*, vol. 11, 1992, pp. 158-178.
17. Nairn, J. A.; and Hu, S.: The Formation and Effect of Outer-Ply Microcracks in Cross-Ply Laminates: A Variational Approach. *Eng. Fract. Mech.*, vol. 41, 1992, pp. 203-221.
18. Bowles, D. E.: Effect of Microcracks on the Thermal Expansion of Composite Laminates. *J. Comp. Mat.*, vol. 17, 1984, pp. 173-187.
19. Nairn, J. A.: The Strain Energy Release Rate of Composite Microcracking: A Variational Approach. *J. Comp. Mat.*, vol. 23, 1989, pp. 1106-1129. (See *errata: J. Comp. Mat.*, vol. 24, 1990, pp. 233-234).
20. Hashin, Z.: Analysis of Cracked Laminates: A Variational Approach. *Mech. of Mat.*, vol. 4, 1985, pp. 121-136.
21. Hashin, Z.: Analysis of Stiffness Reduction of Cracked Cross-Ply Laminates. *Eng. Fract. Mech.*, vol. 25, 1986, pp. 771-778.

22. Laws, N.; and Dvorak, G. J.: Progressive Transverse Cracking in Composite Laminates. *J. Comp. Mat.*, vol. 22, 1988, pp. 900-916.
23. Ogin, S. L.; Smith, P. A.; and Beaumont, P. W. R.: Matrix Cracking and Stiffness Reduction during the Fatigue of a (0/90)_s GFRP Laminate. *Comp. Sci. & Tech.*, vol. 22, 1985, pp. 23-31.
24. Ogin, S. L.; Smith, P. A.; and Beaumont, P. W. R.: A Stress Intensity Approach to the Fatigue Growth of Transverse Ply Cracks. *Comp. Sci. & Tech.*, vol. 24, 1985, pp. 47-59.
25. Flaggs, D. L.: Prediction of Tensile Matrix Failure in Composite Laminates. *J. Comp. Mat.*, vol. 19, 1985, pp. 29-50.
26. Fukunaga, H.; Chou, T. W.; Peters, P. W. M.; and Schulte, K.: Probabilistic Failure Strength Analysis of Graphite/Epoxy Cross-Ply Laminates. *J. Comp. Mat.*, vol. 18, 1984, pp. 339-356.
27. Han, Y. M.; Hahn, H. T.; and Croman, R. B.: A Simplified Analysis of Transverse Ply Cracking in Cross-Ply Laminates. *Proc. Amer. Soc. of Comp., 2nd Tech. Conf.*, 1987, pp. 503-514.
28. Han, Y. M.; Hahn, H. T.; and Croman, R. B.: A Simplified Analysis of Transverse Ply Cracking in Cross-Ply Laminates. *Comp. Sci. & Tech.*, vol. 31, 1988, pp. 165-177.
29. Nuismer, R. J.; and Tan, S. C.: Constitutive Relations of a Cracked Composite Lamina. *J. Comp. Mat.*, vol. 22, 1988, pp. 306-321.
30. Tan, S. C.; and Nuismer, R. J.: A Theory for Progressive Matrix Cracking in Composite Laminates. *J. Comp. Mat.*, vol. 23, 1989, pp. 1029-1047.

APPENDIX

In the variational mechanics analysis of [(S)/90_n]_s laminates [16, 19-21] we define the following constants:

$$C_1 = \frac{1}{E_x^{(1)}} + \frac{1}{\lambda E_x^{(2)}} \quad (16)$$

$$C_2 = \frac{\nu_{xz}^{(1)}}{E_x^{(1)}} \left(\lambda + \frac{2}{3} \right) - \frac{\lambda \nu_{xz}^{(2)}}{3E_x^{(2)}} \quad (17)$$

$$C_3 = \frac{1}{60E_z^{(1)}} (15\lambda^2 + 20\lambda + 8) + \frac{\lambda^3}{20E_z^{(2)}} \quad (18)$$

$$C_4 = \frac{1}{3G_{xz}^{(1)}} + \frac{\lambda}{3G_{xz}^{(2)}} \quad (19)$$

where $E_x^{(i)}$ and $E_z^{(i)}$ are the x - and z -direction moduli of ply group i , $G_{xz}^{(i)}$ is the $x-z$ plane shear modulus of ply group i , and $\lambda = t_1/t_2$. Superscripts (1) and (2) denote properties of the 90° plies and the (S) sublaminates, respectively. t_1 and t_2 are the ply thicknesses of the 90° and 0° ply groups. Defining $p = \frac{C_2 - C_4}{C_3}$ and $q = \frac{C_1}{C_3}$ there are two forms for the function $\chi(\rho)$. When $4q/p^2 > 1$

$$\chi(\rho) = 2\alpha\beta(\alpha^2 + \beta^2) \frac{\cosh 2\alpha\rho - \cos 2\beta\rho}{\beta \sinh 2\alpha\rho - \alpha \sin 2\beta\rho} \quad (20)$$

where

$$\alpha = \frac{1}{2} \sqrt{2\sqrt{q} - p} \quad \text{and} \quad \beta = \frac{1}{2} \sqrt{2\sqrt{q} + p} \quad (21)$$

When $4q/p^2 < 1$

$$\chi(\rho) = \alpha\beta(\beta^2 - \alpha^2) \frac{\tanh \alpha\rho \tanh \beta\rho}{\beta \tanh \beta\rho - \alpha \tanh \alpha\rho} \quad (22)$$

where

$$\alpha = \sqrt{-\frac{p}{2} + \sqrt{\frac{p^2}{4} - q}} \quad \text{and} \quad \beta = \sqrt{-\frac{p}{2} - \sqrt{\frac{p^2}{4} - q}} \quad (23)$$

In the variational mechanics analysis of $[90_n/(S)]_s$ laminates [17] we define some new constants:

$$C_{2a} = -\frac{\nu_{xz}^{(1)}}{3E_x^{(1)}} + \frac{\nu_{xz}^{(2)}}{E_x^{(2)}} \left(1 + \frac{2\lambda}{3}\right) \quad (24)$$

$$C_{3a} = \frac{1}{20E_z^{(1)}} + \frac{\lambda}{60E_z^{(2)}} (8\lambda^2 + 20\lambda + 15) \quad (25)$$

$$C_1^* = \frac{1}{E_x^{(1)}} + \frac{(1+2\lambda)^2}{\lambda^3 E_x^{(2)}} \quad (26)$$

$$C_2^* = -\frac{\nu_{xz}^{(1)}}{3E_x^{(1)}} + \frac{\nu_{xz}^{(2)}}{E_x^{(2)}} \left[\frac{(1+2\lambda)(2+\lambda)}{3\lambda} \right] \quad (27)$$

$$C_3^* = \frac{1}{20E_z^{(1)}} + \frac{\lambda}{60E_z^{(2)}} (2\lambda^2 + 7\lambda + 8) \quad (28)$$

$$C_4^* = \frac{1}{3G_{xz}^{(1)}} + \frac{1+\lambda+\lambda^2}{3\lambda G_{xz}^{(2)}} \quad (29)$$

The function $\chi_a(\rho)$ is expressed in terms of $\chi(\rho)$ and $\chi^*(\rho)$ as

$$\chi_a(\rho) = \frac{2\chi\left(\frac{\rho}{2}\right)}{1 + \frac{C_3\chi\left(\frac{\rho}{2}\right)}{C_3^*\chi^*\left(\frac{\rho}{2}\right)}} \quad (30)$$

where $\chi(\rho)$ is defined above except that we must redefine $p = \frac{C_{2a}-C_4}{C_{3a}}$ and $q = \frac{C_1}{C_{3a}}$. Defining $p^* = \frac{C_2^*-C_4^*}{C_3^*}$ and $q^* = \frac{C_1^*}{C_3^*}$, the new function $\chi^*(\rho)$ has two forms. When $4q^*/p^{*2} > 1$

$$\chi^*(\rho) = 2\alpha^*\beta^* (\alpha^{*2} + \beta^{*2}) \frac{\cosh 2\alpha^*\rho + \cos 2\beta^*\rho}{\beta^* \sinh 2\alpha^*\rho - \alpha^* \sin 2\beta^*\rho} \quad (31)$$

When $4q^*/p^{*2} < 1$

$$\chi^*(\rho) = \alpha^*\beta^* (\beta^{*2} - \alpha^{*2}) \frac{1}{\beta^* \tanh \alpha^*\rho - \alpha^* \tanh \beta^*\rho} \quad (32)$$

In the previous four equations, α^* and β^* are given by Eq. (21) and (23) with p and q replaced by p^* and q^* .

Establishing the Relationship Between Manufacturing and Component Performance in Stretch Formed Thermoplastic Composites

Michael H. Santare, R. Byron Pipes,
A. J. Beaussart, D. W. Coffin, B. J. O'Toole, S. F. Shuler

Department of Mechanical Engineering and
Center for Composite Materials
University of Delaware

56-24
51406

Flexible manufacturing methods are needed to reduce the cost of using advanced composites in structural applications. One method that allows for this is the stretch forming of long discontinuous fiber materials with thermoplastic matrices. In order to exploit this flexibility in an economical way, a thorough understanding of the relationship between manufacturing and component performance must be developed. This paper reviews some of the recent work geared toward establishing this understanding. Micromechanics models have been developed to predict the formability of the material during processing. The latest improvement of these models includes the viscoelastic nature of the matrix and comparison with experimental data. A finite element scheme is described which can be used to model the forming process. This model uses equivalent anisotropic viscosities from the micromechanics models and predicts the microstructure in the formed part. In addition, structural models have been built to account for the material property gradients that can result from the manufacturing procedures. Recent developments in this area include the analysis of stress concentrations and a failure model each accounting for the heterogeneous material fields.

Motivation

The extraordinary properties of collimated fiber composites consisting of continuous fibers suspended in polymeric matrices have been widely acclaimed during the past two decades. These materials were made possible by the invention of synthetic fibers which possess specific strengths significantly greater than conventional monolithic materials. The recent introduction of thermoplastic polymer matrices now offers the potential to develop manufacturing methods for these new composite materials that can take advantage of lower cost conventional manufacturing methods.

Sheet forming of metallic materials is one of the most pervasive manufacturing methods in the contemporary manufacturing technology. However, unlike monolithic metallic sheet, continuous fiber composites possess direction of inextensibility in the fiber direction. For these material systems the dominant modes of deformation during sheet forming are shearing. Extensibility in the fiber direction can, however, be provided by introducing breaks along the fiber length so that the individual fibers are made discontinuous [1]. The development of extensibility in the fiber direction for the collimated fiber composite results in enhanced formability of multiaxial sheet products.

The objective of the present work is to develop the science base for a series of models that can be used to link manufacturing with structural performance. This is shown schematically in Figure 1.

Micromechanics Analysis

The primary objective of the micromechanics analysis is to develop relationships between the primary anisotropic viscosities, η_{ij} and the properties of the oriented fiber assembly and matrix fluid. There have been many studies of the flow of dilute suspensions of fibers and particles in

liquids, for example by Metzner [2] and recently Rogers [3]. The micromechanical analysis presented here, however, addresses a collimated, discontinuous fiber assembly suspended in a viscous matrix fluid which is subjected to relatively small total strains.

Consider an aligned fiber assembly wherein long discontinuous and rigid fibers are arranged in a regular cross-sectional geometry (hexagonal or square array) and suspended in a viscous fluid (Figure 2). At the interface between the fibers and matrix fluid, a no slip condition is assumed. In addition, it is assumed that neighboring fibers can be treated as if they were arranged so that fiber ends in one row are next to fiber centers in adjacent rows. This geometry is possible for a square array, but not for a hexagonal array, where the assumption must be regarded as a simplifying approximation.

Fiber Array Geometric Relations

Consider the geometric arrangements of fibers. For fibers of diameter, D , and arranged in a fixed pattern where the spacing between fibers, S , then the fiber volume fraction, f , is given as:

$$f = F \left(\frac{D}{S}\right)^2 \text{ where } F = \begin{cases} \frac{\pi}{2\sqrt{3}} & \text{(hexagonal array)} \\ \frac{\pi}{4} & \text{(square array)} \end{cases} \quad (1)$$

The following fiber volume fraction parameter is now introduced:

$$\kappa = \frac{1}{1 - \sqrt{f/F}} \quad (2)$$

Effective Viscosities of Oriented fiber Assembly Newtonian Matrix Fluids

If a linear variation in velocity in the direction of the fibers is imposed upon the oriented fiber assembly, the relative velocity of adjacent fibers may be determined by assuming that the fibers travel at the velocity of their centroids (Figure 3). Hence, the relative velocity of two adjacent fibers of length L is given as,

$$\Delta \dot{u} = \dot{\epsilon}_1 L/2 \quad (3)$$

where $\dot{\epsilon}_1$ is the extensional strain rate of the fiber assemblage. Therefore the apparent shear strain rate in the fluid contained between the nearest points of two adjacent fibers is

$$\dot{\gamma} = \frac{(L/D) [\kappa - 1] \dot{\epsilon}_1}{2} \quad (4)$$

The induced shearing strain rate, $\dot{\gamma}$, generates a shearing stress, τ , on the fiber surfaces equal to the product of the fluid shear viscosity, η , and the strain rate, $\eta\dot{\gamma}$. At a cross-section through the fiber midpoints, half of the fibers will carry the total load, and so the fiber tensile stress at the midpoint will be $2\sigma/f$, where σ is the average stress in the system. This force equilibrium implies that the tensile force at the fiber midpoint must equal the total surface shear force over a length $L/2$. This results in the following equation,

$$\tau = \frac{\sigma}{f} (D/L) \quad (5)$$

Combining Equations (1-5) yields the expression for the elongational viscosity, η_{11} , as listed in Table 1.

In order to develop simple relations for the effective shearing viscosities, the fibers are again assumed to behave rigidly and a no slip condition is assumed at the fluid fiber interface. By imposing pure steady state shearing motion, the shearing strain rate of the matrix fluid can be geometrically related to the effective shearing strain rate of the fiber-fluid unit cell. For a Newtonian viscous fluid the shear stress is related to the fluid strain by $\tau = \eta \dot{\gamma}$. This leads to the Newtonian expressions for η_{12} and η_{13} listed in Table 1.

Following the development for the effective transverse shearing viscosity, η_{23} , the effective transverse elongational viscosity, η_{22} , may be determined (for $\eta_{11} \gg \eta_{22}$) and is listed again in Table 1.

Power-Law Matrix Fluids

The previous relationships have all been developed assuming a matrix fluid which follows Newtonian behavior. Consider next the constitutive relations for a matrix fluid which takes the non-Newtonian form of a simple power-law with yield stress, τ_0 :

$$\tau = \eta \dot{\gamma}^m + \tau_0 \quad (6)$$

Incorporating this expression, the anisotropic viscosities for the assembly with power-law fluid can be developed. (See Table 1.)

Carreau Model Matrix Fluids

A deficiency of the simple power-law constitutive relation for a shear thinning fluid is its lack of a finite zero-shear viscosity. Carreau [4] has introduced the following empirical rheological model to describe the non-Newtonian behavior of such a fluid:

$$\eta = \bar{\eta}_0 [1 + (\bar{\lambda} \dot{\gamma})^2]^{(n-1)/2} \quad (7)$$

Where $\bar{\eta}_0 = \eta_0 A_T$, $\bar{\lambda} = \lambda A_T$ with the temperature shift factor $A_T = \exp \xi[(T_0-T)/T]$. The parameters η_0 , λ , n and ξ are determined empirically. The onset of non-linearity is determined by the time constant $\bar{\lambda}$ and the exponent n determines the degree of non-linearity. The value $n=1$ corresponds to a Newtonian fluid and as n decreases the fluid exhibits increased shear thinning. Employing this matrix constitutive relation and again assuming a linear velocity gradient for the

matrix fluid, it is possible to derive new expressions for effective viscosities of the medium as listed in Table 1.

Comparison of Predicted Viscosities to Experimentally Obtained Data

Binding [5] has measured the shearing viscosity versus strain rate for neat polypropylene at 200°C. Employing a least squares approximation, the Carreau equation was fit to the Binding data and the Carreau parameters were determined. A comparison between the Binding data and the Carreau model prediction is shown in Figure 4.

Binding also measured the elongational and shear viscosities of a 25 volume percent glass fiber/polypropylene melt (200°C) suspension utilizing a converging flow orifice die and a capillary die, respectively. When the parameters determined from the curve fit above are combined with the Carreau equations from Table 1, the elongational and shearing viscosities of the glass fiber/polypropylene suspension can be predicted as a function of strain rate. The measured and predicted elongational viscosities of the polypropylene/glass suspension as a function of strain rate are shown in Figure 5. The model predictions shown in Figure 5 correspond to a maximum fiber packing fraction, F , of 0.846 (an average of square and hexagonal array values).

Binding noted that the average fiber aspect ratio of the suspension was 588 prior to the test. Due to fiber breakage which occurred during the flow the post-extrusion fiber aspect ratio was approximately 200. The two predictions for L/D of 588 and 200 bound the data.

The shear rate in the matrix fluid is amplified by the presence of the fibers. For the range in elongational rates of 10^0 to 10^2 s^{-1} in this suspension, the corresponding shear rate in the matrix fluid viscosity is 10^2 to 10^4 s^{-1} . To achieve a better description of the matrix fluid viscosity in the 10^2 to 10^4 s^{-1} shear rate range, a new set of Carreau parameters were chosen.

A summary of the predictions for the anisotropic viscosities of the suspension are shown in Figure 6. Several observations should be made regarding these predictions. First, the prediction for an average aspect ratio (L/D) of 360 shows excellent agreement with the Binding Data. Second, at low shear rates, the elongational viscosity, η_{11} , is approximately 10^4 Pa-s greater than the shearing viscosities of the suspension.

The agreement between the developed relations and the Binding data offer strong support for their validity. This ability to predict the effective viscosities of anisotropic thermoplastic sheet materials by knowing the rheological behavior of only the matrix polymer should prove valuable in the sheet forming technology.

Review of Finite Element Analysis for Forming Processes

Thermoforming of advanced thermoplastic composites has many similarities to metal sheet forming technology. The use of computer-aided techniques in the metal-forming industry has increased considerably in the last several years. The finite element method has become a common tool for the simulation of sheet metal forming processes. The analysis provides useful information about the forming rates, stress and strain distributions. They are also helpful in predicting optimum process conditions and in designing dies and equipment.

The first approach to analyze a metal-forming process is to treat the metal as a deformable solid and to use the displacements as the primary variables. This solid mechanics approach is based on the use of elasto-plastic models.

Elastic effects can be neglected in most metal-forming processes where large, permanent deformations occur. For such cases, a viscoplastic model is adopted to describe the behavior of the deforming material. A general numerical finite-element solution was presented in 1979 by Zienkiewicz and Godbole for viscoplastic materials [6]. This second approach is usually referred to as the flow formulation for forming processes. In this technique, the material is treated as a viscous medium and the velocities are the primary variables. Since the behavior of the composite system at its forming temperature is described in the present work by the constitutive equation for a

viscous, anisotropic medium, it is thus logical to apply the flow formulation to this material. The high degree of anisotropy must be, however, taken into account.

In the flow formulation, the finite element discretization is attained using an analogy with solid mechanics [7] that will be summarized briefly here. The equilibrium equation for an elastic solid is also valid for a viscous medium if dynamic effects are neglected. This is the case for relatively slow forming processes.

In fluid mechanics, the strain-rates are defined by the spatial derivatives of the velocity, v :

$$\dot{\epsilon}_{ij} = \frac{1}{2} \left(\frac{\partial v_i}{\partial x_j} + \frac{\partial v_j}{\partial x_i} \right) \quad (8)$$

This expression is similar to that of strains in the solid mechanics formulation for small deformation problems.

$$\epsilon_{ij} = \frac{1}{2} \left(\frac{\partial u_i}{\partial x_j} + \frac{\partial u_j}{\partial x_i} \right) \quad (9)$$

where u is the displacement.

The constitutive equation for a non-Newtonian viscous fluid is used to describe viscoplastic materials. It can be expressed as

$$\dot{\epsilon}_{ij} = \frac{1}{2\mu} (\sigma_{ij} - \delta_{ij}P) \quad (10)$$

where P is the pressure term and μ is the viscosity of the medium. For incompressible elasticity, the constitutive equation can be written in the following form:

$$\epsilon_{ij} = \frac{1}{2G} (\sigma_{ij} - \delta_{ij}P) \quad (11)$$

The constitutive relationships 10 and 11 have an identical form. There is thus an analogy between incompressible elasticity and creeping flow problems. This analogy allows the adaptation of the finite element technique and programs used in elasticity for viscous flow problems [7]. Strains are simply replaced by strain-rates, displacements by velocities, and the elastic shear modulus G by viscosity, μ .

Numerical Modeling for Thermoplastic Composites

The flow formulation briefly described in the previous section can be combined with the plane stress assumption to model forming processes of thin sheets with plate or shell finite elements. This combination was first introduced in 1983 by Onate and Zienkiewicz [8] in their viscous shell model for metal sheet-forming. In this technique, the constitutive equation for a creeping flow is simplified by the plane stress assumption as in shell theory. Large deformations of viscoplastic sheets are then studied as a series of small deflection steps, each being analogous to a small deformation elastic problem. These authors restricted their study to isotropic metals although they mentioned the validity of their method for anisotropic materials if the rotation of the principal axes of anisotropy is considered.

The constitutive relations introduced in the previous sections are adapted in the present study to perform a finite element analysis derived from the method introduced for sheet metal forming. The following scheme is proposed:

1. Solve for the velocity field "V" in the initial geometry using analogy to elasticity;
2. Update the geometry by "VΔt" where Δt is an appropriate time step;
3. Update the sheet thickness using the incompressibility condition;
4. Update the local fiber orientations;
5. Change the boundary conditions if new points come into contact with a mold surface;
6. Repeat the procedure for the new configuration.

An independent problem is solved at each stage of the deformation in a given configuration. This approximation is reasonable if the time step Δt is chosen so as to limit the displacements to small values. Each stage corresponds then to a small deformation elastic problem. Very large deformations can be followed with this procedure. However, the updating of the mesh may lead to mesh distortion and it may be therefore necessary to redefine the mesh at some point. It should be also noted here that at the present time the problem solved at each stage of the deformation is linear. However, the non-linear constitutive relations may be adapted. An iterative technique is then used at each stage of the solution scheme, as is the case of viscoplastic metals.

2-D Plane Stress Model

The applicability of the flow approach to the case of highly anisotropic materials has been first studied with a 2-D plane stress finite-element code. To take into account the fiber orientation change during the deformation, a vector is associated in this model with each element and represents the local fiber orientation. Because of the high fiber volume ratio, it is reasonable to assume that the fiber orientation moves as a material line. The displacement of the orientation vector is computed after each time step by analogy with elasticity. Consider the vector F denoting the fiber orientation in the mth element. F forms an angle θ with the x-axis of the global referential frame in the initial geometry. The components of F are given after a time-step Δt by:

$$F'_x = \cos\theta_m + \dot{\epsilon}_x \Delta t \cos\theta_m + \dot{\epsilon}_{xy} \Delta t \sin\theta_m - \dot{\omega}_{xy} \Delta t \sin\theta_m \quad (12)$$

$$F'_y = \sin\theta_m + \dot{\epsilon}_{xy} \Delta t \cos\theta_m + \dot{\epsilon}_y \Delta t \sin\theta_m + \dot{\omega}_{xy} \Delta t \sin\theta_m \quad (13)$$

where

$$\dot{\epsilon}_x = \frac{\partial U}{\partial x} \quad \dot{\epsilon}_y = \frac{\partial V}{\partial y}$$

$$\dot{\epsilon}_{xy} = \frac{1}{2} \left(\frac{\partial V}{\partial x} + \frac{\partial U}{\partial y} \right) \quad \dot{\omega}_{xy} = \frac{1}{2} \left(\frac{\partial V}{\partial x} - \frac{\partial U}{\partial y} \right)$$

The velocity field is denoted by U and V in this case. The rotation term $\dot{\omega}_{xy}$ is computed numerically in the same way as the strain rates by using the derivatives of the velocities modeled with the shape functions.

The simulation of an off-axis tensile test for a viscous fiber assembly illustrates well this 2-D model. Figure 7 shows the initial geometry of this example. The initial fiber orientation is 45 degrees. The following theoretical properties are employed: $\eta_{11} = 20\eta_{22}$ and $\eta_{22} = 3\eta_{12}$. The

element chosen here is a nine-node quadratic element with nine integration points. The mesh has 16 elements, and the time step is 2.5 sec. A normal velocity of 1 sec^{-1} is applied to the edge 2-3. The edge 1-4 is clamped. The deformed geometry at different stages is shown in Figure 8. Note that each element is divided in four parts in that figure. The fiber orientation at the center of each element is presented in Figure 9. The fiber orientation varies between 25 and 40 degrees in the geometry obtained after 50 percent of elongation. Although the mesh is quite coarse, this simple example shows clearly the importance of taking into account the fiber rotation during the deformation in the numerical model. The simulation of the web of a curved beam in a thermoforming process and the extension of the present model to the use of continuous fiber systems are discussed in reference [9].

Structural Analysis of Manufactured Components

Manufacturing processes such as sheet forming and stretch forming can be used to produce a variety of composite parts. The use of a long discontinuous fiber material system allows for material stretching over complex curvature parts while maintaining a high percentage of the continuous fiber material properties [10]. Combination of these forming methods and material system allows the production of complex structures such as curved beams as shown in Figure 10. The microstructure of a curved beam is sensitive to the production method and gradients in material properties are expected in both sheet formed [11] and stretch formed [12] beams. Schematic examples of two types of heterogeneity are shown in Figure 11; analysis of these types of beams can be useful in determining the effect of such property gradients on the overall performance of a given beam.

In the following section, the results of two separate analyses are reviewed. The first uses a closed form stress potential approach [13] to investigate the effect of radial heterogeneity on curved beams loaded in pure bending. The stress state is found for beams which can have several different geometries including I, J, T, and rectangular cross-sections. Material properties can be specified independently for each section of the beam, i.e., flange and web can have different properties. Each section of the beam is treated as an individual curved rectangular beam loaded in pure bending and with a constant distributed load on the curved surfaces. Superposition is used to combine the results of the individual sections into the total beam solution. Details of the analysis are provided in reference [11]. Results are shown for comparison with known solutions.

The second analysis technique uses a Rayleigh-Ritz approach [14] to solve the minimum potential energy equation for several curved beam problems including pure bending and a beam with a uniform distributed load. This is an approximate solution which uses an assumed series formulation of the displacement field. The advantage of this method is that it allows for any type of material heterogeneity and can be used to solve other relevant problems such as tensile loaded beams or beams with geometric stress concentrations such as cutouts.

Analysis results have been compared to solutions found by using mechanics of materials and finite element methods. The mechanics of materials solutions are useful for comparing results for beams with homogeneous material properties and the finite element analysis is necessary to solve the problem when the beam has heterogeneous material properties. The first type of analysis has been incorporated into a design tool for analyzing curved beams loaded in pure bending. A wide range of geometric parameters and material properties can be analyzed with relative ease. The second type of analysis is being developed so that a similar tool can be used to analyze curved beams with different loading conditions or geometric configurations.

Results of Structural Analysis

The superposition model, which is used to find stresses and displacements in a curved beam loaded in pure bending, has been verified by comparing results with mechanics of materials and finite element analysis solutions. Several example problems of isotropic beams having I-, T-, or rectangular cross-sections have been examined and the difference between the superposition and

mechanics of materials solutions is less than 1% for all cases. Two-dimensional finite element analysis is used to compare results for a curved heterogeneous anisotropic J-beam. The heterogeneity is introduced into the finite element analysis by varying the material properties in each element of the model.

The validity of the model has been demonstrated and the effect of radial heterogeneity on beam performance can now be determined. The maximum tangential stress and maximum displacement versus heterogeneity are found for a curved J-beam loaded in pure bending. The degree of heterogeneity is varied from approximately a 20% decrease to a 20% increase in stiffness along the radial dimension. The effect of material heterogeneity is highly dependent on the beam geometry which is characterized by the average radius to depth ratio, R/t . Heterogeneity has a considerable effect on the maximum tangential stress in beams with a small radius of curvature, $R/t = 1$, while it has virtually no effect on the stresses in beams with a large radius of curvature. The maximum displacement is effected by heterogeneity for all beam geometries considered, but, the effect is again seen more drastically in beams with small curvature.

The Rayleigh-Ritz technique is used to solve the problem of a curved beam loaded by internal and external pressure. Solutions are compared with exact results for isotropic and axisymmetric anisotropic beams [13], and the difference is within 0.1%. This solution technique is also verified by solving the problem of an infinite plate with a centrally located hole loaded only by an internal pressure where the principle material directions are along the Cartesian axes. This problem is modeled by letting $r_i = 2.54$ cm, $r_o = 76$ cm, $P_i = 1$ Pa, and $P_o = 0$ Pa. The stress concentrations found at $\theta = 0^\circ$ and 90° are within 1% of those found by Lekhnitskii, [13]. A carbon reinforced thermoplastic composite ring with an inner radius of 15.2 cm and an outer radius of 20.3 cm is analyzed for two different fiber arrangements, one with tangentially oriented fibers and the second with fibers aligned in the x-direction. The stress distribution is axisymmetric in the ring with tangentially oriented fibers as shown in Figure 12a while the ring with straight fibers in the x-direction has a slight stress concentration at approximately $\theta = 45^\circ$ as shown in Figure 12b. These results are evidence that the tangential heterogeneity due to non-axisymmetric fiber distribution can effect the stresses in a curved beam loaded by internal and external pressure.

The Rayleigh-Ritz technique is also used to solve the problem of a curved beam loaded in pure bending. Results for isotropic beams compare to within 1% of the elasticity solutions. Results for anisotropic beams with the principle fiber directions along the polar axes also compare to within 1%. The results for beams having heterogeneous material properties are currently being compared to finite element analysis solutions.

Introduction To Notched Composites Failure Theories

The tensile failure of notched composite plates has been studied by many researchers. Waddoups, et al. [15] applied linear elastic fracture mechanics to notched composites. They assumed an intense energy region to exist at the hole which is represented by a characteristic length, 'a'. A crack of length 'a' is used to represent this region and the stress intensity factor, K_1 , is used to predict the notched strength. A parametric study is conducted to determine the effect of 'a' and find which value best represents experimental data.

Nuismer, et al. [16-19], used similar methods known as the point and average stress criteria. These methods use the stress distribution for an infinite plate with a circular hole subject to uniaxial tension. A stress concentration of 3 is obtained for all hole sizes, but the stress intense region is very localized for smaller holes. A larger volume of material is subject to a concentrated stress for plates with a larger hole. Experimental results verify that plates with larger holes have a smaller fracture stress. The point stress criteria assumes that the notched strength is obtained when the stress at a certain distance away from the hole edge, d_0 , reaches the unnotched strength. The average stress criterion assumes that the notched strength is obtained when the average of the stress over a certain distance in front of the hole, a_0 , reaches the unnotched strength.

These methods and several others not mentioned are empirical failure theories. They rely on some parameter which has to be chosen so that the theory matches the experimental data. They

can not be determined from basic material data. Backlund [20] developed the fictitious crack model, which only uses fundamental material parameters such as stiffnesses, unnotched strength σ_0 , and fracture energy G_c , to predict the notched strength of composites. The fracture energy, G_c , is used to represent all the micromechanical fracture mechanisms and damage accumulating in the stress intense region at the edge of the notch. Backlund and Aronsson [21, 22] use this method to model the entire crack formation process. The failure load can also be determined for various shapes of notches.

The Fictitious Crack Model

The basic principle of this method is to model all of the microcracks and local fractures as one fictitious crack with closing stresses acting on its surfaces as shown in Figure 13. The fictitious crack is formed when the unnotched tensile strength s_0 of the material is exceeded. The crack opening, $2v$, increases as the load is increased and the closing stresses are reduced. The relationship between this stress and the crack opening is shown in Figure 14. The stress at the tip of the crack is always equal to the unnotched fracture stress and the closing stress is assumed to be a linearly decreasing function of the crack opening, $2v$. The area under the $s-v$ curve is equal to the fracture energy, G_c . The closing stress is reduced to zero at a limiting value of the crack opening, v_c , and at this point a real crack is assumed to form. Backlund and Aronsson studied several different functional relations between s and v ; the linear relation provided the best approximation to experimental data. The applied load is increased and the crack grows in a stable manner at first and after a critical load it begins to grow in an unstable manner. This critical load is taken as the failure load.

The Numerical Technique

The fictitious crack failure prediction is carried out using finite element analysis. The problem of a rectangular plate with a circular hole is used as an example. Only a quarter of the plate needs to be analyzed due to symmetry and the crack path is assumed to be horizontal as shown in Figure 15. The external load is introduced into the plate by a displacement, d . A stiffness matrix relating external displacement d and crack openings v_i to external load P and crack surface loads F_i is obtained using finite element analysis as shown in Equation 14.

$$\begin{bmatrix} P \\ F_1 \\ F_2 \\ F_3 \\ F_4 \\ F_5 \end{bmatrix} = \begin{bmatrix} k_{11} & k_{12} & k_{13} & k_{14} & k_{15} \\ k_{21} & k_{22} & k_{23} & k_{24} & k_{25} \\ k_{31} & k_{32} & k_{33} & k_{34} & k_{35} \\ k_{41} & k_{42} & k_{43} & k_{44} & k_{45} \\ k_{51} & k_{51} & k_{51} & k_{51} & k_{55} \\ k_{61} & k_{61} & k_{61} & k_{61} & k_{65} \end{bmatrix} \begin{bmatrix} d \\ v_1 \\ v_2 \\ v_3 \\ v_4 \end{bmatrix} \quad (14)$$

All of the crack openings, v_i , are initially set equal to zero representing the undamaged plate. The initiation of damage occurs when the stress at node 1 is equal to the unnotched strength, s_0 . The corresponding nodal force, F_1 , is taken as $(\sigma_0 b t)/2$, where b is the distance between nodes and t is the plate thickness. The external displacement which causes this initiation of damage is found from the second row of equation 1, $d^1 = F_1/k_{21}$ and the corresponding external load is found from row 1, $P^1 = F_1 k_{11}/k_{21}$.

The next step is to allow the crack to open at node 1 and to calculate the external load which makes $F_2 = (\sigma_0 b t)$. Equation 1 can be simplified as shown below since $v_2, v_3,$ and v_4 are equal to zero.

$$\begin{bmatrix} P^2 \\ F_1 \\ \sigma_0 b t \end{bmatrix} = \begin{bmatrix} k_{11} & k_{12} \\ k_{21} & k_{22} \\ k_{31} & k_{32} \end{bmatrix} \begin{bmatrix} d^2 \\ v_1 \end{bmatrix} \quad (15)$$

The relationship between F_1 and v_1 is known from the assumed linear function in Figure 14, $F_1 = (\sigma_0 b t)/2(1 - v_1/v_c)$. Therefore the second two rows of Equation 15 can be solved simultaneously for the two unknowns d^2 and v_1 . The corresponding external load P^2 is then determined from row 1. This procedure is repeated by increasing the crack length by one node at each step.

By coupling this damage zone model with the structural analyses described previously, a failure prediction model for heterogeneous structures can be developed. This work is currently underway.

Conclusions

The effective viscosities were shown to be functions of the fiber aspect ratio, the fiber volume fraction, and the matrix fluid shearing viscosity. The elongational viscosity of the suspension was found to vary as the square of the fiber aspect ratio while the shearing viscosities of the suspension were not related to fiber aspect ratio. All the anisotropic viscosities showed a complex relationship to fiber volume fraction. For a Newtonian fluid, the effective shearing viscosity of the fiber filled fluid can be related to the matrix viscosity through the factor κ , which depends only on the fiber volume fraction and packing geometry. However, the shearing viscosities of many polymeric fluids exhibit Newtonian behavior at low strain rates and power-law behavior at higher strain rates. Consequently, relations were needed for suspensions in which the matrix fluid exhibited non-Newtonian shear thinning behavior. This has been accomplished by considering an assembly of fibers suspended in a power-law fluid with finite yield stress. The relations for predicting the effective viscosities were then extended to include zero-shear viscosity and temperature dependence through incorporating the Carreau model into the existing relations.

The numerical analysis for sheet forming of long, discontinuous fiber reinforced thermoplastics has been investigated in this research. These materials are modeled at their forming temperature as a highly anisotropic, viscous medium. This study demonstrates that a finite element technique developed for the simulation of metal sheet forming processes can be adapted to the case of advanced thermoplastic composites. The first results of the implementation of the proposed method into an existing finite element code are shown. Comparison with experimental results is currently under study. The technique described in this study is believed to show great promise for the future as a helpful tool to study the manufacturing of long, discontinuous fiber reinforced thermoplastics and, possibly, continuous fiber systems. Future studies will include the extension of this work to the case of multidirectional laminates as well as the adoption of the more accurate models for the constitutive equation.

A closed form elasticity solution can be used to solve for the stresses and displacements in a heterogeneous anisotropic curved beam loaded in pure bending. The elasticity analysis, based on the superposition of several two-dimensional solutions, provides results which are in very good agreement with those found from mechanics of materials and finite element analysis. The effect of radial heterogeneity on curved beams loaded in pure bending depends on the geometry of the beam. The maximum stress and deflection in beams with a small average radius to depth ratio is significantly effected by heterogeneous material properties. It is unlikely, however, that radial heterogeneity effects the elastic behavior of most beams used in transport aircraft fuselage

applications since they have an $R/t > 10$; but this heterogeneity could play a part in the failure behavior.

The Rayleigh-Ritz analysis can be used to solve problems with both radial and tangential heterogeneity. Stress concentrations can develop which are a function of both the material properties and the heterogeneity. This type of analysis is currently being used to study the effect of heterogeneity on curved beams subject to several different loading conditions: pure bending, internal and external pressure, and end loading. Geometric heterogeneity, such as a notch or cut-out, is also under investigation.

A damage zone mechanics analysis is being developed to study the failure response of structures where heterogeneous material property fields are present as a result of the manufacturing procedures. This model is theoretically based and only requires knowledge of the unnotched strength and fracture toughness of the material to predict failure near a stress concentration.

These models together can be used to establish the relationship between manufacturing and component performance for a variety of forming methods used in thermoplastic composite part production.

References

1. I. Y. Chang and J. F. Pratte, "LDF Thermoplastic Composites Technology," J. Thermoplastic Comp. Mat., Vol. 4, (1991), pp. 227-252.
2. A. B. Metzner, "Rheology of Suspensions in Polymeric Liquids," J. of Rheology, Vol. 29 (6), (1985), pp. 739-775.
3. T. G. Rogers, "Rheological Characterization of Anisotropic Materials," Composites, Vol. 20, No. 1, (1989), pp. 21-27.
4. P. J. Carreau, "Rheological Equations from Molecular Network Theories," Trans. Soc. Rheol., 16 (1), pp. 99-127 (1972).
5. D. M. Binding, "Capillary and Contraction Flow of Long (Glass) Fiber Filled Polypropylene," Presented at *Flow Processes in Composite Materials*, University College Galway (Ireland), July 4-5, (1991).
6. O. C. Zienkiewicz and P. N. Godbole. Flow of plastic and viscoplastic solids with special reference to extrusion and forming processes. International Journal for Numerical Methods in Engineering, 8:3-16, 1974.
7. O. C. Zienkiewicz. The Finite Element Method. McGraw-Hill, London, third edition, 1977.
8. E. Oñate and O. C. Zienkiewicz. A viscous shell formulation for the analysis of thin sheet forming. International Journal of Mechanical Science, 25(5):305-335, 1983.
9. A. J. Beaussart. Numerical Modeling of Sheet Forming Processes for Thermoplastic Composites. Master's Degree thesis, Department of Mechanical Engineering, University of Delaware, August 1990.
10. J.F. Pratte, W.H. Krueger, and I.Y. Chang. High Performance Thermoplastic Composites With Poly Ether Ketone Matrix. 34th International SAMPE Symposium and Exhibition, Reno, NV, May 8-11, 1989.

11. R.B. Pipes, M.H. Santare, B.J. O'Toole, A.J. Beaussart, D.C. DeHeer, and R.K. Okine. Long Discontinuous Fiber Composite Structure - Forming and Structural Mechanics. Proceedings of the First NASA Advanced Composites Technology Conference, Seattle, Washington, Oct. 29-Nov. 1, 1990, pp. 247-270. NASA CP- 3104.
12. S. Medwin. Long Discontinuous Ordered Fiber Structural Parts. 34th International SAMPE Symposium and Exhibition, Reno, NV, May 8-11, 1989.
13. S.G. Lekhnitskii. Theory of Elasticity of an Anisotropic Body. Mir Publishers, 1981.
14. S.G. Russell. A Rayleigh-Ritz Analysis Methodology for Cutouts in Composite Structures. Proceedings of the First NASA Advanced Composites Technology Conference, Seattle, Washington, Oct. 29-Nov. 1, 1990, pp. 901-920.
15. Waddoups, M. E., J. R. Eisenmann and B. E. Kaminski. Macroscopic Fracture Mechanics of Advanced Composite Materials. J. of Composite Materials, Vol. 5, pp. 446-454, 1971.
16. Whitney, J. M. and R. J. Nuismer. Stress Fracture Criteria for Laminated Composites Containing Stress Concentrations. J. of Composite Materials, Vol. 8, pp. 253-265, 1974.
17. Nuismer, R. J. and J. M. Whitney. Uniaxial Failure of Composite Laminates Containing Stress Concentrations. In Fracture Mechanics of Composites, ASTM STP 593, pp. 17-142, 1975.
18. Nuismer, R. J. and J. D. Labor. Applications of the Average Stress Criterion: Part I - Tension. J. of Composite Materials, Vol. 12, pp. 238-249, 1978.
19. Nuismer, R. J. and J. D. Labor. Applications of the Average Stress Criterion: Part II - Compression. J. of Composite Materials, Vol. 13, pp. 49-60, 1979.
20. J. Backlund. Fracture Analysis of Notched Composites. Computers and Structures, Vol. 13, pp. 145-154, 1981.
21. Backlund, J. and C-G. Aronsson. Tensile Fracture of Laminates With Holes. J. of Composite Materials, Vol. 20, pp. 259-286, 1986.
22. Aronsson, C-G. and J. Backlund. Tensile Fracture of Laminates With Cracks. J. of Composite Materials, Vol. 20, pp. 287-307, 1986.

Term	Newtonian	Power-Law	Carreau
η_{11}	$\frac{\eta f}{2} [\kappa-1] (L/D)^2$	$2^m \eta f [\kappa-1]^m (L/D)^{(m+1)} (\dot{\epsilon}_{11})^{(m-1)}$	$\frac{\eta_0 A_T (\kappa-1) f}{2} (L/D)^2 \left[1 + \frac{A_T^2 (\kappa-1)^2 (L/D)^2}{4} (\lambda \dot{\epsilon}_{11})^2 \right]^{(n-1)/2}$
η_{12}	$\kappa \eta$	$\eta \kappa^m (\dot{\gamma}_{12})^{(m-1)}$	$\eta_0 A_T \kappa \left[1 + (A_T \lambda \kappa)^2 (\dot{\gamma}_{12})^2 \right]^{(n-1)/2}$
η_{23}	$\kappa \eta$	$\eta \kappa^m (\dot{\gamma}_{23})^{(m-1)}$	$\eta_0 A_T \kappa \left[1 + (A_T \lambda \kappa)^2 (\dot{\gamma}_{12})^2 \right]^{(n-1)/2}$
η_{22}	$4 \kappa \eta$	$2^{(m+1)} \eta \kappa^m (\dot{\epsilon}_{22})^{(m-1)}$	$4 \eta_0 A_T \kappa \left[1 + (A_T \lambda \kappa)^2 (\dot{\epsilon}_{22})^2 \right]^{(n-1)/2}$

Table 1. Anisotropic viscosities for long discontinuous fiber thermoplastic composites

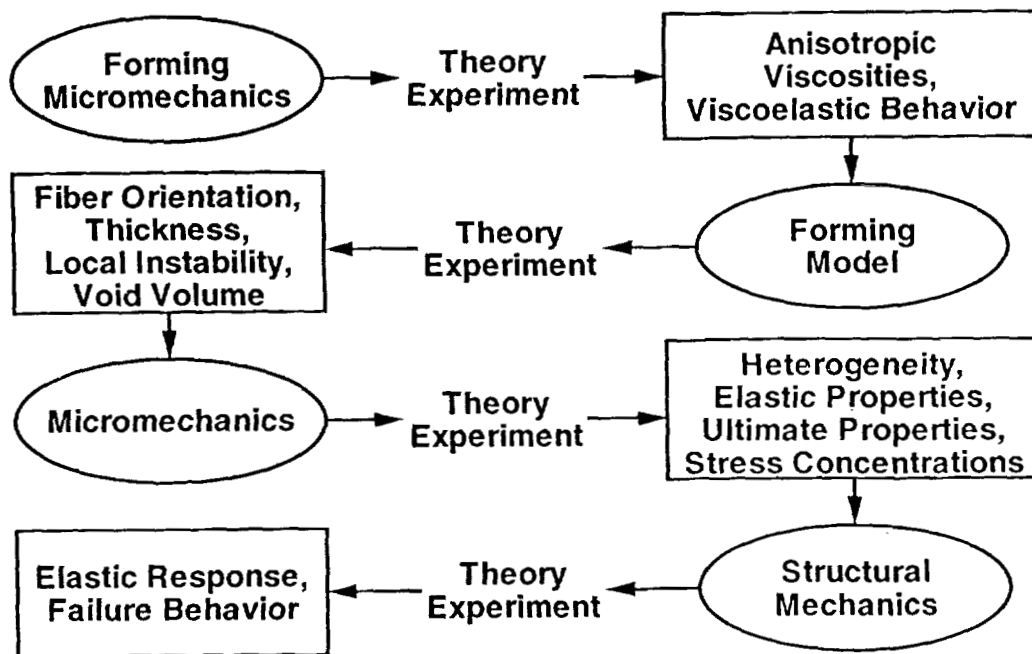


Figure 1. Summary of research plan

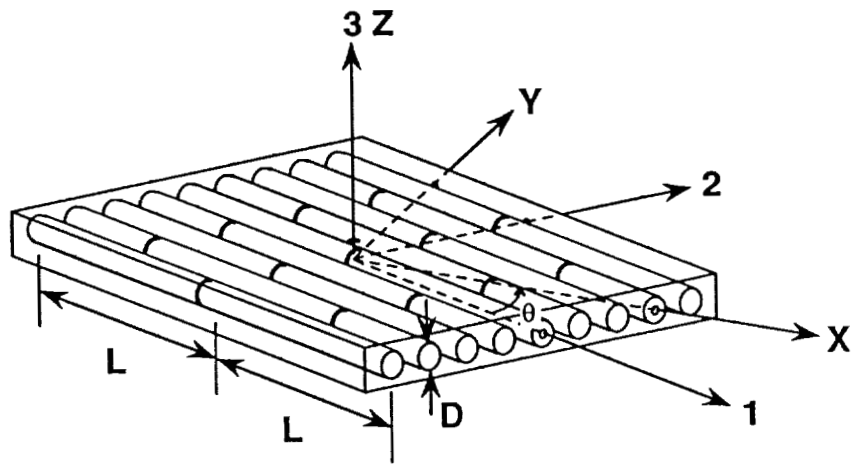


Figure 2. Oriented fiber assembly

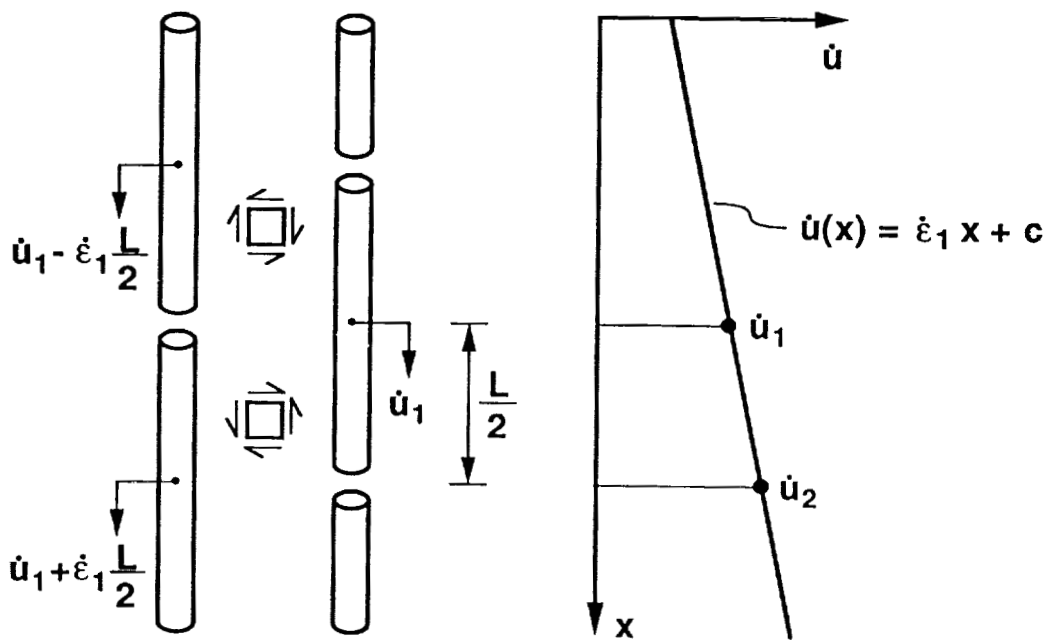


Figure 3. Fiber kinematics in extension

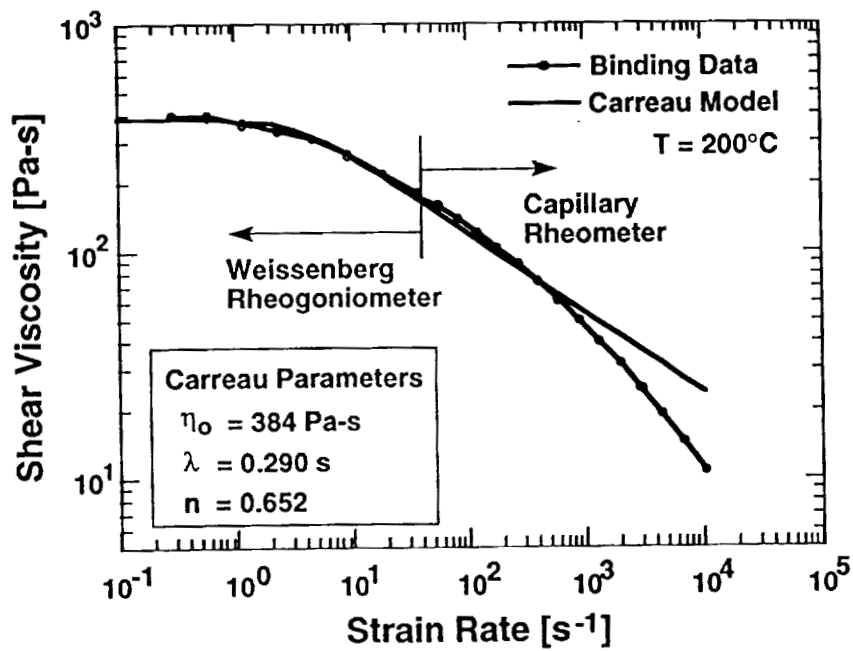


Figure 4. Shearing viscosity vs. strain rate for polypropylene, Binding data and Carreau fit

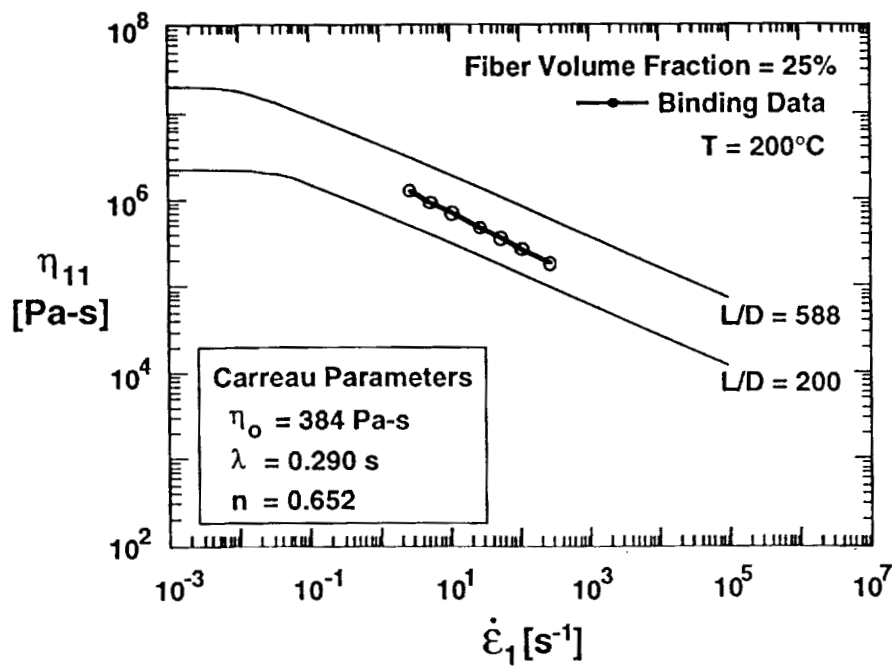


Figure 5. Elongational viscosity vs. strain rate for glass fiber polypropylene

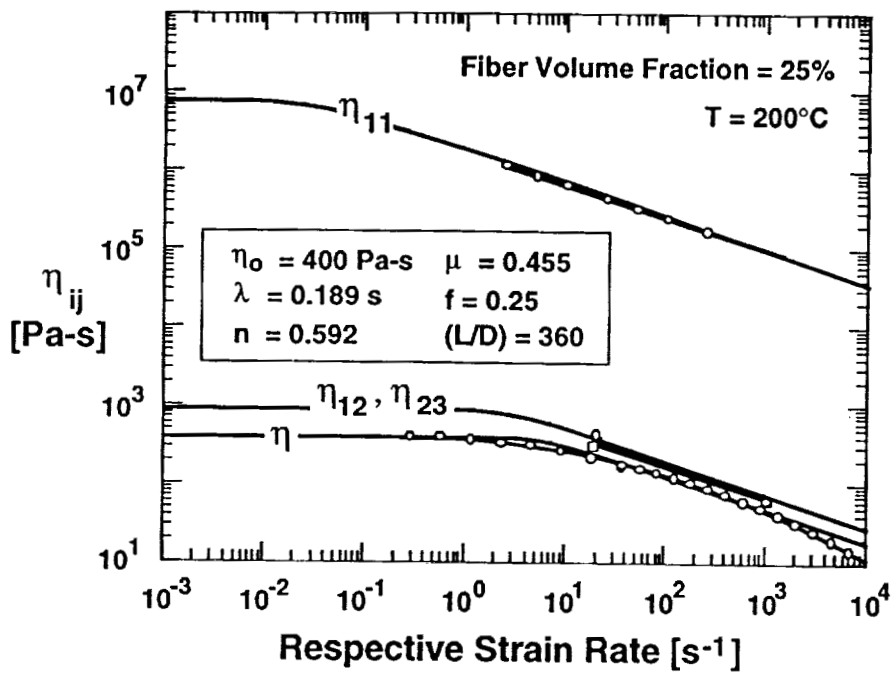


Figure 6. Comparison between predicted and experimentally measured viscosities

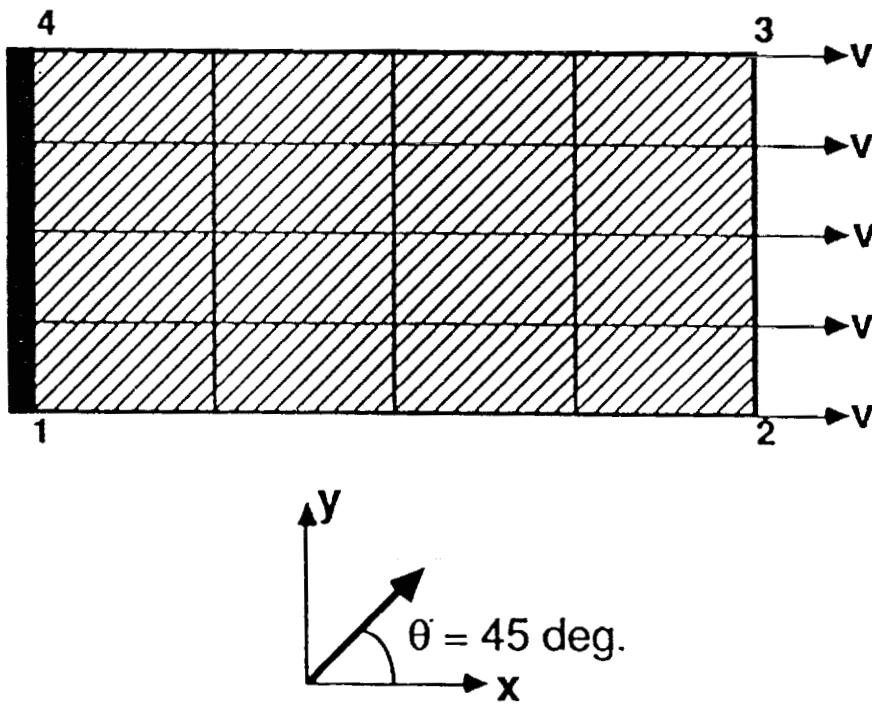


Figure 7. Off axis tensile test, initial geometry of finite element simulation

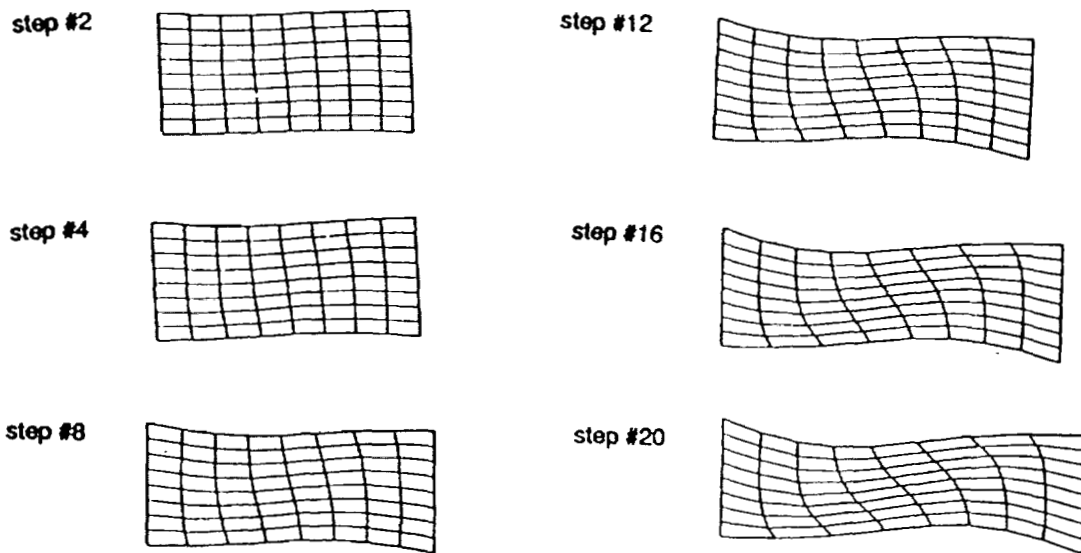


Figure 8. Several stages of the simulated deformation

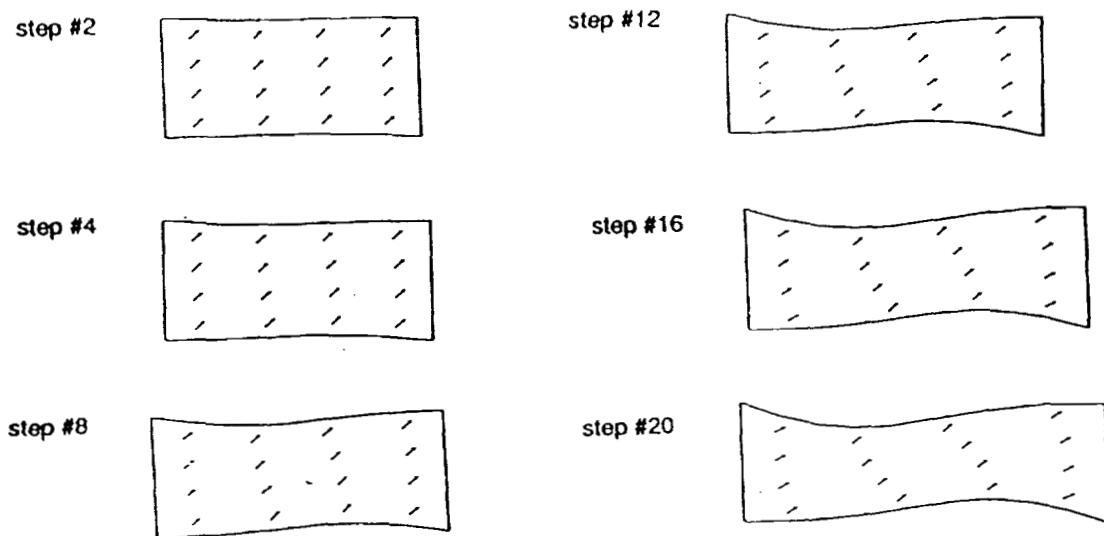


Figure 9. Fiber orientation during simulated deformation

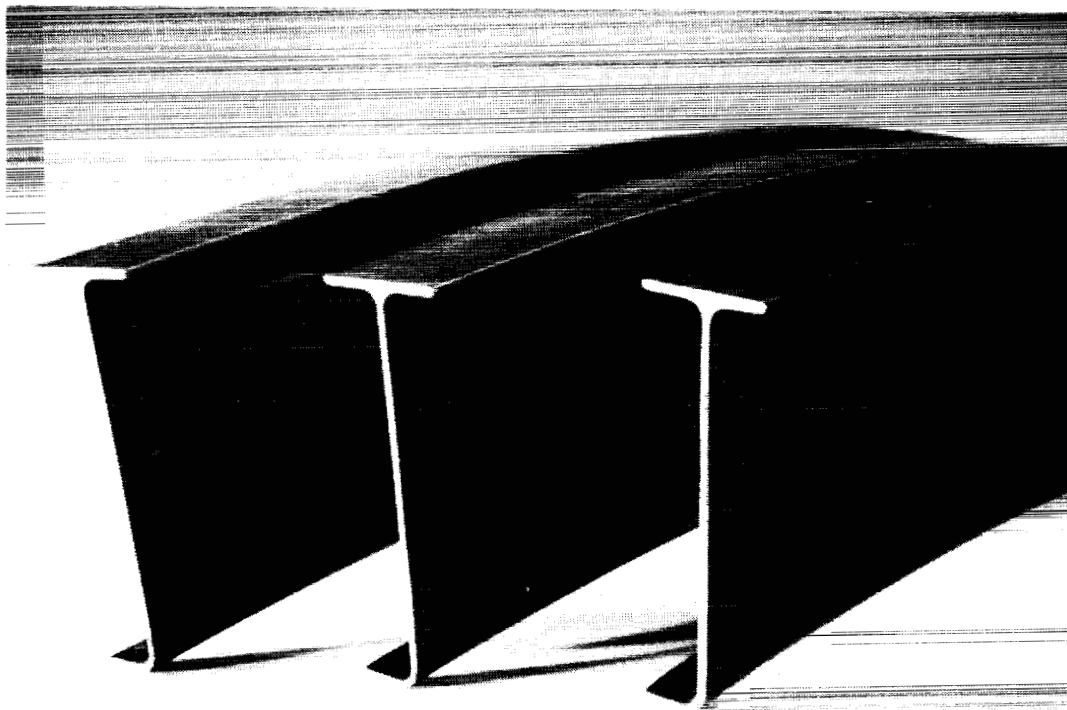


Figure 10. Thermoplastic composite curved beams

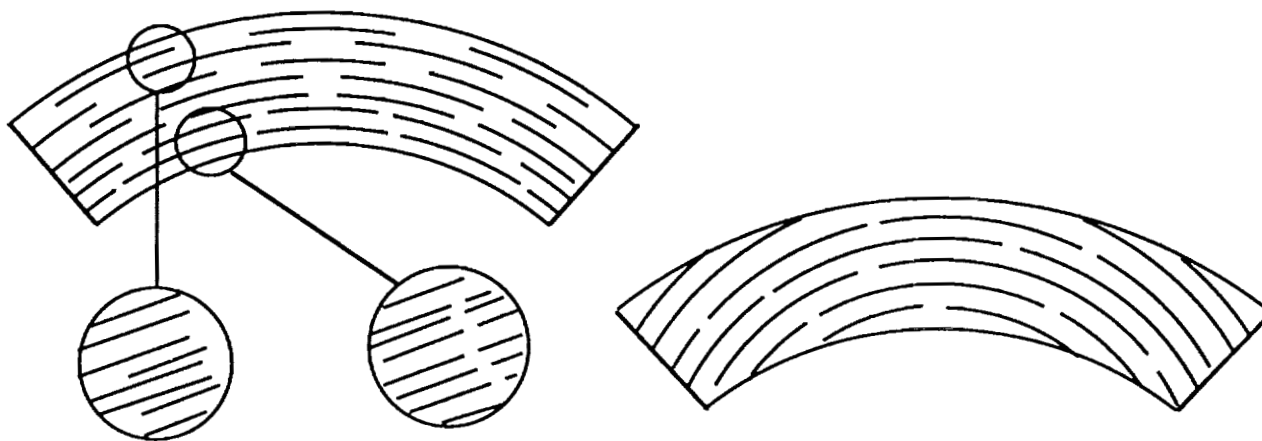


Figure 11. Different types of possible material heterogeneity

Lines of Constant Tangential Stress, Units In psi.

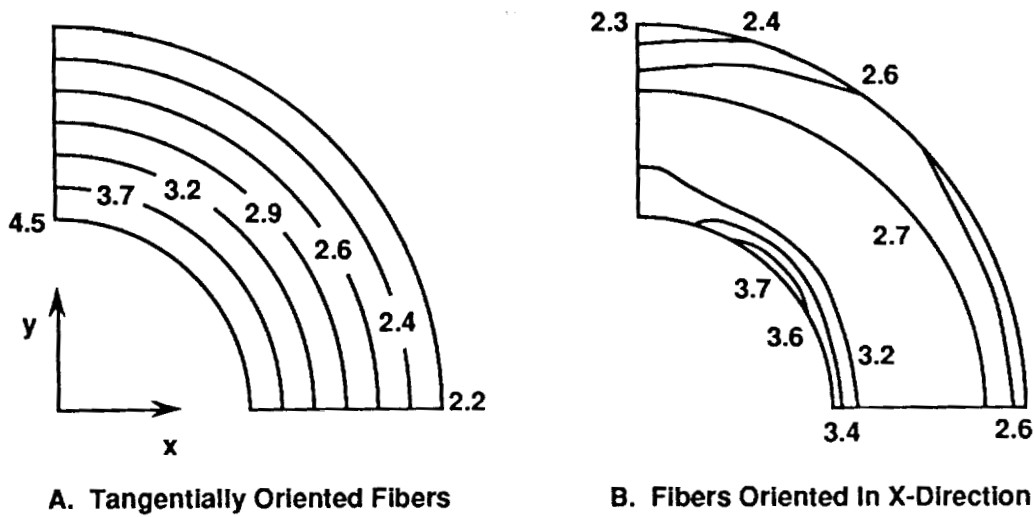


Figure 12. Tangential stress contours in a circular ring loaded by internal pressure

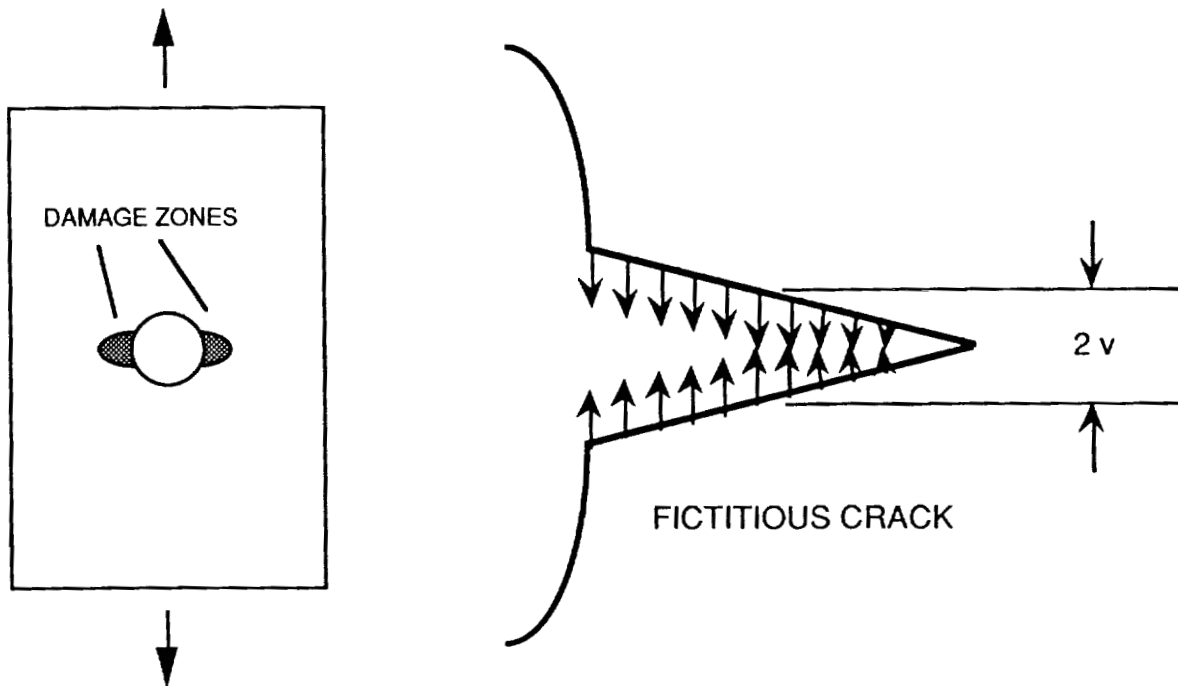


Figure 13: Damaged zone represented by fictitious crack

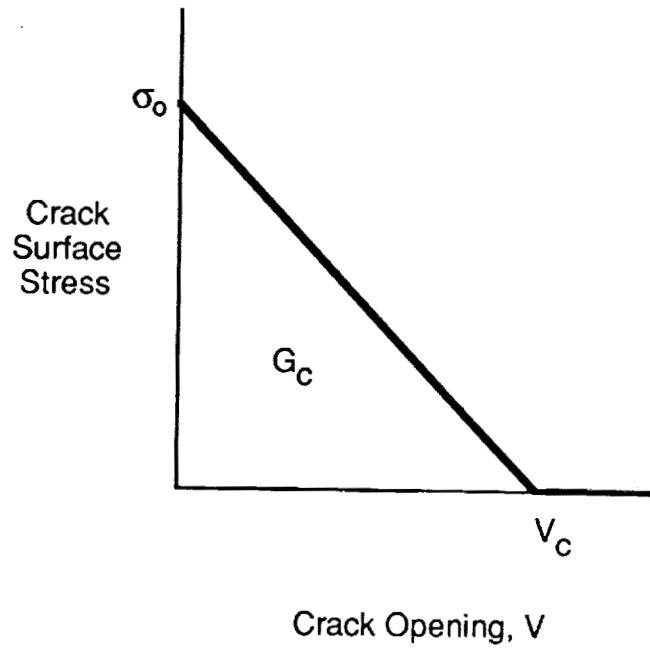


Figure 14: Crack surface stress vs. crack opening

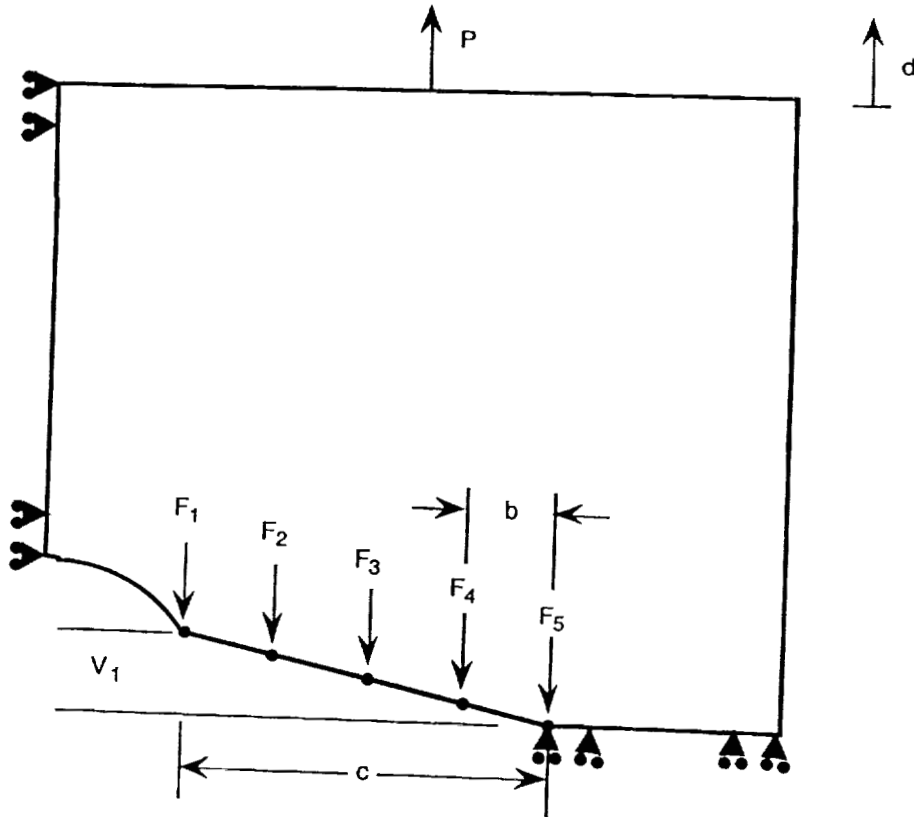


Figure 15: Plate geometry and computational parameters

NOVEL COST CONTROLLED MATERIALS AND PROCESSING FOR PRIMARY STRUCTURES

S. J. Dastin
Grumman Aircraft Systems
Bethpage, New York 11714

57-24
51407

SUMMARY

Textile laminates, developed a number of years ago, have recently been shown to be applicable to primary aircraft structures for both small and large components. Such structures have the potential to reduce acquisition costs but require advanced automated processing to keep costs controlled while verifying product reliability and assuring structural integrity, durability and affordable life-cycle costs. Recently, resin systems and graphite-reinforced woven shapes have been developed that have the potential for improved RTM processes for aircraft structures. Ciba-Geigy, Brochier Division has registered an RTM prepreg reinforcement called "Injectex" that has shown effectivity for aircraft components. Other novel approaches discussed are thermotropic resins producing components by injection molding and ceramic polymers for long-duration hot structures. The potential of such materials and processing will be reviewed along with initial information/data available to date.

INTRODUCTION

The Advanced Composite Technology (ACT) program has shown that textile laminates and enhanced processing such as automated fiber placement can significantly reduce the acquisition cost of advanced composite primary aircraft structures. To satisfy such development and reduce the development time for production implementation, further advancements in materials and processing are needed. Among the industry available developments in the resin transfer molding process is a registered technique called Injectex (R) by Ciba-Geigy. Ciba has also developed a lower than usual density epoxy matrix which can provide intrinsic weight savings without loss of structural integrity.

Several other industry developments that can possibly address the goals of the ACT program are the injection molding of self-reinforcing thermotropic resins and rapid thermal processing of ceramic polymer prepreps for high-temperature structures.

This paper presents the early developments of such technology and is given to review the technical base available and stimulate ideas/improvements to speed successful development of the ACT program.

TEXTILE LAMINATES

Five years ago, the BROCHIER division of Ciba-Geigy in France studied and developed the application of the liquid resin injection process for reducing the acquisition cost of secondary aircraft structures and named the reinforcement for the Resin Transfer Molding (RTM) process INJECTEX. The process, using high-performance graphite fibers at high volume content (i.e., 60 %) and epoxy resins certifiable to aircraft specifications can be suitable for reduced-cost primary structural components.

The technical difficulties of liquid resin RTM manufacturing of structural components for aeronautical applications are:

- Providing void free high fiber volume laminates
- Complete and rapid injection of resin
- Control of fiber orientation and elimination of fiber wrinkling and/or fiber fracture
- High quality, especially for large components.

To address such concerns, Ciba has developed a formable textile reinforcement weave including lightweight tow encasement fibers (servings) to increase resin permeability along the major axis of the woven cloth, a patented reactive chemical binder (epoxy compatible) to hold weave orientations, and the development of low viscosity epoxy resins (<100 cps) to permit complete infiltration at low resin pump pressures to assure minimum fiber disarray. The service temperature of the developed resin systems are 250°F and 350°F.

Laminates manufactured using these materials have been produced within one hour and found to be satisfactory, as determined by NDT, for aeronautical applications. Typical room temperature mechanical properties for a balanced carbon fiber weave and the 250°F resin system are given in Table 1.

Table 1. Injectex Laminate* Properties

	WARP DIRECTION	WEFT DIRECTION
TENSILE		
• STRENGTH, ksi	92	100
• MODULUS, Msi	9.1	9.1
FLEXURE		
• STRENGTH, ksi	113	110
• MODULUS, Msi	9.0	8.1
INTERLAMINAR SHEAR STRENGTH, ksi	7.7	7.4
* 57 VOLUME PERCENT FIBER; <1 VOLUME PERCENT VOIDS		
MR92-0259-005		

Studies have shown that, utilizing vacuum degassed low-viscosity epoxy resins and enhanced permeability woven graphite reinforcements, the liquid injection method of the RTM process can be effective even for large aircraft components. Figure 1 shows the enhancement possible to reduce resin injection time between a standard plain weave 3-ply aramid fabric, 2-ply standard fabric with center ply Injectex, and 3-ply Injectex. As noted in the figure, the all-Injectex fabric wets-out twice as fast as the hybrid fabric which, in turn, is more than twice as fast as the standard fabric.

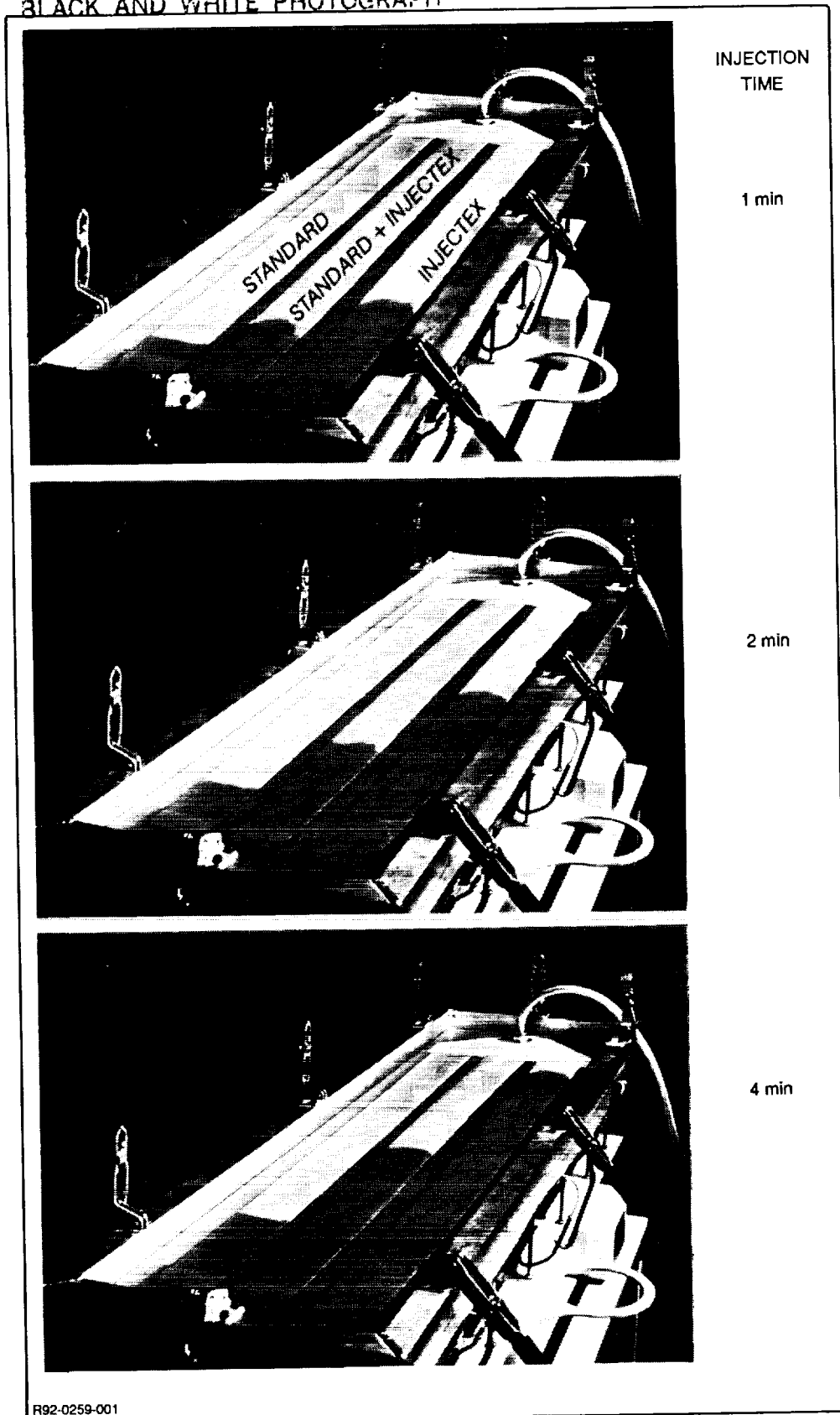


Figure 1. Wet-out factors for resin injection of the RTM process.

Such materials have already been utilized in the Aerospace industry. Typical components using graphite 2-D weaves and epoxy matrices molded by liquid injection RTM include access doors for civil aircraft (Figure 2) and fuselage stiffened panels as shown in Figure 3.

Matrix Enhancement

Some three years ago, Ciba-Geigy developed an improved 250°F hot-wet service temperature epoxy resin suitable for Aerospace applications. Among the attractive features of this resin, designated Vicotex M18, is a 3.7% lower laminate density due to a lower resin specific gravity. This represents an automatic weight savings compared with the currently used graphite laminates, without any known reduction in required structural integrity or durability. Further, resin cost is similar to other multi-func-

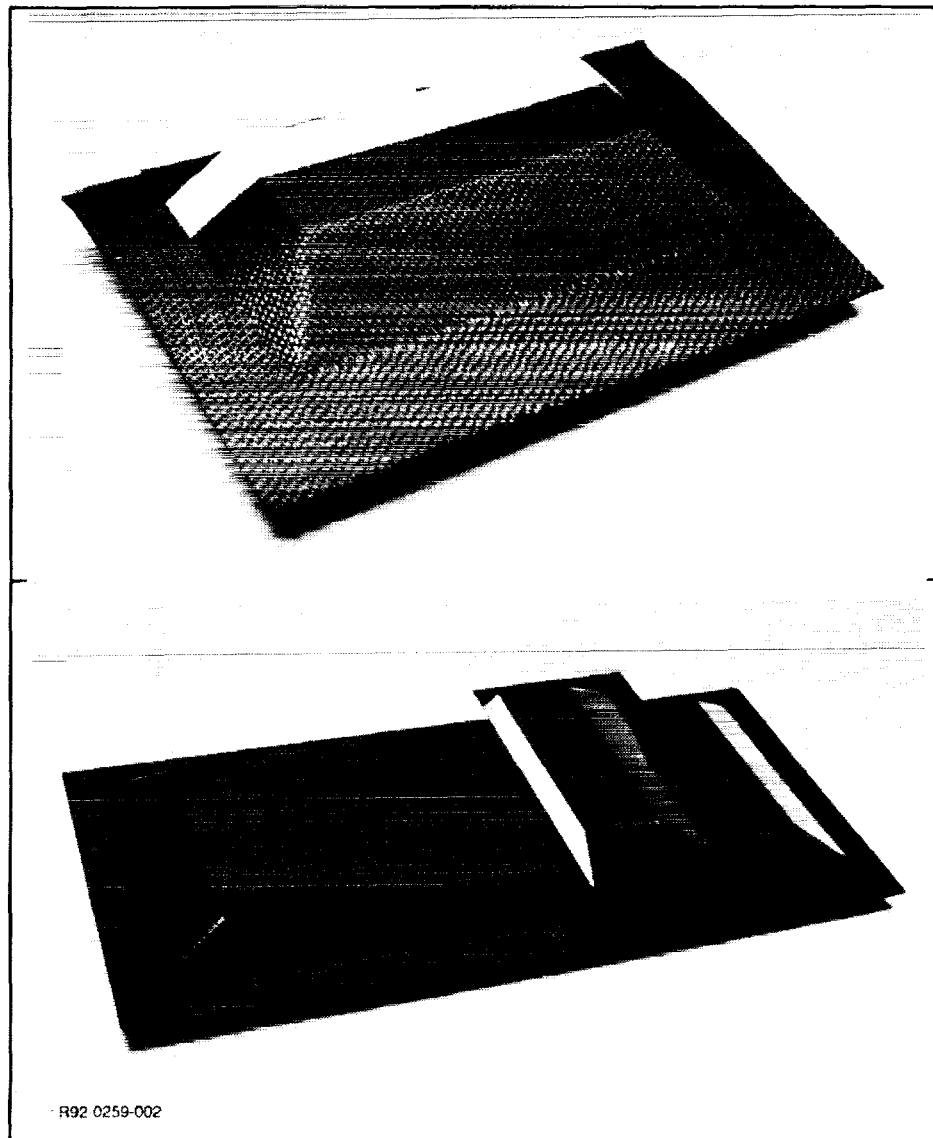


Figure 2. Access doors for civil aircraft

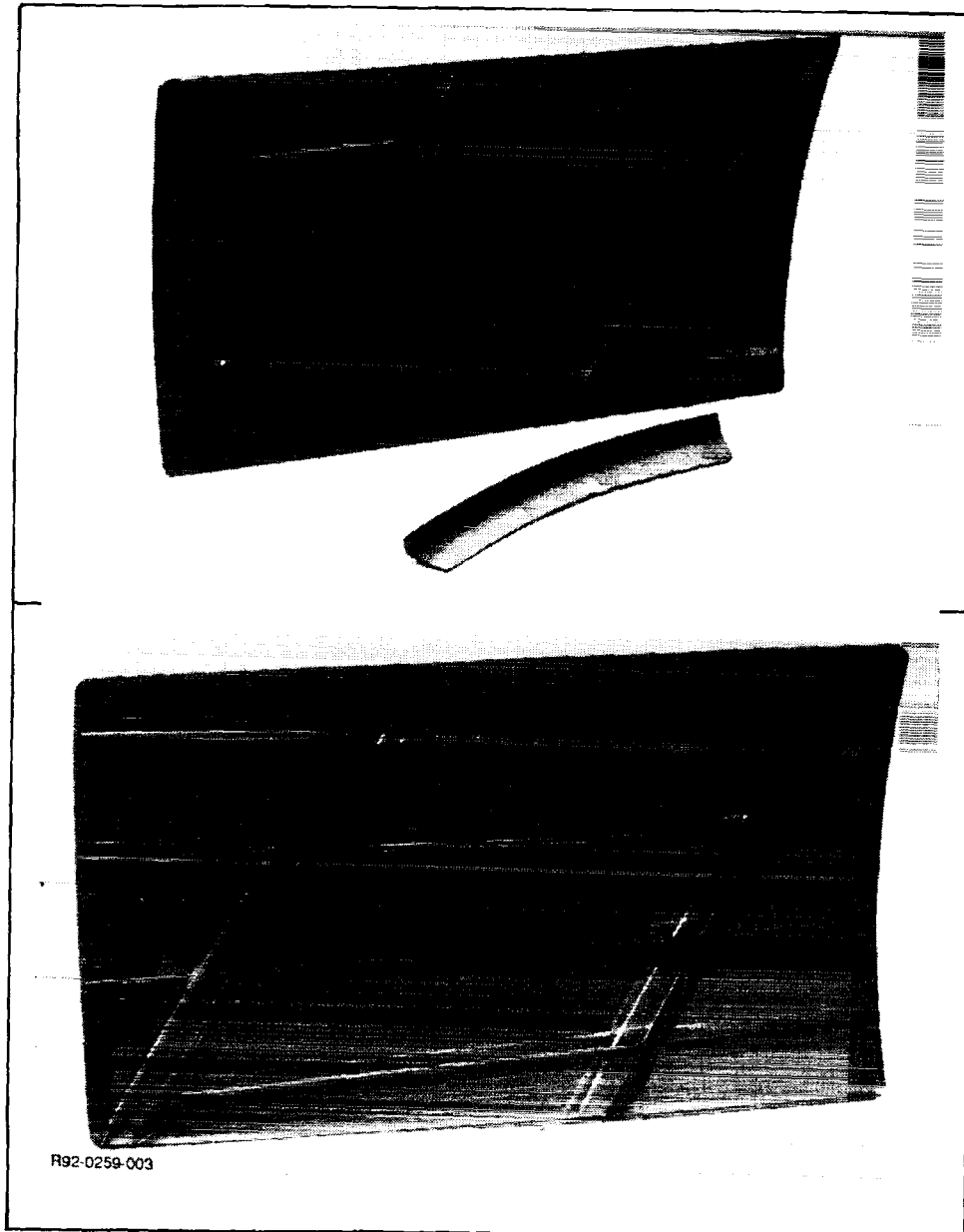


Figure 3. Fuselage stiffened panel.

tional epoxies and does not contain any OSHA restricted components. Typical laminate properties for a unidirectional 197 g/m² prepreg at room temperature using 12K-HTA graphite fiber are given in Table 2.

The resin system was evaluated on intermediate modulus graphite fiber and demonstrated satisfactory properties, including damage tolerance testing, as shown in Table 3.

Currently, to take advantage of the lower resin density, Ciba-Geigy is evaluating this type of formulation with reduced viscosity to allow for resin infiltration RTM for ACT components needed for Grumman structures.

Table 2. M18 Resin Laminate Typical Properties

	AS CURED	AFTER 1000 HR AT 160°F/95% RH
TENSILE 0°		
• STRENGTH, ksi	309	314
• MODULUS, Msi	21	—
TENSILE 90°		
• STRENGTH, ksi	8.8	8.4
• MODULUS, Msi	1.8	—
COMPRESSION 0°		
• STRENGTH, ksi	185	189
FLEXURE 0°		
• STRENGTH, ksi	246	—
• MODULUS, Msi	16	—
INTERLAMINAR SHEAR 0°		
• STRENGTH, ksi	14.0	12.6

MR92-0259-006

**Table 3. Vicotex M-18/Cellon G40-600 (60 V/o)
Laminate Mechanical Properties (at Room Temp)
for Unidirectional Laminates**

0° TENSILE STRENGTH		398 ksi
0° TENSILE MODULUS		25.3 msi
90° TENSILE STRENGTH		11.1 ksi
90° TENSILE MODULUS		1.9 msi
0° COMPRESSION STRENGTH		180 ksi
90° COMPRESSION STRENGTH		32.6 ksi
ILSS		14.1 ksi
OPEN-HOLE-TENSION (QUASI-ISOTROPIC)		137 ksi
±45° TENSION		13.3 ksi
G _{IIC}		6.6 in.-lb/in. ²
FILLED-HOLE-COMPRESSION (QUASI-ISOTROPIC)	• DRY	75.7 ksi
	• WET (95% RH)	67.4 ksi

MR92-0259-007

THERMOTROPIC RESINS

Liquid Crystal Polymers (LCP) form ordered systems, either in solution or in the melt forming matrices, that are anisotropic in the heating or cooling direction and are known as thermotropic materials.

The most popular LCP, a copolyamide in fiber form, is Dupont's Kevlar. The currently studied LCPs are aromatic copolyesters and several are currently commercial realities. The LCP ordered structure provides exceptional mechanical, chemical, and thermal stability properties. Most currently available LCPs are semi-crystalline rigid rod chains, although Dupont has recently introduced an amorphous resin designated HX-2000.

The major semi-crystalline materials are available from Amoco, under the tradename of Xydar, and Hoechst Celanese, under the brand name of Vectra. These resins are solvent-resistant, show very low moisture absorption, and display low coefficients of thermal expansion. Properties in the melt direction are significant, including high matrix modulus and reasonable elongation. The material is effective in long-term stability at 400°F and inherently self-extinguishing.

LCP resins process readily compared to other high-temperature-resistant resins and easily fill molds during injection molding or pultrusions. Currently, these resins are particulate filled to reduce material cost, currently at \$10/lb for volume quantities of material. Some studies are being undertaken for continuous-reinforced LCP suitable for structural components, but the major resin outlets are for electronics, automotive, and microwave cookware. Table 4 shows typical injection-molded properties of the neat resin tested in the melt flow direction.

Table 4. Typical Neat Resin Properties for Xydar G540 at Room Temperature

TENSILE STRENGTH, ksi	21.2
TENSILE ELONGATION, %	1.5
FLEXURAL MODULUS, Msi	2.3
264 psi HEAT DISTORTION TEMP, °F	465
MR92-0259-008	

LCPs are currently of high interest, since forecast of high volumes are expected within the next few years which is expected to reduce current costs. Several Japanese resin suppliers such as Sumitomo, Sekisui, and Nippon Petrochemical, as well as Rhone-Poulenc, Bayer, and BASF of Europe, produce LCP resins. As supply increases along with development of continuous reinforced prepregs, an improved material system will be available for structural components. It is expected that early aircraft parts will be processed by thermoforming as well as injection molding and pultrusion, and utilized for aircraft interiors and secondary structures operating at elevated temperatures. It is forecasted that with increased development the LCP laminates will be utilized for primary aerospace structures across a broad service temperature range. Table 5 provides trade literature data for three specific neat resins from longitudinal test bars prepared to net dimensions by injection molding.

Table 5. Typical LCP Neat Resin Properties at Room Temperature

PROPERTY	MATERIAL DESIGNATION		
	VECTRA A130	XYDAR RC210	HX-2000
DENSITY, g/cc	1.6	1.6	1.3
TENSILE PROPERTIES			
STRENGTH, ksi	20	20	22
MODULUS, Msi	2.2	2.3	2.6
ELONGATION, %	2.3	1.7	0.6
NOTCHED IZOD IMPACT, ft-lb/in.	2.0	2.0	3.7
HEAT DEFLECTION AT 264 psi, °F	446	650	365
MR92-0259-009			

CERAMIC POLYMERS

Currently, Government and Industry development personnel have renewed interest in long-duration hot structures for high-speed commercial aircraft and extremely hot structures for short duration in highly oxidizing environments for hypersonic vehicles. As is known, structural materials that perform under such conditions must be of minimum weight to allow for reasonable payloads. Several ongoing developments in this regard are based on both reinforcing fibers and matrices made from polymer precursors. Hercules and Hexcel, among the current suppliers of polymer prepregs for aerospace structures, are developing ceramic prepregs that hold high promise for high-strength, high-modulus composites suitable for future aircraft structures.

Several U.S. universities are developing specialty materials that could result in affordable structural materials in the ceramic matrix composite category. The University of New Mexico has developed boron nitride fibers from polymer precursors that show microstructure similar to currently used carbon fibers. The fibers are produced by the commercial process of die extrusion fiber spinning. Other non-oxide fibers are under study such as silicon carbide, aluminum nitride, and silicon nitride. Consistent mechanical properties are current limitations, but with continued study it is expected that such problems will be overcome. At the University of Michigan, an economical silicate process is being developed to obtain a low-cost range of polymers and glasses suitable for high-temperature composites. Applications currently of interest are 800°F stable polymers, conductive polymers, and a wide variety of silicon compounds. At the University of Illinois, micro-controlled blended extremely fine powder ceramics have resulted in high mechanical strength. With optimized reinforcements that can resist high temperature and high pressure, hot pressed weight effective aerospace structures will be possible.

In 1990, Rhone-Poulenc of France introduced a carbonitride ceramic fiber with oxidative stability to 2550°F with the trade name Fiberamic. The developed fiber is a continuous textile yarn of 250 to 500 filaments obtained via pyrolysis of polysilazane, as shown in Figure 4. Although the fiber was at the pilot plant scale, production commitment has not yet been announced and is herein noted because the future will surely contain such textiles so that output of the ACT program can be utilized in the current studies for HSCT. Molding developments currently under study for ceramic structural components include high solids injection molding, tough nonporous green preforms, and crack-free fired parts with silicon nitride matrices. Other structural fabrication techniques demonstrated are lamination, corrugation, winding, and thermoforming.

CONCLUSIONS

A number of studies and developing thrusts to enhance and/or enable attainment of low-cost, reliable primary structures for the Aerospace industry are appearing and hold high promise for application to future high-speed commercial aircraft.

The ongoing research is a necessary key ingredient to the industry's technological readiness to reduce implementation time and assure continuing developments. The developments have been focused to

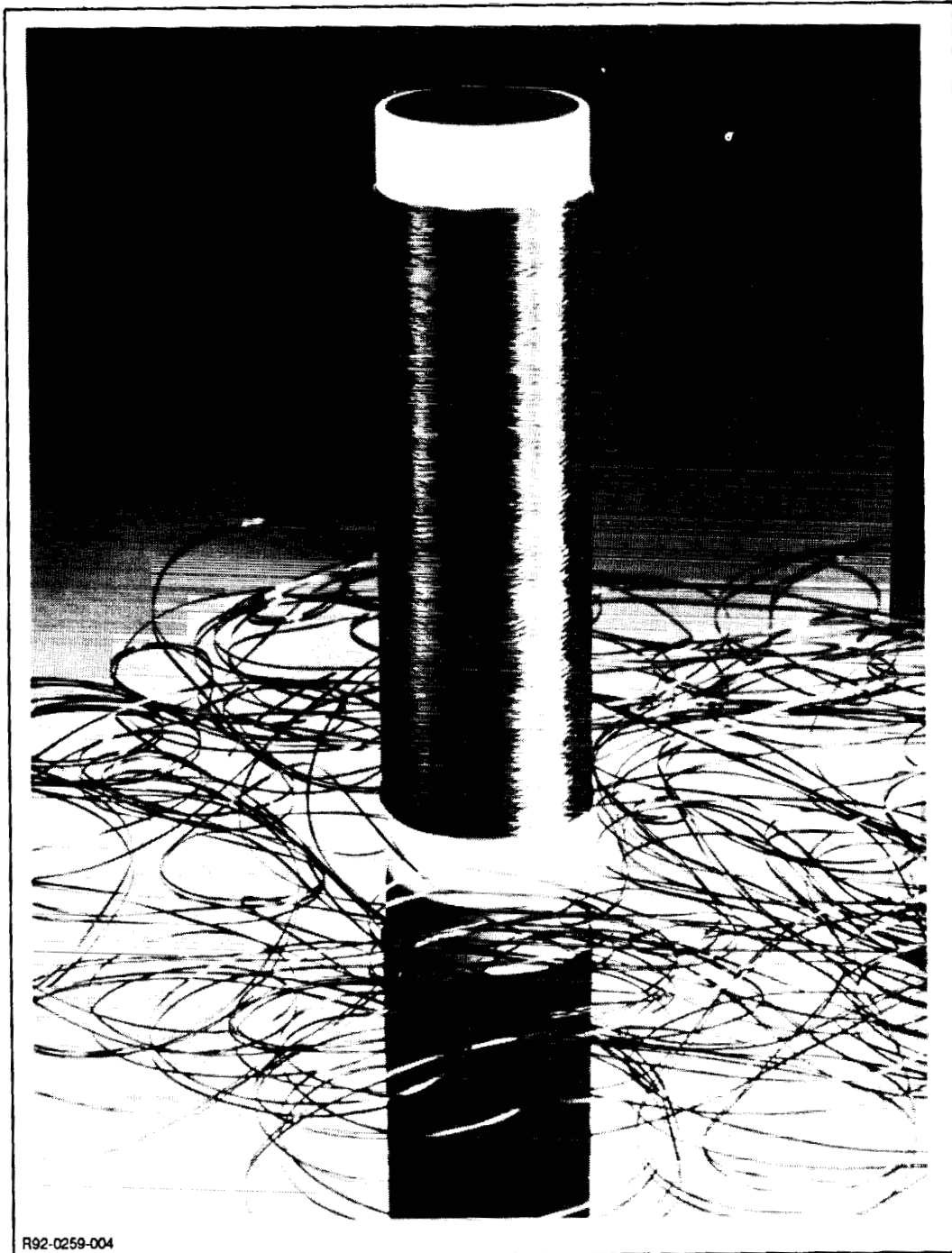


Figure 4. Rhone-Poulenc ceramic fiber--Fiberamic.

the needs of the end-user and, with their willingness to accept some risk, a significant advancement in our airframe industry will shortly become a reality.

THE EFFECTS OF DESIGN DETAILS ON COST AND WEIGHT OF FUSELAGE STRUCTURES¹

G. D. Swanson, S. L. Metschan, M. R. Morris
Boeing Commercial Airplane Group

C. Kassapoglou
Sikorsky Aircraft

58-05
51408

ABSTRACT

Crown panel design studies showing the relationship between panel size, cost, weight, and aircraft configuration are shown with comparisons to aluminum design configurations. The effects of a stiffened sandwich design concept are also discussed. This paper summarizes the effect of a design cost model in assessing the cost and weight relationships for fuselage crown panel designs.

Studies were performed using data from existing aircraft to assess the effects of different design variables on the cost and weight of transport fuselage crown panel design. Results show a strong influence of load levels, panel size, and material choices on the cost and weight of specific designs. A design tool being developed under the NASA ACT program is used in the study to assess these issues. The effects of panel configuration comparing postbuckled and buckle resistant stiffened laminated structure is compared to a stiffened sandwich concept. Results suggest some potential economy with stiffened sandwich designs for compression dominated structure with relatively high load levels.

INTRODUCTION

Boeing is studying the technologies associated with the application of composite materials to transport fuselage as part of the NASA/Boeing Advanced Technology Composite Aircraft Structures (ATCAS) program. As part of this program, a designer's cost model [1, 2, 3] is being developed to quantify the complex interactions of aircraft design criteria, multiple load conditions, and the extensive number of design variables associated with composite structures. Analysis, optimization, and design routines plus a theoretical framework for assessing the cost are being combined into a tool that can aid a design engineer in the understanding and design of many structural components. The cost model effort, Composite Optimization Software for Transport Aircraft Design Evaluation (COSTADE), is being developed in coordination with a number of subcontractors, including Sikorsky Aircraft, University of Washington, Massachusetts Institute of Technology, Dow/United Technologies, and Northrop. The current study uses COSTADE in a developmental form to demonstrate and validate its usefulness for a number of composite fuselage crown panel designs.

¹ This work was funded by Contract NAS1-18889, under the direction of J. G. Davis and W. T. Freeman of NASA Langley Research Center.

Composite structural design can be very complicated if the proper design tools are not available. The aircraft industry has had decades to develop design charts and material allowables to aid the engineer in establishing an efficient aluminum design. This capability is still being developed for composite structures. The concept of a designer's cost model which combines preliminary design tools, laminate analysis, and an ability to handle multiple load conditions and criteria using an optimization routine has significant appeal in closing the existing gap in capability.

An important feature being developed for inclusion in COSTADE is a blending function. In the first part of the current study, the cost efficiency of large panel sizes is studied. The trend, which justifies large composite panels, was also discussed in [1, 3]. Since aircraft loadings are sensitive to their relative location, a large panel will likely have a wide range of loading levels from one end to the other. For example, a fuselage crown panel has higher axial loads at the center of the aircraft and lower loads closer to the tail or the nose. The optimum design at the heavily loaded end of the crown panel will likely be quite different than the optimum design at the lightly loaded end. The optimum design for the entire panel may be different than either of these. Most likely, the optimum will be a compromise between them. The intent of the blending function is to optimize the entire panel, accounting for all the local load variations that occur within the panel. In the current study, the blending was done manually. The lessons learned and the pitfalls encountered are being incorporated into the blending function development. This feature of a designer's cost model is likely to be one of the most important features responsible for reducing the cost of a design and will be discussed in future work.

CURRENT STUDY

The present study is intended to show the applicability of the designers cost model to a fuselage crown panel design for different design configurations. The study is divided into two parts, the first being an evaluation of the crown panel design as a function of aircraft size and load levels. Comparisons to equivalent aluminum aircraft designs are made when possible. The second part of the study is focussed on the effect of panel configuration, specifically the effect of large stiffener spacing and sandwich core. Previous studies [1, 4] suggested that minimum cost is achieved by increasing the stiffener spacing and is often limited by skin buckling constraints. The use of sandwich skins to increase the buckling capability of the skins between stiffeners (stiffened sandwich structure) is addressed.

Design Constraints

Performance Constraints

The criteria used to design a composite fuselage crown panel are very similar to those used for its aluminum counterpart since both structures perform the same function. Many design checks were made to evaluate structural performance for each loading condition. A summary of the constraints used during local optimization are shown in Table 1. Using these criteria to constrain investigations to a feasible design space, structural cost and/or weight was used as an objective function in the optimization routine to find the best possible design.

Of the constraints and guidelines listed in Table 1, the minimum skin buckling, minimum stiffness, and tension damage tolerance constraints tended to be the most critical. The minimum skin buckling constraint limited skin buckling to no less than 38% of the ULTIMATE compression load.

<p>Structural Criteria Related Design Checks</p> <ul style="list-style-type: none">o Ultimate failure strainso Tension damage tolerance (axial and hoop directions)o General panel stabilityo Local buckling/crippling <p>Structural Guidelines</p> <ul style="list-style-type: none">o Minimum overall axial and shear stiffness no less than 90% of an equivalent aluminum designo Minimum skin buckling percentage of 38% ULTIMATE loado Maximum stiffener spacing based on skin area between adjacent stiffeners and frames (16" for the current study)o Minimum skin gage based on impact damage resistance data <p>Composite Laminate Guidelines</p> <ul style="list-style-type: none">o Poisson ratio mismatch between skin and stiffener laminate less than 0.15 for both longitudinal and transverse directionso A minimum of two $\pm 45^\circ$, two 0°, and two 90° plies in any laminateo Ply angle increments of 15° in final laminate <p>Geometric, Configuration, or Manufacturing Constraints</p> <ul style="list-style-type: none">o Maximum stiffener heighto Minimum stiffener flange widthso Stiffener web angle limitations

Table 1: Structural Performance Constraints and Guidelines

The minimum stiffness criteria used was based on 90% of the baseline aluminum airplane fuselage stiffness. This criteria is discussed further in [1].

A longitudinally oriented through penetration that included a central failed frame element was used to evaluate hoop tension damage tolerance. Analytical corrections for configuration, stiffness, pressure, and curvature were included. The damage tolerance analysis used in the present study uses assumed material properties for fracture properties and some assumed load redistribution characteristics. Current investigations into the response of composite structure to this type of damage are ongoing [5, 6]. Further work in this area will be incorporated into the designer's cost model. It is expected that the results will be affected, but the trends will be similar.

The loading conditions applied to the crown panel include both flight loads and internal pressure loads. The critical flight loads are derived from a scan of all the critical load cases used to design the aircraft. The typical tension load distribution and the associated shear loads were discussed in [1]. Maximum

longitudinal tension, compression, and shear cases were determined from the existing loads data. Two pressure cases are also used to design the fuselage structure. An ULTIMATE pressure load case (18.2 psi pressure differential) is applied without any additional flight loads. This case is critical in the crown for frame loads and for the longitudinal splices. A FAIL-SAFE pressure load (9.6 psi pressure differential) is used to evaluate the tension damage tolerance in the hoop direction.

Cost Constraints

The relationship between the design details and the cost of a given structure is often hidden in the data provided by a cost estimator since these estimates are based on process and manufacturing parameters. It is the intention of the present study to approach cost estimation such that it forms a framework which allows the relationship between the design details and cost to be bridged [2]. The framework approach, as it is currently conceived, will relate the cost and design variables through a series of coefficients and functions defined in a Design Build Team (DBT) environment [7]. In this environment, the factory flow and the process steps used at any given company can be defined within the framework and these relationships can be used to optimize the structure to its desired objective function.

The cost algorithm in the current study is based on data collected during the crown panel [7, 8] and keel panel [9] global evaluation study of Boeing's ATCAS program. During global evaluation, a comprehensive manufacturing plan was compiled for each design to support a detailed cost estimate. The estimate included the recurring labor and material cost of 300 ship sets and the non-recurring costs. Six crown designs were evaluated and include both hat stiffened skins and sandwich panel designs. The four keel designs include similar concepts. In an earlier study [1], a limited cost relationship for a hat stiffened crown panel was established. This relationship assumed that the stiffener spacing was limited between 10" and 20", overall panel size was unchanged and no changes to the processes or manufacturing steps would be allowed. Additional relationships were developed for the present study to broaden these assumptions.

In the first part of the present study, a number of different design configurations are analyzed for composite material applications in which both the size of the crown panel and its diameter were varied. Two cost centers that are affected by a change in panel size were assumed to be constant in the cost relationship from [1]. These are the tooling and bagging costs. Since detailed cost data were available for the smaller keel panel designs, tooling and bagging costs could be established as a function of area. The variation of the tooling and bagging costs were assumed to vary linearly with size. These additional relationships are shown in Figure 1.

In the second part of this study, the effects of increasing the stiffener spacing to very large values were considered. The major effect of the stiffener spacing variation, not accounted for in the original relationship [1], was the bagging costs. The cost relationship [1] incorrectly tied the bagging costs to the design variable associated with the number of stiffeners. Although this assumption was reasonable for the limited range of stiffener spacings used in [1], the limiting case of no stiffeners yielded incorrect cost trends. Bagging costs from the detailed cost estimate for sandwich crown panel designs (Family D [7]) provided an estimate of the bagging costs for a similar size panel without stiffeners. A relationship was defined based on a linear variation of bagging costs with stiffener spacing. These additional relationships are also included in the equations shown in Figure 1.

The larger stiffener spacing resulted in a lower panel cost [1] and was limited in most cases by a minimum skin buckling constraint. It was assumed that by increasing the ability of the skin to resist buckling, a larger stiffener spacing, hence a lower panel cost, could be achieved. One approach to increasing the skin buckling resistance was to add core material to the skin laminate, effectively creating a stiffened sandwich structure. The addition of core to the design had a significant effect on the cost. The cost relationships relating to the core were extracted from the detailed cost estimate for the sandwich crown panel design [7]. The core costs were broken down into cost equations and are shown in Figure 1.

Cost relationships like this must be used carefully since much of the estimate is based on speculation of factory flow and technology development. A more general approach to cost modeling is currently being developed and will eventually be incorporated into the COSTADE program. As with the current approach, a more general theory will include design details and material properties as independent variables, providing insight into the general effect of criteria and design practice on the cost of a composite structure. It is intended that the general cost relationship structure may be customized by a user to fit any factory for which data is available.

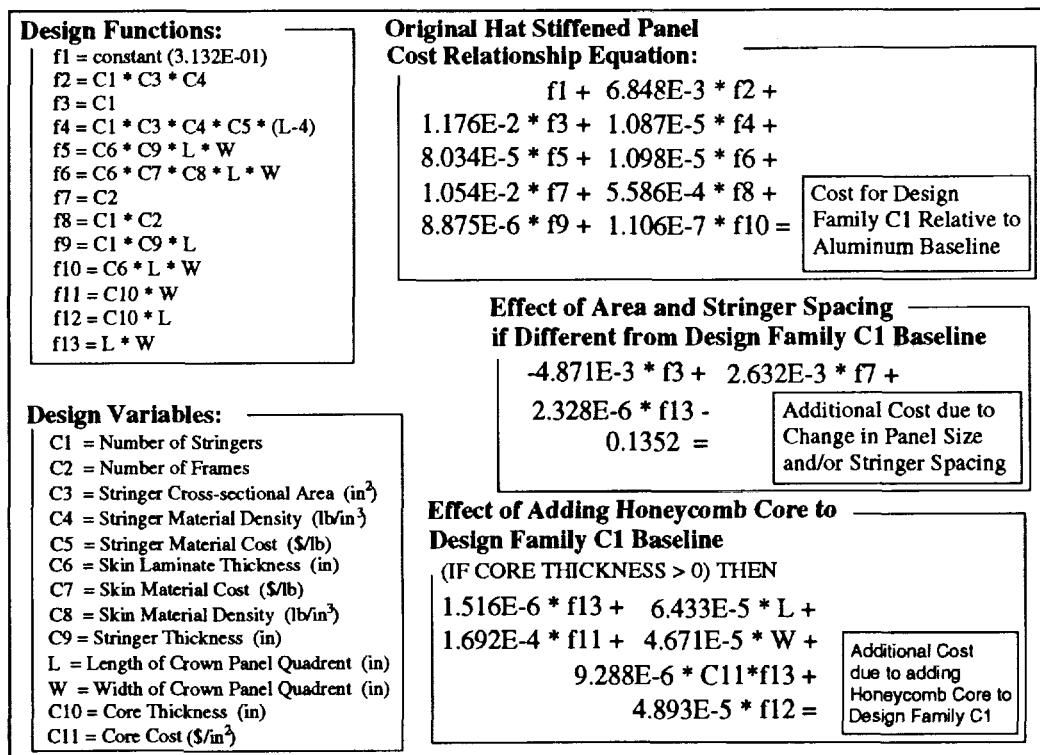


Figure 1: Cost Relationships used in Current Study

PART 1: THE EFFECT OF SIZE ON CROWN PANEL DESIGN

The first part of the study is intended to address the issue of size on the cost and weight of a crown panel. Loads and criteria from a number of existing aircraft were used as the basis for the study. Aircraft size ranged from a relatively short, small diameter to a very long, large diameter transport aircraft. The relative sizes of the aircraft used are shown in Figure 2. The fuselage crown panel from

section 46 aft of the wing was used. Loads in the crown panels were a function of the diameter, aft fuselage length, mass distribution, and structural load paths, just to name a few. As is shown in Figure 3, the load distribution on the crown panel is fairly consistent in that the axial loads decrease as a function of fuselage station and that the smaller aircraft have overall lower load levels.

In addition to the axial loads, hoop loads are a function of the diameter. A larger diameter fuselage has larger hoop loads. From Figure 2 it is observed that the larger diameter tends to be accompanied by a longer aft fuselage length, coupling the axial and hoop load levels. A ratio of hoop load to axial load may be an appropriate term to keep in mind when comparing configurations.

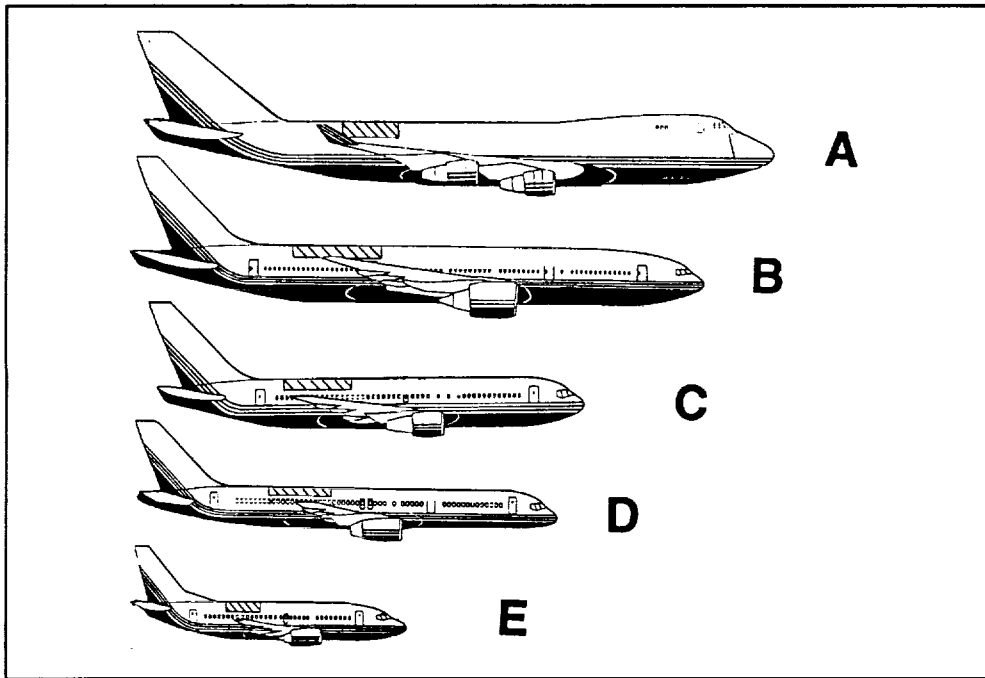


Figure 2: Aircraft Configurations and Crown Panel Locations used for Current Study

Effects of Size on Composite Cost and Weight

Composite crown panel designs were derived based on aircraft shown in Figure 2, using appropriate loads, geometry, and design criteria for each configuration. Design constraints listed in Table 1 were applied. AS4²/938³ tow material was used as the primary material for the present study. The potential cost and/or weight savings of using other materials types such as a material with a higher modulus or a tougher resin is discussed in a following section. A brief summary of the design results is listed in Table 2.

² AS4 is a graphite fiber system produced by Hercules, Inc.

³ 938 is a epoxy resin system produced by ICI/Fiberite.

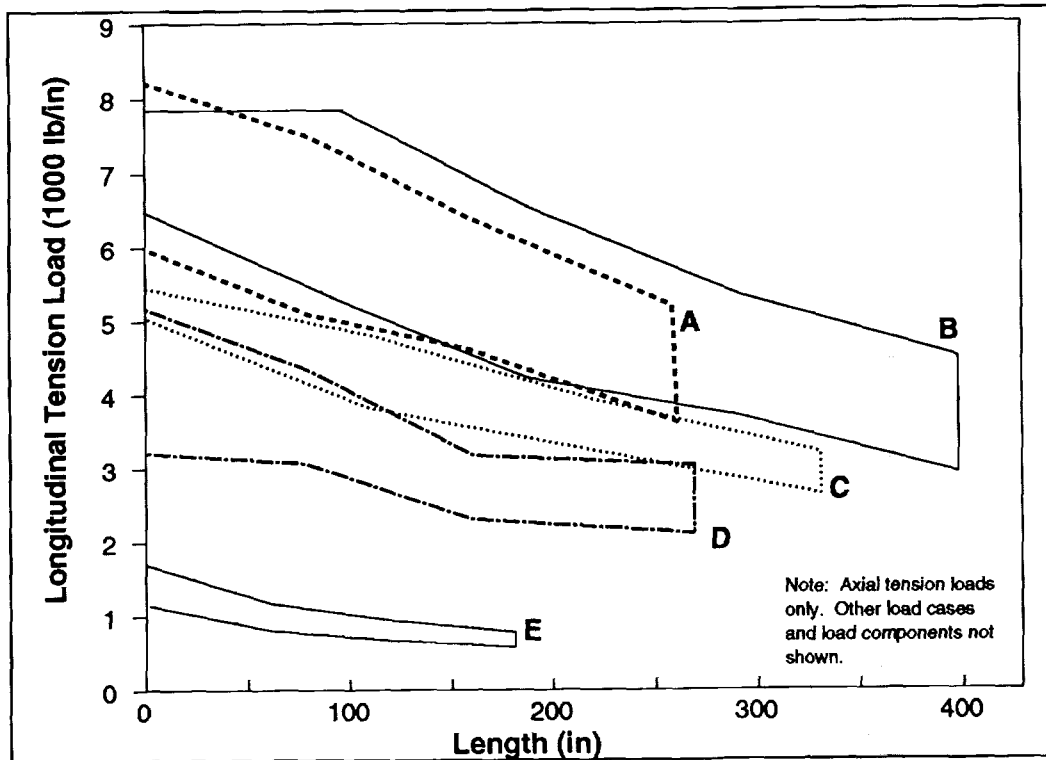


Figure 3: Crown Panel Load Envelope Comparison of Aircraft Configurations used for Current Study

	Radius (in)	Maximum Axial Tension Load (lb/in)	Minimum Axial Tension Load (lb/in)	Maximum Number of skin plies	Minimum Number of skin plies	Length (in)	Width (in)
A	128	8209	3600	18	14	260	213
B	122	7800	3100	18	16	398	211
C	99	5400	2700	14	12	330	150
D	74	5200	1960	14	12	270	180
E	74	1710	800	10	10	180	170

Crown Panel Structure - Section 46	AS4/938 Tow Material (35% R. C.)
Hat Stiffened Panel -	$E_{11} = 19.2e6$ psi
Stiffener Spacing 16"	$E_{22} = 1.36e6$ psi
Pressure Loads:	$\nu_{12} = 0.32$
9.6 psi Fail-safe	$G_{12} = 0.72e6$ psi
13.6 psi Ultimate (with flight loads)	
18 psi Ultimate (acting alone)	

Table 2: Data Relating to Designs used in Size Study

The effect of different panel lengths on the cost and weight were assessed. For this study, the crown panel width was held constant for each configuration and the length was varied. The section 46 crown panel length was measured from the aft wheel well bulkhead location. This implies that the longer crown panel lengths include more of the lightly loaded structure typical of the extreme aft crown panel. This effect is seen in the comparison of crown panel weight to the overall size shown in Figure 4. Trends for the four largest aircraft (A-D) show a lighter crown panel weight per unit area as the panel size increases, reflective of the greater amount of lightly loaded structure included in the larger panel sizes. Aircraft configuration E is constant as a function of size. This is indicative of a smaller aircraft that has a relatively low longitudinal loading, causing the design to be dominated by the hoop loading condition, which is constant along the length.

One important note to make regarding Figure 4 is the difference in the relationship of weight with size for a given configuration and the relationship with size between the aircraft configurations. It is often tempting in a study of this type to draw a line between points based on different aircraft configurations and claim a relationship between size and weight. If that were done, a misleading trend could be obtained.

In addition to the weight comparisons, cost data based on the relationships presented in Figure 1 were used to establish the comparative costs of the composite crown panels as a function of size. These data are presented in three forms, relative cost (Figure 5), relative cost normalized to the area (Figure 6), and relative cost normalized to the panel weight (Figure 7). In each figure, the cost is shown as a function of size for each configuration, with the data point showing the actual crown panel design point. In each figure, the recurring labor and material cost and the nonrecurring cost for airplane B are shown. The economy obtained with larger sizes is apparent in the recurring labor and non-recurring (tooling) components. The recurring material is less influenced by size and tends to follow a relationship similar to the weight trends discussed earlier.

An important point to note in Figures 5 through 7 is the lack of economy for very small panels. The effect of tooling costs and recurring labor costs become very large for small panel sizes. This is especially noticeable in Figures 6 and 7 where the cost is normalized to the panel area and weight, respectively.

As discussed earlier for the weight relationship, drawing conclusions using data from different airplane configurations can be easily misinterpreted. Even though the trends in Figures 5 and 6 show a relatively small scatter between the configurations (13% for 40000 in²), the trends are definitely a function of both the aircraft size and load levels. These trends are much greater in Figure 7 where the cost is normalized to the panel weight ("dollars per pound"). A design engineer may make decisions based on a curve fit of the five data points in Figure 7 and not the actual relationship between "dollars per pound" and size for a given configuration. In this case, the cost estimate could have significant error, leading to an incorrect design decision.

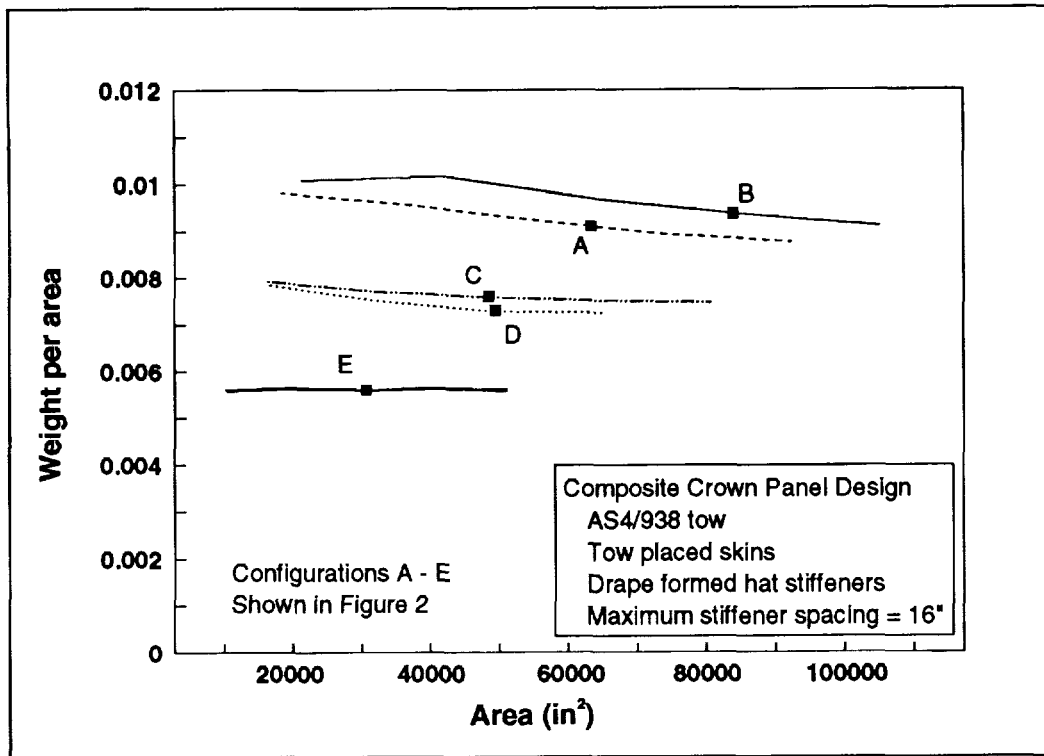


Figure 4: Effect of Crown Panel Size on Weight

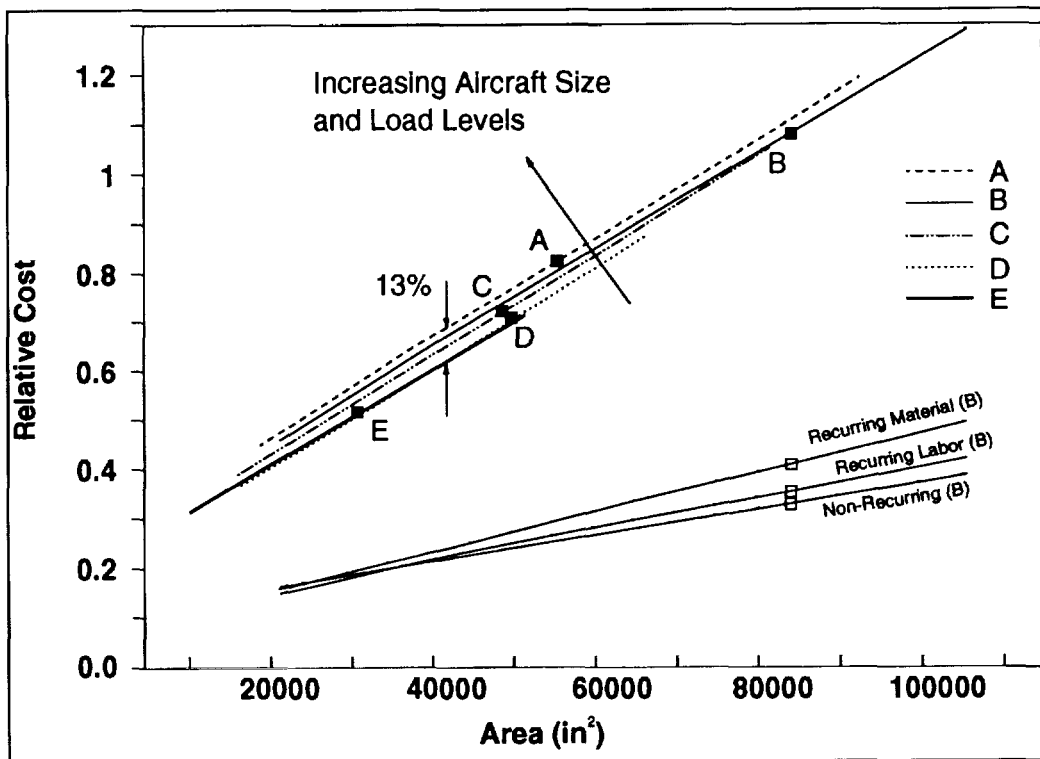


Figure 5: Effect of Crown Panel Size on Relative Cost

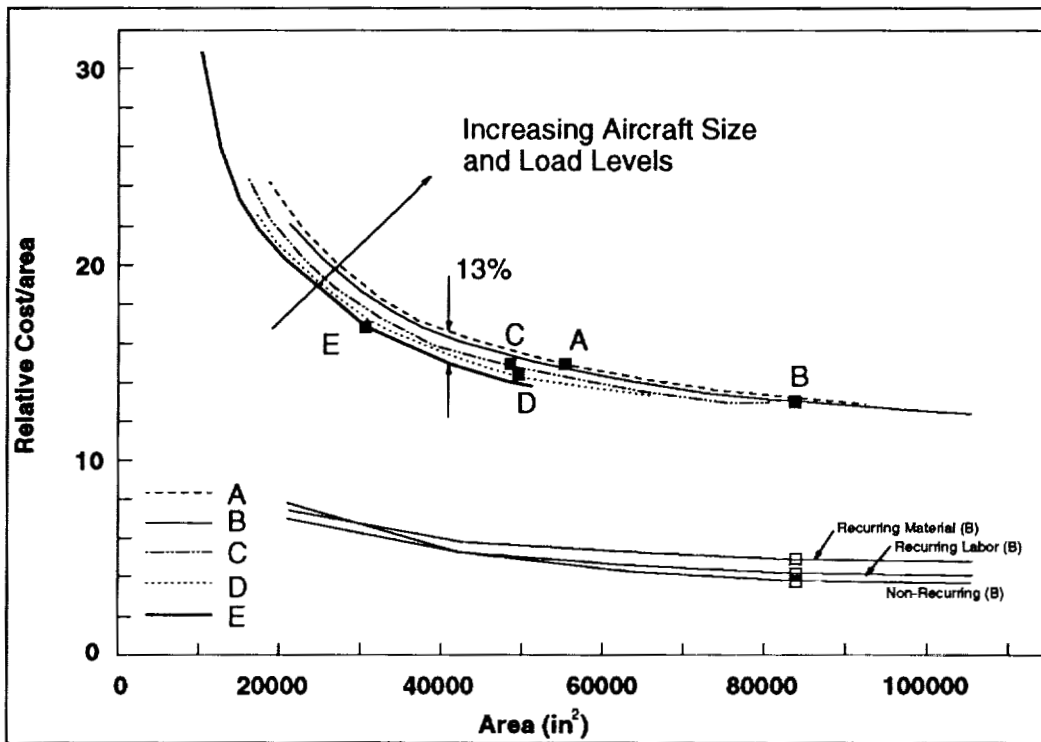


Figure 6: Effect of Crown Panel Size on Cost Normalized by Area

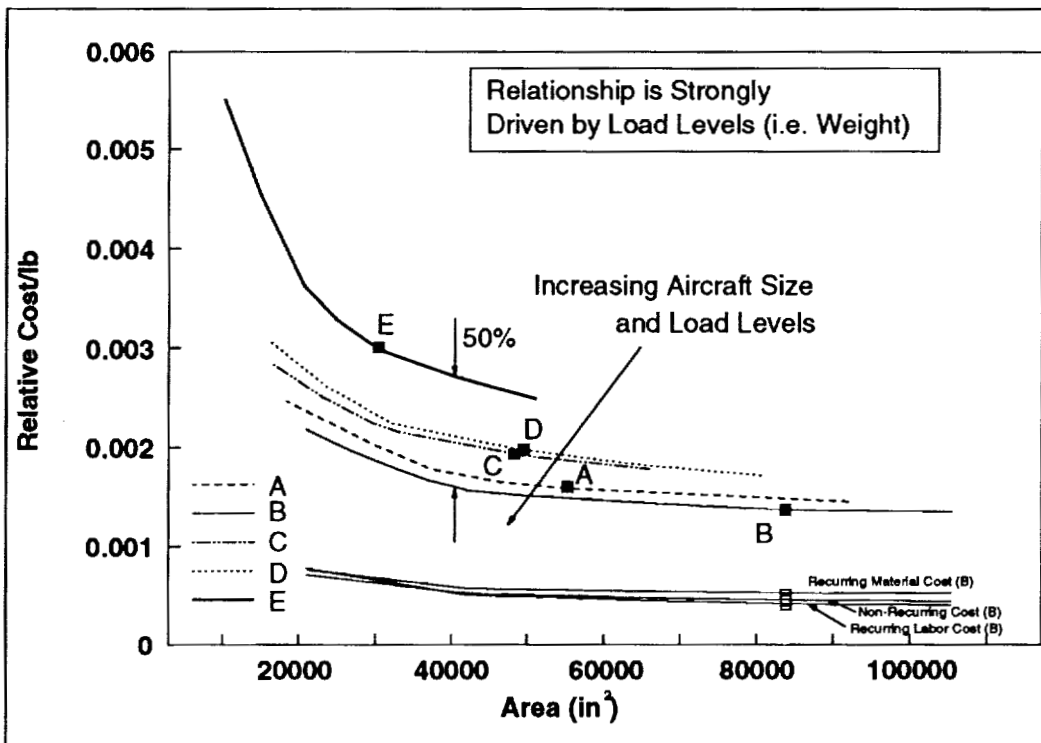


Figure 7: Effect of Crown Panel Size on Cost Normalized to Panel Weight

Cost and Weight Comparison of Composite and Metal Designs

It is often desirable to compare an emerging technology to an existing one to better understand the benefits and drawbacks of the new technology and where to invest future resources. In the world of composite materials, comparison is often made to the aluminum design, the backbone of today's commercial airframe industry. A comparison of aircraft configuration B is shown relative to an equivalent aluminum design in Figure 8. One of the most important points to note in the figure is that the metal design is not shown as a point but rather as a range of cost and weight. The aluminum design community is constantly looking for ways to lower the cost and/or weight of the design, as is the composite material community. The line in Figure 8 defining the "Current Aluminum Technology" represents the latitude that an airframe design engineer has based on a specific program's goals to minimize cost at the expense of weight, or visa versa. This decision relates to many economic factors. The location of an aluminum design within this range can greatly affect how the emerging composite design is compared.

For the composite design, the data point in Figure 8 represents a crown panel with hat stiffeners using a tow placed AS4/938 material system. This point represents the first hardware application of COSTADE. The details describing this data point are shown in Figure 9 along with some of imposed constraints. These constraints included higher axial loads and a larger crown panel size, based on updated load and geometry information since the original design [1]. Other constraints included that the aft laminate remain unchanged from the original design due to the existing material and laminate database and test plans on the Boeing ATCAS program. These load increases and laminate constraints are typical of real world design processes.

From this data point, the design engineer can trade a number of alternatives based on overall program direction to minimize cost, weight, or some combination of the two based on some level of dollars spent per pound of weight saved. The envelope drawn around the composite design point is an estimate of the range this particular crown panel design can be moved during cost and weight trade studies.

It is at this stage in the design process that many of the material decisions on aircraft programs are made. Material requirements for the tension load dominated crown panel may differ from the material requirements of other parts of the fuselage such as the keel [9]. For the particular crown panel application shown in Figure 8, the apparent toughness for large damage sizes exhibited by the tow placed AS4/938 material system suggests that it is a better choice than the resins typically described as tough [5, 6]. The medium modulus AS4 fibers were traded against higher modulus fibers which tend to be more expensive. The resulting weight savings associated with the higher modulus fiber was not sufficient to overcome the lower cost of the AS4 fiber for the assumed value of a pound of weight used in the current study.

Another material considered to have merit for crown panel applications is a hybrid material. In the current study, a hybrid material is defined as a material system that combines graphite and fiberglass fibers within a lamina to increase the damage tolerance. The resulting material has a lower effective modulus than an all graphite material, resulting in design criteria such as stiffness and stability to become more critical. As shown in Figure 8, hybrid applications tend to reduce cost due to the lower material cost, but tend to add weight due to an increased material density and the effect of stiffness and stability on the design. A lowering of these constraints tends to reduce the design weight without significant impact on cost.

The risk associated with the cost estimate is also shown in Figure 8. This is shown in two parts, the risk of the material price projections and the risk of emerging technologies not being developed. These risks are subjective, yet show that the costs are still at the same general cost level of the lower weight aluminum design space.

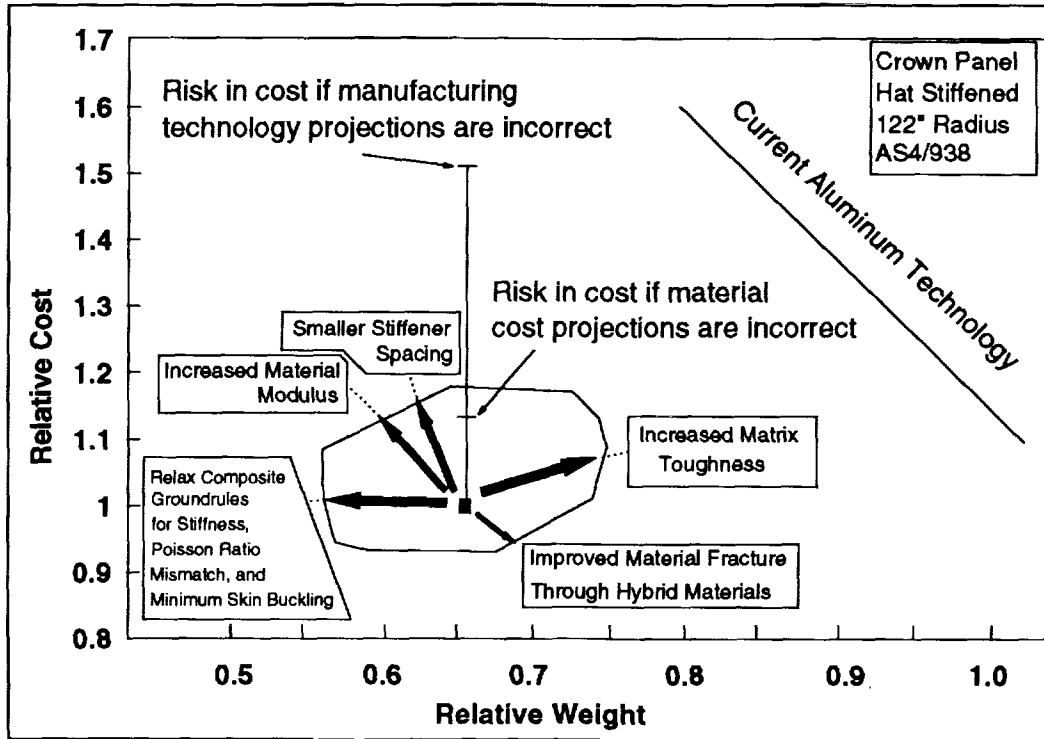


Figure 8: Comparison of a Composite Crown Panel Design to an Equivalent Aluminum Design

Weight Comparison of Composite and Aluminum Configurations

A comparison relating potential weight savings for composite structures to another design can be made by comparing the stress levels and densities of the aluminum design and the competing composite design. In general, for a given load, a higher stress level generally represents less required material in the design. If two materials are at an equivalent stress level, the weight savings would be directly proportional to their densities. In Figure 10, a comparison of the potential weight savings between the five composite crown panel designs and their aluminum counterparts is shown. Note that the shaded area represents the region of weight variance in the metal design described in Figure 8. It is important to note that the aluminum designs were based on many different assumptions over many years and may be different if designed in today's economy.

An assumed relationship between the potential weight savings and axial load level is shown in Figure 10 for the five configurations used in the current study. For a given diameter, a family of curves exists that relate the weight savings to the load level based on a maximum allowable aluminum stress level. If the maximum aluminum stress level is constant, the weight savings potential increases as the longitudinal load level increases, until a limiting composite stress level is reached.

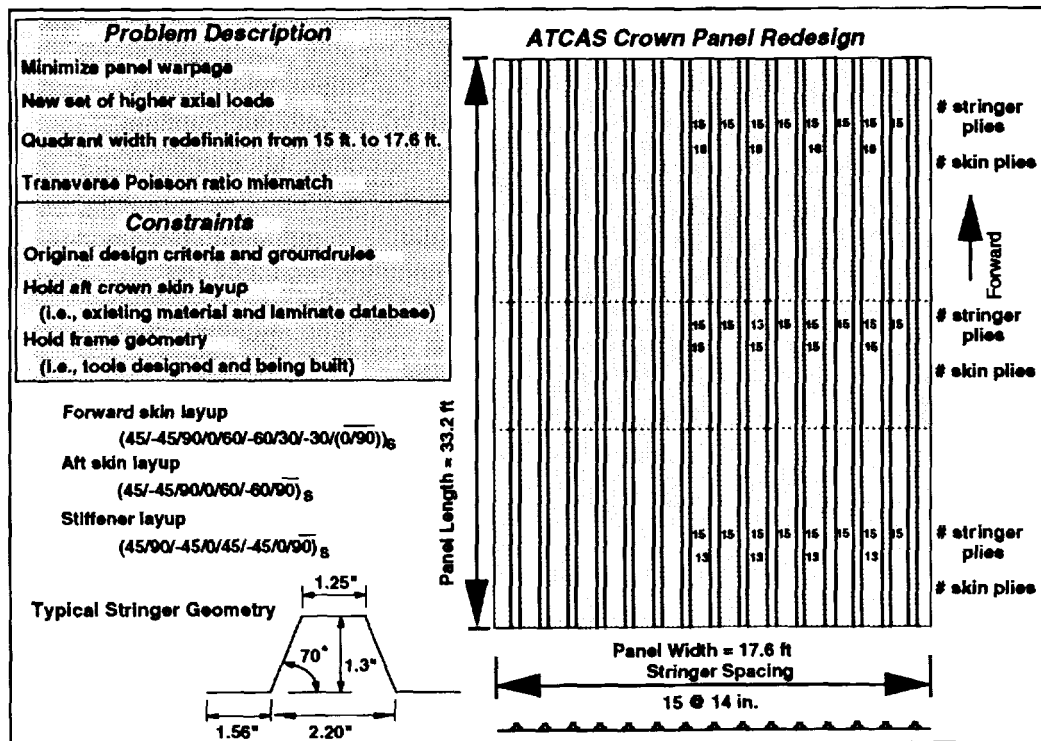


Figure 9: Crown Panel Design Result Using COSTADE

Note that a small, short fuselage tends to have low axial loads, making it appear unattractive for composite applications. However, the composite design was based on a material system chosen for minimum cost. When a weight emphasis is placed on the design, as was described in Figure 8, other material and criteria decisions may make the weight savings potential more attractive at this extreme end of the design envelope. In addition, longitudinal load levels logically increase as the fuselage length increases for a given diameter. For a typical family of airplanes, growth in the fuselage length typically occurs to satisfy customer requirements. A decision to choose a material system must take that growth into account. Finally, very light gage material is used in the aluminum design for the smaller aircraft. Additional weight, in the form of skin doublers (tear straps) under the frame are not reflected in the stress levels used to establish the trends in Figure 10. These factors will again tend to make the composite design more attractive.

PART 2: EFFECTS OF CONFIGURATION

To improve the buckling resistance of the skin panel, the introduction of a sandwich core to the skin, effectively creating a stiffened sandwich configuration, is compared to a more typical stiffened configuration. The tendency of sandwich core to reduce weight for larger spacings and its effect on cost is investigated. Previous studies [1, 4] discussed cost and weight trends for more typical stiffened skin designs. Decreased cost associated with fewer stiffeners (i.e. larger stiffener spacings) came at the penalty of increased weight. Optimum stiffener spacing was determined by the premium value (dollars per pound) that customer or manufacturer is willing to pay to save a pound of weight.

In this part of the current study, three configurations are considered: 1) a hat stiffened skin with no skin buckling allowed below Ultimate load, 2) a hat stiffened design with postbuckled skin, subject to a 38% minimum buckling requirement, 3) a hat stiffened sandwich panel constrained to be buckle resistant below Ultimate loads. A schematic of the three concepts and a photograph of some manufacturing demonstration articles representative of these concepts is shown in Figure 11.

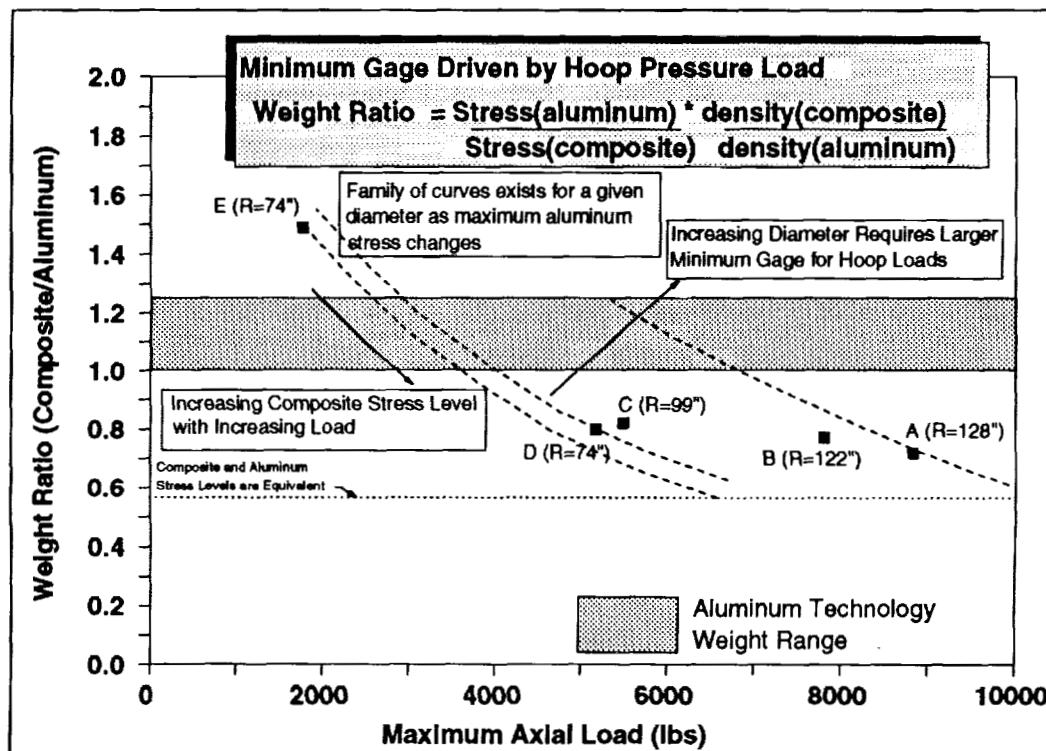


Figure 10: Comparison of a Composite Crown Panel Weight Savings Potential Relative to an Equivalent Aluminum Design

Effects of only applying stability constraints on stiffened sandwich design

Because skin stability plays such an important role in defining the crown panel stiffener spacing requirements, a simplified design study was undertaken that included only one compression load condition constrained by skin buckling, general instability, and local stiffener buckling. An additional constraint of face wrinkling was included for the stiffened sandwich designs. The three configurations shown in Figure 11 were optimized for minimum weight using the geometry of aircraft B from Figure 2. Two load levels, 1000 lb/in, typical of an aft crown panel compression load and 3000 lb/in, typical of a forward crown panel compression load, were considered. The cost values were based on the equations presented in Figure 1. This exercise was undertaken to provide information on whether the stiffened sandwich would be an attractive alternative without doing a fully constrained crown panel design.

The results of this study are shown in Figures 12 and 13. For the stiffened sandwich structure, a range of As/Ds values is used. This ratio couples the stiffener cross-sectional area (As) and the stiffener spacing (Ds). Note that in both figures, the weight is increasing with stiffener spacing while the cost is

decreasing with stiffener spacing. This is the same type of trend shown in [1, 4]. In these graphs, the value of saving weight is not accounted for in the relative cost relationships. Determining the benefits of lighter weight on the effective cost of different configurations would be needed to choose the most cost effective configuration.

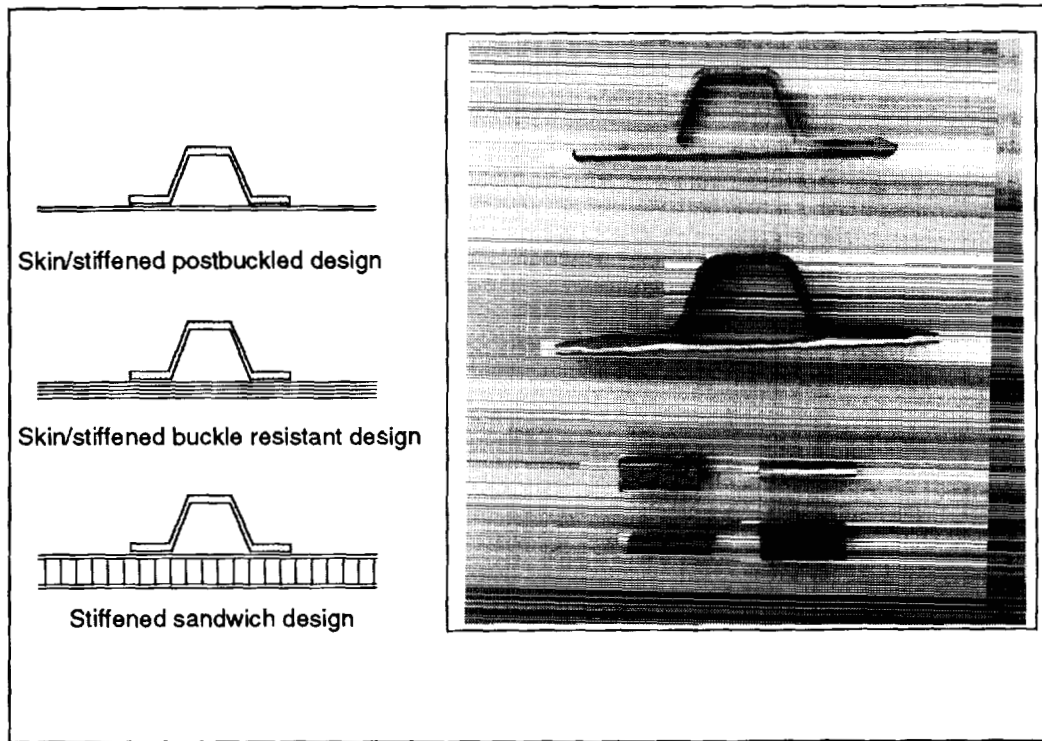


Figure 11: Configurations used in Stiffener Spacing Study

At 1000 lb/in, the postbuckled design is marginally heavier than the stiffened sandwich design, with the buckling resistant stiffened laminate significantly heavier. However, the postbuckled design was clearly more cost efficient than the other configurations at this load level. The cost saved by the lower weight of the stiffened sandwich did not overcome the additional cost of adding core to the design. The extra material used in the buckling resistant stiffened laminate made that configuration the heaviest. The cost, however, was essentially equivalent to the stiffened sandwich.

At 3000 lb/in compression, the relationships change. The best postbuckled design occurs when the stiffener spacing is small, yet it is not as weight efficient as the stiffened sandwich at any stiffener spacing. The cost effectiveness of the stiffened sandwich and the postbuckled design are essentially equivalent at this load level, with a slight advantage to the stiffened sandwich. The buckling resistant stiffened laminate is by far heavier and more expensive than the other two configurations.

The results of this initial, buckling only, study indicate that stiffened sandwich structure may be a good candidate to minimize the cost and weight of a stability dominated structure, given that the panel was subjected to relatively high compression loads. The next logical step, and the final part of the current study, is to determine the effects of stiffened sandwich given all of the design constraints outlined in Table 1 for a crown panel design.

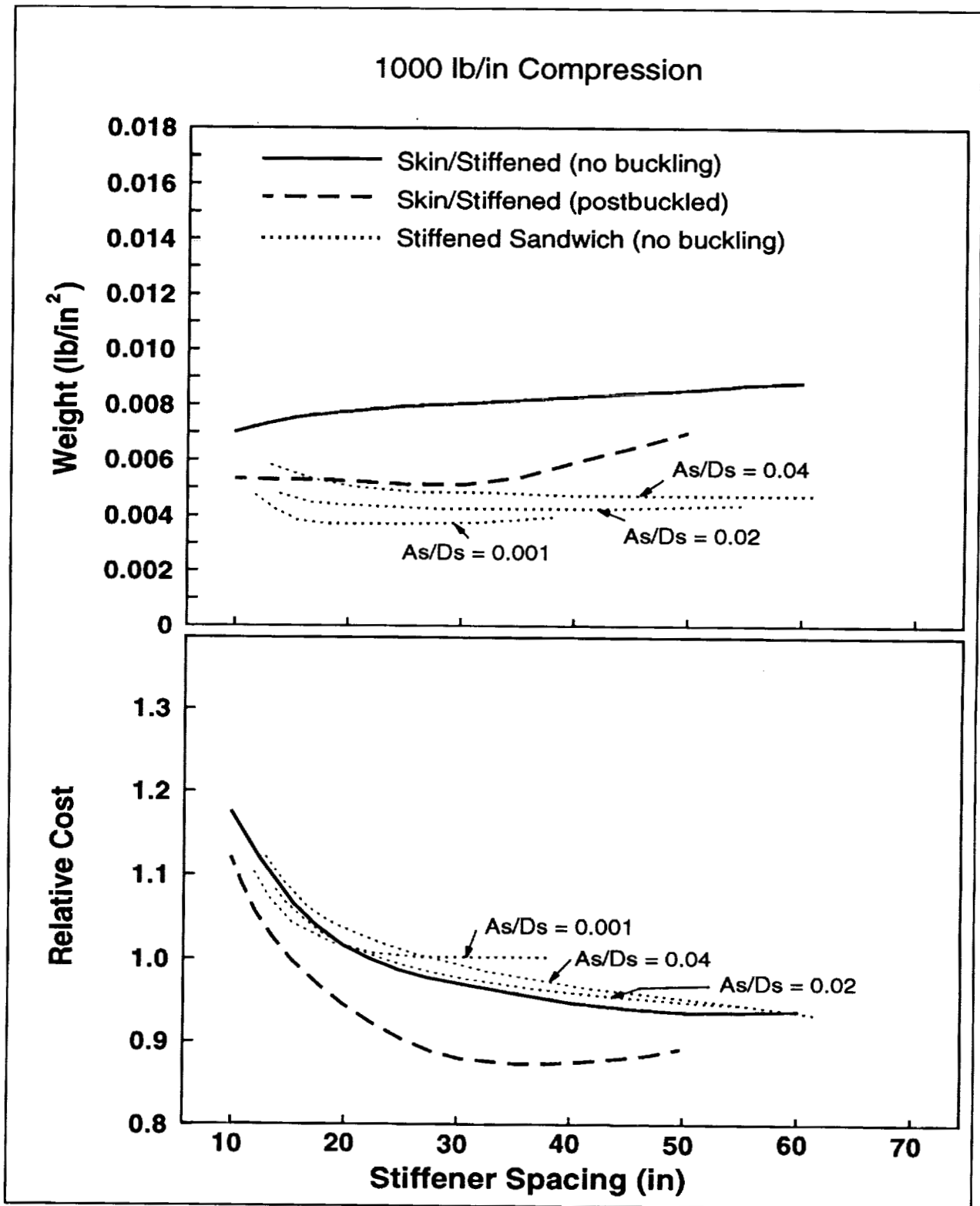


Figure 12: Cost and Weight Design Trends for Stiffened Panels Subjected Only to Buckling Constraints (1000 lb/in Compression)

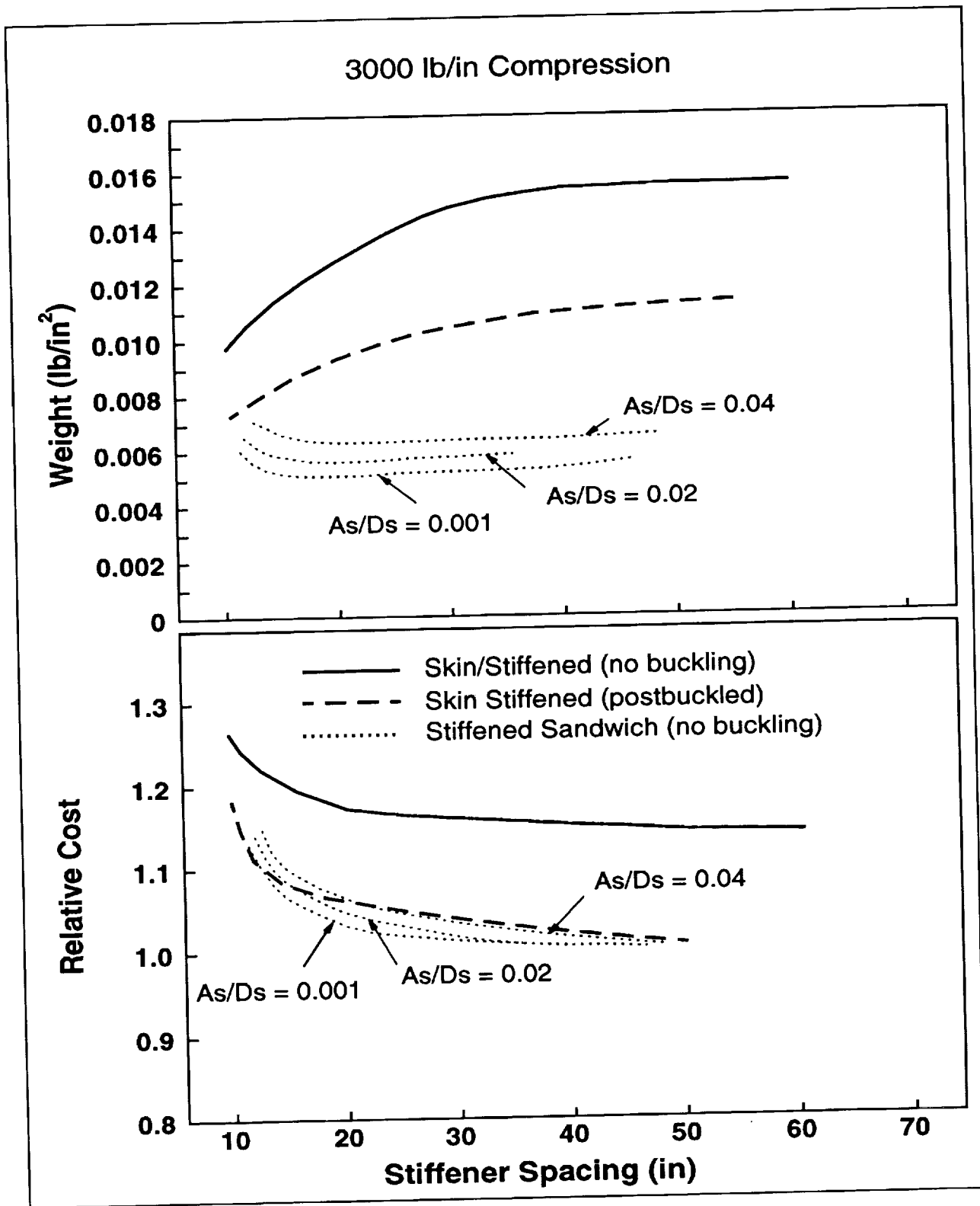


Figure 13: Cost and Weight Design Trends for Stiffened Panels Subjected Only to Buckling Constraints (3000 lb/in Compression)

Effects of Crown Panel Design Criteria on Stiffened Sandwich

In the last part of this study, a forward and an aft crown panel design are considered using the same three configurations presented in Figures 12 and 13. These designs include the effects of the criteria listed for the crown panel in Table 1. The costs do not reflect any additional value for weight savings.

Many of the analysis routines in the current version of the designer's cost model are based on simplified preliminary analysis design tools. Further development of some of these tools is ongoing and will be incorporated when complete. One of the analysis methods being developed is the tension damage tolerance assessment of a stiffened, orthotropic structure [5, 6, 10]. Currently, the cost model has a simplified damage tolerance routine that has proven to be inadequate for certain conditions. To address the effect of the stiffener spacing on the fully constrained design, some modifications to the tension damage tolerance analysis were made. It was assumed that up to a 20" axial damage size would be tolerated without any effect of load redistribution to the stiffening members for stiffener spacings larger than 20".

Other analysis routines that are to be added include a panel warpage assessment [11] and a stiffened and unstiffened sandwich analysis. Currently these are not yet incorporated. The sandwich analysis in this final part of the current study was calculated by a design engineer using the currently available design charts, spreadsheets, and lamination computer codes. It is interesting to note, and a big incentive for the cost model development, that the time needed to generate the analysis trends for the stiffened sandwich was on an order of magnitude longer than to develop similar trends using the cost model for both the buckling resistant and postbuckled hat stiffened panel designs. The many load cases and criteria that are checked in the process of developing a design can become cumbersome when doing an analysis by hand. The trends in time saved will be amplified even more when an entire panel is considered with many changing load levels. The blending function currently being developed for the cost model will address this situation.

The results of the fully constrained crown panel design for the lightly loaded (aft) and heavily loaded (forward) ends are shown in Figures 14 and 15, respectively. For small stiffener spacings, similar cost and weight trends to [1, 4] are observed for the stiffened laminate designs, with the post buckled design showing more cost and weight efficiency than the design constrained to resist buckling. At these smaller spacings, minimum skin buckling, axial and hoop damage tolerance, and axial stiffness tended to have the lowest margins of safety.

As stiffener spacings approached the frame spacing (22"), the revised damage tolerance analysis was implemented. In addition, the buckling mode shape of the skin between the stiffeners also approaches a critical point as the stiffener spacing approaches the same value as the frame spacing. Larger stiffener spacings affect the number of buckling waves across the skin bay between stiffeners. The required skin thickness to resist this buckling mode is such that the hoop damage tolerance is no longer critical for the larger stiffener spacings. The area labeled "transition zone" in the figure refers to the area where the critical design constraints are changing. Designs in this area are questionable in that small changes in any load or constraint may trigger different design constraints to be critical. Beyond this "transition zone," the design is driven by the axial damage tolerance and the buckling constraints. Little difference is seen between the postbuckled and buckle resistant stiffened skin designs in this region. For these larger stiffener spacings, postbuckling is no longer an effective way to save weight since a significant amount of material is needed to satisfy the minimum buckling constraint and the

stiffeners are less and less effective as the spacings increase. Reduced weight and cost as a function of stiffener spacing in this region is directly proportional to the reduction in the number of stiffeners.

The best stiffened sandwich design for both cost and weight is the limiting case of an unstiffened sandwich panel. The increased bending stiffness of the sandwich relieves the pressure effects at the notch tip and improves the buckling resistance of the skin. The addition of the core material, however, is a source of increased weight and significant cost. For the lightly loaded aft design, shown in Figure 14, the best sandwich design (large stiffener spacing) is both heavier and more expensive than the best postbuckled design (small stiffener spacing). The added axial and hoop loads along with the tension damage tolerance constraints require additional skin material in the sandwich beyond what is needed for the buckling constraint, resulting in somewhat different trends than shown in Figure 12 for stability only. The compression loads applied to both of these cases are similar.

For the more heavily loaded forward crown design shown in Figure 15, similar trends exist as were shown in Figure 14. The major difference is that the relationship between the best postbuckled design and sandwich design is much closer, suggesting that the higher loads make the sandwich design more favorable, a trend consistent with the buckling only results discussed earlier. For keel applications where very high compression loads occur, this trend would tend to favor the sandwich design [9].

Conclusions

A design study investigating the effects of size and configuration of a composite crown panel was undertaken. Results indicate that both aircraft geometry, load intensities, and material decisions can greatly affect the cost and weight of the designs. Larger crown panel sizes tended to be more economical. Comparison to aluminum technology utilized a concept of comparing feasible design regions, since both composite and aluminum designs can vary depending on weight and cost targets. The range of weight and cost in which a feasible design can be found is based on decisions that an engineer can make regarding material, geometry, and criteria.

The effect of stiffened sandwich, as compared to postbuckled and buckle resistant structure, suggests that for stability dominated designs, a stiffened sandwich concept can be weight effective without significant cost differences. This trend becomes more attractive for larger compression loads. When the remaining load conditions and design constraints typical of a crown panel are applied, the trend changes such that a sandwich structure without stiffeners is still not as efficient in both cost and weight as a postbuckled design. The trends suggest that as the load increases, the difference between these two concepts is less. A stiffened sandwich design may be a benefit for more heavily loaded compression panels.

The benefits of a design cost model in this type of study are evident. For the stiffened sandwich study, design constraints were not yet incorporated into the model, forcing a design engineer to run the trade studies using conventional analysis and available design tools. For the fully constrained crown panel design, the time needed to complete the trade study for the stiffened sandwich as compared to both stiffened laminate designs was an order of magnitude longer. The understanding gained by seeing the effects of the design on both cost and weight is a great benefit to an engineer. Further development of the cost model to include the sandwich constraints, along with warpage constraints, improved damage tolerance analysis, a blending function to handle load variations, and a more general cost framework are ongoing.

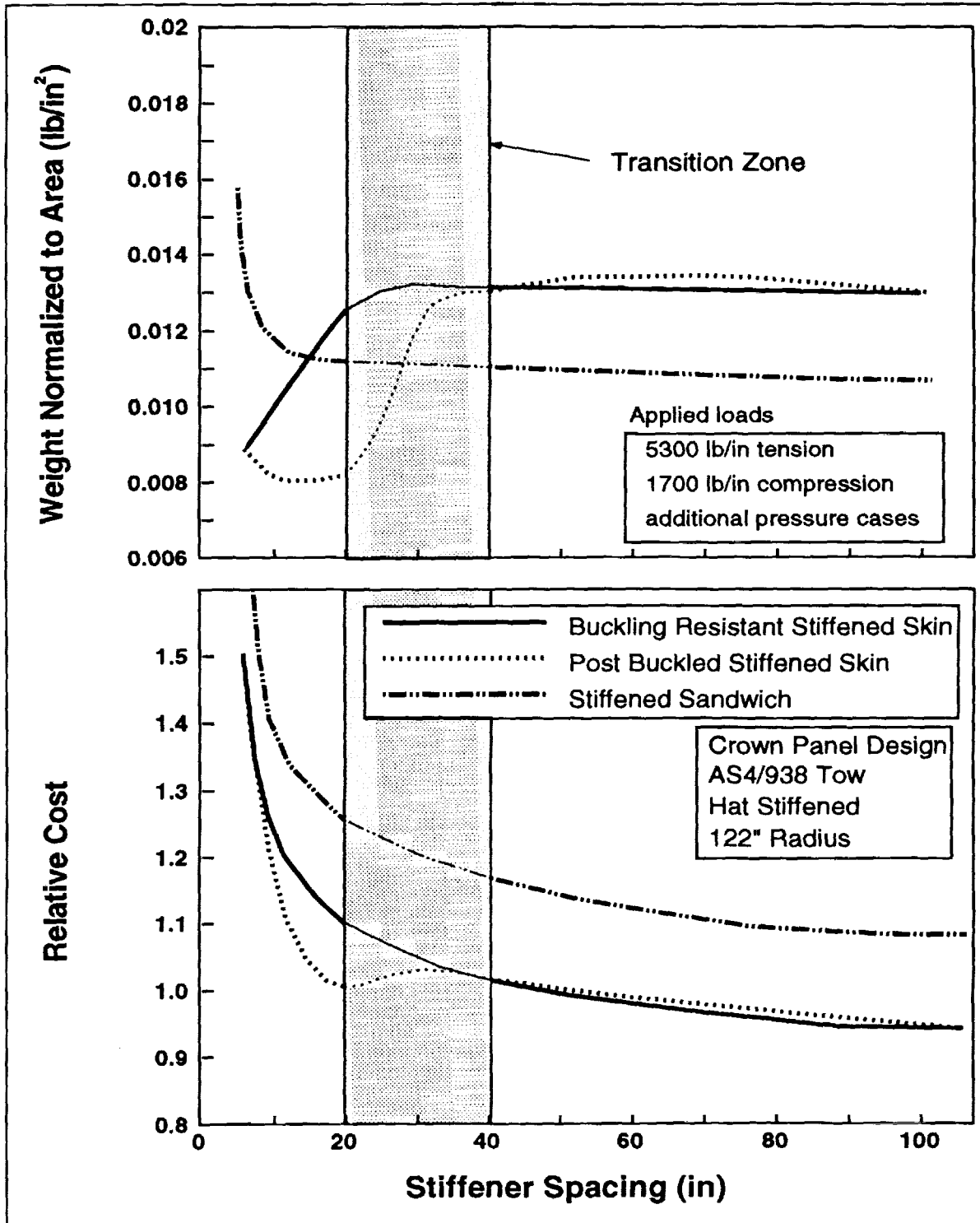


Figure 14: Cost and Weight Design Trends for Stiffened Panels Subjected to Crown Panel Design Constraints (Lightly Loaded Aft Crown Panel)

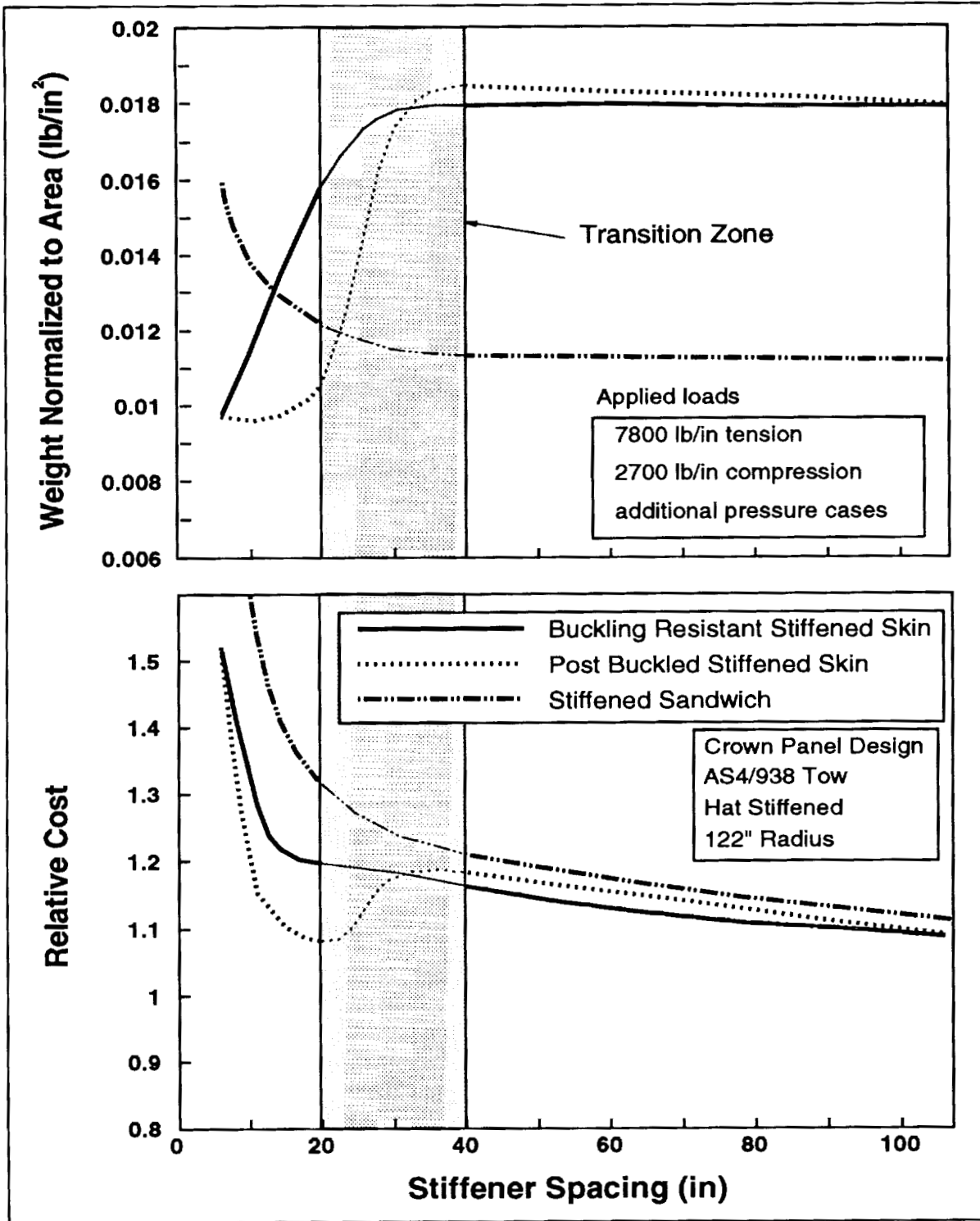


Figure 15: Cost and Weight Design Trends for Stiffened Panels Subjected to Crown Panel Design Constraints (Heavily Loaded Forward Crown Panel)

References

1. G. D. Swanson, L. B. Ilcewicz, T. H. Walker, D. Graesser, M. Tuttle, Z. Zabinsky: "Local Design Optimization for Composite Transport Fuselage Crown Panels," In Proceedings of the Ninth DoD/NASA/FAA Conference on Fibrous Composites in Structural Design, Lake Tahoe, NV, FAA Publication, 1991.
2. W. T. Freeman, L. B. Ilcewicz, G. D. Swanson, T. Gutowski: "Designer's Unified Cost Model," In Proceedings of the Ninth DoD/NASA/FAA Conference on Fibrous Composites in Structural Design, Lake Tahoe, NV, FAA Publication, 1991.
3. Z. Zabinsky, M. Tuttle, D. Graesser, G. D. Swanson, L. B. Ilcewicz: "Multi-Parameter Optimization Tool for Low-Cost Commercial Fuselage Crown Designs," First NASA Advanced Composites Technology (ACT) Conference, October 30 -November 1, 1990, NASA CP-3104.
4. C. Kassapoglou, A. J. DiNicola, and J. C. Chou: "Innovative Fabrication Processing of Advanced Composite Materials Concepts for Primary Aircraft Structures," NASA Contractor Report 189558, February 1992.
5. T. H. Walker, W. B. Avery, L. B. Ilcewicz, C. C. Poe, C. E. Harris: "Tension Fracture of Laminates for Transport Fuselage, Part 1: Material Screening," In Proceedings of the Ninth DoD/NASA/FAA Conference on Fibrous Composites in Structural Design, Lake Tahoe, NV, FAA Publication, 1991.
6. T. H. Walker, W. B. Avery, L. B. Ilcewicz, C. C. Poe, C. E. Harris: "Tension Fracture of Laminates for Transport Fuselage, Part 2: Large Notches," In Proceedings of the Third NASA Advanced Composites Technology (ACT) Conference, Long Beach, CA, June 8 - 11, 1992, NASA CP-3178.
7. L. B. Ilcewicz, T. H. Walker, K. S. Willden, G. D. Swanson, G. Truslove, and C. L. Pfahl: "Application of a Design-Build-Team Approach to Low Cost and Weight Composite Fuselage Structure," NASA Contractor's Report 4418, 1991.
8. T. H. Walker, P. J. Smith, G. Truslove, K. S. Willden, S. L. Metschan, C. L. Pfahl: "Cost Studies for Commercial Fuselage Crown Design," In Proceedings of the Ninth DoD/NASA/FAA Conference on Fibrous Composites in Structural Design, Lake Tahoe, NV, FAA Publication, 1991.
9. B. W. Flynn, M. R. Morris, S. L. Metschan, G. D. Swanson, P. J. Smith, K. H. Griess, M. R. Schramm, R. J. Humphrey: "Global Cost and Weight Evaluation of Fuselage Keel Design Concepts," Third NASA Advanced Composite Technology Conference, NASA CP-3178.
10. L. B. Ilcewicz, P. J. Smith, and R. E. Horton: "Advanced Composite Fuselage Technology," Third NASA Advanced Composite Technology Conference, NASA CP-3178.
11. G. Mabson, B. W. Flynn, R. Lundquist, G. D. Swanson, P. Rupp: "Dimensional Stability of Curved Panels with Cocured Stiffeners and Cobonded Frames," Third NASA Advanced Composite Technology Conference, NASA CP-3178.

Session VII

**AUTOMATED FIBER PLACEMENT
TECHNOLOGY**

Session Chairman: William T. Freeman, Jr.
NASA Langley Research Center

**AUTOMATED FIBER PLACEMENT—EVOLUTION
AND CURRENT DEMONSTRATIONS**

Carroll G. Grant, Hercules Aerospace Company
Program Manager, NASA ACT Contracts
Composite Structures Group
Bacchus, Works, Magna, Utah 84044

59-24
57409

Vernon M. Benson, Hercules Aerospace Company
Manager, Composite Structures Technology
Composite Structures Group
Bacchus Works, Magna, Utah 84044

ABSTRACT

The automated fiber placement process has been in development at Hercules since 1980. Fiber placement is being developed specifically for aircraft and other high performance structural applications. Several major milestones have been achieved during process development. These milestones are discussed in this paper.

The automated fiber placement process is currently being demonstrated on the NASA ACT program. All demonstration projects to date have focused on fiber placement of transport aircraft fuselage structures. Hercules has worked closely with Boeing and Douglas on these demonstration projects. This paper gives a description of demonstration projects and results achieved.

CONFERENCE

Third NASA Advanced Composites Technology Conference
8 – 11 June 1992, Long Beach, California

AUTOMATED FIBER PLACEMENT EVOLUTION

Hercules filament winding experience dates back to 1957. We have used this experience to develop a new automated process to accurately place and compact prepreg tow material that meets the requirements for aircraft applications. The automated fiber placement process (also known as automated tow placement) has been significantly improved over the last 10 years and is now production ready.

In the late 1970s, Hercules identified composite aircraft and space structures as possible applications for automated filament winding. Although filament winding was ideal for rocket motor cases, it was not necessarily a good process for aircraft and space structures. These parts were seldom symmetrical bodies of revolution; many had complex compound curvatures with concave surfaces. Filament winding relied on tension and geodesic paths to keep the material in place and was limited in ply angle orientation capability. On complex structures, filament winding was not practical. Automated tape layup was limited to relatively flat surfaces, and the process was very immature at the time.

A machine was needed that would lay material down at any orientation from 0 to 90°, and that could handle both symmetrical bodies of revolution and complex contoured surfaces. Structures fabricated on this machine needed to be equivalent in performance properties to structures fabricated with prepreg tape and fabric materials. It appeared that the machine would be a hybrid of filament winding, tape laying, and some new technology.

In 1980, the design of a six-axis machine that could follow complex contoured surfaces while placing and compacting material directly on the surface was started by Hercules engineers at the Clearfield, Utah filament winding facility. It was originally called "advanced filament winding" or "six-axis filament winding."

Two years later, the design was complete and procurement of machine elements was under way. In 1983, Hercules assembled the first six-axis machine. This machine incorporated a three-roll wrist (designed for the robotics industry) along with a horizontal profile machine modeled after the state-of-the-art filament winding machines designed and built by Hercules for in-house use.

The delivery system consisted of a standard dry fiber creel, a series of redirects, a hot melt resin impregnation station, and a sophisticated delivery head. The delivery head was capable of delivering 12 tows of material. It was designed to cut one tow at a time, and add one tow at a time when commanded by the software. The cutter and the adder were indexed by two small stepper motors. The tows came in on one level, but were spaced approximately one tow width apart to allow clearance for the cutter and adder for each tow. The tows were converged back together as the tray cavities came closer together. The final delivery roller consisted of a segmented roller, with each segment capable of compacting two tows at a time. These roller segments floated individually to provide compaction of contoured surfaces, while allowing individual fiber speeds across the band.

The new machine and process were distinguished from standard filament winding by being designated "fiber placement," because the individual tows of fiber were now being placed precisely on the surface of the part and compacted in place as they were applied. Another name often used today is "automated tow placement."

The machine and process described above were used to fabricate the Sikorsky ACAP tailcone (Figure 1). Although the ACAP part was successfully fabricated, a

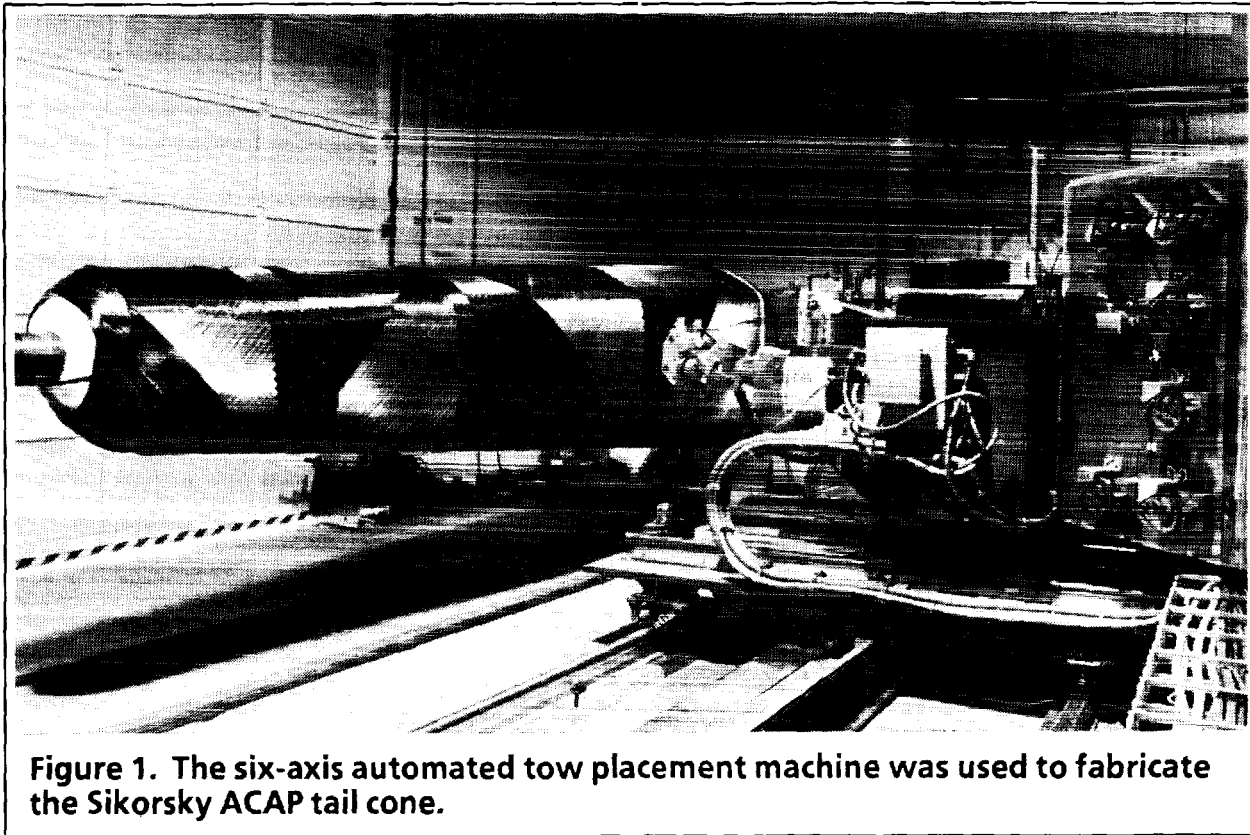


Figure 1. The six-axis automated tow placement machine was used to fabricate the Sikorsky ACAP tail cone.

combination of filament winding and fiber placement methods was used. A need to improve the technology in several areas became apparent because the operation did not proceed as smoothly as the theory indicated. However, it was a significant step in the evolution of fiber placement.

The software required to program the six-axis machine was developed by Dr. Russ Wilhelmsen, a mathematician and computer scientist with a special ability to manipulate spatial geometries. Development and refinement of an off-line programming system for fiber placement has progressed significantly over the past several years.

From the early machine and delivery system to the production ready system available today, there have been many improvements (Figure 2). The more significant evolutionary steps are outlined in the following paragraphs.

MACHINE DEVELOPMENT MILESTONES

Prepreg Tow

Impregnation of dry fiber with a hot melt resin delivery system on the machine had some definite cost advantages. However, resin content control was a problem because the process featured a variable rate with stop and go inconsistencies. Prepreg tow was ordered from material suppliers starting in 1985. The first materials

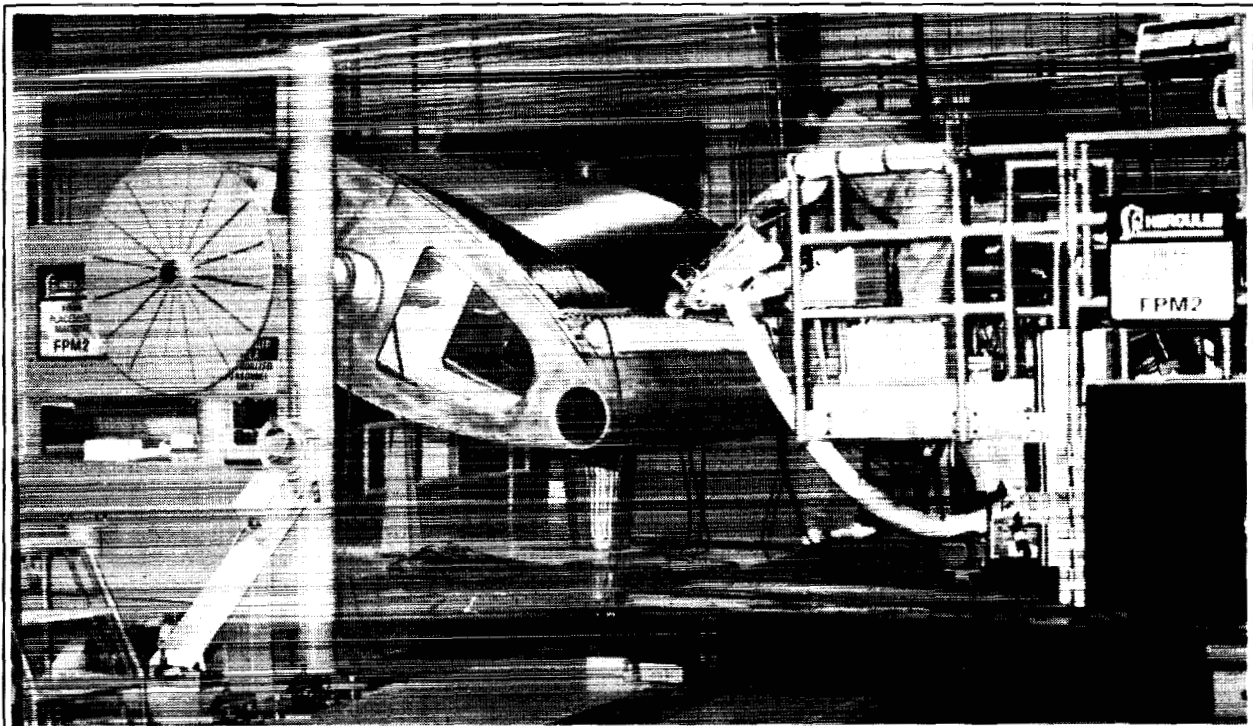


Figure 2. The seven-axis automated tow placement machine incorporates many improvements over earlier machines and delivery systems.

used were made from solvent-based impregnation systems. The materials worked well as long as the residual solvent level was well controlled. Too much solvent made the material very sticky and soft. Mechanical properties testing on the Large Fuselage MANTECH Program showed how difficult it was to get all the residual solvent out of the tow during final part cure. This resulted in lower Tg properties for parts made using solvated prepreg tow.

To improve Tg properties, the Hercules Materials group developed a hot melt prepreg tow process for the Large Fuselage Program (later known as the V-22 Aft Fuselage Demonstration). Since then, the Hercules hot melt prepreg tow process has been greatly refined. Today's process delivers a well-controlled material form for fiber placement. The cost of prepreg tow today is slightly higher than prepreg tape because of the low volume in use. It will become a lower cost material form than prepreg tape as the volume increases.

Bi-Directional Tensioners

One of the key elements in fiber placement is the maintenance of a low, consistent tension. The early delivery creels were capable of applying tension, but did not have the ability to respond to a slack fiber condition, which occurs regularly in fiber placement as a result of the wrist motion on complex surfaces. Simple mechanical devices were used on fiber placement machine No. 1 (FPM1) to keep fibers tight. Fiber placement machine No. 2 (FPM2) was equipped with tensioners

that would allow material to pay out as needed and would take up material on the spool if it attempted to go slack, all the time maintaining constant tension on each tow.

Refrigerated Creel

Prepreg tow does not use backing paper and is spooled on a way wound package to facilitate removal. Some materials can be spooled at room temperature and unspooled successfully, but the majority of them will not. Hercules added refrigeration to the fiber delivery creels to prolong the life of the material, to allow for clean unspooling, and to protect the material from slump when it was not rotating. This has reduced the problems in the creel to near zero.

Ribbonization

Thermoset prepreg tow is in a soft pliable material form. When it is manufactured, the supplier tries to control the width and thickness profile of each tow. Typically, a width control of ± 0.025 inches can be guaranteed by the prepreg supplier for a way wound package. After the spools are loaded onto the fiber placement delivery creel, the fiber must pass through several redirects before it enters the delivery head. Depending on the severity of the fiber path (based on wrist position for a given geometry), the soft pliable tow will often change shape slightly while traveling this path. With a stringent requirement to deliver the individual tows onto a structure with no more than a 0.030-inch gap or overlap between tows or between bands of tows, the tow width variations just described could easily exceed the gap/overlap requirements. To avoid the inconsistencies described, Hercules developed a technique to ribbonize (control the width and thickness of each tow) within the delivery head. This has allowed us to deliver a wide variety of materials and to accommodate last minute design changes from customers. This ribbonizing module can be easily removed from the head if it is not required.

Two Tier Delivery

To accommodate individual tow cut and add mechanisms, the tows in the delivery head are separated into two tiers with a one-tow width separation between each tow. The two tiers of tows are merged together near the delivery point. This allows a straight tow path through the head. The individual actuators for each tow allow any tow or combination of tows to be cut or added back in simultaneously.

Heavy Duty Wrist

A new roll-bend-roll wrist was designed and put into use on FPM2 to accommodate the high compaction forces and newer generation delivery heads. This new wrist was a Hercules design and incorporated a series of compact motor and non-backlash gear assemblies into a wrist package that maintain a high degree of flexibility on each of the three axes.

Large Crossfeed Travel

For large parts with severe cross section changes and for parts where material must be placed on the end of the part near the shaft or rotational centerline, a flexible wrist and a large crossfeed travel are required. Hercules designed FPM2 with 8.5 feet of crossfeed travel, and 1.5 feet of that travel beyond the spindle centerline. This feature was very helpful in fabricating the V-22 aft fuselage, a demonstration boat hull, and a 4-foot diameter sphere. It is also useful to meet production schedules that require the manufacture of widely different part geometries.

Synchronization

To have a tow start and stop accurately on the surface of a part required the development of synchronized motion between the rate at which new tows were being added and the rate at which material is being applied to the surface of the part. It also required look aheads in the software. These features were accommodated in later generations of the delivery head.

Heating and Cooling Zones

Over years of making parts, Hercules learned that strategic heating and cooling of the tows as they are delivered aided in the effective processing of the materials. The tows are cooled to reduce tack and to stiffen them so that they can be fed or pushed. The tows are heated in the ribbonizer to condition their width/thickness control, and are heated slightly at the laydown point to increase the tack characteristics (resin dependent).

Direct CATIA and IGES CAD Link to Off-Line Programming

To ensure that the complex surfaces being programmed are identical to the ones used in the product and tool design of the structures, Hercules developed direct transfer links from CATIA and IGES to feed three-dimensional CAD data to the fiber placement machine's off-line programming system. This direct link allows a rapid, accurate transfer of surface data.

Simulation Software

The need for the ability to estimate manufacturing times before the parts are actually built became apparent early in machine development. Hercules developed software to simulate the actual manufacturing times based on a given part geometry and the kinematics of the machine in which it is to be processed. This is a great help in planning work schedules, estimating costs, and in evaluating design changes to the machine. Hercules also has graphic simulation of the machine applying the material to the structure that can be used to verify that everything is in order before part fabrication.

Data Logging

The machine control system software has been customized over the years to provide a variety of useful data for the fiber placement operator and engineer. Some of these data include: laydown rates, off part times, machine down times, time stamps, system diagnostics, ply and circuit data, time to complete, etc.

These are only some of the significant areas where the evolution of the fiber placement machine technology at Hercules has been apparent. The other measure of the advances in technology can be seen by the quality and types of parts that are being fabricated today. The NASA ACT Program is a good illustration of some of the current work.

CURRENT DEMONSTRATIONS

Hercules ACT Program

The Hercules NASA ACT Program was established to demonstrate and validate the low cost potential of the automated tow placement process for fabrication of commercial aircraft primary structures. It is currently being conducted as a cooperative program in collaboration with the Boeing ATCAS program. Hercules is

responsible for fabrication of test panels that are representative in design of commercial aircraft fuselage Section 46 crown, keel, and side quadrants. Boeing is responsible for panel design and testing (Table I). All panels are fabricated using the automated tow placement process.

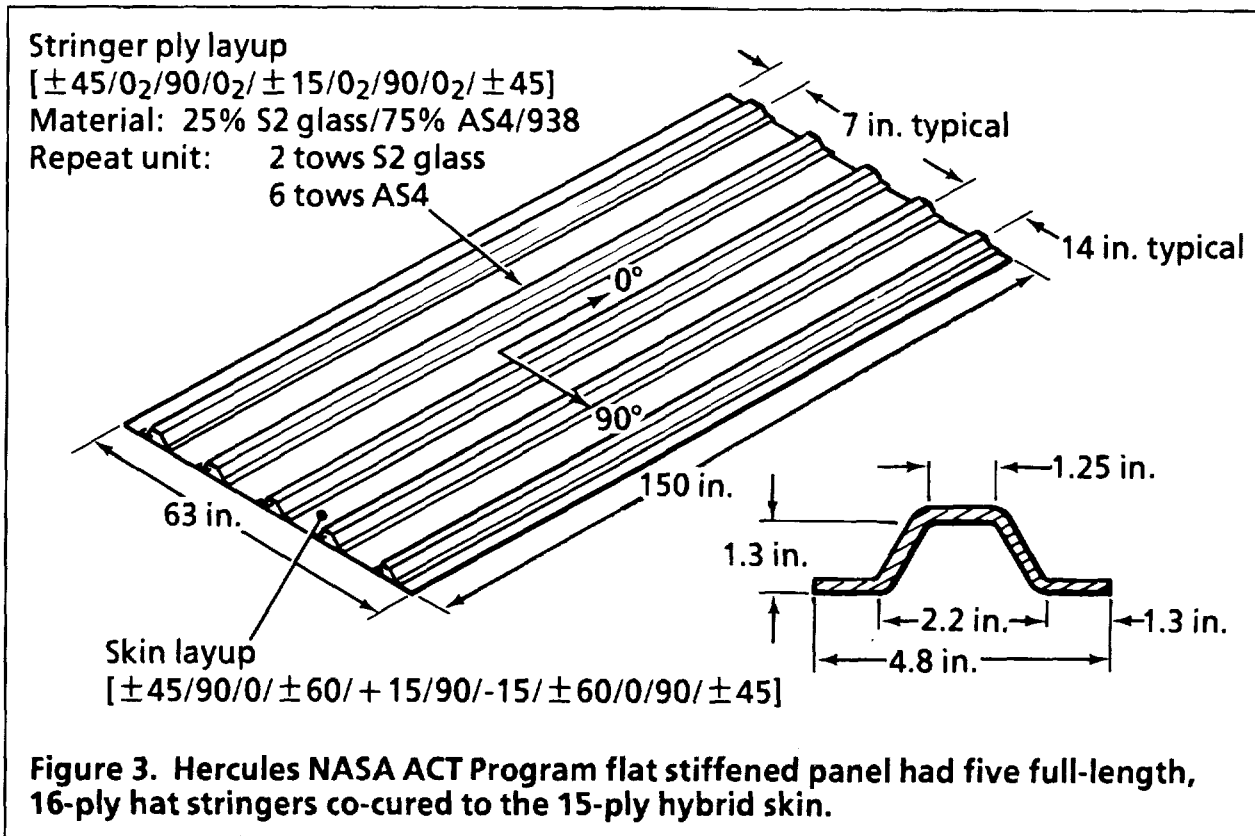
Table I. Test Matrix for Boeing/Hercules ACT Program Integration

Fuselage Quadrant	Test Article	Undamaged Elements	Tension with Damage	Shear with Damage	Comp. with Damage	Bi-Tension with Damage	Comp/Shear with Damage
Crown	Flat, unstiffened skin panels, 60 inch X 150 inch		2				
Crown	Flat, stiffened panels, 63 inch X 150 inch		1				
Crown	Curved, stiffened panels, 65 inch X 72 inch					1	
Keel	Flat, coupons, 35 inch X 60 inch				1		
Keel	Flat, stiffened panels, 30 inch X 44 inch				6		
Keel	Curved, stiffened panels, 30 inch X 44 inch						1
Window belt	Tension coupons with thick taper 35 inch X 60 inch	1					
Window belt	Curved panel with taper and cutout, 40 inch X 40 inch		1				
Window belt	Panel with double window frame 40 inch X 40 inch			1			

Program activities to date have focused on the fuselage crown quadrant. The Hercules program includes four large test panels for the crown task. Stiffened, unstiffened, flat, and curved panels have been fabricated for tension testing. A hybrid material form was used on two of the panels and the other two panels were made with all graphite materials. The hybrid material consisted of 25% S2 glass and 75% AS4 6K fiber. The glass and graphite tows were impregnated with Fiberite 938 resin. The glass/graphite hybrid material form is produced on the tow placement machine in a 24-tow band with repeat units of two tows of glass and six tows of graphite. The all graphite material form was AS4 6K fiber impregnated with Fiberite 938 resin.

The flat unstiffened panels were both 63 inch \times 150 inch 15-ply tension fracture panels. One panel was 100% graphite and the other was made with the glass/graphite hybrid material form. Both panels were autoclave cured using a 350°F and 100 psi cure cycle. Both panels looked good, and no defects were found with NDI. These panels were fabricated in July 1991 and were delivered to Boeing for testing. Both panels were tested and results were excellent when compared to prepreg tape layup panels.

The 63-inch \times 150-inch flat stiffened hybrid panel was cured and delivered in early 1992. This panel was stiffened with five full-length 16-ply hat stringers that were co-cured to the 15-ply hybrid skin (Figure 3). The hat stringers were also made



with the glass/graphite hybrid material form. The hat stringers were kitted from a flat tow-placed hybrid panel and were hot drape formed. The formed stringers were trimmed to size and fitted with a molded silicon rubber cure mandrel. The stringer/cure mandrel assemblies were located to the panel inside mold line (IML) (Figure 4). A layer of film adhesive was laid up under the skin flanges of each hat stringer. A peel ply was used on the panel outside mold line (OML) and IML surface. After the stringers were located, a molded graphite flex caul was installed on the IML of the panel assembly. The assembled panel was then vacuum bagged and autoclave cured at 350°F. After cure, the panel was trimmed to size, and the molded silicon rubber stringer cure mandrels were removed without difficulty. Quality of the panel was good, and no defects were found with NDI (Figure 5). Boeing will test this panel for axial damage tolerance.

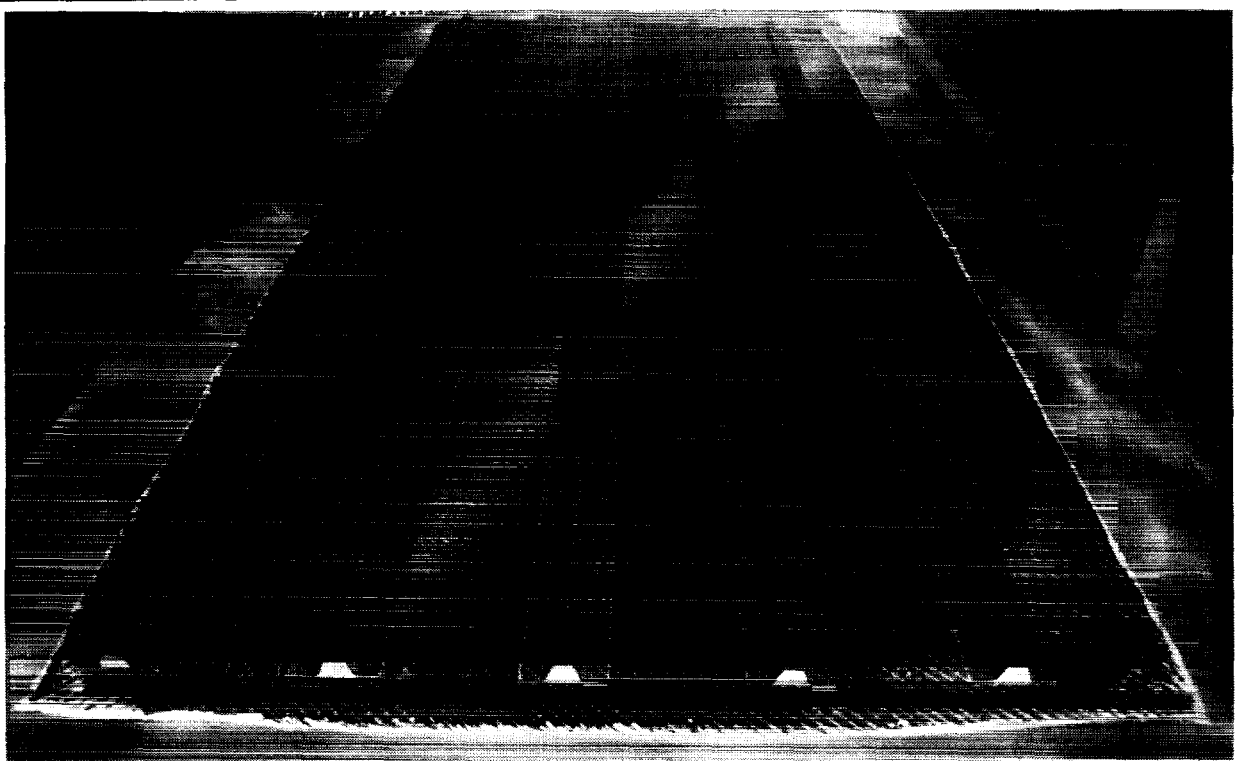


Figure 4. The hybrid panel/skin/stringer assembly was located to the panel IML.

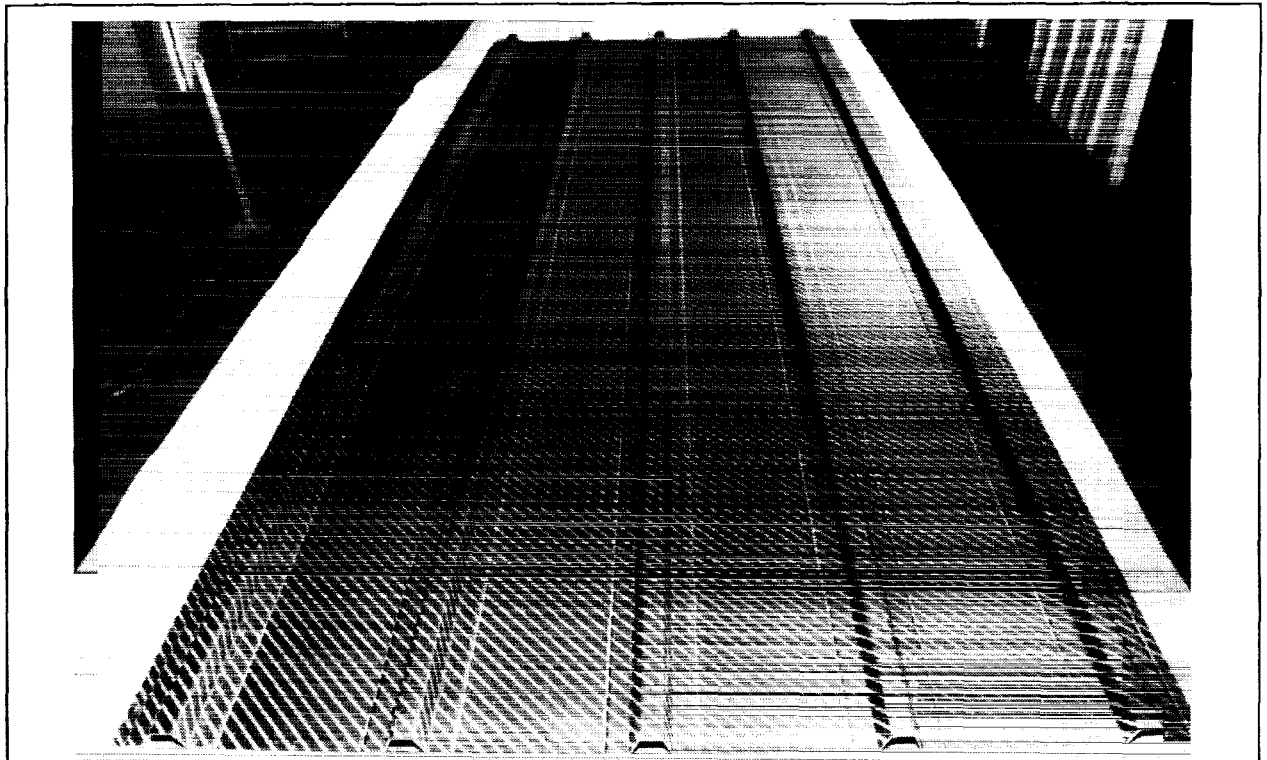


Figure 5. The cured hybrid panel quality was good; no defects were found with NDI.

The only curved panel for the crown task of this program is a large 65 inch \times 72 inch panel with a 122-inch radius. This panel will have four hat stringers and three braided resin transfer molded (RTM) "J" frames. The stringers are co-cured with the panel skin and the precured frames are co-bonded to the skin. Fabrication of this panel is similar to the flat stiffened hybrid panel, except for the IML tooling to achieve the co-bonded frames. Both the skin and stringers were made on the tow placement machine. Skin and stringers are all graphite AS4 6K/938. Stringers are kitted from a flat tow-placed panel and are hot drape formed. The IML tooling is somewhat different in that the molded flex cauls are not full length, but are short pieces that are positioned over the skin/stringers between the frames. The frames are on 22-inch centers. The panel will be assembled and cured on an Invar OML cure mold. At the time this paper was prepared, the tow placement operations were finished and cure of the panel was expected late in May 1992. The tow-placed skin and stringers were stored in a freezer.

Activities on the keel task of the Hercules program will start in mid 1992. Designs for the keel test panels are being defined by Boeing. Hercules new 8553 toughened epoxy resin has been selected for the keel test panels.

Hercules ACT Subcontracts

Hercules currently has subcontracts from the Douglas ICAPS Program and the Boeing ATCAS Program (Table II). All Hercules NASA ACT-related subcontracts are based on the automated tow placement process, and all subcontracts to date have been fuselage related. Our subcontract from Douglas for tow placement of subscale fuselage panels was mostly completed in 1991. The contract has not been closed, and we are talking with Douglas about extending and modifying the contract for additional work scope. We have several ongoing Boeing ATCAS subcontracts at this time, and several subcontracts were completed during the past year.

Table II. Hercules ACT Subcontracts

Boeing ATCAS	<ul style="list-style-type: none"> • Flat tear strap panels (4 each) • Flat stiffened panel 63 inch \times 150 inch • 3-foot \times 5-foot curved stiffened panels (2 each) • 7-foot \times 10-foot curved stiffened panels (2 each) • 7-foot \times 10-foot curved stiffened panel (1 each) • 8-foot \times 12-foot Invar cure mold
Douglas ICAPS	<ul style="list-style-type: none"> • 4-foot \times 5-foot curved stiffened panel (6 each)

The manufacturing processes used to fabricate subscale fuselage panels for Douglas and Boeing were similar, but had distinct differences. Both the Boeing and Douglas Panels had tow placed skins and co-cured stringers. The Douglas design used "J" stringers, while the Boeing design used hat stringers. The Douglas panel stringers were hand laid up with prepreg tape, and the Boeing panel stringers were tow-placed material that was hot drape formed. Both panels were assembled and cured on an OML mold to achieve surface smoothness. The Douglas design has

mechanically attached frames, and the Boeing design has a co-bonded frame. Boeing also mechanically attached the frames on one of their large 7-foot X 10-foot panels. The manufacturing processes used on both the Douglas and Boeing panels have been very successful. The quality of panels produced has been excellent.

Douglas ICAPS

The subcomponent panels fabricated for the ICAPS Program were 4-foot X 5-foot curved panels on a radius of 118 inch. The tow-placed skins were 12 plies thick and the tape layup stringers were 20 plies thick. The panels were stiffened with six "J" stringers and three mechanically attached frames. The frames were attached to a shear tee that "mouse holed" over the stringers and was bonded to the panel skin. These shear tees also had a 4-ply doubler beneath them that was co-cured to the skin IML. The bonding of the shear tees and the attachment of the frames were done at Douglas.

The tooling concept for the ICAPS panels was somewhat different than anything used previously at Hercules. Our objective was a low cost, low risk tool concept to achieve a skin-to-stringer co-cure. Surface smoothness was also a consideration in selection of our tool concept. The stiffened test panels simulated aircraft fuselage skin; thus, the OML surface needed to be as smooth as possible. Some other objectives to be achieved with our tool concept were a uniform skin thickness, close tolerance in spacing of the stringers, and net shape of the stringer achieved during the panel cure process. To accomplish these objectives, we used a low cost aluminum mandrel to tow place the panel skins, which were then transferred to an OML mold for cure. The OML cure mold achieved the skin smoothness we wanted. The stringer spacing tolerance, uniform skin thickness, and net shape stringers were accomplished by using a molded caul sheet on the IML side of the panel during cure (Figure 6).

The IML flex caul was laid up on a master model machined from monolithic graphite (Figure 7). The model was machined to a 118-inch concave radius. Detail was also machined for the stringers and shear tee doublers. A thin, 4-ply, molded caul was laid up on the master model using prepreg graphite tooling fabric. The flex caul was cured at 250°F and postcured at 350°F.

The tooling concept was very successful. The tooling was simple and easy to use. We produced six 4-foot X 5-foot panels for delivery to Douglas. All the panels were of excellent quality.

The fabrication process proved to be very simple and easy to duplicate. The 12-ply skins were tow placed on the aluminum mandrel and transferred to the aluminum OML cure mold (Figure 8). This was accomplished by setting the mandrel down on the cure mold and releasing the skin. The panel skin was then aligned to reference marks on the OML mold. The shear tee doublers were located to the skin IML by aligning to marks on the tool. The previously formed J-stringers were fitted

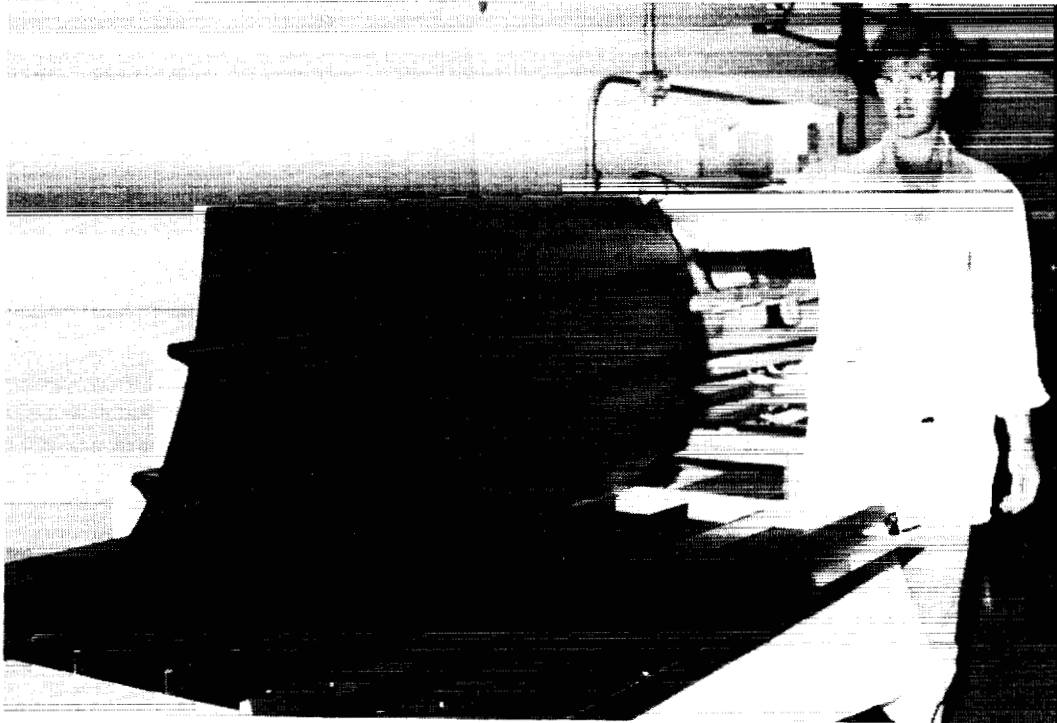


Figure 6. By using a molded IML flex caul, stringer spacing tolerance, uniform skin thickness, and net shape stringers were accomplished.

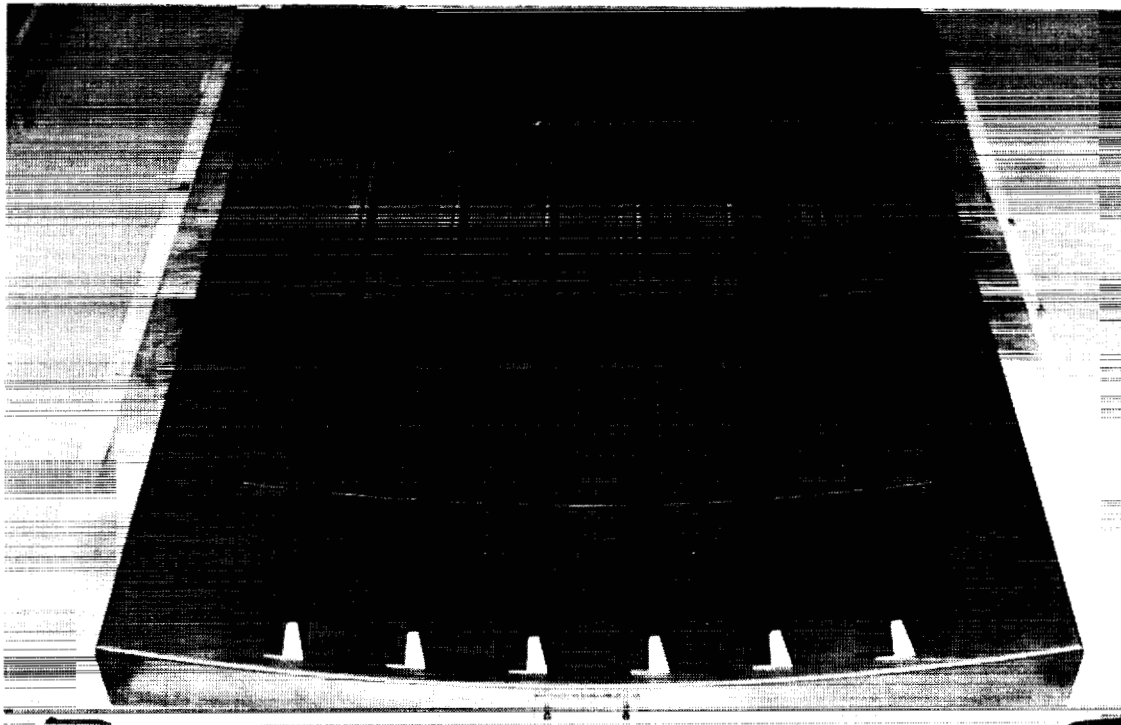


Figure 7. The IML flex caul was laid up on a monolithic graphite master model.

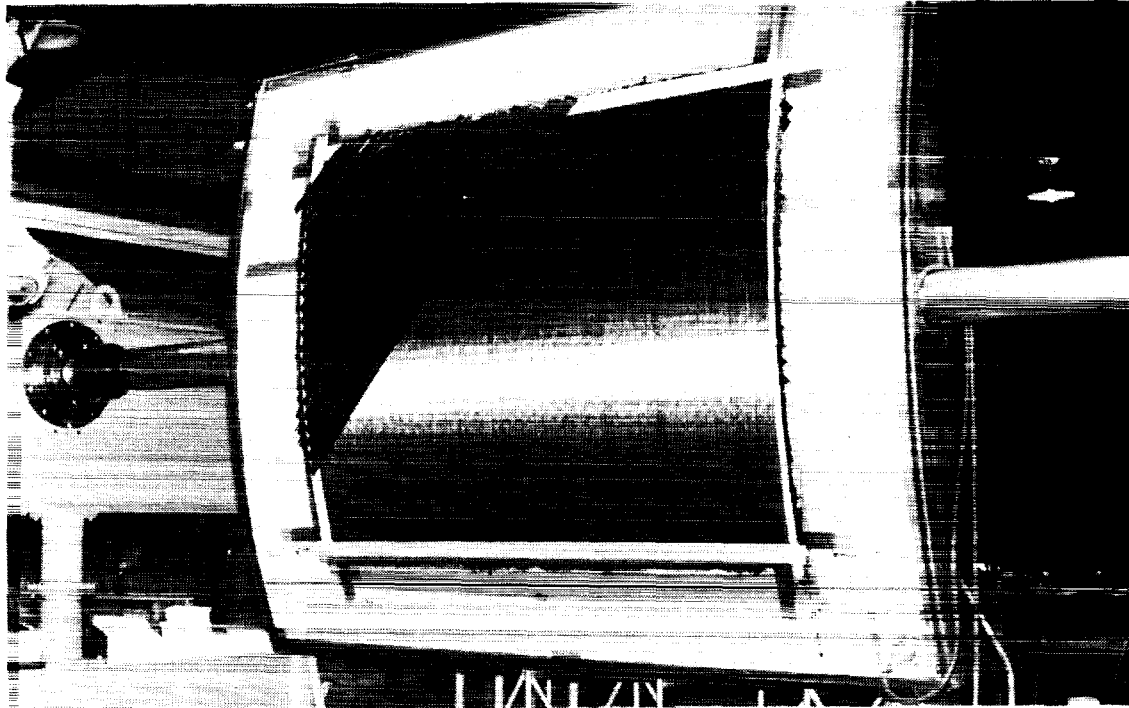


Figure 8. Tow placement of 4-foot × 5-foot skins for Douglas ICAPS panels was a simple, easy to duplicate fabrication process.

with a stringer cure mandrel, and the stringer/cure mandrel assemblies were positioned to the IML of the panel skin. Stringers were positioned using alignment marks on the tool. The molded graphite flex caul was located over the skin/stringer assembly and pressed down to the skin IML. Pressing the flex caul down corrected any error in stringer position. The completed assembly was vacuum bagged and cured in the autoclave.

After cure, the assembly was debagged and the tooling pieces were removed (Figure 9). The flex caul came off the panel with no problems. The stringer cure mandrels were removed by using T handles that screw into the sides of the cure mandrels. Removing the stringer tools was not a problem. The panel was deburred and trimmed to net dimension.

Dimensional and ultrasonic inspections were performed on each panel. No problem areas were discovered during NDI. Stringer spacing was well within tolerance. Overall quality of the panels was excellent (Figure 10).

Boeing ATCAS

Several subcontracts from the Boeing ATCAS Program are ongoing at the present time and several have been completed during the past year. We have fabricated both tooling items and tow-placed test panels for the ATCAS Program.

ORIGINAL PAGE
BLACK AND WHITE PHOTOGRAPH



Figure 9. Removal of tooling from the Douglas ICAPS panel was completed with no problems.

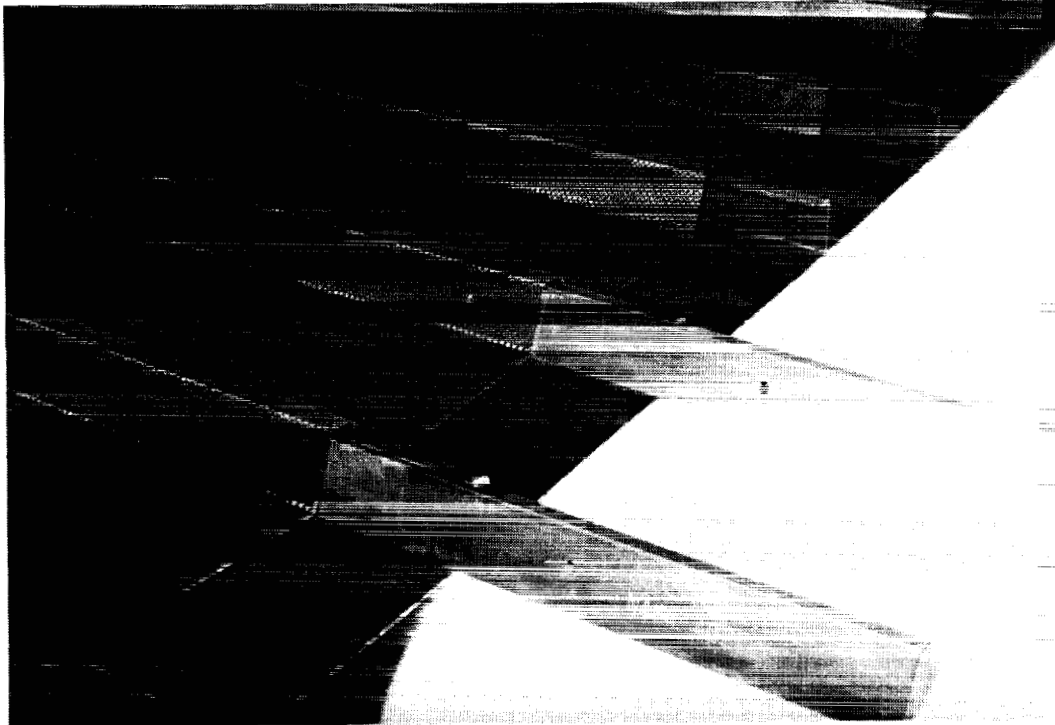


Figure 10. Stringer spacing was within tolerance, and overall panel quality was excellent.

All ATCAS panels to date have been crown quadrant designs. We have made flat unstiffened coupon panels and stiffened subscale crown panels for testing.

The Boeing designed manufacturing process for large Section 46 crown quadrants is similar to that used on the Douglas ICAPS subcomponent panels. The major exception is the co-bonded frames instead of mechanically fastened frames. Co-bonding of the precured braided RTM frames requires somewhat more complex IML tooling. The molded graphite flex caul cannot be a one-piece, full-length tool, but must be cut into short pieces that nest between the frames, which are located on 22-inch centers. Each caul piece must be sealed against the frames to prevent excessive resin bleed. Co-bonding the frames also requires a low coefficient of thermal expansion (CTE) OML cure mold to minimize tool growth at 350°F cure temperatures. Excessive tool growth would result in a mismatch in the skin radius and the radius of the precured frame that could cause a weak bondline. An Invar cure mold was used to cure panels with co-bonded frames.

The Boeing crown panel design is stiffened with hat section stringers instead of the "J" stringers used on the Douglas panel. Removing cure mandrels from a closed hat stringer proved to be a considerable problem. A machined metal mandrel with a silicon overwrap was tried first, and was very difficult to remove after cure. A molded silicon rubber mandrel was tried, and removing these tools after cure was not a problem. The combination of the molded silicon rubber stringer cure mandrel and the IML flex caul produced a very good quality hat stringer.

The master model used to layup the IML flex caul for the ATCAS 7-foot×10-foot panel was machined from REN 550 tooling board (Figure 11). We had used a machined monolithic graphite model for the Douglas ICAPS panels. The REN board model was of lower cost than a monolithic graphite model, and we used a low temperature cure tooling prepreg for the molded caul. The cured flex caul was postcured at 400°F. The REN model was machined in a flat configuration because its originally intended use was for a large flat stiffened panel. We used this flat master model to layup the caul for the 122-inch radius 7-foot×10-foot panels. The caul worked very well.

The OML cure mold used to cure the 7-foot×10-foot panels was made with an Invar tooling plate (Figure 12). The Invar plate was rolled to the 122-inch radius and the backup structure was welded on. The tool surface was then machined to the close tolerance radius. A frame fixture that bolts onto the cure mold was also made from Invar. This fixture clamps the frames and holds them in place during panel cure. The Invar cure mold was a very expensive tool.

We have subcontracts from the Boeing ATCAS Program to fabricate three 7-foot×10-foot stiffened crown panels. Two of these panels will have the co-bonded frames and one will have mechanically attached frames. The panel with the mechanically attached frames was finished first. The skin and stringers were cured in early April 1992. At the time this paper was prepared, work was in process on the 7-foot×10-foot panel with co-bonded frames.

ORIGINAL PAGE
BLACK AND WHITE PHOTOGRAPH

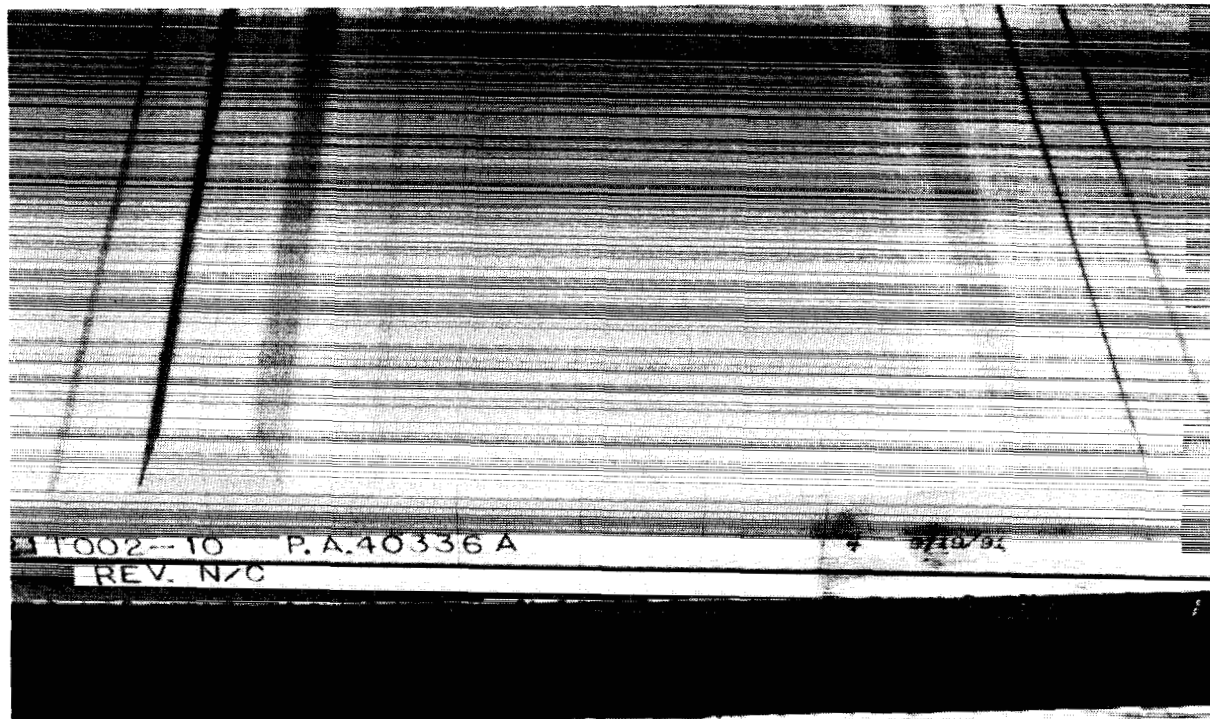


Figure 11. A REN board model was used for the flex caul.

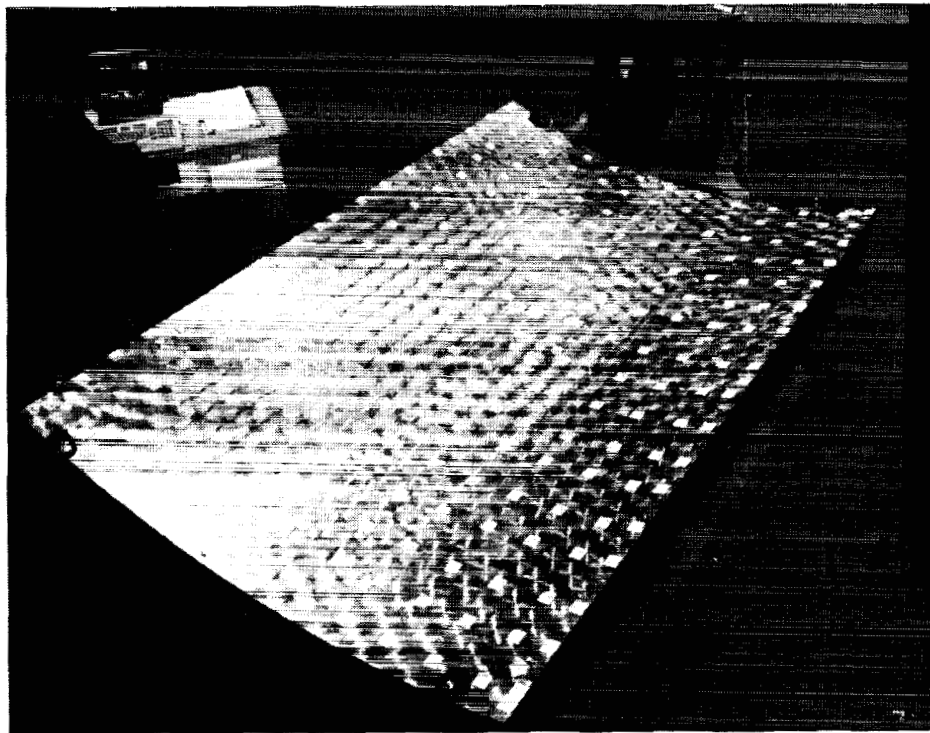


Figure 12. An Invar OML cure mold was used to cure the 7-foot \times 10-foot panels.

The manufacturing process used on the ATCAS crown panels is similar to that used on the Douglas ICAPS panels, except for stringer fabrication and co-bonding the frames. The 13-ply panel skins were tow placed on a two-sided oval mandrel (Figures 13 and 14). The mandrel radius is 122 inches on both sides. The two-sided mandrel configuration was used only because the tow placement machine in its current configuration will not accept a 20-foot diameter cylindrical mandrel, which would be used to produce four crown panels on one tool. The tow-placed skins were transferred from the aluminum mandrel to a holding fixture and stored in a 0°F freezer while the stringers were being made.

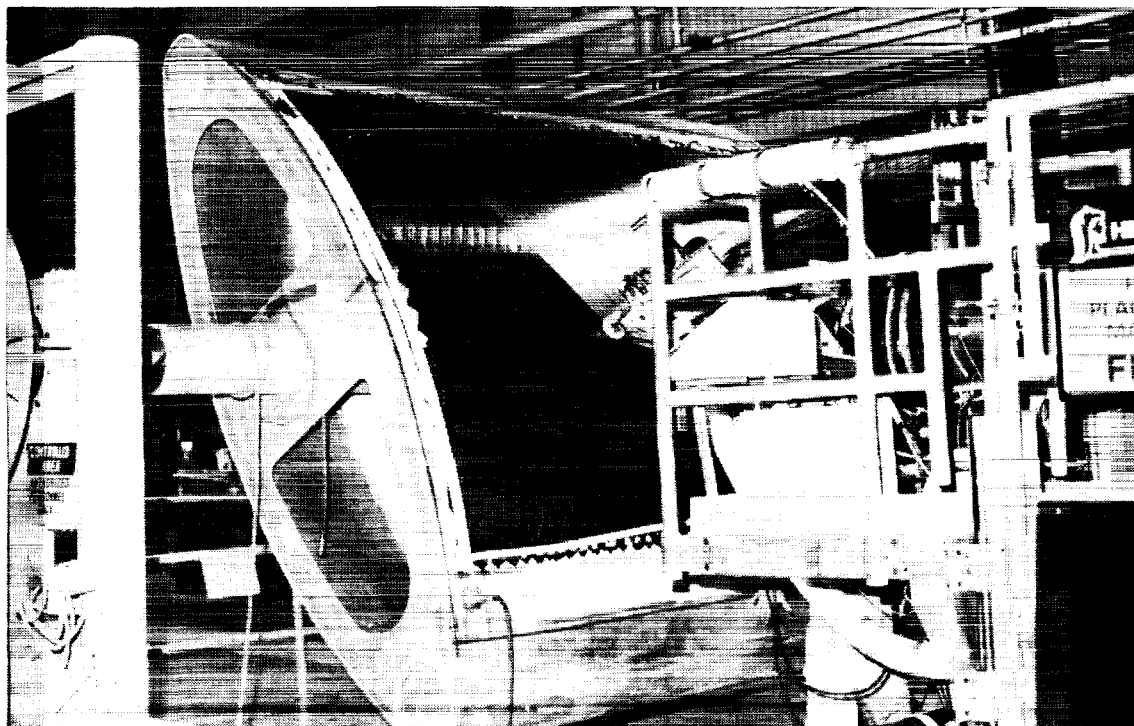


Figure 13. The ATCAS 13-ply crown panel skins were tow-placed on a two-sided oval mandrel.

The hat stringers were also fabricated with tow-placed material. A 13-ply flat panel was tow placed and the stringer charges were kitted from this panel. A machined aluminum female mold was used to hot drape form the stringers. The forming mold was heated in an oven. After the tool was removed from the oven, the flat stringer charges were laid up on the tool. As the material warmed up, it was hand worked down into the female mold. The molded silicon stringer cure tool was then pressed into the hat stringer. The mold and stringer were bagged and hot compacted. After compaction, the stringer was trimmed to size and stored in the freezer until all six stringers were finished and the panel was ready to be assembled.

ATCAS 7-foot × 10-foot panels were assembled on the 122-inch radius Invar cure mold. A peel ply was laid down on the tool surface. The panel skin was taken out of the 0°F freezer and nested in the Invar cure mold. Strips of film adhesive were cut and laid up on the skin IML where the hat stringers were located. The film adhesive was only beneath the stringer skin flanges. The stringers were taken out of

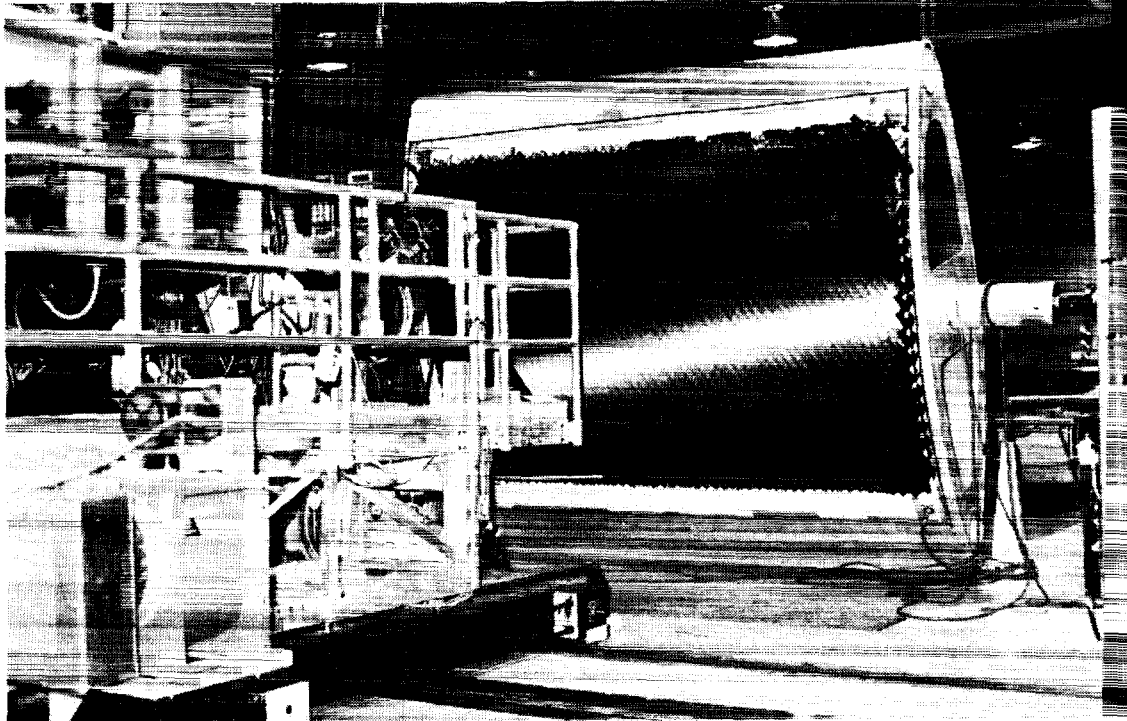


Figure 14. Tow placement of crown panel skins was accomplished on a 122-inch radius mandrel.

the freezer and located to the skin IML (Figure 15). A straight edge was used to ensure that the stringers were straight and precisely located. A peel ply was then cut and laid up on the assembled panel IML. The molded graphite flex caul was positioned on the assembled panel IML (Figures 16 and 17). The flex caul was taped to the Invar cure mold on all sides and the assembly was vacuum bagged.

The assembly process for the ATCAS 7-foot \times 10-foot panels with co-bonded frames differed somewhat from the process described above. Everything was the same up to where the stringers were assembled to the skin. At this point, the process changed. The precured RTM frames were located to the skin IML with a layer of film adhesive between the frame and skin. The frames were held in place with the frame clamp fixture described earlier in this paper. With the frames located and clamped down, the flex cauls were installed. The flex cauls for the co-bonded panel were short pieces that nested between the frames, which were located on 22-inch centers. We used a peel ply on the IML of the co-bonded panel as well. After the flex cauls were pressed down to the skin IML, the assembly was taped and a molded silicon bag was installed on the assembly. The bag was sealed and the panel assembly was ready for autoclave cure.

As previously discussed, the 7-foot \times 10-foot crown panel that had mechanically attached frames was cured in early April 1992. Quality of the cured panel was excellent. Cosmetic appearance of the panel was very good, and no defects were found with NDI (Figure 18).



Figure 15. During assembly, stringers were located to the skin IML using a straight edge to ensure precise location.



Figure 16. The molded graphite IML flex caul was positioned on the assembled panel IML.

ORIGINAL PAGE
BLACK AND WHITE PHOTOGRAPH

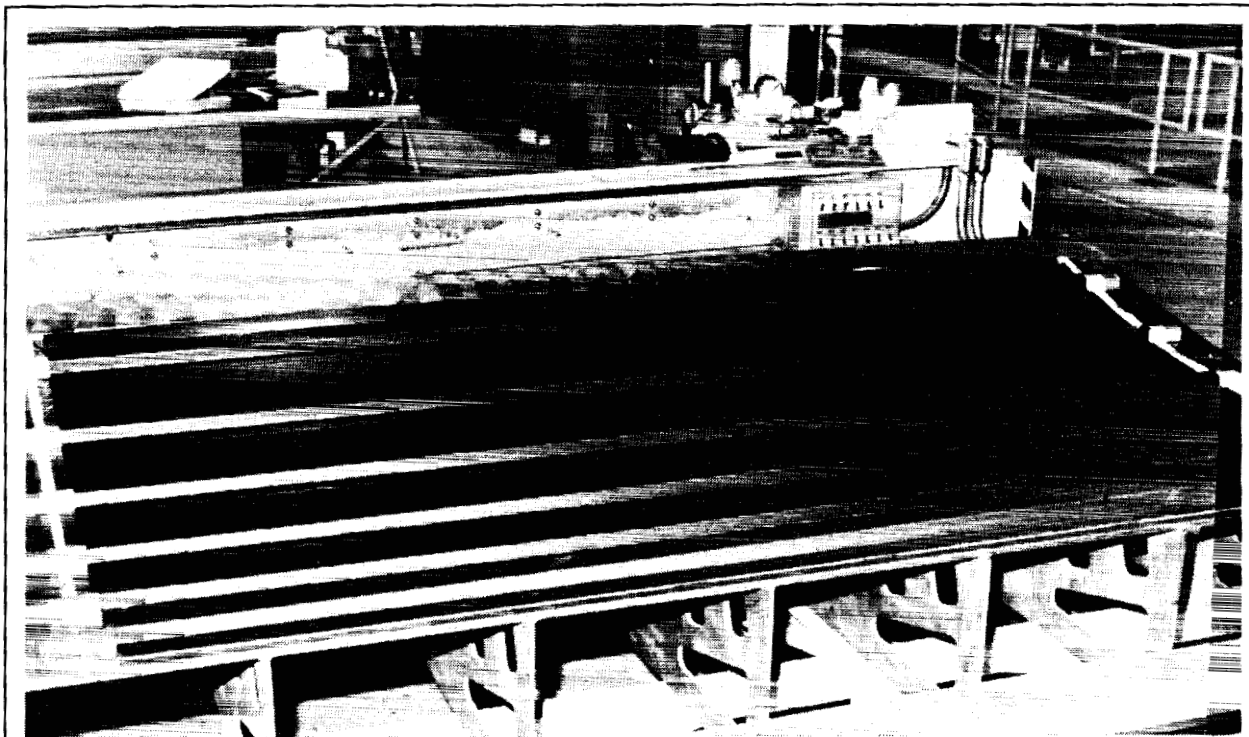


Figure 17. Boeing ATCAS crown panel was assembled and ready for cure.

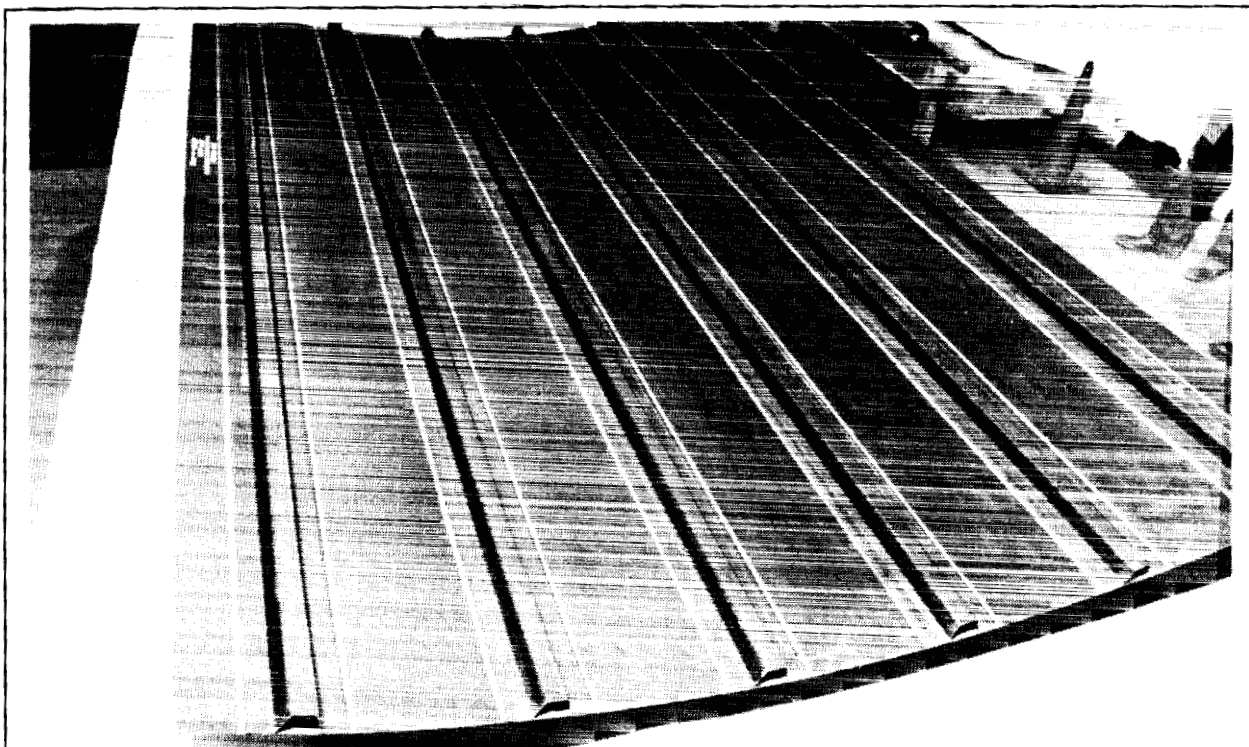


Figure 18. Boeing ATCAS crown panel had a very good cosmetic appearance; no defects were found with NDI.

Hercules manufacturing process was very successful in producing a large tow placed skin with co-cured hat stringers (Figures 19, 20, and 21).



Figure 19. ATCAS crown panel hat stringer.

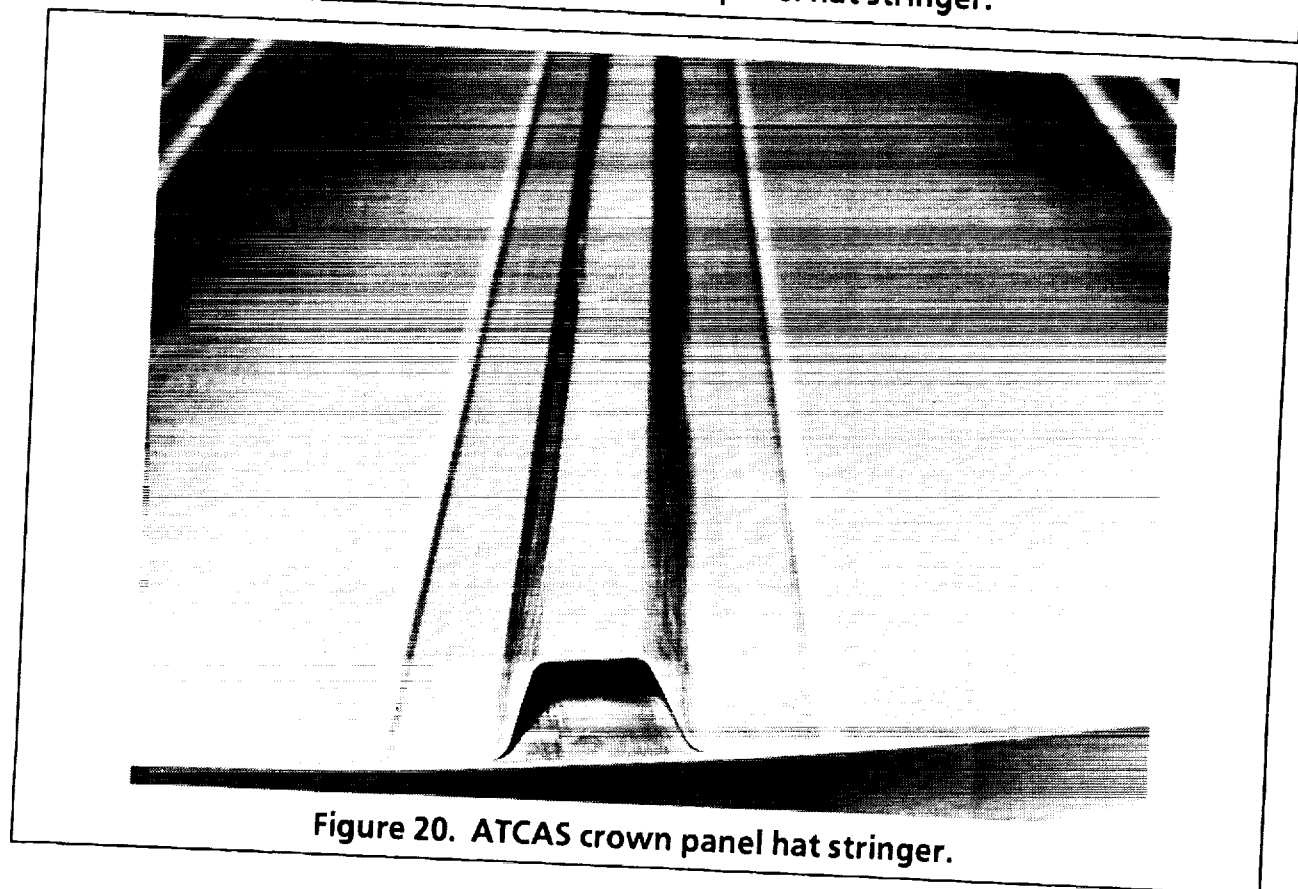


Figure 20. ATCAS crown panel hat stringer.

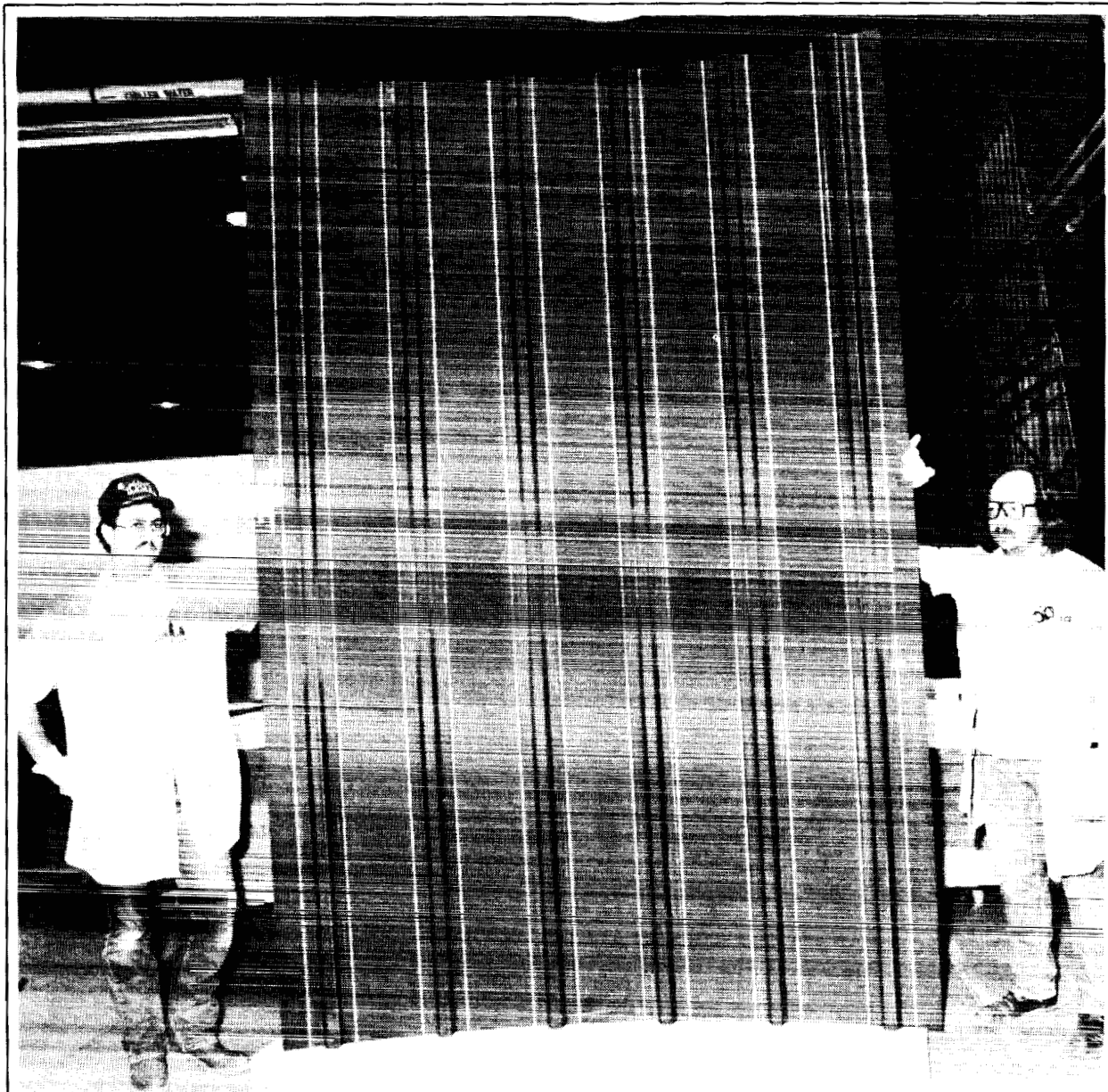


Figure 21. Boeing ATCAS crown panel.

The panel with the co-cured stringers and co-bonded frames will be cured in late May 1992. This process was successfully demonstrated on small demonstration panels. We believe it will also be successful on the 7-foot \times 10-foot crown panels.

SUMMARY

The process used to fabricate subscale crown panels with co-cured stringers and mechanically attached frame sections appears to be lower in risk than the co-bonded

frame process. The tooling concept uses fewer tooling pieces and lower cost tooling. Panels can be cured on an aluminum cure mold instead of the low CTE Invar mold. The full-length, one-piece IML flex caul has produced excellent results every time it has been used. The combination of the OML cure mold and IML molded caul produces a consistent, excellent quality panel. This process uses tried and proven composite structures manufacturing techniques (OML caul mold), and combines them with the automated tow placement process to achieve cost effectiveness. We believe this process is now production ready.

The process used to fabricate subscale crown panels with co-cured stringers and co-bonded frame sections would probably have lower recurring costs because the frame assembly effort is eliminated. At the time this paper was prepared, Hercules had not cured one of the large 7-foot \times 10-foot ATCAS panels with co-bonded frames; therefore, our data for this process were limited to small process trial panels. We believe this process will need more development, but when it is fully mature, it will be very attractive for commercial aircraft crown panel production.

Both processes are based on automated tow placement of fuselage crown panels on a cylindrical mandrel that is large enough to allow fabrication of four panels in one winding. The tow placement test panels made for the NASA ACT Program have performed well in compression-after-impact and tension fracture testing. The automated tow placement process appears to be ideally suited for production of commercial aircraft fuselage structures.

Response of Automated Tow Placed Laminates to Stress Concentrations

Douglas S. Cairns¹, Larry B. Ilcewicz², and Tom Walker²

510-24
51410

Abstract

In this study, the response of laminates with stress concentrations is explored. Automated Tow Placed (ATP, also known as Fiber Placement) laminates are compared to conventional tape layup manufacturing. Previous tensile fracture tests on fiber placed laminates show an improvement in tensile fracture of large notches over 20% compared to tape layup laminates. A hierarchical modeling scheme is presented. In this scheme, a global model is developed for laminates with notches. A local model is developed to study the influence of inhomogeneities at the notch tip, which are a consequence of the fiber placement manufacturing technique. In addition, a stacked membrane model was developed to study delaminations and splitting on a ply-by-ply basis. The results indicate that some benefit with respect to tensile fracture (up to 11%) can be gained from inhomogeneity alone, but that the most improvement may be obtained with splitting and delaminations which are more severe in the case of fiber placement compared to tape layup. Improvements up to 36% were found from the model for fiber placed laminates with damage at the notch tip compared to conventional tape layup.

Introduction

As advanced composites continue to be utilized in large, primary structures, a need exists to identify and quantify those parameters affecting fracture performance. Structures are typically manufactured from thin (0.127 mm) prepreg tape (305 mm wide), laminated and cured in an autoclave. Obviously, manufacturing large structures with even moderate volume production schedules will require alternative processing. One such alternative is Automated Tow Placement (ATP), also known as Fiber Placement (FP). This manufacturing technique has the advantage that fabrication production rates may be increased and the production may be automated. This fabrication method, as developed by Hercules, is shown in Figure 1.

In Figure 1, individual tows are placed on a creel and passed through a robotic head. A rotational axis, along with manipulation of the robotic head, allows placement of these individual tows. Unlike conventional filament winding, where compaction is provided via tensioning of the tows, fiber placement provides compaction via roller pressure. This versatility allows for manufacturing structures which are not axisymmetric and may even contain concave surfaces. Consequently, the designer is not constrained to near geodesic paths. In addition, individual tow cut and add allows for in-situ thickness control. These individual tows allow for intra-ply hybridization as well.

¹Hercules Materials Company, Composite Products Group, Magna, UT

²Boeing Commercial Airplanes, Structures: Advanced Composites, Seattle, WA

This manufacturing process results in a tow to tow architecture which is different from standard prepreg tape laminated structures. Small gaps and laps can form between the tows, which are approximately 2.54 mm wide and between bands, which are 30 mm or greater. This can result in localized inhomogeneities. This is illustrated in Figure 2 for a $[-45/+45/90/+30/-30/\bar{0}]_n$ laminate configuration. Figure 2 is a Computer Aided Design (CAD) generated model of the ply by ply and tow by tow buildup in a localized region of a structure. Each line represents the boundary between tows. The regions where lines cross represent potential lap/gap sites. The minimum spacing is approximately 1.5 tow widths or 3.8 mm. As a result, this manufacturing process introduces another level of inhomogeneity which is greater than the thickness of individual plies. As with other alternative forms such as woven materials, it is improper to view fiber placement as a material form, especially with respect to fracture. Therefore, a need exists to understand the influence of this inhomogeneity on performance.

Impetus

The fiber placement architecture can result in improved fracture properties under tensile loading applications as shown in Figure 3a [1,2]. This improvement in fracture is an important parameter for improving Boeing's advanced fuselage performance as shown in Figure 3b. This improvement has the largest influence on decreasing weight with improved costs compared to conventional prepreg tape laminates. The motivation behind this study is to understand the tensile fracture performance of fiber placed structures.

Model Description

Global Model

To study the influence of notches, a global two-dimensional finite element model was constructed. A mesh for this model is shown in Figure 4. The model is a half symmetry model (important later) about the left hand side, which is fixed vertically at the bottom and has a uniform vertical displacement at the top to simulate testing. This layup is AS4/3501-6 in a $[-45/+45/90/+30/-30/\bar{0}]_n$ stacking configuration [3]. The region of interest is near the tip of the crack. Hence, logarithmic mesh refinement was utilized at the tip.

For greater accuracy near the crack tip, a hybrid membrane element based on the Hellinger-Reissner principle Π_R was used [4,5]. In this formulation, assumed fields for the stress and displacements are utilized.

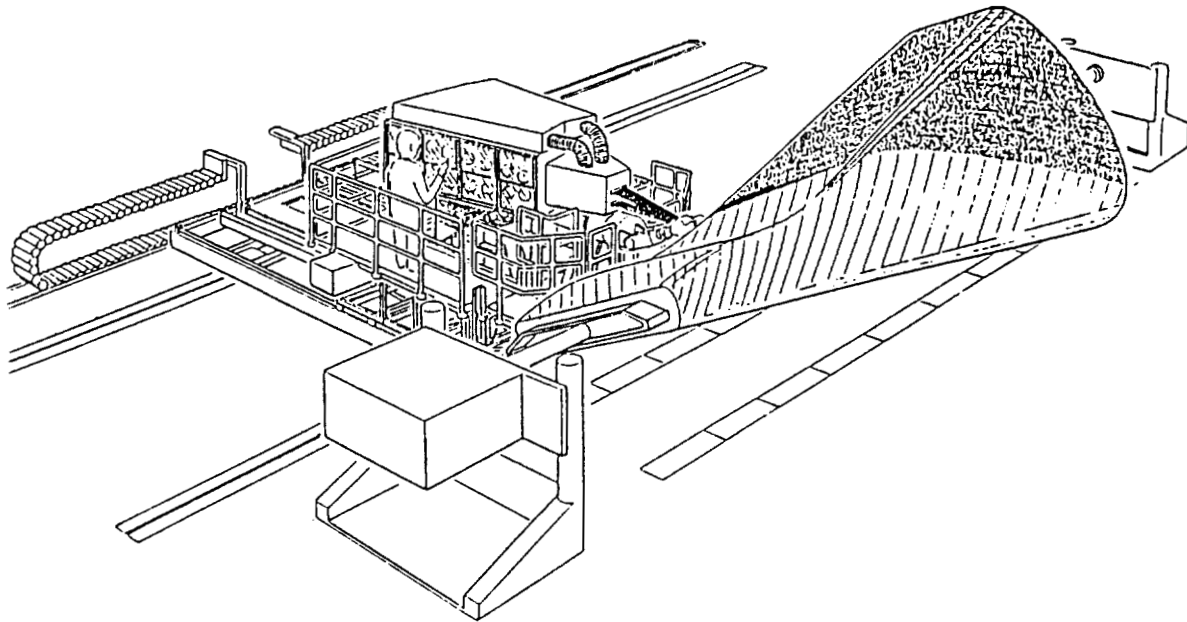
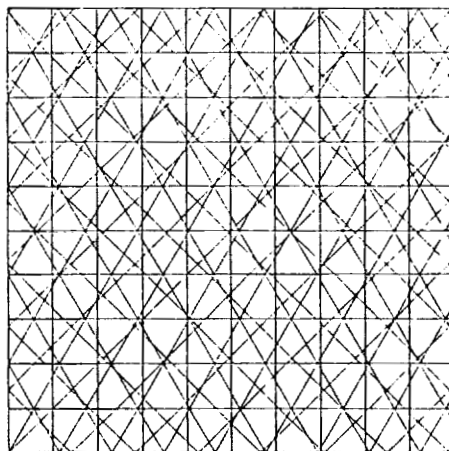


Figure 1. Fiber Placement (Automated Tow Placement) Process



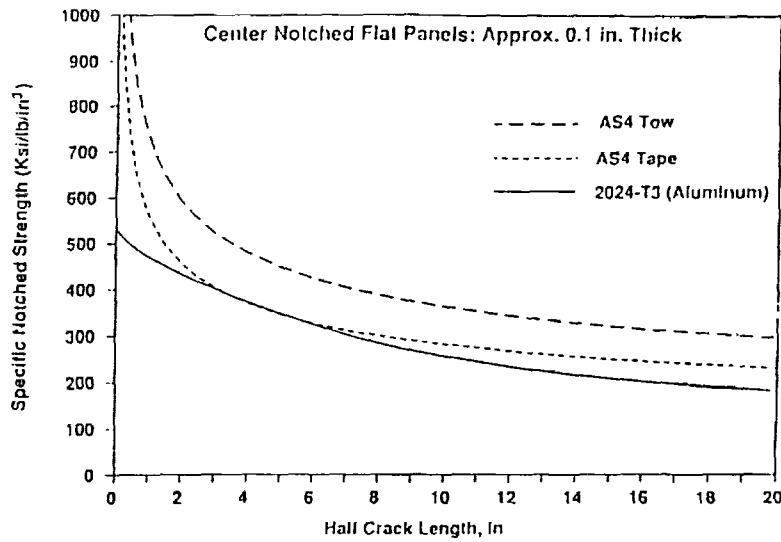
CAD-generated local region

25.4 mm X 25.4 mm Region, 2.54 mm tow width
 $[-45/+45/90/+30/-30/\bar{0}]_s$ AS4/3501-6

Cross-over points represent potential lap (overlap) or
 gap (space) regions

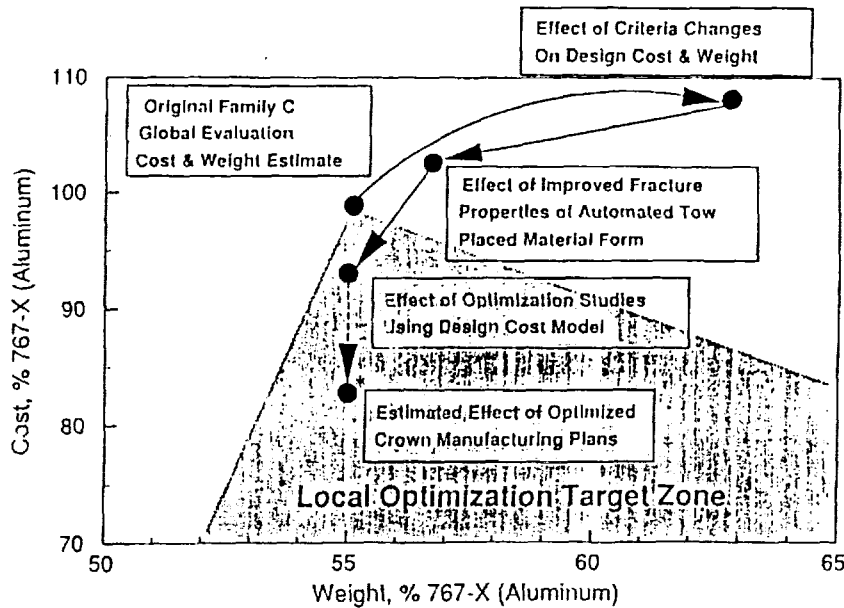
Figure 2. Resulting Fiber Placement Architecture for
 $[-45/+45/90/+30/-30/\bar{0}]_s$ Laminate

Tension Residual Strength Curves Normalized By Material Density



a) Improvement in Tensile Fracture

Progress in Crown Local Optimization



b) Impact of Improvement on Weight and Cost of Advanced Fuselage Structure

Figure 3. Improvement in Performance for Automated Tow Placement versus Tape

$$\begin{aligned}
 \sigma &= P\beta & a) \\
 u &= Nq & b) \\
 Du &= Bq & c)
 \end{aligned}
 \tag{1}$$

$$\Pi_R = \int_V \left[-\frac{1}{2} \sigma^T S \sigma + \sigma^T (Du) \right] dV \quad d)$$

where

σ is stress
 P is the interpolating function for the stress
 u is the displacement vector
 N is the displacement interpolating function
 q is the nodal displacement
 D is the kinematic operator matrix
 B is the operator matrix in terms of nodal displacements
 S is the element compliance
 and V is the elemental volume.

Invoking the stationary condition $\delta\Pi^R$ equal to zero and condensing out the β parameters yields an elemental stiffness matrix k , in terms of the nodal displacements of the form:

$$k = G^T H^{-1} G \quad a)$$

where

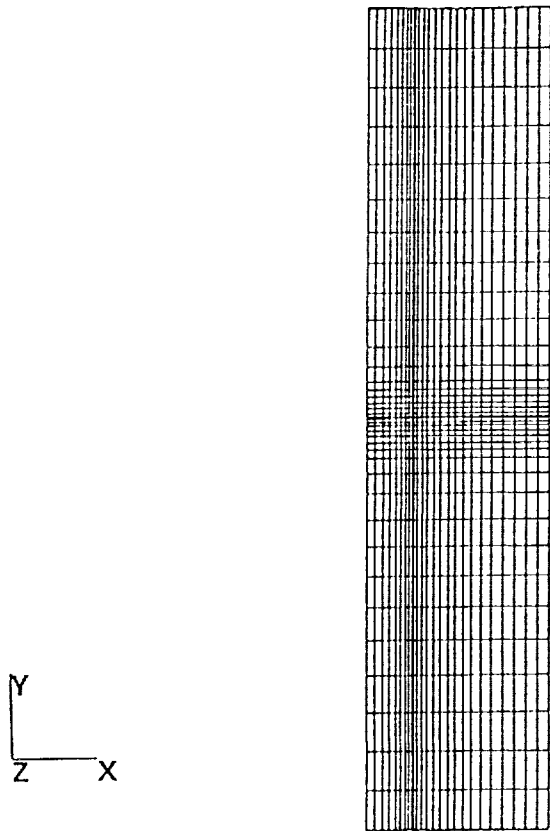
$$G = \int_V P^T B dV \quad b) \tag{2}$$

$$H = \int_V P^T S P dV \quad c)$$

Local Model

The local model is illustrated in Figure 5. This model is a half symmetry, 25.4 mm high by 50.8 mm wide. The darkened areas represent elements which have different membrane stiffness properties to represent laps or gaps. To bound the problem with respect to inhomogeneity, laps were modeled as double stiffness regions, while the gaps were modeled as resin regions. The distance between laps/gaps represents the minimum inhomogeneity spacing. The elements are sized to approximate the 0.76 mm maximum lap/gap which is specified in fiber placement.

Displacements were invoked around the perimeter from least squares fitting of the displacements obtained from the global model. The local model is slightly more compliant than the global model. Consequently, an error norm ratio for stresses along the perimeter in the global region and the local region was constructed. The results were multiplied by this first order correction [6].



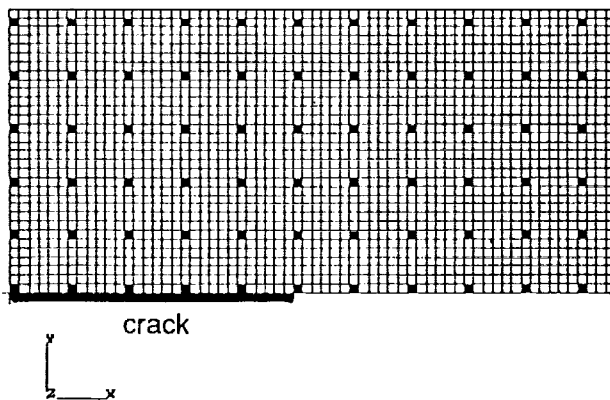
Global Model Description

559 mm long, 254 mm wide,
63.5 mm central notch,

Symmetry about Y-axis
Uniform Y displacement at top,
Fixed in Y at bottom

4 node isoparametric
displacement, 5 beta assumed
stress hybrid elements

Figure 4. Global Finite Element Mesh



Local Model Description

50.8 mm X 25.4 mm local model
symmetry about X axis
perimeter displacements from
Global model

darkened areas represent
local lap/gap sites
gap - resin
lap - higher stiffness
inclusion

larger areas varied to simulate
hybrid panels

Figure 5. Local Finite Element Mesh
(darkened areas represent areas of inhomogeneity)

Failure Criterion - Basis for Comparisons

The Whitney-Nuismer Average Stress Criterion was implemented on a strain basis to compare the results between models in the near field region [7]. This was implemented as:

$$SR = \frac{\epsilon_0}{\frac{1}{a_0} \int_a^{a+a_0} \epsilon(r, \theta) dr} \quad (3)$$

where SR is the ratio of far-field strain to near-field strain
 ϵ_0 is the far-field strain of interest
 a_0 is the averaging parameter (assumed to be a material constant)
and $\epsilon(r, \theta)$ is the strain along a path in the critical direction
(not necessarily perpendicular to the applied load)

Using a progressive failure criterion, the failure of the 0° ply in the $[-45/+45/90/+30/-30/0]_s$ laminate was determined to be critical. This fiber-dominated failure was utilized as the basis of comparison.

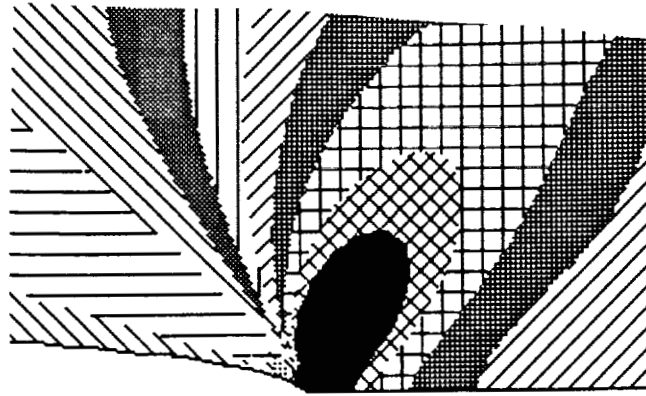
Results

Influence of Inhomogeneity

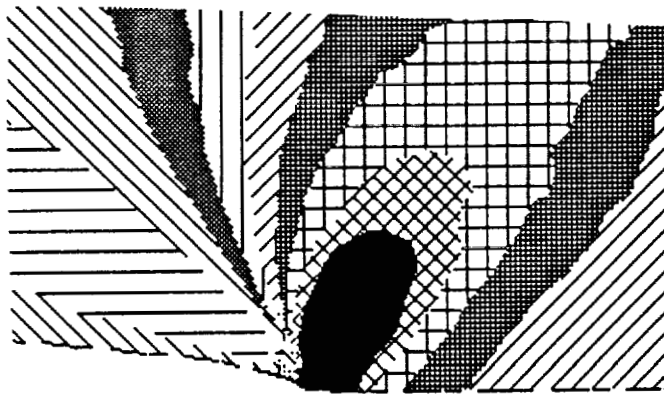
As stated above, the fiber placement process results in an architecture which has local inhomogeneities. To determine the effect of these inhomogeneities, the local model was used to determine average strain near the crack tip. An averaging parameter a_0 of 3.81 mm was used based on previous tests on AS4/3501-6 [8]. The near-field ϵ_y strain isocontours are shown in Figure 6a. This strain field is a classical plane stress isocountour. In Figure 6b is the strain field for gaps (resin areas, i.e. compliant inclusions) in the darkened regions shown in Figure 5. Notice that small perturbations in the strain field can be seen around the perimeter of the isocountours. The case where all of the inhomogeneity sites are laps (double thickness membrane regions, i.e. stiff inclusions) is shown in Figure 6c. Large perturbations in the strain isocontours can be seen here.

The average strain in the case of laps divided by the baseline average strain is approximately 0.97. The average strain ratio for the case of laps (stiff inclusions) was found to be 0.89. Consequently, a slight improvement over the baseline results can be expected to be gained on the basis of inhomogeneity alone.

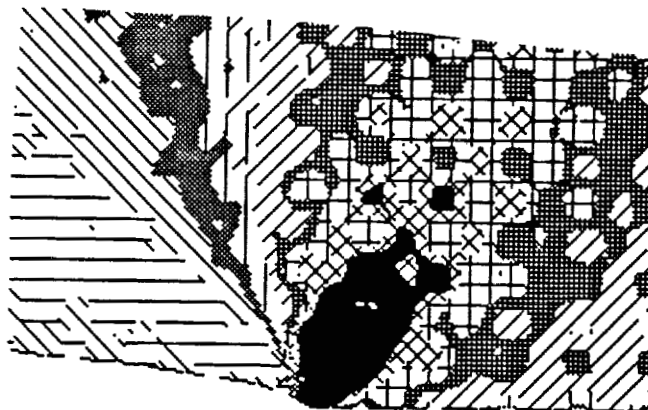
A model of intraply glass/carbon hybrids was also conducted. The fiber placement process allows for introducing intraply hybridization via individual tows. This results in large, inhomogeneous regions. Large all carbon regions exist, and no benefit for local average strain results was found for the case of intraply hybridization. The relative improvement for inhomogeneity is shown in Figure 7.



a) Baseline (homogeneous case, smooth strain isocontours)



b) Gaps (resin pocket inhomogeneities from gap, small perturbation in strain)



c) Laps (stiff inclusion from overlap, large perturbation in strain)

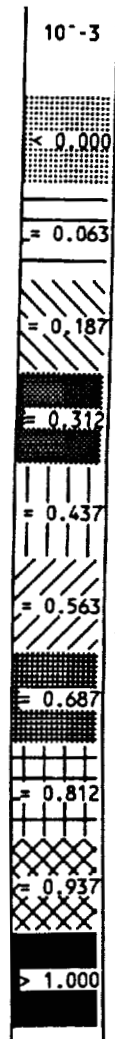


Figure 6. Local Inhomogeneity Effect on Strain Field

It is important to note that these studies are bounding cases. That is, the assumptions of proximity and buildup of laps/gaps is rather severe. Actual improvement from inhomogeneity alone can be expected to be less. The experimentally determined ratio of fiber placed laminates to tape laminates is approximately 0.795 as shown in Figure 3a. This is much better than the 0.89 ratio determined for the case of laps. Consequently, the influence of inhomogeneity on the strain field alone cannot completely explain the benefits. This does not, however, preclude the inhomogeneity from affecting the damage type and progression during fracture.

Influence of Damage

The results above indicate that inhomogeneity is not solely responsible for the improvement from tape to tow. Clearly, some other mechanisms provide the improvements. While the inhomogeneity has a moderate influence on the strain field, it is expected to have a large influence on damage progression during fracture. In Figure 8 are shown dye-enhanced radiographs of tape layup and fiber placed, notched, fractured laminates. Notice the much larger damage zone ahead of the crack tip in the case of fiber placed laminates compared to the tape layup laminates at final fracture. This damage size is on the order of the size of the original notch. The influence of laps/gaps on splitting and delamination has been postulated previously [1,2]. The goal here is to quantify the influence of these damage types on final fracture.

The damage produced is three dimensional. Different plies split and delaminate. A complete, three dimensional model of these damage types would be quite complicated. To model splitting and delaminations with some degree of pragmatism, a stacked membrane model was developed. In this model, membrane elements are stacked to simulate ply-by-ply lamination. Delaminations were introduced by releasing nodes through the thickness. Splitting was introduced by releasing nodes in the plane [9]. Therefore, while interlaminar stresses cannot be accurately modeled, the influence of constraints by surrounding plies and material can be modeled in the plane of a ply. This technique was found to be simple and practical. The stacked membrane region is illustrated in Figure 9. Here, the half-symmetry is necessary, since the presence of membrane extensional-shear coupling ($A_{1\theta}$ and $A_{2\theta}$ in classical laminated plate theory) may be important.

Splitting alleviates the influence of the sharp notch and acts as a crack blunting mechanism in composites. This is illustrated in Figure 10. The surrounding plies are shown in Figure 10a, while deformation of the 0° ply is shown in Figure 10b. The node is released adjacent to the notch allowing shear lag to occur. Various splitting lengths were modeled (up to 0.8 times the notch length of $2a$). Delaminations also alleviate the influence of the notch. The delamination allows plies to deform independently. This can also lower strains ahead of the notch. A variety of delamination sizes were modeled (up to 0.8 times the notch length of $2a$).

Combined splitting plus delaminations provides the most benefit. In Figure 11 is illustrated the deformation of surrounding plies and the 0° ply with a split plus delaminations in the surrounding plies. Notice that the material ahead of the crack tip

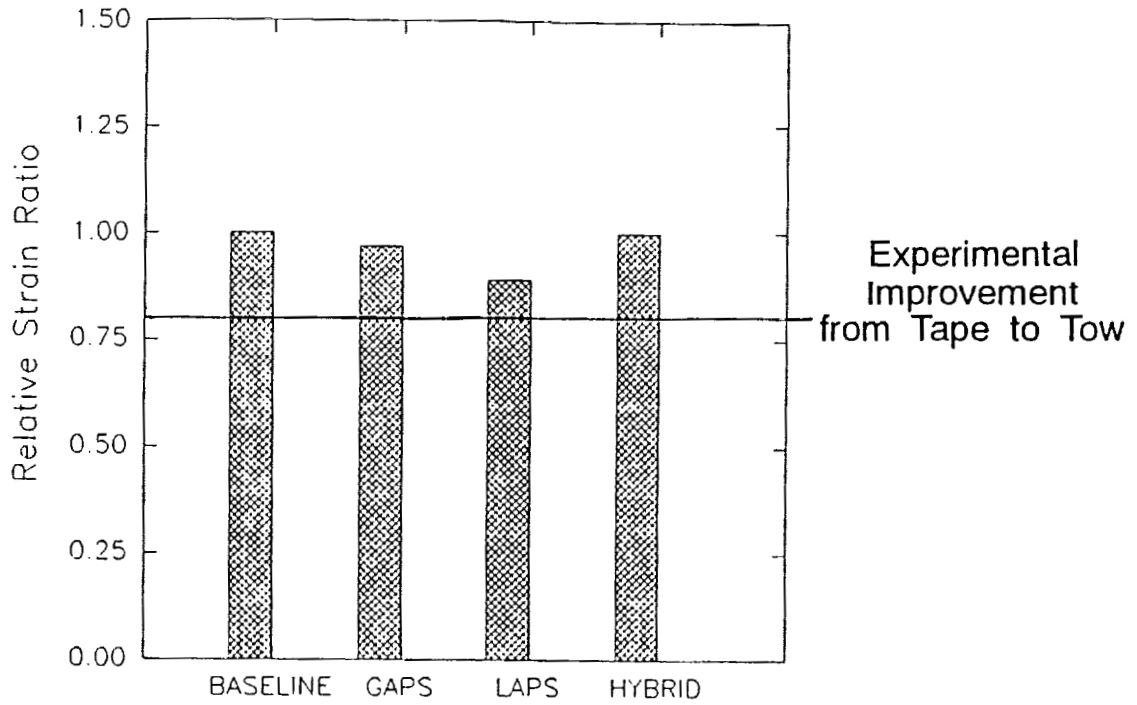


Figure 7. Local Inhomogeneity Effect on Tensile Fracture Performance

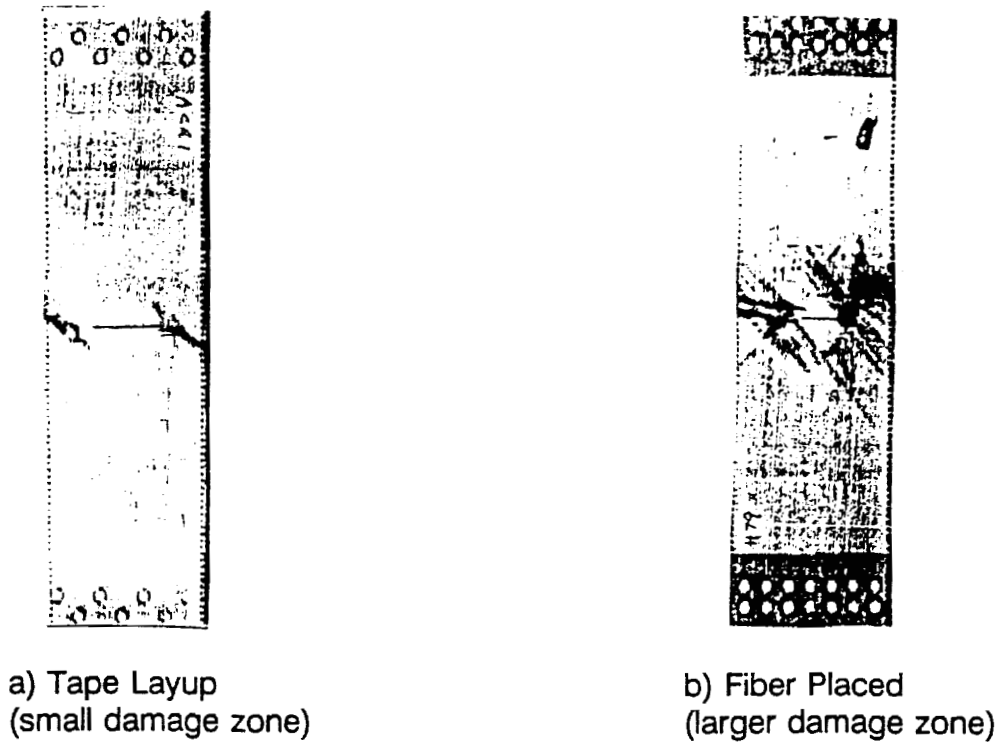
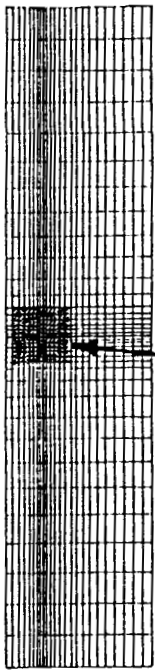


Figure 8. Dye-Enhanced Radiograph of Notch Damage Differences Between Tape and Tow

*Original figure unavailable.



Model Features

Stacked membrane region for ply-by-ply analysis

Damage Modeling

Interply connectivity released to simulate delaminations

Intraply connectivity released to simulate splitting

Combinations

Relative average strain utilized for comparisons

Stacked Membrane Region

Figure 9. Stacked Membrane Model

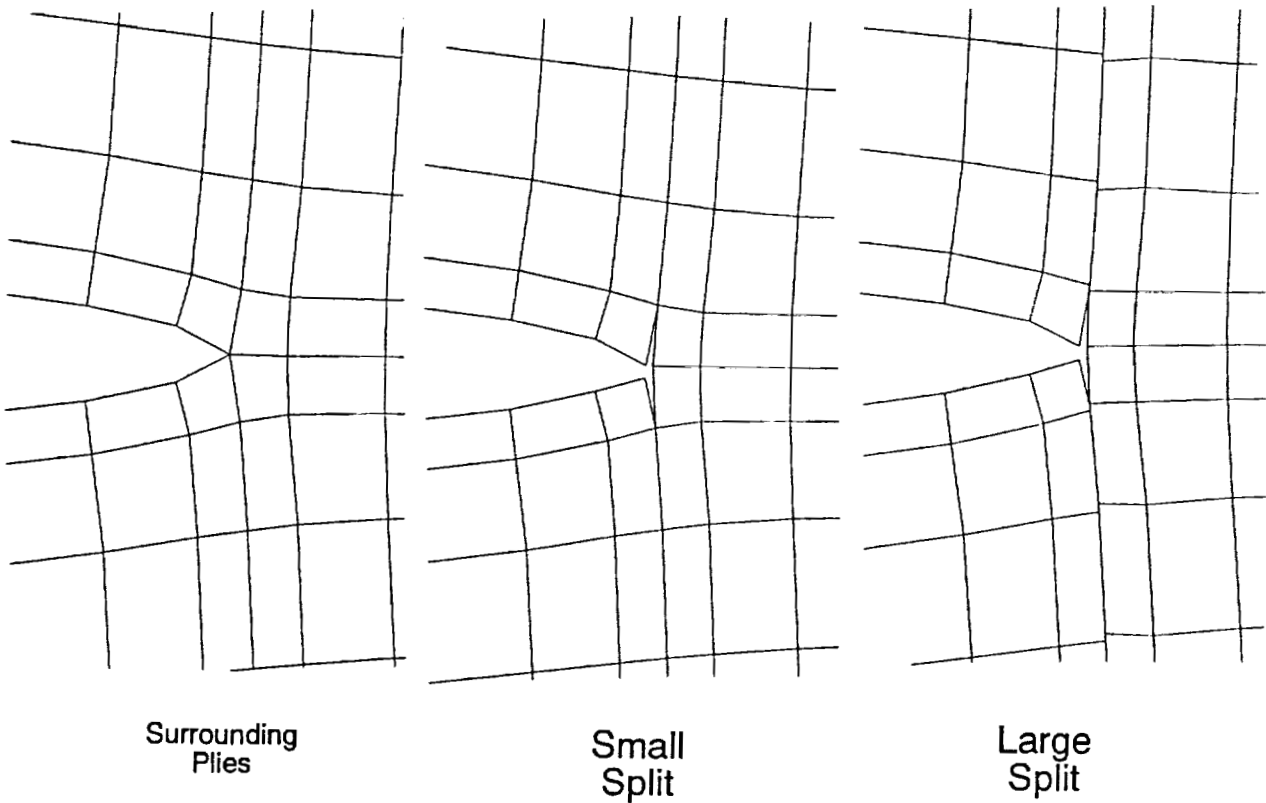


Figure 10. Splitting at Notch Tip

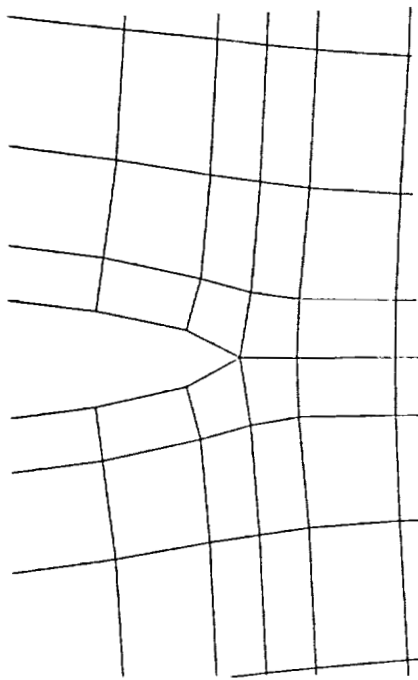
acts almost completely independently from the material behind the crack tip. This deformation is plotted on the same scale as shown for Figure 9.

Isocountours for the ϵ_y strain are shown in Figure 12. The surrounding plies again exhibit classical plane stress behavior in Figure 12a, while the split ply distributes strain over a larger region in Figure 12b. Also, the isocountours are much more uniform than in Figure 12a. Higher, localized strains can be seen above and below the crack as stress is reintroduced via shear lag.

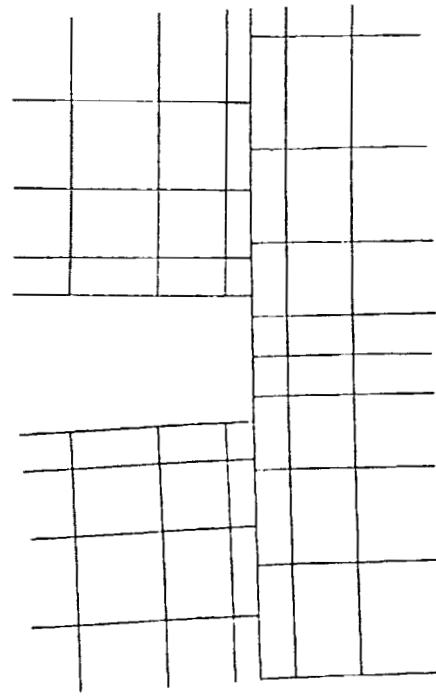
The influences of these various damage types on average strain compared to baseline results are shown in Figure 13. The $\sqrt{d/a}$ is the square root of the half damage size divided by original half crack length. For all damage types, the damage has little effect, until a large enough damage size is present to redistribute the local strain field. This occurs between $\sqrt{d/a}$ equal to 0.2 to 0.4. Splits alone or delaminations alone cannot explain the benefit of experimentally observed improvement from tape to tow. A combination of damage types provides the most benefit.

Conclusions and Recommendations

A study of the influence of inhomogeneity and damage on the tensile fracture performance of structures manufactured from fiber placement has been conducted. A global hybrid finite element model was constructed, and a local inhomogeneity model was constructed to explore strain fields near the crack. The results indicate that inhomogeneity can provide some benefit, but cannot completely explain the experimentally observed improvement in tensile fracture of laminates manufactured from conventional prepreg tape to laminates manufactured from fiber placement. A ply-by-ply stacked membrane model was utilized to study the influence of splitting, delaminations, and combined damage. The stacked membrane approach was found to be a practical two-dimensional method of analyzing damage which is essentially three dimensional. Additional configurations need to be examined to determine limitations. The influence of damage types, which are enhanced with fiber placement appears to play a greater role in the improvement compared to the inhomogeneity effects alone. Splitting provides some improvement, as well as delaminations. However, up to 36% improvement was provided by combined delaminations and splits for the damage sizes studied here. This interesting phenomenon warrants further research. In particular, while the enhancement from fiber placement is clearly beneficial for tensile fracture, it is necessary to determine if these damage types are beneficial for fracture of structures loaded in compression and shear as well.

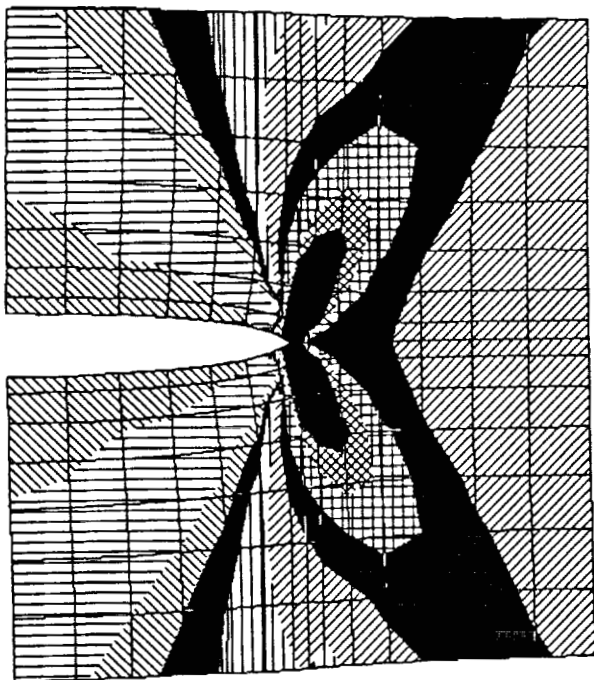


Surrounding Plies

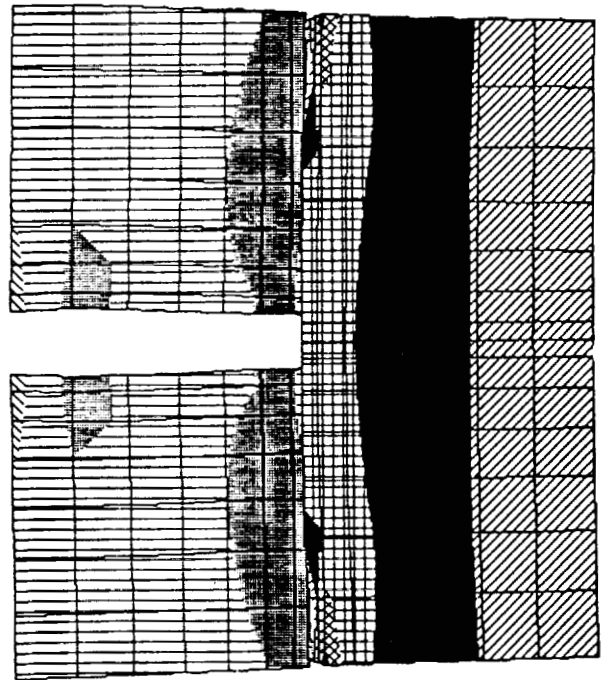


Delaminations plus Splits

Figure 11. Delaminations plus Splits



a) Surrounding Plies



b) Delaminations plus Splits

Figure 12. Isostrain Contours with Splitting Plus Delaminations

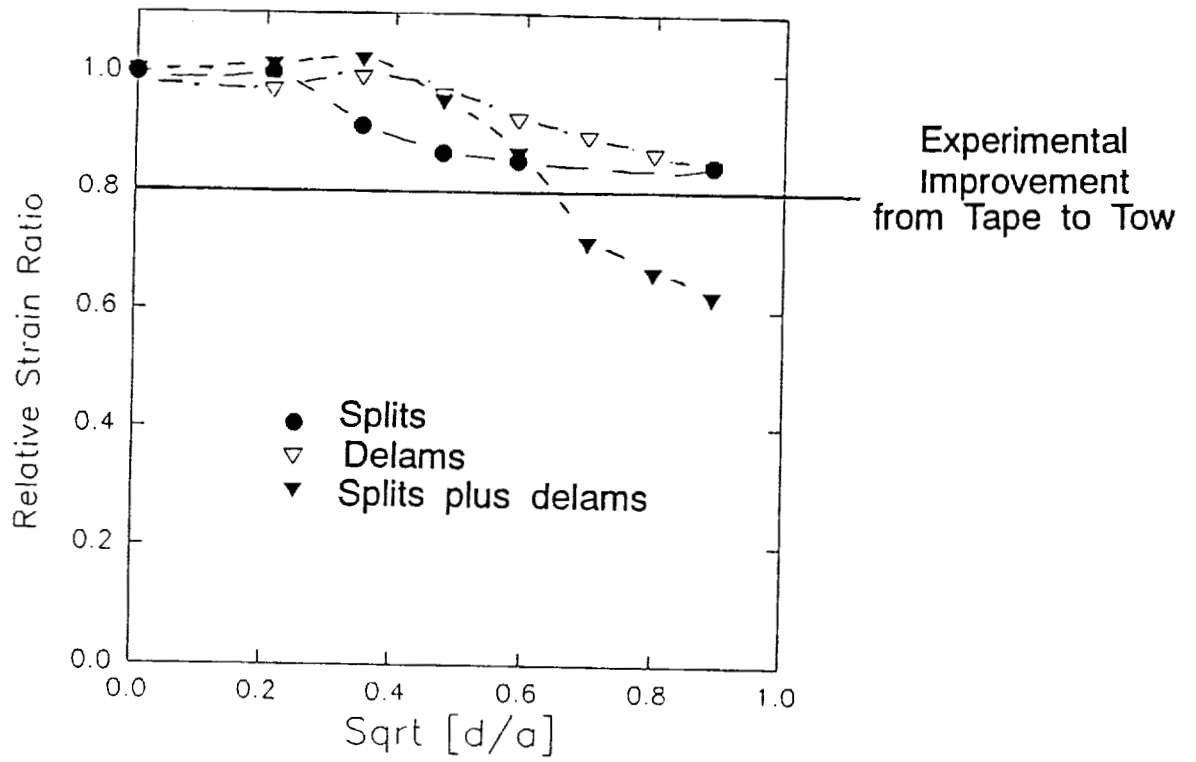


Figure 13. Improvement in Fracture for Various Damage Types

References

1. Walker, T., Avery, W., Ilcewicz, L., Poe, C.C., Jr., and Harris, C.E., "Tension Fracture of Tow-Placed Laminates for Transport Applications", **Ninth DoD/NASA/FAA Conference on Fibrous Composites in Structural Design**, November 4-7, 1991.
2. Walker, T. and Ilcewicz, L.B., "Mechanical Tests and Analysis Predictions," **Proceedings of the Boeing/NASA review of ATCAS**, Contract NAS1-18889, May 15, 1991.
3. **Hercules Prepreg Tape Materials Characterization Data Package**, Fibers: AS4, IM6, IM7 & IM8, Resins: 8551-7, 8551-7A, 8552, 3501-6, Hercules Composite Products Group, Magna, Utah, November, 1988.
4. Washizu, K., **Variational Methods in Elasticity and Plasticity**, Third Edition, Pergamon Press, Elmsford, New York, 1982.
5. Pian, T.H.H., "Derivation of Element Stiffness Matrices by Assumed Stress Distributions," **AIAA Journal**, Vol. 5, No. 1, 1964, pp. 1333-1336.
6. Cook, R.D., **Concepts and Applications of Finite Element Analysis**, John Wiley and Sons, New York, New York, 1981, pp. 210-211.
7. Whitney, J.M. and Nuismer, R.J., "Stress Fracture Criteria for Laminates Containing Stress Concentrations," **Journal of Composite Materials**, Vol. 8, 1974, pp. 253-265.
8. Cairns, D.S. and Lagace, P.A., "Residual Tensile Strength of Graphite/Epoxy and Kevlar/Epoxy," **Composite Materials: Testing and Design (Ninth Conference)**, American Society for Testing and Materials, Reno, NV, 1988.
9. Kortschot, M.T. and Beaumont, P.W.R., "Damage-Based Notch Strength Modeling: A Summary," **Composite Materials: Fatigue and Fracture (Third Volume)**, ASTM STP 1110, T.K. O'Brien, Ed., American Society for Testing and Materials, Philadelphia, 1991, pp. 596-616.

**MECHANICAL CHARACTERIZATION OF TWO THERMOPLASTIC
COMPOSITES FABRICATED BY AUTOMATED TOW PLACEMENT**

Larry C. Dickinson
Lockheed Engineering and Sciences Co.
Hampton, Virginia

Jerry W. Deaton
NASA Langley Research Center
Hampton, Virginia

511-24
51411

ABSTRACT

AS4/PEEK towpreg and IM7/Radel 8320 slit tape were used to make flat panels by automated tow placement. The panels were tested in notched and un-notched tension, notched and un-notched compression and compression after impact (CAI) at room temperature and under hot/wet conditions (notched and un-notched compression and CAI only). The properties were compared with AS4/PEEK tape laminate properties found in the literature. The tow placed AS4/PEEK material was stronger in tension but weaker in compression than the AS4/PEEK tape laminates. The tow placed AS4/PEEK was stronger but less stiff than the tow placed IM7/Radel 8320 in all compression tests. The IM7/Radel performed better in all other mechanical tests. The IM7/Radel outperformed the AS4/PEEK in all CAI tests.

INTRODUCTION

Advanced polymeric composite materials offer significant potential for weight savings and performance advantages over traditional aircraft materials. A major goal of the NASA Advanced Composite Technology (ACT) program is to develop these materials for use in primary structure of commercial aircraft. Compared to metallic materials, composites offer tailorability of properties along with very high specific strength and stiffness. However, laminated composite structures are expensive to manufacture and less damage tolerant than desired. If advanced composites are to be used in the primary structure of commercial aircraft, the problems of high cost and low damage tolerance must be overcome.

When first introduced, thermoplastic composites such as graphite/PEEK were heralded as offering a solution to the low damage tolerance of traditional graphite/epoxy laminates. Although the improved toughness of thermoplastic matrix composites is well documented, their high cost relative to traditional materials has prevented their widespread use in aircraft structures.

Much effort has been made to reduce the cost of manufacturing composite structure by using processes such as filament winding and automated tow placement. While the filament winding process has been utilized in the aerospace industry for some time, it is generally restricted to certain volumetric shapes and cannot manufacture a concave form. A specialized form of filament winding called automated tow placement (ATP) or fiber placement is capable of manufacturing simple volumetric shapes, flat panels and complex (including concave) shapes. The process uses a multi-axis robotic machine (ref. 1) to lay down multiple tows as a band, forming a laminated structure (see figure 1). The band location and angles are precisely controlled with material cut, add and compaction features incorporated into the process. ATP has been identified as a cost effective automated manufacturing process capable of producing the large complex shapes needed for the next generation of commercial aircraft (ref. 1 and 2). While demonstrating cost saving potential, most ATP work has been done with thermoset materials, which often have poor damage

tolerance. There is little published data for tow placed thermoplastics.

The objective of this work was to evaluate the potential of using cost effective ATP in conjunction with damage resistant thermoplastic materials to fabricate composites for use as primary aircraft structure. The approach was to select two graphite/thermoplastic (Gr/Tp) material systems, fabricate flat panels by ATP and perform standard tests to evaluate the mechanical properties. The ATP material properties were also compared to the properties of tape laminates. The mechanical property characterization included notched and un-notched tension and compression, compression after impact, and environmental degradation under hot/wet (H/W) conditions.

MATERIALS AND PROCESSING

The thermoplastic material systems evaluated in this study were AS4/PEEK towpreg and IM7/Radel-8320 (formerly Radel-X) slit tape. The two materials were selected from several which were available from suppliers and capable of being tow placed. AS4/PEEK was selected so that comparisons could be made to existing data on AS4/PEEK prepreg tape material. The IM7/Radel material offered somewhat different constituent material properties and processing temperatures than the AS4/PEEK. Tables 1 and 2 show the fiber and resin properties for the two material systems (ref. 3-6).

Under contract to NASA Langley, Hercules Aerospace Company, Composite Products Group used automated tow placement to manufacture the flat composite panels with the above materials. A modest development effort was made to "auto-consolidate," or "consolidate on the fly." In an auto-consolidation process, the thermoplastic material is heated to its processing temperature and consolidated in-situ with a compaction roller. Early efforts involved making small hoops or cylinders with a filament winding machine. The development work was done with AS4/PEEK. A special fiber placement head was developed to apply heat as the tows were laid down on the tool or part. A Sylvania hot air flameless

torch was selected as the heat source. The manufacture of quality (low void content) filament wound rings was found to be fairly easy. However, the manufacture of the flat panels was found to be quite difficult. Two significant problems were identified.

First ply adhesion was found to be very difficult in the tow placement of flat panels. The first layer of the composite must adhere to the tool or mandrel so that subsequent plies can be added successfully. The material must adhere to the tool at high processing temperatures and yet easily release from the tool once processing is complete. This problem is less significant when "tacky" thermosets are used or when the first ply can be completely wrapped under tension around a volume of revolution. To overcome the problem of first ply adhesion in the flat panels of this study, the panels were manufactured oversized (see figure 2). An AS4/PEEK bi-direction tape (woven material) was mechanically fastened to the flat tool outside the perimeter of the required panel area. During the lay-down of the first layer, the beginning and end of each pass adhered to the bi-directional tape. Once the second ply was placed the first ply seated down in the correct position with minimal gaps or overlaps. Once all the layers were laid down, the excess material was then trimmed away leaving a panel of the required size.

The second major difficulty encountered in auto-consolidation of the flat panels was related to the difference between tow placement and filament winding processes. The development work was done with a filament winding machine. However, automated tow placement was used to make the flat panels. In the filament winding of thermoplastic materials, the winding head stays in contact with the mandrel or composite part making consolidation "on the fly" simpler. Reference 7 discusses process development of in-situ consolidation of ring-type specimens and cylinders with filament winding. In tow placement the fiber placement head accelerates from a still position, traverses a set distance and then decelerates to a complete stop where the tow is cut. The head is then lifted from the surface of the panel and indexed to another position. The unavoidable variation in material lay-down rate and discontinuity of contact between the placement head and composite part creates a complicated process control problem for in-situ consolidation. The AS4/PEEK towpreg was fairly insensitive to this variation. However the IM7/Radel was very sensitive to the process

parameters; hence, the extent of in-situ consolidation was not constant across any given lay-down pass. Only 40% consolidation (based on visual observation and past experience by the contractor) was achieved near the beginning and end of each pass while around 75% consolidation was accomplished near the middle of each pass. To achieve full consolidation on the fly specific attention needs to be given to controlling the heat source as a function of machine speed (open-loop feedback) or material temperature (closed loop feedback).

Due to the complexity of auto-consolidation with tow placement, full consolidation was not achieved "on the fly" at any lay-down rate. However, as auto-consolidation was not the goal of the research, the processing was completed by vacuum bag/autoclave cycles in a manner similar to that used for tow placed thermoset parts. Autoclave pressure was 200 psi for both material systems. The maximum processing temperatures were 720°F and 650°F for the AS4/PEEK and the IM7/Radel, respectively. Ultrasonic testing was conducted by Hercules to insure quality and determine the extent of consolidation. The panels were reprocessed in the autoclave several times until nearly void free.

The flat panels were made with a quasi-isotropic lay-up, $[45/0/-45/90]_{3s}$ for un-notched tension and $[45/0/-45/90]_{6s}$ for compression and notched tension. Completed panels were again ultrasonically tested at NASA Langley to verify quality, void free panels.

TEST METHODS AND PROCEDURES

Tension, compression, 90° compression, notched tension, notched compression and compression after impact (CAI) testing was performed with the quasi-isotropic flat panels. Specimen configurations are shown in figure 3. Test procedures as described in reference 8 were followed unless otherwise stated. Three specimens were tested for each configuration with the exceptions of 90° compression and room temperature CAI where two

specimens (each) were tested. Specimens were instrumented with 350 ohm back-to-back strain gages as shown in figure 3. Data were gathered with a 16-bit resolution A/D micro-computer-based data acquisition system. Tension tests (notched and un-notched) were performed in a 50 kip electro-hydraulic test machine equipped with hydraulic grips at a constant stroke of 0.05 in./min. All compression tests were performed in a 120 kip hydraulic test machine at a constant rate of 0.05 in./min.

Tension specimens were un-tabbed, but each end had a coarse grit paper and Lexan film between the knurled grips and specimen. The un-notched compression test utilized a specimen configuration and fixture developed at NASA Langley to evaluate the compression properties of composites. The test is referred to as short block compression (SBC). The SBC fixture, shown in figure 4, applies end loading while preventing a brooming type failure. The CAI test specimens were impacted with a low-velocity air gun apparatus which fires a 1/2-in. diameter aluminum ball (0.0065 lb mass). An impact energy of 1500 in.-lb/in. of specimen thickness was used (approximately 550 ft/sec velocity, equalling 30 ft-lb of energy). Impacted panels were loaded in a special fixture, shown in figure 5. The fixture utilizes clamped ends and simple support knife edges on each side. The specimens are end loaded and the clamped ends prevent brooming failures. The impacted specimens were C-scanned after impact, before compression testing to determine the extent of the impact damage. Fiber volume fraction for each large panel was determined by acid digestion of small samples obtained from different locations within each panel (ref. 9).

While the majority of the testing was performed on unconditioned specimens at laboratory conditions, some environmental testing was performed on notched and un-notched compression (three specimens each) and CAI specimens (one specimen). Specimens were immersed in 160°F water for 45 days. The specimens were weighed before and after exposure to determine moisture gain and then instrumented with strain gages. The specimens were then tested at 180°F, usually within one or two hours. This type test is referred to as hot/wet (H/W) testing.

RESULTS AND DISCUSSION

The results of the mechanical testing are presented as averages in tables 3 through 5. The fiber volume fractions ranged from 53.9% to 57.2% for the AS4/PEEK and 63.6% to 64.0% for the IM7/Radel. Normalizing the mechanical properties to a 60% fiber volume fraction did not significantly affect property trends or comparisons; hence, data shown are actual test values. Typical stress-strain plots for each material are shown in figure 6. Moduli were calculated by a linear regression over the range of 0.1% to 0.3% strain to avoid initial loading artifacts.

Tension Properties

The quasi-isotropic tow placed AS4/PEEK and IM7/Radel tensile properties are shown in figure 7 along with quasi-isotropic AS4/PEEK tape (prepreg) laminate data from reference 10. The bars represent the average values listed in the tables and the lines drawn through the bars indicate the full range of the repeat tests. The tow placed AS4/PEEK composite was slightly stronger than the AS4/PEEK tape composite (10%), but both possessed similar moduli. It should be noted that the tension testing of the tape material in reference 10 was performed with a 48 ply quasi-isotropic material while the tension testing of the tow placed material was performed with a similar layup of only 24 plies.

Comparing the two tow placed materials, the IM7/Radel had an approximately 32% greater un-notched tensile strength and modulus than the AS4/PEEK. This fact is not surprising in that tension properties are dominated by fiber behavior. IM7 fiber has a significantly greater strength (30%) and modulus (21%) than AS4 fiber (see table 1). The two composite systems exhibited similar tensile failure strains and in-plane Poisson's ratios (tables 3 and 4). Both the AS4/PEEK and IM7/Radel exhibited approximately 50% lower

tensile strength when tested with a 0.25-in. diameter hole.

Compression Properties

Figure 8 illustrates the room temperature and hot/wet compression properties of the quasi-isotropic tow placed AS4/PEEK and IM7/Radel composite materials. Again, the bars represent the average values and the lines drawn through the bars indicate the full range of the repeat tests. Also shown in figure 8 are the room temperature compression properties of quasi-isotropic AS4/PEEK tape (prepreg) laminate data from reference 10. The AS4/PEEK tow placed material compares closely with the AS4/PEEK tape material. The tape material was slightly stronger and stiffer (5% and 8% respectively).

When comparing the compression properties of the two tow placed composites, the AS4/PEEK was slightly stronger while the IM7/Radel had a significantly higher modulus. The tow placed AS4/PEEK was 8% stronger in un-notched compression strength and experienced a 35% greater ultimate strain than the tow placed IM7/Radel (see tables 3 and 4). The IM7/Radel compression modulus was 24% higher than that of the AS4/PEEK. Since compressive failure is strongly dependent on matrix properties, the higher compression strength and ultimate strain of the tow placed AS4/PEEK may be attributed to the higher modulus of PEEK compared to Radel (see table 2). The higher compressive modulus of the IM7/Radel may be explained by the higher modulus of the IM7 (43 Msi) fiber as compared to AS4 (36 Msi).

Both tow placed materials suffered a similar reduction in strength for notched compression (approximately 40%) and for hot/wet compression (approximately 15%). The AS4/PEEK specimens experienced 0.1% to 0.2% moisture gain during the 45 day soak of the H/W test while the IM7/Radel absorbed 0.4% to 0.5%. The IM7/Radel seemed more sensitive to the hot/wet notched testing as it retained only 46% of its room temperature un-notched compressive strength while the AS4/PEEK retained 55%. A similar trend was found

for the ultimate strains in H/W and notched compression (see tables 3 and 4). However, the moduli for both materials remained relatively unaffected by environmental testing (see figure 8).

The two tow placed quasi-isotropic materials were also tested in the 90° direction (see tables 3 and 4). One would expect the longitudinal (0°) and transverse (90°) properties to be comparable for a quasi-isotropic layup. While the 0° and 90° moduli were similar for both the AS4/PEEK and the IM7/Radel tow placed materials, both materials showed 6 to 7% higher strength in 90° compression than in 0° compression. A similar finding was reported for the AS4/PEEK tape laminate of reference 10 where the 0° and 90° direction strengths (both tension and compression) were significantly different. The higher compression strength in the 90° direction may be related to the fact that there are two 90° plies together at the center of the laminate. In effect there is one thick 90° ply at the midplane of the laminate and there is one less 90° ply interface than there are 0° ply interfaces.

Compression After Impact Properties

The room temperature and hot/wet compression after impact properties of the tow placed AS4/PEEK and IM7/Radel are shown in figure 9, along with the room temperature CAI data for AS4/PEEK tape from reference 11. The compression strengths (un-impacted) shown are repeated from figure 8 and the CAI data are from table 5 and reference 11. The numbers in parentheses at the top of the columns indicate the damage areas as determined from C-scans taken after the impact event. A target impact energy of 30 ft-lb (1500 in.-lb/in. of thickness) was used in the current investigation, as stated earlier. One AS4/PEEK specimen was inadvertently impacted at only about 15 ft-lb. This value is listed in table 5 but not included in figure 9.

As can be seen in figure 9, the CAI strength of the AS4/PEEK tow placed material compares closely with the AS4/PEEK tape material of reference 11, both being impacted with

an air gun at 1500 in.-lb/in. Although the actual impact energies varied somewhat (see table 5), and albeit the tow placed AS4/PEEK was somewhat stronger in un-notched compression, the tow placed IM7/Radel had a 26% greater room temperature CAI strength than the AS4/PEEK. The IM7/Radel retained 43% of its un-impacted strength while the AS4/PEEK retained only 32%. Even the one AS4/PEEK specimen inadvertently impacted at about 1/2 of the targeted impact energy was not stronger than the impacted IM7/Radel specimens. The higher strength of the IM7/Radel compared to AS4/PEEK is consistent with the smaller damage area (almost half) of the IM7/Radel. Some of this difference in strength between the two materials may be attributed to the different fibers. For example, reference 11 compared quasi-isotropic IM7/PEEK and AS4/PEEK tape laminates and found the IM7/PEEK to have approximately 10% greater CAI strength. While the higher strength of the IM7 fibers over AS4 may have contributed to the higher CAI strength of the IM7/Radel, the difference is large enough to suggest that the Radel matrix contributed more to the better CAI characteristics than the PEEK matrix. It is the properties of the matrix material which contribute most to impact and CAI behavior (ref. 11).

The hot/wet CAI data shown in figure 9 and tables 2-5 for the tow placed materials indicate that the IM7/Radel also retained more of its room temperature compressive strength in hot/wet CAI testing when compared to the AS4/PEEK. The IM7/Radel retained about 46% of its hot/wet un-impacted strength while the AS4/PEEK retained about 38% of its hot/wet un-impacted strength.

While the IM7/Radel material demonstrated smaller damage areas and higher CAI strengths, neither material demonstrated outstanding damage tolerance. A measure of merit for the CAI test is for the material to have a CAI strength of 40 ksi after a 1500 in.-lb/in. of thickness energy drop weight impact (ref. 12). While the materials of this study did not meet this measure of merit, the low CAI strengths may be partially attributed to the type of impact. The tow placed materials of this study were impacted with an air gun. When compared to drop weight impacting, it has been shown repeatedly that the higher velocity impact of an air gun firing an aluminum ball causes larger damage area and lower CAI strength. Reference 11 reported that quasi-isotropic AS4/PEEK tape laminates, impacted at 1500 in.-lb/in., had an

air gun CAI strength of about 31 ksi and a drop weight CAI strength of approximately 48 ksi, a 55% difference. It is important to note that the specimen geometry and boundary conditions during impact were also different. Reference 13 presents CAI data for two-phased toughened epoxy matrix materials subjected to both types of impact at 1500 in.-lb/in. The drop weight impact resulted in 33 to 55% higher CAI strengths and 50 to 61% smaller impact damage areas (ref. 13). These data suggest that direct comparisons between CAI data obtained from the two types of impact tests should be avoided. Although a drop weight type impact test was not performed for this work, in light of the results presented in reference 11, the air gun impacted CAI properties suggest that the ATP thermoplastic materials would meet the measure of merit.

CONCLUDING REMARKS

Two graphite/thermoplastic composite materials, AS4/PEEK towpreg and IM7/Radel 8320 slit tape, were used to make quasi-isotropic $[45/0/-45/9]_{ns}$ flat panels by automated tow placement. An attempt at auto-consolidation was made. Consolidation on-the-fly was found to be a complex but potentially viable process needing more research and development to become useable for full consolidation of thermoplastic composites. The tow placed composites of this study were partially consolidated in-situ and then fully consolidated with a more traditional vacuum bag/autoclave process.

Un-notched tension, notched tension, un-notched compression, notched compression, compression after impact and hot/wet tests were performed with the two tow placed composite materials. The properties of the tow placed quasi-isotropic AS4/PEEK laminates were compared with quasi-isotropic AS4/PEEK tape properties found in the literature. The tow placed AS4/PEEK material was somewhat stronger in tension but also somewhat weaker in compression than the AS4/PEEK tape laminates. The CAI properties of AS4/PEEK tape and tow placed materials were similar.

Comparing the two tow placed materials, the IM7/Radel demonstrated a significantly higher modulus in both tension and compression than the AS4/PEEK. The IM7/Radel also had a higher tensile strength. These better properties can be related to the higher strength and stiffness of the IM7 fiber as compared to the AS4. The AS4/PEEK was stronger in compression than the IM7/Radel. This higher compressive strength can be ascribed to the higher modulus of the PEEK resin as compared to Radel. The IM7/Radel outperformed the AS4/PEEK in all CAI tests.

While the CAI strengths did not indicate high levels of damage tolerance in these tests, this fact may be attributed in part to the type of impact test. These materials may have shown a significantly better CAI strength if tested with a drop weight impact instead of an air gun impact. The above findings suggest that these materials may be suitable for aircraft structure; however, the real potential of tow placed thermoplastics lies in the manufacturing process. If effective, low cost auto-consolidation can be successfully achieved, tow placed thermoplastics will compete more favorably with other materials under development.

REFERENCES

1. Anderson, R. L.; and Grant, C. G.: Advanced Fiber Placement of Composite Fuselage Structures. *First NASA Advanced Composites Technology Conference*, NASA Conference Publication 3104, 1991.
2. Bullock, F.; Kowalski, S.; and Young, R.: Automated Prepreg Tow Placement for Composite Structures. *35th International SAMPE Symposium*, April 2-5, 1990.
3. Hercules Incorporated Product Data Sheets, 847-5 and 8-68-1, June 1989.
4. Amoco Performance Products Incorporated Preliminary Product Data Sheet. January 1990.
5. Johnston, N. J.; Towell, T. W.; and Hergenrother, P. M.: Physical and Mechanical Properties of High-Performance Thermoplastic Polymers and their Composites, *Thermoplastic Composite Materials*, Elsevier Science Publishers B. V. 1991, pp 27-71.

6. Margolis, J. M.: *Engineering Thermoplastics*, Dekker, New York, 1985.
7. Rowan, J. H. C.; Askander, R. N.: Filament Winding of High Performance Thermoplastic Composites. *Materials and Processing - Move into the 90's*, Elsevier Science Publishers B. V., Amsterdam, 1989.
8. Standard Tests for Toughened Resin Composites, Revised Edition. NASA RP-1092, July 1983.
9. Standard Test Method for Fiber Content of Resin-Matrix Composites by Matrix Digestion. *Annual Book of ASTM Standards*, ASTM D3171-76, Volume 15.03, 1990.
10. Baker, D. J.: Mechanical Property Characterization and Impact Resistance of Selected Graphite/PEEK Composite Materials. NASA TM 102769, April 1991.
11. Srinivasan, K. and Tiwari, S. N.: Impact Response of Composite Materials. NASA-CR-187,896, February 1991.
12. Boeing Material Specification BMS-8-276.
13. Cano, R. J. and Dow, M. B.: Properties of Five Toughened Matrix Composite Materials. NASA TP 3254, 1992.

Table 1. Fiber Properties

Property	AS4	IM7
Tensile strength (ksi)	590	770
Tensile modulus (Msi)	36	43.6
Tensile strain (%)	1.65	1.81
Specific gravity	1.80	1.78
Cost 6K tow, 0-100 lbs(\$/lb)	28	62

Table 2. Resin Properties

Property	PEEK	Radel
Tensile yield strength (ksi)	13.6	11
Tensile modulus (Msi)	0.515	0.415
Tensile strain (%)	>40	100
Specific gravity	1.32	1.37
Tg (°F)	290	430
Processing temp. range (°F)	660-770	650-730

Table 3. AS4/PEEK Mechanical Properties, [45/0/-45/90]_{ns}

Property	n	Strength (ksi)	Modulus (Msi)	Ultimate strain (%)	Possion's ratio	Fiber vol. fract. (%)
Tension	3	97.5	6.60	1.51	0.31	53.9
Compression	6	87.3	6.10	1.67	0.32	57.2
90° compression	6	92.7	5.99	1.85	0.31	57.2
H/W compression	6	75.0	5.84	1.45	0.32	57.2
Notched tension	6	59.6*	6.66	0.76	—	57.2
Notched compression	6	55.1*	6.34	0.92	—	57.2
H/W notched compression	6	47.8*	6.14	0.81	—	57.2

* Strength based on gross cross-sectional area

Table 4. IM7/Radel Mechanical Properties, [45/0/-45/90]_{ns}

Property	n	Strength (ksi)	Modulus (Msi)	Ultimate strain (%)	Possion's ratio	Fiber vol. fract. (%)
Tension	3	130.0	8.68	1.48	0.31	63.6
Compression	6	79.9	7.59	1.08	0.33	64.0
90° compression	6	85.7	7.51	1.26	0.32	64.0
H/W compression	6	66.1	7.57	0.92	0.33	64.0
Notched tension	6	67.8*	8.33	0.81	—	64.0
Notched compression	6	46.6*	7.91	0.59	—	64.0
H/W notched compression	6	36.9*	7.75	0.49	—	64.0

* Strength based on gross cross-sectional area

Table 5. Compression After Impact Results, [45/0/-45/90]_{6s}

Specimen	Impact energy (in.-lb/in.)	Damage area (in.²)	Strength (ksi)
AS4/PEEK			
1*	770	1.91	33.3
2#	1410	5.19	28.2
3	1430	4.49	27.5
IM7/Radel			
1	1470	2.11	34.9
2	1520	2.82	34.3
3#	1530	2.60	30.5

Hot/wet test.

* Not included in average plotted in figures.

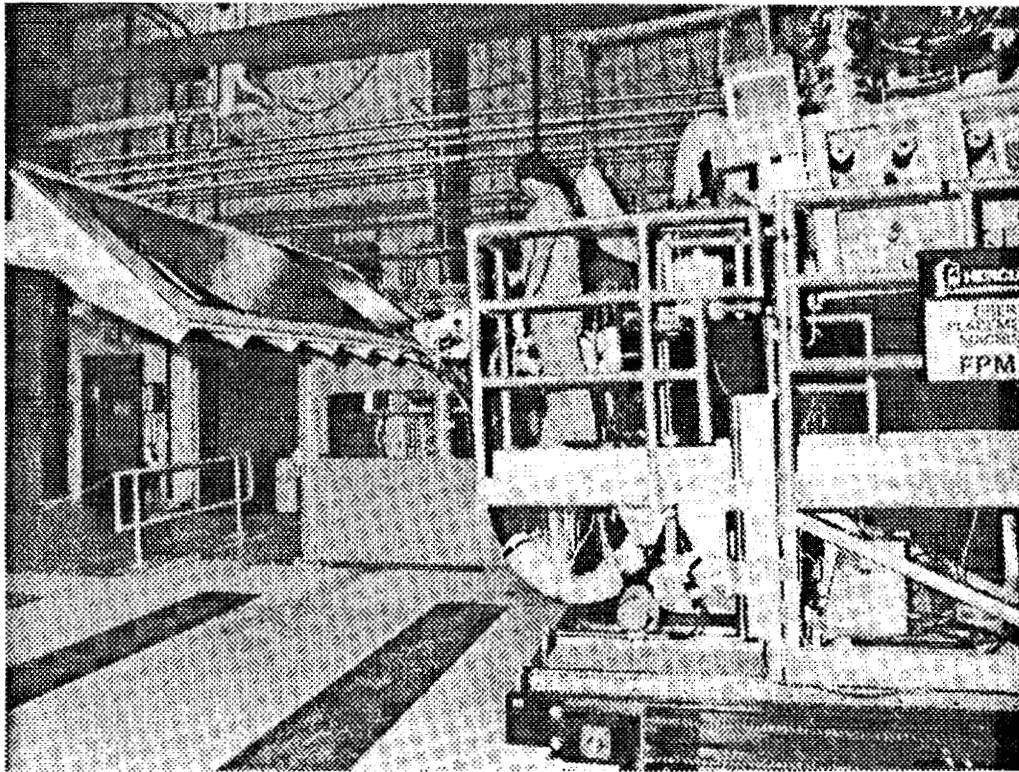
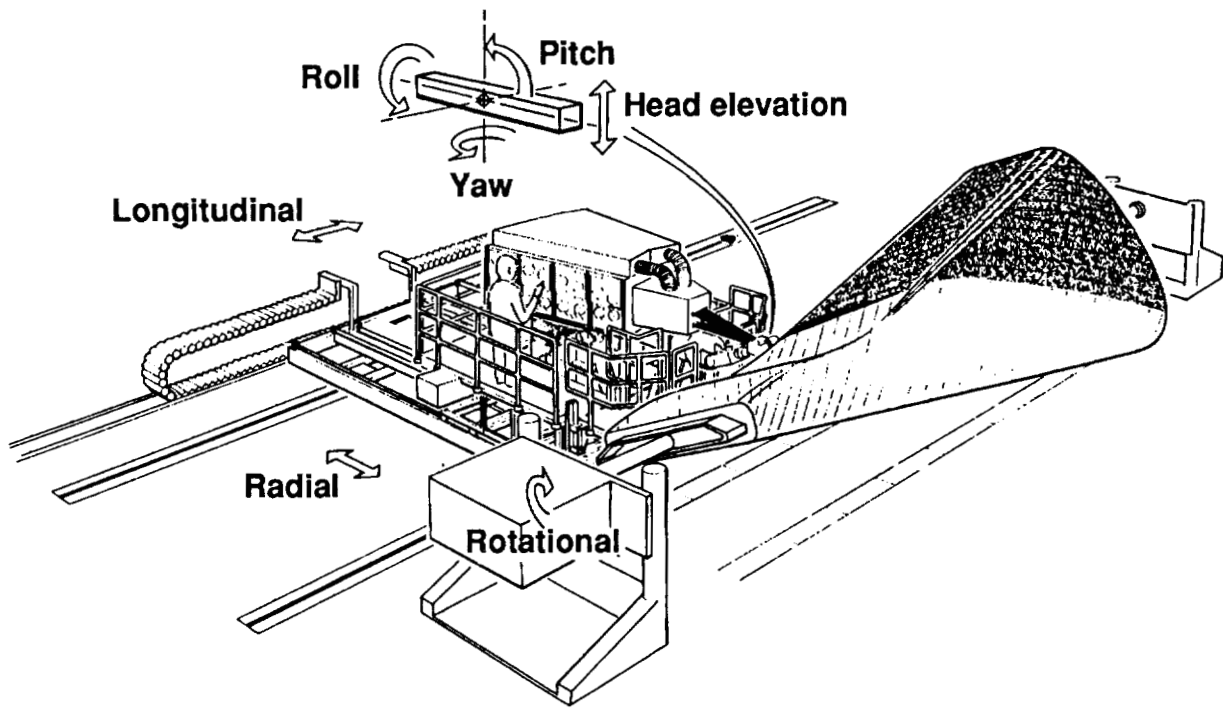


Figure 1. Automated tow placement machine, schematic and photograph (ref. 1).

C-3

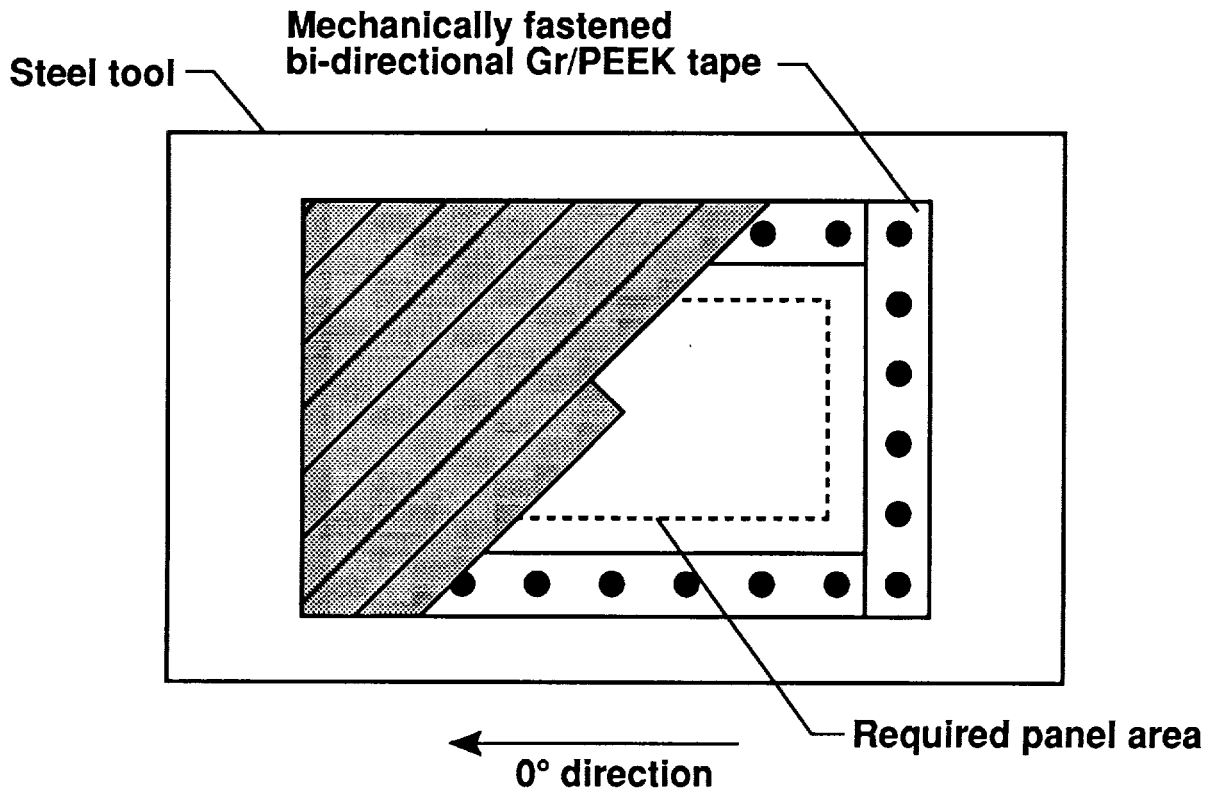


Figure 2. Schematic of first ply adhesion technique.

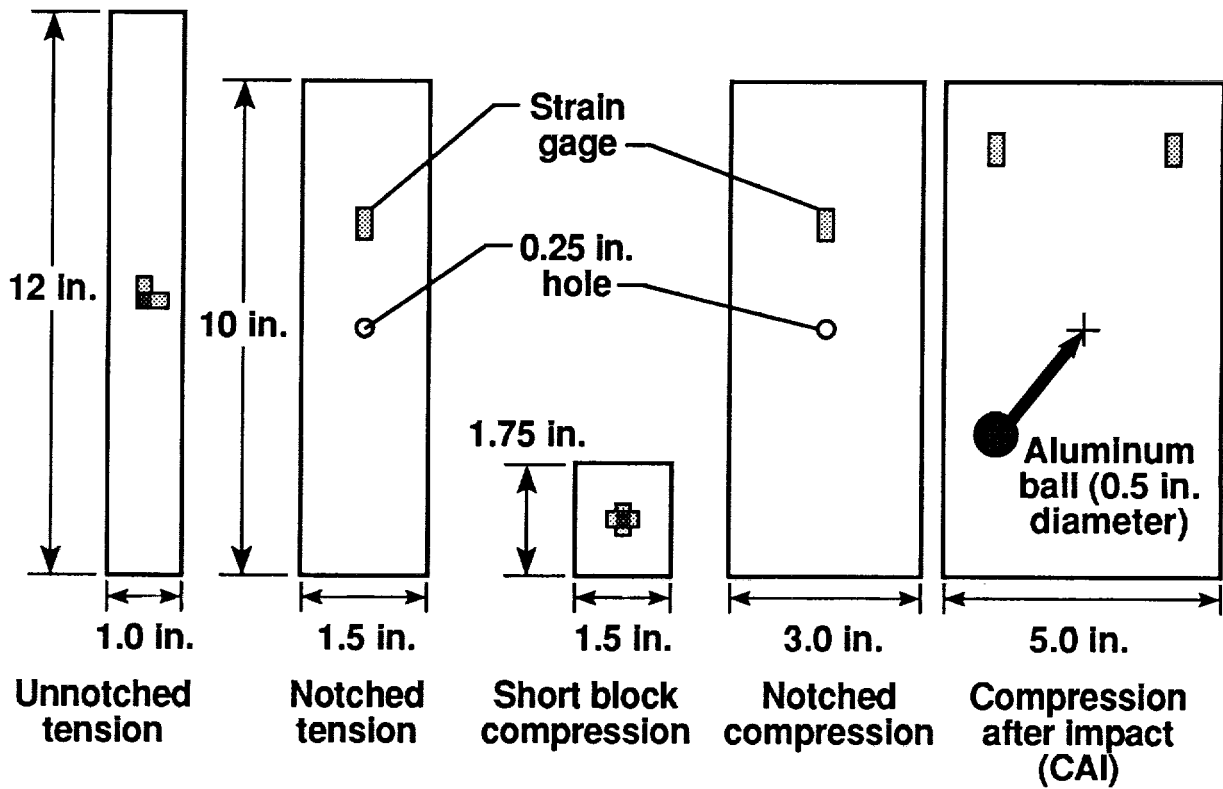


Figure 3. Test specimen configurations.

ORIGINAL PAGE
BLACK AND WHITE PHOTOGRAPH

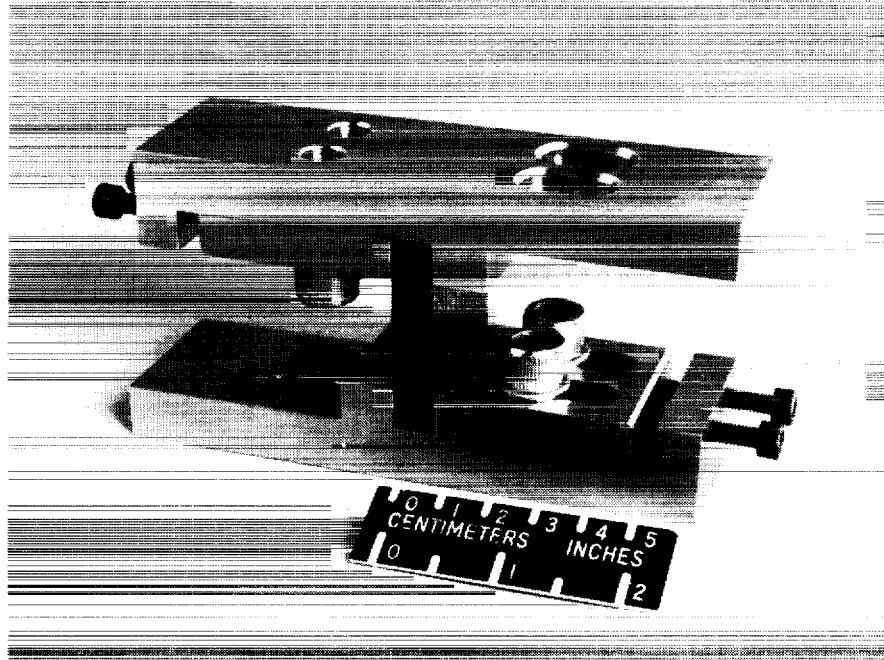


Figure 4. Short block compression test fixture.

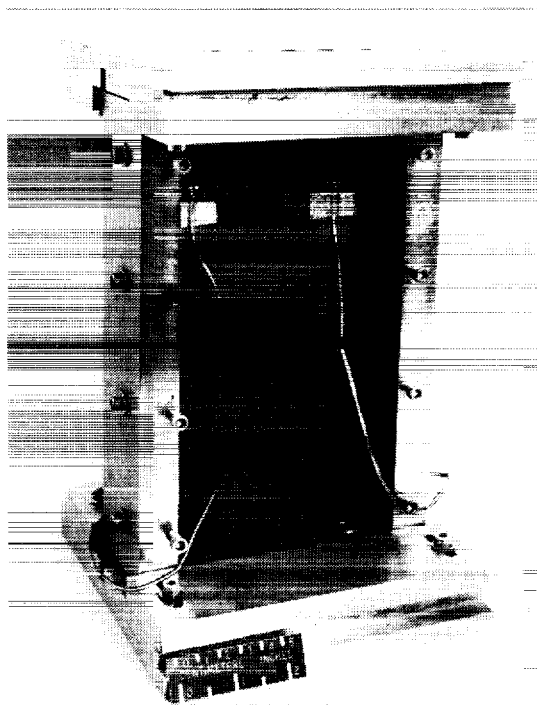


Figure 5. Compression after impact test fixture.

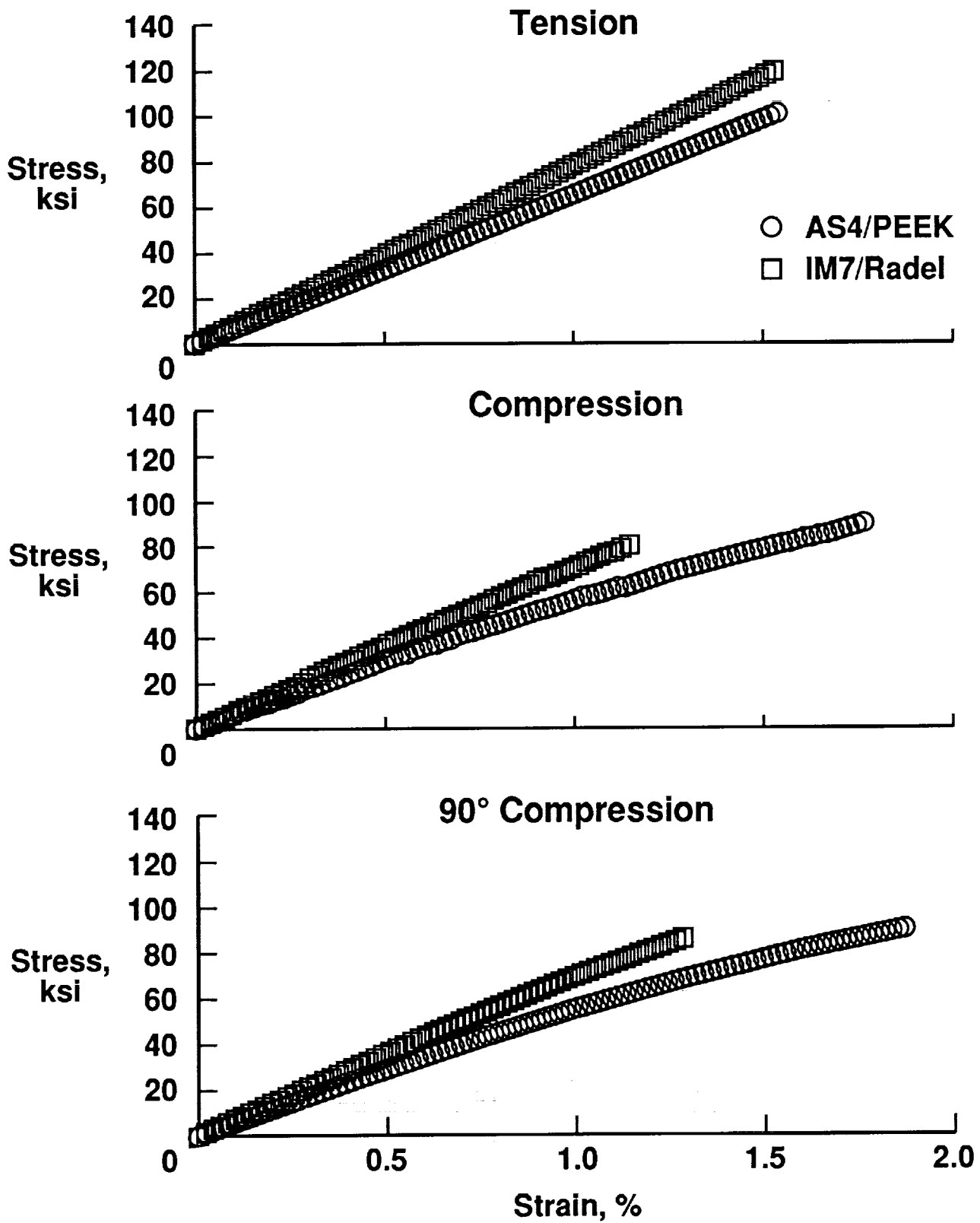


Figure 6. Typical stress-strain curves for tow placed quasi-isotropic graphite/thermoplastic composites.

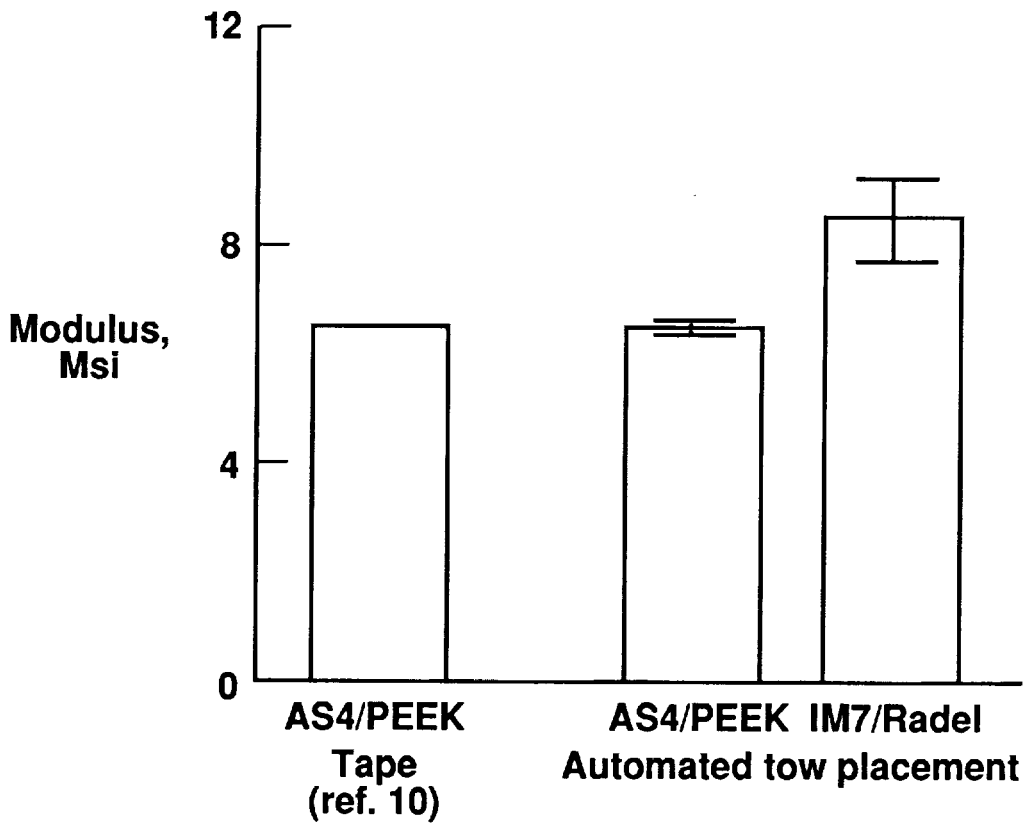
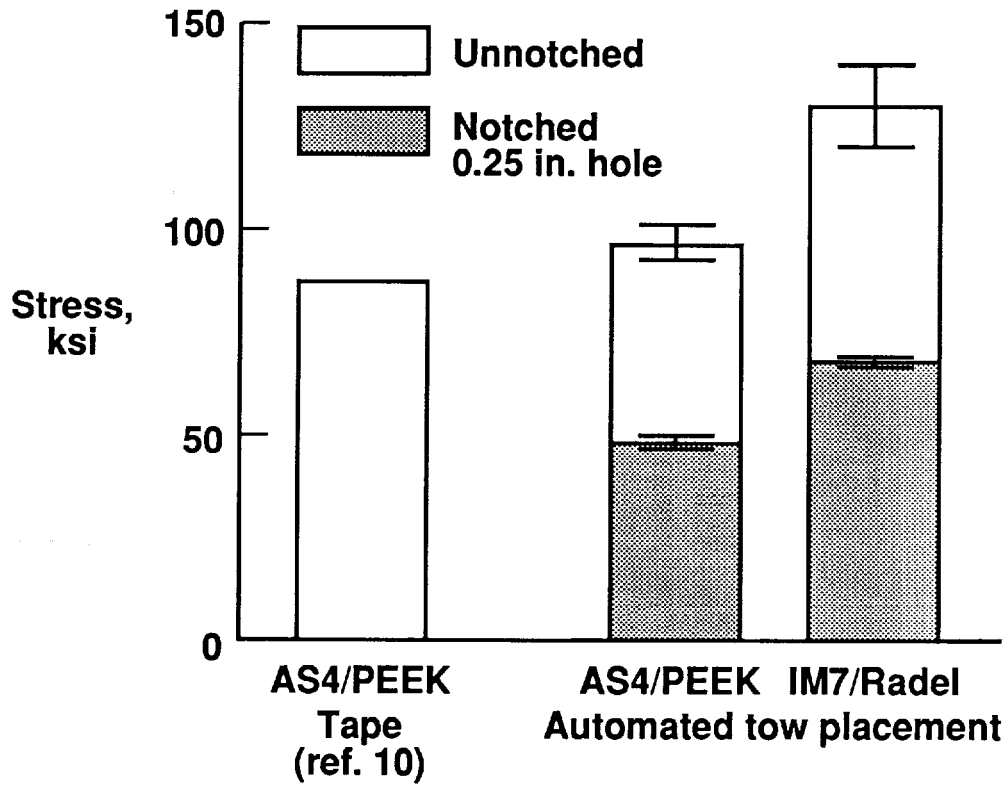


Figure 7. Notched and un-notched room temperature tension strengths and moduli of tow placed quasi-isotropic graphite/thermoplastic composites.

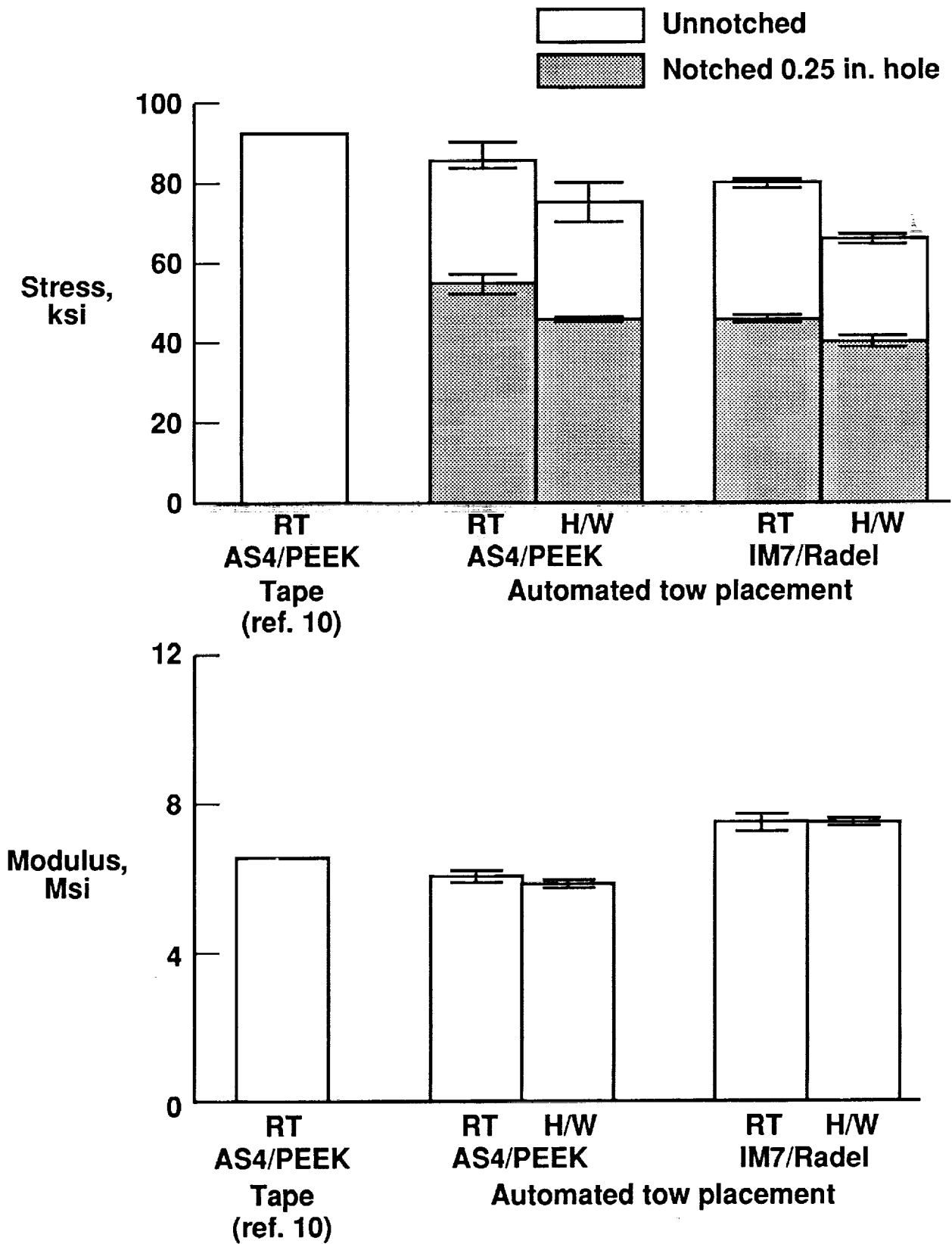


Figure 8. Notched and un-notched room temperature and hot/wet compression strengths and moduli of tow placed quasi-isotropic graphite/thermoplastic composites.

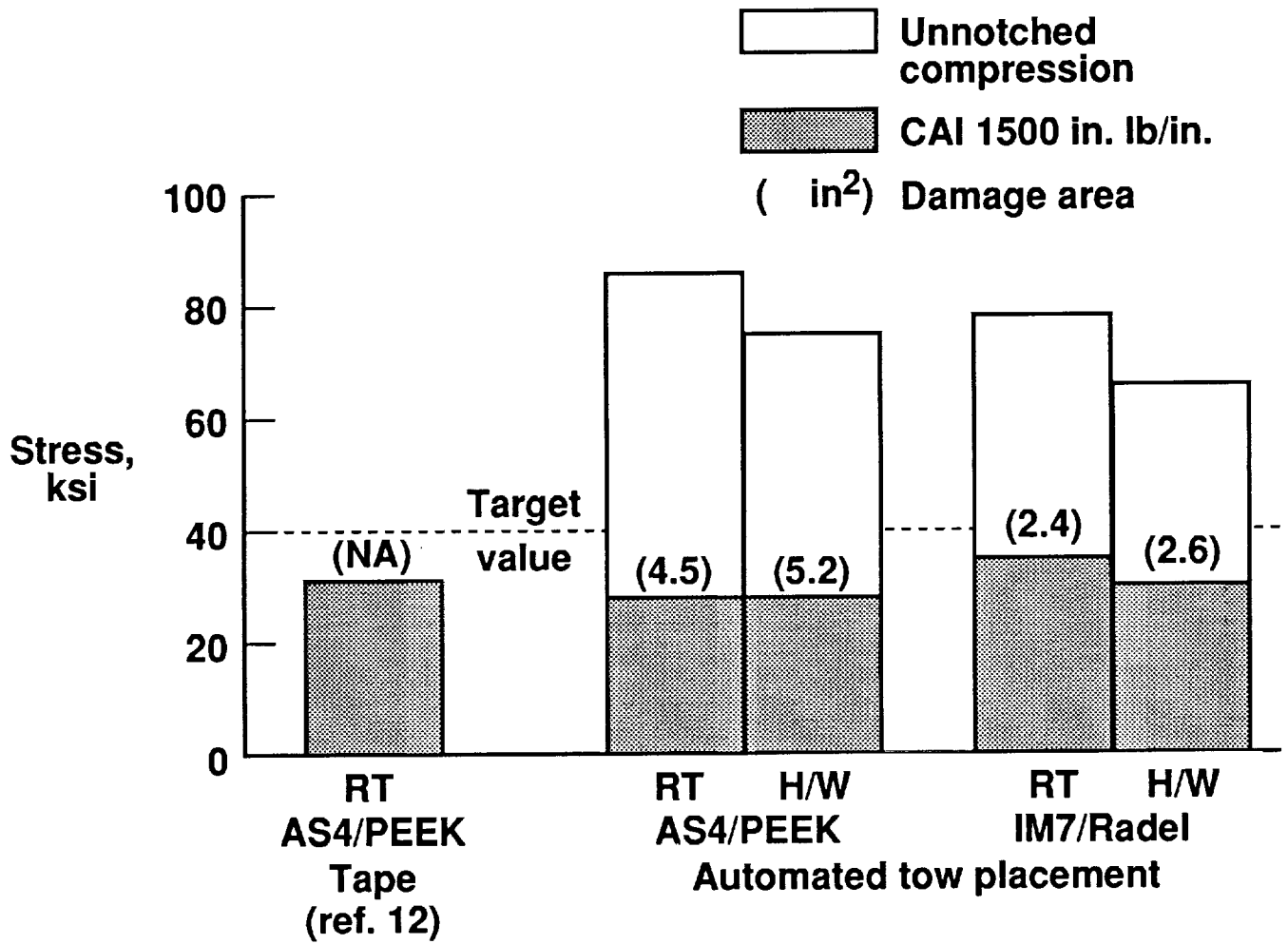


Figure 9. Compression and compression after impact strengths of tow placed quasi-isotropic graphite/thermoplastic composites.

Manufacturing Scale-up of Composite Fuselage Crown Panels ¹

K. Willden, M. Gessel
Boeing Commercial Airplanes
Seattle, Washington

C. Grant, and T. Brown
Hercules Aerospace
Magna, Utah

512-24
61412

ABSTRACT

The goal of the Boeing effort under the NASA ACT program is to reduce manufacturing costs of composite fuselage structure. Materials, fabrication of complex subcomponents and assembly issues are expected to drive the costs of composite fuselage structure. Several manufacturing concepts for the crown section of the fuselage were evaluated through the efforts of a Design Build Team (DBT) (Ref. 1). A skin-stringer-frame intricate bond design that required no fasteners for the panel assembly was selected for further manufacturing demonstrations. The manufacturing processes selected for the intricate bond design include Advanced Tow Placement (ATP) for multiple skin fabrication, resin transfer molding (RTM) of fuselage frames, innovative cure tooling, and utilization of low-cost material forms. Optimization of these processes for final design/manufacturing configuration was evaluated through the fabrication of several intricate bond panels. Panels up to 7 ft. by 10 ft. in size were fabricated to simulate half scale production parts. The qualitative and quantitative results of these manufacturing demonstrations were used to assess manufacturing risks and technology readiness for production.

INTRODUCTION

Large manufacturing demonstration panels were designed to meet the ATCAS program objectives. Manufacturing risk, technology readiness, and cost for an optimized panel configuration were evaluated. The crown panel design used the cost advantages of the ATP process for skin and stringer fabrication and braiding and RTM technologies for frame fabrication. Additionally, intricate tooling for cocuring the skin and stringers and cobonding the frames in one cure cycle was developed (Figure 1, Refs. 2, 3 and 4). The crown panel assembly was further optimized such that one tool served as the panel assembly tool and the cure tool.

¹ This work was funded by Contract NAS1-18889, under the direction of J.G. Davis and W.T. Freeman of NASA Langley Research Center

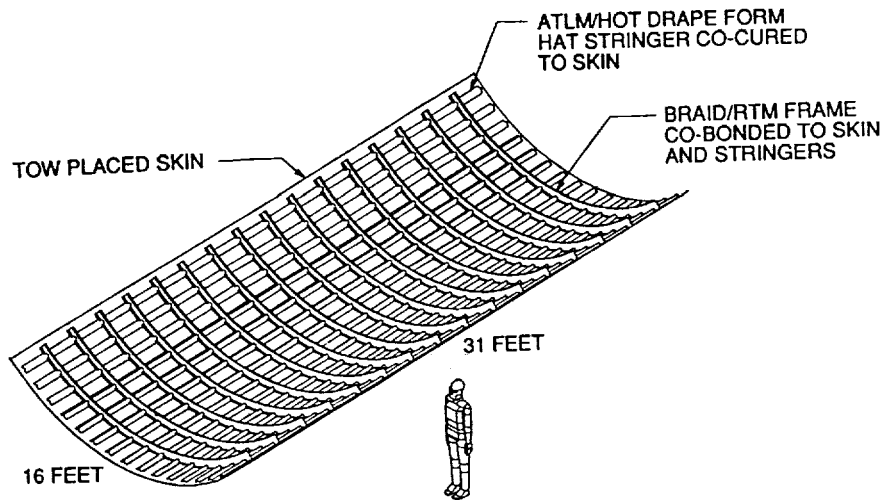


Figure 1: Intricate Bond Panel Configuration

Innovative IML cure tooling concepts were critical to the success and cost reduction of the intricate bond design. The tooling was optimized through a series of tool trials to reduce manufacturing risk and increase the part quality and structural performance. Scale-up issues were considered such that manufacturing concepts demonstrated on small panels would accommodate large panels without increasing manufacturing risks. Several types of manufacturing demonstration panels were identified to validate the tooling and intricate bond process (Figure 2).

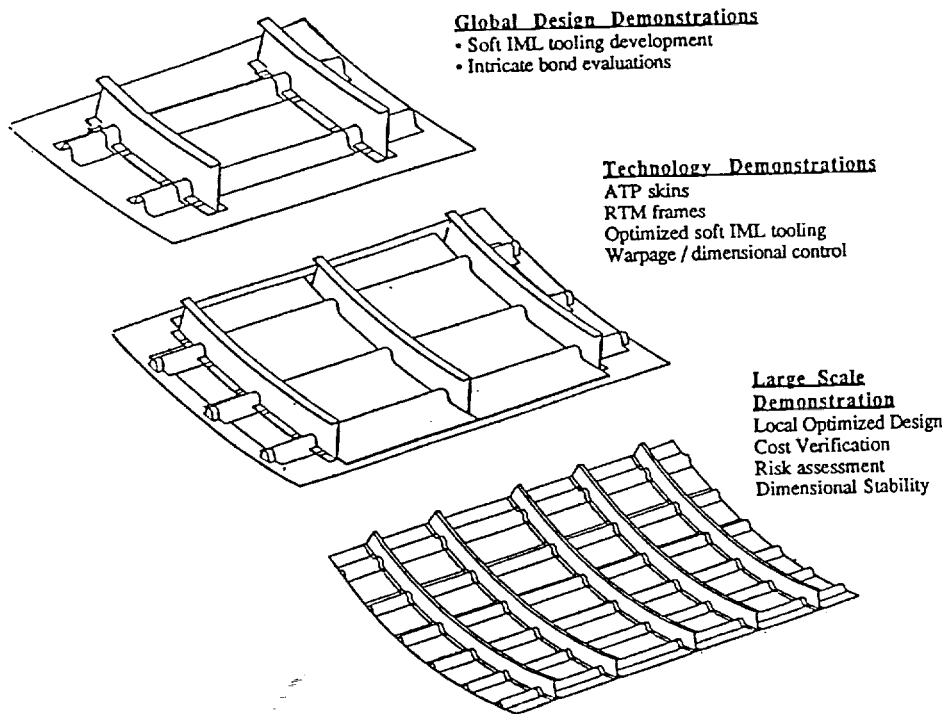


Figure 2: Manufacturing Technology Demonstrations

Manufacturing Demonstration

The initial IML tooling concepts were optimized by fabricating two-frame, two-stringer flat and curved panels (Figure 3). Panels 3 ft. by 5 ft. were fabricated at Hercules with the same soft IML tooling concept. These panels used ATP skins, drape formed stringers, and RTM frames (Figure 4). The results of these panels were used to optimize the tooling for the 7 ft. by 10 ft. manufacturing demonstration.

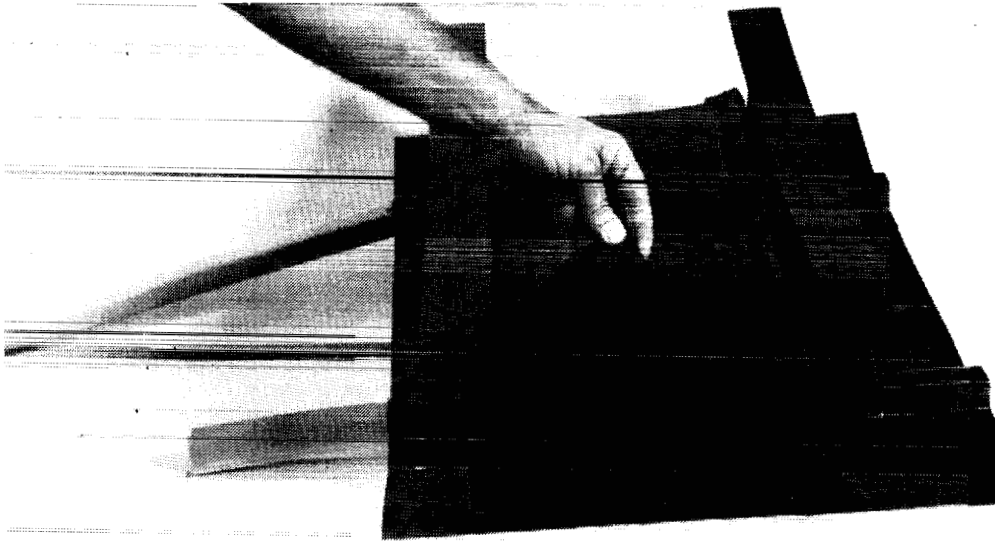


Figure 3: IML Tooling Trials

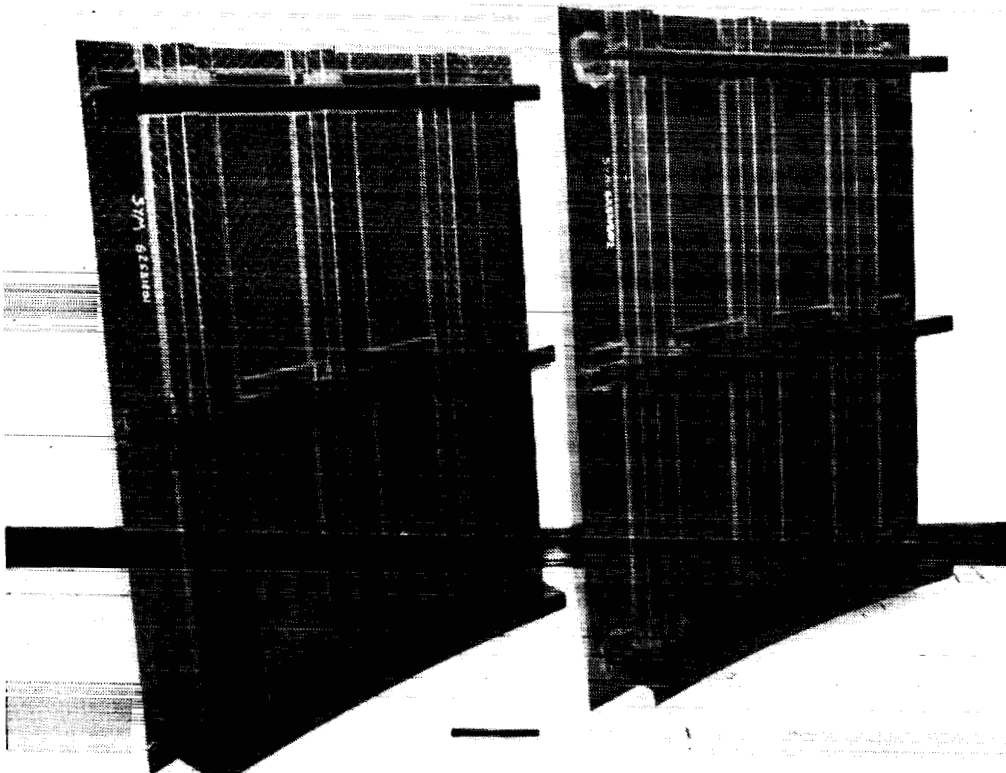


Figure 4: 3 ft. by 5 ft. Intricate Bond Panels

Inspection of the two 3 ft. by 5 ft. panels showed several manufacturing anomalies that required additional development of the stringer cure mandrels and soft IML tooling. Figure 5 shows excess resin in frame flange radii that bled from the stringer and skin. Since the cauls had net molded stiff corners, any significant frame mislocation created a gap for resin flow during the cure.

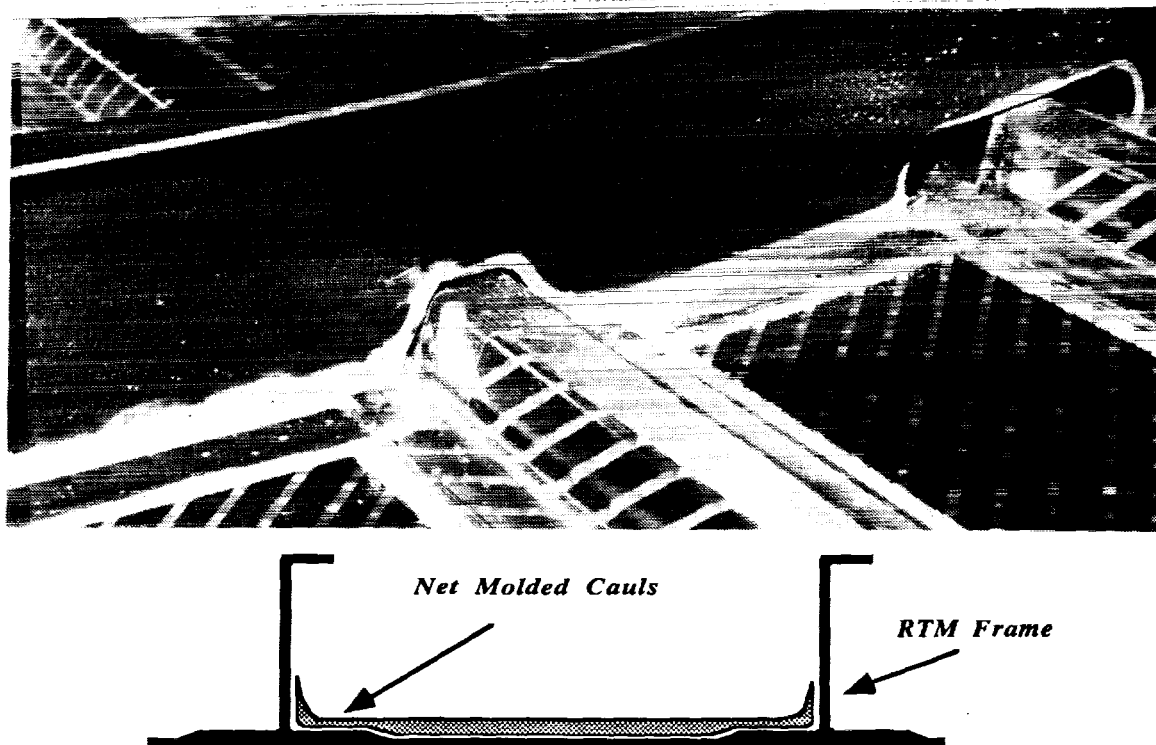


Figure 5: IML Tooling Results (3 ft. by 5 ft. Intricate Bond Panel)

The cauls were redesigned without the molded corners for more flexibility to prevent the resin from bleeding into the frame flange radius (Figure 6). This new concept was assessed by fabricating a 3 ft. by 5 ft. panel. The caul redesign required the addition of mouse hole plugs to transfer autoclave pressure to the stringers and minimize potential bag bridging at the frame-stringer intersections.

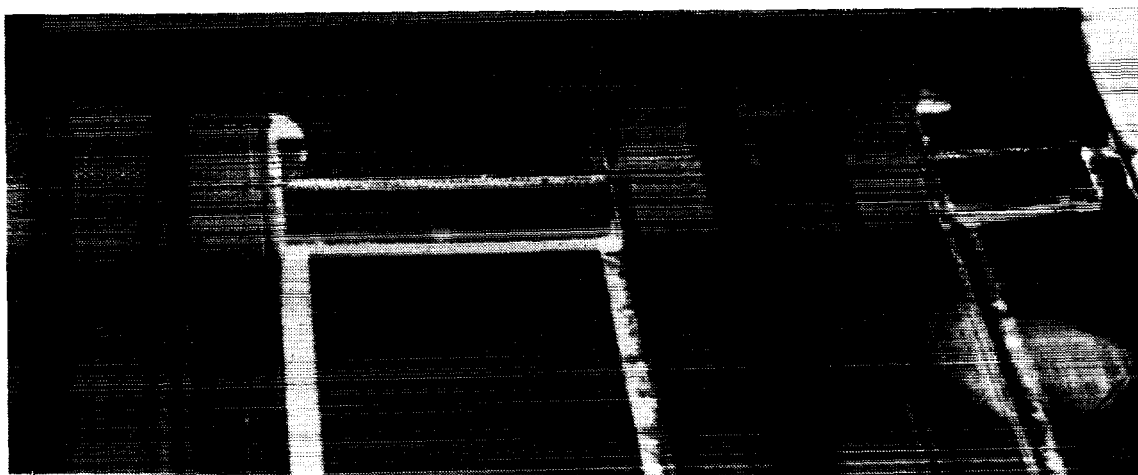


Figure 6: Modified Caul Results (3 ft. by 5 ft. Intricate Bond Panel)

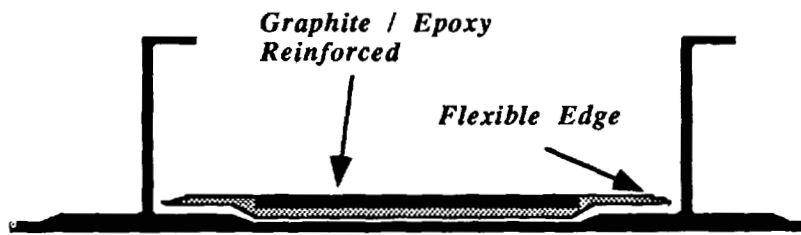


Figure 6 (cont.): Modified Caul Results (3 ft.by 5 ft. Intricate Bond Panel)

Stringer gage thickness and location were difficult to control with the original IML tools. Because the stringer laminates could not be fully compacted prior to cure, the excess bulk gage thickness caused an interference fit between the caul and the stringer charge. This interference fit caused the hat cavity of the caul to spread open which compromised stringer location tolerance (Figure 7). To minimize this problem the stringer drape forming process and caul design were modified.

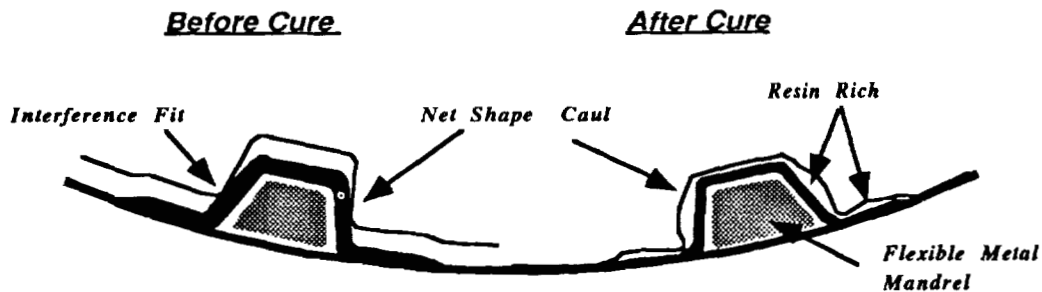
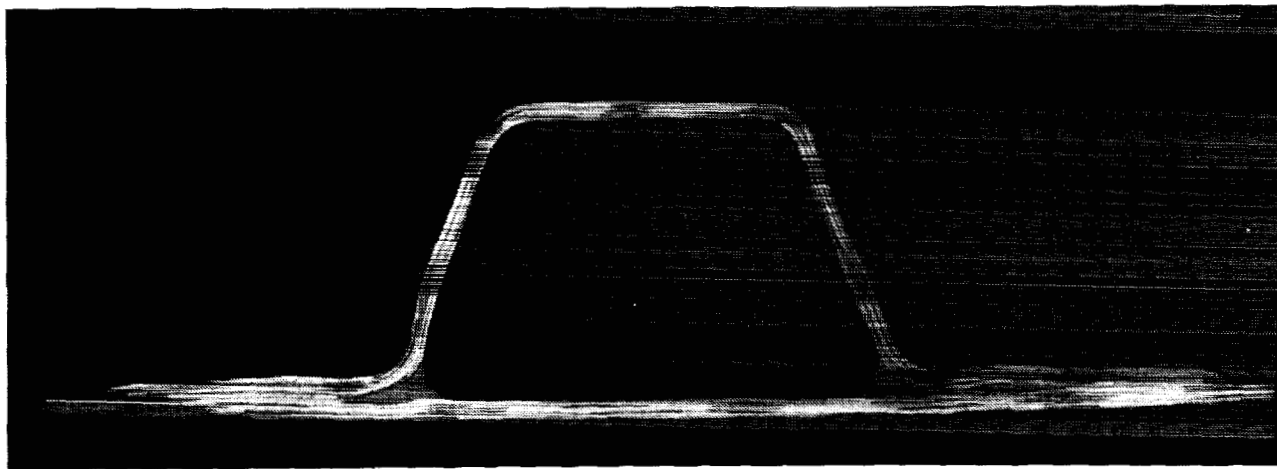


Figure 7: Unstiffened Caul Results (3 ft.by 5 ft. Intricate Bond Panel)

The cauls were redesigned with four plies of graphite prepreg between the stringers and up to ten plies to stiffen the stringer shape. To compensate for the stringer bulk thickness, net sized and over sized cauls were evaluated. A two stringer panel ten feet in length was fabricated to evaluate an over sized (+0.030 in.) and a net shaped caul. Results from both cauls show an improvement of stringer cross sectional shape and gage thickness control. The over sized cauls controlled the stringer gage thickness better than the net shape cauls (Figure 8).

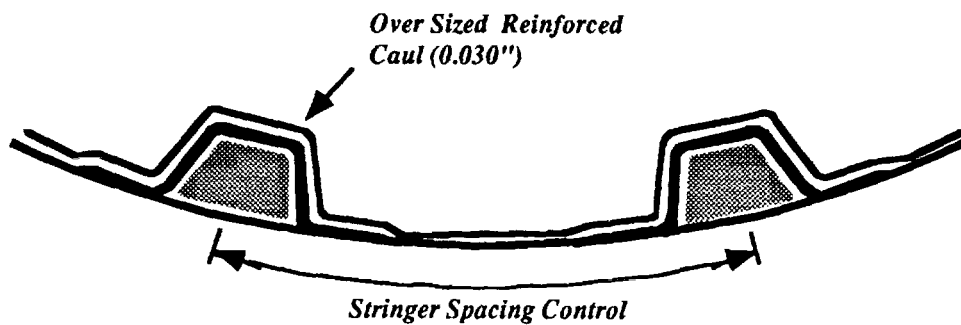
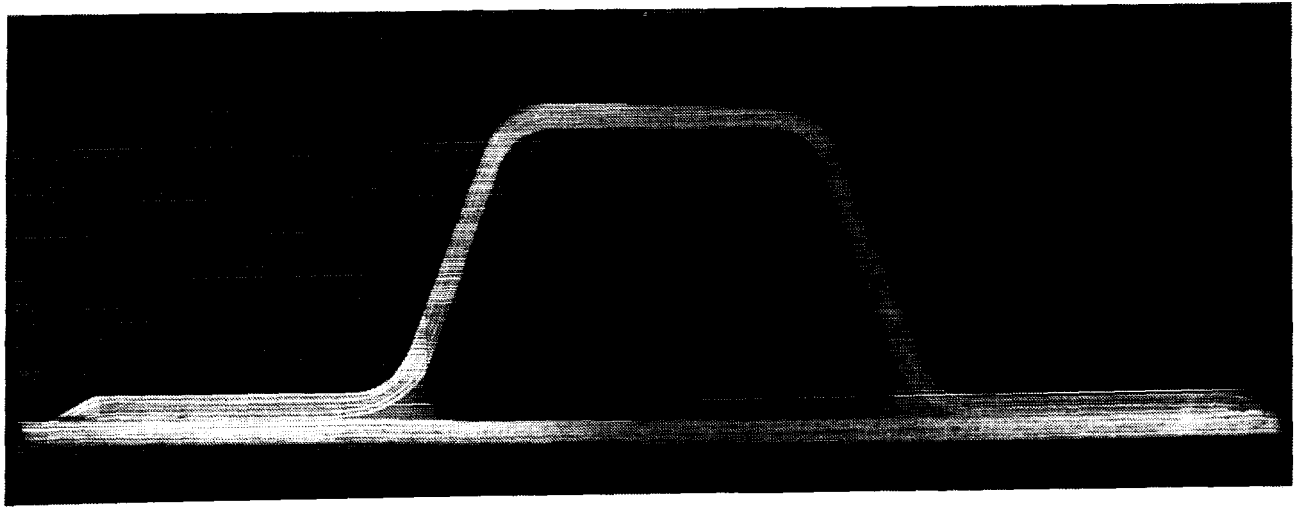


Figure 8: Results of Oversized Stiffened Caul Trials

The over sized caulk was designed to be used with a higher expansion stringer tool such as rubber. During cure the mandrel expands and applies pressure to the stringer laminate without deforming the stiffened cauls. The net shape caulk was designed to be used with low thermal expanding stringer cure tools. This tooling concept was used in the fabrication of the 3 ft. by 5 ft. panel. The cure mandrels were flexible, low CTE (coefficient of thermal expansion) metal mandrels designed for an after cure clearance of 0.015 in. between the mandrel and stringer. Extraction of the metal mandrels from the hat stringers proved difficult due to an interference fit between the stringer and mandrel. Further evaluations with FEM models (Ref. 5) revealed that the large adhesive noodle in the bottom corners of the hat stiffeners caused this interference fit (Figure 9). This was a result of the difference in CTE between the stringer laminate and adhesive. To minimize this effect, a smaller radius noodle or a lower CTE radius filler material could be used. Another option is the rubber mandrel could be molded to net shape eliminating the need for a radius noodle. The oversized stiffened cauls and net shaped silicone molded mandrels were selected as the tooling option for the 7 ft. by 10 ft. panels.

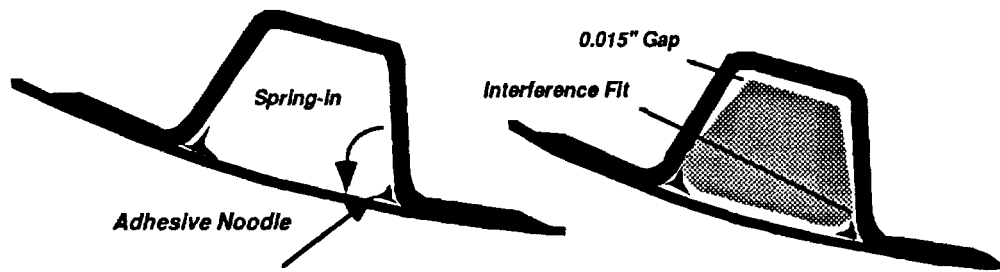


Figure 9: Mandrel Interference

Fuselage Frame Development

Under the fuselage frame development program, 8 ft. frames were fabricated for the intricate bond design. One of the critical requirements for cobonding the frame to the skin was the tolerance control of the 122 in. frame radius. The development of 3 ft. frames with aluminum tooling provided insight for scale-up for 8 ft. frames. The processing conditions and tooling for resin transfer molding of two 3 ft. frames at a time were developed so that the same processing conditions and tooling would be applicable for the 8 ft. frames (Ref.6). The tool was designed for resin impregnation to be independent of the frame length.

The 8 ft. frame preforms were fabricated on a 144 carrier braider. A swing arm was constructed to drive the braiding mandrel through the center of the braider at a controlled speed to maintain fiber orientation (Figure 10). The preform consisted of six plies of triaxial braided AS4 fiber. The bias ± 66 degree fibers were 6k tow and the axial fibers were 18k tows. Preform distortion from handling was minimized by integrating the mandrel as part of the RTM mold. The mandrel and attached preform were inserted into the RTM mold cavity. Prior to closing the mold a simple cut and fold operation of the three outer plies was done to form the bottom flanges of the two "J" frames. The braided preform was impregnated with Shell RSL 1895 resin and cured in a convection oven and strip heaters were also attached to the outside of the tool for preferential heating.

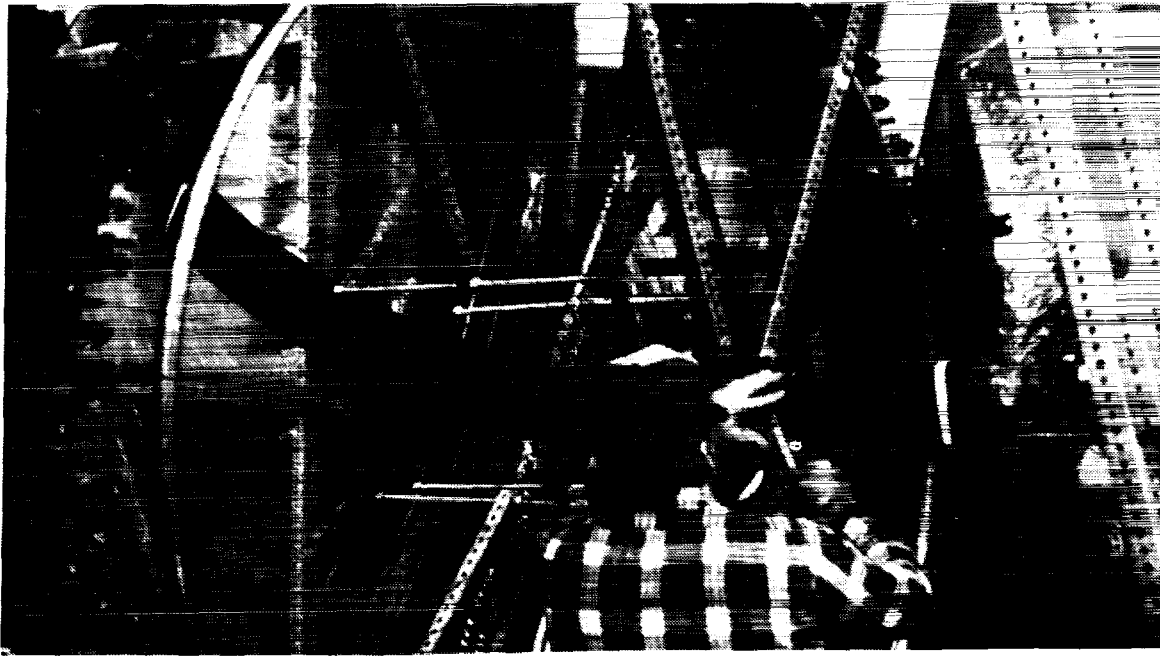


Figure 10: Braiding Frame Preform

Dimensional inspection of the 3 ft. frames revealed a 1° spring-in of the bottom frame flange. The amount of web twist shown in Figure 11 required less than 2 lbs. of force to remove. The gage thickness variations on all flange and web areas were held to ± 0.010 in. The part was designed for a 121.89 in. radius but the measured radius was 122.16 in.

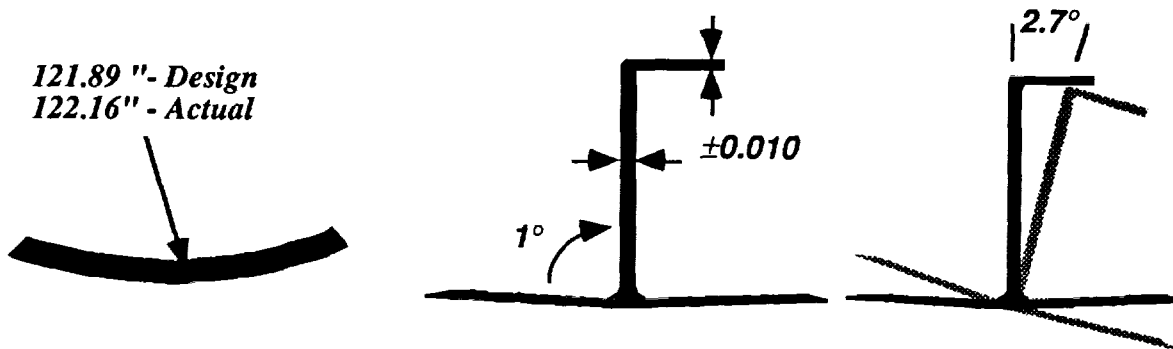


Figure 11: Tolerance Control of the 3 ft. Frames

A finite element model of the aluminum RTM tool during cure was evaluated which indicated a 122.34 in. radius at 350° f. The use of aluminum material for a larger frame would cause high residual stresses during tool cool down due to this change in radius. Therefore, tooling material for the 8 ft. cure tool was changed to Invar 36 so that the CTE mismatch between the frame and RTM tool would be minimized. Since Invar 36 has a lower heat up rate than steel or composite, strip heaters and a convection oven were used.

Thirty five 8 ft. frames were processed with the Invar RTM mold (Figure 12). Inspection was performed on the frames with and without mouse holes cut outs. The frames without mouse holes met the desired frame radius of 121.90 in. ± 0.010 in. but sprung open to 123.00 in. after the

mouse holes were cut into it. Less than 20 lbs was required to fit the frame to the 121.89 in. radius during panel assembly. The Invar RTM mold was machined to compensate for the 1° spring-in. Frame spring-in measurements indicated that no spring-in occurred; therefore, the frames were molded with a 1° spring-out. The web twist was .1° compared to 2.7° twist measured with the frames made with the aluminum tool.

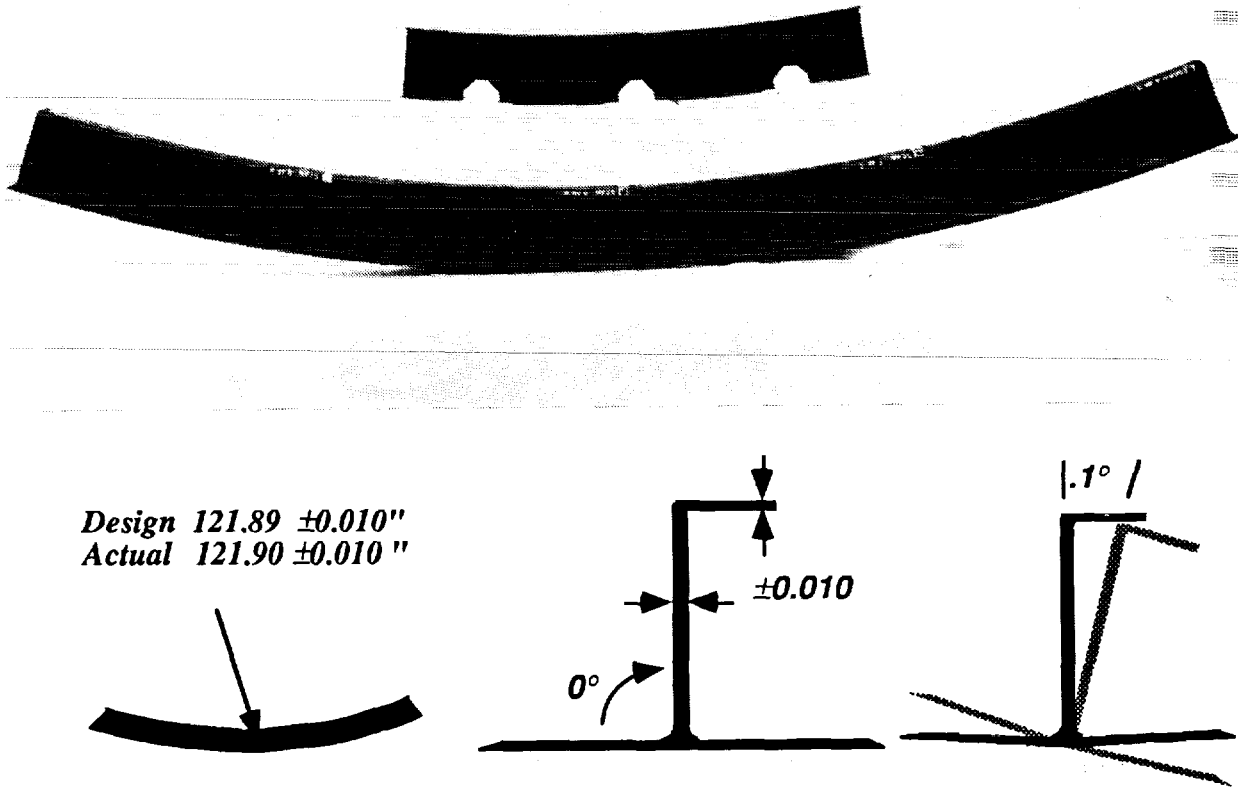


Figure 12: 8 ft. RTM Frame Inspection

Surface porosity was found in the same region of each frame during initial RTM processing. Processing variations and enlarged resin ports eliminated this problem. Inspection of the frames with TTU techniques (@ 6 db) showed long narrow defects running parallel to the axial fibers. Photomicrographs were compared to TTU results from various sections of the frame. In areas where white axial streaks occurred, the axial fibers from each ply were aligned to form resin rich areas and high fiber volume areas (Figure 13a,b). This significant variation in density produced a signature similar to a defect. Photomicrographs of areas with no transmission loss revealed that the axial tows of the six plies were offset resulting in a more nested configuration. The photomicrographs also showed no signs of porosity or internal micro-cracks.

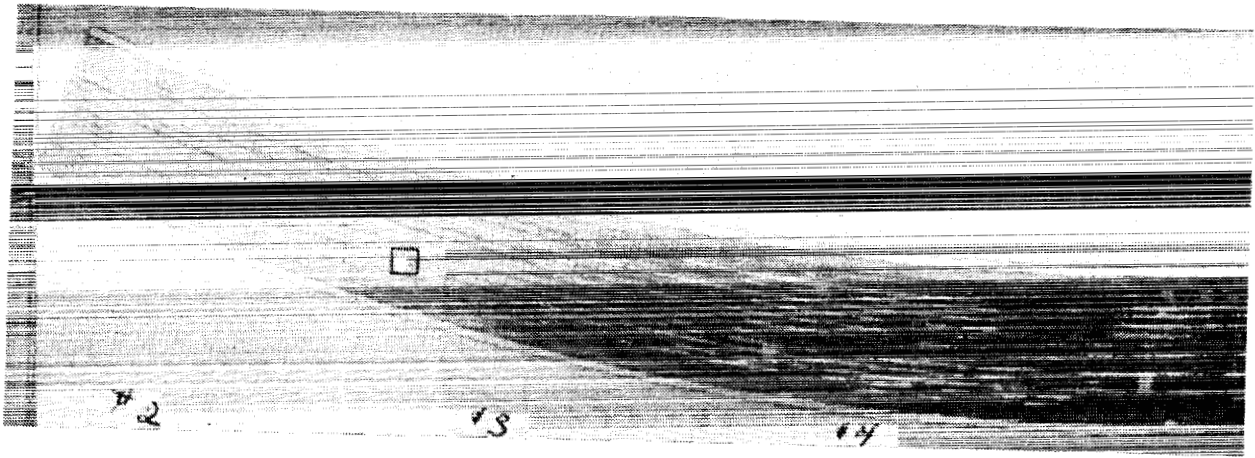


Figure 13a TTU of RTM Frames (6 db loss)



Figure 13b Stacked Axial Yarns

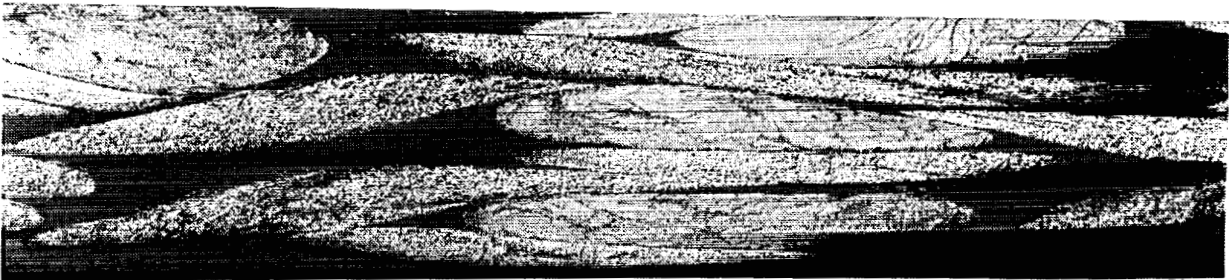


Figure 13c Nested Axial Yarns TTU of RTM Frames

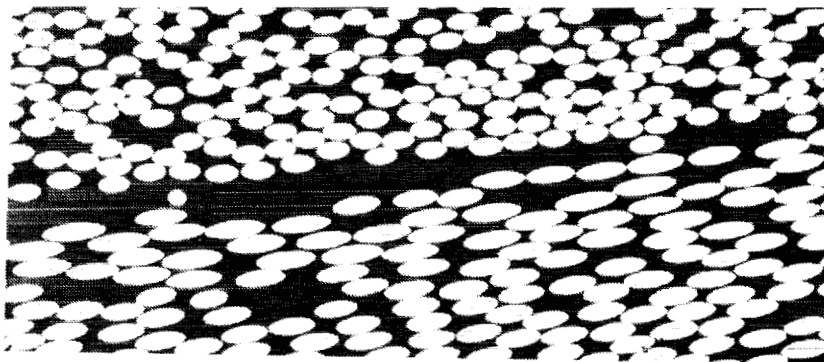


Figure 13d Architecture Resin Wet Out

Intricate Bond Panel Fabrication

IN an effort to demonstrate manufacturing feasibility for large quadrant panels, RTM frames and IML tooling was again used with the ATP process to fabricate a 7 ft. by 10 ft. intricate bond panel. The 7 ft. by 10 ft. skin and stringer charges were fiber placed at Hercules with the four inch wide band head. After the stringer charges were individually trimmed, they were formed into the hat stringer shape with a one step drape forming process. A silicone cure mandrel and an aluminum female tool were used to form the hat section. Prior to placement of the stringers on the skin, adhesive was placed on skin stringer interface areas (Figure 14). The IML cauls aided in locating stringers on the skin (Figure 15).

Prior to locating the RTM frames, adhesive film was applied to the bottom frame flanges. The frames were then positioned with the aid of frame finger clamps positioned along the length of the Invar cure tool (Figure 16). The frame fingers maintained frame spacing during the cure but allowed the frames to move normal to the skin. Once the frames were positioned, the precured two ply pressure bridge was located in each frame mouse hole (Figure 17). The cauls were then placed between frame bays (Figure 18). The cauls were designed so that they would overlap each other in the mouse holes areas to control resin flow. Once the silicone plugs were placed in each mouse hole, the textured silicone bag was placed over the assembly (Figure 19, 20). This bagging approach minimized the amount of non-reusable bagging material and associated labor. Neither breather or separator film was used between the cauls and the IML surface.

After cure the silicone bag and stringer mandrels were removed. The panel was inspected and all frame and stringer bond lines were defect free (Figure 21). One small void was detected in the stinger-skin bond area but was determined to meet production requirements. Examination of the stringer cross section showed good control of the resin flow for stringer shape and spacing. Laminate wrinkling in the stringers did occur near each two-ply mouse hole pressure bridge. Resin flow control was also maintained at all stringer frame intersections. The designed frame spacing was 22.00 in. +0.000, -0.050 in. compared to the desired frame spacing of 22.00 in. \pm .030.

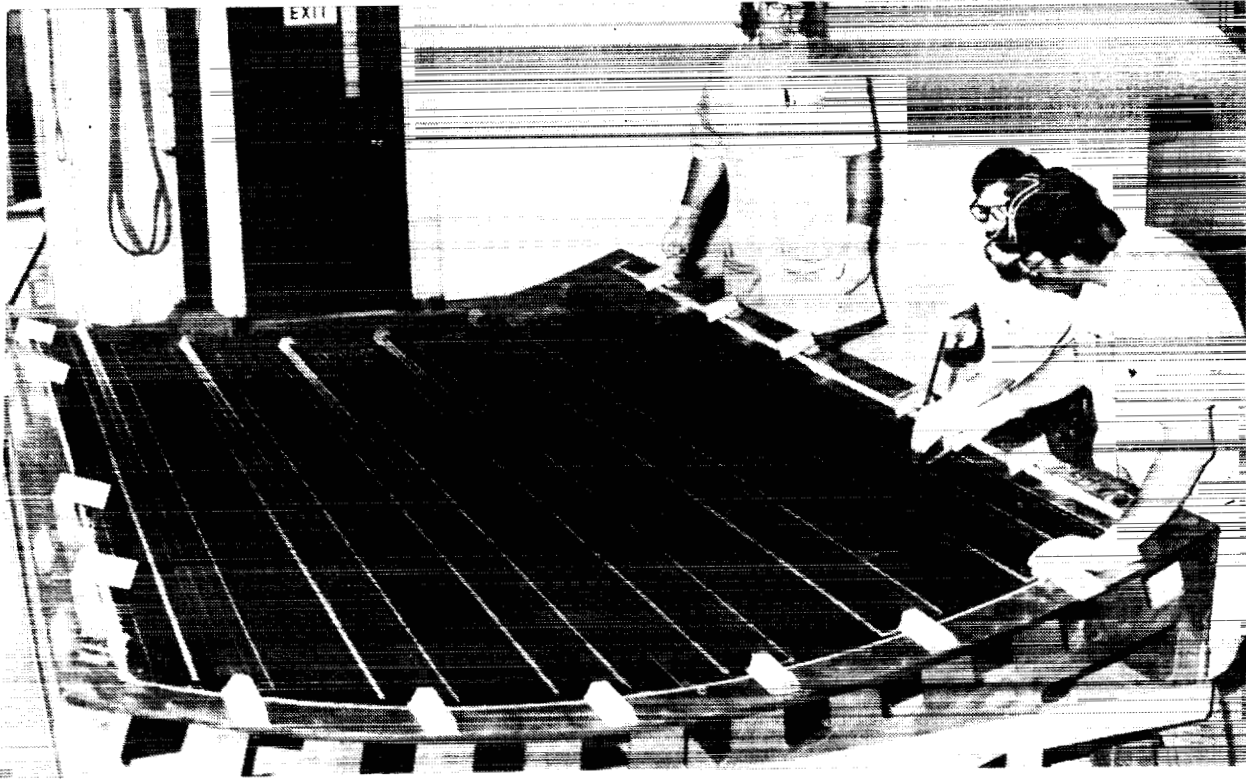


Figure 14: Stringer Placement



Figure 15: Locating Stringers with IML Cauls

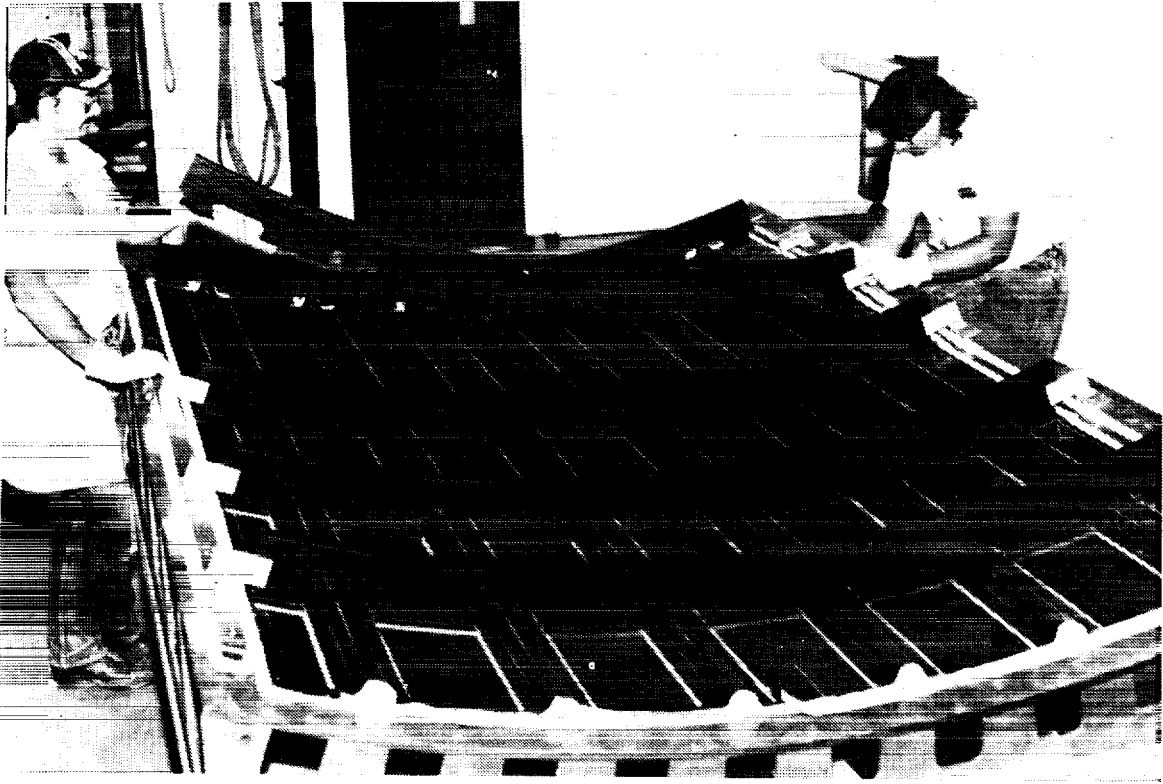


Figure 16: Loading Frames into Assembly Fingers



Figure 17: Installation of Mouse Hole Pressure Bridges

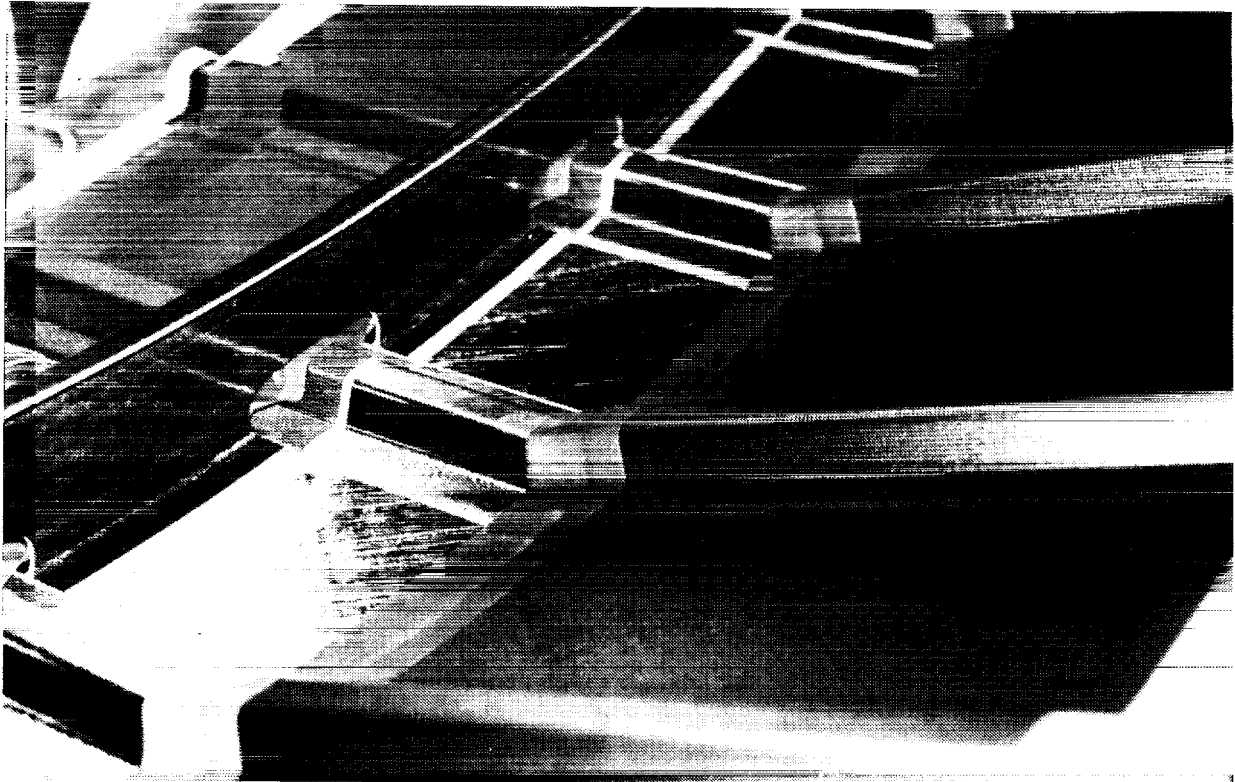


Figure 18: Installation of Cauls

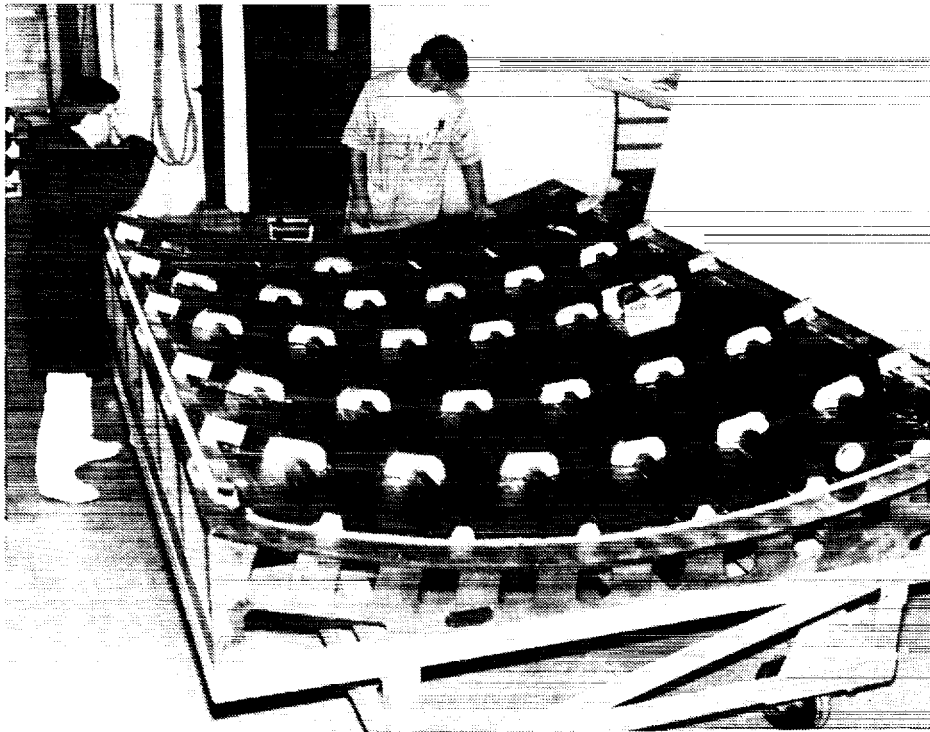


Figure 19: Installation of Pressure Intensifiers

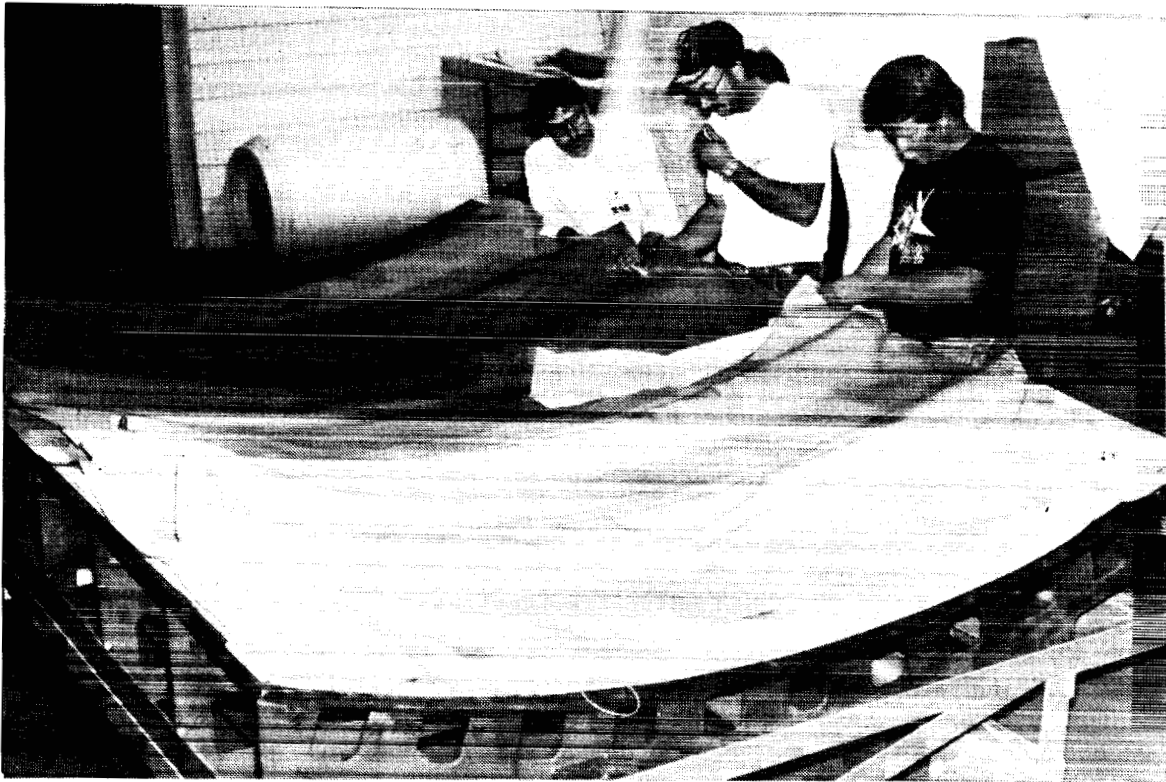


Figure 20: Reusable Cure Bag

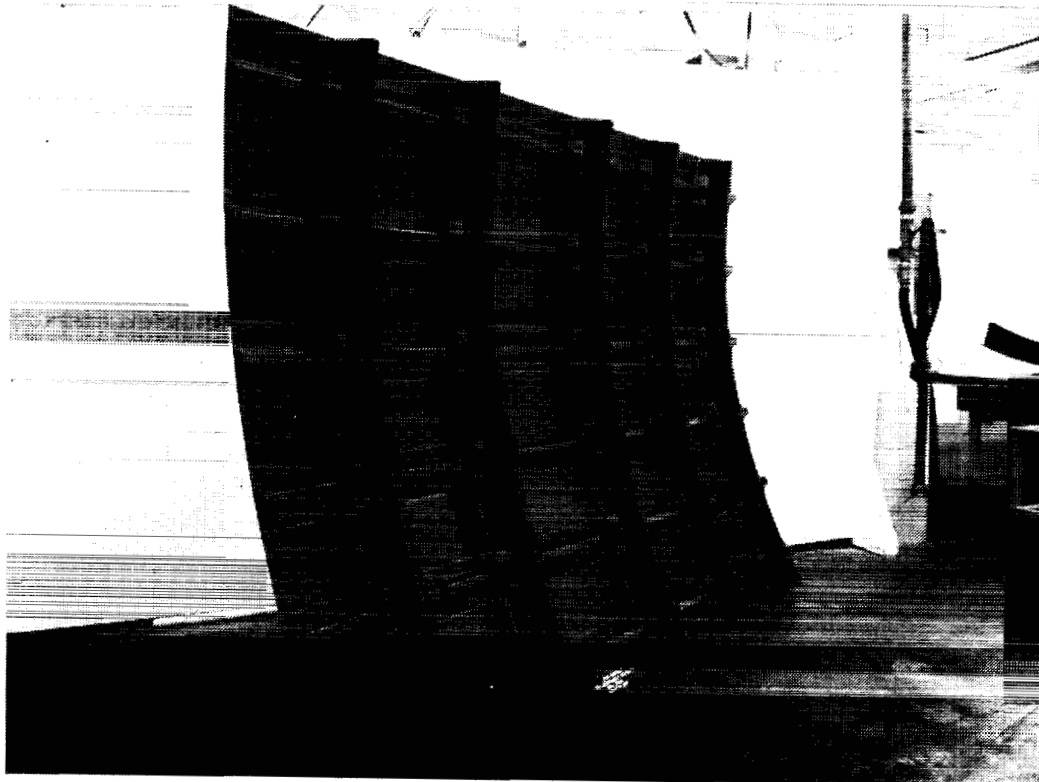


Figure 21: 7 ft. by 10 ft. Intricate Bond Panel

Conclusion

The fabrication of the 7 ft. by 10 ft. composite crown panel showed the potential for large quadrant panel fabrication. The use of fiber placed skins and stringers and the resin transfer molding of long frames were also demonstrated and optimized to further reduce risk and cost. One of the major technology risks evaluated was the ability to cure the skin and stringers and co-bond the frames to the skin at the same time without sacrificing quality. This was accomplished with dimensionally accurate RTM frames and unique IML tooling that reduced panel warpage. Initial measurements indicate that the tooling concepts did control frame and stringer spacing for subsequent quadrant panel assembly.

This development program is still in progress and additional evaluations for structural performance, warpage, and dimensional stability will be conducted. Additional intricate bond panels will be fabricated to evaluate cost and manufacturing anomalies. Cost and learning curve data for the fabrication of the frame, skin and stringer will be evaluated with the use of a cost model to determine optimal cost for production rates. Optimization of the RTM frames will continue with the evaluation of additional braided architectures to increase the structural performance.

REFERENCES

1. L.B. Ilcewicz, T.H. Walker, G. Truselove, K. Willden, G.D. Swanson, and C. Pfahl, "Application of a Design-Build-Team Approach to Low Cost and Weight Composite Fuselage Structure," NASA CR-4418, NAS1-18889, May 15, 1989.
2. T.H. Walker, P. Smith, G. Truselove, K. Willden, S. Metschan, C. Pfahl, " Cost Studies for Commercial Fuselage Crown Designs", First NASA Advanced Composite Technology Conference, Seattle, WA, October 29-November 1, 1990, NASA-CP-3104
3. L.B. Ilcewicz, P. Smith, T.H. Walker, R. Johnson, " Advanced Technology Composite Aircraft Structures", First NASA Advanced Composite Technology Conference, Seattle, WA, October 29-November 1, 1990, NASA-CP-3104
4. K.S. Willden, S. Metschan, V. Starkey, " Process and Assembly Plans for Low Cost Commercial Fuselage Structure", First NASA Advanced Composite Technology Conference, Seattle, WA, October 29-November 1, 1990, NASA-CP-3104
5. R. Lundquist, B. Flynn, G. Swanson, and G. Mabson, "Dimensional Stability of Curved Panels with Cured Stiffeners and Cobonded Frames", presented at the Third NASA Advanced Composite Conference, Long Beach, Ca, June 8-11, 1992. NASA CP-3178
6. M.J. Fedro, K.S. Willden, " Characterization and Manufacture of Braided Composites for Large Commercial Aircraft Structures", presented at the Ninth DoD/NASA/FAA Conference on Fibrous Composites in Structural Design, Lake Tahoe, Nevada, November 4-7, 1991

**DIMENSIONAL STABILITY OF CURVED PANELS WITH
COCURED STIFFENERS AND COBONDED FRAMES¹****G. E. Mabson, B. W. Flynn , G. D. Swanson****Boeing Commercial Aircraft Group**

S13-24

51413

R. C. Lundquist**Boeing Computer Services****P. L. Rupp****University of Washington****ABSTRACT**

Closed form and finite element analyses are presented for axial direction and transverse direction dimensional stability of skin/stringer panels. Several sensitivity studies are presented to illustrate the influence of various design parameters on the dimensional stability of these panels. Panel geometry, material properties (stiffness and coefficient of thermal expansion), restraint conditions and local details, such as resin fillets, all combine to influence dimensional stability, residual and assembly forces.

INTRODUCTION

Composite material structure can show considerable curing-induced dimensional changes. These dimensional changes are primarily the result of coefficient of thermal expansion and stiffness mismatch in the part and/or tool. Resin chemical shrinkage (i.e. resin decrease in volume during cure after it gains some stiffness properties) may also contribute to the problem (Ref. 1). Dimensional changes often cause assembly problems, such as excessive shimming and/or induced residual forces. This paper describes the effort directed toward the prediction of cure-induced dimensional changes associated with composite skin/stringer panels. The intention is to include dimensional change predictions during the design phase of the panel development effort in order to minimize any adverse effects on performance and manufacturing cost.

Material properties of the composite material can vary with temperature and viscoelastic response may also complicate analysis procedures. Flat unstiffened panels fabricated with unsymmetric laminates subjected to temperature changes have been shown to require geometric nonlinear analyses to accurately describe the panel's response (Ref. 2).

¹ This work was funded by Contract NAS1-18889, under the direction of J. G. Davis and W. T. Freeman of NASA Langley Research Center

In order to include skin/stringer panel dimensional stability constraints in the optimization program (COSTADE, Ref. 3) being developed in the Boeing ATCAS program, closed form solutions are being developed. The short computational times usually associated with this type of solution should allow the optimizer to operate effectively.

Figure 1 is a photograph of a representative composite skin/stringer panel. The out-of-plane displacements of this panel (Figure 2) show cure induced curvatures along the length of the stiffeners (axial direction) and also transverse to the stiffeners (transverse direction).

The closed form solutions for dimensional stability fall into two categories: axial predictions and transverse predictions.

NOMENCLATURE

a, b, c	constants	P	axial load
A'	classical laminated plate theory A-prime matrix	R	radial direction, radius
B'	classical laminated plate theory B-prime matrix	s	symmetric
D'	classical laminated plate theory D-prime matrix	t	total
E	Young's modulus	T	temperature, tangential
F	thermal force resultants, force	u, v	displacements
g	global	w	width, displacement
G	thermal moment resultants, shear modulus	x, y, z	coordinates
i	element number, inner	$1, 2, 3$	material principal directions
I	moment of inertia	α	coefficient of thermal expansion
L	length	ϵ	normal strain
M	moment	γ	shear strain
N	number of elements in cross-section	κ	curvature
		ν	Poisson's ratio
		θ	angle

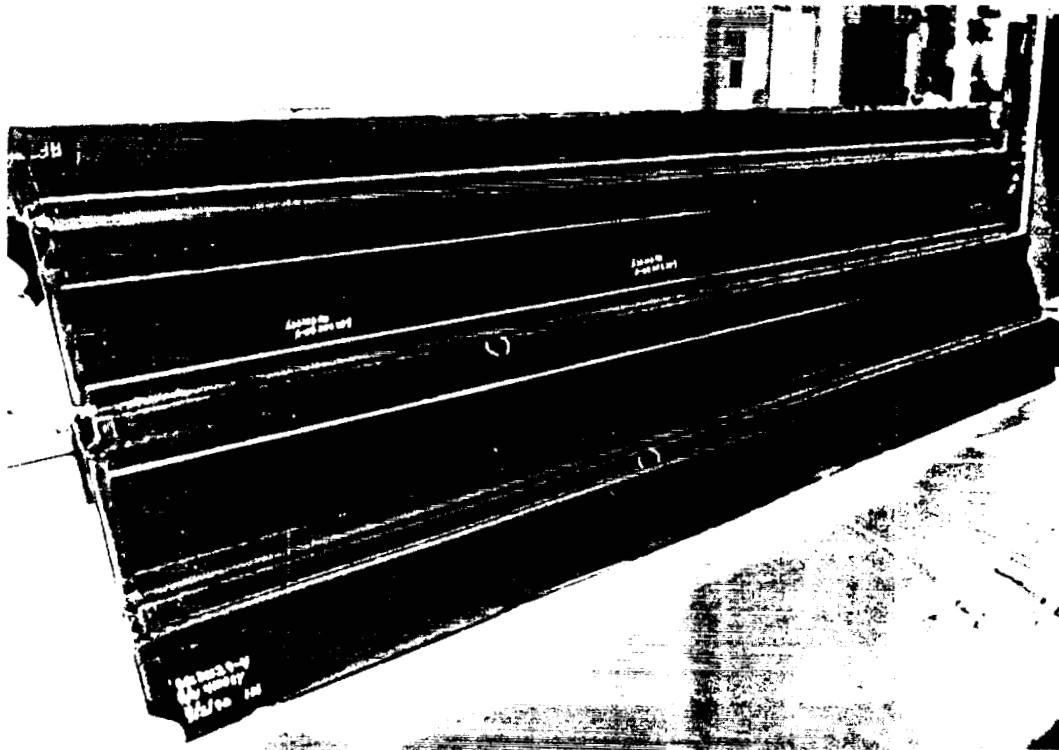
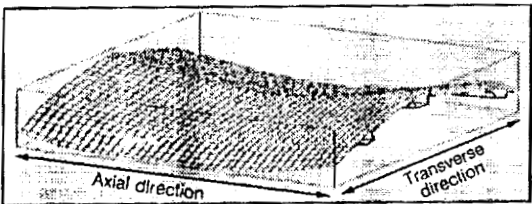
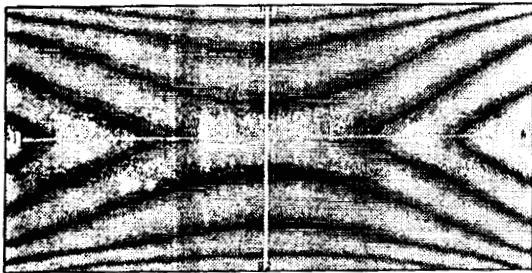


Figure 1 Representative Composite Skin/Stringer Panel

Experiment Results Obtained Using Shadow-Moire Technique



1 Fringe = 0.045 in

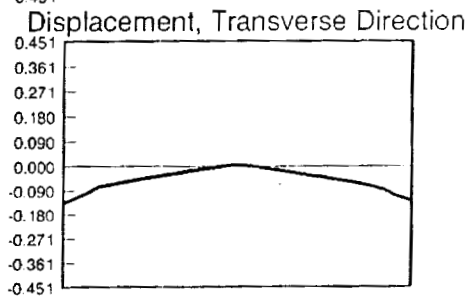
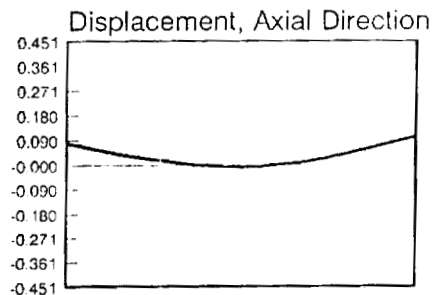


Figure 2 Typical Out-of-Plane Displacements of Representative Skin/Stringer Panels

AXIAL DIRECTION DIMENSIONAL STABILITY

Axial direction dimensional changes can result from stiffener/skin combinations that have axial coefficients of thermal expansion that vary over their cross-section (e.g. different layup in the skin and stiffener). This appears to be the primary cause of axial out-of-plane dimensional changes in skin/stringer panels stiffened in one direction only.

Axial direction dimensional changes can produce waviness in aircraft fuselage structures and therefore can affect aerodynamic properties. Reduced aerodynamic drag may be achieved by designing initial waviness into fuselage panels so that loading during nominal flight conditions counteracts the initial waviness and results in a smooth panel.

Excessive axial dimensional changes may contribute to tool extraction difficulties and the generation of residual forces.

A complex composite beam bending analysis including thermal loading was generated. This analysis was incorporated into a beam bending computer program by adding the coefficient of thermal expansion calculations and thermal loading capabilities. A beam cross-section made from composite material laminates is modelled as an assembly of elements as follows:

1. Each element in the cross-section is straight but may be oriented at an arbitrary angle.
2. Each element in the cross-section obeys classical laminated plate theory. Unbalanced and/or unsymmetric laminates are permissible.
3. Compatibility of axial strain is enforced for all elements in the cross-section. The axial strain is assumed to be bilinear (i.e. $\epsilon_x = a + b y + c z$).

This analysis procedure is essentially the same as classical beam theory, modified for composite materials. Appendix A presents the development of this analysis.

Measurements of out-of-plane displacements were performed on sixteen different nominally flat skin/stringer panel configurations at each of three temperatures. These panels incorporated different thicknesses, layups, stringer types, materials and stringer spacings. Closed form and finite element analyses were performed to predict the axial direction results. Figures 3 and 4 present these comparisons for six of the forty-eight different conditions tested.

The finite element analysis used plate elements, small displacements and constant material properties to model the complete panels. Figure 5 presents the skin/stringer panel finite element geometry used. As the closed form solution is based on beam theory, coupling between the transverse and axial directions is not modelled. The finite element plate style model does include this coupling. The closed form and finite element predictions agree to within approximately ten percent.

The test data and predictions compared well for some panel configurations (Figure 3) but not as well for others (Figure 4). Including the effects of variable material properties with temperature, large displacements, chemical shrinkage and "spring in" of curved laminates in the web/skin area may improve the finite element predictions.

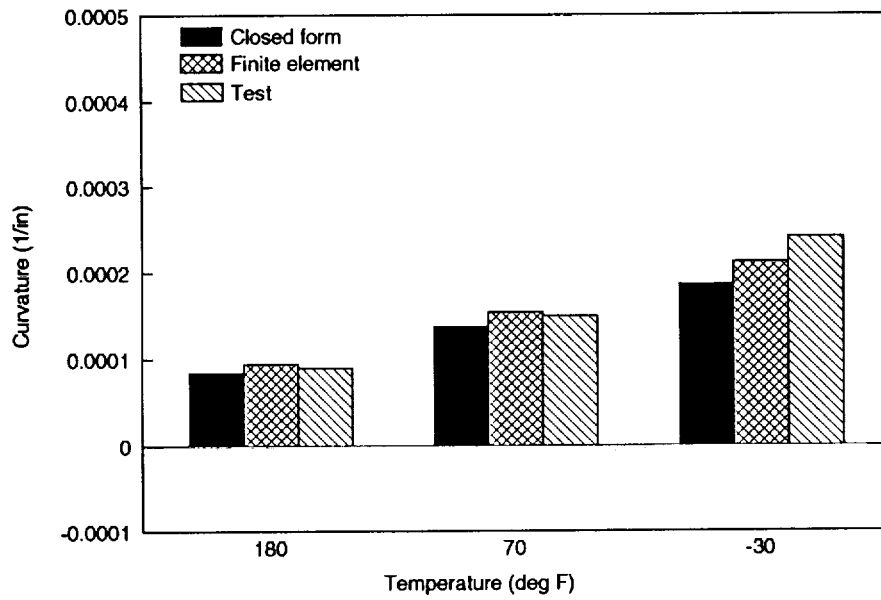


Figure 3 Comparison of Axial Direction Curvature Predictions and Test Data (29-8A)

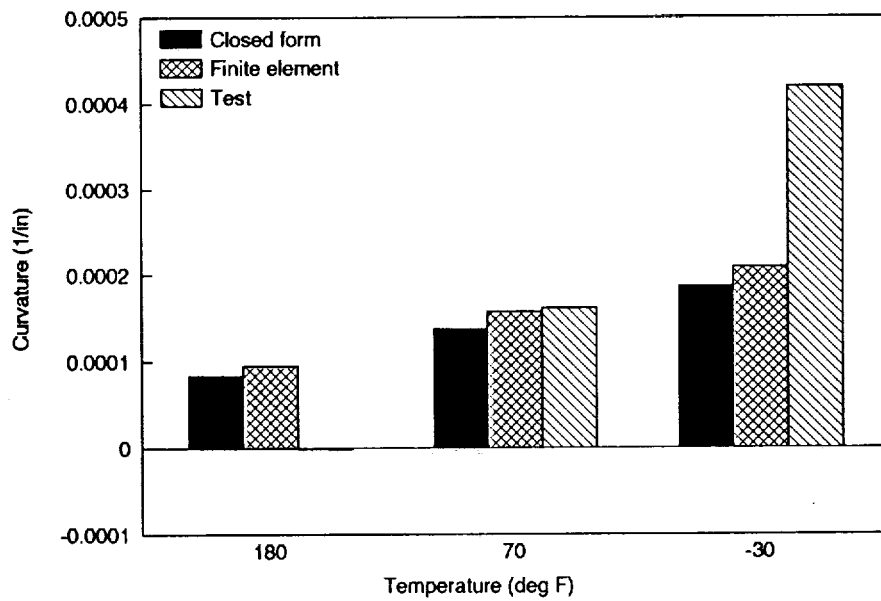


Figure 4 Comparison of Axial Direction Curvature Predictions and Test Data (29-8B)

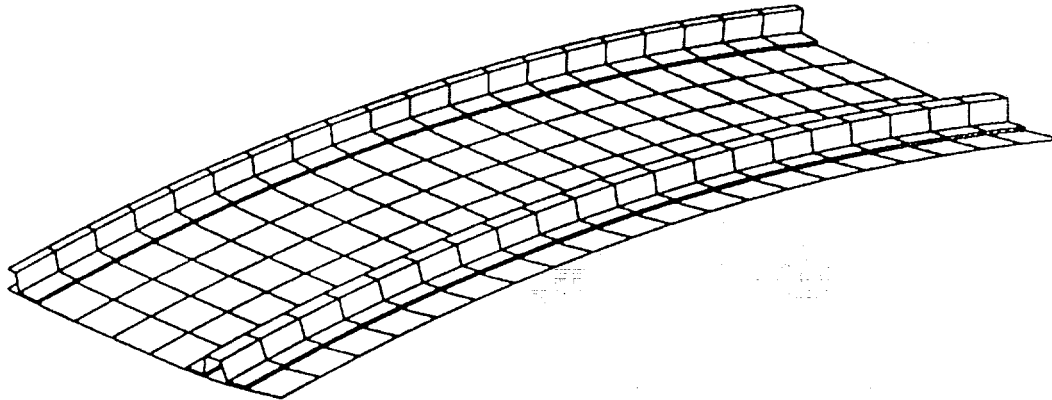


Figure 5 Finite Element Model of Complete Skin/Stringer Panel

Axial Beam Dimensional Stability Sensitivity Studies

Beam Laminate Design Effects

To illustrate the effect of designing beams with elements having different stiffnesses and coefficients of thermal expansion, a sensitivity study on a simple T-section was performed.

The simple T-section, shown in Figure 6, was analyzed for unrestrained thermally induced curvature and for the applied moment required to exactly counteract the curvature (i.e. straightening moment). The laminate in element 2 is held constant as quasi-isotropic $(0/45/-45/90)_s$ AS4²/938³, while the laminate for element 1 is varied. The base laminate for element 1 is also quasi-isotropic; however, the effects of adding additional zero degree plies to its midplane are investigated. Figure 7 presents the unrestrained curvature resulting from a temperature shift. Note that there is an extreme value of curvature when seven additional zero degree plies are added to element 1.

Figure 8 presents the straightening moment for a temperature shift. Note that this straightening moment monotonically increases with additional zero degree plies in element 1. Figures 7 and 8 indicate that element stiffnesses, coefficients of thermal expansion and section geometry all combine to affect thermal curvatures, as well as the straightening moments required to counteract those curvatures.

² AS4 is a graphite fiber system produced by Hercules, Inc.

³ 938 is a resin system produced by ICI/Fiberite.

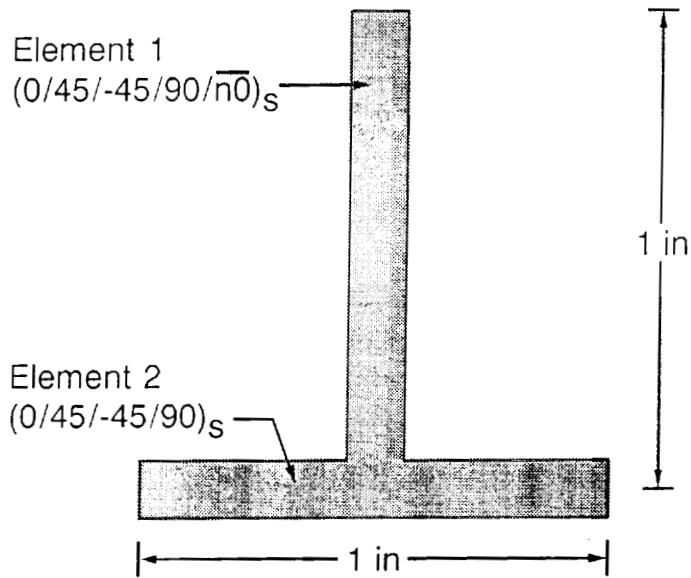


Figure 6 T-Section Beam Geometry

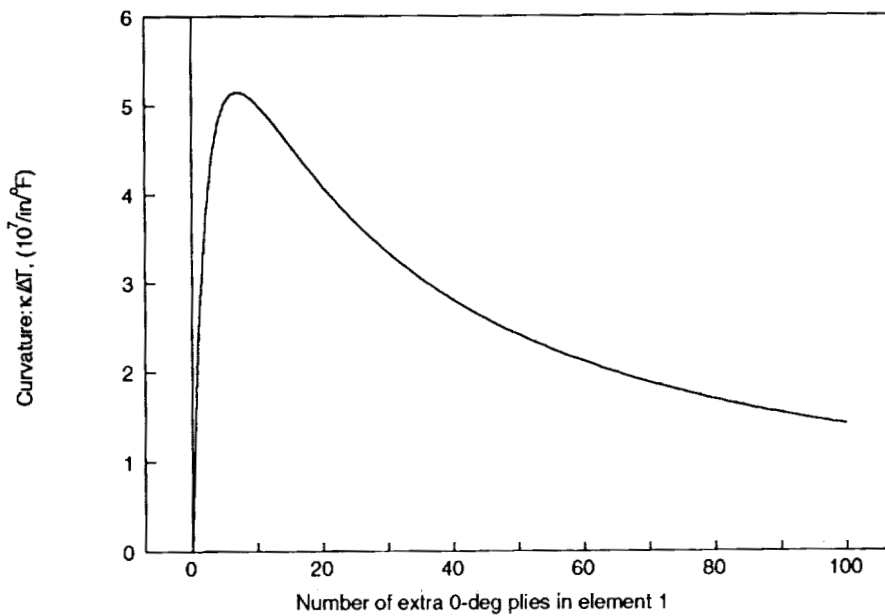


Figure 7 Curvature for T-Section Beam

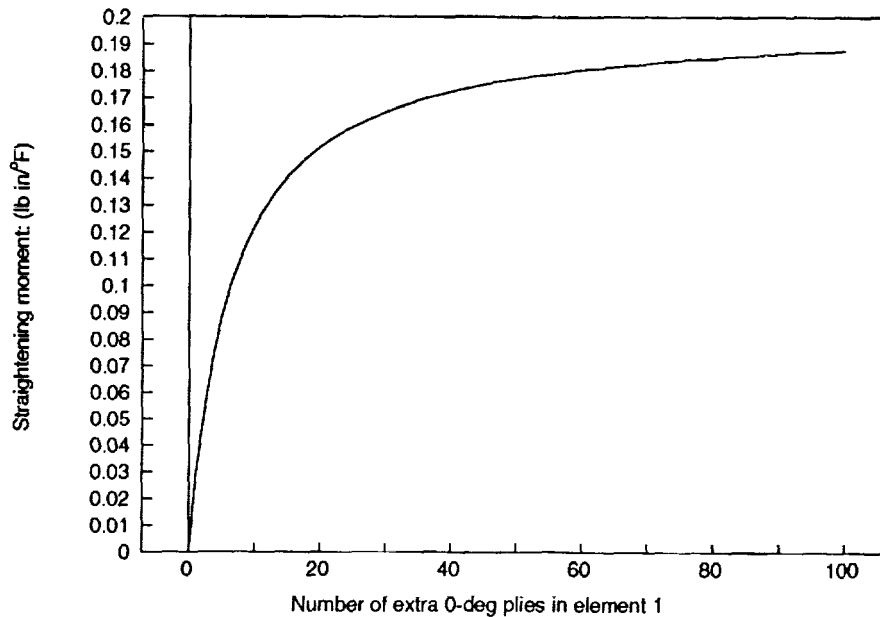


Figure 8 Straightening Moment for T-Section Beam

Beam Support Effects on Dimensional Stability and Assembly Forces

A continuous beam with multiple simple supports was analyzed as a representation of an assembled panel. The supports act as points of attachment as shown in Figure 9. Thermally induced curvature in the beam may result in residual and assembly forces being reacted at the supports. The beam takes the shape shown in Figure 10.

The residual forces are the reaction forces at the supports when the beam is in its final assembled form. If the beam is mechanically fastened to the supports, different support reactions are induced depending upon the order of support attachment. The assembly forces are the reactions induced during assembly. If the beam is attached to all supports simultaneously, in cobonded or cocured structure for example, the support reactions develop as the part cools. In these cases, assembly forces are reduced to be equal to the residual forces.

The maximum magnitude displacements and reaction forces are shown in Figures 11 and 12. Increasing the number of supports decreases the beam displacements at the expense of increasing residual and assembly forces.

Aerodynamic considerations may determine the acceptable out-of-plane displacements of axial panel stiffeners. Beam support strengths may require the residual and assembly forces to be minimized.

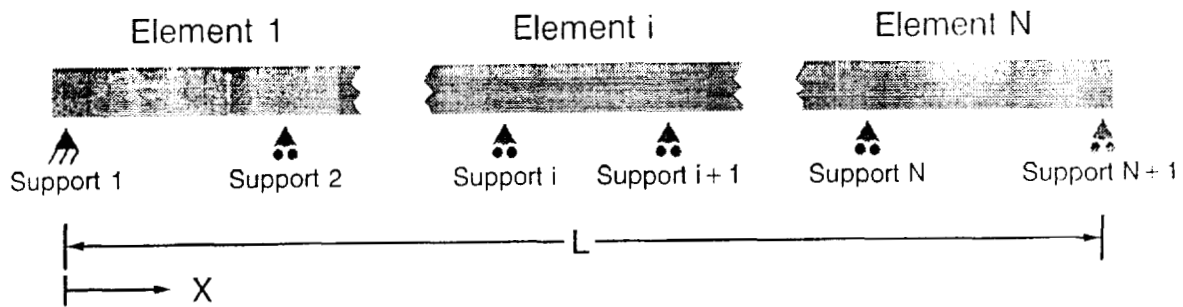


Figure 9 Continuous Beam with Multiple Simple Supports

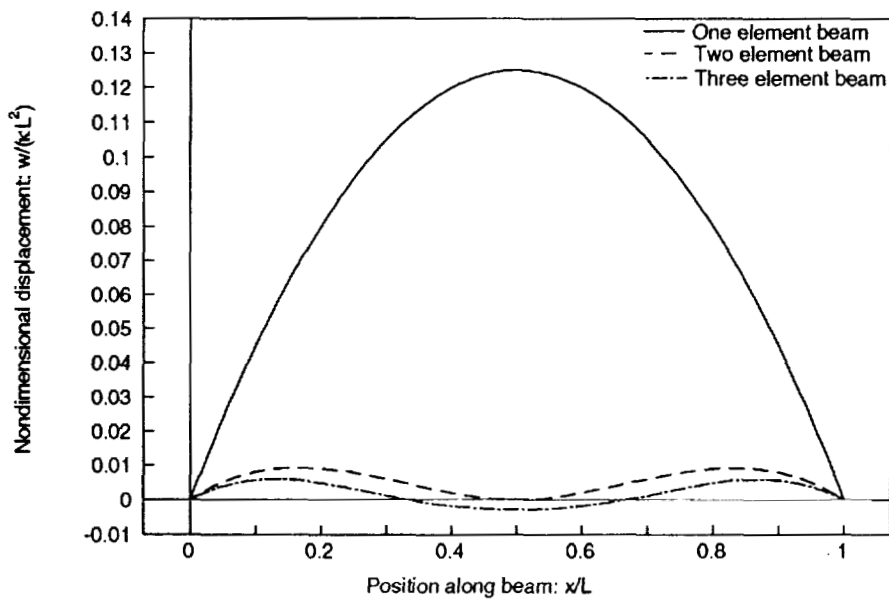


Figure 10 Displacement for Continuous Beams with Multiple Simple Supports

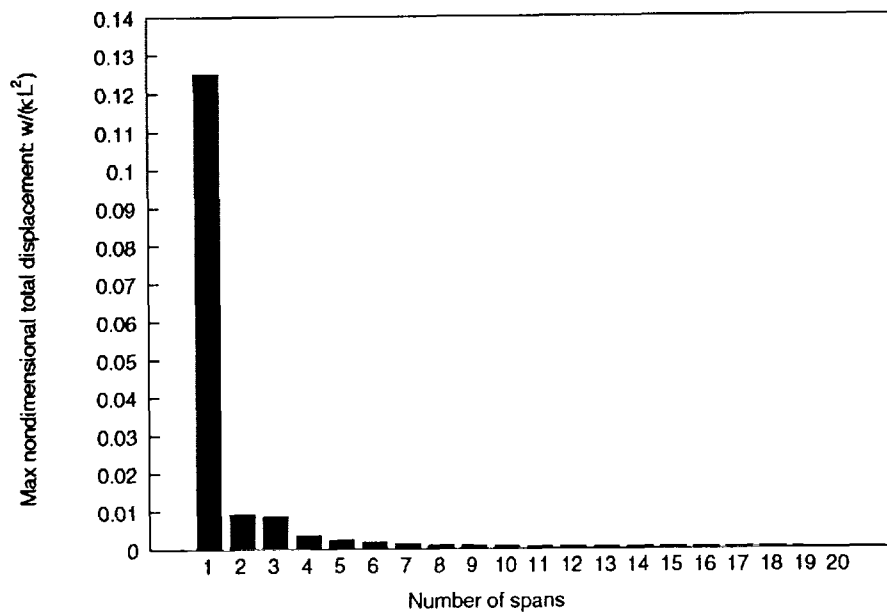


Figure 11 Maximum Out-of-Plane Displacements for Continuous Beams with Multiple Simple Supports

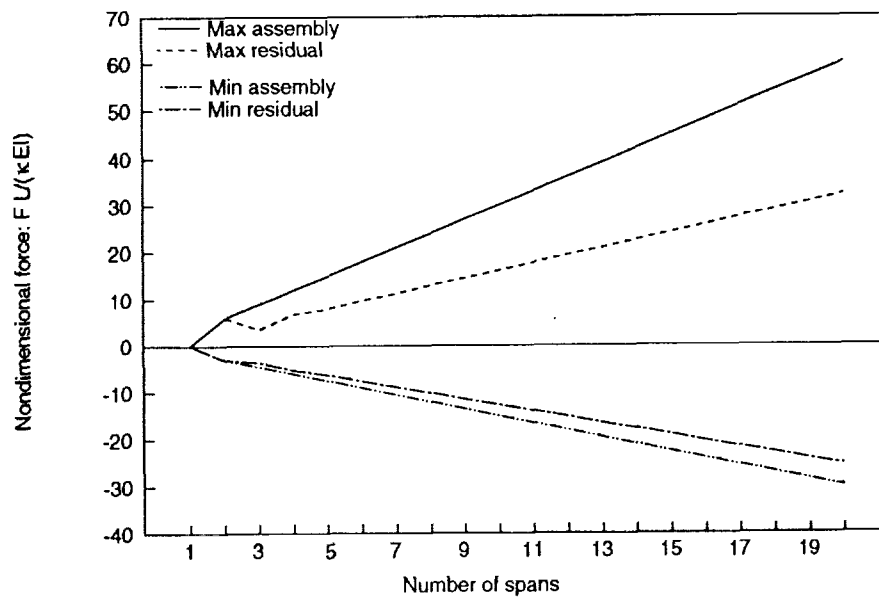


Figure 12 Assembly and Residual Forces for Continuous Beams with Multiple Simple Supports

TRANSVERSE DIRECTION DIMENSIONAL STABILITY

Transverse direction dimensional changes can result from a number of phenomena:

1. Unsymmetrical skins.
2. Unsymmetrical skin/stiffener flange combinations.
3. "Spring in" effect of curved elements at the stiffener/skin interface.
4. Resin pools or fillets.
5. Laminate thickness variations in resin rich or starved areas.

The resin pooling and laminate thickness variations (items 4 and 5 above) can be reduced significantly by modifying the cure tooling. Unsymmetrical skins and skin/stiffener flange combinations may require large displacement theories to accurately describe their response (Ref. 2).

Transverse Direction Dimensional Changes Due to "Spring In"

Symmetric curved composite laminates "spring in" when subjected to a temperature drop (i.e. cure temperature to operating temperature shift). This effect is evident whenever there is a significant difference between the coefficients of thermal expansion in the in-plane and through-the-thickness directions. This phenomenon has caused tool designers to include the effect in the design of tools for fabricating composite parts.

An exact plane strain solution for curved composite laminates subjected to a pure moment or temperature shift is presented in Ref. 4. This analysis solves the equilibrium equations separately in each ply of a laminate, and then assembles the ply solutions together using the appropriate boundary conditions at each ply interface. Stresses, strains and displacements are predicted throughout the laminate. This solution can be used to predict "spring in" angles for arbitrary laminates.

The curved laminate section that joins the stiffener web to the skin/flange combination of a stiffened panel can result in local "spring in" effects. In this situation, the skin and the roving material in the interface will provide some restraint to the curved laminate, as shown in Figure 13. To illustrate this restrained "spring in" phenomenon, an analysis is presented for the 8 ply quasi-isotropic (0/45/-45/90)_s family of laminates for both the skin and curved section. The stacking sequence in both the skin and curved section is varied and "spring in" effects are predicted. Several unsymmetrical laminates were also analyzed for unrestrained "spring in." In this analysis the filler material is ignored. The restraint provided by the skin is assumed to be a pure moment only. The slopes of the skin and curved laminate are forced to be equal where these two laminates join (Figure 13).

The predicted "spring in" angle changes due to a -280°F temperature shift in unrestrained curved laminates are shown in Figure 14. Note that all of the symmetrical laminates are predicted to have virtually the same "spring in." The simple equation (see Equation 1 below) for the homogeneous single ply case compares quite well with the exact plane strain solution for symmetrical laminates. Note that the laminate value of α_R , rather than the lamina value α_3 , is used.

$$\text{"Spring in" angle} = \theta \Delta T (\alpha_T - \alpha_R) \quad (1)$$

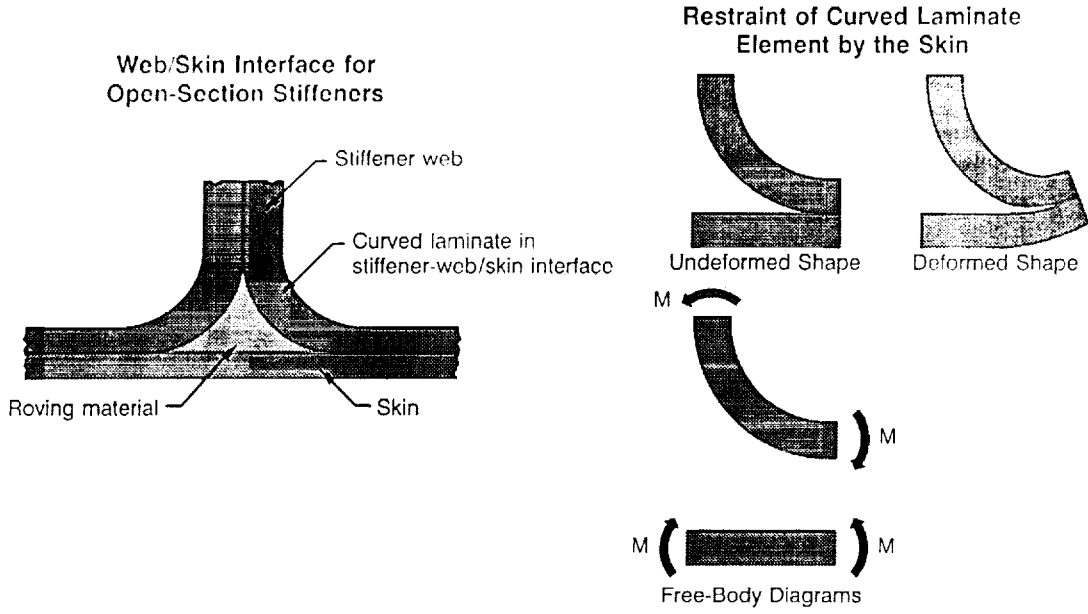


Figure 13 Stiffener Web/Skin Interface

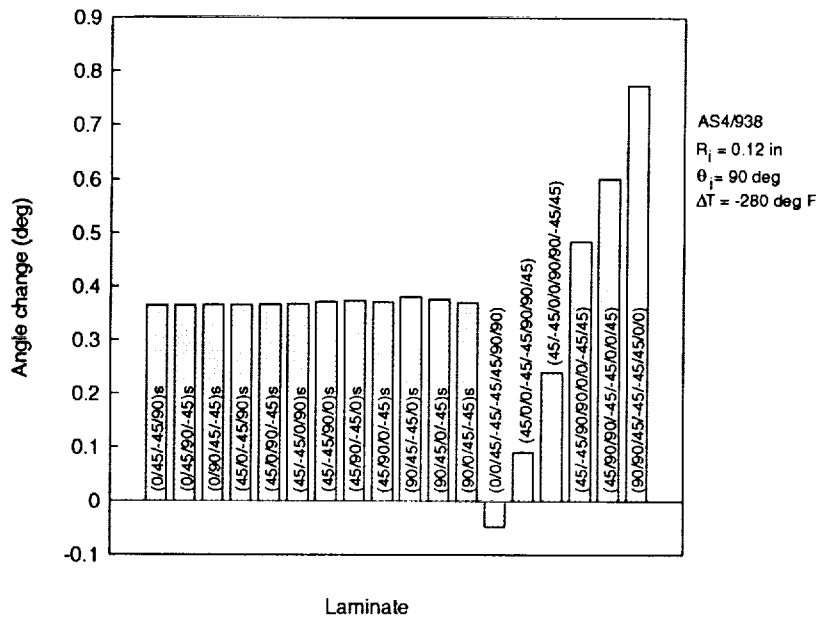


Figure 14 Stacking Sequence Effect on "Spring In" Angle Change for Unrestrained Curved Laminate

Note that unsymmetrical laminates can cause drastic changes in "spring in" response. "Spring out" can be induced in this manner. Ref. 5 presents a design of an aircraft leading edge using unsymmetrical laminates to control "spring in" effects.

The "spring in" angle change due to a -280°F temperature shift when a $(0/45/-45/90)_s$ and a $(90/45/-45/0)_s$ skin laminate provide restraint is shown in Figures 15 and 16, respectively. The ply stacking sequences of these quasi-isotropic skin laminates significantly affects the predicted "spring in" associated with the stiffener web/skin interface.

The angle change predictions presented are based on constant material properties and small displacements. Chemical shrinkage has not been included here. The effective stress-free temperature used in the analysis was the cure temperature. Additional material property evaluations and improved boundary conditions are necessary to refine this analysis.

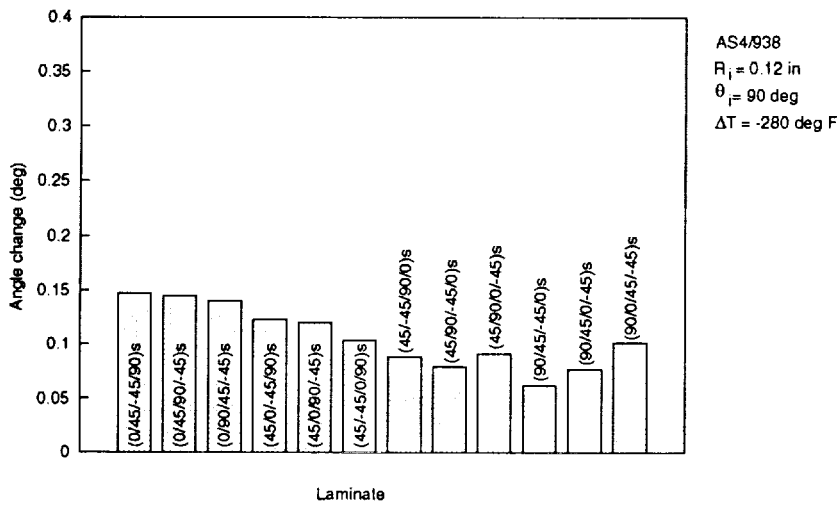


Figure 15 Stacking Sequence Effect on Angle Change for $(0/45/-45/90)_s$ Skin Restraint

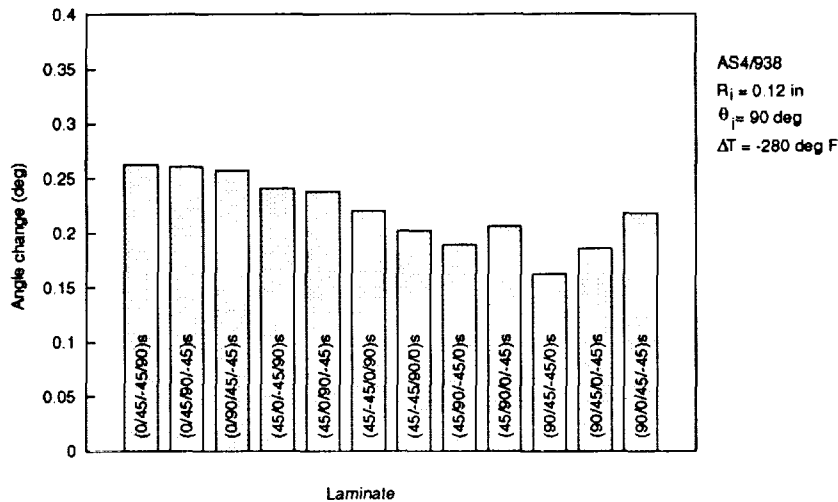


Figure 16 Stacking Sequence Effect on Angle Change for (90/45/-45/0)_s Skin Restraint

Closed Section Stiffener Transverse Direction Dimensional Changes

A closed form solution was developed to model the transverse direction dimensional changes of hat section stiffeners. The hat section is modelled as an assembly of straight and curved elements as shown in Figure 17. Plane strain conditions are imposed in the x - y plane (i.e., $\epsilon_z = \gamma_{xz} = \gamma_{yz} = 0$). The straight elements are assumed to obey classical laminated plate theory. For the curved elements, the plane strain solution (Ref. 4) is used for the pure moment and temperature shift, whereas classical laminated plate theory is used for the axial loading and varying moment. Slope and displacement compatibility is enforced at element interfaces. External temperature shifts provide the loading. Appropriate boundary conditions are applied to the left ends of elements 1 and 2 to enforce symmetric response of the overall cross-section.

This closed form solution was validated by comparing its predictions with a finite element analysis. In the finite element analysis, each ply was modelled with a separate solid element using ABAQUS (Ref. 6). Plane strain conditions were imposed by applying the appropriate boundary conditions. The closed form and finite element predictions compare favorably as shown in Figure 18.

Measurements were obtained on the skin of a section of a hat stiffener. Figure 19 presents the closed form predictions and test data. Both thermal and chemical shrinkage effects are included in the predictions. The temperature shift used was simply the difference between the cure temperature and the test temperature. The chemical shrinkage value used ($\epsilon_1 = 0, \epsilon_2 = \epsilon_3 = -0.0015$) was taken from Reference 1. Reasonable agreement of the analysis and test data is indicated.

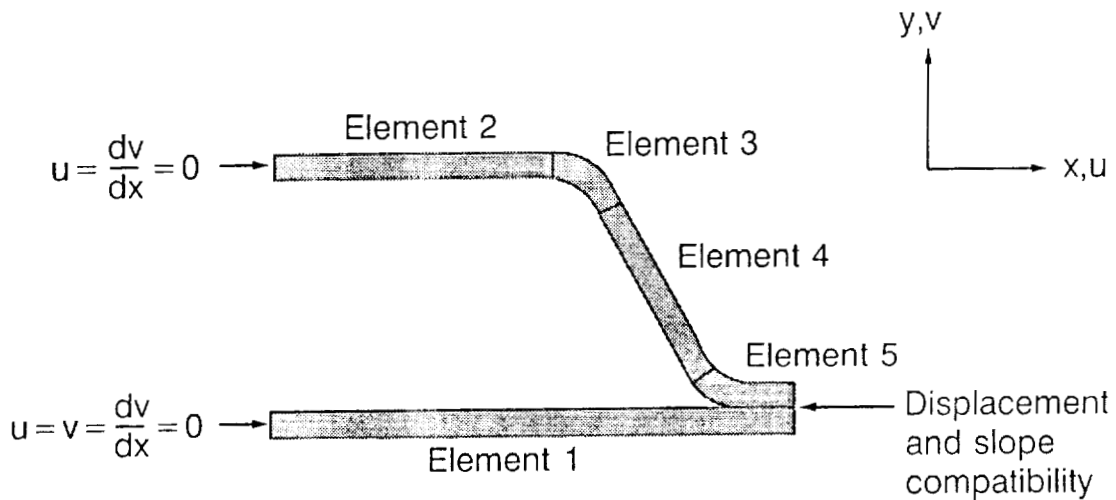


Figure 17 Hat Section Closed Form Solution Model

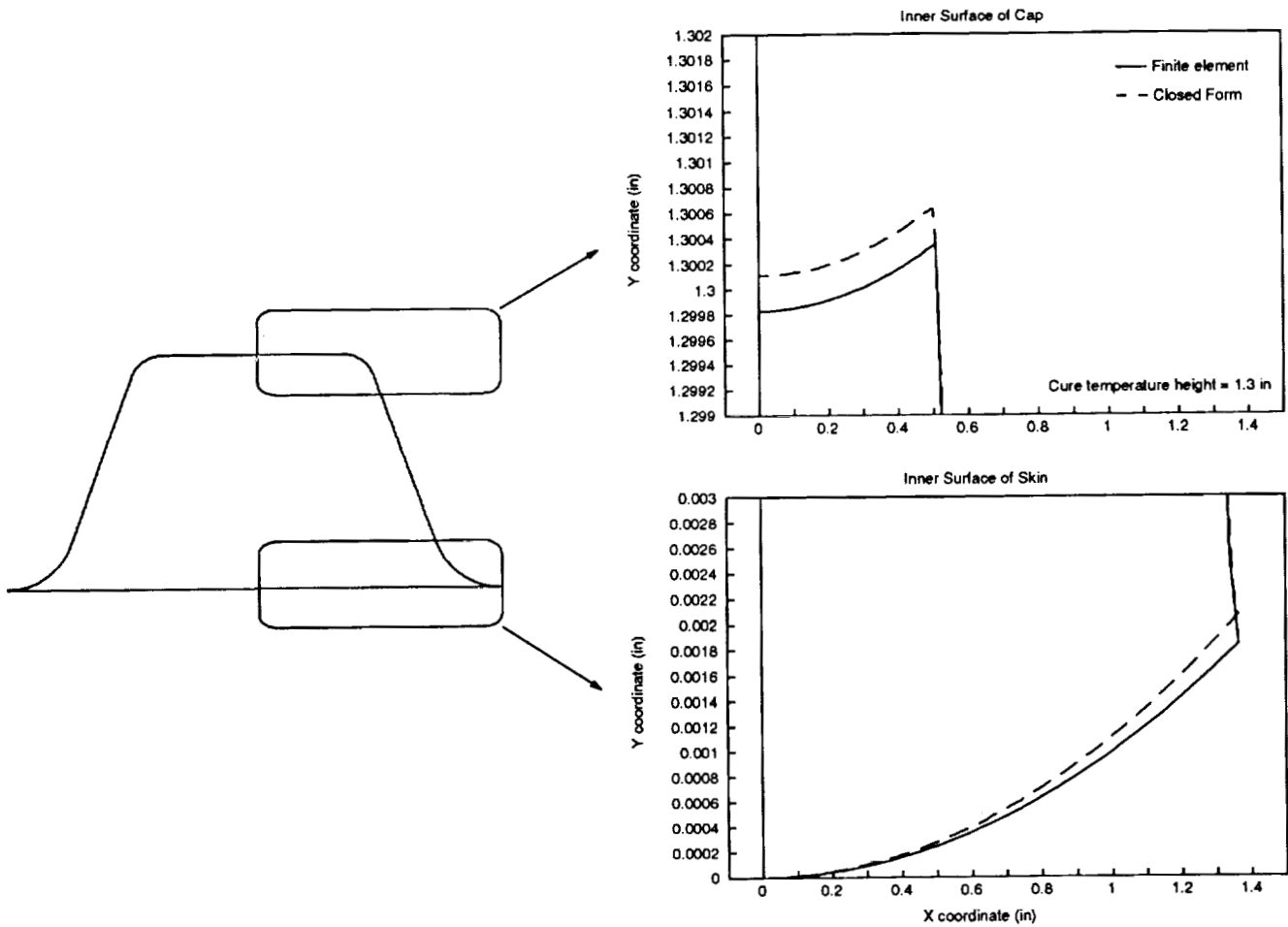


Figure 18 Comparison of Closed Form and Finite Element Analyses for Transverse Direction Dimensional Stability of Hat Sections (Ambient Conditions)

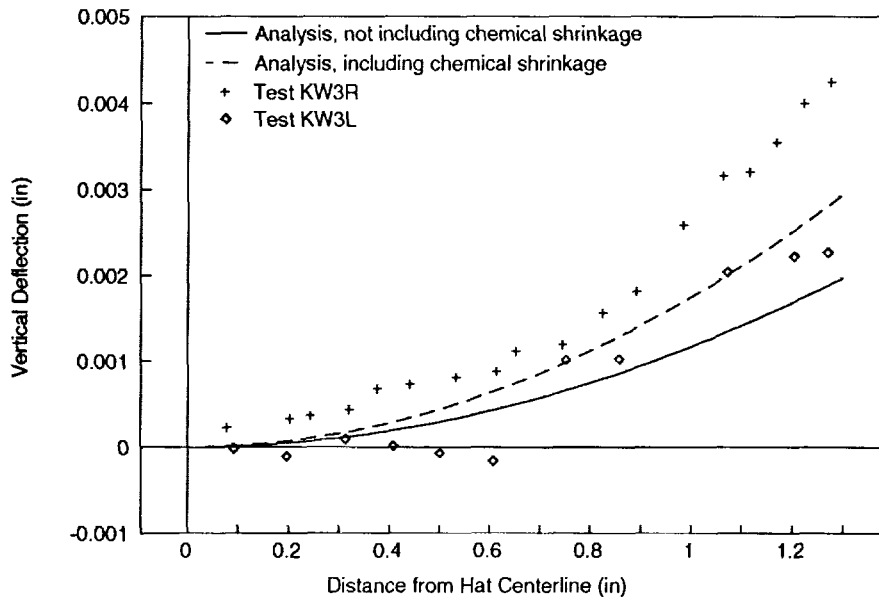


Figure 19 Hat Section Skin Deformation Analysis and Test Comparison (Ambient Conditions)

Mandrel Extraction Analysis

In an effort to understand the difficulties encountered in removing layered aluminum mandrels from certain Boeing ATCAS hat stiffeners, finite element models of the hat section, with and without the resin fillet shown in Figure 20, were performed.

Predictions of the aluminum mandrel position were also made. Results of these analyses are presented in Figures 21 and 22. Note the dramatic influence of the fillet on the deformation of the cross-section. The "no resin fillet" model predicts no interference between the mandrel and hat. The model that includes the resin fillet predicts interference on elements 2 through 4. This appears to be a major contributor to the mandrel extraction problems encountered. Dimensional changes in the axial direction may also have aggravated the mandrel extraction problems.

CONCLUSIONS

Closed form and finite element analyses have been presented for axial direction and transverse direction dimensional stability of skin/stringer panels.

Section geometry, material properties (stiffness and coefficient of expansion) and restraint conditions all combine to influence axial direction dimensional stability and residual and assembly forces. Mechanically attached stiffeners induce larger assembly forces than similar cocured or cobonded ones.

Unsymmetrical laminates may be used to control "spring in" in unrestrained curved laminates. The ply stacking sequences of laminates significantly affect the "spring in" response for restrained curved laminates.

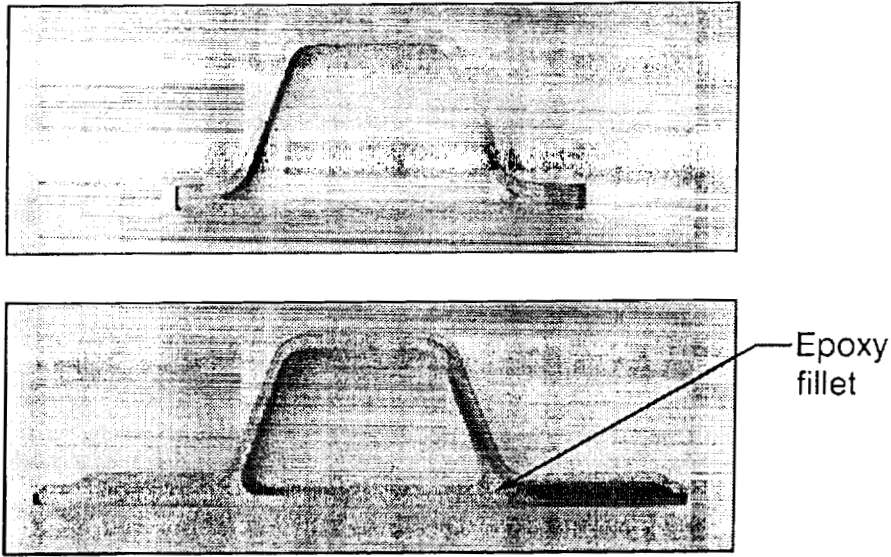


Figure 20 Photograph of Hat Section Stiffener Without and With Fillet

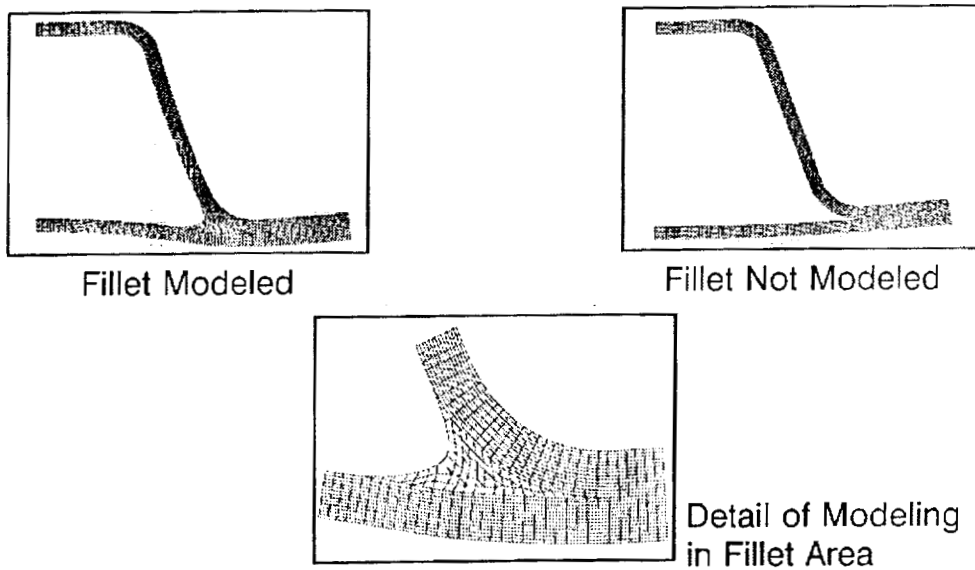


Figure 21 Plane Strain Finite Element Model Results for Hat Section Stiffener Cross-Sections (Amplified Displacements for Ambient Conditions)

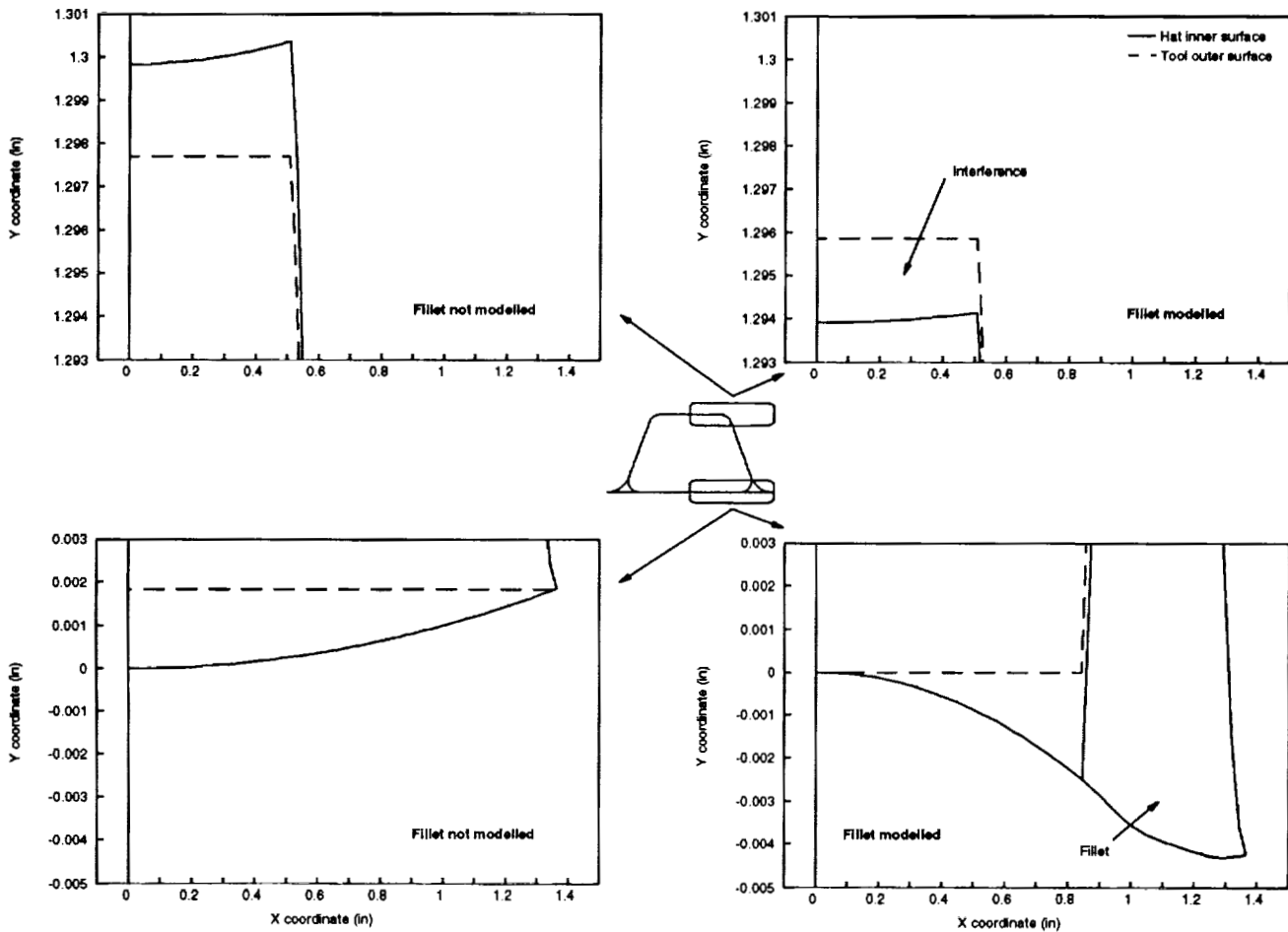


Figure 22 Effect of Fillet on Transverse Direction Dimensional Stability and Tool Extraction for Hat Section Stiffeners (Ambient Conditions)

Resin fillets have a drastic influence on transverse direction dimensional stability.

Closed form analyses compare well with small displacement, constant material property finite element analyses for both axial and transverse direction dimensional stability predictions.

Further work is required in the following areas:

1. Large displacement finite element modelling of skin/stringer panels.
2. Nonconstant material property finite element modelling.
3. Include transverse direction "spring in" in finite element complete panel models.
4. Generate chemical shrinkage, effective stress-free temperature material properties.
5. Include dimensional stability analyses into COSTADE.
6. Further investigation of dimensional stability issues caused by tool/part coefficient of thermal expansion mismatch.

REFERENCES

1. Nelson, R. H. and Cairns, D. S.: *Prediction of Dimensional Changes in Composite Laminates During Cure*, 34th International SAMPE Symposium, May 8-11, 1989, pp. 2397-2410.
2. Hyer, M. W.: *Some Observations on the Cured Shape of Thin Unsymmetric Laminates*, Journal of Composite Materials, Vol. 15, 1981, pp 175.
3. Freeman, W. T., Ilcewicz, L. B., Swanson, G. D. and Gutowski, T.: *Designer's Unified Cost Model*, Proceedings of the Ninth DoD/NASA/FAA Conference on Fibrous Composites in Structural Design, FAA Publication, 1991.
4. Mabson, G. E. and Neall, E. P.: *Analysis and Testing of Composite Aircraft Frames for Interlaminar Tension Failure*, Presented at the National Specialist's Meeting on Rotary Wing Test Technology of the American Helicopter Society, Bridgeport, Connecticut, Mar. 15-16, 1988.
5. Nolet, S. C. and Sandusky, P. M.: *Impact Resistant Hybrid Composite For Aircraft Leading Edges*, SAMPE Quarterly, Vol. 17, No. 4, July 1986, pp. 46-53.
6. *ABAQUS User's Manual Version 4.8*. Copyright 1989 by Hibbitt, Karlsson & Sorensen Inc.

APPENDIX A

COMPOSITE BEAM SECTION ANALYSIS INCLUDING THERMAL LOADING

The response of a single element is modelled as shown in Figure A1. Note that the element coordinate system origin ($y = 0, z = 0$) chosen is the location where no x -direction curvature results due to axial loads on the element (i.e. $B_{11}' = 0$). This location is the element midplane for symmetric laminates.

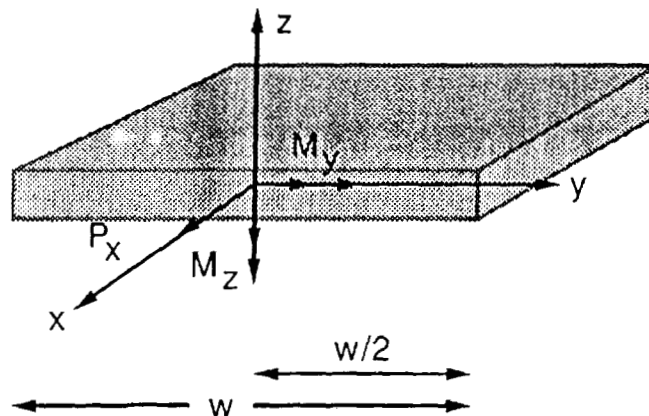


Figure A1 Element Coordinate System and Loading

The axial strain for an element due to the load and moments (P_x, M_y, M_z) and thermal loading in the element coordinate system is

$$\epsilon_x = A_{11}' P_x / w + A_{11}' F_1 + A_{12}' F_2 + A_{16}' F_3 + B_{12}' G_2 + B_{16}' G_3 + y \left[12 A_{11}' M_z / w^3 + z (D_{11}' M_y / w + B_{21}' F_2 + B_{61}' F_3 + D_{11}' G_1 + D_{12}' G_2 + D_{16}' G_3) \right] \quad (A1)$$

For a multi-element cross-section, Figure A2 illustrates the global coordinate system used. The total load and moments about the global coordinate system origin ($y_g = 0, z_g = 0$) are

$$P_{xt} = \sum_{i=1}^N P_{xi} \quad (A2)$$

$$M_{yt} = \sum_{i=1}^N (M_{yi} \cos \theta_i + M_{zi} \sin \theta_i + P_{xi} z_i) \quad (A3)$$

$$M_{zt} = \sum_{i=1}^N (M_{zi} \cos \theta_i - M_{yi} \sin \theta_i + P_{xi} y_i) \quad (A4)$$

For arbitrary loads (P_{xp}, M_{yp}, M_{zp} and thermal) applied to the cross-section at the global origin, the unknowns are the element loads P_{xi}, M_{yi}, M_{zi} (in each element coordinate system) and the axial strain constants a, b and c where

$$\epsilon_x = a + b y_g + c z_g \quad (A5)$$

The above equation is written with respect to the global coordinate system.

This results in $3N+3$ unknowns.

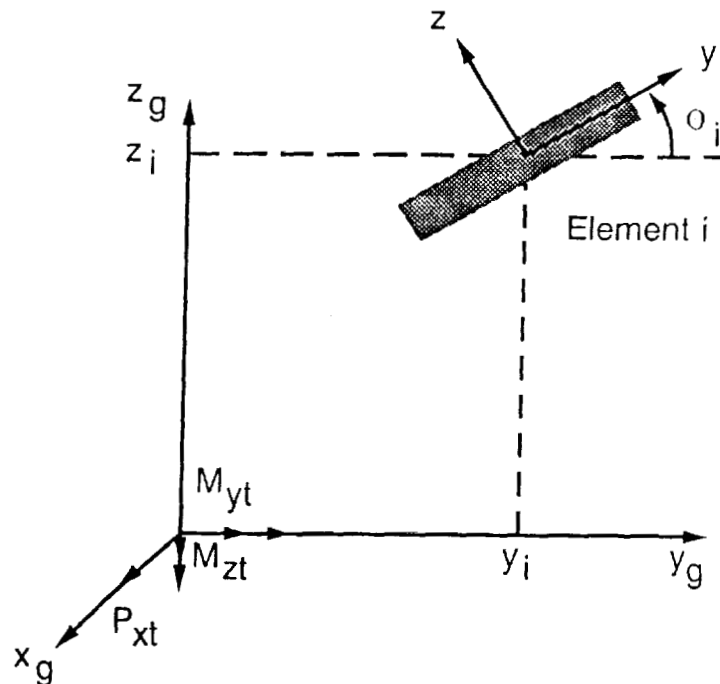


Figure A2 Global Coordinate System and Loading

The equations to be solved are equations A2, A3 and A4 and for each element:

$$\begin{aligned}
 a = & A_{11}' P_{xi} / w_i + A_{11}' F_1 + A_{12}' F_2 + A_{16}' F_3 + B_{12}' G_2 + B_{16}' G_3 \\
 & + y_i (-12 A_{11}' M_{zi} \cos \theta_i / w_i^3 \\
 & + (B_{21}' F_2 + B_{61}' F_3 + D_{11}' M_{yi} / w_i + D_{11}' G_1 + D_{12}' G_2 + D_{16}' G_3) \sin \theta_i) \\
 & + z_i (-12 A_{11}' M_{zi} \sin \theta_i / w_i^3 \\
 & - (B_{21}' F_2 + B_{61}' F_3 + D_{11}' M_{yi} / w_i + D_{11}' G_1 + D_{12}' G_2 + D_{16}' G_3) \cos \theta_i)
 \end{aligned} \tag{A6}$$

$$\begin{aligned}
 b = & 12 A_{11}' M_{zi} \cos \theta_i / w_i^3 \\
 & - (B_{21}' F_2 + B_{61}' F_3 + D_{11}' M_{yi} / w_i + D_{11}' G_1 + D_{12}' G_2 + D_{16}' G_3) \sin \theta_i
 \end{aligned} \tag{A7}$$

$$\begin{aligned}
 c = & 12 A_{11}' M_{zi} \sin \theta_i / w_i^3 \\
 & + (B_{21}' F_2 + B_{61}' F_3 + D_{11}' M_{yi} / w_i + D_{11}' G_1 + D_{12}' G_2 + D_{16}' G_3) \cos \theta_i
 \end{aligned} \tag{A8}$$

This results in $3N+3$ equations.

**TENSION FRACTURE OF LAMINATES FOR TRANSPORT FUSELAGE
PART II: LARGE NOTCHES¹**

**T. H. Walker, L. B. Ilcewicz
Boeing Commercial Airplane Group**

**D. R. Polland
Boeing Defense and Space Group**

**C. C. Poe, Jr.
NASA Langley Research Center**

514-24
51414

ABSTRACT

Tests were conducted on over 200 center-crack specimens to evaluate (a) the tension-fracture performance of candidate materials and laminates for commercial fuselage applications and (b) the accuracy of several failure criteria in predicting response. Crack lengths of up to 12 inches were considered. Other variables included fiber/matrix combination, layup, lamination manufacturing process, and intraply hybridization. Laminates fabricated using the automated tow-placement process provided significantly higher tension-fracture strengths than nominally identical tape laminates. This confirmed earlier findings for other layups, and possibly relates to a reduced stress concentration resulting from a larger scale of repeatable material inhomogeneity in the tow-placed laminates. Changes in material and layup result in a trade-off between small-notch and large-notch strengths. Toughened resins and 0°-dominate layups result in higher small-notch strengths but lower large-notch strengths than brittle resins, 90°- and 45°-dominated layups, and intraply S2-glass hybrid material forms. Test results indicate that strength-prediction methods that allow for a reduced order singularity of the crack-tip stress field are more successful at predicting failure over a range of notch sizes than those relying on the classical square-root singularity. The order of singularity required to accurately predict large-notch strength from small-notch data was affected by both material and layup. Measured crack-tip strain distributions were generally higher than those predicted using classical methods. Traditional methods of correcting for finite specimen width were found to be lacking, confirming earlier findings with other specimen geometries. Fracture tests of two stiffened panels, identical except for differing materials, with severed central stiffeners resulted in nearly identical damage progression and failure sequences. Strain-softening laws implemented within finite element models appear attractive to account for load redistribution in configured structure due to damage-induced crack tip softening.

¹ This work was funded by Contract NAS1-18889, under the direction of J. G. Davis and W. T. Freeman of NASA Langley Research Center

INTRODUCTION

Boeing's program for Advanced Technology Composite Aircraft Structure (ATCAS) is studying manufacturing and performance issues associated with a wide body commercial transport fuselage (Ref. 1). Tension damage tolerance and pressure containment are major technical issues to solve for fuselage structures. Although composites are generally thought to have excellent tension properties, only limited data exists on the performance of configured composite shell structures with large through-penetrating damage and are subjected to combined load conditions, including pressure. A collaborative effort between Boeing and NASA is committed to collecting a database and solving the technical challenges associated with composite fuselage damage tolerance.

The tension fracture studies for the crown region include seven types of tests, as shown in Figure 1. The upper row illustrates uniaxial tension tests, while the lower row contains those for biaxial tension. The numbers shown parenthetically are the specimen quantities. Significant progress has been made towards completion of the testing. As of June 1992, the tests remaining include several flat tear-strap panels and the curved stiffened panels. The focus of this paper is the coupon and large unstiffened panel tests, but the results obtained from the large stiffened panel tests conducted during May of 1992 are also briefly discussed. A discussion of the curved tear strap panel test, also conducted during May of 1992, and the plans for the curved stiffened panels are contained in Reference 2.

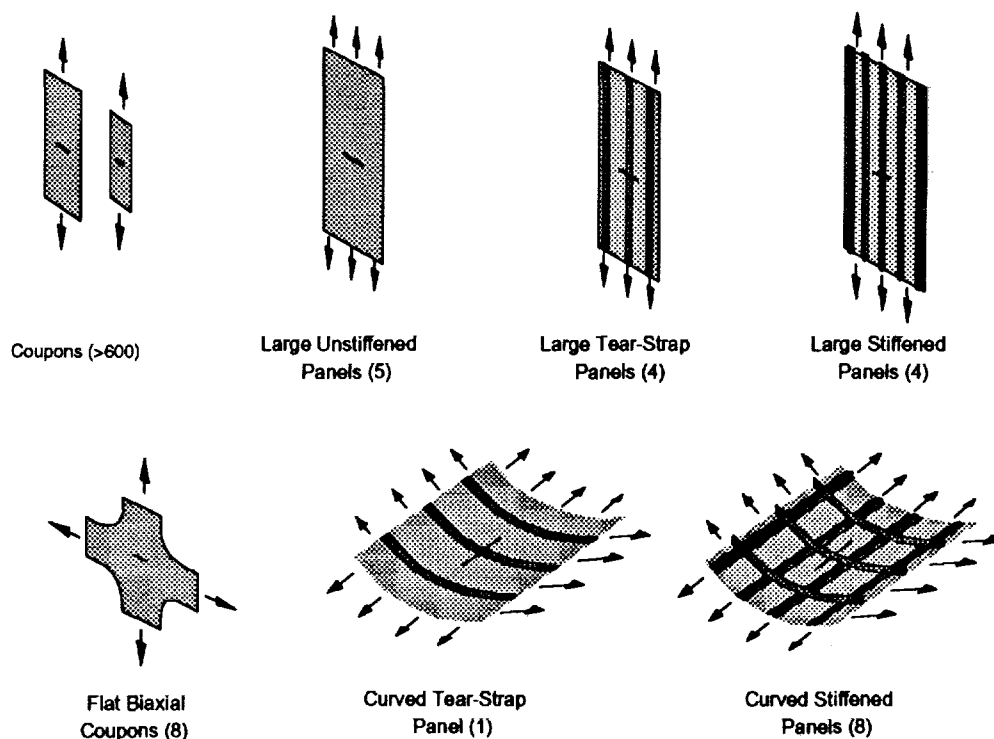


Figure 1. ATCAS tension fracture testing.

This paper is the second in a series on ATCAS tension fracture studies. The first paper (Ref. 3) discussed several significant experimental and theoretical findings. Experimental

results were based on 430 uniaxial tension tests of specimens with notch sizes between 0.25 and 5.0 inches. The most important findings are summarized below.

1. Laminates fabricated using the advanced tow-placement process were found to have significantly higher tension fracture performance than identical laminates that were fabricated by hand layup from nominally identical prepreg tape (i.e., the same fiber, fiber bundle size, resin, resin content, areal weight and ply thickness). This improvement was hypothesized to relate to a larger scale of repeatable material inhomogeneity in the tow-placed laminates.
2. Brittle-resin laminates tested with sharp penetrations created by an impact event and machined slits of comparable dimension displayed similar strengths for the thinnest laminates tested ($t = 0.074$ in.). For thicker brittle-resin laminates ($t = 0.118$ in.), the machined slit resulted in approximately 25% lower strengths than the through-penetration. For toughened-resin laminates, the through-penetration specimens provided 22% lower strengths than the machined slit coupons.
3. Classical finite width correction factors did not properly account for the differences between notched strengths of specimens with width-to-notch-length ratios ($W/2a$) of 2 and 4. This was found to be true for a range of fibers, matrices, fabrication techniques and layups.
4. Intraply hybridization with higher strain fibers reduced the sensitivity of a material to changes in notch length. Significant precatastrophic damage was observed in such laminates.
5. Increased matrix toughness was found to increase the sensitivity of the material to changes in notch size. A representative toughened-matrix system, IM7²/8551-7³, was found to have 35% higher strength at 0.25 in. notch sizes than a brittle-matrix system with a nearly identical fiber, IM6⁴/937A⁵. However, the advantage had turned into a 7% disadvantage for 2.5 in. notches. This behavior was suggested to relate to reduced matrix damage in the vicinity of the notch tip for the toughened-matrix material, which in turn limits stress relief.
6. Layup was found to affect notch strength for a single notch size and the sensitivity to changes in notch length.
7. Classical fracture toughness values obtained from experimental data increased with increasing notch size.

² IM7 is a graphite fiber system produced by Hercules, Inc.

³ 8551-7 is a resin system produced by Hercules, Inc.

⁴ IM6 is a graphite fiber system produced by Hercules, Inc.

⁵ 937A is a resin system produced by ICI/Fiberite

8. Four failure criteria were evaluated for accuracy in predicting the effect of notch size. Failure criteria that used a classical crack-tip stress-field singularity of 0.5 were less successful in predicting the test results than methods using 0.3.

Significant efforts have been conducted in understanding the damage tolerance of stiffened metallic structure (e.g., Ref. 4, 5). Competing failure mechanisms in such structure are skin fracture, stiffener strength, and rivet yielding. Consideration of the inelastic behavior of the material has been found to be important in properly predicting the interaction between these competing failure mechanisms. It was also found that stiffener bending is an important aspect to predicting load redistribution and stiffener strength. Similar failure mechanisms exist for composite structure with bonded stiffening elements. Skin fracture and stiffener strength both remain important, and delamination of the stiffener from the skin replaces rivet yielding, since both control the local load transfer into the stiffening element in their respective configurations. It is likely, then, that local damage growth in composite materials is important in predicting strengths of configured composite structure since it is the mechanism by which composite materials exhibit significant inelastic behavior. Additional discussions of failure mechanisms for configured composite structure are contained in Reference 1.

EXPERIMENTS

Test Matrix

Nearly two-hundred coupons and five large flat unstiffened panels have been tested since the initial paper on ATCAS tension fracture activities (Ref. 3). A summary of the test specimen configurations and quantities are contained in Figure 2. Laminates were made of combinations of three fiber (AS4⁶, S2-Glass⁷, IM7) and two resin (938⁸, 8551-7) types. The first two materials indicated in the figure, AS4/938 tape and AS4/938 tow, provided a direct comparison of laminates fabricated using the tow-placement and hand layup processes. The IM7/8551-7 system represented the toughened-resin class of materials. Intraply hybrid materials, consisting of alternating bands of differing fibers within some or all of the laminate plies as shown schematically in Figure 3, were included to further evaluate their attractive fracture characteristics.

Several laminates representative of crown applications were considered, including aft (Crown3, 2/4/6, 4/4/4) and forward (Crown4) portions of the ATCAS study section. Most laminates were tested in the directions corresponding to both the axial and hoop directions of the fuselage.

⁶ AS4 is a graphite fiber system produced by Hercules, Inc.

⁷ S2 is a glass fiber system produced by Owens-Corning Fiberglas, Corp.

⁸ 938 is a resin system produced by ICI/Fiberite

Material	Laminate	Notch Type:			Machined Slit														
		Unnotched	0.250	0.250	0.438	0.500	0.500	0.750	0.875	0.875	1.250	2.000	2.500	8.000	9.000	12.000			
		Notch Size:	N/A	N/A	N/A														
		Width:	1	2	3	1	2	3.5	2	3.5	3	3.5	3.5	10	8	10	36	36	60
		Length:	12	12	12	12	12	12	12	12	12	12	12	30	24	30	90	90	150
		W/2a:	N/A	N/A	N/A	4	8	8	4	7	4	4	4	8	4	4	4.5	4	5
		Test Temperature:	RT	RT	RT	RT	RT	RT	RT	RT	RT	RT	-75F	RT	RT	RT	RT	RT	RT
AS4/938 Tape	Crown3-Hoop			5						5				4					
AS4/938 Tow	2/4/6-Axial	3	3		3	3					3					2			
	2/4/6-Hoop	3	3		3	3					3					2			
	Crown3-Axial		4		3						2	2							
	Crown3-Hoop		4	5	3					5	2	1		5	2				1
	Crown4-Axial	3			3						3				2				1
25%-Glass Hybrid	Crown3-Axial		4		4						2	2							
	Crown3-Hoop		4		4						2	2			2				
	Crown4-Axial	3			3						3				2				1
Hoop Hybrid	4/4/4-Axial		3																
	4/4/4-Hoop		3		3			2	3		3				2				
IM7/8551-7 Tape	Crown3-Axial	3			3	3	2				3			2		2	1		
	Crown3-Hoop	3			3	3	2				3			2		2		1	

Layups:
Crown3 = [45/-45/90/0/60/-60/90/-60/60/0/90/-45/45]
Crown4 = [45/-45/90/0/60/-60/15/90/-15/-60/60/0/90/-45/45]
2/4/6 = [-45/90/45/90/0/90]s
4/4/4 = [-45/90/45/0/0/90]s (90-deg plies are 50% AS4/938 and 50% S2/938 with 8-tow repeat unit)
Note: 0-deg direction = Axial direction

Figure 2. Specimen configurations and number of replicates for tension fracture testing.

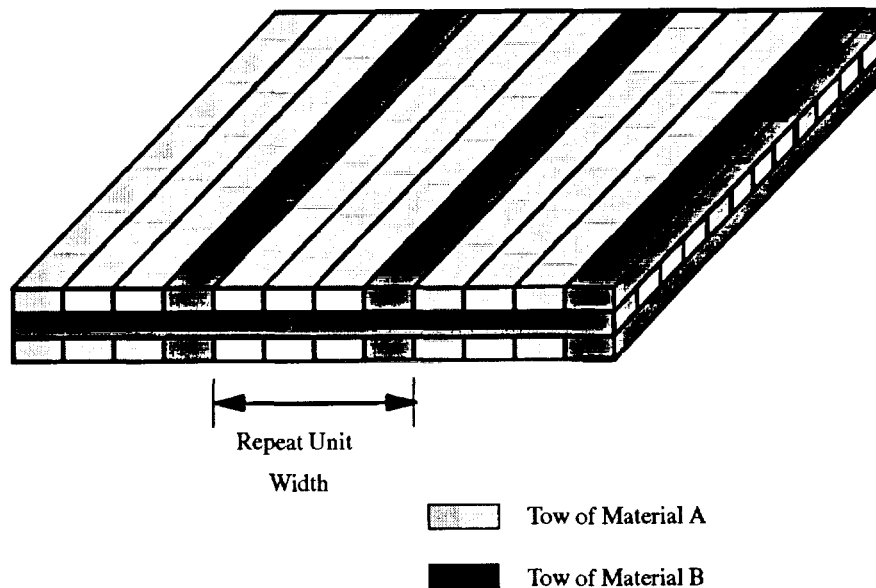


Figure 3. Schematic of intraply hybrid material.

Other variables considered included notch length, $W/2a$, test temperature, and load rate. Notch sizes ranged from 0.25 to 12.0 inches. Specimens with $W/2a = 4$ and 8 were tested to further evaluate the limits of isotropic finite width correction factors. Limited tests were conducted at reduced temperature (-75°F). The notch type for all tests was limited to machined central slits, for manufacturing convenience and repeatability, and since previous data provided some, although not conclusive, indications that machined slits were

either equivalent or conservative for some materials when compared with sharp penetration damage.

The two 5-stringer fracture panel configurations are illustrated in Figure 4. Both panels were identical in geometry and layup, with hat stringers at 14 inch spacing. The first panel was fabricated entirely from AS4/938 tow and the second using an intraply hybrid of 75% AS4/938 and 25% S2/938 with an 8 tow repeat unit. Both contained a centered, single-bay skin notch (14 in.) that also severed the central hat stringer.

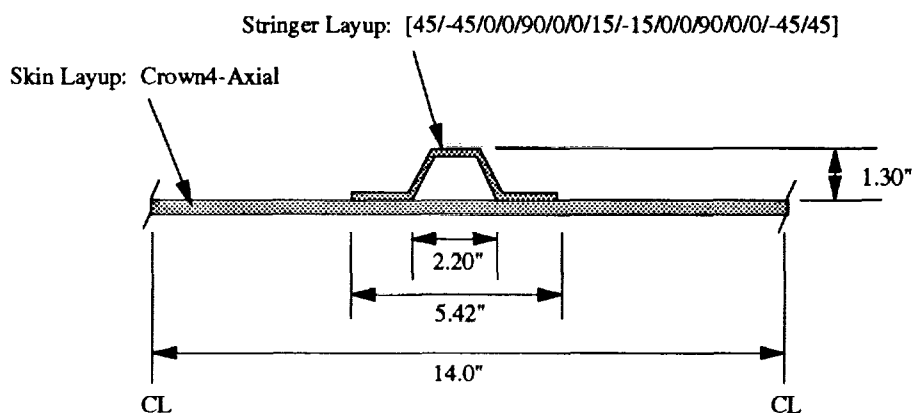


Figure 4. Stiffened fracture panel configurations.

All laminates in the test matrix were fabricated from material with a fiber volume of approximately 57% (corresponding to a resin content of 35% for graphite/epoxy systems). The fiber tows used in the tape materials were 12K. To maintain approximately equal tow spread for all intraply hybrid fiber types, tow-placed laminates were fabricated using 6K tows of AS4 and 20-end 750 yd./lb. S2-glass.

Panel Fabrication

The tow-placed laminates were fabricated on the Hercules 7-axis fiber placement machine using a 32-tow Cut-and-Add head. The tape panels were fabricated from 12 inch wide prepreg tape using standard hand layup techniques. All panels were autoclave cured at 350°F. The nominal cured ply thickness for both tow and tape materials was 0.0074 in. Through transmission ultrasonics was used to non-destructively inspect each panel after cure to ensure laminate quality. Measurements indicated that all panels fabricated were within specified limits.

The stiffened panels were also fabricated on the Hercules 7-axis fiber placement machine using the 32-tow Cut-and-Add head. The skin and stringer charges were tow-placed separately. The stringer charges were then trimmed and hot-drape-formed at approximately 150°F to the hat-section shape. The panels were assembled, with flexible aluminum-wafer and silicone rubber stringer mandrels (Ref. 6) being used for the non-hybrid and hybrid panels, respectively. Both panels were then covered with a thin graphite caul plate that included the intended stringer cross-section, bagged, and cured at 350°F.

Difficulties were encountered in removing the aluminum-wafer stringer mandrels from the non-hybrid panel, resulting in many areas of delamination along the skin/stringer bondline. In only one section of the test panel, however, did the delamination extend beyond the adhesive noodle, as shown in Figure 5. This region was remote from the crack-tip, and mechanical fasteners were placed through this approximately 12 in. long partial delamination to preclude premature failure of the test panel. The silicone mandrels were removed without incident from the hybrid panel, and no significant delaminations were noted.

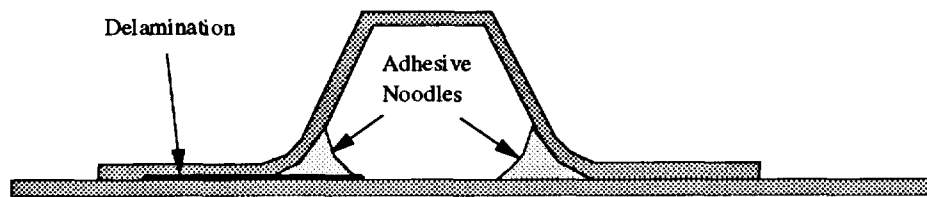


Figure 5. Location of skin/stringer disbond prior to panel testing.

Specimen Machining

The coupons were cut to slightly oversized dimensions using a band saw, then sanded to final dimensions. A 125 surface finish was designated for all cut edges. The slits were created by drilling two 0.070 inch diameter holes at the crack tip locations, then connecting them using an abrasive waterjet cutter.

The 10 in. x 30 in. coupons were tabbed with 10 in. x 3 in. tabs on both sides of each end to preclude failure in the grips. The tabs were fabricated from various graphite/epoxy materials with each tab having a nominal thickness of approximately 0.070 inches. They were bonded to the test specimens with a 0.010 inch thick 250°F cure film adhesive. Peel plies were used on the tab bonding surfaces, while the test specimens were prepared for bonding by lightly grit blasting the bonding surfaces, followed by a solvent wipe to remove any loose material.

The three 60 in. x 150 in. flat unstiffened panels were prepared in a manner similar to the 10 in. x 30 in. coupons. All three panels featured a center slit created by drilling two 0.070 inch diameter holes 12 inches apart, which were subsequently connected using an abrasive waterjet cutter. Precured 60 in. x 13.2 in. tabs fabricated from graphite/epoxy prepreg tape with a [-45/45/-45/45/0/90/0/45/-45/45/-45] stacking sequence were adhesively bonded on both sides of each end with a 0.010 inch thick 250°F cure film adhesive.

The two 60 in. x 150 in. flat stiffened panels were shortened to (a) eliminate delaminations caused by stiffener mandrel removal on the AS4/938 panel and (b) enable the panels to fit within the test frame constraints. The as-tested length of the AS4/938 panel was 126 in. while the hybrid panel was 137 in. long. As with the other panels, two 0.070 in. diameter holes were drilled 14 inches apart in the center of the panel to locate the crack tips. These holes were then joined using a hand-held narrow kerf diamond cutoff saw. As previously mentioned, the center stringer was severed resulting in the center slit extending to the

middle of each adjacent skin bay. Doublers 14.5 in. long fabricated from graphite/epoxy 250°F cure prepreg plain weave fabric with a $[\pm 45, 0/90, \pm 45, 0/90, \pm 45]_{10}$ stacking sequence were secondarily cured on the panel, with a 0.005 in. thick layer of 250°F cure film adhesive used between the doubler plies and the panels to improve the doubler bond. The doublers extended between stiffener flanges on the stiffened side only. This, combined with machined aluminum grip plates, resulted in load application to the panel neutral axis. Sixty 0.375 in. diameter fasteners were used to attach aluminum grip plates to each end of the panel. Load was directly introduced into the skin and stiffener flanges, but no attempt was made to directly load the stiffener webs or caps.

Test Procedures

The smaller coupons were loaded in monotonic tension to failure. Strain measurements were made using either remote extensometers or strain gages. The large unstiffened and stiffened panels tests were conducted as a series of load-unload sequences to successively higher loads. Non-destructive inspections, in the form of x-rays and/or pulse-echo, were performed after each unloading. These larger panels were extensively instrumented, including strain gages and shadow Moiré (to measure out-of-plane displacements of the crack edges).

UNSTIFFENED TEST RESULTS

The average nominal failure stress (i.e., failure load divided by the product of the number of plies and the nominal ply thickness) for each specimen and unstiffened panel configuration is listed in Figure 6. The following discussions will highlight the important findings.

Coupon Tests

A major finding during the second phase of the ATCAS tension fracture studies, observed at MIT by Lagace and McManus under ATCAS subcontract, was the confirmation of the previously observed 10-25% tension fracture improvements of tow-placed laminates over similar tape laminates, for a layup other than that tested in previous ATCAS experiments. These results are shown for a quasi-static strain rate in Figure 7. In addition to its higher fracture strength, the tow-placed laminate was found to exhibit less strength reduction with increasing strain rate than does its tape counterpart for strain rates up to 2.04 in./in./min. The importance of strengths at higher strain rates is related to the potential high-speed blade penetration event and the ensuing cabin-pressure release.

Material	Laminate	Notch Type:			Machined Slit													
		Notch Size:	Unnotched			0.250	0.250	0.438	0.500	0.500	0.750	0.875	0.875	1.250	2.000	2.500	8.000	9.000
Width:	Length:	W/2a:	RT	RT	RT	RT	RT	RT	RT	RT	RT	RT	RT	RT	RT	RT	RT	RT
AS4/938 Tape	Crown3-Hoop				89.21						40.40					29.46		
AS4/938 Tow	2/4/6-Axial	58.02	59.09			39.41	41.29					30.35				25.00		
	2/4/6-Hoop	142.75	131.27			75.04	91.59					63.71				48.14		
	Crown3-Axial		58.03			35.03						30.03	27.86					
	Crown3-Hoop		83.67	85.47		65.45						50.88	51.98	51.68		42.06	38.90	22.51
	Crown4-Axial	66.02				40.13						33.29				29.91		21.98
25%-Glass Hybrid	Crown3-Axial		53.24			30.93						32.82	28.79					
	Crown3-Hoop		76.02			57.95						50.94	52.87			41.06		
	Crown4-Axial	60.08				39.26						35.35				31.80		27.10
Hoop Hybrid	4/4/4-Axial		94.91															
	4/4/4-Hoop		80.87			51.16			50.03	58.34		46.87				40.03		
IM7/8551-7 Tape	Crown3-Axial	81.84				51.06	50.30	44.18				39.13		40.12		31.96	22.49	
	Crown3-Hoop	130.14				83.47	72.01	62.73				55.18		49.84		37.10		18.57

Layups:
 Crown3 = [45/-45/90/0/60/-60/90/-60/60/0/90/-45/45]
 Crown4 = [45/-45/90/0/60/-60/15/90/-15/-60/60/0/90/-45/45]
 2/4/6 = [-45/90/45/90/0/90]_s
 4/4/4 = [-45/90/45/0/0/90]_s (90-deg plies are 50% AS4/938 and 50% S2/938 with 8-tow repeat unit)
 Note: 0-deg direction = Axial direction

Figure 6. Nominal failure stresses for unstiffened fracture tests.

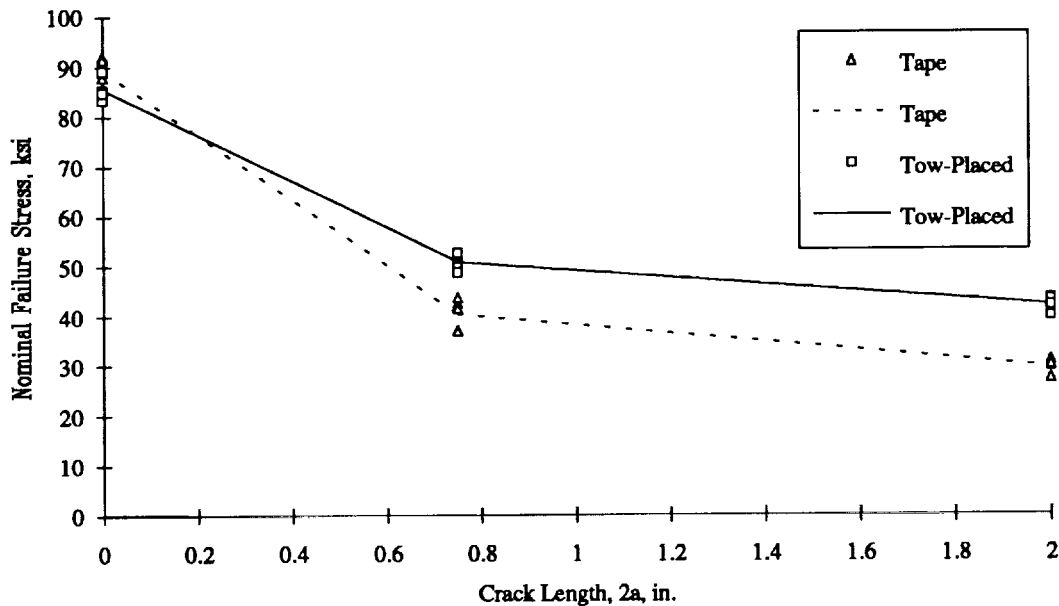


Figure 7. Fracture strengths of tow-placed and tape AS4/938 laminates measured under MIT subcontract (Lagace and McManus).

Two intraply hybrid concepts were considered at the coupon level. In the first concept (i.e., 25%-Glass Hybrid), all plies were hybridized with 25% S2-glass. In the second (i.e.,

Hoop Hybrid), only the hoop direction plies were hybridized (50% S2-glass), similar to buffer-strip concepts widely studied in the past (e.g., Refs. 7, 8). All tests of the Hoop Hybrid were conducted with the notch perpendicular to the glass strips. As shown in Figure 8, the 25%-Glass Hybrid had superior fracture performance for the notch sizes below 2.5 inches, but its advantages over the Hoop Hybrid diminish with increasing crack length. At notch lengths above 2.5 inches, the Hoop Hybrid is likely to have the higher strengths. A significant drawback to this material concept, however, is the directionality of its improved fracture performance; notches oriented other than perpendicular to the glass strips will likely result in significantly lower strengths. Damage progression was shown by x-rays to be significantly different for the two hybridizing concepts. Growth in the Hoop Hybrid was severely antisymmetric, appearing to follow the glass strips, while growth in the 25%-Glass Hybrid was more uniform around the crack tip.

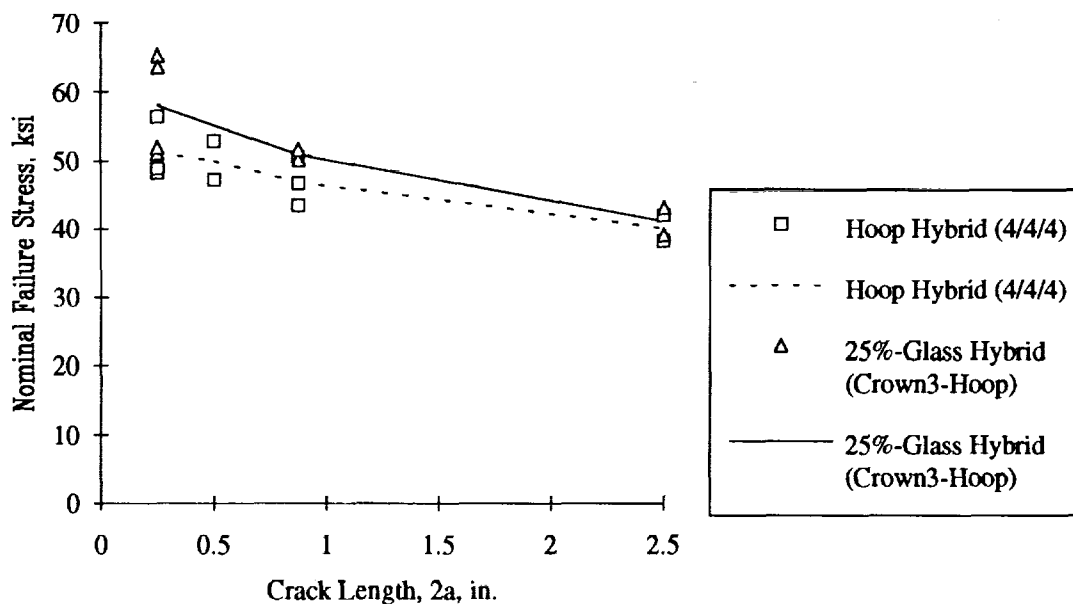


Figure 8. Failure strengths of intraply hybrid concepts.

Results obtained comparing notched strengths at reduced and ambient temperatures are shown in Figure 9. For the AS4/938 material, the more 0°-dominated laminate (Crown3-Hoop) exhibited no reduction in strength due to the reduced temperature, while the 90°-dominated laminate (Crown3-Axial) exhibited a 7% decrease. This likely relates to a combination of (a) the reliance of the 90°-dominated laminate on the matrix for load transfer around the notch and (b) the embrittlement of the matrix at the reduced temperature. Similar results were observed for the 25%-Glass Hybrid material.

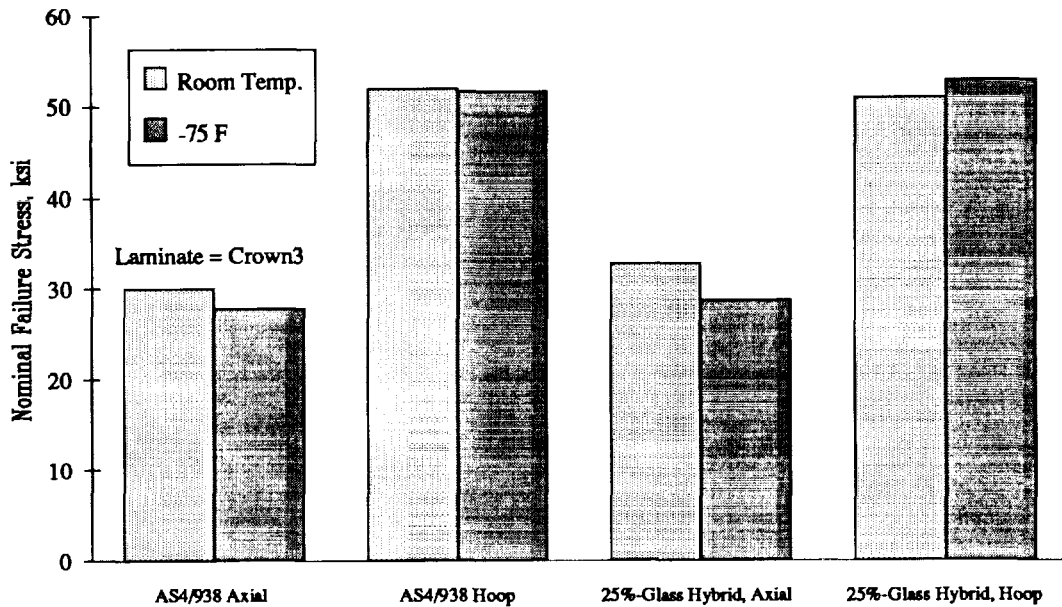


Figure 9. Effect of temperature on tension fracture strength.

Large Panel Tests

Five laminate/material combinations were tested with notch sizes of 8 inches or greater. Small-notch coupons were also tested for each of these combinations, and the results are summarized in Figure 10. Each point in the figure represents the average value of all tests conducted with $W/2a$ between 4.0 and 5.0 for a specific notch size and laminate/material combination. A considerable range of behavior was observed, and confirms earlier ATCAS findings that the small-notch strength of a particular laminate/material combination had little direct relationship with its large-notch strength. Other relationships observed in the data are discussed in the following paragraphs.

The effect of varying the material for each of two laminates is shown in Figures 11 and 12. In Figure 11 it can be seen that, for the Crown3-Hoop laminate, the IM7/8551-7 material provided higher small-notch strengths than the AS4/938 but lower strengths at notch lengths above approximately 2 inches. This confirms earlier ATCAS findings of a cross-over. It is also similar to the trade-off between yield strength and fracture toughness observed in aluminum alloys, where the small notch strengths and large notch strengths of the composites assume the roles of the yield strength and fracture toughness of the aluminum, respectively. A similar compromise is seen between the AS4/938 and the 25%-Glass Hybrid for the Crown4-Axial laminate in Figure 12, where the former has higher strengths with notch lengths below approximately 0.5 inches, and lower strengths above. The 25%-Glass Hybrid was nearly notch-insensitive, exhibiting only a 20% reduction in strength as notch lengths varied from 0.25 to 12 inches.

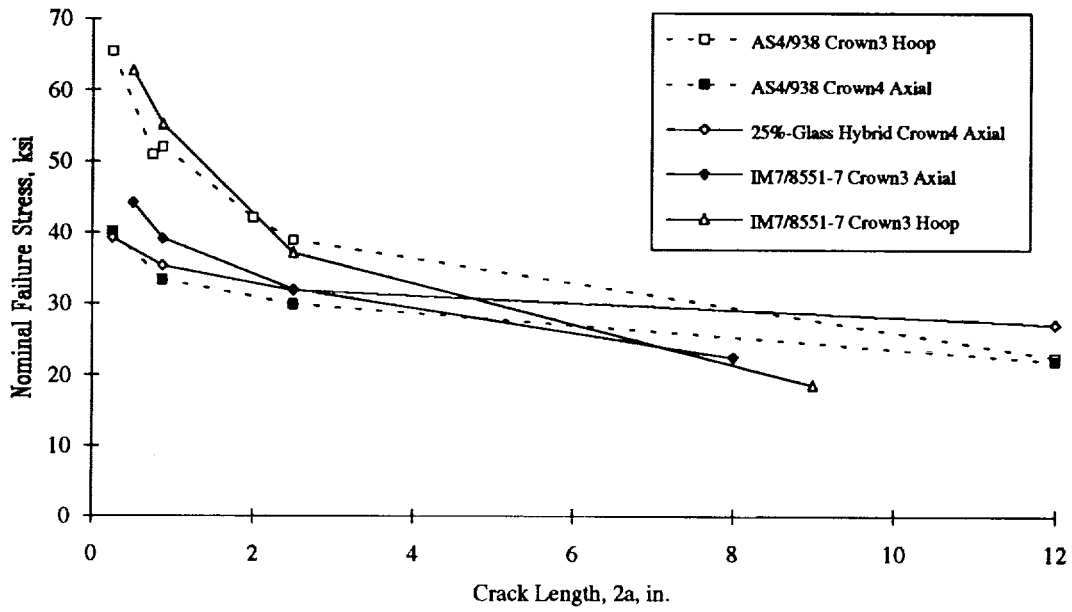


Figure 10. Tension fracture performance of laminate/material combinations tested with large notches.

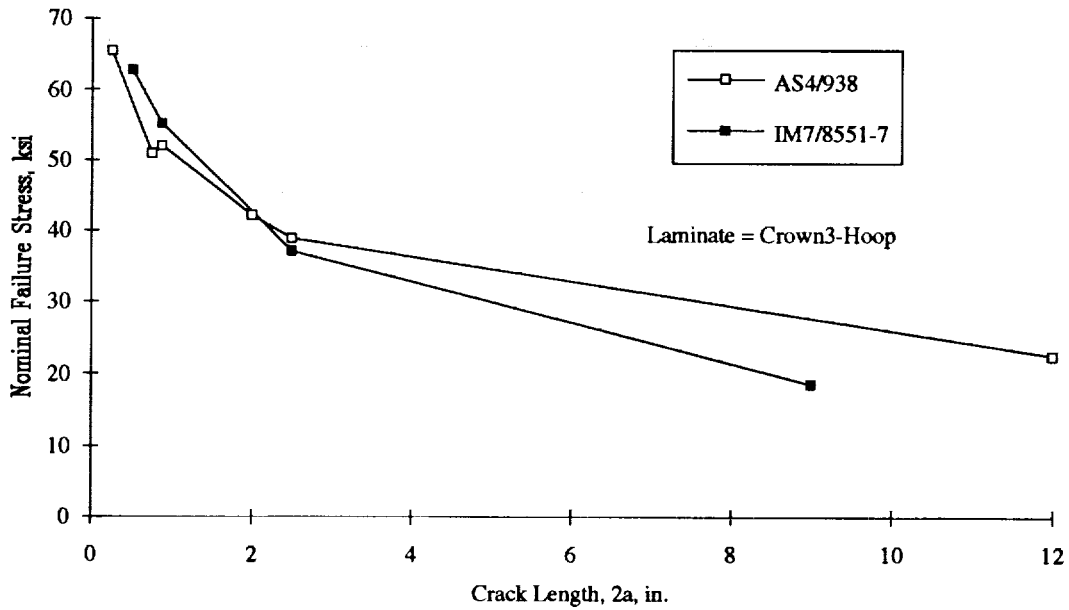


Figure 11. Material influence on fracture strength for the Crown3-Hoop laminate.

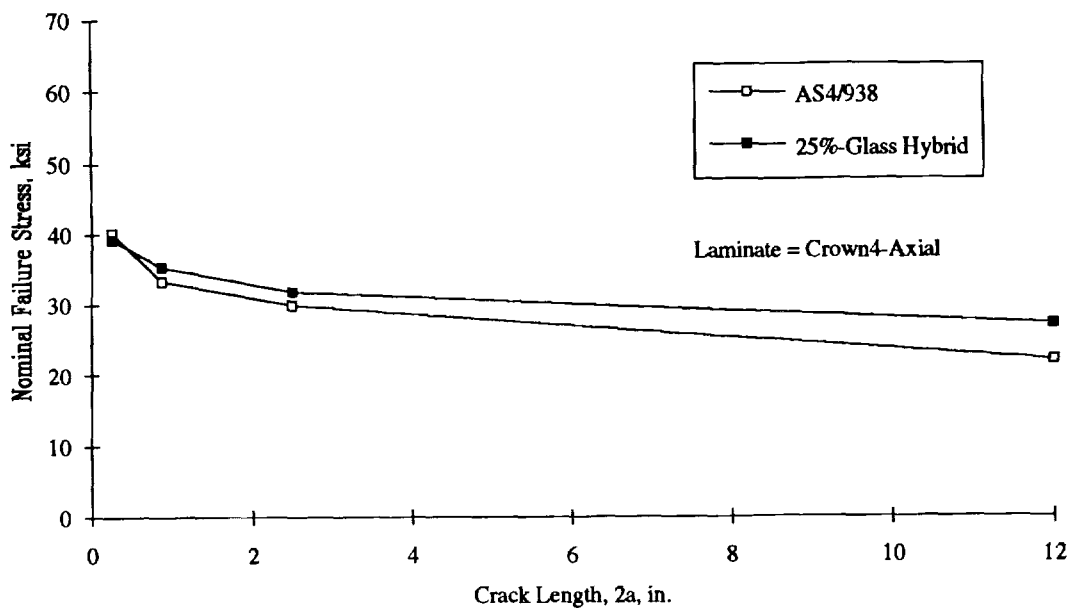


Figure 12. Material influence on fracture strength of the Crown4-Axial laminate.

The effect of varying the layup for each of two materials can be seen in Figures 13 and 14. A similar trade-off between small-notch and large-notch strengths is observed for both the AS4/938 and IM7/8551-7 material systems. In both cases, the laminate with the higher modulus parallel to the loading direction exhibited strengths that were larger for small notches but lower for large notches. The notch size at which the cross-over occurs, however, is significantly larger than that observed for material differences. The stress versus strain plots for notched panels with differing layups show that relatively soft laminates have significantly higher failure strains and work to fracture. This observation is an important finding in support of composite skin design. Additional discussions on the use of soft-skin/hard-stiffener designs to achieve structural damage tolerance is given in Reference 1.

The results of these laminate/material combinations were also compared by observing the convergence of the classical stress intensity factor (K_{IC}) with increasing crack length, as shown in Figure 15. As was observed in previous ATCAS studies, K_{IC} increased with notch length for all laminate/material combinations. In the extreme cases, the stress intensity factor of the stiffer of the two IM7/8551-7 laminates had converged to an approximately constant value at a notch length of approximately 2 inches while that of the 25%-glass hybrid was still increasing rapidly at a 12 inch notch length. A similar requirement for large notch testing has been observed in obtaining converged plane-stress fracture toughnesses for ductile aluminum alloys, as illustrated in Figure 16.

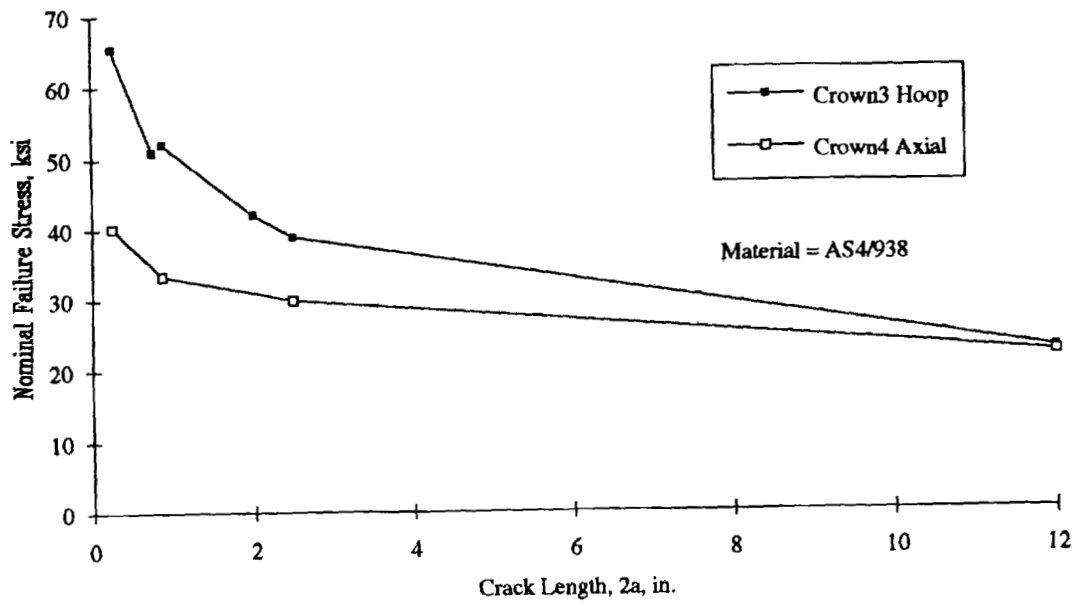


Figure 13. Laminate influence on fracture strength of AS4/938.

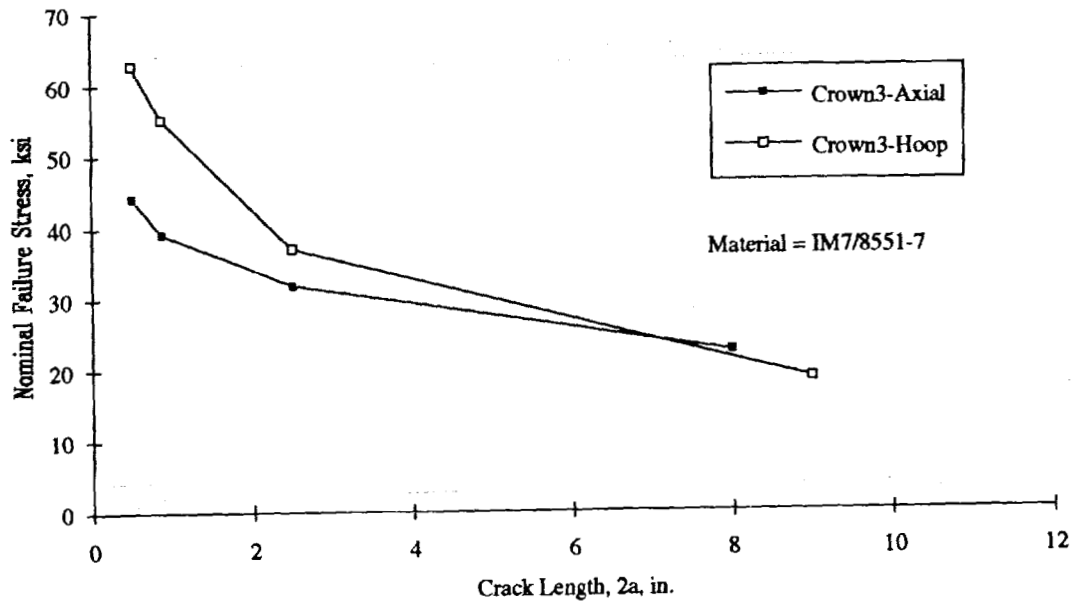


Figure 14. Laminate influence on fracture strength of IM7/8551-7.

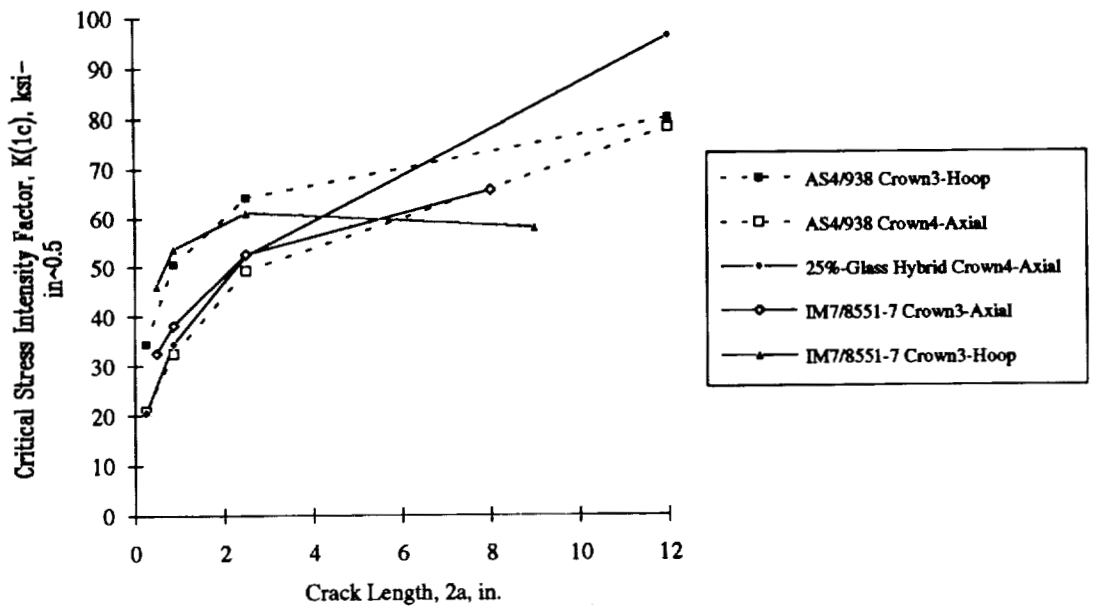


Figure 15. Convergence of classical fracture toughness with increasing crack length.

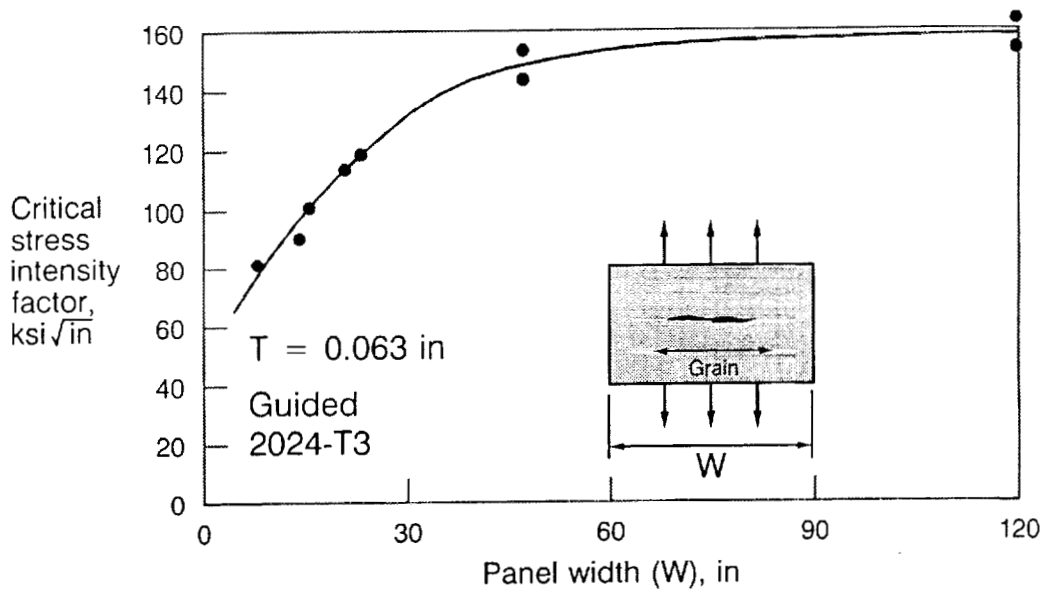


Figure 16. Plane-stress fracture toughness convergence of 2024-T3 (Ref. 9).

ANALYSIS OF UNSTIFFENED RESULTS

Finite Width Corrections

Correcting failure strengths for finite width effects provides the basis for comparison of different specimen configurations. Numerical methods have been employed to show that isotropic finite width correction factors (FWCF) differ from their orthotropic counterparts by less than 3% for specimen-width-to-crack-length ratios ($W/2a$) greater than 2 (Refs. 10, 11). Any of the several expressions for isotropic FWCFs may therefore be used. In the current studies, the nominal notched strengths for specimens with $W/2a = 4$ and 8, corrected for finite width according to

$$\sigma_N^{\infty} = FWCF * \sigma_N \quad (1)$$

where

$$FWCF = \sqrt{\sec\left(\frac{\pi a}{W}\right)} \quad (2)$$

(Ref. 10) were used to further assess the validity of using isotropic FWCFs. The isotropic FWCFs for these two cases are approximately 4% and 1%, respectively. If the finite-width correction factor properly accounts for all differences between the two specimen geometries, the datasets for each of these $W/2a$ values should fall on a single curve when the corrected strengths are plotted versus notch length.

Four laminate/material combinations were evaluated in such a manner. For each of these combinations, the FWCFs were underpredicted for the $W/2a = 4$ specimens, although by less than previously observed for $W/2a = 2$ data when compared with $W/2a = 4$. Representative comparisons are contained in Figures 17 and 18. As indicated in Reference 3, specimen edge-delamination, crack-tip softening due to matrix damage, and buckling adjacent to the unsupported crack surfaces may result in larger interactions between the notch-tip stress field and the specimen edges than analytically predicted.

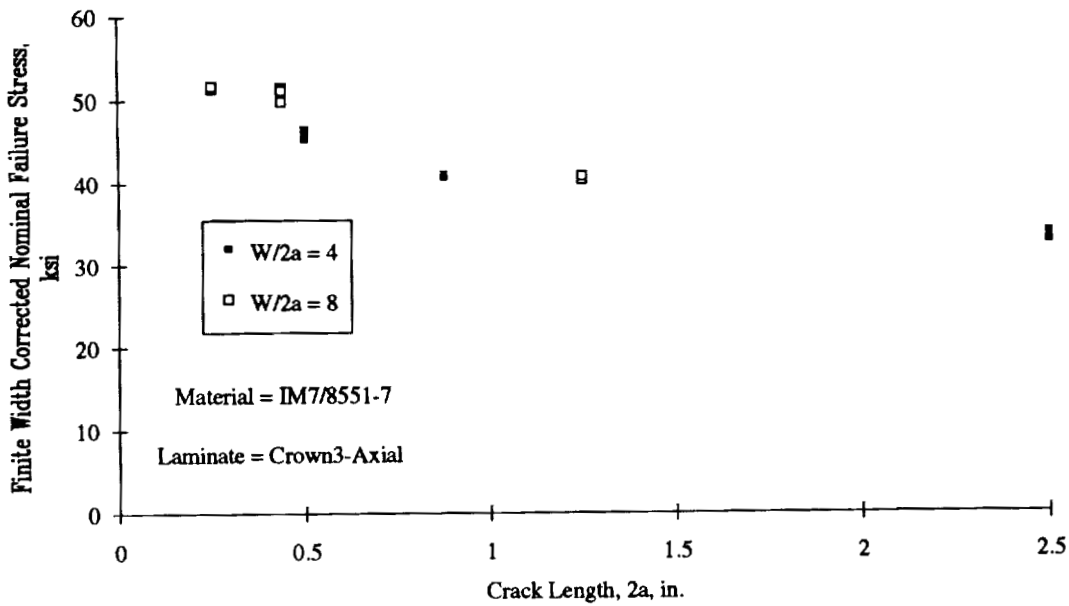


Figure 17. Comparison of finite width corrected strengths for IM7/8551-7 specimens with $W/2a = 4$ and $W/2a = 8$.

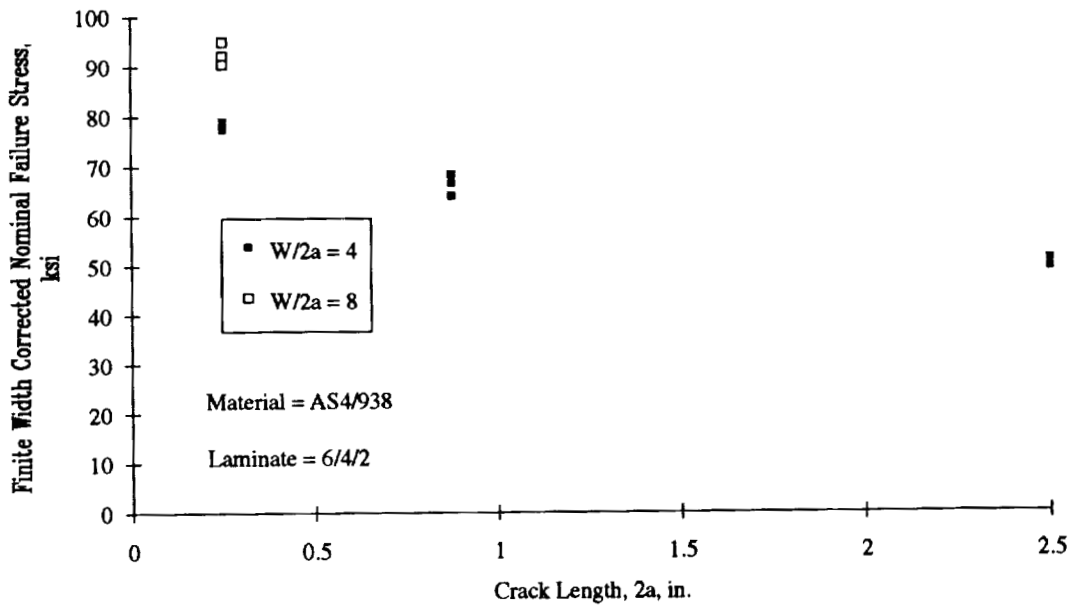


Figure 18. Comparison of finite width corrected strengths for AS4/938 specimens with $W/2a = 4$ and $W/2a = 8$.

Comparison with Experimental Strengths

Previous evaluation of strength prediction models focused on four primary candidates: linear elastic fracture mechanics (LEFM), Whitney-Nuismer point stress (WN), Poe-Sova (PS), and Mar-Lin (ML). Reference 3 contains a brief discussion of these methods and compares the functionality of each. Several major behavioral characteristics were noted when all methods were calibrated through a single notch-length/failure-strength point. For this calibration, the unnotched strength used in the LEFM, WN and PS methods was assumed to be the product of the laminate modulus and the fiber failure strain. For the ML method, the exponent was assumed, leaving only the composite fracture toughness to be determined.

The WN and PS methods were found to be functionally equivalent. The effect of the characteristic dimensions used in these methods is to reduce the small notch strength predictions from the parent LEFM curve. As crack lengths increase, differences between these characteristic-dimension methods and LEFM converge to a constant value that is small in comparison with the prediction. The order of the stress singularity in the vicinity of the crack tip controls the large notch strength, with reduced singularities predicting higher strengths. Comparison with experimental results indicated that these reduced singularities were required to accurately predict the large notch strengths from smaller notch strengths for most material/laminate combinations tested. The lone exception to this finding was an IM7/8551-7 laminate.

Similar evaluations were conducted in the current study for the 5 laminate/material combinations for which large notch strengths were obtained. In each case, the LEFM, PS, and ML methods were calibrated through the average strength with a 2.5 in. notch. The ML exponent, n , was varied to determine the singularity providing the best prediction of the largest-notch strength. The results for the two IM7/8551-7 laminates are shown in Figures 19 and 20. For the stiffer Crown3-Hoop laminate, LEFM and PS ($n = 0.5$ for both methods) provided the best correlation with the largest notch strengths, while for the less-stiff Crown3-Axial laminate, the ML method with $n = 0.3$ provided good results. A similar *trend* was observed in the results obtained from the AS4/938 laminates, shown in Figures 21 and 22, although at a reduced singularity value. The stiffer Crown3-Hoop laminate required $n = 0.3$, while the softer Crown4-Axial laminate required $n = 0.2$. The results for the hybrid laminate, shown in Figure 23, indicated the need for $n = 0.1$.

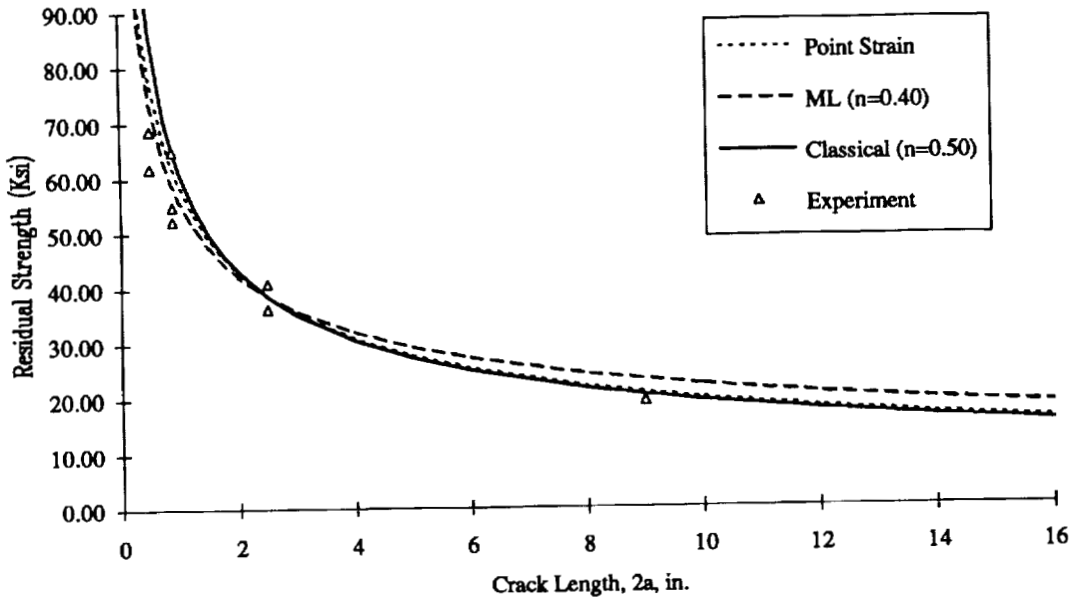


Figure 19. Comparison of IM7/8551-7, Crown3-Hoop experimental results with different failure criteria.

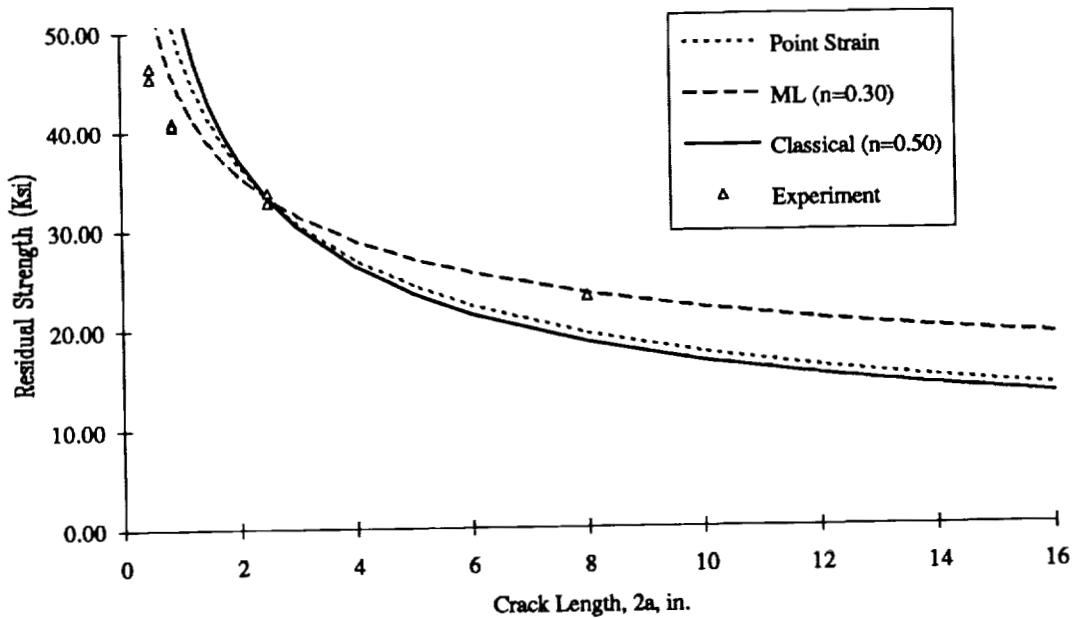


Figure 20. Comparison of IM7/8551-7, Crown3-Axial experimental results with different failure criteria.

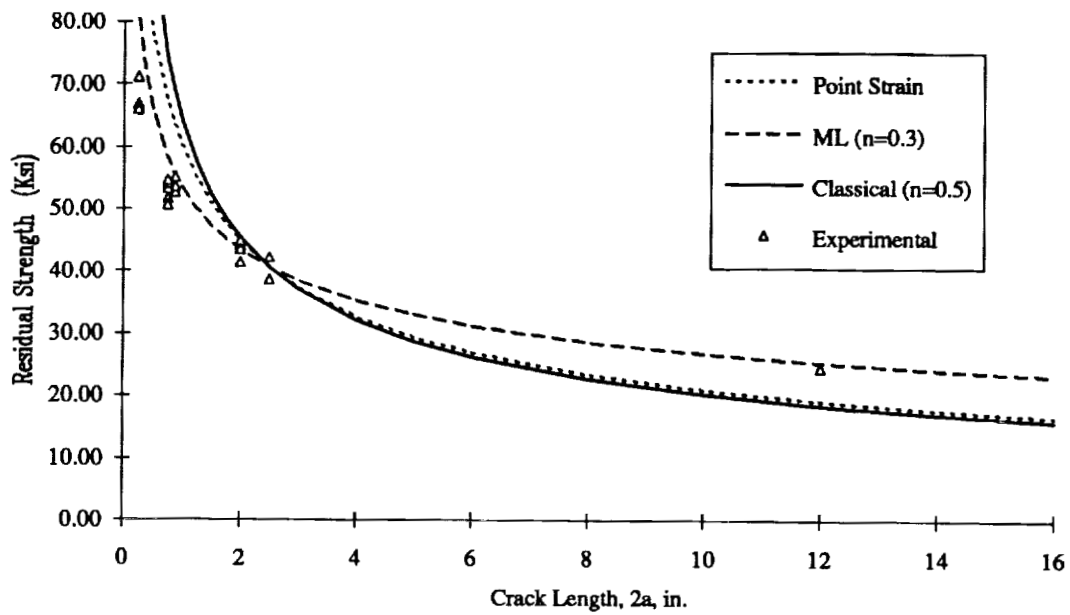


Figure 21. Comparison of AS4/938, Crown3-Hoop experimental results with different failure criteria.

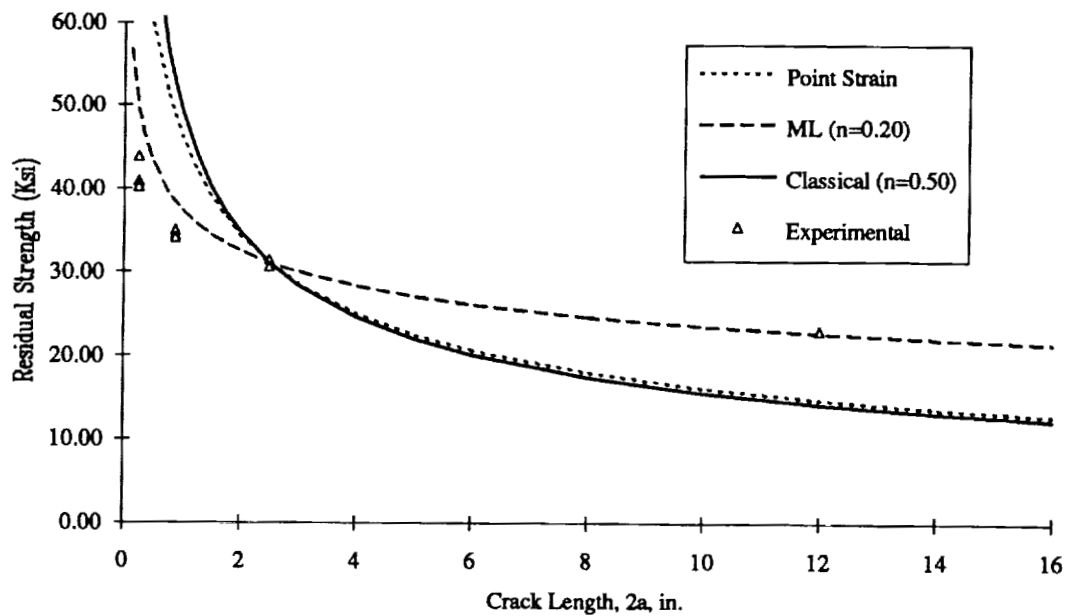


Figure 22. Comparison of AS4/938, Crown4-Axial experimental results with different failure criteria.

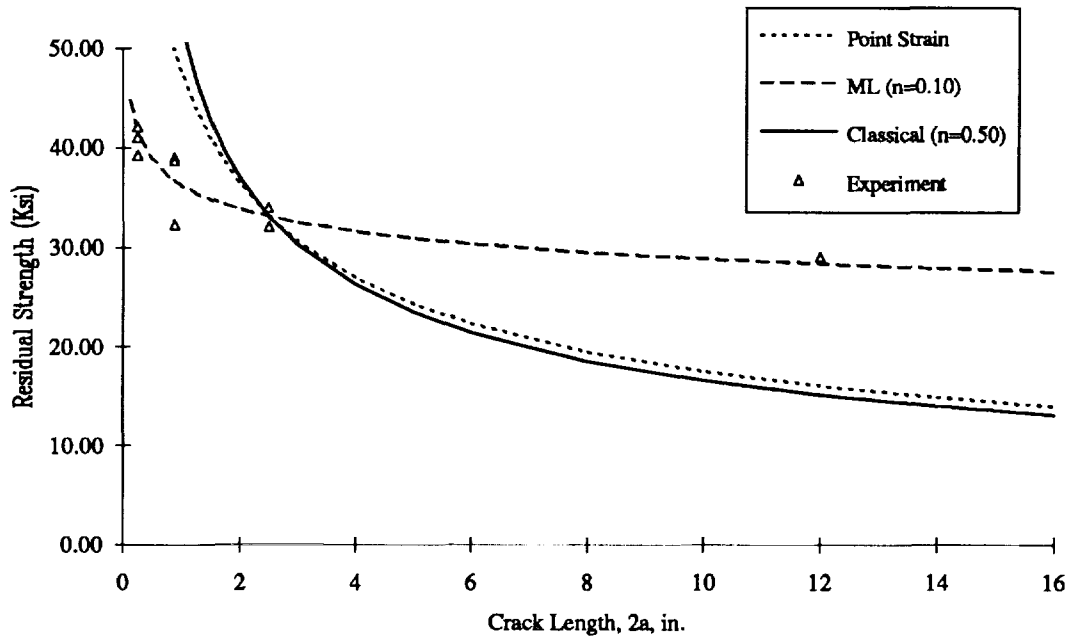


Figure 23. Comparison of 25%-Glass Hybrid, Crown4-Axial experimental results with different failure criteria.

The best-fit curves for the large-notch laminate/material combinations are shown in Figure 24. Variations in laminate and material can result in strengths that differ by a factor of 2 at large notch sizes representative of damage tolerance scenarios. For a stiffened panel design controlled by tension loads and large damage tolerance, selection of the most desirable laminate/material combination for skin and stiffener can help optimize weight and associated cost.

Most of these results suggest that methods based on the classical square-root stress-field singularity are not capable of predicting strengths for a large range of notch sizes, and that reduced-singularity methods may be more accurate. It is important to understand, however, whether the reduced-singularity stress fields are physically occurring, or whether the methods are just accounting for the effects of pre-failure damage. As discussed in reference to Figures 15 and 16, convergence to a true plane-stress fracture toughness (assuming a square-root singularity) may require very wide specimens. Net section yielding for narrow coupons or small notches tends to mask the true fracture properties of high toughness aluminum alloys such as 2024-T3 unless nonlinear methods (e.g., J-integral) are used to interpret test results.

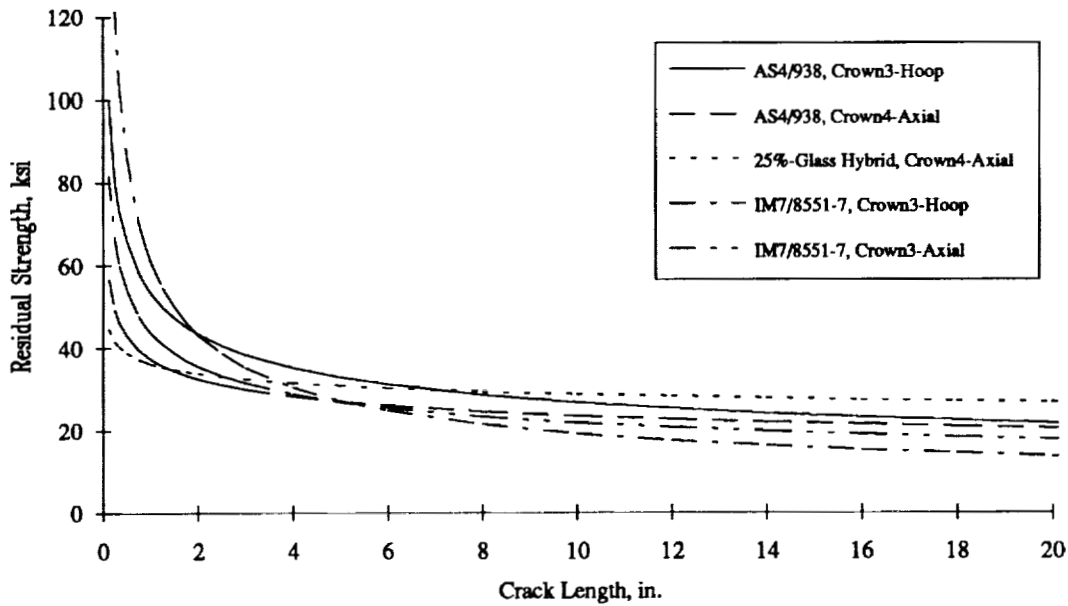


Figure 24. Comparison of theoretical predictions for all laminate/material combinations tested with large notches.

Comparisons with Measured Crack-Tip Strain Distributions

To determine the behavior of the crack-tip strain field, strains measured on the larger panels *prior to any crack-tip damage creation* were compared with theoretical prediction based on a relationships for a through-thickness crack in an specially orthotropic material subjected to mode I loading (Ref. 12). The strain predictions as a function of the distance ahead of the crack tip, r , are given by

$$\epsilon_y(r) = \epsilon_y^{\infty} \xi \sqrt{\frac{a}{2r}} * FWCF \quad (3)$$

where

$$\xi = \left[1 - \nu_{yx} \sqrt{\frac{E_x}{E_y}} \right], \quad (4)$$

$FWCF$ is the finite-width correction factor given in equation (2), ϵ_y^{∞} is the far-field strain (taken as the measured value for predictive purposes), and a is the half-crack length. This relationship is accurate for distances ahead of the crack tip that are less than 10% of the crack length. A method for predicting *strain* distributions ahead of the crack tip in a reduced-singularity stress field was sought but not located in the literature.

The comparisons for each of the five large-notch laminate/material combinations are contained in Figures 25 through 29. As shown in Figure 25, the Crown3-Hoop IM7/8551-7 laminate most closely matches the predicted strain distribution. As previously discussed, failure predictions for this laminate/material combination were also most accurately predicted using the classical square-root stress-field singularity. All other laminates exhibited measured strains significantly higher than predicted over most of the distances considered. In several cases, the measured strains indicated a possible cross-over approaching the crack-tip, with the actual strains being lower than predicted. The higher-than-predicted strains may account for the previously discussed underprediction of finite width effects.

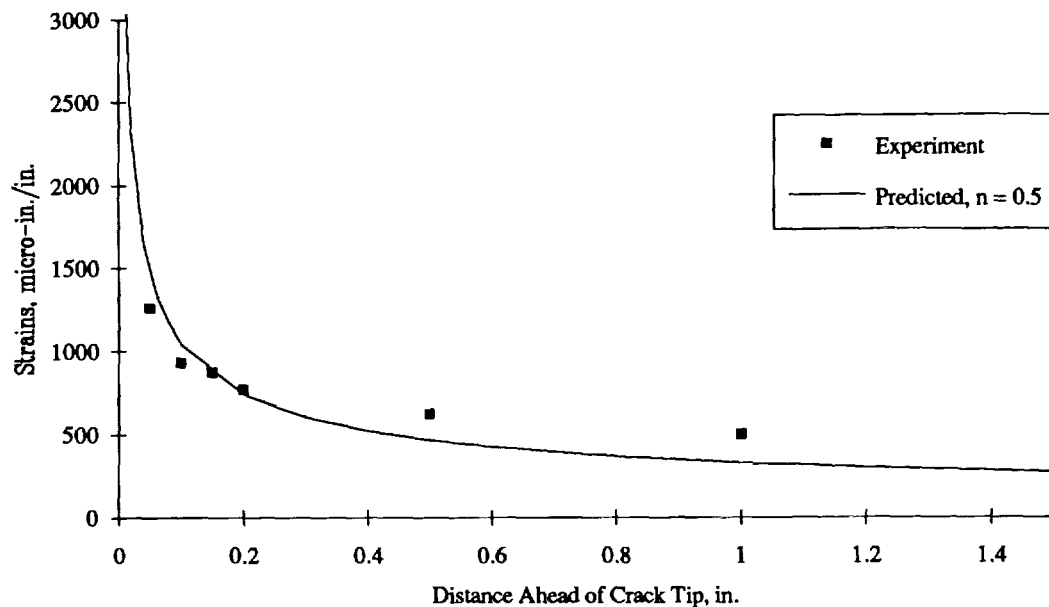


Figure 25. Comparison of predicted and measure crack-tip strains for IM7/8551-7, Crown3-Hoop laminate with an 9 inch notch.

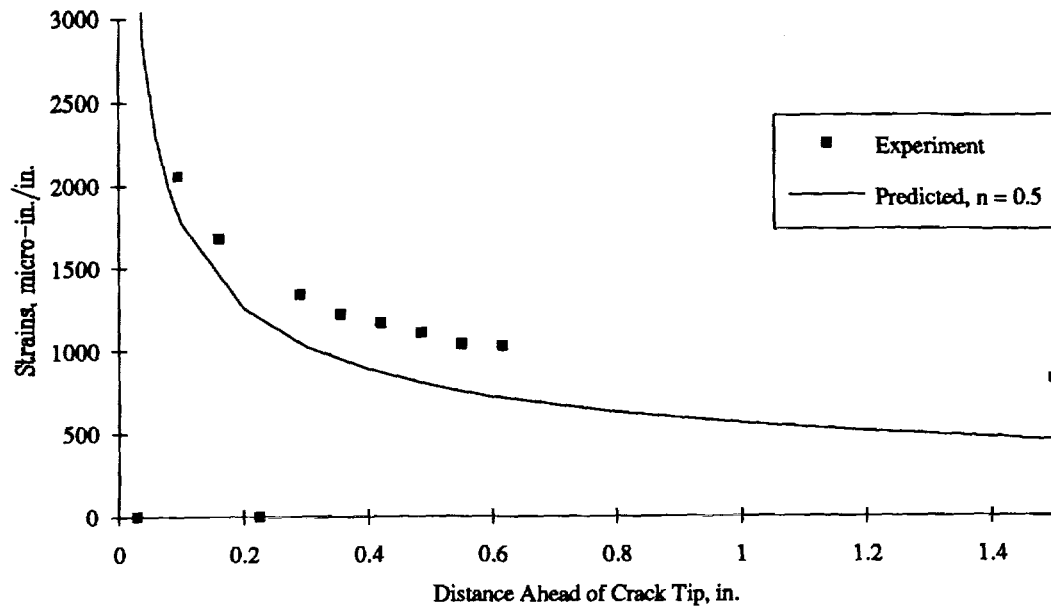


Figure 26. Comparison of predicted and measure crack-tip strains for IM7/8551-7, Crown3-Axial laminate with an 8 inch notch.

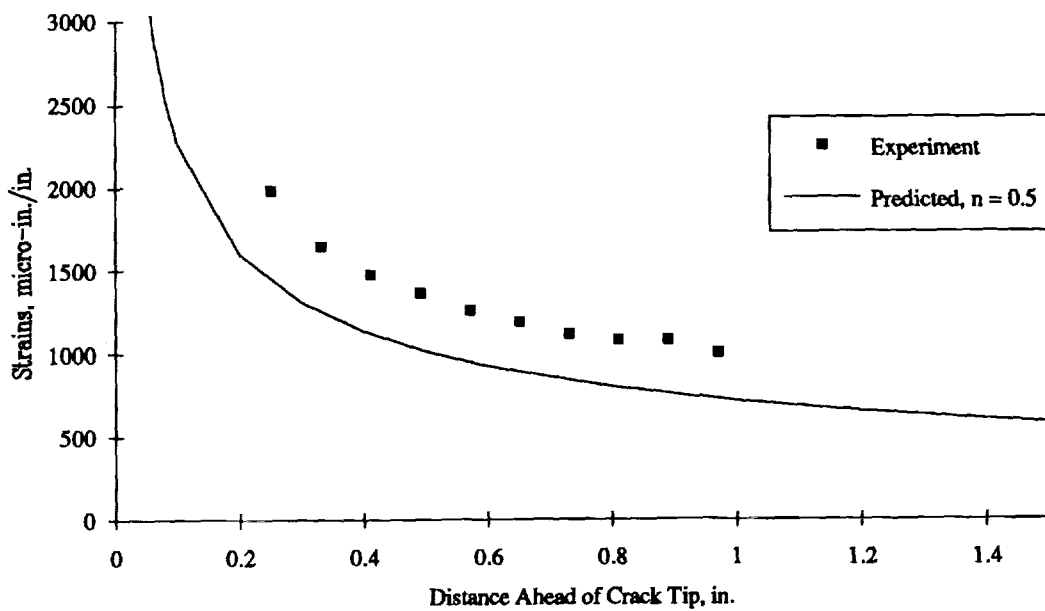


Figure 27. Comparison of predicted and measure crack-tip strains for AS4/938, Crown3-Hoop laminate with a 12 inch notch.

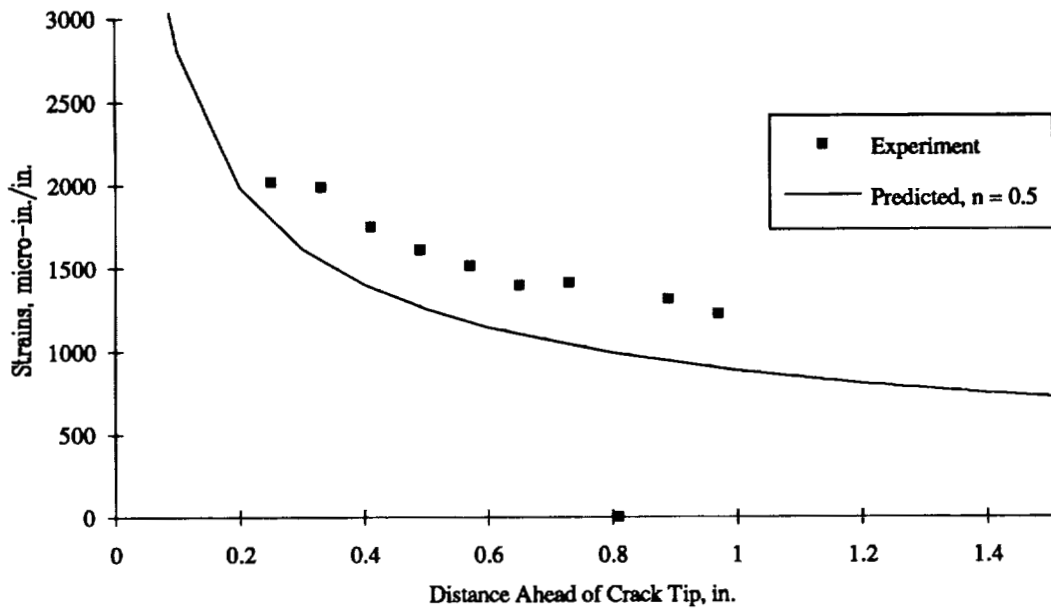


Figure 28. Comparison of predicted and measure crack-tip strains for AS4/938, Crown4-Axial laminate with a 12 inch notch.

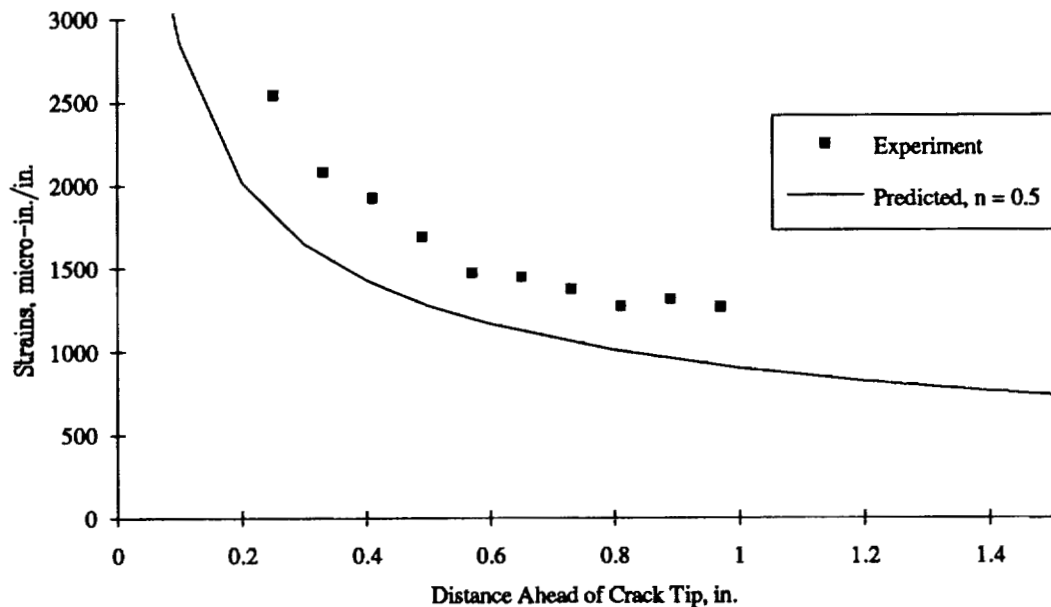


Figure 29. Comparison of predicted and measure crack-tip strains for 25%-Glass Hybrid, Crown4-Axial laminate with a 12 inch notch.

Another interesting characteristic, seen most clearly in Figures 28 and 29, are the undulations in the measure strains. Undulations of similar magnitude have been analytically observed over similar distances using simplified models of the larger scale of repeatable material inhomogeneity (Ref. 13). This implies that such inhomogeneities are affecting the response of the tow-placed laminates, and may be the cause of the high measured strains. In addition, it gives further support to the hypothesis that such inhomogeneities are related to the improved tension-fracture performance of the tow-placed laminates. Additional work is planned to generate more detailed models of tow-placed microstructure.

Alternative methods of accounting for the inhomogeneous microstructures of composites include generalized continua. Additional degrees-of-freedom that account for local rotation exist in Cosserat theories. These theories have found some application to mechanics problems involving stress concentrations in composites (e.g., Refs. 14, 15) and metals (Ref. 16). Attempts will be made to apply Cosserat theories to predict strain distributions shown in Figures 25 through 29.

Strain plots in this section suggest that past empirical modifications to fracture mechanics for thin composite laminates (e.g., characteristic dimension corrections, reduced singularities) correct for more than pre-catastrophic damage. Hypothetically, some composites smear the notch stress concentration over a wider area, resulting in stronger interactions with plate boundaries. As pre-catastrophic damage accumulates, such interactions are expected to become stronger. Future analysis developments are needed to quantify these effects, since they have important implications to scaling test results, material selection, and design for structural load sharing. Without analysis, expensive large-scale tests will be needed to show the full potential of composites.

STIFFENED PANEL RESULTS

Experimental

The failure strengths for the two 5-stringer flat fracture panels are compared with those for the unstiffened panels of the same skin laminate in Figure 30. Both panels failed in a nearly identical pattern. From each crack tip, a damage zone progressed in a stable manner within the skin to the adjacent stringer. Strain gages on adjacent stringers showed higher strains as skin damage approached, indicating increased load sharing that helped arrest the damage. The final failure sequence was initiated by the extension of a shallow skin delamination beyond the adjacent stringers, decoupling them from the majority of the skin, reducing load transfer to the stringers, and allowing catastrophic skin damage growth. Since the failure was controlled by the skin fracture (i.e., growth to the adjacent stiffeners and beyond, following loss of local load sharing with the stiffeners), it is not surprising that the 23% improvement observed between the graphite and hybrid panels in the unstiffened configuration was almost identically translated into the stiffened configurations.

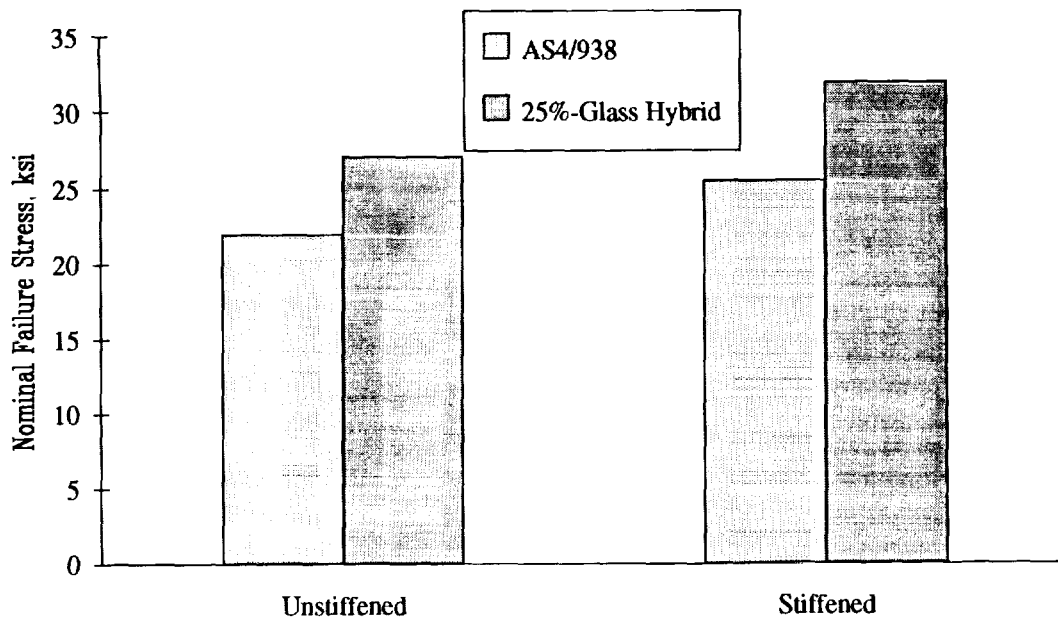


Figure 30. Failure strengths of unstiffened and stiffened fracture panels.

Analytical Considerations

A thorough discussion of failure predictions for the stiffened panels will be addressed in future documents. Briefly, however, accurate predictions for both of these panels were obtained using the following approach. The panel failure *strain* was obtained by predicting the fracture stress for a 2-bay (28 inch) notch in an *unstiffened* skin using the ML method and dividing this stress by the skin modulus. The ML parameters were obtained from small and large notch test results for the skin laminate. The panel failure *load* was then obtained by multiplying the predicted failure strain by the axial stiffness of the *stiffened* panel. This technique implicitly assumes (a) structural redundancy is such that with a severed element, the skin damage effectively grows to the adjacent stringers in a stable manner, and (b) after damage grows under the stiffener, load sharing becomes negligible and final failure occurs at the skin failure strain for a 2-bay notch.

While this method accurately predicted the two panels tested, more general methods are required to address the wide variety of structural arrangements and damage locations encountered on commercial fuselage. These methods must successfully address the three primary failure mechanisms: skin fracture, stiffener strength, and skin/stiffener debonding. The importance of skin fracture is indicated by its control of the failure of both stiffened panels. The effect of stiffening elements on load redistribution is also important, both in terms of (a) predicting stiffener strength and (b) the effects of skin stress reduction on damage progression. The significance of this latter issue is illustrated by the similarity of the damage-progression and failure sequences exhibited by the two stiffened-panel tests.

The ML method with variable singularity has demonstrated the ability to semi-empirically predict skin failure for a wider range of crack lengths. However, it is limited to use as an interpolation tool or as applied in Reference 3 for conservative extrapolation. In addition, if it does not accurately predict the stress and strain distributions prior to any crack-tip damage formation, it is not useful in predicting structural load redistribution as the damage zone progresses.

The finite element method appears to provide the flexibility and accuracy for a multitude of configurations encountered in aircraft structure. Two methods exist to account for the effects of damage progression on load redistribution in finite element models. Progressive damage methods that degrade various stiffness properties of individual elements as specified failure criteria are met (e.g. Ref. 17) have shown some success in modeling damage growth in specimen configurations. The magnitude of the calculations, however, provides a significant obstacle to incorporating them into the complex models required for stiffened structure.

Strain-softening models (e.g., Ref. 18, 19), however, appear to have the required simplicity. Such models have been successfully used in the reinforced concrete industry, and provide the ability to capture the global load redistribution that occurs as the crack-tip region is softened by damage formation, without the computational concerns of detailed progressive damage models. These strain softening models use a nonlinear stress-strain law that allows for a decreasing load-carrying capability of the material as strains increase beyond a critical value, as shown in Figure 31. A range of softening laws have been proposed. In finite element models, nonlinear springs can be used to simulate this behavior. The models can be calibrated using small-notch test results, then extended to large-notch configurations. Issues associated with modeling and calibrating bending stiffness reductions are being evaluated. These reductions are of concern for most structural configurations, where out-of-plane loading, load eccentricities, and bending loads are common.

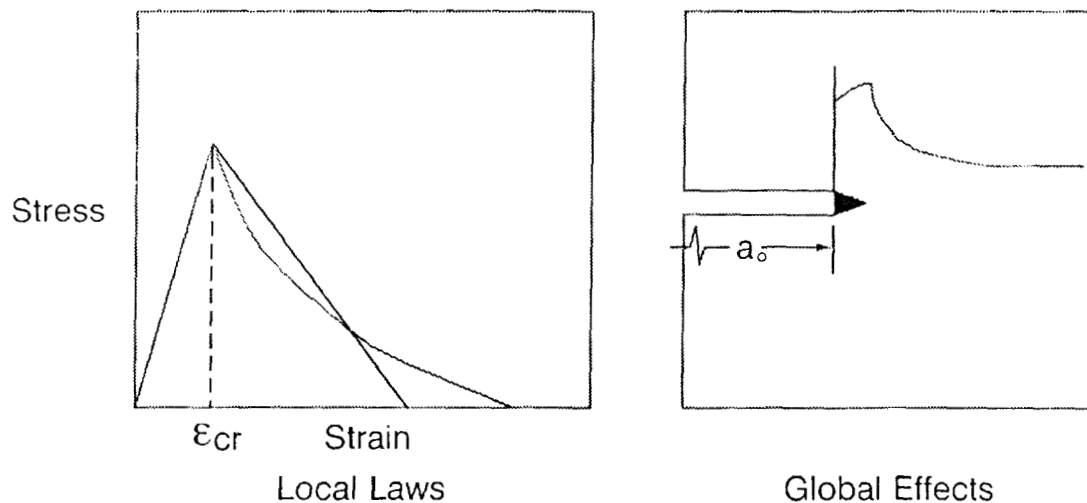


Figure 31. Strain-softening modeling approach.

CONCLUSIONS

Collaborative efforts between Boeing and NASA have continued to address the issues associated with transport fuselage pressure damage tolerance. Previous test results from 430 flat fracture coupons were augmented with an additional 200 coupons and extended into the large-notch and structural regimes with 5 large unstiffened panels and 2 large stiffened panels.

The additional tests confirmed some earlier findings and identified additional behaviors. Tow-placed laminates continue to exhibit 10 to 25% performance improvements over identical tape laminates. Large notch results indicated a trade-off between strength (small-notch strength) and toughness (large-notch strength), as shown in Figure 32. Higher strength but lower toughness resulted from toughened-resin materials and hard (0° -dominated) laminates. Lower strength and higher toughness was caused by brittle-resin materials, soft laminates and intraply hybridization with S2-Glass. Larger scales of repeatable material inhomogeneity appeared to result in improved toughness with little effect on strength. Matrix toughness appeared to have a larger influence on the behavior than laminate type.

Other performance characteristics were also identified. Temperature had little effect on 0° -dominate laminates but reduced strengths of 90° -dominated laminates by approximately 10%. Differing intraply hybridization architectures resulted in differing damage progression and distinct sensitivities to changes in notch length.

Classical methods of correcting for finite specimen width were found to underpredict actual width effects for relatively benign specimen geometries. This confirmed earlier

findings for more severe configurations and indicates that the stress/strain distributions within the coupons do not conform to the assumptions of the classical methods. Similar problems are expected when trying to quantify structural configuration factors. This has important considerations relating to efforts to standardize material screening tests and structural scaling laws. An understanding of the effects of specimen geometry and interactions with material type and laminate layup are essential to optimal material selection and structural design.

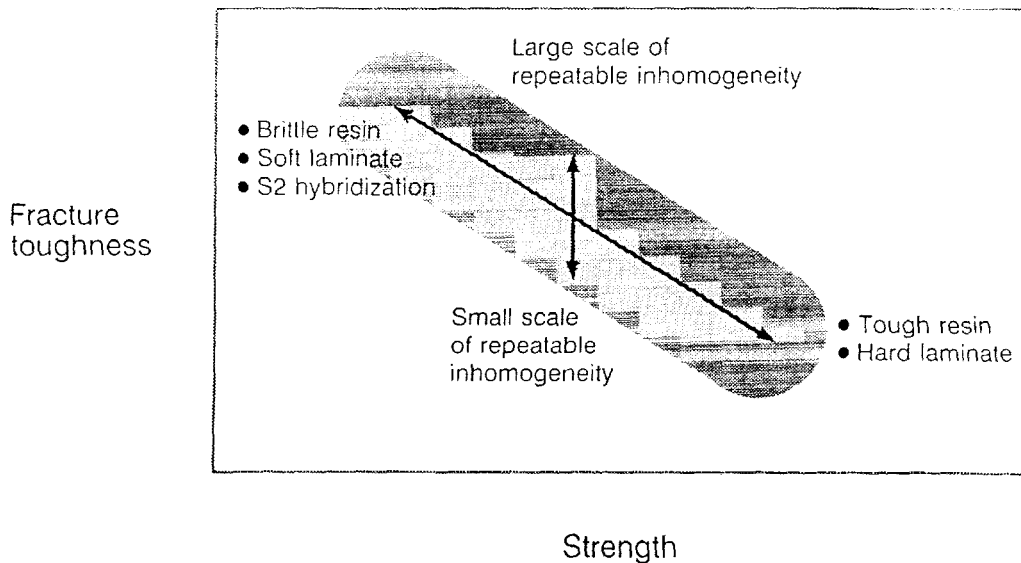


Figure 32. Strength-toughness trade-off in composite materials.

Classical fracture strength models were found to be inaccurate for predicting the large-notch strengths of four of the five laminate/material combinations tested. Measured pre-damage crack-tip strain distributions were significantly higher than assumed in classical methods for the same four laminate/material combinations. The exception in both cases was a 0° -dominate laminate fabricated from IM7/8551-7. The higher strains may result in (a) finite width effects that are stronger than expected and (b) inaccurate strength predictions. The Mar-Lin method was found to predict the large-notch strengths from small notch results through the use of a reduced stress-field singularity. Variations in the singularity modeled the differing sensitivities to changes in notch lengths observed in the test results.

Two stiffened panel fracture tests, each with a severed skin-bay and stiffening element, were conducted. The panel fabricated from AS4/938 exhibited a strength approximately 23% below that of an identical panel fabricated from an intraply hybrid of 25% S2/938 and 75% AS4/938. Skin fracture controlled the final failure of both panels, with load redistribution to the intact stiffening elements significantly affecting the damage growth prior to failure. Strain softening models were identified as attractive for addressing the global load redistribution effects of local damage progression.

REFERENCES

1. Ilcewicz, L. B., Smith, P. J., and Horton, R. E., "Advanced Composite Fuselage Technology," *3rd NASA Advanced Composites Technology Conference*, NASA CP-3178.
2. Smith, P. J., Koch, W. J., Bodine, J. B., and Preuss, C. H., "Design, Analysis, and Fabrication of a Pressure Box Test Fixture for Tension Damage Tolerance Testing of Curved Fuselage Panels," *3rd NASA Advanced Composites Technology Conference*, NASA CP-3178.
3. Walker, T. H., Avery, W. B., Ilcewicz, L. I., Poe, C. C., Jr., and Harris, C. E., "Tension Fracture of Laminates for Transport Fuselage - Part I: Material Screening," *Second NASA Advanced Technology Conference*, NASA CP 3154, pp. 197-238, 1991.
4. Broek, D., *The Practical Use of Fracture Mechanics*, Kluwer Academic Publisher, 1989.
5. Chang, J. B., and Rudd, J. L. (eds.), *Damage Tolerance of Metallic Structures: Analysis Methods and Applications*, ASTM STP 842, 1984.
6. Willden, K., Metschan, S., Grant, C., and Brown, T., "Composite Fuselage Crown Panel Manufacturing Technology," *Second NASA Advanced Technology Conference*, NASA CP 3154, pp. 263-291, 1991.
7. Poe, C. C., Jr., and Kennedy, J. M., "An Assessment of Buffer Strips for Improving Damage Tolerance of Composite Laminates," *J. of Composite Materials Supplement*, Vol. 14, pp. 57-70, 1980.
8. Kennedy, J. M., "Damage Tolerance of Woven Graphite/Epoxy Buffer Strip Panels," NASA TM 102702, 1990.
9. Swift, T., "Damage Tolerance in Pressurized Fuselages," *14th Symposium of the International Committee on Aeronautical Fatigue - New Materials and Fatigue Resistant Aircraft Design*, 1987.
10. Awerbuch, J., and Madhukar, M. S., "Notched Strength of Composite Laminates: Predictions and Experiments -- A Review," *J. of Reinforced Plastics and Composites*, Vol. 4, pp. 1-159, 1985.
11. Konish, H. J., Jr., "Mode I Stress Intensity Factors for Symmetrically-Cracked Orthotropic Strips," in *Fracture Mechanics of Composites*, ASTM STP 593, American Society for Testing and Materials, pp. 99-116, 1975.
12. Poe, C. C., Jr., and Sova, J. A., "Fracture Toughness of Boron/Aluminum Laminates with Various Proportions of 0° and $\pm 45^\circ$ Plies," NASA Technical Paper 1707, 1980.

13. Cairns, D., Walker, T., and Ilcewicz, L., "Response of Automated Tow Placed Laminates to Stress Concentrations," *3rd NASA Advanced Composites Technology Conference*, NASA CP-3178.
14. Nakamura, S., and Lakes, R. S., "Finite Element Analysis of Stress Concentration Around a Blunt Crack in a Cosserat Elastic Solid," *Computer Methods in Applied Mechanics and Engineering*, Vol. 66, pp. 257-266, 1988.
15. Nakamura, S. Benedict, R., and Lakes, R. S., "Finite Element Method for Plane Micropolar Elasticity," *International Journal of Engineering Sciences*, Vol. 22, pp. 319-330, 1984.
16. Chong, W., and Zhi-Da, C., "Microrotation Effects in Material Fracture and Damage," *Engineering Fracture Mechanics*, Vol. 38, No. 2/3, pp. 147-155, 1991.
17. Chang, F. K., and Chang, K. Y., "A Progressive Damage Model for Laminated Composites Containing Stress Concentrations," *J. of Composite Materials*, Vol. 32, pp. 834-855, 1987.
18. Mazars, J. and Bazant, Z. P. (eds.), *Crackin And Damage: Strain Localization and Size Effect*, Elsevier Applied Science, 1988.
19. Llorca, J., and Elices, M., "A Cohesive Crack Model to Study the Fracture Behaviour of Fiber-Reinforced Brittle-Matrix Composites," *International Journal of Fracture*, Vol. 54, pp. 251-267, 1992.

Impact Damage Resistance of Composite

Fuselage Structure, Part 2¹

by

Ernest F. Dost, Scott R. Finn,

Daniel P. Murphy, and Amy B. Huisken

The Boeing Company, Seattle, WA

515-24
51415

Introduction

The strength of laminated composite materials may be significantly reduced by foreign object impact induced damage. An understanding of the damage state is required in order to predict the behavior of structure under operational loads or to optimize the structural configuration. Types of damage typically induced in laminated materials during an impact event include transverse matrix cracking, delamination, and/or fiber breakage. The details of the damage state and its influence on structural behavior depend on the location of the impact. Damage in the skin may act as a soft inclusion [1] or affect panel stability [2], while damage occurring over a stiffener may include debonding of the stiffener flange from the skin.

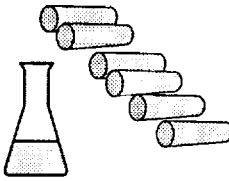
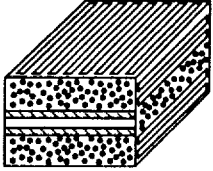
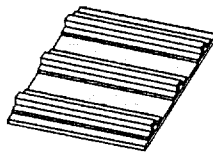
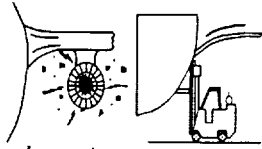
An experiment to characterize impact damage resistance of fuselage structure as a function of structural configuration and impact threat was performed [3]. A wide range of variables associated with aircraft fuselage structure such as material type and stiffener geometry (termed, intrinsic variables) and variables related to the operating environment such as impactor mass and diameter (termed, extrinsic variables) were studied using a statistically based design-of-experiments technique. The experimental design resulted in thirty-two different 3-stiffener panels. These configured panels were impacted in various locations with a number of impactor configurations, weights, and energies. The results obtained from an examination of impacts in the skin midbay and hail simulation impacts were documented in [3]. The current discussion is a continuation of that work with a focus on non-discrete characterization of the midbay hail simulation impacts and discrete characterization of impact damage for impacts over the stiffener.

¹ This work is being funded by Contract NAS1-18889, under the direction of J.G. Davis and W.T. Freeman of NASA Langley Research Center.

Nine variables associated with aircraft fuselage structure and six variables associated with potential foreign object impact threats were investigated to determine the relative importance of each variable to different composite failure modes. The intrinsic variable levels (e.g., 938 epoxy versus 977-2 toughened epoxy for the variable: Matrix type) were chosen based on performance and assembly requirements for a widebody transport aircraft fuselage. The extrinsic variable levels (e.g., flat versus spherical for the variable: Impactor shape) were selected to represent a wide range of potential threats from runway debris to dropped tools.

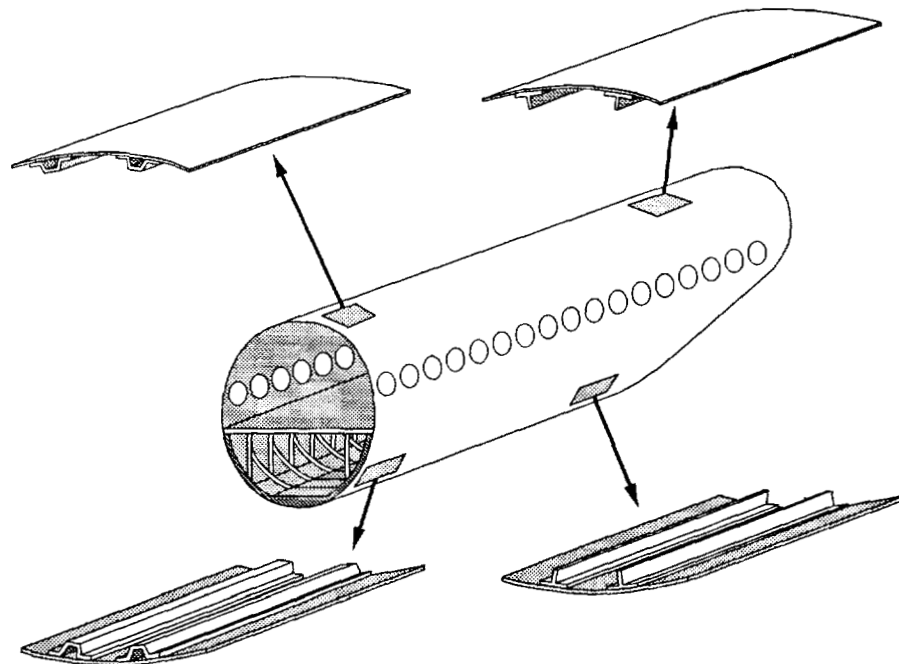
The experiment was designed as a fractional factorial, resolution IV designed experiment [4] in order to study this large number of variables with a relatively small number of specimens. Fourteen variables were included directly in a designed experiment which defined 32 three-stiffener panels. The fifteenth variable was built into each panel by placing a layer adhesive between the skin and two of the three stiffeners during panel assembly. One-hundred and ten inch long panels were fabricated which included both thick and thin sections of equal length, separated by a 10 inch tapered region. This introduced a split-plot aspect to the experiment [5], creating two sizes of experimental units. The intrinsic variables, except laminate thickness, are "whole-plot" variables, while the extrinsic variables along with laminate thickness are "sub-plot" variables. The highly fractionated nature of this experiment created some confounding of effects. Main effects are confounded with three-factor and higher order interaction effects, and two-factor interaction effects are confounded with other two-factor effects.

Intrinsic and Extrinsic Variables Studied

Intrinsic Variables			Extrinsic Variables
Material Variables	Laminate Variables	Structural Variables	
			
<ul style="list-style-type: none"> Fiber <ul style="list-style-type: none"> ● AS4 ● IM7 Resin <ul style="list-style-type: none"> ● 938 (3501-6) ● 977-2 Fiber volume <ul style="list-style-type: none"> ● 0.480 ● 0.565 Material form <ul style="list-style-type: none"> ● Tape ● Tow 	<ul style="list-style-type: none"> Stiffener layup <ul style="list-style-type: none"> ● Hard ● Soft Skin layup <ul style="list-style-type: none"> ● Hard ● Soft Thickness <ul style="list-style-type: none"> ● Thick <ul style="list-style-type: none"> ● Skin 0.18 in ● Stiffener 0.12 in ● Thin <ul style="list-style-type: none"> ● Skin 0.09 in ● Stiffener 0.06 in 	<ul style="list-style-type: none"> Stiffener type <ul style="list-style-type: none"> ● Blade ● Hat Stiffener spacing <ul style="list-style-type: none"> ● 7 in ● 12 in Stiffener adhesive layer <ul style="list-style-type: none"> ● With ● Without 	<ul style="list-style-type: none"> Impactor mass <ul style="list-style-type: none"> ● 0.62 lbm ● 13.9 lbm Impact energy (skin/stiffener) <ul style="list-style-type: none"> ● 200 in-lb/350 in-lb ● 1,200 in-lb/1,600 in-lb Impact temperature <ul style="list-style-type: none"> ● 70°F ● 180°F Impactor diameter <ul style="list-style-type: none"> ● 0.25 in ● 1.0 in Impactor tup shape <ul style="list-style-type: none"> ● Flat ● Spherical Impactor stiffness <ul style="list-style-type: none"> ● 0.4 Msi ● 30 Msi

The panel configurations and materials chosen for the impact damage resistance designed experiment are representative of a variety of locations around the fuselage. The fuselage crown is a tension dominated structure and hence a wide stiffener spacing and thin skin gages can be used. The fuselage lower side-panel on the other hand is combined compression/shear dominated and requires a close stiffener spacing and thicker gages. A matrix with high interlaminar toughness may be required for the lower side-panel when considering the high levels of impact energy resulting from runway debris impacts. The crown, however, has hail impact as a design criteria and may not require costly toughened materials to resist damage from these events. The panels built for this experiment have combinations of the variables covering a range of locations on the fuselage.

Fuselage Locations Represented by Test Panels

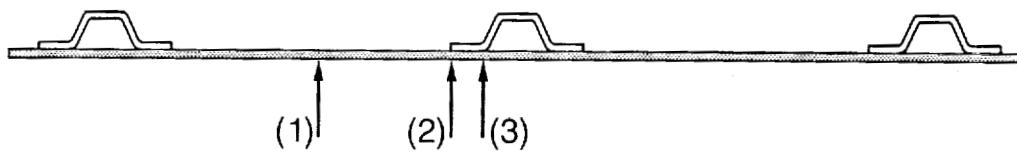


NASA/BOEING
ATCAS

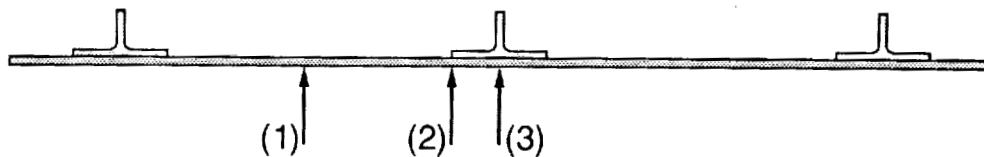
ED-03
FL2014.03 s

The damage states associated with the impact locations shown below were studied on all 32 impact damage resistance panels. These locations were believed to represent those most critical for stiffened structure of this sort. Various responses (e.g., C-scan area) were measured at each impact site. Statistical analyses of the results for each impact location were analyzed as if each location were a separate parallel experiment.

Impact Locations Studied



- (1) Hail simulation
- (2) Edge of stiffener attachment flange
- (3) Base of stiffener web



NASA/BOEING
ATCAS

ED-04
FL2014.04 s1h

The purpose of this experiment was to determine the response of configured fuselage structure to foreign object impact. The responses measured for the impact locations discussed previously included: a) maximum force during the impact event for the stiffener web and flange edge impacts, b) local flexural stiffness of the midbay hail simulation impacts, c) matrix damage associated with load redistribution failures, and d) matrix damage which could act as an initial flaw for stiffener separation under operational loads.

Measured Responses

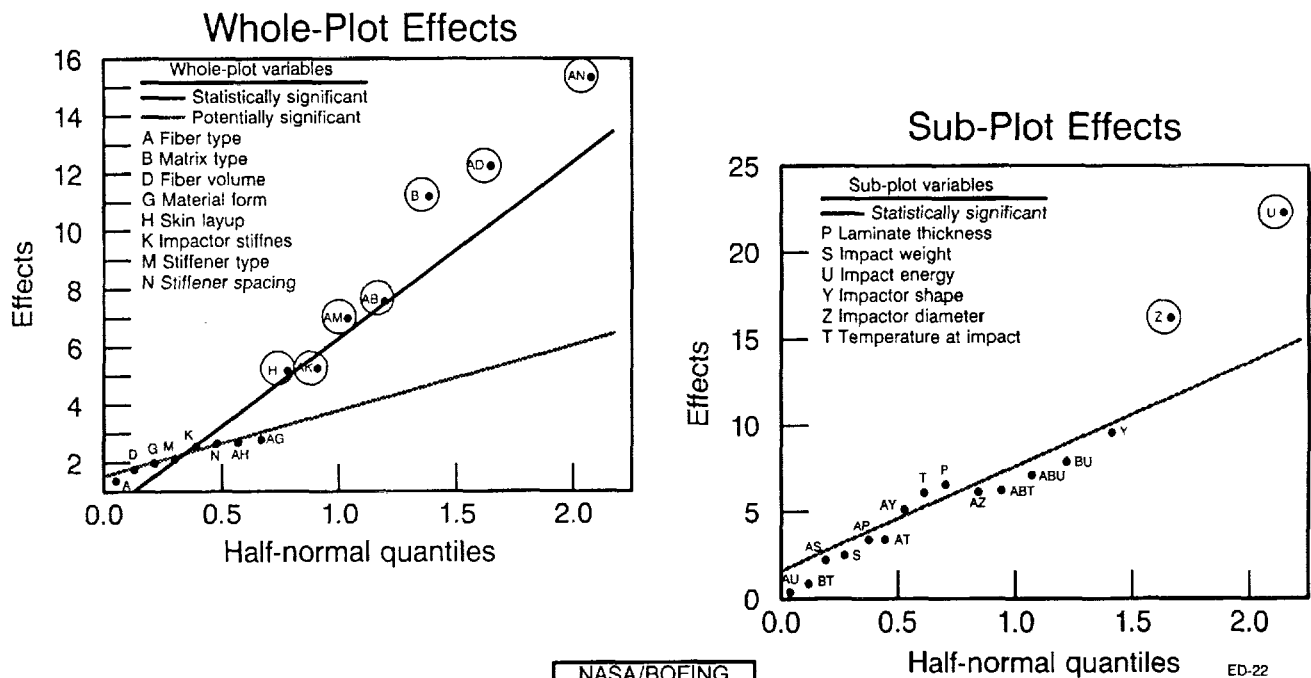
- Maximum force
- Local flexural stiffness
- Localized core-damage area
- Stiffener flange separation
 - Area (stiffener cocured with adhesive)
 - Area (stiffener cocured without adhesive)
 - Ratio (with adhesive/without adhesive)

The highly fractionated and non-replicated nature of this experimental design made it impossible to use a straightforward Analysis of Variance (ANOVA) model to analyze the data. In such situations, there are two different techniques which may be employed. The first is to use a reduced ANOVA model, in which some of the higher-order interactions are *a priori* assumed to be insignificant. The corresponding sums of squares are pooled to form a residual sum of squares which is used as an estimate of the experimental error. The second option is to construct half-normal plots [6] of the effect estimates. The split-plot [5] aspect of this experimental design made the pooling of higher-order interaction terms very arbitrary. For this reason, the second option was chosen to analyze the results.

The half-normal plot is a plot of the absolute values of the ordered effect estimates against $\phi^{-1}(i/(n+1))$, where i is the rank of the particular effect estimate, n is the number of effect estimates to be plotted, and ϕ^{-1} is the inverse of the standard normal probability distribution. This is based on the ANOVA assumption that the effect estimates will constitute a random sample from some normal distribution if no significant effects exist. A lack of significant effects will result in the half-normal probability plot being approximately linear. A large deviation from the linear pattern indicates a significant effect. The split-plot aspect of this experimental design was accounted for by constructing two half-normal plots, one corresponding to the whole-plot effects and the other to the half-plot effects.

Statistical Data Analysis

Half-Normal Plots

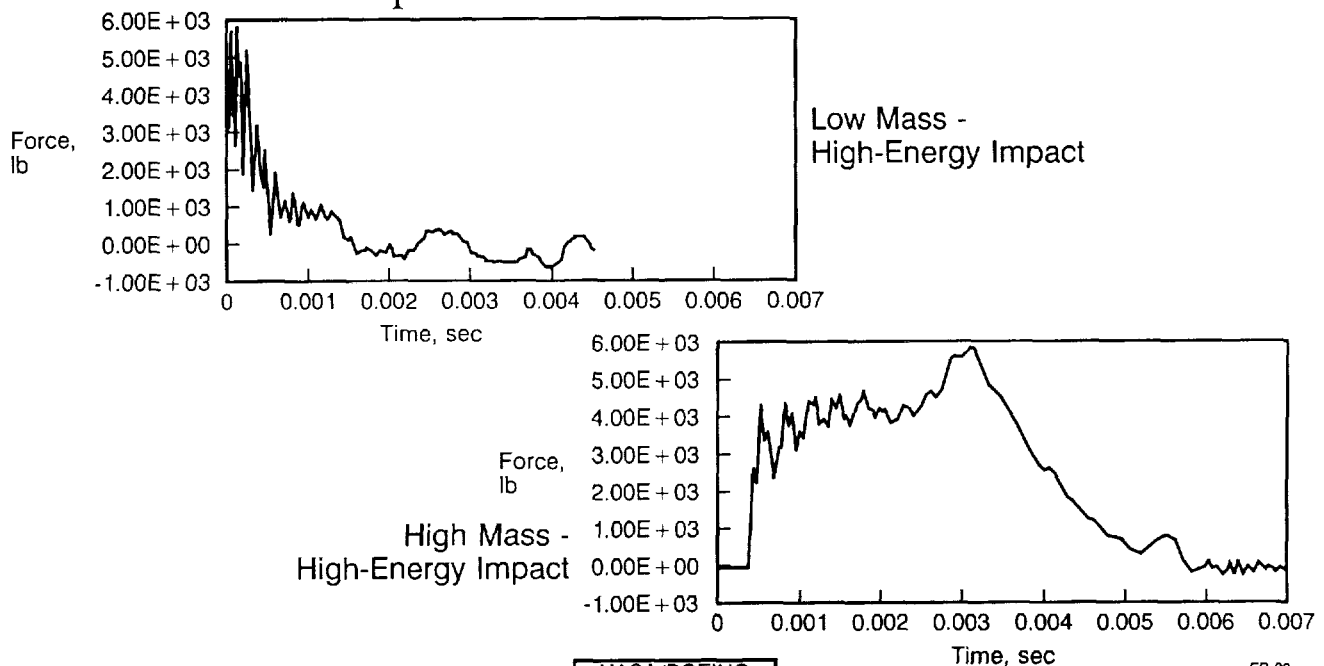


Response Measurement Definition

The majority of impacts were performed with an instrumented impactor (i.e., impactor contains a load cell). The load cell recorded impact force as a function of time, while initial impactor velocities were measured using a set of light gates. These data were numerically integrated to calculate velocity, displacement, and energy as a function of time [7]. Plotted below are force versus time results for both a high mass and a low mass impact on two different panels for a fixed impact energy level. A large number of different metrics can be defined to characterize these impact events, including the maximum force, force at first load drop, duration of the event, and frequencies of the oscillations. Additionally, calculated values such as maximum deflection or absorbed energy can be used to characterize the impact event. Recent work has suggested that maximum force may be a better measure than impact energy for comparing impact damage resistance on different sized parts. Therefore, for this study we selected maximum force as our response variable.

Maximum Force (During Impact Event)

Response Measurement Definition



NASA/BOEING
ATCAS

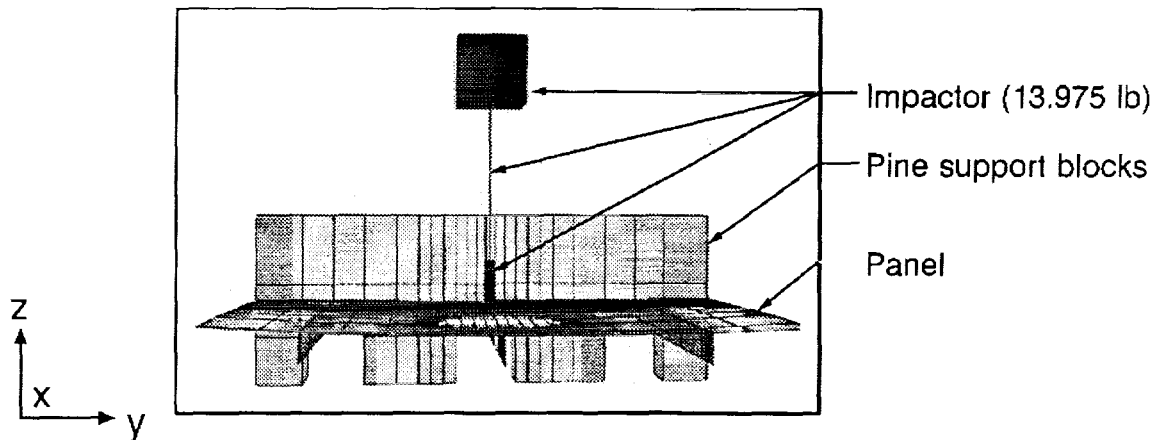
ED-20
FL2014.20 s1h

Finite element modeling of several of the impact events was performed to gain understanding into interactions of the stiffeners and skin, and the interactions of the impactor and panel. Such analyses, if sufficiently accurate, would provide valuable information pertaining to strain levels throughout the test specimen and would allow for extrapolation of test panel data to predict aircraft structure response. These analyses are technically very challenging in that they require the prediction of the dynamic response of an extremely nonlinear system. The large lateral deflections and coupling between the skin, stiffeners, and the clamped pine support blocks are complex.

Analytical simulations of six test events in which no detectable damage was found were conducted using the explicit, nonlinear structural dynamics finite element analysis code DYNA3D [8]. The critical distinction of an explicit code from the standard implicit code (e.g., NASTRAN, STAGSC-1) is that in solving a transient problem, the solution can be advanced in time without solving large systems of equations, (i.e., the equations of motion of a structural system are uniquely uncoupled). This permits the local incorporation of nonlinear phenomena such as plasticity, impact, penetration, and large deflections without having to periodically reformulate the entire problem.

The panels were modeled with shell elements and a linearly elastic orthotropic material description. Modeling the pine support blocks with solid elements was found to be a key factor in obtaining accurate results. Solid elements with linear elastic pine properties realistically reproduced the local out of plane rotation of the panel at its boundaries, which was shown to contribute as much as 40% of the lateral deflection as measured by the instrumented impactor. The impactor was modeled with solid elements for the tup, beam elements for the load cell, and lumped mass elements for the mass behind the load cell.

DYNA3D Model Geometry



Model Statistics

- 983 node points
- 212 continuum (8-node brick) elements
- 576 Hughes-Liu shell elements
- 3 Hughes-Liu beam elements
- Run time: 62 CPU sec - CRAY Y-MP

NASA/BOEING
ATCAS

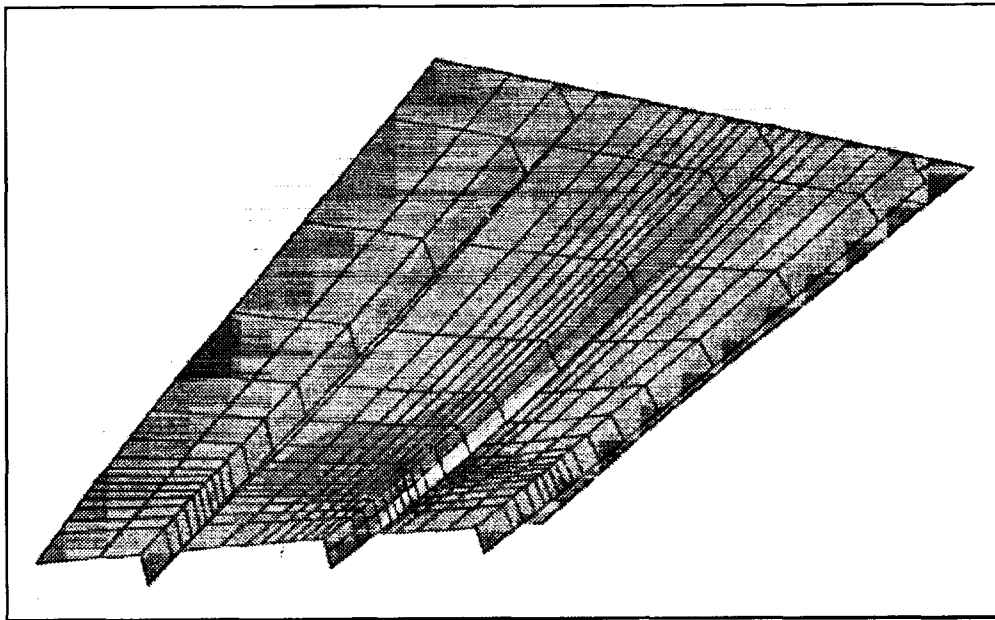
ED-05

FL2014HR.05 h/h

A large variety of computed values can be extracted from a DYNA3D simulation. Stresses, strains, forces, and the motion of the individual elements and node points can be plotted as a function of time. In addition, "snapshots" of the entire structure can be obtained at any time of interest within the period of simulation. The example shown here displays the deformed geometry of the model (wooden supports and impactor excluded for clarity) with the lower surface strains plotted on the structure. The magnitude of strain is indicated by the shades of gray distributed across the figure. These snapshots allow rapid identification of "hot spots" (i.e., areas of high strain) and areas of interest, while the time histories allow quick determination of the time and magnitude of maximum response. A series of snapshots can be combined, allowing for an animated display of the model response. By viewing its motion and a range of stress and strain components as their values vary with time, valuable insights to the response of the test event can be gained. The visual interaction of membrane and flexural modes is of particular interest, as is the time lag between the peak response in the panel and in the peak responses of the stiffeners.

DYNA3D Stiffener Impact Analysis

Surface Strains

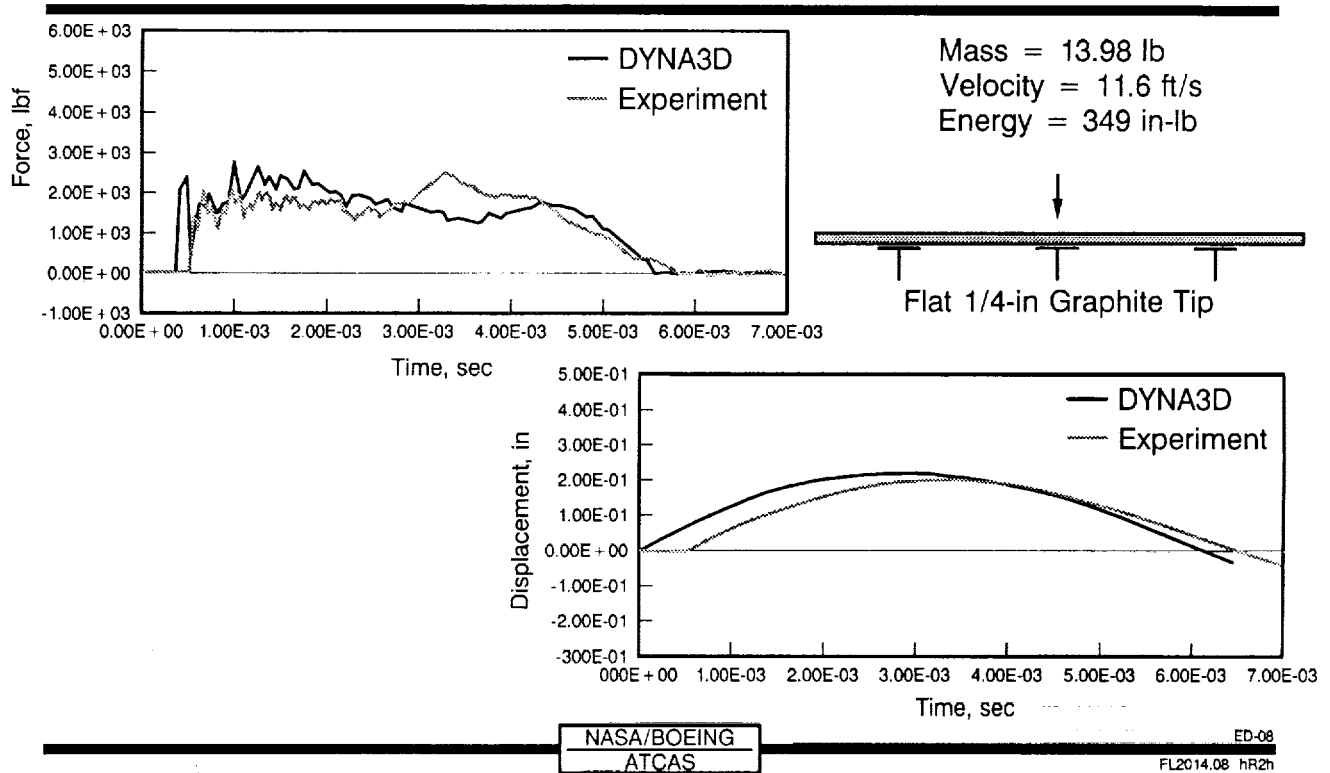


NASA/BOEING
ATCAS

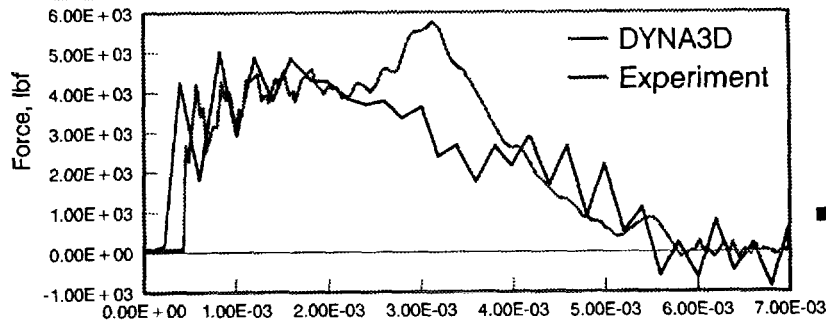
ED-06
FL2014HR.06 h1h

In the next two figures, the calculated responses are compared to test data for two impact events occurring over the centerline of blade stiffeners. Both of these tests were performed on "thick" panels with closely spaced stiffeners, resulting in a rather stiff target. Note that the time scale of the DYNA3D result is shifted to permit a distinction to be made from the test data. Note also that the impact energy for the second test is nearly five times that of the first, while the peak responses (force and displacement) are only doubled. In both tests the displacement response is very accurately predicted. In the force versus time comparisons, the duration of the low frequency response is very well predicted, as is the high frequency component of the response. Peak forces are, in general, accurately predicted for the first 2.5 milliseconds (msec) and the last 3 msec. However, at about 3 msec the analysis underpredicts the force levels. This has been observed in all of the studies made, and the source of the error is not completely understood. A local numerical instability of the finite elements representing the impactor tip (known as "hourglassing") is observed in this portion of the analysis, and may be responsible. However, further analyses should be conducted to investigate this effect further. Recovery of strain energy from indentation of the panel by the impactor might also be a source of additional force in the impactor's transducer. The shell elements used for all analyses to date cannot reproduce this phenomenon, but solid elements or nonlinear springs could easily be added to the impact region to explore this possibility.

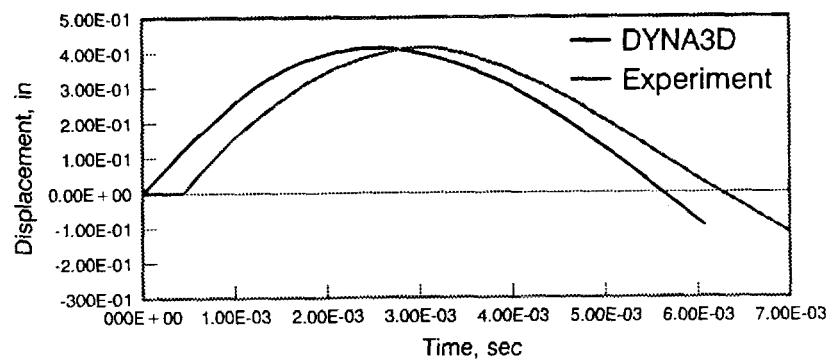
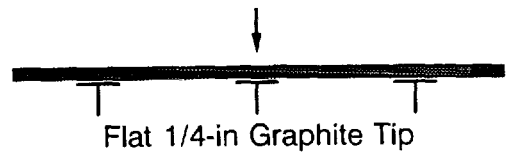
Blade Stiffener Centerline Low-Energy Impact



Blade Stiffener Centerline High-Energy Impact



Mass = 13.98 lb
Velocity = 24.7 ft/s
Energy = 1,589 in-lb



NASA/BOEING
ATCAS

ED-09
F2014.09 hR2h

Significant Effects

The maximum forces for both the stiffener flange edge and stiffener web impacts were analyzed using half-normal plots as previously discussed. The statistical analysis showed the variables listed below to have significant effects on the maximum force developed during the impact event. The letter preceding each variable indicates the impact location for which the listed variable was found to be significant. A variable is significant for both sets of impacts if both letters are listed. In addition to the five main effects, 2 sets of two-way interactions are important. Each set of confounded two-way interactions also included four additional interactions which were not listed for brevity.

There are several observations to be made concerning these results. The first is that impact mass has a stronger effect on impact force than the impact energy. It should be noted that the higher energy impacts tended to perforate the panel, limiting the influence of this variable on maximum force. The variables associated with the impactor geometry (shape and diameter) have a strong influence on the peak forces. The two-way interactions that are listed were chosen because the individual variables also appear as main effects; therefore, the likelihood of these interactions being significant is greater than that of the other interactions with which they are confounded.

Maximum Force

Significant Effects

Impact location	Variable	Low level	High level	Result
F,W	Impact mass, lbm	0.62	13.97	Decreased
F,W	Laminate thickness, in	0.089	0.18	Increased
F,W	Impact energy, in-lb	350	1,600	Increased
F,W	Impactor diameter, in	0.25	1.00	Increased
F,W	Impactor shape	Flat	Spherical	Decreased

Important Interactions

W Laminate thickness - Impactor diameter or Impactor mass - Impactor shape or ?

F Impactor shape - Impactor diameter or Laminate thickness - Impact mass or ?

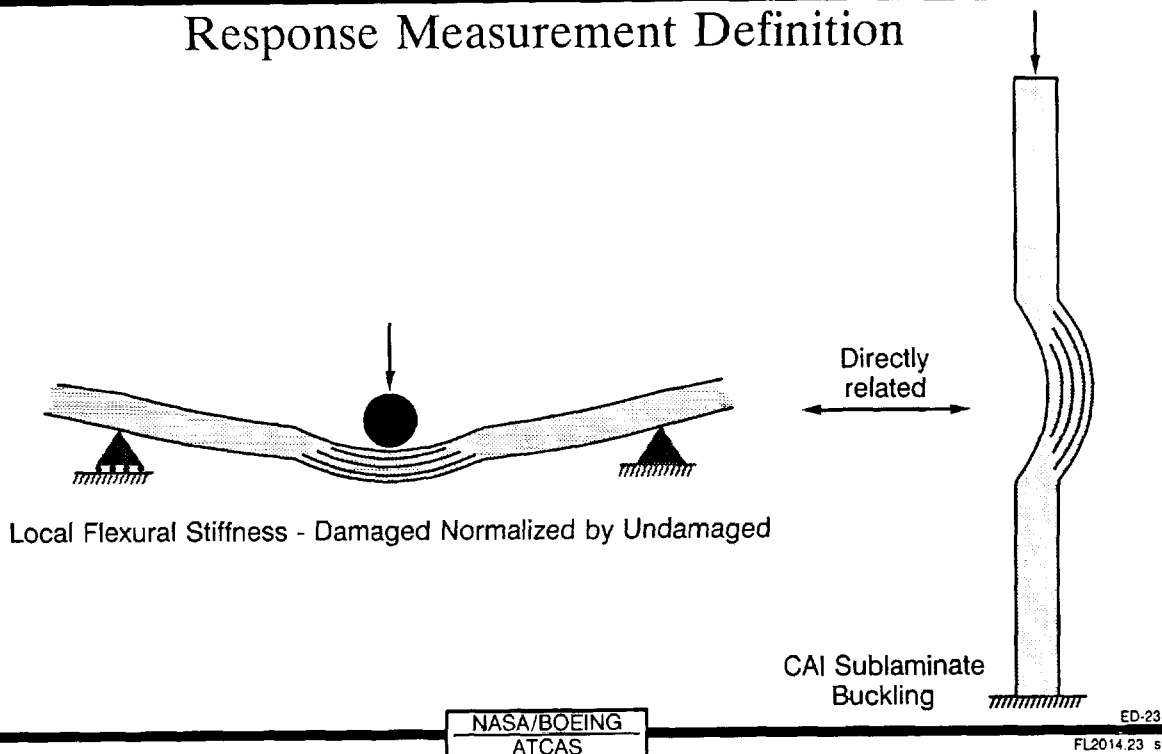
F (flange) W (web)

Response Measurement Definition

Impact damage in a composite laminate generally consists of some combination of matrix damage and fiber failures. The performance of a laminate with damage is related to the stability of sublaminates created by the matrix damage [1,9,10] and the extent of fiber failures [11]. The damage region behaves as a "soft zone" under load, with loads redistributing around buckled sublaminates and broken fibers. The local out-of-plane (flexural and transverse shear) stiffness of the damage zone should relate directly to the stiffness of the damage region under load. A quantitative measure of this flexural stiffness may allow the direct calculation of the influence of the damage on structural performance without detailed determination of the through-thickness location of all delaminations, transverse cracks, and fiber breaks.

Local Flexural Stiffness

Response Measurement Definition

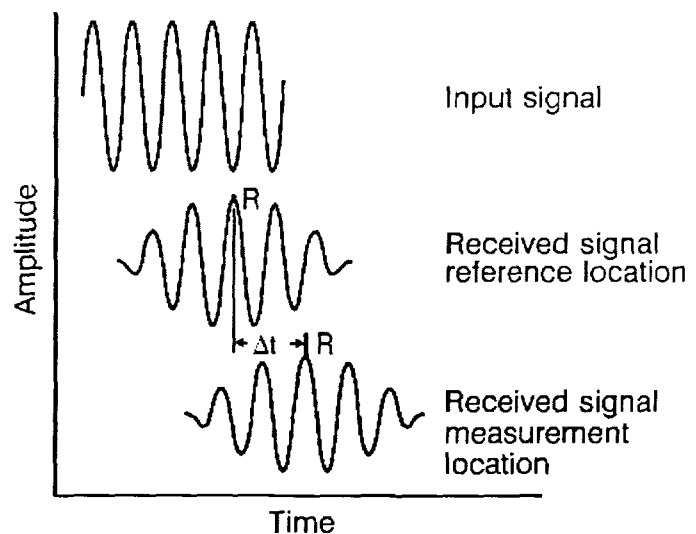
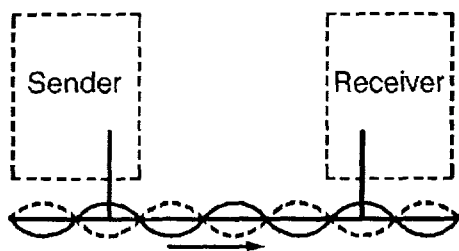
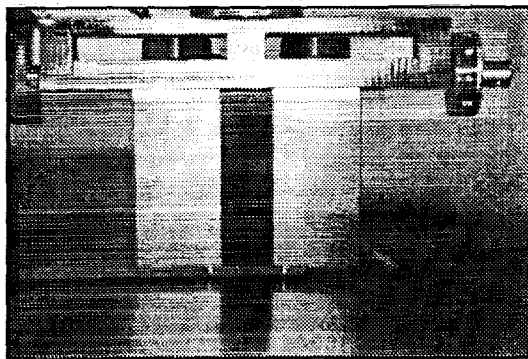


An inspection method based on flexural wave propagation [10,12] was used to estimate stiffness reductions in panel mid-bay regions subjected to hail simulation impacts. Measurements of phase velocity for flexural wave propagation were made at four different frequencies (14, 25, 40, and 84 kHz) for both undamaged and damaged regions of the panels using a ZETEC Sondicator model S-9.

Phase velocity was measured in the undamaged regions using a probe with variable spacing (separation distance) between the transmitter and the receiver. An oscillating transverse load was applied through the transmitter, introducing flexural waves in the panel as illustrated below. The phase velocity was determined by monitoring the change in the received signal as the separation distance was increased.

In the damaged regions, phase velocity was measured using a probe with a fixed separation distance (0.75"). The probe was initially placed over an undamaged reference location where the phase velocity had already been measured. The probe was then moved in small increments to the center of the damaged region. The phase velocity was determined from the change in the received signal from the reference location to the measurement location.

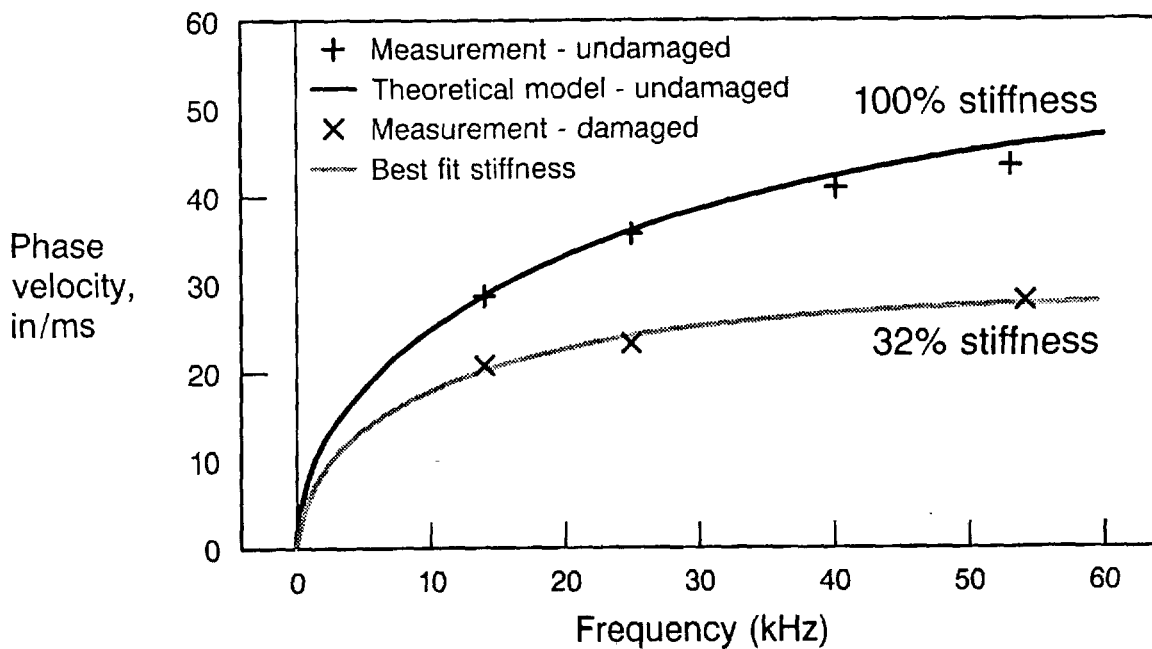
Flexural Wave Damage Characterization



Phase velocities for the undamaged regions of the stiffened panels were predicted using the theoretical formulation of Tang, et al [13]. This formulation is based on laminated plate theory and includes the effects of transverse shear deformation and rotary inertia. The agreement between predicted and measured phase velocities was typically within 5% for the 32 panels studied. The comparison for one typical panel is shown in the figure.

The measured phase velocities in the damaged regions were lower than those in the undamaged regions. Since the measurements were made in the 0 degree direction, this decrease can be attributed to a reduction of the bending stiffness (D_{11}) and the transverse shear stiffness (A_{55}) in this direction [13]. In obtaining the estimates of stiffness reduction, D_{11} and A_{55} were assumed to be reduced by the same percentage. The theoretical model was used iteratively to determine what value of stiffness reduction gave the best fit to the data. An example is shown in the figure.

Stiffness Determination From Dispersion Curve

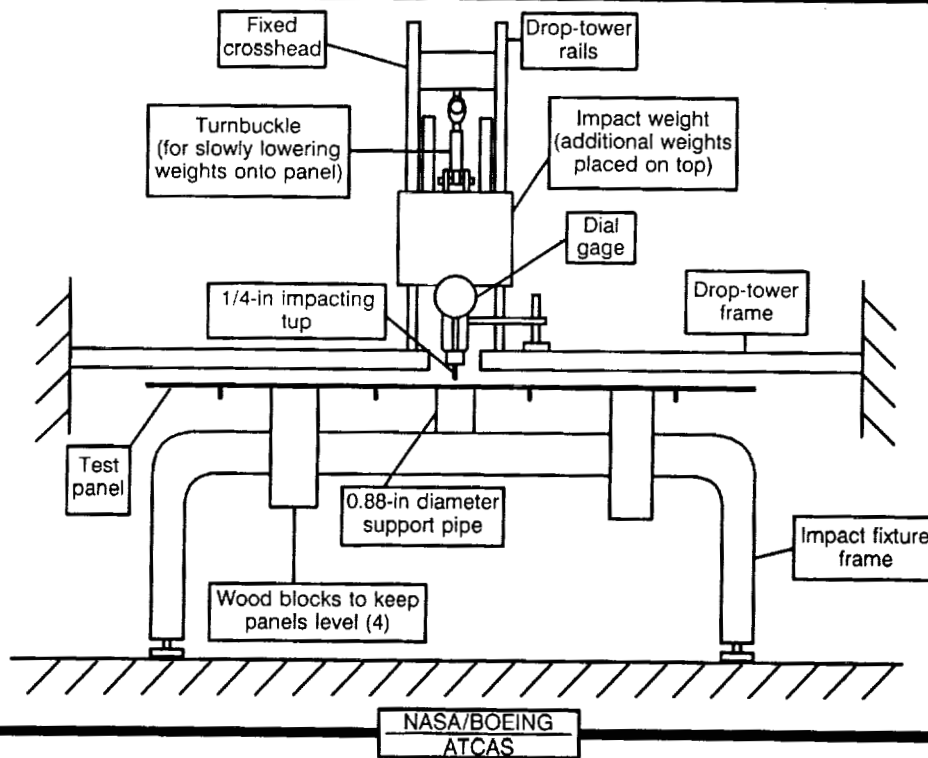


Mechanical bending tests were also performed on the panels for direct comparison to the stiffness estimates from the flexural wave inspections. Standard mechanical test machines could not be used because of the large size of the three-stringer panels (removal of the damaged regions from the panel was undesirable). Instead, a modified DYNATUP impactor at Integrated Technologies, Inc. was used to measure the load/deflection behavior.

The damaged region was centered over a ring shaped support (0.88" diameter) and a transverse load applied to the center of the region through a 0.25" diameter impact tup. Weights were then added to the cross-head and deflections measured using a dial indicator. The stiffness was taken to be the slope of the load versus deflection curve. Measurements were also made in an undamaged region of the panel to normalize the readings.

The large size of the panel in comparison to the test region created experimental difficulties. In particular, alignment of the panel was difficult and tipping of the panel was observed during some of the tests. The accuracy of these test results was estimated to be within 20 percent.

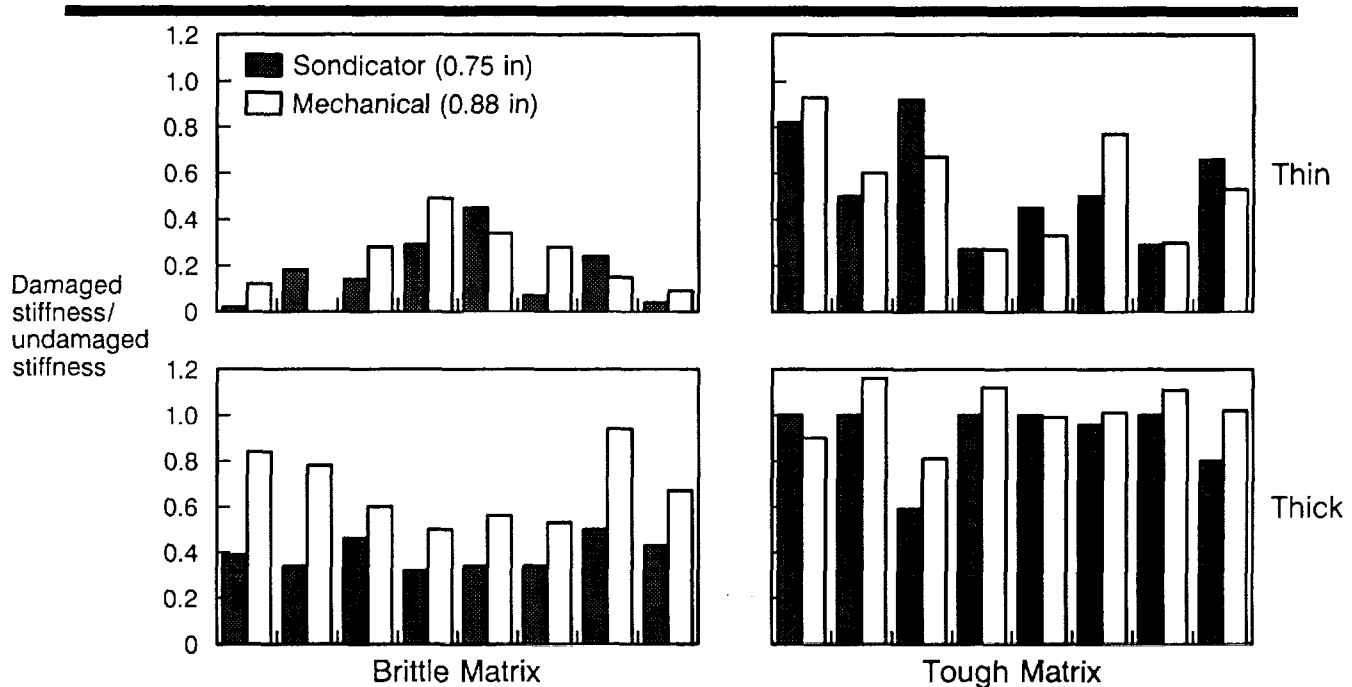
Mechanical Stiffness Tests



The normalized mechanically-measured stiffnesses are compared to the reduced stiffnesses measured using flexural wave propagation for all thirty-two hail simulation impacts. Note, each experimental run represents different combinations of the test variables (i.e., no replication of tests). The experimental runs were grouped by panel thickness and matrix toughness. The stiffness reduction resulting from the hail simulation impacts was strongly related to these two variables. The least stiffness reduction corresponded to the thicker panels with the tougher matrix materials. These results agree with the results of [3].

The stiffnesses measured in the flexural wave inspections agreed qualitatively with the those measured in the mechanical tests. However, the flexural wave inspections generally indicated a greater stiffness reduction than the mechanical tests. Some of this difference may have resulted from the inaccuracies in the mechanical tests. In addition, the flexural wave inspections were conducted in one direction only, whereas the mechanical measurements were related to the stiffnesses in multiple directions.

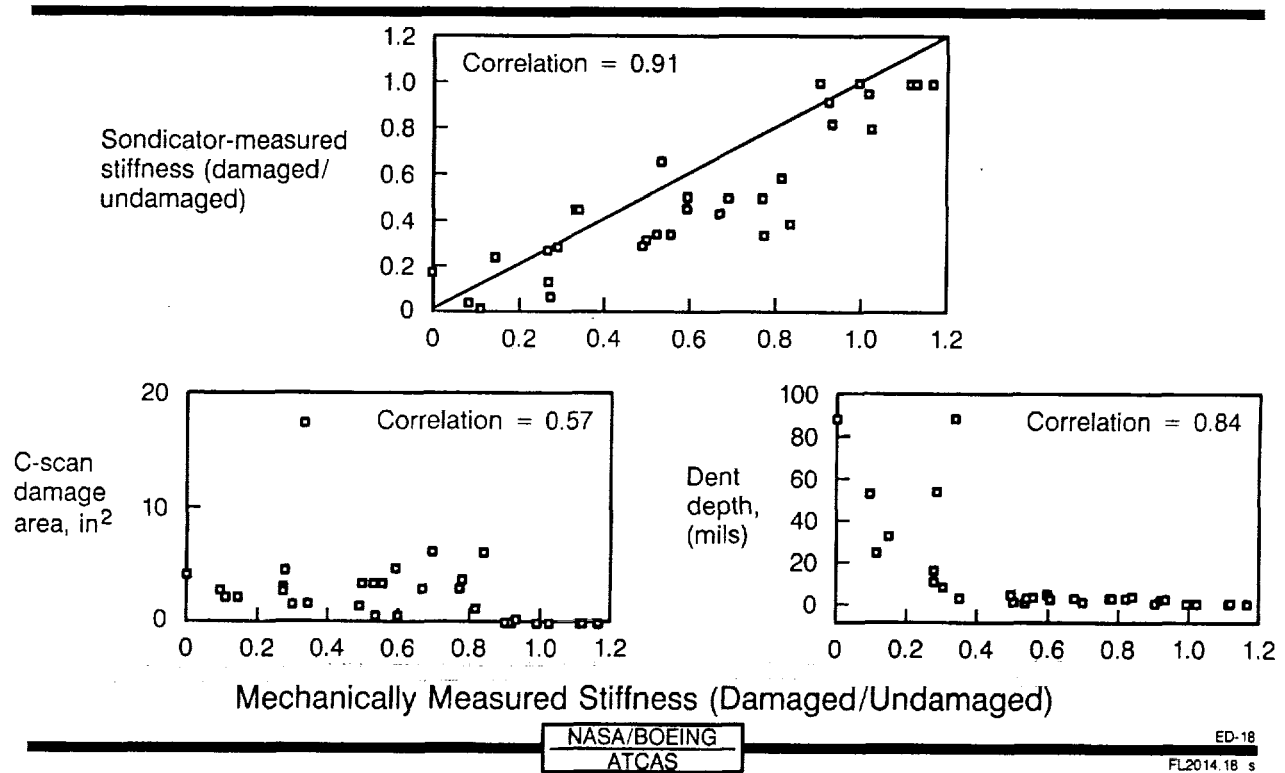
Comparison of Mechanical Tests and Sondicator Measurements



The correlation between the mechanical measurements and the results of the flexural wave inspections was investigated. In addition, the mechanically measured stiffnesses were also compared to more traditional non-destructive measurements for assessing damage. The agreement was quantified using a Spearman rank correlation. The flexural wave inspection gave a better correlation to the mechanical stiffnesses than either the damage area measured by the C-scan or the indentation depth.

It should be noted that the mechanical measurements were made over a region smaller than the impact-damaged region for most panels. In order to fully characterize the damage, both the local stiffness reduction and the size of the damage area may be necessary. The size of the damaged region can be obtained through either flexural wave inspections or more traditional ultrasonic techniques.

Correlation With Mechanically Measured Stiffness



Significant Effects

The reduced stiffnesses generated via the flexural wave measurements on the hail simulation impacts were analyzed using half-normal plots. Matrix type and laminate thickness were found to be statistically significant, as would be expected from observation of the previous figures. For comparison, important effects when examining the planar damage area response of the hail simulation impacts from Part 1 [3] were Matrix type and an interaction between Matrix type and Laminate thickness. Only three confounded two-way interactions are present because the extrinsic variables were eliminated from the hail simulation impacts. Fiber type may be considered significant if a more liberal interpretation of the half-normal plots is taken.

Local Flexural Stiffness

Significant Effects

Impact location	Variable	Low level	High level	Result
H	Laminate thickness, in	0.089	0.18	Increased
H	Matrix type	938	977-2	Increased
H	Fiber type*	AS4	IM7	Increased

Important Interactions

H Fiber type - Matrix or Fiber Volume - Material Form

H ~~or Stiffener type - Stiffener spacing~~

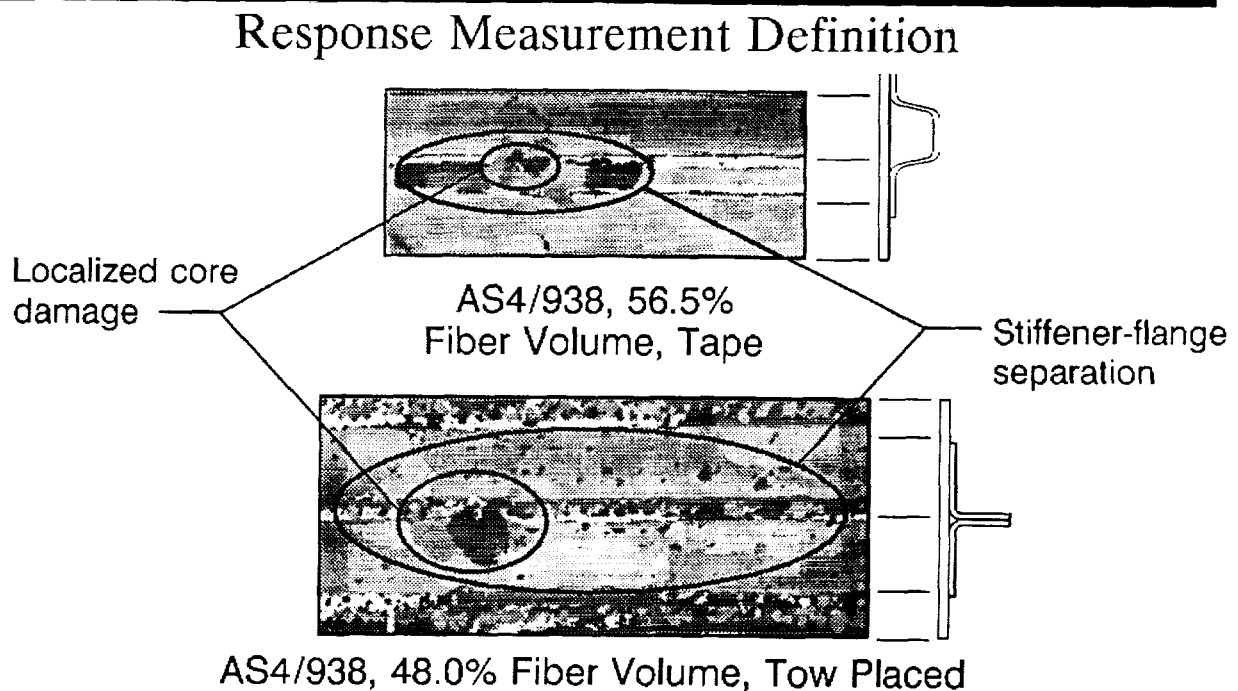
H (Hail simulation)

* Potentially significant.

Response Measurement Definition

Matrix damage created in the stiffener flange edge and stiffener web impacts was studied using pulse-echo ultrasonics. These ultrasound results were presented as C-scans, with different colors representing a variation in depth of a reflective surface, such as a delamination or the back surface of the laminate. The matrix damage found in the stiffener impacts consisted of both a localized region of delaminations with interconnecting transverse cracks and a separation of the stiffener flange from the skin. The local region of damage is expected to effect the post-impact performance of the laminate through sublaminar stability and load redistribution similar to that observed in unstiffened laminate CAI tests. The stiffener flange separation region could act as an initial flaw in a stiffener separation event.

Matrix Damage



NASA/BOEING
ATCAS

ED-10

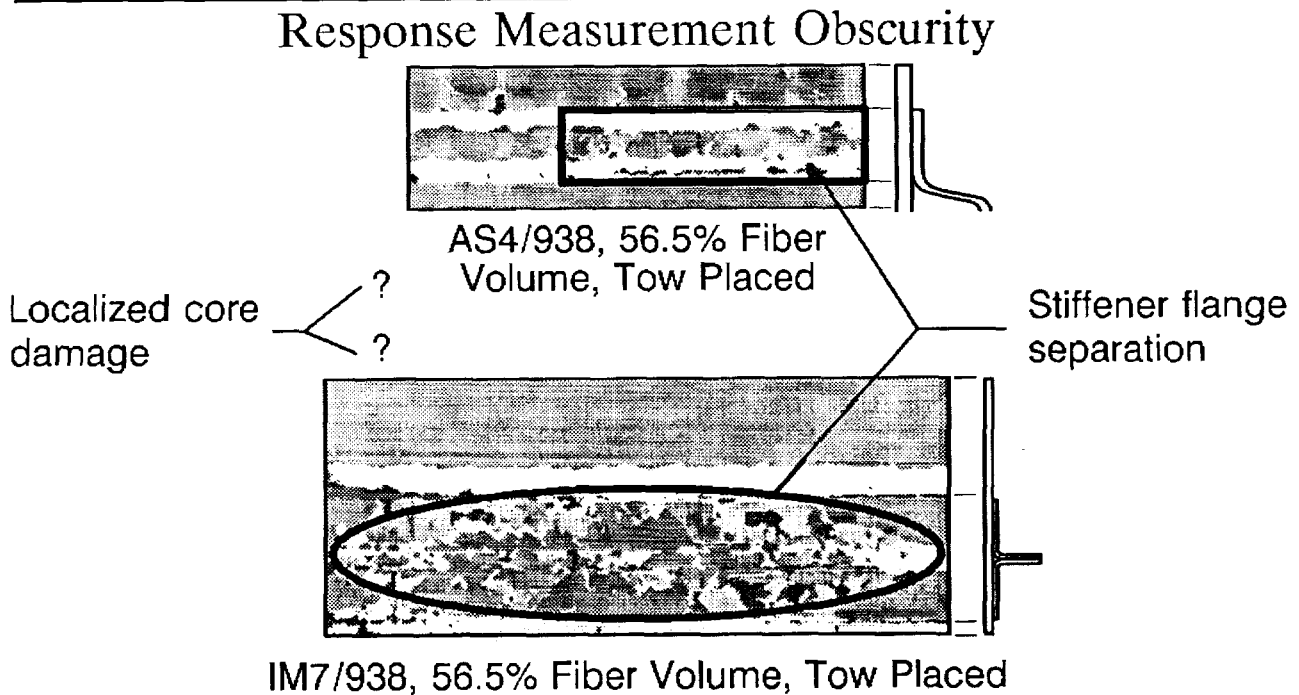
FL2014HR.10 sR1b

Response Measurement Obscurity

Interpretation of the C-scan results was not always straightforward. The region associated with localized core damage was not always distinguishable from the stiffener separation area. Statistically, the missing data reduced the number of degrees of freedom in the results, lowering the resolution on certain variables.

The boundaries of the stiffener separation area were sometimes obscured by "noise" in the C-scans (e.g., signals caused by the tow placement microstructure). The subjective nature of some of the stiffener separation area measurements introduced uncertainty in the measurements. The variation created by this uncertainty adds to the overall experimental noise, which is accounted for by the statistical analysis.

Matrix Damage



NASA/BOEING
ATCAS

ED-11
FL2014HR.11 s

Significant Effects

The stiffener flange separation areas for both the flange edge and web impacts were analyzed using half-normal plots. The statistical analysis showed the variables listed below to significantly affect stiffener flange separation area created during the impact event. The letter preceding each variable indicates the data set (flange edge or web impact) for which the listed variable was found to be significant. A variable is significant for both sets of impacts if both letters are listed. In addition to the four main effects listed, four sets of two-way interactions are important. Each set of confounded two-way interactions listed include 4 others which were not listed for brevity.

Several observations can be made from these results. It is observed that matrix toughness influences the size of the separation area for the stiffener web impacts, although the influence is reduced when a layer of adhesive exists between the stiffener flange and the skin. The thicker panels tended to have more separation area than the thin panels for the stiffener flange edge impacts.

Stiffener-Flange Separation Area

Significant Effects

Impact location	Variable	Low level	High level	Result
F,W	Impact energy, in-lb	350	1600	Increased
W*	Matrix type	938	977-2	Decreased
F,W	Impactor diameter, in	0.25	1.00	Increased
F	Laminate thickness, in	0.089	0.18	Increased

Important Interactions

F,W	Material form - Skin layup (stiffener layup)	or	Matrix type - Stiffener type	or ?
F,W	Laminate thickness - Impactor energy	or	Fiber type - Fiber volume	or ?
W*	Matrix type - Impact energy	or	Material form - Laminate thickness (stiffener layup)	or ?
W*	Matrix type - Impactor diameter	or	Skin layup - Laminate thickness	or ?

*More important for no adhesive case F (flange) W (web)

Significant Effects

The localized core damage area data sets for both the stiffener flange edge and stiffener web impacts were analyzed using half-normal plots. The statistical analysis showed the variables listed below to have significant effects on the localized core damage area created during the impact event. The letter preceding each variable indicates the data set for which the listed variable was found to be significant. A variable is significant for both sets of impacts if both letters are listed. In addition to the four main effects listed, three sets of two-way interactions are important. Each set of confounded two-way interactions listed includes four others which were not listed for brevity.

Several observations can be made from these results. It is observed that matrix toughness influences the localized core damage area for both the stiffener flange edge and stiffener web impacts. Stiffener type was statistically significant, with the hat stiffener having less localized core area. These results have been influenced by missing data points, resulting in lower resolution for the variables studied.

Localized Core-Damage Area

Significant Effects

Impact location	Variable	Low level	High level	Result
F,W	Impact energy, in-lb	350	1600	Increased
F,W	Impactor diameter, in	0.25	1.00	Increased
F,W	Matrix type	938	977-2	Decreased
F,W	Stiffener type	Blade	Hat	Decreased

Important Interactions

F	Matrix type - Impactor diameter	or	Skin layup - Laminate thickness	or ?
F	Impact energy - Impactor diameter	or	Material form - Skin layup (stiffener layup)	or ?
W	Material form - Impactor diameter	or	Stiffener type - Impact energy	or ?

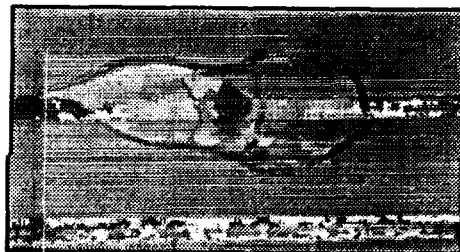
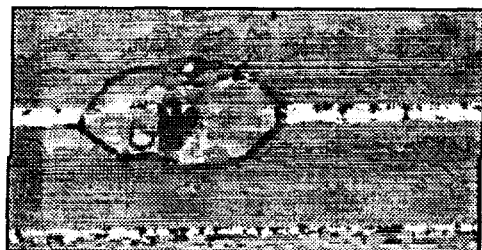
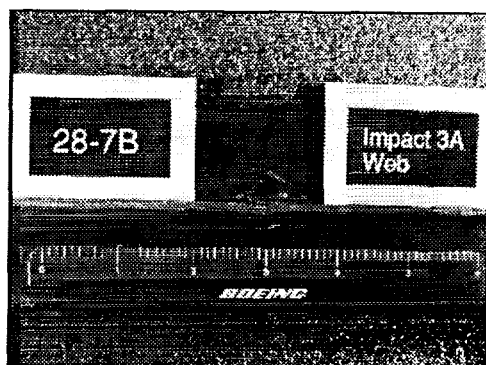
F (flange) W (web)

Response Measurement Definition

The influence of structural adhesive between the uncured skin and stiffener on stiffener separation area created during an impact event was examined. Two stiffener web impacts were performed on each panel, one on a stiffener with adhesive at the flange/skin interface and one on a stiffener without adhesive. The stiffener flange separation area for the stiffener without adhesive was divided by the separation area for the stiffener with adhesive. The larger the ratio the less influence the adhesive layer has on damage size. These results apply only to the stiffener separation area. The effect of an adhesive layer on other damage modes, such as fiber failure, has not been considered yet.

Stiffener Flange Separation Area - Adhesive/No Adhesive Ratio

Response Measurement Definition



NASA/BOEING
ATCAS

ED-12

FL2014HR 12 b1h

Significant Effects

Only three variables were found to be statistically significant for this data set. An increase in the ratio corresponds to the adhesive layer having less influence on the stiffener flange separation area. Based on these results, the addition of an adhesive layer is most beneficial for thin blade stiffened structure. The influence of the Skin layup variable could result from layers just outside of the flange to skin interface becoming critical locations for separation. The effect of Skin layup on stiffener separation should be further examined in future work.

Adhesive-to-No-Adhesive Ratio

Significant Effects

Impact location	Variable	Low level	High level	Result
W	Laminate thickness, in	0.089	0.18	Increased
W	Skin layup	Soft	Hard	Increased
W	Stiffener type	Blade	Hat	Increased

W (web)

NASA/BOEING
ATCAS

ED-30
FL2014.30 h1h

The focus of the work accomplished in both Parts 1 and 2 of this study was to determine the statistically important variables and variable interactions for each measured response. Based on the results of this work, future impact damage studies for composite structure should consider, at a minimum, several levels of the extrinsic variables Impactor diameter and Impactor shape. A range of impact energies should also be included. The findings related to the intrinsic (structural design) variables have provided guidance to the NASA/Boeing ATCAS team on both material selection and structural test requirements and procedures. In addition, significant insight was gained into the impact phenomena and related criteria.

Summary

- Maximum force is strongly related to impactor mass.
- Flexural wave dispersion provides direct measure of local damage performance.
- Stiffener flange separation area is smaller when using a matrix with high interlaminar toughness.
- Stiffener-flange separation area increases with increasing thickness.
- Adhesive layer between skin and stiffener is most important for thin blade-stiffened structure.
- Impactor geometry and interactions between variables have strong influence on all measured responses.
- Teamwork is key to obtaining successful results.

This experiment has involved the efforts of a large number of people from various organizations within and outside of The Boeing Company. The authors wish to acknowledge all the personnel listed below for their technical support.

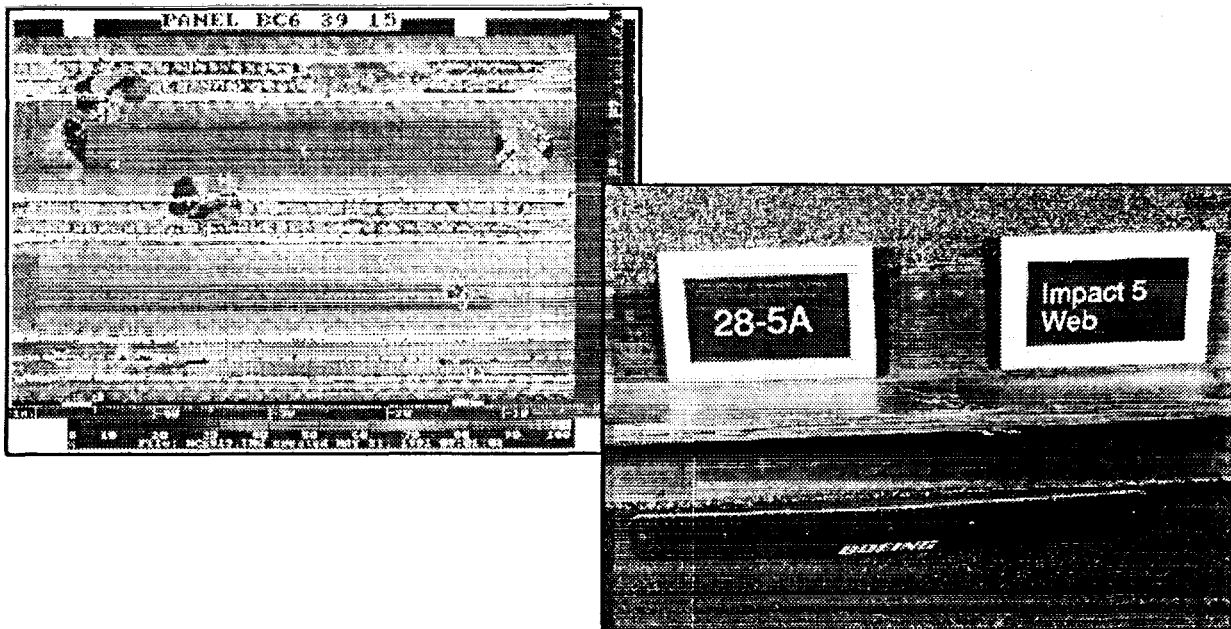
Contributors

Bill Avery - Boeing ATCAS Team	Larry Ilcewicz - Boeing ATCAS Team
Roger Bennett - University of British Columbia	John Linn - Boeing Quality Assurance R&D
Todd Brown - Hercules Inc.	Bill Motzer - Boeing Quality Assurance R&D
Greg Colvin - Zetec Inc.	Derek Newkirk - University of Washington
Gordon Cox - Boeing Manufacturing R&D	Linda Nuanez - Boeing Manufacturing R&D
Brian Coxon - Integrated Technology Inc.	G. Pageau - University of British Columbia
Daniel Delfosse - University of British Columbia	Anoush Poursartip - University of British Columbia
Chris Eastland - Integrated Technology Inc.	Ponce Puzon - Boeing Industrial Engineering
Chuck Fitch - Zetec Inc.	Peter Smith - Boeing ATCAS Team
Dodd Grande - Boeing Materials Technology	Reza Vaziri - University of British Columbia
Carroll Grant - Hercules Inc.	Kurt Willden - Boeing ATCAS Team
Rich Groh - University of Washington	Rod Wishart - Integrated Technology Inc.
Ray Horton - Boeing ATCAS Team	Mark Wood - Boeing Manufacturing R&D

The results and observations presented to date have focused on individual responses only. Although this approach has provided significant insight into important aspects of impact damage resistance in composite fuselage structure, the results from the individual responses should be integrated to create a complete understanding. The relationships between criteria (visibility), applicable load levels (safe-flight, limit, or ultimate), and the types, magnitudes, and locations of the damage states must be understood in order to enhance the design optimization process.

Future Work

Integrate Understanding of Various Measured Responses



NASA/BOEING
ATCAS

ED-13
FL2014hr.13 b

References

1. Dost, E. F., Ilcewicz, L. B., and Gosse, J. H., "Sublaminar Stability Based Modeling of Impact Damaged Composite Laminates," Proc. of 3rd Tech. Conf. of American Soc. for Composites, Technomic Publ. Co., 1988, pp. 354-363.
2. **Dost, E. F., Ilcewicz, L. B., and Avery, W. B., "The Effects of Stacking Sequence On Impact Damage Resistance and Residual Strength for Quasi-Isotropic Laminate," Composite Materials: Fatigue and Fracture, ASTM STP 1110, 1991.**
3. **Dost, E. F., Avery, W. B., Ilcewicz, L. B., Grande, D. H., and Coxon, B. R., "Impact Damage Resistance of Composite Fuselage Structure, Part I," Proc. of Ninth DoD/NASA/FAA Conf. on Fibrous Composites in Structural Design, FAA Publication, 1991.**
4. Wheeler, D. J., Understanding Industrial Experimentation, Statistical Process Controls, Inc., Knoxville, TN. 37919.
5. Milliken, G. A. and Johnson, D. E., Analysis of Messy Data. Volume1: Designed Experiments, Van Nostrand Reinhold Co., NY, 1984.
6. Milliken, G. A. and Johnson, D. E., Analysis of Messy Data. Volume2: Nonreplicated Experiments, Van Nostrand Reinhold Co., NY, 1989.
7. Winkel, J. D. and Adams, D. F., "Instrumented Drop Weight Impact Testing of Cross-Ply and Fabric Composites," Composites 16 No. 4, October 1985.
8. Whirley, R. G. and Hallquist, J. O., "DYNA3D - A Nonlinear, Explicit, Three-Dimensional Finite Element Code for Solid and Structural Mechanics - User Manual," University of California, Lawrence Livermore National Laboratory, Rept. UCRL-MA-107254, 1991.
9. **Ilcewicz, L. B., Dost, E. F., and Coggeshall, R. L., "A Model for Compression After Impact Strength Evaluation," Proc. of 21st International SAMPE Technical Conference, Soc. for Adv. of Material and Process Eng., 1989.**
10. **Dost, E. F., Finn, S. R., Stevens, J. J., Lin, K. Y., and Fitch, C. E., "Experimental Investigations into Composite Fuselage Impact Damage Resistance and Post-Impact Compression Behavior," Proc. of 37th International SAMPE Symposium & Exhibition, Soc. for Adv. of Material and Process Eng., 1992.**
11. Cairns, D. S. and Lagace P. A., "Residual Tensile Strength of Graphite/Epoxy and Kevlar/Epoxy Laminates with Impact Damage," Massachusetts Institute of Technology, TELAC Report 88-3, April, 1988.
12. Lamb, H., "On Waves in an Elastic Plate," Proc. of the Royal Society of London, Series A, 1917.
13. Tang, B., Henneke, E. G., and Stiffler, R. C., "Low Frequency Flexural Wave Propagation in Laminated Composite Plates," Proc. of Acousto-Ultrasonics: Theory and Application, 1988.

*References in bold were published while under Contract NAS1-18889.

DESIGN, ANALYSIS, AND FABRICATION OF A PRESSURE BOX TEST FIXTURE FOR TENSION DAMAGE TOLERANCE TESTING OF CURVED FUSELAGE PANELS¹

P. J. Smith, J. B. Bodine, C. H. Preuss
Boeing Commercial Airplane Group.

516-24
51416

W. J. Koch
Boeing Computer Services

ABSTRACT

A pressure box test fixture was designed and fabricated to evaluate the effects of internal pressure, biaxial tension loads, curvature, and damage on the fracture response of composite fuselage structure. Previous work in composite fuselage tension damage tolerance, performed during NASA contract NAS1-17740, evaluated the above effects on unstiffened panels only. This work extends the tension damage tolerance testing to curved stiffened fuselage crown structure that contains longitudinal stringers and circumferential frame elements. The pressure box fixture was designed to apply internal pressure up to 20 psi, and axial tension loads up to 5000 lb/in, either separately or simultaneously. A NASTRAN finite element model of the pressure box fixture and composite stiffened panel was used to help design the test fixture, and was compared to a finite element model of a full composite stiffened fuselage shell. This was done to ensure that the test panel was loaded in a similar way to a panel in the full fuselage shell, and that the fixture and its attachment plates did not adversely affect the panel.

INTRODUCTION

The objective of Boeing's Advanced Technology Composite Aircraft Structures (ATCAS) program (NAS1-18889) is to develop an integrated technology and demonstrate a confidence level that permits the cost- and weight-effective use of advanced composite materials in primary structures of future commercial transport aircraft. The emphasis of the program is on pressurized fuselages. A significant portion of a typical commercial transport fuselage is designed by either tension from internal pressure and/or flight loads (see Figure 1), therefore the specific emphasis of this paper is on this tension critical structure such as the fuselage crown. The approach of the ATCAS program was to build on tension fracture coupon data with larger unstiffened and stiffened panel analyses and tests to culminate with the analysis and test verification of configured crown panels.

¹ This work was funded by Contract NAS1-18889, under the direction of J. G. Davis and W. T. Freeman of NASA Langley Research Center

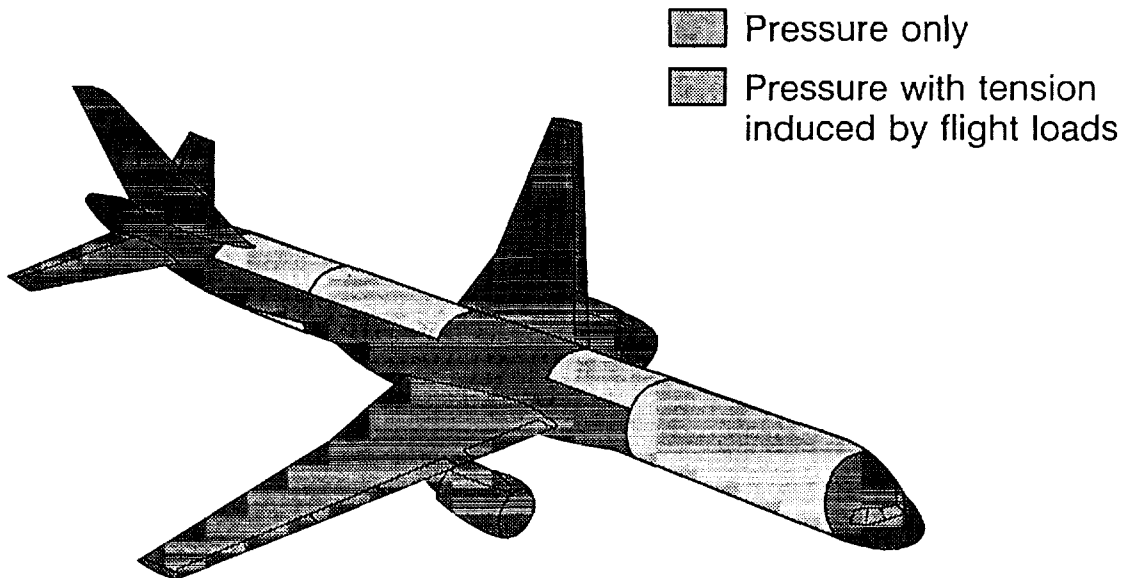


Figure 1. Tension-dominated commercial fuselage structure.

The effects of internal pressure on the tension damage tolerance and pressure containment of composite structure are not understood, and it is essential that this insight be gained if composite materials are to be used for the basic fuselage monocoque of commercial transport aircraft.

The design envelope for the ATCAS development program is that fuselage section of a wide body aircraft immediately aft of the main gear wheel well, called section 46 on Boeing airplanes. This section 46 is 32 feet long and 122 inches radius. After initial studies the section was divided into three quadrants, crown, side and keel, these being shown in Figure 2. As was seen in Figure 1 the crown quadrant is designed by hoop tension due to internal pressure and axial tension due to flight loads at the forward end, and hoop tension in the aft part of section 46. The fuselage aft of the wing is loaded by the wing and horizontal stabilizer as a beam in bending during flight maneuvers with typically the crown in tension and the keel in compression, with load reversal during negative flight maneuvers.

The presence of the cutouts in the fuselage for the wing center section and the main landing gear wheel well just ahead of the section 46 produce high axial loads from flight maneuvers at the forward end which decay toward the rear of the section. These flight induced loads can be present with or without the internal cabin pressure and the structure needs to be evaluated for those load combinations which may be critical. The flight induced axial loads are augmented by the bulkhead loads from the cabin pressure, and negated slightly by the Poisson's effect of the hoop loads induced by the cabin pressure. For a typical metal commercial fuselage the forward end of the section 46 crown tends to be critical for axial flight loads combined with internal pressure, and the aft end is usually critical for the hoop tension generated by the internal cabin pressure alone. Fuselage

structure constructed with composite materials, which have different failure modes than metal, may be critical for other combinations of flight and pressure loads, such as axial tension and pressure at the forward end of the section 46, and axial compression with pressure at the rear of the section.

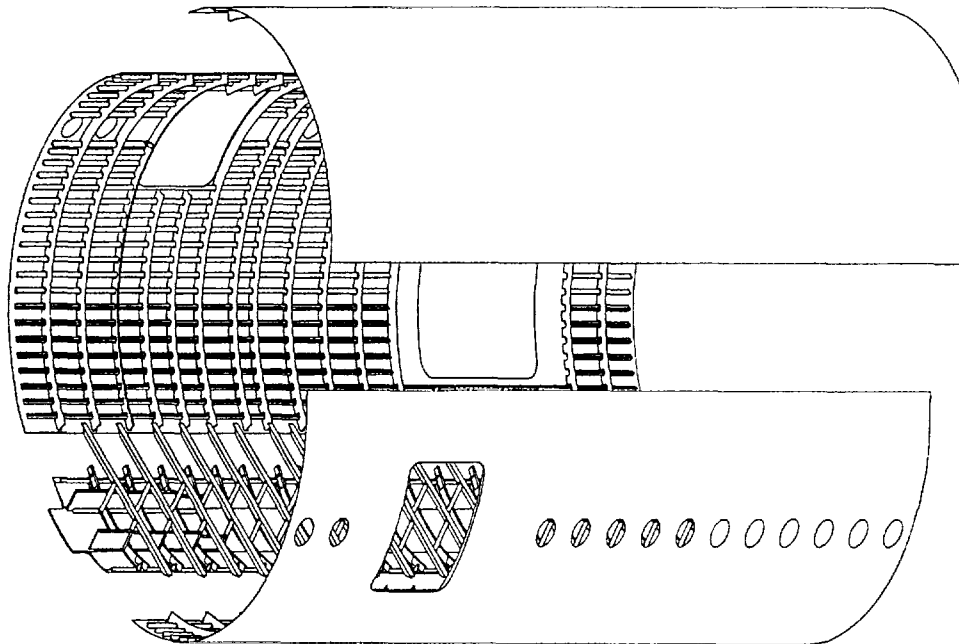


Figure 2. Quadrant approach to Boeing fuselage section 46.

Figure 3 summarizes the ultimate strength and damage tolerance requirements for commercial aircraft primary structures. These requirements are based on those of the Federal Aviation Requirements, specifically those of Part 25 Airworthiness Standards for Transport Category Airplanes, paragraph 25.301 through 25.571. The requirements for damage tolerance and pressure containment are set down in paragraph 25.571 which states that an evaluation of the strength, detail design, and fabrication must show that catastrophic failure due to fatigue, corrosion, or accidental damage will be avoided throughout the operational life of the airplane. These damage tolerance strength requirements are commonly referred to as fail-safe and include residual strength requirements for discrete source damage sustained by the airframe that the crew are aware of and for which the flight loads are reduced. However, fuselage pressure cabin structure must be able to withstand discrete source damage, such as that inflicted by uncontained engine fragments, with normal operating cabin pressure. Consequently the likely damages from discrete sources may be significantly larger than damages that may go undetected until normal maintenance inspections, thus making fuselage pressure designed structure more critical than other primary structural components. To this end testing of curved fuselage configured panels under axial and internal pressure induced loads is essential in order to build the confidence level necessary to allow composite materials to be effectively utilized in commercial transport fuselages.

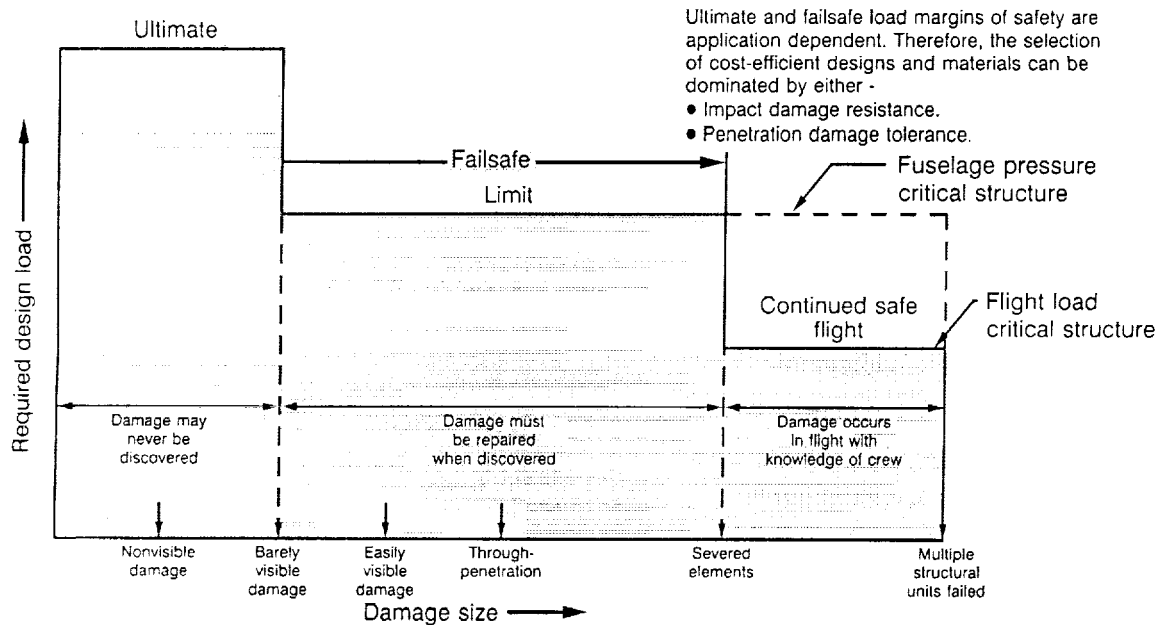


Figure 3. Strength and damage tolerance requirements for commercial aircraft primary structure.

TEST FIXTURE REQUIREMENTS

The maximum design loads considered for the pressure box fixture were derived from the initial design studies of the crown area of an aft section of a 244 inch diameter commercial transport fuselage. These design loads are summarized in Table 1 and show both ultimate and fail-safe loads. The maximum ultimate axial load was taken from the forward end of the section at the top centerline. This axial load, from an ultimate vertical gust load case with internal cabin pressure, includes the bulkhead load of $PR/2$ and the negating Poisson's effect of the cabin pressure. The pressure associated with this ultimate axial load is derived from the maximum cabin pressure relief valve setting combined with the expected external aerodynamic pressure. The maximum internal pressure of 18.2 psi is obtained from the maximum pressure relief valve setting alone multiplied by a factor of 2.0. The ultimate loads are those that may be applied to panels that have no damage that is visible to the naked eye. This includes impact damage up to barely visible, the upper level being 200 foot-pounds of energy inflicted by a 1.0 inch diameter steel ball.

The maximum fail-safe axial load is simply that load from the ultimate gust case above with the 1.5 factor removed. The pressure combined with this maximum fail-safe load is the normal operating cabin pressure plus the expected external aerodynamic pressure. The maximum fail-safe load case for pressure acting alone is the normal operating cabin pressure plus the expected external aerodynamic pressure both multiplied by a 1.15 factor.

Load condition	Axial load, lb/in	Hoop load, lb/in
Ultimate ▷ a. 2 x (maximum pressure relief valve setting) = 18.2 psi b. 1.5 x (maximum flight loads + (maximum pressure relief valve setting + expected external aerodynamic pressure = 9.15 psi))	--- 5000	2220 1675
Fallsafe ▷ a. limit flight loads + (normal operating differential pressure + expected external aerodynamic pressure = 8.75 psi) b. 1.15 x (normal operating differential pressure + expected external aerodynamic pressure) = 10.1 psi	3333 ---	1067 1228

▷ Maximum test-box loads for undamaged test panels or panels with barely visible damage.

▷ For visibly damaged structure (i.e., skin, frames, and stringers severed).

Table 1. Pressure box fixture design loads.

The pressure box fixture was designed to be capable of applying the above loads multiplied by a safety factor of 2.0. The fixture was strength checked for positive margins of safety with this factor applied against the yield strengths of the materials used. This conservative procedure ensures that not only does the fixture have more than adequate strength, but fixture deformations under load will be minimized. The 2.0 factor also ensures adequate durability under repeated static load cycles.

TEST PANEL CONFIGURATIONS

The pressure box fixture will be used to test different types of curved panels. The first panel that has actually been tested in the fixture is a 122 inch radius curved panel, 63 inches arc width by 72 inches long. The panel, shown in Figure 4, was tow-placed with AS4²/938³ material and is stiffened by three cobonded circumferential tear-straps fabricated from AS4/3501-6⁴ fabric. These tear-straps simulate the skin flanges of circumferential cobonded frames. The intent of this panel configuration, which would not be suitable for an actual fuselage shell which has to be stiffened by frames and stringers or sandwich core, is to provide some insight into the effects of damage growth in skins in the presence of frame flanges. When considering typical metal stiffened fuselage shell

² AS4 is a graphite fiber system produced by Hercules, Inc.

³ 938 is a resin system produced by ICI/Fiberite.

⁴ 3501-6 is a resin system produced by Hercules, Inc.

structures, the presence of the stringers and frames and their method of attachment to the skins have significant effects on damage growth and damage tolerance of the total skin panels. These effects are labeled configuration factors and were derived from elastic-plastic analysis or tests to aid in calculating the residual strength of the structure in the presence of differing amounts of damage. The panel with the tear-straps, representing frame flanges, is intended to provide a link between the unstiffened panel fracture strength analysis and tests, and the stiffened panels.

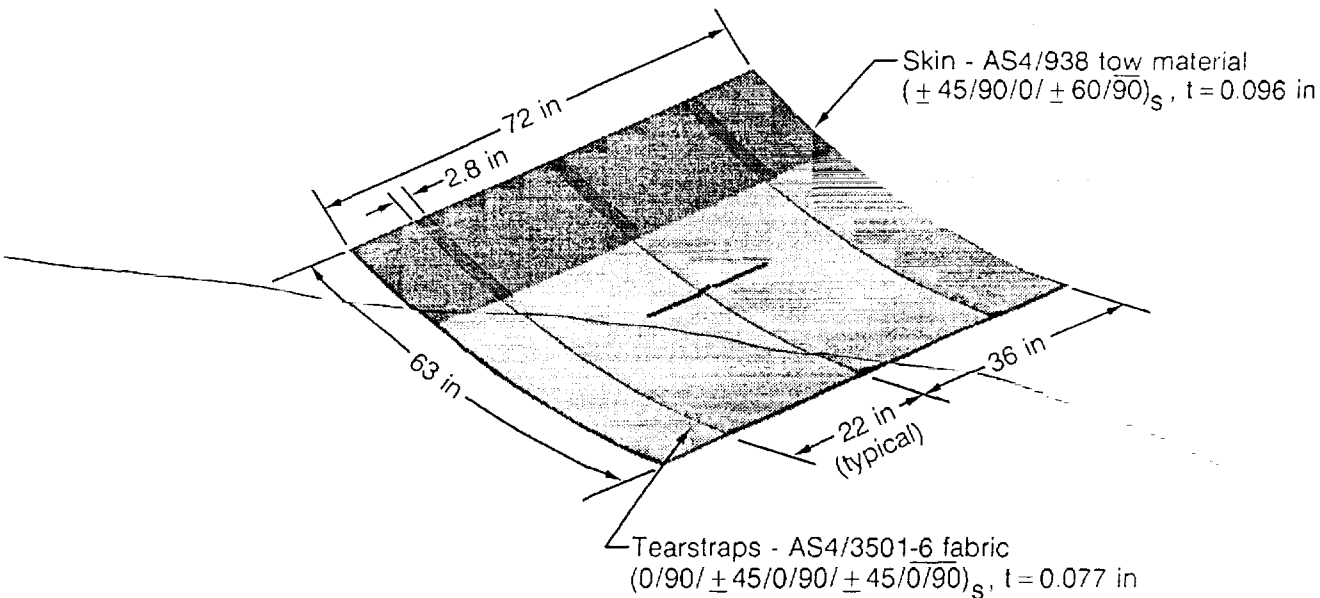


Figure 4. Curved tear-strap test panel configuration.

The second test panel configuration is representative of the crown structure that has been optimized for weight and cost in the ATCAS program. The skin, fabricated of tow-placed AS4/938 material, is stiffened by four longitudinal cocured enclosed hat-stringers of the same material, and three triaxially braided resin transfer molded circumferential frames fabricated from AS4/1895⁵. Figure 5 presents this panel configuration with the frames mechanically attached to the skins. The second and third panels will have four longitudinal stringers and three frames cobonded to the skins. The stiffened panels will provide insight on configuration factors for stiffened panels, loaded with internal pressure and/or axial loads, that have through penetration type damages. These damages will include skin, skin and frame, and skin and stringer severed on different panels. The differences between the cobonded and mechanically fastened frame flange/skin interfaces will provide data on their configuration effects on the damage tolerance of the panels.

⁵ 1895 is a resin system produced by Shell Development Co.

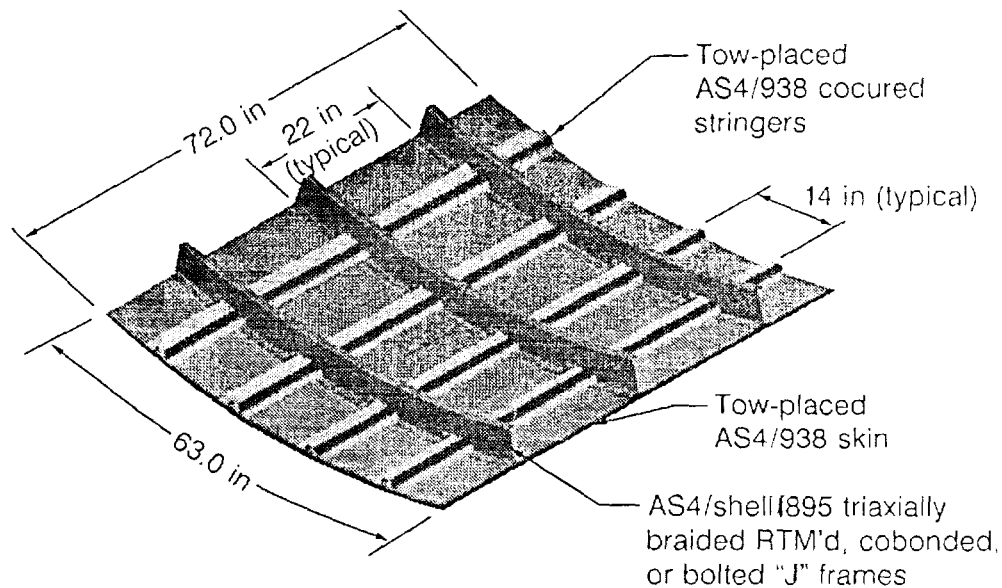


Figure 5. Fuselage crown test panel configuration.

PRESSURE BOX TEST FIXTURE CONFIGURATION

The pressure box was initially conceived as a fixture for the testing of stiffened panels of a fixed configuration. After discussions with NASA, and the creation of the Benchmark test program, the need for testing panels with differing configurations arose. Also the tension fracture work highlighted the need for some test data for curved panels, without frames and stringers, but with circumferential tear-straps representing frame flanges. The fixture configuration is not conducive to quick change over from one panel type to another. The requirement for axial loading necessitates attachment details and loading plates that have differing centers of gravity, or waterlines, so that for each panel axial loads are applied at the respective panel waterline. This must be achieved within reasonable limits so as to reduce any bending that may be applied to the test panel to a minimum. The use of pairs of load actuators at each end to apply axial load further complicates the set-up in that the actuators now must be on butt lines as well as waterlines due to the panel curvature. One modification, that may be made for the later Benchmark tests that NASA has scheduled for this fixture, is that of eliminating one axial load actuator at each end so that the differing panel butt line problem is removed.

Figure 6 shows an overall view of the pressure box fixture with the curved tear-strap panel installed. The dual axial load actuators can be seen at each end of the test panel, and the hoop load reactions on each side to react the internal pressure. Along each edge of the test panel are the individual double lap attachment fingers which apply axial load, or react the hoop loads from internal pressure. These attachments are individualized in order that they do not pick up transverse loads which would be diverted from the test panel. The test panels with frames and stringers, when installed, will also have individual hoop

reaction members for each frame in addition to the skin reactions. These will be configured such that the frame stiffness is continuous for as far as practical through the hoop reaction systems. The weight of the attachment and loading plates is considerable, so a counterbalance system is used to ensure that this weight is not applied to the test panel. All of the test fixture components are fabricated from various steel and aluminum alloys, ranging from A-36 low strength steel for the pressure box and frame weldments, A-514 medium strength steel for the grip fingers and hoop attachment plates, 4340 high strength steel for the actuator clevis fittings and hoop turnbarrels, to 7075 aluminum for the tether straps and access doors in the pressure box itself.

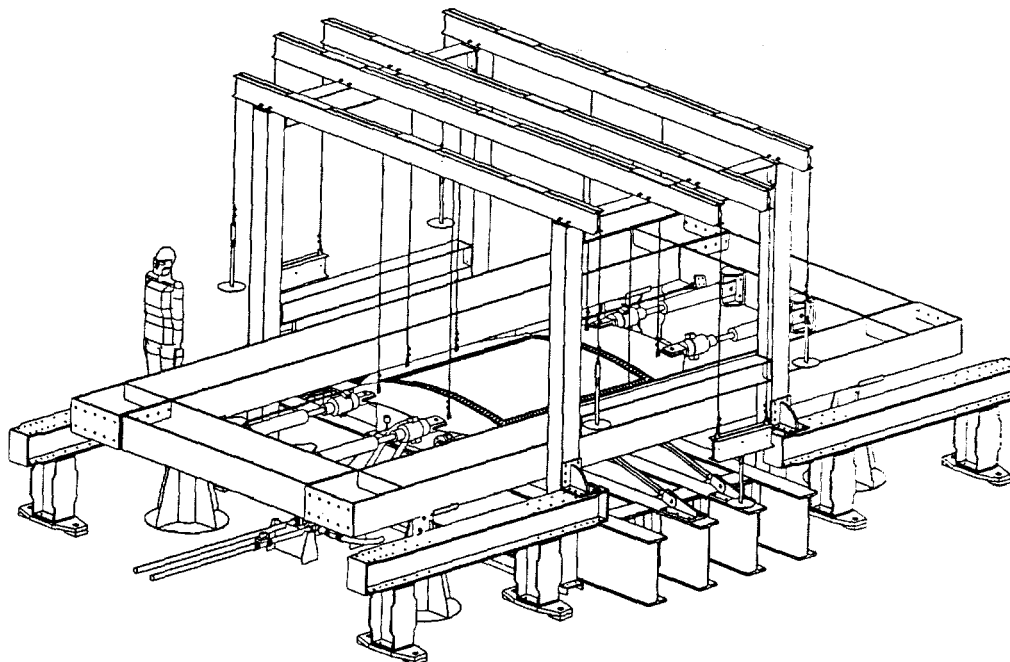


Figure 6. Pressure box test fixture.

Figure 7 presents a view of the fixture with the test panel removed so that the pressure seal and the interior of the pressure box may be seen. When the box is pressurized, the seal, being flexible, inflates slightly, thus causing the test panel to float, therefore the seal had to be designed such that no extraneous loads are applied to the test panel. The seal is fabricated from a fluoroelastomer/Kevlar laminate and is based on the advanced flexible tooling developed for the fabrication of the stiffened crown panels (Ref. 1). The seal is fabricated and autoclave cured in four sections, and bonded in each corner with a single lap shear splice. The single lap shear splice configuration was tested for strength prior to incorporation in the design. The seal is mechanically attached to both pressure box and test panel, and these attachment areas of the seal are reinforced with an aluminum strip to provide bearing strength. As the test panel floats when under internal pressure due to the seal inflating, a means of adjusting the alignment of the panel is necessary. This adjustment is provided by the turnbarrels in each of the hoop reaction systems. The overall size of the fixture is 25 feet in length, 20 feet in width, and 12 feet in height; this includes the overhead support beams for the counterweight system and shadow moire equipment.

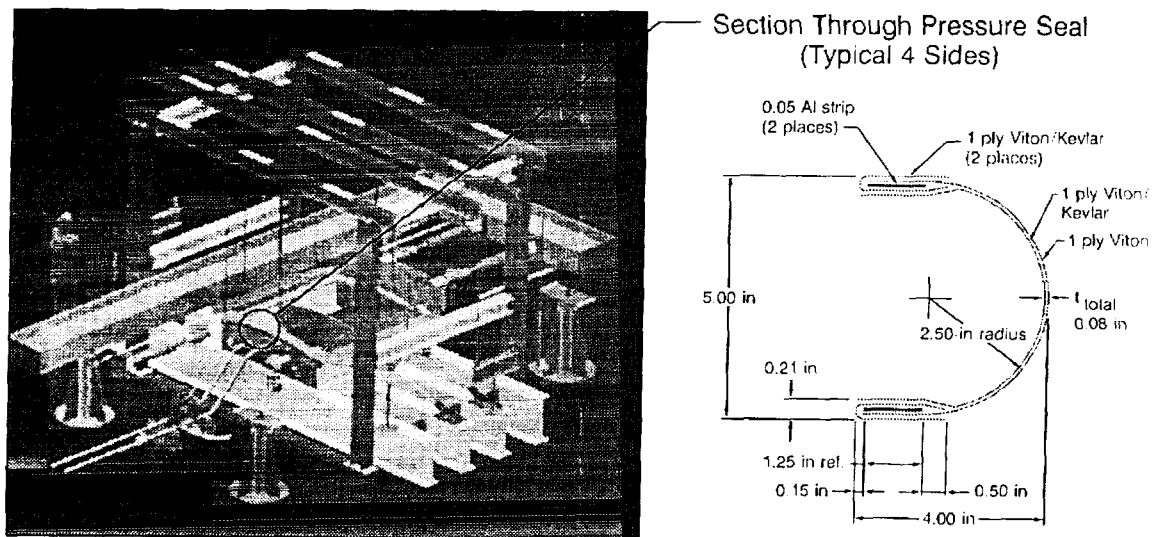


Figure 7. Pressure box seal detail.

PRESSURE BOX FIXTURE ANALYSIS AND DESIGN

A NASTRAN finite element model (FEM) was made of the pressure box fixture and test panel to help minimize the boundary effects of the fixture on the behavior of the test panel under load. As shown in Figure 8 only a quarter of the fixture and panel was included in the model due to symmetry. Another and important reason for the FEM analysis is to help understand the test results especially from panels with damage. From previous work (contract NAS1-17740, *Development of Composites Technology for Fuselage Structures in Large Transport Aircraft*) it was seen that the test panel dimensions needed to be very large if the effects of the fixture on the test panel are to be negligible, and this approach is impractical because of the increased costs of both test panels and the fixture.

A complete shell FEM was created at NASA Langley Research Center (LaRC) to support this work, and compared to a model of the test panel with symmetric boundary conditions, as well as the model of the complete test fixture and test panel. These FEM runs indicated that the fixture needed to be as stiff as possible in order to best approximate full fuselage shell boundaries for the test panel, so the attachment plates, individual grip fingers, hoop reaction members, and load plates were all changed to steel from aluminum. The FEM analyses also highlighted the need for hoop reaction nearer the fixture corners, so the reaction members were moved closer to the corners. A summary of the design revisions based on the FEM effort is shown in Figure 9.

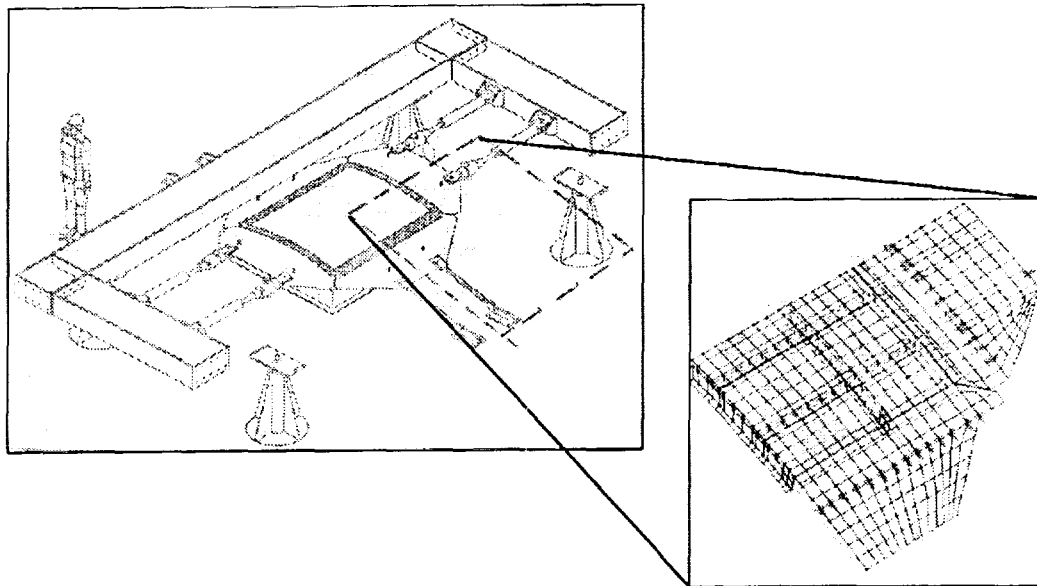
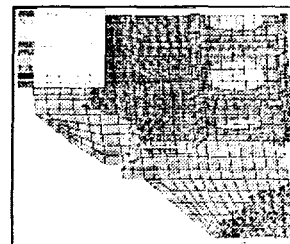
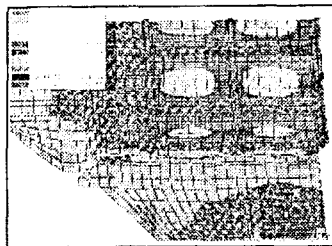


Figure 8. Finite element model of pressure box fixture and test panel.

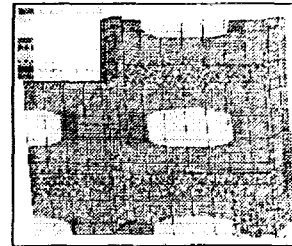
- Reduced "overhang" seal pressure from 9 in to 1.75 in
- Modified stiffness ratio of skin and frame-hoop reaction members to approximate full fuselage boundaries
- Adjusted axial-load plate neutral axis to match test panel
- Shifted frame reaction attachment points to neutral axis of frame
- Added more attachment points near corner of test panel



Model of Actual Test Panel Without Damage



Model of Five-Bay Test Panel Without Damage



Model of Test Panel With Symmetric Boundaries

Figure 9. Design revisions to the pressure box fixture based on finite element modeling

The length of the stiffened test panel was a concern in that there are only three frame bays, and with the center frame and skin severed, just one intact frame bay on each side. The proximity of the fixture attachment plates could have a significant effect on the load

redistribution around the ends of the damage in the center bay, thus making analysis of the test results difficult. Figure 10 presents the actual three bay test panel with a 22 inch skin notch and central frame severed under internal pressure loading of 10 psi. Figure 11 shows the test panel with an additional frame at each end with the same damage and loading as the three bay panel. There are differences in the stress field in the center bay, but these were not considered sufficient enough to warrant the additional length for the five bay panel.

Further evidence that analysis is absolutely necessary to be able to interpret the results of damage tolerance tests of configured panels in a pressure box fixture is presented in Figure 12. Figure 12 shows circumferential frame hoop loads plotted against distance from the shell crown centerline in degrees. These loads were extracted from full shell FEM analyses, performed by NASA LaRC personnel, and are those produced in the frame by a flight load case combined with 10.35 psi cabin pressure. The frame load plots are for a frame with and without severing damage. Also shown are the loads for the intact frames one and two bays away from the severed frame. It can be seen that when a frame is severed the axial loads in that frame in the vicinity of the damage are much disturbed, and do not become normal for a considerable distance, approximately 50 degrees from the damage. The shaded area of the figure indicates that portion of the shell that the pressure box test panels represent. Indeed it would require a pressure box test section measuring 9 feet arc length to allow the frame loads to be redistributed completely for a panel with a severed frame. The loads in the intact frame one bay forward are also much changed, and it can be seen that the pressure box would need to have a test panel that has five frames. This would indicate a total test panel length of almost 10 feet. The cost of such test panels would be on the order of three times as much as the current panels, with potentially a more costly fixture.

Notwithstanding the limits of the test fixture, effective FEM analyses of the pressure box and test panels, and the full shell, together with sufficient testing, will enable engineers to gain an understanding of the damage tolerance of configured composite crown panels. This will aid in the design of future composite fuselage structure, such that testing of large fuselage sections may be conducted with confidence.

PRESSURE BOX TEST PROGRAM

The intended pressure box test program will be in three phases. The first phase, shown in Table 2, consists of tests conducted on test panels designed and fabricated by Boeing as part of the ATCAS contract. The second phase, shown in Table 3, will consist of tests conducted on test panels designed and fabricated by Boeing as part of a Task Assignment contract (NAS1-19349). The third phase, which will not be discussed here, will consist of panels designed and fabricated by Douglas as part of their ACT contract (NAS1-18862).

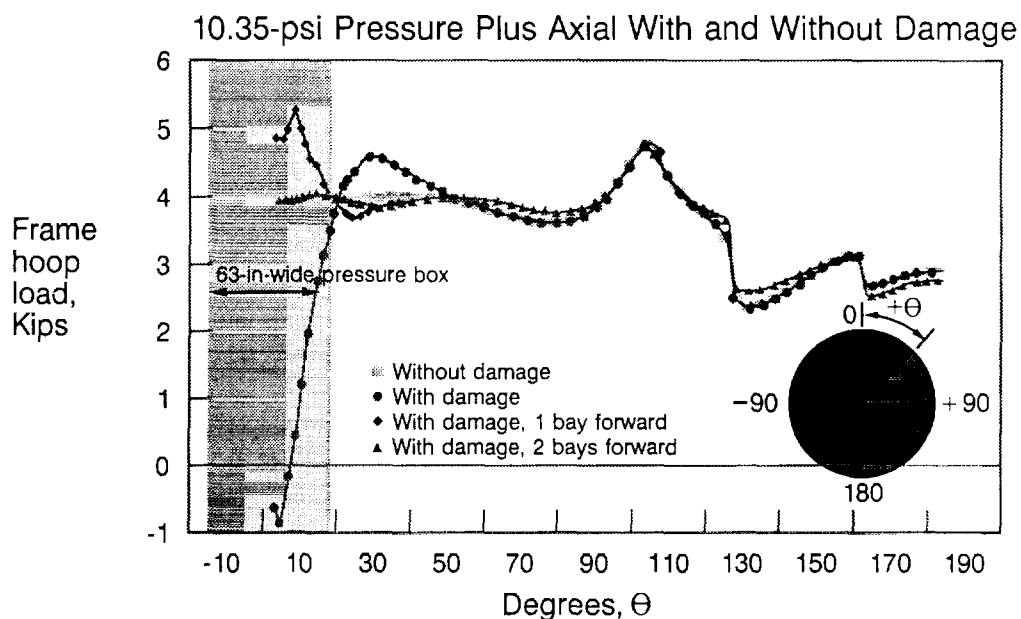


Figure 12. Circumferential frame hoop loads from full shell finite element analysis.

The first three panels in the phase 1 program will be tested at Boeing, the first being a tear-strap panel (reference Figure 4), the second and third being stiffened with frames and stringers (reference Figure 5). After the testing of the third panel is completed, the fixture will be disassembled, shipped to LaRC, and reassembled with Boeing coordination. The fourth panel, also stiffened with frames and stringers, will feature a repair of severing damage by American Airlines. The repair will be designed by Boeing based on the results of a current repair analysis and test program, with the actual repair performed by American Airlines personnel at their composite repair facility at Tulsa. This panel will be tested by NASA with Boeing coordination, after the pressure box fixture is moved from Boeing to LaRC.

Phase two of the test program will comprise the testing of five additional crown stiffened panels with varying details and damages. Table 3 lists all of these panels, their configurations, and testing scenarios. Both hoop tension critical damages and axial tension critical damages are included in the total program. Also hybrid skins will be featured on two of the phase two panels. The potential for enhanced tension fracture performance of hybrid panels has been demonstrated in ATCAS tension fracture work (Ref. 2). As was stated above, the design and fabrication of the panels for phase two are funded through a separate NASA contract. All of these panels will be tested at LaRC, with Boeing coordination.

Panel No.	Panel Description	Test Sequence	Panel test loads		Damage
			Internal Pressure	Axial Load \triangleright	
1	63" x 72" curved panel with 3 cobonded circumferential tear straps \triangleright	a) Strain survey with limit cabin pressure b) Strain surveys with increasing internal pressure	9.0 psi Up to 3.0 psi	380 lb/in —	a) None b) 22" longitudinal notch severing skin and central tear strap
2	63" x 72" curved panel with 4 cocured hat stringers and 3 bolted circumferential frames (min. gauge crown)	a) Strain surveys to limit cabin pressure b) Strain surveys with internal pressure only, then failure	9.0 psi 9.0+ psi	550 lb/in —	a) None b) 22" longitudinal notch, severing skin and central frame
3	63" x 72" curved panel with 4 cocured hat stringers and 3 cobonded circumferential frames (min. gauge crown)	a) Strain surveys to ultimate cabin pressure b) Strain survey to limit internal pressure only, then to failure	18.2 psi 9.0+ psi	1100 lb/in —	a) None b) 22" longitudinal notch, severing skin and central frame
4	63" x 72" curved panel with 4 cocured hat stringers and 3 cobonded circumferential frames (min. gauge crown)	a) Strain survey to ultimate cabin pressure b) Strain surveys to ultimate flight loads & cabin pressure	18.2 psi 13.5 psi	1100 lb/in 5000 lb/in	22" longitudinal notch, severing skin and central frame, repaired by American Airlines

\triangleright Includes representative longitudinal bulkhead pressure loading of PR/2.

\triangleright Predicted failure with damage of 5.0 psi internal pressure only

Table 2. Pressure box test program - Phase 1.

Panel No.	Panel Description	Test Sequence	Panel test loads		Damage
			Internal Pressure	Axial Load \triangleright	
5	63" x 72" curved panel with 3 cobonded circumferential frames and 4 cocured hat stringers	a) Strain survey up to limit cabin pressure and flight loads b) Load to failure with cabin pressure and flight loads	9.0 psi 9.0+ psi	550 lb/in 550+ lb/in	22" longitudinal notch, severing skin and central frame
6	63" x 72" curved panel with 3 cobonded circumferential frames and 3 cocured hat stringers (minimum gage crown area)	a) Strain survey to ultimate cabin pressure only b) Strain survey to limit cabin pressure and flight loads c) Strain survey to limit cabin pressure and flight loads, then failure	18.2 psi 9.0 psi 9.0+ psi	1100 lb/in 550 lb/in 3400+ lb/in	a) B.V.I.D. \triangleright on skin over central frame b) 2" central long. notch sev. skin at mousehole c) 14" circumferential notch, severing skin and central stringer
7	63" x 72" curved panel with 3 cobonded circumferential frames and 3 cocured hat stringers (Fwd. crown area)	Strain survey to limit cabin pressure and flight loads, then failure	9.0+ psi	5200+ lb/in	14" circumferential notch, severing skin and central stringer
8	63" x 72" curved panel with 3 bolted circum. frames and 4 cocured hat stringers (Hybrid skin - AS4/S2 fibers with 938 resin) fwd. crown	Strain survey to limit cabin pressure and flight loads, then failure	9.0+ psi	5200+ lb/in	30" circumferential notch, severing skin and two stringers
9	63" x 72" curved panel with 4 cocured hat stringers and 3 bolted circumferential frames (Hybrid skin - AS4/S2 fibers with 938 resin) min. gauge	a) Strain survey to limit cabin pressure b) Strain survey up to limit cabin pressure, then failure	18.2 psi 9.0+ psi	1100 lb/in —	a) None b) 22" longitudinal notch, severing skin and central frame

\triangleright Includes representative longitudinal bulkhead pressure loading of PR/2

\triangleright B.V.I.D. - Barely visible impact damage

Table 3. Pressure box test program - Phase 2.

TEST RESULTS

Phase 1 has commenced with testing of the first panel being completed. This panel, designated panel No. 1 in Table 2, was a curved tear-strap stiffened panel as presented in Figure 4. The test panel was instrumented with uniaxial and rosette strain gages, and deflection indicators. Shadow moire was used to provide a map of total panel deflections. The first test of the panel was a strain survey up to 9.0 psi internal pressure, with the panel undamaged. This first test run enabled the pressure box fixture and its systems to be checked out, and to understand how the panel was reacting to the internal pressure, comparing the strain and deflection to those from the FEM analysis. Axial load was applied to the panel, simultaneous with the internal pressure, to represent the bulkhead pressure present in transport fuselage cabins. The axial load applied was, in fact, lower than the load of 550 lb/in that correctly represents the bulkhead load associated with a limit cabin pressure of 9.0 psi. The test results indicated that the fixture was applying loads to the test panel correctly, and that the strains and deflections were similar to those predicted by the FEM analysis, except along the edges of the panel, especially in the corners. The FEM is not modeling these areas correctly, and more detail is needed in the model in order to match the fixture stiffness in the corners. The test panel was inspected for test induced damage. The inspection indicated that no damage had occurred.

The panel was then damaged with a 22 longitudinal inch central notch, severing the skin and the central tear-strap. The panel was again inspected with pulse echo in order to understand the complete damage to the panel prior to testing. Additional strain gages were cemented to both sides of the skin and tear-strap in the vicinity of both ends of the notch. A rubber seal was bonded to the inside of the skin, sealing the notch, and the panel was loaded with internal pressure up to 2.5 psi, combined with the corrected axial load of 150 lb/in. After this test run the panel was again inspected with pulse echo equipment to ascertain if damage growth had occurred. The inspection indicated that damage to the panel sustained by this loading sequence was minimal, and the panel was then loaded again. This time the loading was internal pressure alone. This represents a load condition consisting of cabin pressure combined with a flight maneuver that loads the fuselage crown with axial compression. This load combination is considered critical for minimum gage structure. An analysis of an unstiffened shell with the mechanical properties of the tear-strap skin and with a 22 inch longitudinal notch, indicated that catastrophic failure would occur at 5.0 psi internal pressure. Therefore, with the need to be able to inspect and dissect the panel after the test to compare with the results of various non-destructive evaluation (NDE) techniques, the panel was loaded to 4.5 psi and then unloaded. The pulse echo equipment indicated some damage growth at the ends of the notch, but more accuracy was needed. The flexural stiffness on the panel around the notch tips was measured using an advanced NDE technique that utilizes flexural wave dispersion. This technique is discussed in Reference 3. Figure 13 presents some of the results of these flexural stiffness measurements. It can be seen that close to the notch tip, the panel flexural stiffness has been reduced significantly, with the stiffness increasing as the distance from the notch tip increases. This change in stiffness indicates, as did the pulse echo inspection, that some damage growth had occurred.

The panel will be removed from the fixture so that further inspection can take place. After these inspections from both sides of the panel, sections will be cut from the panel so flexural and axial stiffnesses can be determined by mechanical test, and the results compared to those from the NDE equipment. In the mean time the fixture will be readied for testing of the stiffened panels.

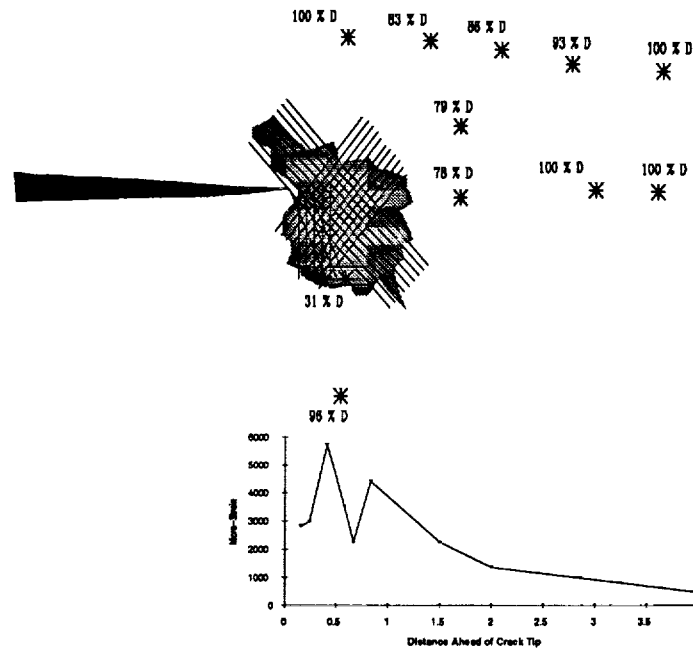


Figure 13. Effects of notch tip damage.

SUMMARY

In summary a pressure box test fixture has been designed and fabricated for the testing of curved fuselage panels. Analysis has aided considerably in the design process. The FEM analyses of both the fixture and test panels, together with the modeling work of full fuselage shells at LaRC, has resulted in a fixture that will be utilized by Boeing and NASA for tension damage tolerance testing of fuselage crown panels.

Testing has started with the first test completed. The pressure box fixture worked very well, in particular the flexible seal that was designed and fabricated in this work. As the testing continues with the stiffened panels, the analysis support at Boeing and LaRC will provide failure predictions and help understand the stress fields in the test panels. The tension damage tolerance data base that will result from both phases of the pressure box test program will help provide confidence for the effective application of advanced composites to commercial aircraft fuselage structures.

REFERENCES

1. K. Willden, S. Metschan, C. Grant, T. Brown, "Composite Fuselage Crown Panel Manufacturing Technology," NASA CP-3154, Second NASA Advanced Composites Technology Conference.
2. T. H. Walker, L. B. Ilcewicz, D. R. Polland, C. C. Poe, Jr., "Tension Fracture of Laminates for Transport Fuselage, Part II: Large Notches," NASA CP-3178, Third NASA Advanced Composites Technology Conference.
3. E. F. Dost, S. R. Finn, D. P. Murphy, A. B. Huisken, "Impact Damage Resistance of Composite Fuselage Structure, Part 2," NASA CP-3178, Third NASA Advanced Composites Technology Conference.

GLOBAL COST AND WEIGHT EVALUATION OF FUSELAGE KEEL DESIGN CONCEPTS

B.W. Flynn, M.R. Morris, S.L. Metschan,
G.D. Swanson, P.J. Smith, K.H. Griess,
M.R. Schramm, and R.J. Humphrey

Boeing Commercial Airplane Group

517-05
51417

ABSTRACT

The Boeing program entitled Advanced Technology Composite Aircraft Structure (ATCAS) is focused on the application of affordable composite technology to pressurized fuselage structure of future aircraft. As part of this effort, a design study was conducted on the keel section of the aft fuselage. A design build team (DBT) approach was used to identify and evaluate several design concepts which incorporated different material systems, fabrication processes, structural configurations, and subassembly details. The design concepts were developed in sufficient detail to accurately assess their potential for cost and weight savings as compared with a metal baseline representing current wide body technology. The cost and weight results, along with an appraisal of performance and producibility risks, are used to identify a globally optimized keel design; one which offers the most promising cost and weight advantages over metal construction. Lastly, an assessment is given of the potential for further cost and weight reductions of the selected keel design during local optimization.

INTRODUCTION

The objective of Boeing's Advanced Technology Composite Aircraft Structure (ATCAS) program¹ is to develop an integrated technology and demonstrate a confidence level that permits the cost- and weight-effective use of advanced composite materials in primary structures of future aircraft. The emphasis of the program is on pressurized fuselages. The specific emphasis of the work documented in this paper is on the keel section of the aft fuselage.

A design study of the keel was conducted such that several different concepts were developed in sufficient detail to yield accurate cost and weight estimates. Fabrication and assembly plans were considered early in design development as they have proven to be major cost centers (Reference 1). The composite concepts are compared against a 1995 metallic baseline. The design envelope (i.e., size, loads, and configuration constraints) corresponds to an aft fuselage section (referred to as "Section 46") of an aircraft with a diameter of 244 inches. The loads are characteristic of a commercial aircraft which is 80% the size of a 747.

The ATCAS program utilizes a three step design process which is described in detail in Reference 1. The first step is the selection of a "baseline" concept for each area of the fuselage: crown, side panels, and keel. The

¹ This work was funded by Contract NAS1-18889, under the direction of J.G. Davis and W.T. Freeman of NASA Langley Research Center.

selected baseline concepts are those judged to have the greatest potential for cost and weight savings, combined with an acceptable risk.

The second design step is "global optimization" in which preliminary designs are developed in sufficient detail to determine significant cost and weight differences between the baseline concepts and other potentially low-cost/low-weight concepts, as well as the aluminum counterpart. A cost and weight analysis is performed for each different concept. New concepts are then generated within each design family by trading design features in different combinations, leading to the identification of a "best" design for each family, and an understanding of which design details most significantly influence its cost and weight. The cost and weight results, as well as an assessment of the risks associated with each concept, contribute to the selection of a globally optimized design. The completed efforts of the global optimization step, as they relate to the keel, are reported in this paper.

The third step, termed "local optimization," takes the most attractive design from step 2 and optimizes individual design elements (e.g., skin, core, frame, floor beam, etc.), while continually evaluating how changes to the design impact cost centers in a global sense. Local optimization of the keel quadrant had only just begun at the time of this writing; however, based on a review of the results from global evaluation, some of the potential cost and weight savings which could be realized during local optimization have been identified and are included.

Note that the term "design family" refers to a group of design concepts sharing similar geometry, structural performance, and manufacturing cost characteristics. The design families considered in the ATCAS studies have been previously reported (Reference 1). Use of design families provides an efficient method of performing cost and weight trade studies.

DESIGN CONDITIONS

Keel Quadrant Definition

The subject of this design study is the keel quadrant of Section 46 of a wide body airplane — one which has a fuselage diameter of 244 inches and is approximately 80% the size of a 747. Section 46 is the area of pressurized fuselage just aft of the wing-to-body intersection.

The fuselage cross section is divided into four quadrants as a baseline for the ATCAS program (Figure 1). The keel comprises the lower quadrant. The keel quadrant is relatively small due to a configuration constraint imposed by a cargo door on the right side. The stiffened skin, frames, splices, and cargo floor support structure associated with the keel are all included as part of the design trades discussed herein.

Loads

The critical load case for the keel panel is a flight maneuver which causes body bending and puts the keel in compression. The resulting loads are multiplied by a factor of 1.5 to an ULTIMATE condition. The compression load is introduced into the forward end of the keel section as a concentrated force as the loads are carried around the large cutouts which accommodate the wing center section and wheel well (Figure 2). Typical aluminum designs carry these concentrated loads through two massive keel beams, or chords, which are mechanically attached to the stiffened keel skin. The concentrated load is transferred rapidly from the keel beams into the stiffened skin and then sheared out into the rest of the panel. The resulting keel skin compression and shear load contours are shown in Figures 3a and 3b, respectively. The figures show the axial load levels increasing rapidly at the forward end of the panel as the skin picks up load from the keel beams, then leveling off and gradually decreasing toward the aft end. The highest shear loads are in evidence in the areas adjacent to the forward end of the keel beams. Note also the jump in loads in the area near the side panel cargo door opening.

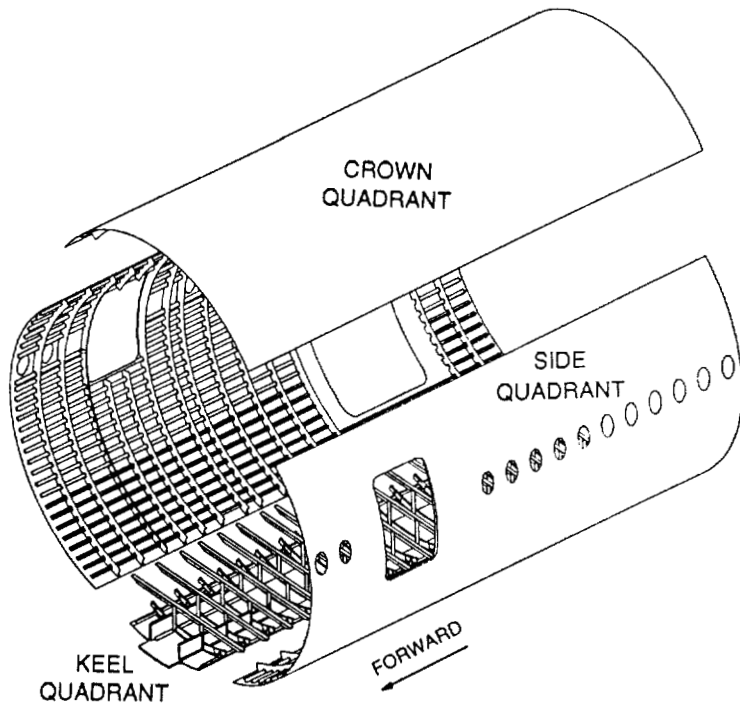


Figure 1: Exploded View of Fuselage Quadrants

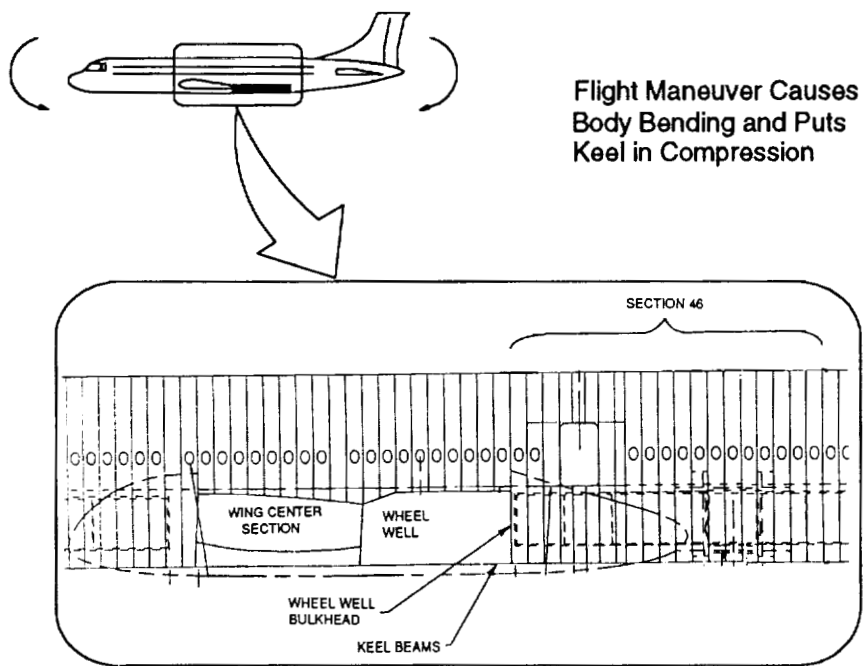


Figure 2: Load Paths in Keel Panel

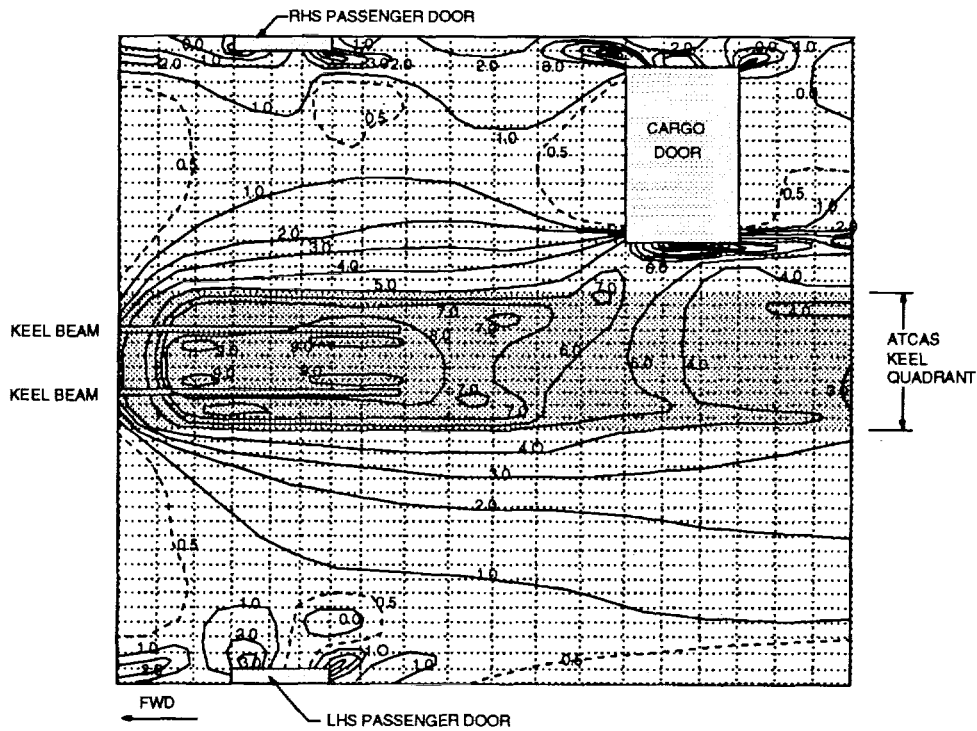


Figure 3a: Keel Panel Compression Loads (k/in)
 (discrete keel beam loads not included)

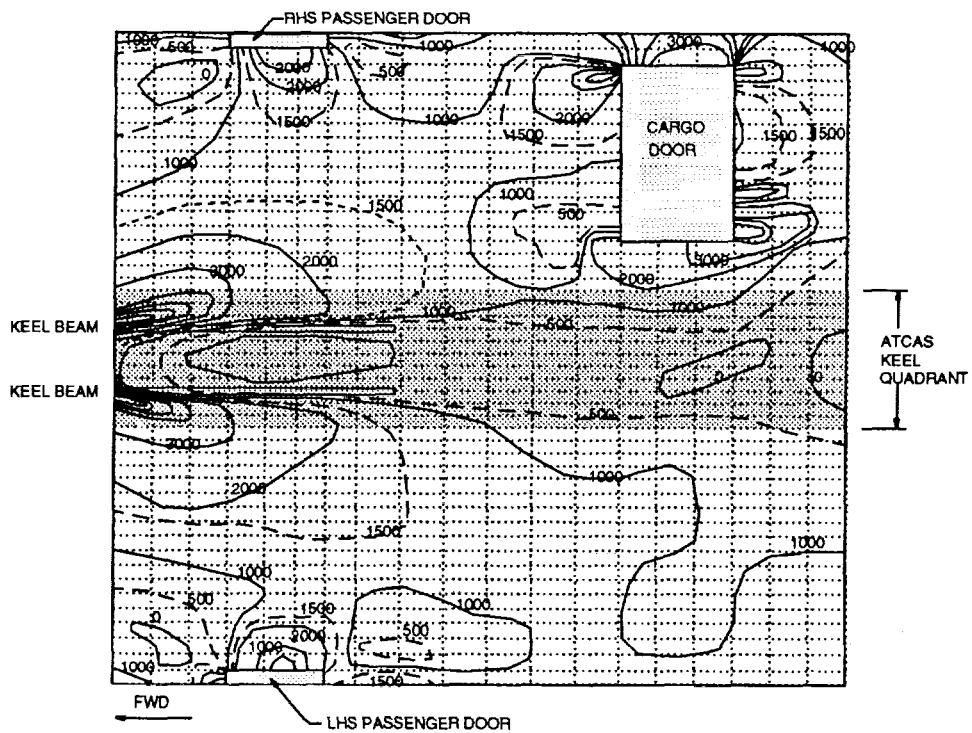


Figure 3b: Keel Panel Shear Loads (lb/in)

The compression load case discussed above is without internal pressure. The same maneuver with flight pressure, although it calls for reduced allowable strains due to the presence of hoop tension, is generally not critical for the keel panel since the axial compression loads are also reduced by the bulkhead pressure. However, an additional load case of ULTIMATE pressure (18.2 psi) acting alone was considered in the design of the keel in the circumferential or hoop direction, particularly with respect to the longitudinal splice joints. ULTIMATE pressure represents two times the maximum positive pressure differential and corresponds to a hoop direction line load of 2220 lb/in for a fuselage with a 122" radius.

Two FAILSAFE tension load conditions were checked for residual strength requirements in a damaged skin panel. The first is equal to 80% of the LIMIT axial tension load and is applied to a panel with a transverse through penetration across one stringer. (The LIMIT axial tension load is obtained by assuming a 40% reversal of the maximum compression load.) The second FAILSAFE condition is a pressure load acting on a panel with a through penetration across one frame, perpendicular to the hoop loading direction. For this damage state, an internal pressure equal to the differential operating pressure plus the aerodynamic pressure times a 1.15 safety factor is applied, resulting in an applied internal pressure of 10.3 psi and a hoop direction line load of 1260 lb/in.

Several load cases were checked in sizing the frames, including ULTIMATE pressure (18.2 psi), flight loads, and a crash condition. Each of the flight load cases was also evaluated when combined with a 13.65 psi pressure load (75% ultimate pressure, or 1.5 x maximum positive pressure differential). A flight load case was used to size the cargo support structure which carries loads from the roller trays supporting the cargo containers.

Material Considerations

A number of different material systems were considered for the trades of the keel panel designs. Two fiber types were considered: high stiffness IM6² and low cost AS4³. Similarly, the lower cost of 3501-6⁴ untoughened resin was traded against the improved compressive performance of the toughened 977-2⁵ resin. The need for local stress redistribution in the keel skins favored the use of high resin content systems, despite the resulting sacrifice of stiffness as compared with lower resin content materials (Reference 2). In the Family D sandwich structures, both Rohacell⁶ foam and graphite honeycomb core materials were considered.

Structural Criteria

The keel panel was sized to preliminary design cutoff strains which were derived based on ULTIMATE and FAILSAFE damage scenarios. Actual strain values are a function of the laminate thickness and the specific material system employed. For the gages and materials used in the keel panel, the design compression strains ranged from about .0037 to .0048.

The keel panel is also required to be tension damage tolerant. In the hoop direction the structure must show good for cabin pressure with a through penetration damage that includes one frame and adjacent skin bays severed. It must also show good for 80% limit axial tension load with a through penetration that includes one stringer and adjacent skin bays severed.

² IM6 is a graphite fiber system produced by Hercules, Inc.

³ AS4 is a graphite fiber system produced by Hercules, Inc.

⁴ 3501-6 is a resin system produced by Hercules, Inc. For the purposes of this study, its properties were assumed to be equivalent to those of the 938 resin system produced by ICI/Fiberite.

⁵ 977-2 is a resin system produced by ICI/Fiberite.

⁶ Rohacell is a foam core produced by Rohm Tech.

In order to preserve handling qualities and passenger ride comfort, limits have been placed on the overall fuselage bending and torsional stiffness. These translate into axial (EA) and shear (Gt) stiffness requirements for each portion of the complete fuselage barrel, including the keel panel. The current minimum requirement is established as 90% of the stiffness of the baseline aluminum structure.

The minimum margin of safety against buckling is set at 20% to account for uncertainties such as initial imperfections. Wide column stability of stringers and post-buckled skin is based on an effective width approach, with the column length defined by the frame spacing. Initial buckling of the skin between stringers is not allowed to occur below 40% of ultimate load. Additionally, the maximum Poisson ratio mismatch at the skin/stringer and skin/frame interfaces is limited to 0.15 to help prevent stringer and/or frame pop-off.

In sizing the frames, the assumed effective skin width is the full 21 inches (frame spacing) for 18.2 psi pressure acting alone and for 13.65 psi combined with flight loads. This is because the skin is in hoop tension for pressure cases and buckling won't occur. For flight loads without the pressure, only 5 inches of the skin (including that under frame flange) is assumed effective.

DESIGN STUDIES

Background

Two keel panel designs were developed for each of two design families (C and D). Family C is a skin/stringer/frame geometry with both stringers and frames cobonded or cocured to the laminate skin. Family D (the baseline concept for the keel) is a sandwich geometry with cobonded frames to provide hoop stiffening. All designs were developed using the design build team (DBT) approach (Ref. 1), whereby design decisions are based on the input of all pertinent disciplines (e.g., design, manufacturing, cost analysis, materials, structures, quality control).

For each design a comprehensive fabrication and assembly plan was developed to provide sufficient detail for accurate cost estimates. The assumptions used in generating the cost estimates should be noted, as they are important in understanding the relationships between design and cost. The first ground rule calls for a production rate of 5 shipsets per month with non-recurring costs burdened over 300 shipsets. The second ground rule establishes a \$100/hr wrap rate for recurring labor and \$75/hr for non-recurring labor. All labor, tooling, and material estimates are expressed in 1995 dollars, and material order quantities are based on the Section 46 keel panel only. The estimates are the result of a step-by-step appraisal of the process sequence interaction with each design detail. Important cost drivers such as machine capabilities, process limits, material utilization rates, rate tooling, learning curves, and shop variance were all included in the estimates. It should be noted that roughly half of a typical estimate is based on process steps which have labor standards developed from current production composite parts.

The following subsections describe each keel design and its corresponding manufacturing plans, controlling criteria, and cost/weight results.

Family C Designs

Design C1

Design Description. The Design C1 keel assembly is shown in Figure 4. The design incorporates discrete aluminum (7150) keel chords which are mechanically fastened to a skin/stringer panel. Load is introduced into each keel chord from the forward section via a combination of two titanium (6AL-4V) splice straps with Inconel bolts, and direct bearing via an aluminum compression plate which fills the gap between each pair of Section 45 and Section 46 keel beams. The curved skin is flattened where it attaches to the keel chords which are external

to the skin OML. A layer of fiberglass protects against corrosion between the aluminum keel beams and the composite skin.

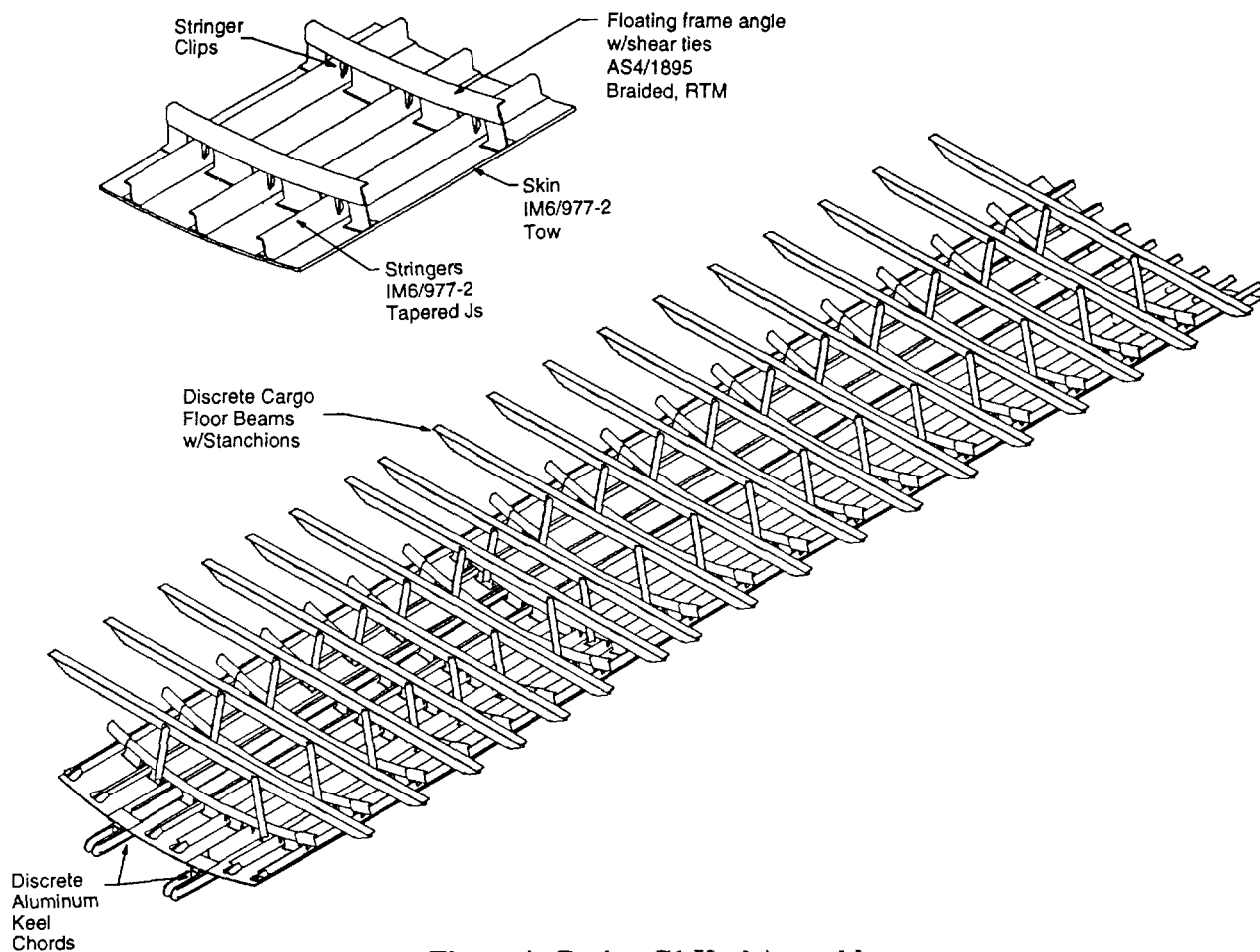


Figure 4: Design C1 Keel Assembly

The J stringers taper down in thickness proportional to the decreasing loads in the forward to aft direction. Where necessary, the width of the stringer base also varies to accommodate attachment to the keel chords. Stringers are spaced approximately 10-11" apart. The skin thickness is constant across the width of the panel in approximately the forward third of its length, then varies to match the asymmetrical loading (due to the cargo door cutout) in the remainder of the panel. The rate at which skin plies are dropped is limited by the ability of the precured stringers to conform to the profile of the cobonded skin. The design reflects a maximum drop rate of approximately 1 ply every 5 inches. Both skin and stringer use IM6/977-2 material.

The multi-piece frames include shear ties, an inner angle section, and stringer clips. The shear ties are blade sections which are cobonded to the skin in the areas between the stringers. The frame angle is mechanically fastened to the shear ties and to the webs of the J stringers via the stringer clips. The frame angles and shear ties use AS4/1895⁷ type material; the clips use AS4/3501-6.

⁷ 1895 is a resin system produced by Shell Chemical Co.

The cargo support structure for Design C1 features a discrete J-section cargo floor beam and two T-section stanchions. Angles are provided at the roller tray locations to support the flanges of the floor beam. The beam and support angles use fabric, the stanchions use tape; all are pultruded with AS4/3501-6 equivalent material.

Manufacturing Plans. The baseline fabrication method originally chosen for the keel skins employed batch processing using the same equipment and the same 360° tooling as the crown (Reference 1). This approach was abandoned as a result of cost studies done on the actual keel designs. Although larger charge sizes usually result in higher material laydown rates, a point of diminishing returns is reached where gains in the production rate do not justify the increased tooling, handling, storage life, and storage costs. The fabrication method selected for the Design C1 keel skin is tow placement on a two-at-a-time clamshell winding mandrel followed by a transfer of the skin to an OML cure tool (Figure 5). An OML tool is employed due to the criticality of the attachment of the aluminum keel chords to the outside of the skin panel. Viton bagging provides the IML surface.

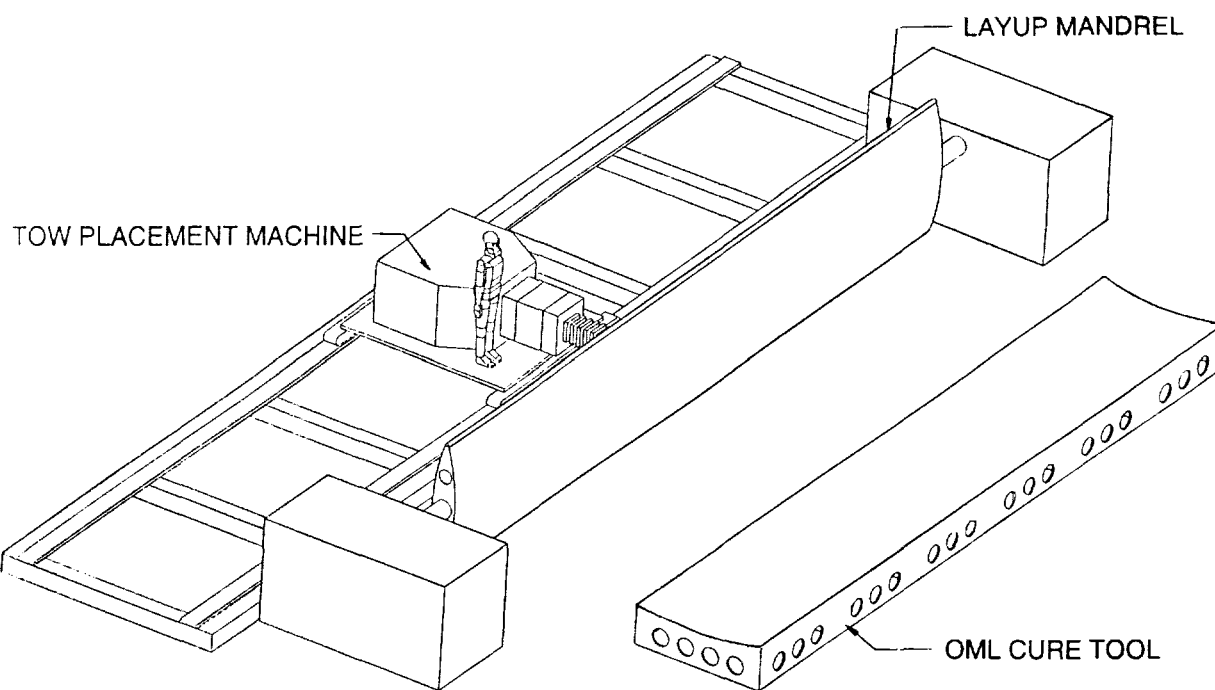


Figure 5: Tow Placement of C1 Keel Skin

Due to the large number of ply drops in the skin, the IML surface exhibits significant contour change. Use of a multi-piece frame minimizes the amount of RTM frame tooling required to match the contour. The shear ties and the frame angles to which they attach are cut from triaxially (2-D) braided/RTM J-sections. The stringer clips are pultruded. The tapered J stringers utilize automated layup and automated hot drape forming. Both the stringers and shear ties are precured and cobonded to the skin.

The keel chords are machined from aluminum extrusions. They are mechanically attached to the cured panel with a cocured fiberglass isolator at the interface. The compression plates carrying load into the keel chords are machined after casting a pattern in the void between the two assembled in-line keel chords of Sections 45 and 46. The longitudinal panel lap splice incorporates an automated layup and hot drape formed cured stringer along with automated fastening due to the clear access. The fuselage frame is then attached to the shear ties

using thermoplastic rivets. Stringer clips and the braided/RTM frame splices are then fastened in place, followed by completion of the aft circumferential splice joint. The pultruded cargo floor beam and stanchions are then assembled to the keel panel. The installation is completed after the forward circumferential splice attachment is achieved.

Design Drivers. Figure 6 is a schematic showing where specific design issues tend to be critical in the Design C1 keel panel. The figure shows the important areas of load redistribution: the keel beam to skin joint, and the areas of high shear adjacent to the keel beam. Most of the stiffened skin panel is dominated by axial compression and the minimum stiffness requirements. Minimum skin buckling becomes a driver toward the aft end where skin gages are lighter, especially in the area of increased load near the cargo door opening. Although axial loads are lower in the far aft end, the corresponding reduction in skin gages is limited by hoop tension damage tolerance.

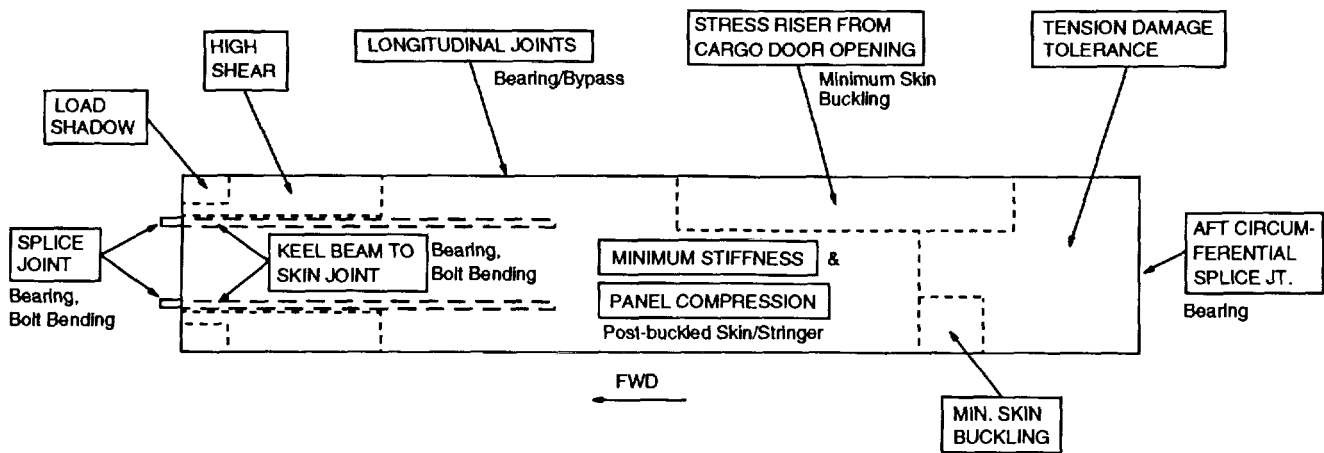


Figure 6: Critical Issues for Design C1 Keel Panel

Fastener bearing in the aft circumferential splice joint controls the skin thickness at that location, which is sized to allow the use of only two rows of fasteners per side. The longitudinal joints are controlled by bearing/bypass strength under combined hoop tension and shear loads.

At the forward splice of each keel chord the ULTIMATE compression condition relies on the bolts and splice plates to react all of the bending load but only the axial load up to LIMIT. The remaining axial load up to ULTIMATE is reacted in direct bearing by the compression plate. For the ULTIMATE tension and LIMIT compression loads the compression plate is assumed ineffective and all axial and bending loads are reacted through the bolts and splice plates. The titanium splice plates are sized not only to carry the loads but also to provide the desired bolt load distribution. High strength Inconel bolts are used for their capability to resist bolt bending.

Strain compatibility of the keel chords with the attached composite skin/stringer panel restrains the aluminum from being loaded to its full capability. The flanges of each T-section keel chord are bolted through both the skin and the bottom flanges of the J-stiffener above to provide the maximum bearing area in the composite material. For this reason the width of the keel beam web directly controls the required width of the adjacent J stiffener. The forward depth of the tapered keel chord, and therefore the rate of taper, is limited by its effect on panel bending loads due to eccentricities.

The thermal mismatch between the aluminum keel beam and the Gr/Ep stiffened skin was found not to be a critical issue for the C1 keel panel. The greatest thermally induced loads occur at about -40°F when the keel

chords contract, thus adding to the compression loads in the attached skin. However, existing material test data indicate that the increase in compression damage tolerant allowable strains for the cold environment (with respect to hot/wet allowables) more than make up for the added thermal strains. The cold condition is therefore not a critical load case.

The frames were sized to provide the stiffness required to prevent general instability of the fuselage. Strength checks were also conducted and revealed the flight loads were not critical once the stiffness criteria were met. The minimum cross section of the multi-piece frame occurs over the stringer where the inner angle spans between shear ties. The frame must also react out-of-plane loads due to eccentricities in the longitudinal load path of the stiffened skin and distribute concentrated loads from the cargo support structure. The fasteners connecting the inner frame angle to the shear ties carry both these reaction loads and the shear flow acting along the length of the frame.

The cargo support structure for Design C1 uses a large cargo floor beam and a minimum number of stanchions (two) to beam out the loads acting at the locations of the eight roller trays. The floor beam is critical for bending strain due to flight loads. The upper flanges of the J-section floor beam are supported against bending by mechanically fastened clips at the roller tray locations.

Design C2

Design Description. The Design C2 keel assembly is shown in Figure 7. Design C2 is similar to Design C1 in that it incorporates a skin stiffened with cobonded, precured J stringers. Rather than discrete keel chords, however, Design C2 utilizes a thick laminate skin to carry the high compressive loads which exist at the forward end of the keel. The thick laminate acts as a panelized keel beam by spreading the equivalent material of the discrete keel chords across a wide section of the keel panel. This panelized keel beam tabs out from the forward end of Section 46 to accept load from the forward section via two bolted titanium (6AL-4V) splice plates. Both D Family designs have similar panelized keel beam and joint details.

The Design C2 J stringers maintain constant geometry the full length of the panel. Blade stringers, also of constant geometry, are used along the longitudinal splice joints; however, these are fastened in place rather than cobonded. As in Design C1, the stringers are spaced approximately 10-11" apart. The thick skin in the forward center of the panel tapers down to the sides and to the aft end where the loads are lighter. The asymmetrical skin thicknesses in approximately the aft two-thirds of the panel reflect the loads in that area. Because the Design C2 panel uses IML tooling, the precured stringers have a smooth surface to bond to and do not limit the rate of ply drops in the skin as they did in Design C1 which uses OML tooling. While the IML tooling pushes the skin thickness variations to the outside, the greatest ramp rates occur in the forward portion of the panel which is inside the fairing. Aerodynamic smoothness is therefore maintained. Both skin and stringers are AS4/3501-6 material.

The frames, which are cobonded to the skin, are one-piece triaxially (2-D) braided Js with mouse holes over the stringers. Clips fasten the stringer webs to the frames at the mouse hole locations. Frames are made of AS4/1895 type material and clips are AS4/3501-6.

The cargo support structure for Design C2 is similar to that for Design C1 in that it features discrete floor beams and stanchions; however, Design C2 uses a larger number of smaller sized elements. The six stanchions are C-channels, the cargo floor beam is a J-section. Angles are provided at the roller tray locations to support the flanges of the floor beam. The stanchions, beam, and support angles all use tape; all are pultruded with AS4/3501-6 equivalent material.

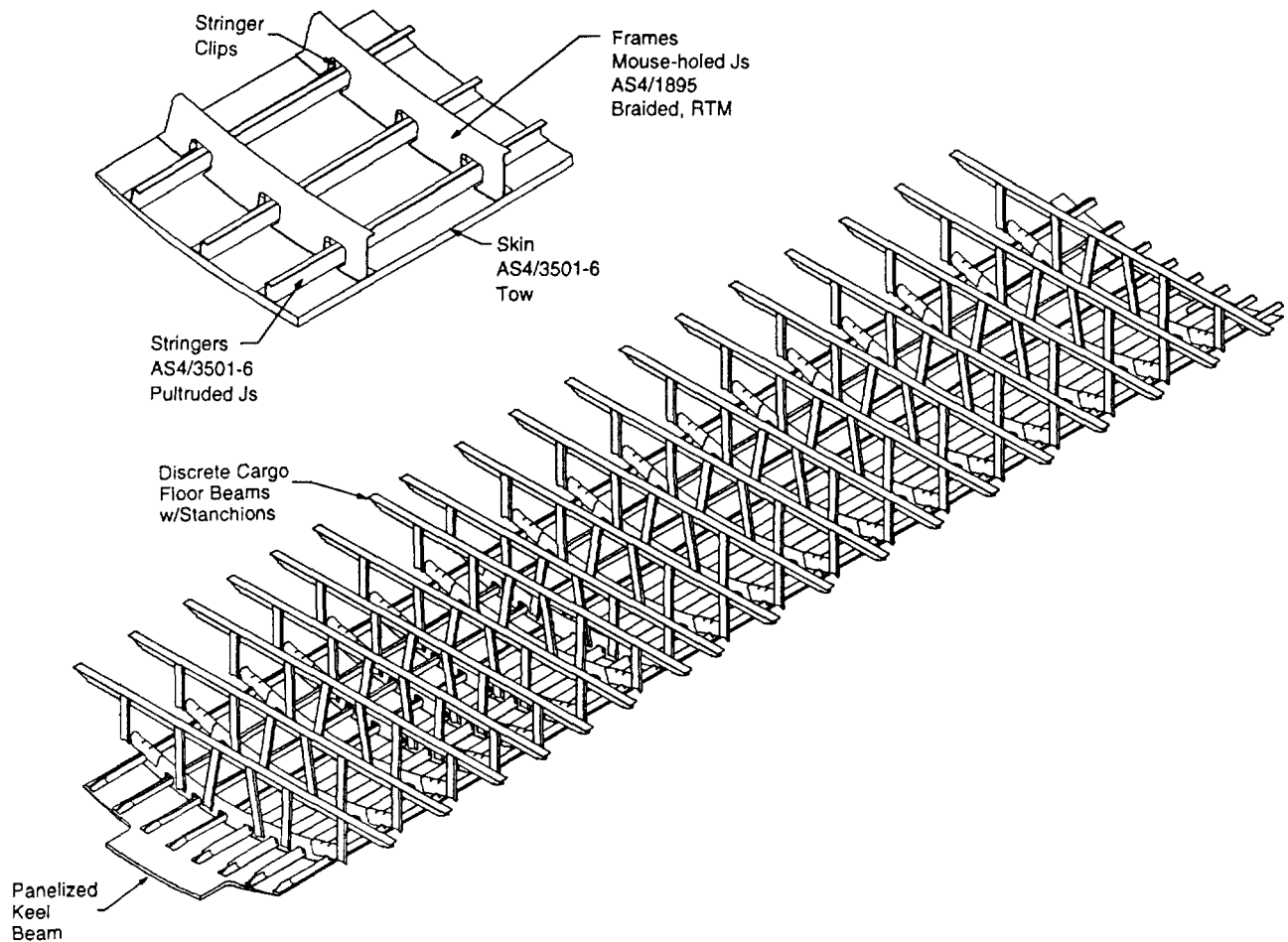


Figure 7: Design C2 Keel Assembly

Manufacturing Plans. The keel skin for Design C2 is tow placed directly over the cure tool, as illustrated in Figure 8. The use of IML tooling resulted in a constant IML surface allowing for the use of a one piece braided/RTM frame. The use of constant gage J stringers allows for the efficient use of pultrusion. The precured frames and stringers are located in the IML tool and the skin is tow placed over the details. The subsequent oven/vacuum bag operation cures the skin and cobonds it to the frames and stringers.

The stringers at the longitudinal lap splices are automated dry fabric layup pultrusions. As with Design C1, the clear access allows for automated fastening. The automated layup hot drape formed and cured frame splices are then installed, after which the aft circumferential splice is completed. The pultruded cargo floor beams and stanchions are then assembled to the keel panel. The installation is completed with the forward circumferential splice attachment.

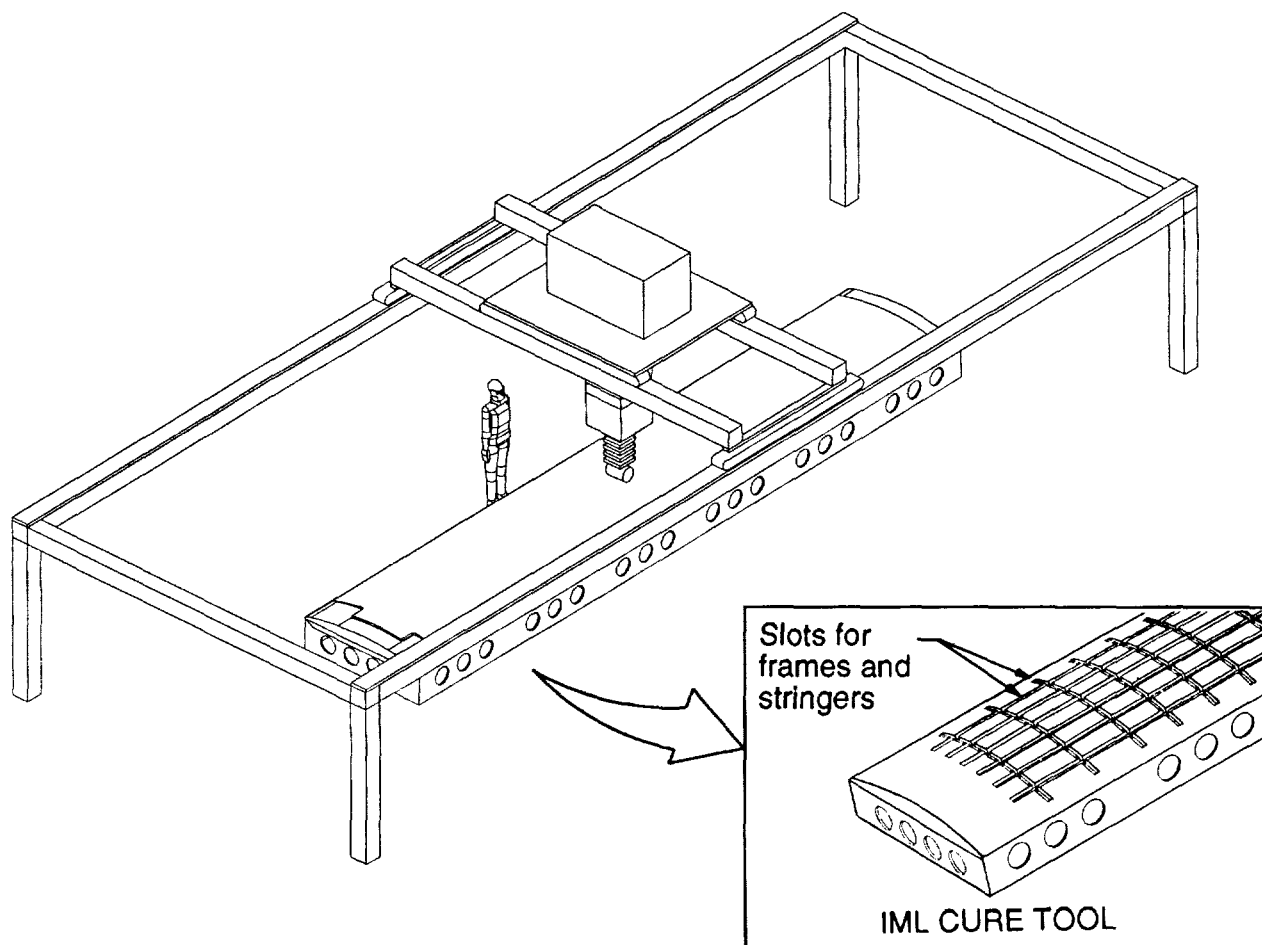


Figure 8: Tow Placement of Design C2 Panel

Design Drivers. Figure 9 shows in schematic form the areas where certain design issues are critical for the Design C2 keel panel. Many of the design drivers are similar to those shown for Design C1. The major area of difference is at the forward end where Design C2 has a very thick skin acting as a panelized keel beam in place of discrete keel cords. The thick skin easily satisfies the minimum shear stiffness requirement, which only becomes a design driver toward the aft end where the panelized keel beam has tapered out. As plies are dropped from the thick laminate, bending loads are introduced due to eccentricities in the load path, and add to the compression strains which dominate the forward two-thirds of the panel. As in Design C1, the skin in much of the aft end is controlled by minimum skin buckling. However, tension damage tolerance does not drive the skin gages in the aft end of Design C2 as it did Design C1. This is due to the better tension fracture performance under large crack sizes demonstrated by the AS4/3501-6 system as compared with AS4/977-2.

Like Design C1, the longitudinal joints are controlled by bearing/bypass strength, and the aft circumferential splice joint is critical for fastener bearing. The required skin thicknesses at the joints for Design C2 are sometimes greater due to the lesser bearing properties of the AS4/3501-6 material. The forward splice joint at the panel tab out is bearing and bypass critical. Note that this forward splice joint design, unlike Design C1, has no direct bearing capability and the full ULTIMATE compression load is carried through the bolts and splice plates. The titanium splice plates were sized to provide a fairly uniform bolt load distribution and to hold the joint to only three rows of fasteners per side.

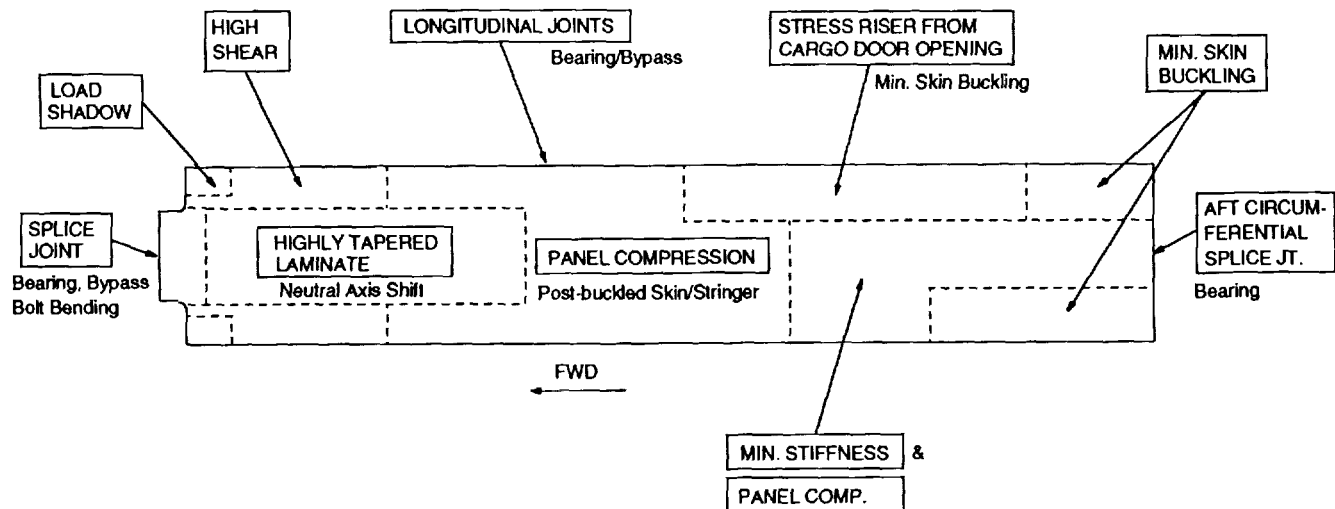


Figure 9: Critical Issues for Design C2 Keel Panel

The frames are stiffness designed to prevent general instability. The most strength critical area is where the mouse holes are cut from the frame cross section to accommodate the stringers. Pressure combined with flight loads results in the most severe combination of axial and bending loads, producing a maximum strain at the inner edge of the frame. The effect of stress concentrations at the mouse holes is not a design driver since the edge of the mouse hole cutout is in the middle of the bending section, away from the more highly stressed frame inner edge.

The cargo support structure for Design C2 utilizes a six stanchion configuration with supports directly beneath the roller trays. This greatly reduces the bending loads in the floor beam as compared with Design C1, and the floor beam of Design C2 is downsized accordingly. Design C2 also provides greater stiffness than Design C1 and, as a result, may improve the functioning of the cargo handling equipment. Like Design C1, Design C2 includes mechanically fastened clips at the roller tray locations to support the upper flanges of the J-section floor beams against bending.

Family C Cost Results

Cost results for the Family C keel designs are shown in Figure 10. The figure shows costs for the total keel assembly and for each of the six major processes which comprise it. These costs are further categorized into nonrecurring costs and recurring material and labor costs. All costs are expressed as a relative percentage of the total metal keel baseline cost.

The total cost for Design C1 is 103% and Design C2 is 82% of the total metal keel baseline cost. Note that this cost data is for the non-optimized composite designs, and is therefore intended primarily to identify the differences between variations within the design family. Cost comparisons between the metal and the globally optimized composite designs are given later.

The panel fabrication and assembly (including keel chords) is 34% of the total metal keel panel cost for Design C1 and 26% for Design C2. The labor cost is affected in two main areas. The first is the skin fabrication in which Design C1 utilizes a winding mandrel and subsequent transfer to the cure tool, while Design C2 calls for material placement directly on the cure tool. The winding mandrel approach of Design C1 provides a slightly improved layup rate as compared with Design C2, but not enough to justify the increased tooling and handling costs. The second area affecting labor costs is the tooling approach. The IML tool of Design C2 simplifies the procedure for bagging and locating stiffening elements. This results in significant labor cost savings over the

OML tooling approach of Design C1, although the savings are offset somewhat by the higher cost of the more complex IML tool.

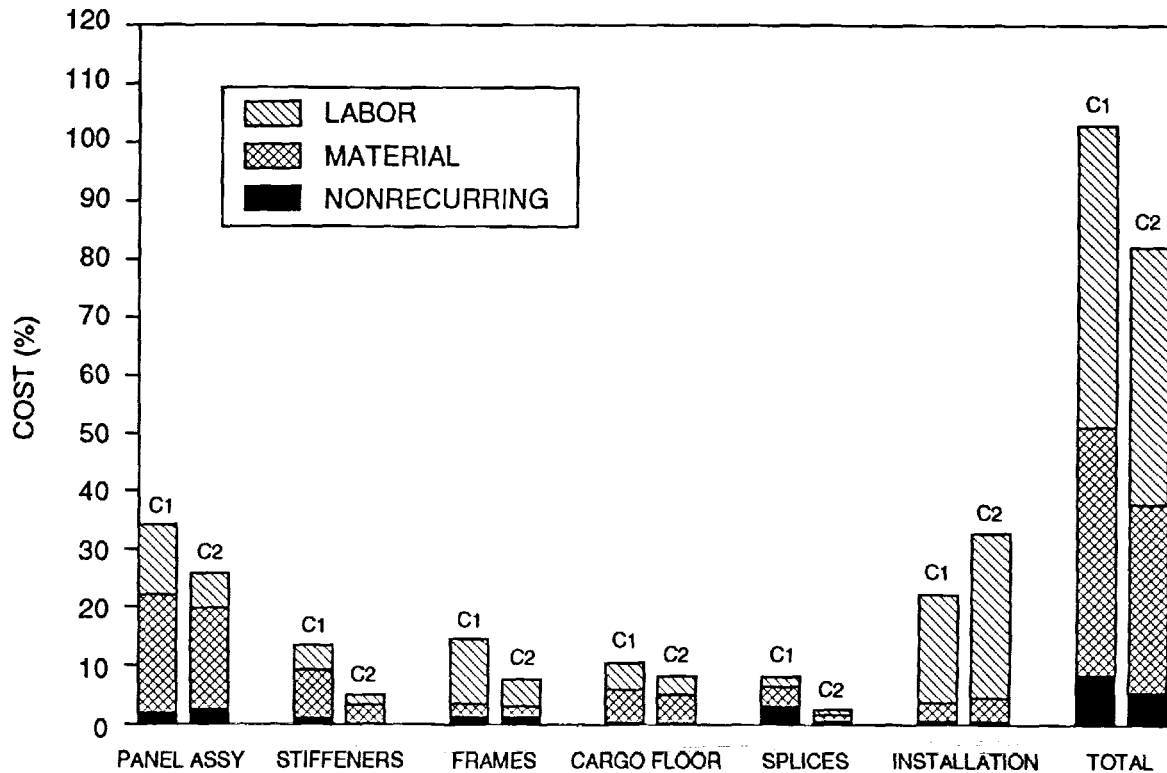


Figure 10: Family C Cost Results

The panel material costs are also affected in two main areas. The first difference results from the IM6 fiber used in Design C1 which is 32% more expensive than the AS4 fiber used in Design C2. The second difference arises from the material used in the keel beam designs: aluminum for the discrete keel chords of Design C1, AS4/3501-6 for the panelized keel beam of Design C2. The raw material cost per pound for the aluminum is only 62% of the AS4/3501-6 material; however, after machining and assembly are taken into account, the cost per pound of the aluminum keel chords jumps to 131% of the composite panelized keel beam.

Stiffener fabrication was 13% (Design C1) and 5% (Design C2) of the total metal keel panel cost. Significant labor savings result for the Design C2 stringers which are constant section and can therefore be pultruded. The stringers for Design C1 are required to be tapered and utilize automated layup and manual hot drape forming. While automating the hot drape forming process would help improve the efficiency of the Design C1 stringer fabrication, the large batch sizes inherent in pultrusion would be hard to better. The differences in material costs between the two designs was due to the use of the more expensive IM6 fiber for Design C1 along with a design that requires a large amount of material wastage. The stringers for Design C2 utilized the less expensive AS4 fiber along with automatically stacked and lightly stitched dry tape preform.

Frame fabrication amounted to 15% of the total metal keel panel cost for Design C1 and 8% for Design C2. The labor cost doubled for the multi-piece frame used in Design C1, due largely to the assembly, as compared with the one piece frame used in Design C2.

Cargo floorbeam fabrication was 11% (Design C1) and 8% (Design C2) of the total metal keel panel cost. The use of prestacked dry tape preforms for both stanchion and floorbeam pultrusions of Design C2 versus the automated dry fabric layup and kitting in Design C1 is responsible for most of the difference in labor costs.

The splice fabrication was 8% (Design C1) and 3% (Design C2) of the total metal keel panel cost. The primary reason for the difference between the two Family C designs is the design of untapered parts allowing the consistent use of pultrusion in Design C2.

The keel panel installation was 22% (Design C1) and 33% (Design C2) of the total metal keel panel cost. The first major difference between the two is the design of the cargo support structure: a two stanchion configuration for Design C1, six stanchions for Design C2. This has a significant effect on cost (7% for Design C1 versus 17% for Design C2), while providing only a minimal improvement in weight for Design C2. The second major difference is the forward splice design. Design C1 splices its discrete keel chords in a manner similar to the current metal technology. Design C2 utilizes a double shear tab out splice. While the two approaches are very different, the resultant costs are about the same.

Family C Weight Results

The weight results for the non-optimized Family C keel designs are shown in Figure 11. Weights are given for the total keel assembly and for each of the same six major processes used in the cost comparisons. All weights are expressed relative to the total metal keel baseline weight. Design C1 shows a total weight 87% of the metal baseline; Design C2 is 88%. Only minor differences between the weights of the various designs were found.

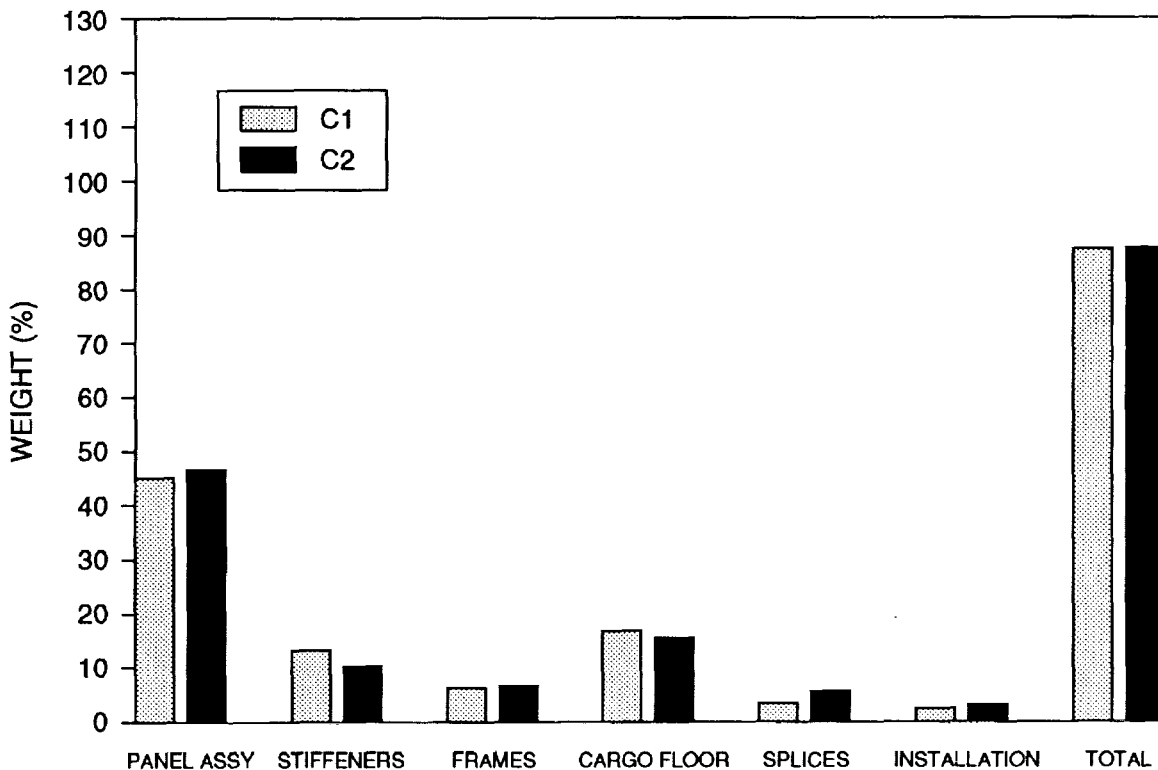


Figure 11: Family C Weight Results

Family D Designs

Design D1

Design Description. The Design D1 keel assembly is shown in Figure 12. The design utilizes a thick laminate to carry the high compressive loads which exist at the forward end of the keel, and transitions to sandwich construction as the loads reduce further aft. The thick laminate acts as a panelized keel beam by spreading the equivalent material of the discrete keel chords across a wide section of the keel panel. The panelized keel beam tabs out from the forward end of Section 46 to accept load from the forward section via two bolted titanium (6AL-4V) splice plates. Moving to the rear of the panel, the thick laminate is tapered out, and the change in thickness is made up by an insert of core material which allows the inner radius of the panel to remain constant along its length. The constant inner radius reduces the number of individual frames which would otherwise need to be manufactured. The sandwich construction eliminates the need for stringers. The panel incorporates panned-down edges to provide a solid laminate for splicing to adjacent structures. A blade stiffener is fastened to the skin along each panned-down longitudinal splice edge to provide stability.

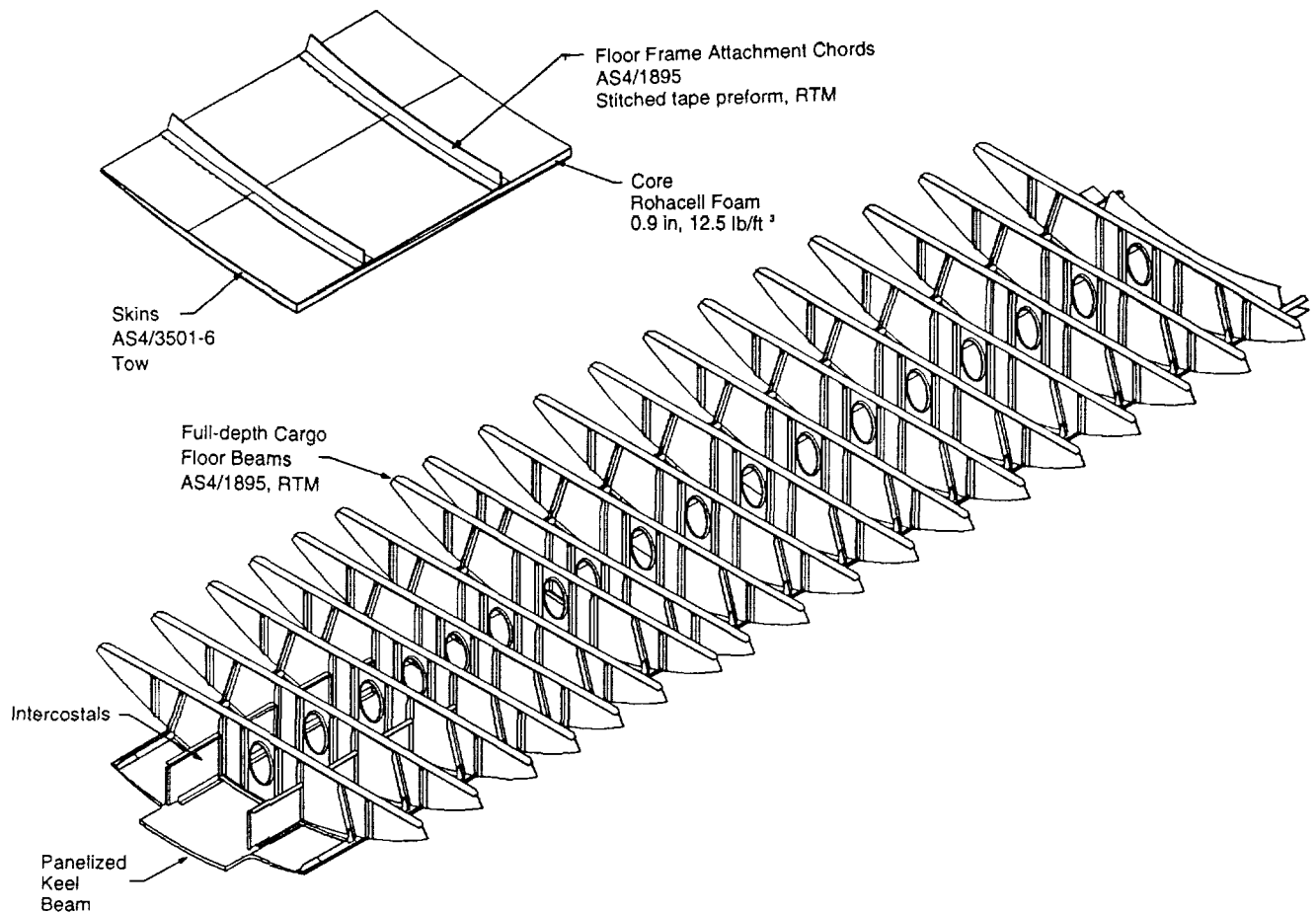


Figure 12: Design D1 Keel Assembly

The frames in the D1 keel section are integral with the cargo support structure to form a full-depth beam. This is accomplished by cobonding blades onto the skin and then mechanically fastening these to the stiffened web which comprises the rest of the frame/cargo beam. At the forward end of the keel panel, intercostals are used to

stabilize the thick "skin" against buckling. These are also accomplished by fastening to blades which have been cobonded to the skin.

Design D1 utilizes a 12.5 lb/ft³ foam core material, and the sandwich skins are high resin content (42%) tow placed AS4/3501-6. The full-depth cargo floor beam is fabric material equivalent to AS4/1895. The longitudinal edge stiffeners are AS4/3501-6 type material in stitched tape form. Design variations D1A and D1B were developed to evaluate different materials and processes for the intercostals, intercostal attachment blades, and frame blades. All intercostal blades and frame blades use AS4 type fiber; however, Design D1A uses fabric prepreg and 3501-6 type resin, while D1B uses stitched tape preform and 1895 type resin. Intercostals are AS4/1895 type stitched tape for D1A and AS4/ACP-2(PEEK)⁸ thermoplastic for D1B.

Manufacturing Plans. Design D1 uses IML tooling in order to standardize all the frame and intercostal attachment chords which are precured, fitted into slots in the tool, and cobonded to the panel. Two manufacturing methods are identified for the attachment chords. The first method (D1A) employs hand layup prepreg fabric which is hot draped formed, assembled, and cured. The second method (D1B) utilizes prestacked tape and resin transfer molding.

The skins are fabricated in a manner similar to Design C1; however, due to the use of IML tooling, a concave winding tool is required (Figure 13). After the precured attachment chords are in place, the tow placed skin is transferred to the cure tool. Vacuum pressure is used to hold the skin panel to the winding tool until it can be located directly over the cure tool.

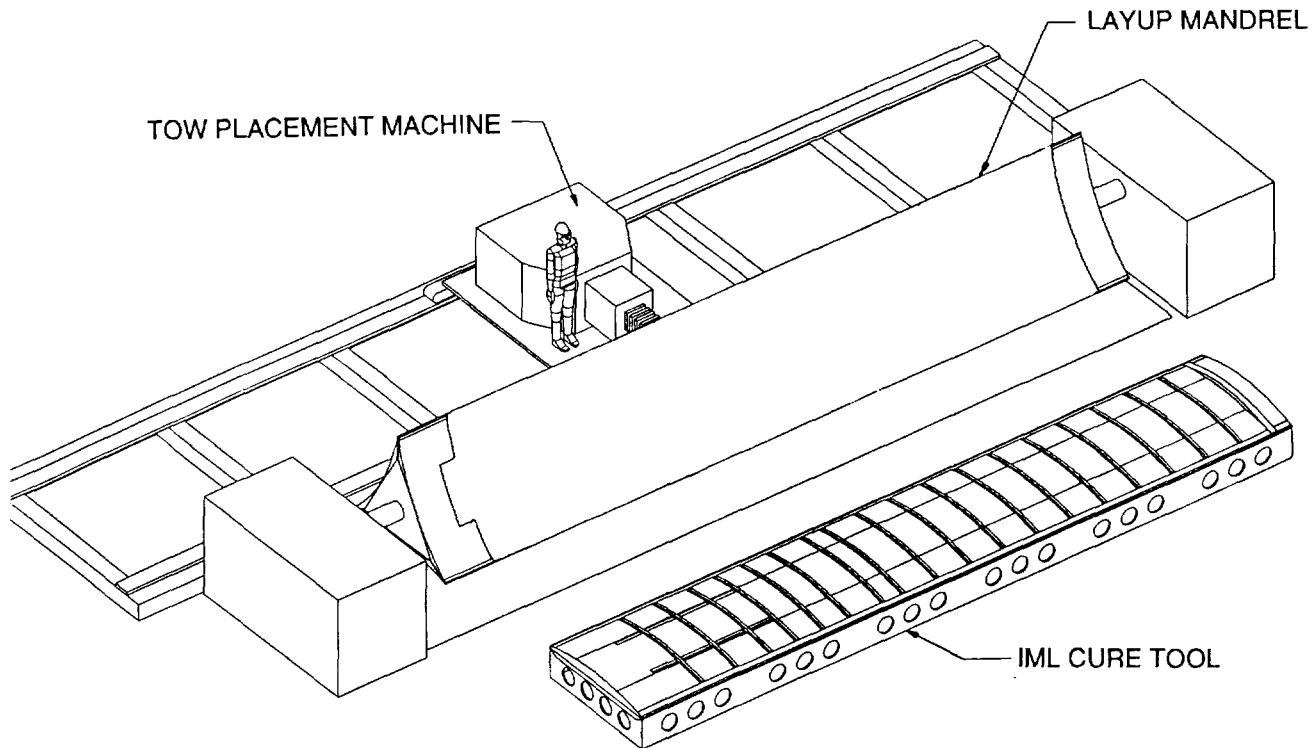


Figure 13: Tow Placement of Design D1 Keel Skin

⁸ ACP-2 is a resin system produced by ICI/Fiberite, Inc.

The fabrication of the Rohacell core with its double taper and curvature represents a significant challenge in fabrication, handling and locating. The OML surface of the core is cut prior to the forming of the curvature. Then, after an oven/vacuum bag operation has induced curvature into the core while it is in the forming tool, barrel cutters are used to trim the IML surface. The foam core is then located onto the cure tool, with the inner skin and precured attachment chords already in place, and the outer skin is placed over the core. The assembly is then oven/vacuum bag cured.

Design D1 includes a full depth resin transfer molded cargo floor beam. Individual dry preform stiffening elements are located into the cure tool, followed by the web charge. The dry preform is then resin infused, cured and trimmed. Intercostals are resin transfer molded for D1A and pressformed thermoplastic for D1B.

Once the sandwich panel with cobonded attachment chords is completed, the longitudinal lap splice is accomplished using a stitched tape pultruded stringer along with automated fastening due to the clear access. The aft circumferential splice joint is then completed. This step is followed by the installation of the full depth cargo floor beams which are fastened to the co-bonded chords. The stitched tape/RTM or thermoplastic intercostals are then installed in the first four bays at the forward end. Then the pultruded frame splices are mechanically fastened. Lastly, the forward splice installation is completed using two titanium splice plates.

Design Drivers. Figure 14 is a schematic showing where specific design issues tend to be critical in the Family D Designs for the keel panel. The forward end is driven by the areas of high shear and panel compression, much like Design C2 which also has a panelized keel beam. Without stiffeners however, Design D1 requires intercostals in the first four bays to provide panel stability. The absence of stiffeners also requires the sandwich skins to remain fairly thick toward the aft end of the keel. As a result, neither the minimum shear stiffness or the tension damage tolerance requirements become critical. As the thick laminate transitions to a sandwich structure, the rate of ply drops in the longitudinal direction is limited by the resulting shifts in the neutral axis, which add bending loads. Along the panned-down longitudinal edges, blade stiffeners are attached to compensate for the loss of bending stiffness (and therefore column stability) provided by the sandwich construction.

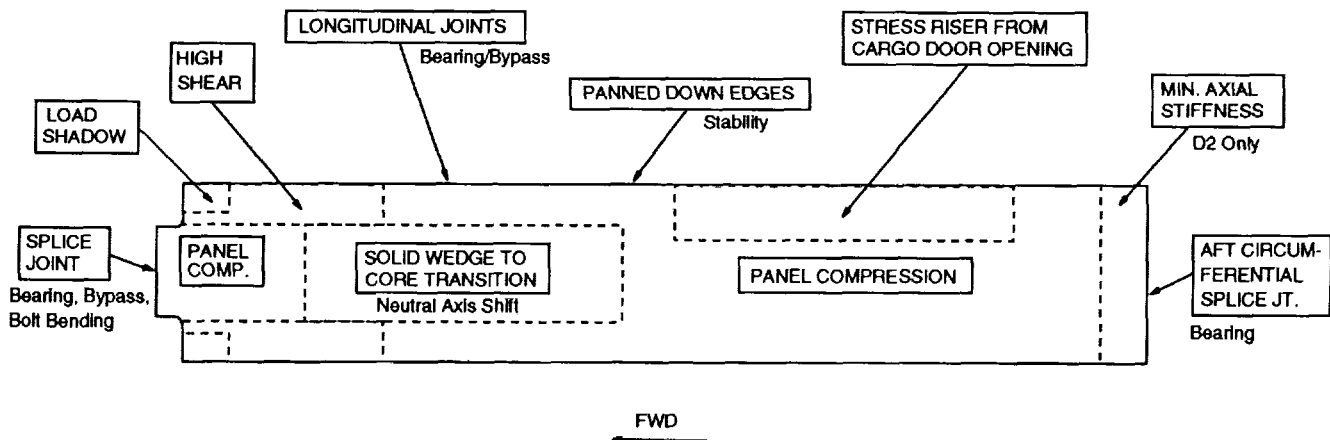


Figure 14: Critical Issues for Design Family D Keel Panels

The intercostals are designed to provide a reaction equal to 7% of the compressive load in the panel they are stabilizing. The most forward intercostal is therefore the most highly loaded, and is sized accordingly. The differences between the D1A and D1B intercostals reflect the properties of the different materials. The addition of a vertical stiffener to break up the buckle pattern and allow a thinner gage was considered but dismissed as

too expensive for the amount of weight saved, especially since a minimum intercostal thickness is nevertheless required at the attachment to the skin-bonded blade where fastener bearing is critical.

The panned-down edges of the sandwich panel provide joint details much like the Family C Designs. The longitudinal joints are controlled by bearing/bypass strength, and the aft circumferential splice joint is critical for fastener bearing. The forward splice joint at the panel tab out is very similar to that of Design C2.

The full-depth cargo floor beam acts as a stiffened post-buckled shear beam. Per the established criteria, the web of the beam was not allowed to buckle below 40% ULTIMATE load. The lower chord of the beam is formed by the blade-section frame which is cobonded to the skin panel. The upper chord is reinforced against flange bending as required beneath the roller trays by an integral angle and/or the ends of the vertical web stiffeners. The access hole cut from the center of the beam is reinforced around its edges with an upstanding flange.

Design D2

Design Description. The Design D2 keel assembly is shown in Figure 15. The D2 design is very similar to D1, with a panelized keel beam transitioning to a sandwich structure. The major differences between the two D designs are the materials and the configuration of the frames and cargo support structure. The D2 skins use toughened resin 977-2 with AS4 fibers. The sandwich core is a 6.0 lb/ft³ graphite/thermoplastic honeycomb. An edge filler of 12.5 lb/ft³ Rohacell foam is provided where machining the honeycomb to a knife edge would prove too difficult.

Design D2 has discrete cargo floor beams supported by two stanchions, all using AS4/3501-6 type material. The beams are pultruded Js made from fabric, with an integral radius filler running full length to support flange bending. The stanchions are pultruded Ts made from stitched tape. The stanchions fasten into the frames, which are Js fashioned from triaxially (2-D) braided material, equivalent to AS4/1895. The frames are cobonded to the skin. The D2 intercostals are very similar to those for D1 except the material is AS4/3501-6 prepreg fabric.

Manufacturing Plans. The method of fabrication for Design D2 utilizes an IML tool similar to that of Design D1. The IML tool provides standardization of all of the pultruded intercostal attachment chords and braided/RTM frames which are cobonded to the skin panel. As in Design D1, the IML tool is notched to accept the precured attachment chords and frames. Unlike Design D1, however, the skins for Design D2 are tow placed directly onto the cure tool. The thermoplastic honeycomb core is trimmed net and then formed into its curved shape. The core is transferred to the cure tool, with the inner skin, frames, and attachment chords already in place, and then the outer skin is tow placed over the core. The subsequent oven/vacuum bag operation yields a cured skin panel with cobonded attachment chords and frames.

The longitudinal lap splice is achieved using an automated layup dry fabric/pultruded stringer along with automated fastening due to the clear access. The frame splices are completed, followed by the aft circumferential splice joint. Then the pultruded floor beams and stanchions are fastened to the keel panel frames. The pressclave thermoset intercostals are then installed in the forward first four bays. The forward splice installation is then completed using two titanium splice plates.

Design Drivers. The drivers for the Design D2 keel panel are very similar to those for Design D1, and Figure 14 is again applicable in identifying the areas of critical design issues. The forward end is sized very closely to Design D1 because the splice joint at the tab out is the controlling factor. Further aft however, the toughened material used in Design D2 allows thinner skin gages and higher ramp rates for ply drop-offs. At the very aft end, the reduction of skin thickness is limited by the minimum axial stiffness requirement.

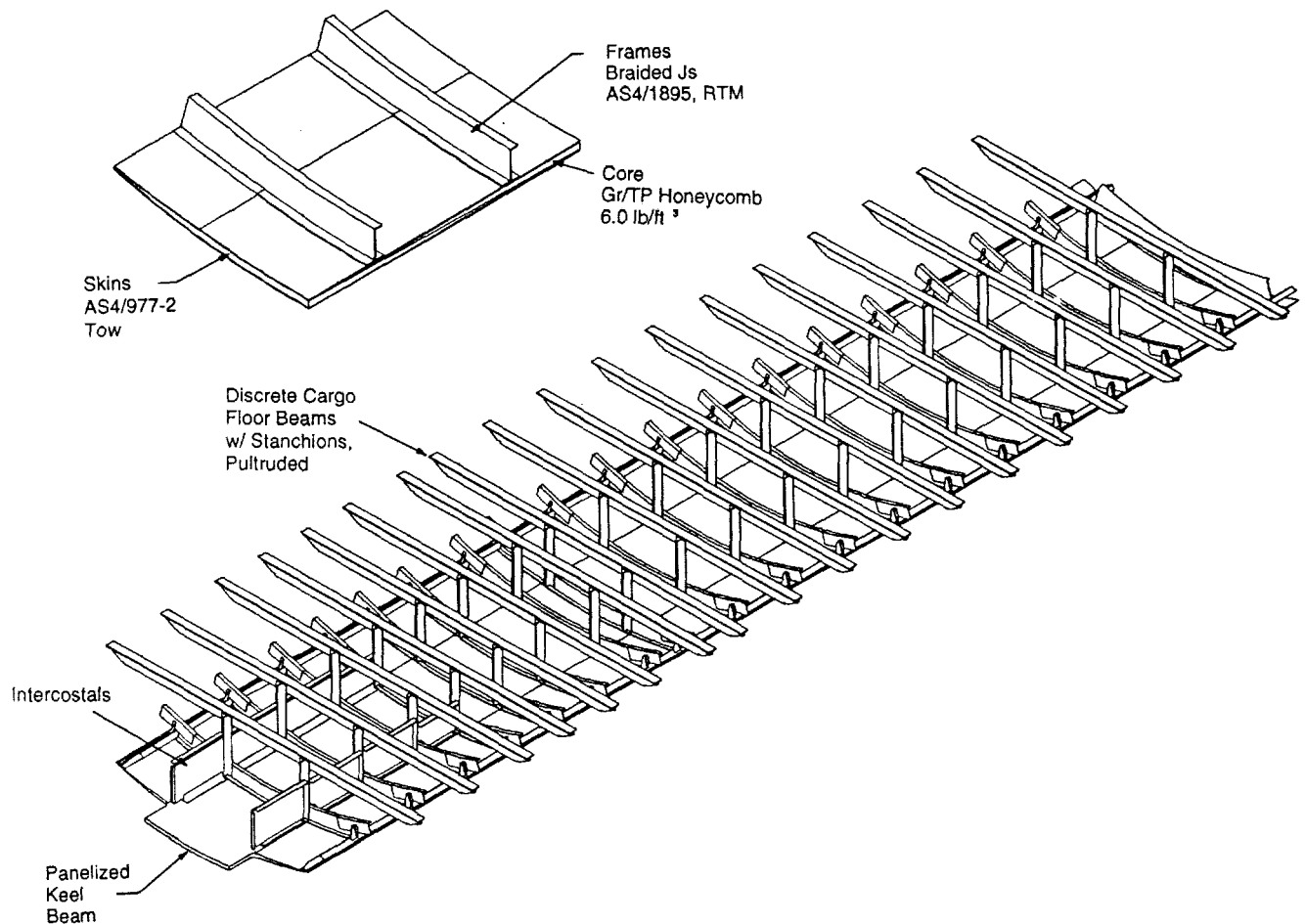


Figure 15: Design D2 Keel Assembly

The cargo support configuration for Design D2 is similar to Design C1, except the angles supporting the top flanges of the J-section floor beam are integral and run the full length of the beam. The two stanchions of Design D2 stand vertically, rather than slightly angled as in Design C1. The frames were sized in a manner similar to those of Design C2, without the complication of mouse holes.

Family D Cost Results

Cost results for the Family D keel designs are shown in Figure 16. The costs are expressed as a percentage of the metal keel baseline cost. The figure gives the total cost for the keel assembly and also a breakdown into six major processes. These costs are further broken down into nonrecurring costs and recurring material and labor costs.

The total cost was 117% (Design D1) and 119% (Design D2) of the metal baseline. Again, note that this cost data is for the non-optimized Family D composite designs, and is intended primarily to identify the differences between variations within the design family. Cost comparisons between the metal and the globally optimized composite designs are given later.

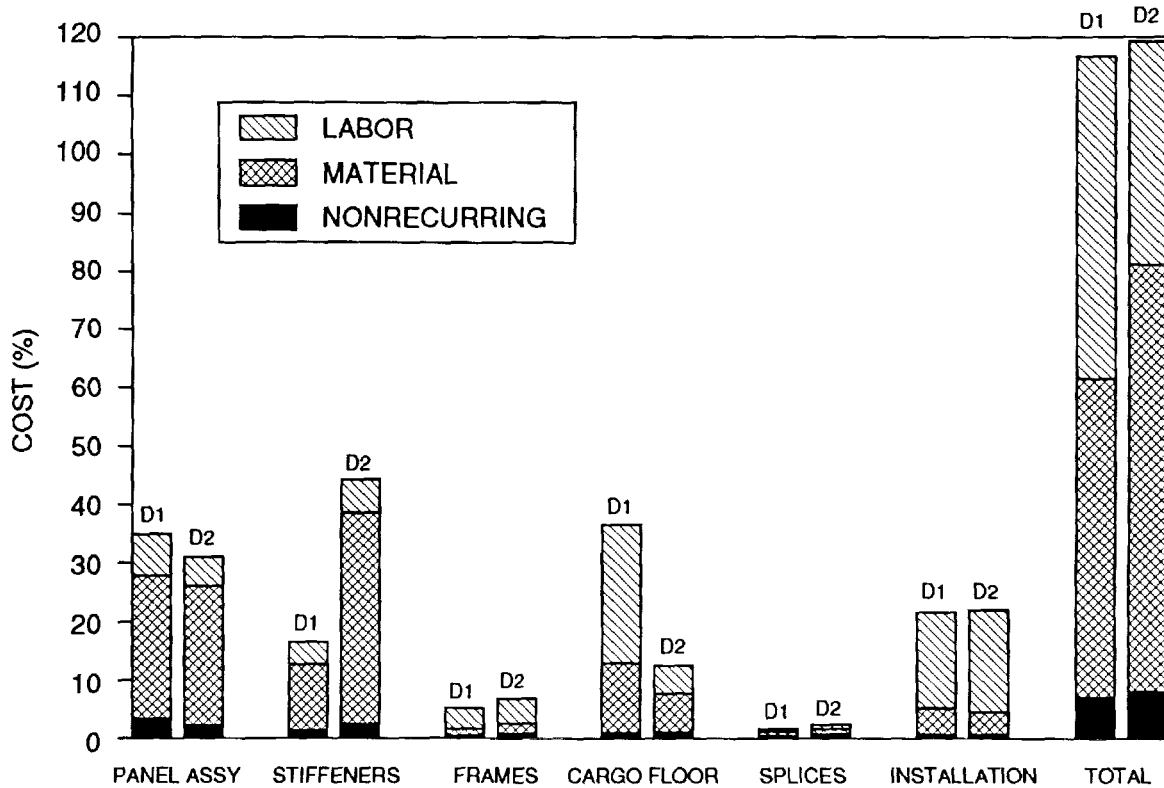


Figure 16: Family D Cost Results

The keel panel fabrication and assembly was 35% of the total metal keel panel cost for Design D1 and 31% for Design D2. As was the case with Family C, an improved material laydown rate in the winding method of Design D1 skin fabrication does not justify the additional tooling cost and labor steps associated with the process. Although only a six inch bandwidth was used for Design D1, increasing it to match the twelve inch bandwidth of Design D2 still wouldn't significantly reduce the overall cost. Automated fiber placement directly on the cure tool, as utilized in Design D2, offers a cost advantage.

Fabrication of the core and stiffening elements is 17% (Design D1) and 44% (Design D2) of the total metal keel panel cost. The major cost center of this process was the material cost associated with the core. While the thermoplastic honeycomb core used in Design D2 was half the weight of the Rohacell core used in Design D1, the associated material cost was 36% of the aluminum baseline versus only 11% for the Rohacell core. Most of the difference in labor costs between the two designs was due to the fabrication and assembly of the edge bands required for Design D2.

The frame fabrication was 5% (Design D1) and 7% (Design D2) of the total metal keel panel cost. While the two designs employed different fabrication methods, the cost difference was largely insignificant. However, direct comparisons are difficult due to the fundamental difference in the designs and the way in which the frames integrate with the cargo floor structure.

The cargo floor frame fabrication was 37% (Design D1) and 13% (Design D2) of the total metal keel panel cost. The difference in labor was due largely to the preforming of web stiffener charges and manual assembly of the full depth cargo floor beam of Design D1. Design D2, which utilizes pultrusion for its cargo floor beams and stanchions, takes advantage of the efficiency of large batch sizes and little touch labor. The material costs were also higher for Design D1 due to the higher weight, material cost, and wastage inherent in the full depth design.

Splice fabrication is 1.6% (Design D1) and 2.3% (Design D2) of the total metal keel panel cost. There were only slight differences between the two splice designs and processes.

Keel panel installation is approximately 22% of the total metal keel panel cost for both Design D1 and D2. The major difference in assembly was the installation of the cargo floor structure. While very different in procedure, the Design D1 full depth design cost 7.6% while the two stanchion configuration of Design D2 cost 6.6%.

Family D Weight Results

The weight results for the non-optimized Family D keel designs are shown in Figure 17. Weights are given for the total keel assembly and for each of the same six major sub-assemblies used in the cost comparisons. The weights given are relative to the total metal keel baseline weight.

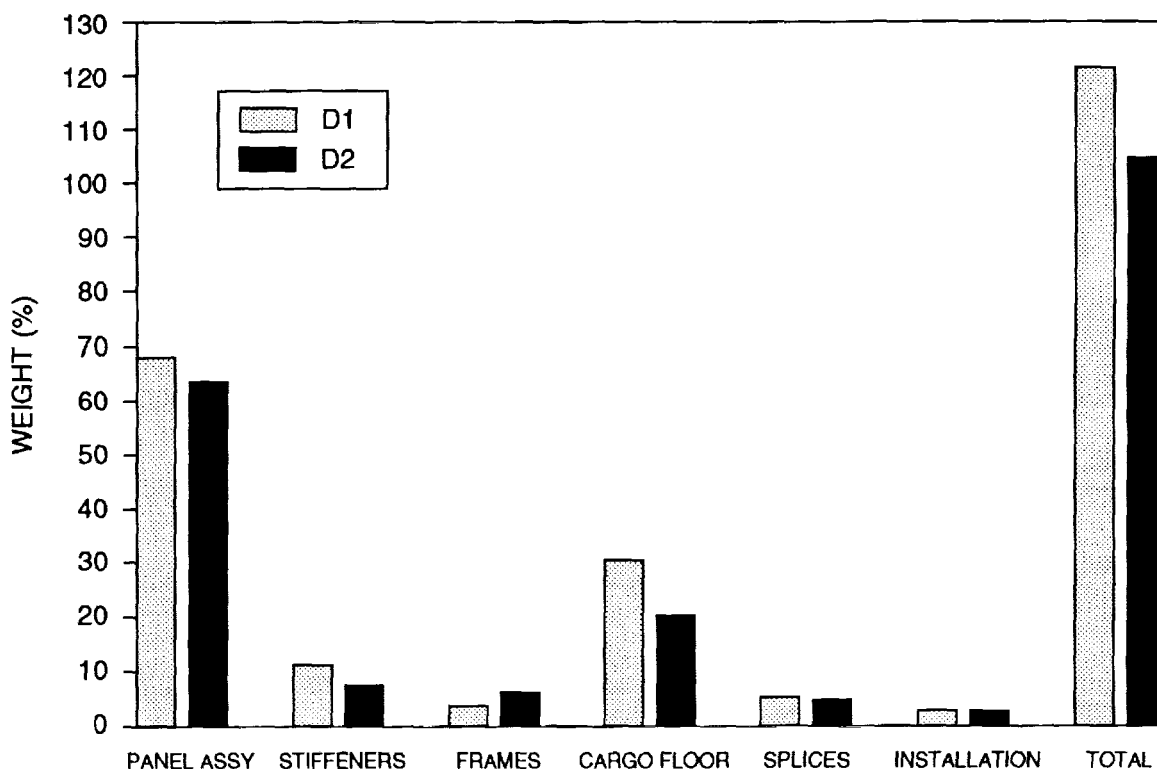


Figure 17: Family D Weight Results

The total weight is 121% (Design D1) and 105% (Design D2) of the baseline metal weight. The major cause of the weight difference is the dissimilarity between cargo floor structure designs: The full depth cargo floor beam of Design D1 is 30% of the total metal baseline weight, while the discrete floor beam/two stanchion configuration of Design D2 is only 20%. Other factors benefiting the Design D2 weight are thinner skin panel gages, which result from the use of toughened material, and the lighter thermoplastic core.

GLOBAL OPTIMIZATION

The previous section described four design concepts for a keel panel, two from Family C (bonded skin/stringer) and two from Family D (sandwich), and presented an evaluation of the cost and weight estimates for each. To

more fully understand the potential of each family, "new" designs, beyond those studied in detail, were created by modifying and/or combining attractive elements of the original four concepts. The costs and weights of these new designs were estimated using engineering judgement based on the detailed values obtained for the original designs. This process is referred to as "mix-and-match." The goal of the mix-and-match effort was to arrive at an "optimum" design within each family.

In addition to the mix-and-match activity, steps were taken to eliminate inconsistencies in the criteria and analysis assumptions governing the designs of the two families. For instance, the difference in laminate orthotropy between the Family C and Family D designs penalized the weight of the Family D design. A harder, thinner laminate was applied instead to Designs D1 and D2 to account for this disparity. These extra designs are designated D1c and D2a. Also, the analyses were updated to incorporate more recent insight into the tension damage tolerance of specific material systems, cargo floor frame stiffness requirements, effective widths, and core density requirements. Other modifications to the original designs addressed the effects of tough resin (as opposed to brittle), a six stanchion cargo floor beam (as opposed to two), and stringer fabrication methods on the cost and weight of the keel design. A summary of both the original and modified designs is presented in Table 1, along with each design's total cost and weight relative to the baseline metal configuration.

Table 1: Results of the Global Evaluation Mix and Match Exercise

Design	Comments on Design	Skin Material	Core/Stringer Material	Cargo Frame Description	Relative Cost	Relative Weight
D1a	Original global evaluation design (Sandwich concept)	AS4/3501-6 42% R.C.	Rohacell (12 pcf)	Full depth design Hand L/U (fabric)	1.18	1.22
D1b	Original global evaluation design (Sandwich concept)	AS4/3501-6 42% R.C.	Rohacell (12 pcf)	Full depth design Stitch tape RTM	1.17	1.21
D1c	D1b with harder, thinner skins (Sandwich concept)	same as D1b	same as D1b	same as D1b	1.10	1.06
D1d	D1c with process change (Tow place on cure tool per D2b)	same as D1b	same as D1b	same as D1b	1.07	1.06
D2	Original global evaluation design (Sandwich concept)	AS4/977 42% R.C.	Hexcell HFT-G (6 pcf)	2 stanchion design Pultruded	1.19	1.05
D2a	D2 with harder, thinner skins (Sandwich concept)	same as D2	same as D2	same as D2	1.12	0.90
D2b	D2a with adjustment for layup rate to be consistent with other assumptions	same as D2	same as D2	same as D2	1.13	0.90
Dw	Combination of D2b material and layup, D1a core, 2 stanchion frame from C1	AS4/977 42% R.C.	Rohacell (12 pcf)	2 stanchion design from Design C1	0.83	0.90
Dx	Dw with D1d material and layup	AS4/3501-6 42% R.C.	same as Dw	same as Dw	0.83	0.95
Dy	Dw with a 6 stanchion frame design from design C2	AS4/977 42% R.C.	Rohacell (12 pcf)	6 stanchion design from Design C2	0.91	0.89
Dy'	Dy with lighter core aft, corrected floor beam & stanchion stiffness, reduced fwd eplice	AS4/977 42% R.C.	Rohacell (12 pcf fwd, 9 pcf aft)	6 stanchion design from Design C2	0.90	0.83
Dz	Dy with an estimate for the effects of an In situ foam core. (Included for comparison only)	same as Dy	In situ foam core	same as Dy	0.86	0.92
C1	Original global evaluation design (Bonded skin/stringer)	IM6/977 42% R.C.	CTLM hot drape "J" (Alum chord)	2 stanchion design Pultruded	1.03	0.87
C1a	C1 with corrections to account for analysis errors and lower margins of safety	same as C1	same as C1	same as C1	1.02	0.86
C1b	C1a with an AS4/3501-6 material system	AS4/3501-6 42% R.C.	same as C1, but AS4/3501-6	same as C1	0.94	0.91
C1c	C1a with an AS4/977 material system	AS4/977 42% R.C.	same as C1, but AS4/977	same as C1	0.95	0.87
C2	Original global evaluation design (bonded skin/stringer)	AS4/3501-6 42% R.C.	Pultruded "J" panelized chord	6 stanchion design	0.82	0.88
C2a	C2 with corrections for analysis errors and lower margins of safety	same as C2	same as C2	same as C2	0.83	0.89
C2b	C2a with an AS4/977 material system	AS4/977 42% R.C.	same as C2, but AS4/977	same as C2	0.82	0.84
C2c	C2b with drape formed stringer fabrication from family C1 used	same as C2b	same as C1c	same as C2	0.85	0.84
C2c'	C2c with corrected floor beam and stanchion stiffness, reduced fwd eplice	AS4/977 42% R.C.	pnizd, hot drape Js, AS4/977	6 stanchion design same as C2	0.85	0.80

The best combinations for each design family are designated C2c' and Dy'; these are highlighted in Table 1. Both include the use of AS4/977-2 (toughened resin system) and a six stanchion design for the cargo floor beam. It should be noted that the two stanchion design used in these studies was less expensive to produce and slightly heavier than the six stanchion design, but after further consideration, only the six stanchion design was felt to satisfy the design requirements due to an imposed stiffness criteria. Also note that cost and/or weight could potentially be saved by using a sandwich design with in situ foam (Dz) or a stiffened skin with bonded, pultruded Js (C2b); however, the process and performance development required to achieve these designs presents too great a program risk within the scope of global evaluation. Such options may be revisited in the local optimization phase.

The costs and weights for the globally optimized keel designs are shown in Figures 18 and 19, respectively. The total cost of the optimized Family C design (C2c') was 85% of the metal baseline; the total cost of the optimized Family D design (Dy') was 90%. Weight comparisons reveal the C2c' design to weigh 80% of the metal baseline, while Dy' is 83% of the metal keel weight.

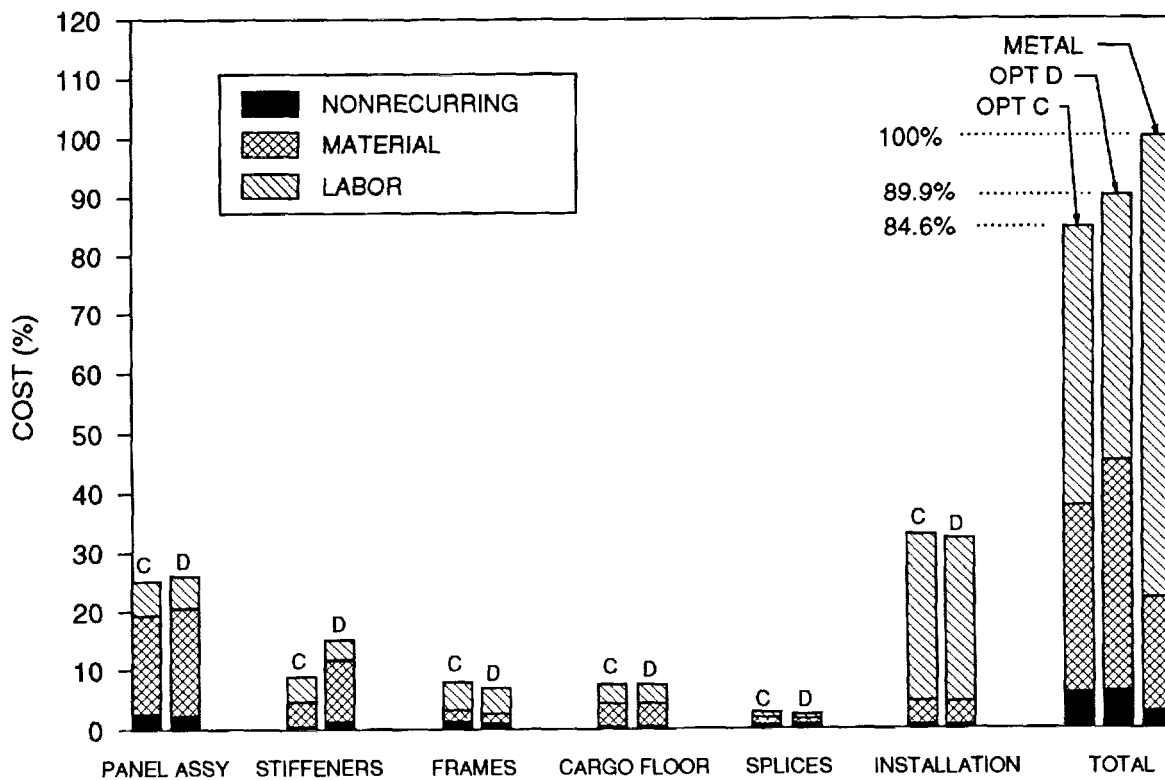


Figure 18: Cost Results for Globally Optimized Keel Designs

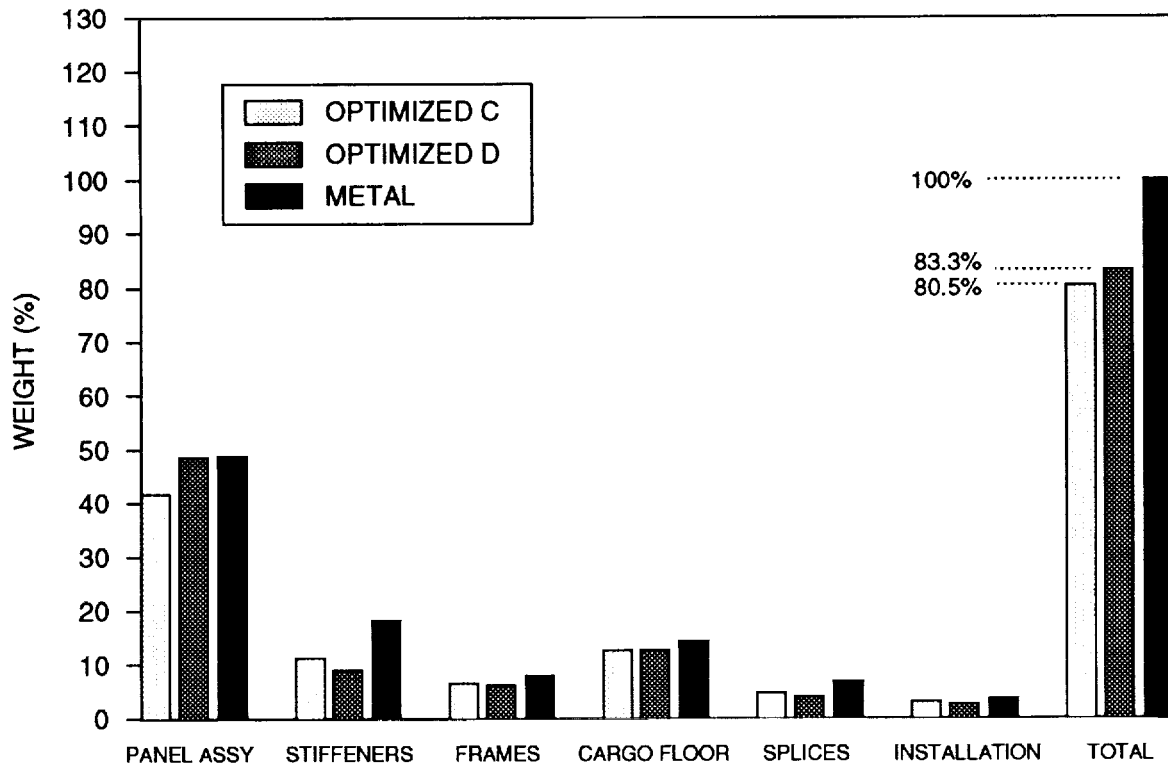


Figure 19: Weight Results for Globally Optimized Keel Designs

SELECTION RATIONALE

The cost and weight results of the globally optimized keel designs for each family are shown in Figure 20, along with results for the original four designs and the metal baseline. The sloped line reflects a typical performance value of weight.

The Design Build Team (DBT) approach was used to down-select to a single design family for keel panel local optimization. The down-select decision was based on both the cost/weight results reported above and the risk issues associated with each design concept. The risks related to manufacturing process development, performance development, and program demonstrability are listed in Table 2 for design families C and D.

One process risk for both families is the cure of thick laminates, although Hercules has had good success with laminates up to 3/4" thick. Most other process risks for Family D relate to the core: its machining, cleaning, and handling. Cleaning is an issue for both the C and D Design IML tools with their narrow slots. Tooling development for the C Family J stiffeners is another process risk item.

The performance risks for Family D again relate primarily to the core. Damage resistance, moisture ingress, and repair of thick skin and sandwich structure are all concerns. Design C performance also requires the development of thick skin repairs. The bonded elements of Family C carry risks associated with repair, durability, and damage tolerance, as well as load eccentricities in the areas of stringer runouts. If an OML tool is used for the Family C concept, achieving a high integrity bond between the stiffener and the stairstep ply drops becomes a risk.

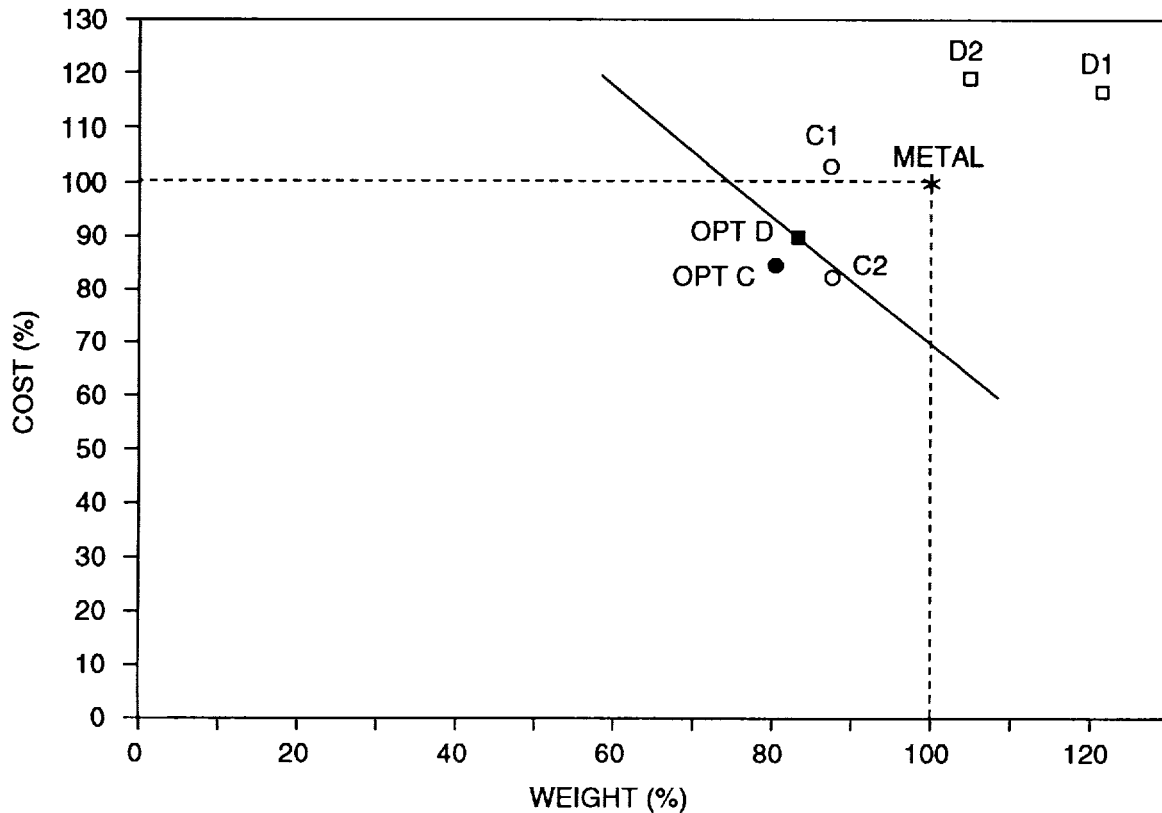


Figure 20: Cost/Weight Results Summary

Program risks result when the level of effort required to fully investigate certain technical issues threatens to outweigh the available resources of time, manpower, and budget. An example is the cost of an IML tool for the Family C concept which is considered to be prohibitively high for our demonstration purposes. This would require us to adapt an OML tool to simulate an IML tool, a task which is much more easily accomplished for the sandwich designs. Time is a factor in that many of the technical issues associated with the Design C keel concept have yet to be addressed. More effort has been expended to date on the Family D keel technical issues, however much core development remains to be done.

The cost and weight performances of the C and D Family designs were not greatly different. With this in mind, and after evaluating the relative risks of each concept, the consensus was that Family D would be selected for local optimization of the keel panel.

POTENTIAL FOR LOCAL OPTIMIZATION

The local optimization process provides the opportunity to further refine the selected concept within the cost constraints defined by global optimization. Material, geometric and laminate variables affecting cost and weight are considered during local optimization, as well as improvements in the manufacturing processes. A locally optimized design will also incorporate any developments in the understanding of the technical/economic issues identified during global evaluation.

Table 2: Risk Issues for Keel Design Concepts

	C FAMILY	D FAMILY
MANUFACTURING PROCESS DEVELOPMENT RISK	<ul style="list-style-type: none"> • Thick laminate cure • Cleaning of IML tool • Tooling for J stiffeners • Stringer splices 	<ul style="list-style-type: none"> • Cure of thick laminate with tapered core • Machining, handling, cleaning of core • Cleaning of IML tool
PERFORMANCE DEVELOPMENT RISK	<ul style="list-style-type: none"> • Stiffener bond to stairstep ply drops w/ OML tooling • Durability and damage tolerance of bonded elements • Repair of thick skins • Repair of bonded stringers • Load eccentricities (stringer runout) 	<ul style="list-style-type: none"> • Damage resistance of core • Moisture ingress • Repair of thick skin • Repair of sandwich, bondline • Core development
PROGRAM RISK	<ul style="list-style-type: none"> • Cost of IML tool is prohibitive for demonstration purposes • Schedule for working technical issues 	<ul style="list-style-type: none"> • Core screening, development

Material costs are a major factor in the recurring costs. An optimum balance will be sought between material cost and performance, especially in the skins and core where the majority of the material resides. A toughened resin system has shown advantages for the keel skins; however, the degree of toughness can be altered to maximize compressive performance without unduly sacrificing the required tension damage tolerance for large crack scenarios. A wide variety of core materials will be screened to determine which can demonstrate the required stiffness, strength, and damage resistance while maintaining a low density. Foam core, honeycomb, in situ foam, fiber-filled foam, foam-filled honeycomb, and multi-layered syntactic foam are all being considered as candidate core structures for the keel panel. Both glass and graphite fibers of various layups will be evaluated for the honeycomb cores, as will thermoset and thermoplastic resins.

Major geometric variables to be considered include frame spacing, frame height and width, core thickness, and alternate cargo floor beam and stanchion cross sections. Major laminate variables include ply orientations, stacking sequences, and ply drop rates. COSTADE (References 3, 4, 5), a software design tool that incorporates cost and structural mechanics constraints with an optimization algorithm, will be used to support studies on the effects of material, geometric, and laminate variables. COSTADE was used during local optimization of the crown panel and will be further developed to support the keel design.

Several potential manufacturing improvements will be surveyed during local optimization of the keel. One area of potential improvement is the core fabrication. The results of the current core fabrication and performance trials could have a significant effect on the process used. Also, an investigation into the key process drivers of

advanced tow placement as they relate to a highly tapered skin may yield higher efficiencies. Another cost-saving measure could result from removing the frame cap charge as was done in the ATCAS crown frames. The curing of the panel assembly could also see some processing improvements brought about by modified bagging and tooling approaches. The pultrusion process, which has a significant impact on the keel design, needs to be better understood in terms of both processing requirements and design/process interactions.

Insight gained from ongoing studies to understand associated technology issues will be incorporated into the design and analysis of the keel during local optimization. Included will be developments in analysis techniques (i.e., optimization procedures, residual strength analysis) and results from related test efforts (i.e., core strength, ply drop tests, fracture tests, impact damage resistance, material screening). Additionally, the structural criteria on which the analysis is based will be revisited to verify its applicability. For instance, the minimum stiffness requirement, which drives the skin thickness over much of the panel, was conservatively set at 90% of the baseline aluminum. If a lower value were acceptable, additional weight savings would be realized.

Figure 21 shows an estimate of the total potential cost and weight savings which may be realized as a result of the local optimization effort.

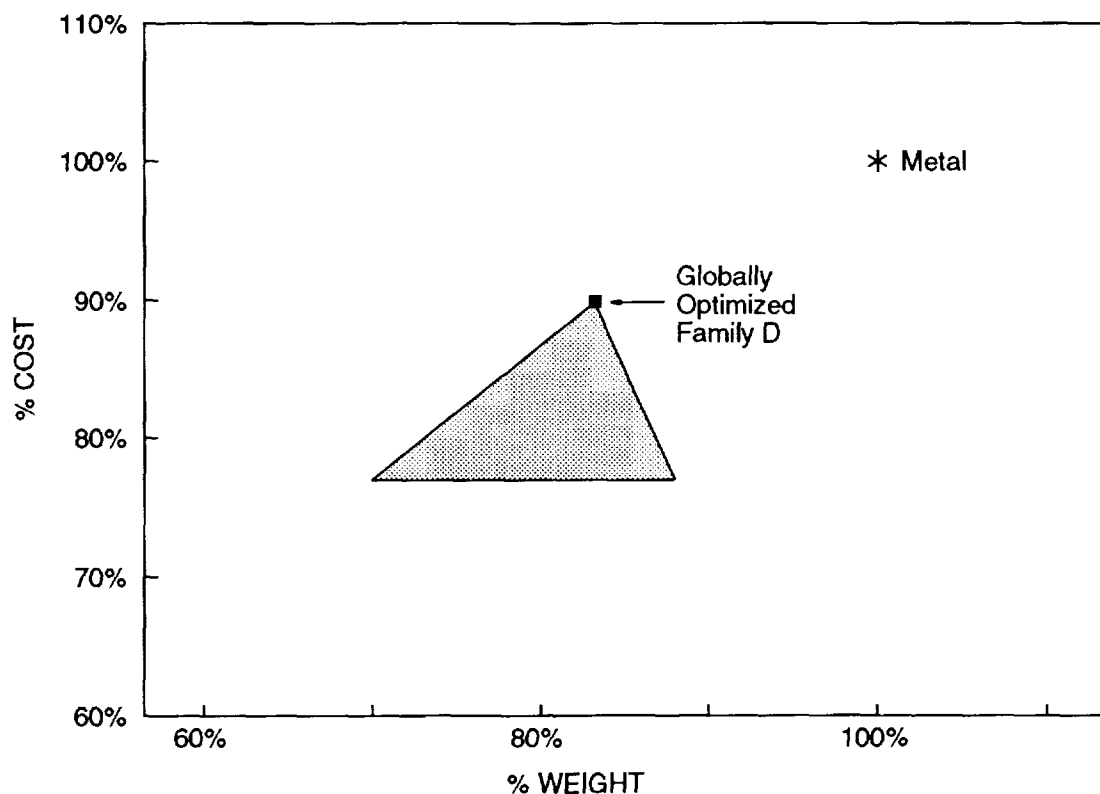


Figure 21: Local Optimization Potential

SUMMARY

Two designs from each of two families were developed for global optimization of the keel quadrant. Both Design Families C and D were considered in the study. Family C is a structural skin stiffened with bonded stringers and frames. Family D is a sandwich construction with bonded frames. Each design was sized considering critical load cases, damage tolerance, and attachment details. A detailed fabrication and assembly plan was developed for each design. These were then used to estimate weight, material costs, and labor rates.

Both recurring and nonrecurring (minus capital equipment) costs were estimated according to specific groundrules (e.g., 300 shipsets at a rate of 5 per month).

The designs within each family differed in material types, manufacturing processes, and structural variables. These differences helped to distinguish a range of cost and weight variation for each family. Design trades within a family yielded data on cost and weight centers, and helped to identify interactions between design variables. Such data is crucial to local optimization studies. Studying two designs per family also provides a convenient means of checking for errors in the cost estimating tasks (e.g., data entry, plotting) by analyzing the cost results and the differences between designs.

The majority of weight for all designs resides in the stiffened panel (skin and stringers/keel chords for Family C; facesheets, core, and intercostals for Family D). This is especially true in the forward end where gages are larger to accommodate the highly concentrated loads near the wheel well cutout. The skin gages in the more lightly loaded aft end tend to be driven by minimum skin buckling (Family C only), hoop tension damage tolerance, and/or the minimum stiffness criteria. Skin gages near panel edges are controlled by joint bearing and/or bypass requirements. The frames and cargo support structure were stiffness rather than strength designed and showed only a small weight advantage over the metal design.

Cost estimates for all designs revealed recurring costs to comprise over 90% of the total cost. For the composite designs, the labor and material portions of the total recurring cost are not dramatically different; the labor costs being only slightly greater. In the metal baseline however, labor costs are significantly larger than the material costs. Within a single design, the relationship between the labor and material cost components can vary widely for individual fabrication and assembly steps. For instance, panel bonding consists almost entirely of labor costs, while batch tow placement processing of skins is dominated by material costs. The breakdown of cost estimates to this and lower levels of detail is necessary in order to attack cost centers in local optimization.

Fabrication and assembly of the skin/sandwich panel and its stiffening elements is the largest cost component. Installation of the cargo floor frames and panel splices comprises another major cost center. The majority of the cost savings realized by the composite designs over the metal baseline result from the fabrication of the splice elements and the cargo floor structure.

As was the case in an earlier study of the crown quadrant (Reference 1), the switch to a high performance fiber to reduce skin weight was not found to be cost effective. This relates to the trade between a higher material purchase price and the costs saved from added performance capability. The economically acceptable increase in cost per unit weight savings was considered in this evaluation. Material cost and weight design trades such as performed in this keel study are useful in determining an acceptable increase in material cost per added performance. Note that these relationships are likely to be application specific due to differences in design drivers.

Design concepts for each family studied were globally optimized by mixing and matching the best design features, and by correcting any inconsistencies in the analysis and criteria applied to them. The globally optimized designs for both Families C and D include AS4/977-2 (toughened resin system), a panelized keel beam (as opposed to discrete keel chords), and a six stanchion cargo floor frame. Both designs are cost and weight competitive relative to the metallic benchmark, even though both of the original non-optimized Family D designs were heavier and more costly than the baseline. The optimized Family C design presented a 15% cost savings and 20% weight savings as compared with the metal baseline. The optimized Family D showed 10% cost savings and 17% weight savings.

Based on these cost/weight results, and an assessment of risks associated with each design, a single design family was selected for further study in local optimization. The risks in question relate to the development of manufacturing processes, performance characteristics, and the ability to demonstrate the chosen concept within the confines of program schedule and budget. Family C was judged to have the greater risk, due in large part to

questions surrounding the durability and damage tolerance of bonded stringers, and due to the prohibitive cost of an IML tool for program demonstration purposes. The sandwich designs are more adaptable to an OML type process. In view of these risks, and the fact that the costs and weights of the C and D Family designs were not greatly different, Family D was chosen for keel local optimization.

Local optimization is planned to further refine Family D and attack cost centers identified during the global evaluation phase. Attempts to reduce material costs will include studies of skins with varying degrees of toughness. An extensive screening of core materials will also be conducted. A software design tool that includes cost and structural mechanics constraints for keel panels will be used to support optimization of design variables such as laminate and core thicknesses, ply orientations, and stacking sequences. The manufacturing approach to panel subassembly and the use of composite fasteners will also be evaluated. The local optimization effort will incorporate any developments in related technology studies. Advanced analysis techniques, test data, and refinements of the structural design criteria could all lead to improvements in the cost and weight results of the keel quadrant.

REFERENCES

1. Ilcewicz, L.B., T.H. Walker, et al, "Application of a Design-Build Team Approach to Low Cost and Weight Composite Fuselage Structure," NASA CR-4418, December 1991.
2. Grande, D.H., B.W. Flynn, E.F. Dost, L.B. Ilcewicz, W.B. Avery, "Studies on Toughened Material Forms for Composite Fuselage Keel Applications," in the Proceedings of the Sixth Technical Conference of the American Society for Composites, 1991.
3. Swanson, G.D., L.B. Ilcewicz, T.H. Walker, D. Graesser, M. Tuttle, Z. Zabinsky, "Local Design Optimization for Composite Transport Fuselage Crown Panels," In Proceedings of the Ninth DoD/NASA/FAA Conference on Fibrous Composites in Structural Design, Lake Tahoe, NV, FAA Publication, 1991.
4. Freeman, W.T., L.B. Ilcewicz, G.D. Swanson, T. Gutowski, "Designer's Unified Cost Model," In Proceedings of the Ninth DoD/NASA/FAA Conference on Fibrous Composites in Structural Design, Lake Tahoe, NV, FAA Publication, 1991.
5. Zabinsky, Z., M. Tuttle, D. Graesser, G.D. Swanson, L.B. Ilcewicz, "Multi-Parameter Optimization Tool for Low-Cost Commercial Fuselage Crown Designs," First NASA Advanced Composites Technology (ACT) Conference, October 30-November 1, 1990, NASA CP-3104.

Session VIII

DESIGN/ANALYSIS TECHNOLOGY

Session Chairman: James H. Starnes, Jr.
NASA Langley Research Center

DESIGN AND EVALUATION OF A FOAM-FILLED HAT-STIFFENED PANEL CONCEPT FOR
AIRCRAFT PRIMARY STRUCTURAL APPLICATIONS

Damodar R. Ambur
NASA Langley Research Center
Hampton, VA 23665-5225

5/8-05
51418

INTRODUCTION

Geodesically stiffened structures are very efficient in carrying combined bending, torsion, and pressure loading that is typical of primary aircraft structures. They are also very damage tolerant since there are multiple load paths available to redistribute loads compared to prismatically stiffened structures (Refs. 1,2). Geodesically stiffened structures utilize continuous filament composite materials which make them amenable to automated manufacturing processes to reduce cost. The current practice for geodesically stiffened structures is to use a solid blade construction for the stiffener. This stiffener configuration is not an efficient concept and there is a need to identify other stiffener configurations that are more efficient but utilize the same manufacturing process as the solid blade.

This paper describes a foam-filled stiffener cross section that is more efficient than a solid-blade stiffener in the load range corresponding to primary aircraft structures. A prismatic hat-stiffener panel design is then selected for structural evaluation in uni-axial compression with and without impact damage. Experimental results for both single stiffener specimens and multi-stiffener panel specimens are presented. Finite element analysis results are presented that predict the buckling and postbuckling response of the test specimens. Analytical results for both the element and panel specimens are compared with experimental results.

FOAM-FILLED STIFFENER CONCEPT

In order to make the solid-blade stiffener shown in Figure 1 more efficient, it is necessary to position the 0° material away from the skin to increase the bending stiffness. When such a stiffener concept is applied to a geodesically stiffened structural configuration, the tooling design becomes extremely complicated if the tooling must be removed after curing. It is cost effective to leave the tooling in the hat stiffener if the material for the tool is light in weight and has the necessary processing characteristics for curing and adequate mechanical properties to support the stiffener and skin elements when loaded. In a typical manufacturing process, the overwrap material is first placed in a female tool and unidirectional material is tow placed to form a predominantly 0° material stiffener cap. A pre-machined foam insert is then placed in the tool to complete the stiffener. Skin material of the required thickness is then tow placed to complete the assembly which is then cured to produce the geodesically stiffened structure. As a first step toward evaluating this stiffener concept for geodesically stiffened structures, a prismatic stiffener panel study was undertaken which is the subject of this paper.

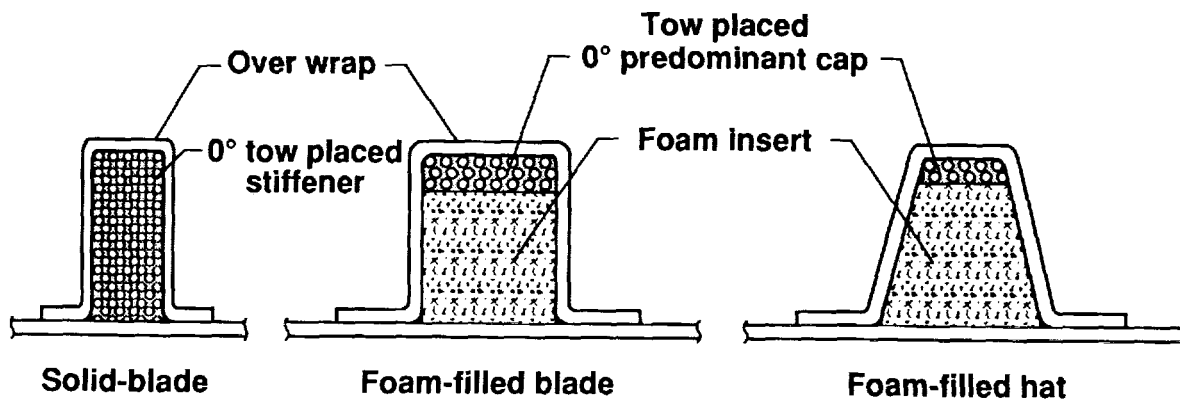


Figure 1. Foam-filled stiffener concepts.

STRUCTURAL EFFICIENCY OF FOAM-FILLED-STIFFENER PANEL CONCEPTS

A design study was performed to compare the structural efficiency of the foam-filled structural concepts with the simpler, efficient, and more widely used hat-stiffener concept. The results presented in Figure 2 correspond to a 30-inch-long and 24-inch-wide panel with four stiffeners across the width. The unidirectional tape material used in this study is the Hercules Inc. AS4/3502 graphite-epoxy system with Rohacell WF-71 foam as the core material. This four-stiffener configuration is structurally the most efficient for load cases above 6,000 lb/in. and has also been adapted for lower load cases in this study. A constrained optimization for minimum weight was performed using the Panel Analysis and Sizing COde (Ref. 3) and the results for a range of axial loads from 3,000 to 20,000 lb/in. are presented herein. Results for solid-blade stiffened panel are also included in this figure for reference.

The results show that the foam-filled hat-stiffened panel is lighter than the conventional hat-stiffened panel by about 6.5 percent at 6,000 lb/in. and by about 10 percent at 20,000 lb/in. The foam-filled blade-stiffened panel appears to perform better than the hat-stiffened panel above 16,000 lb/in. The foam-filled hat-stiffener panel is lighter by about 20 percent when compared to the solid-blade concept. Hence, If the foam-filled hat-stiffened concept is used in stiffened structures, a substantial weight savings is possible over the entire load range considered. A foam-filled hat-stiffener panel design for 3,000 lb/in., which corresponds to a fuselage structure, has been chosen for further evaluation.

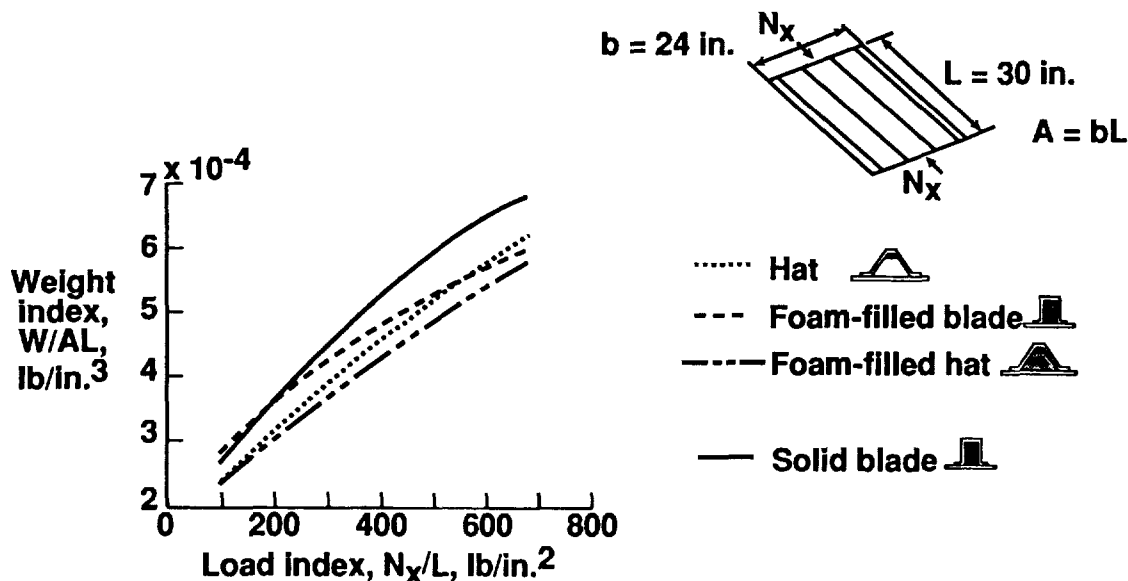
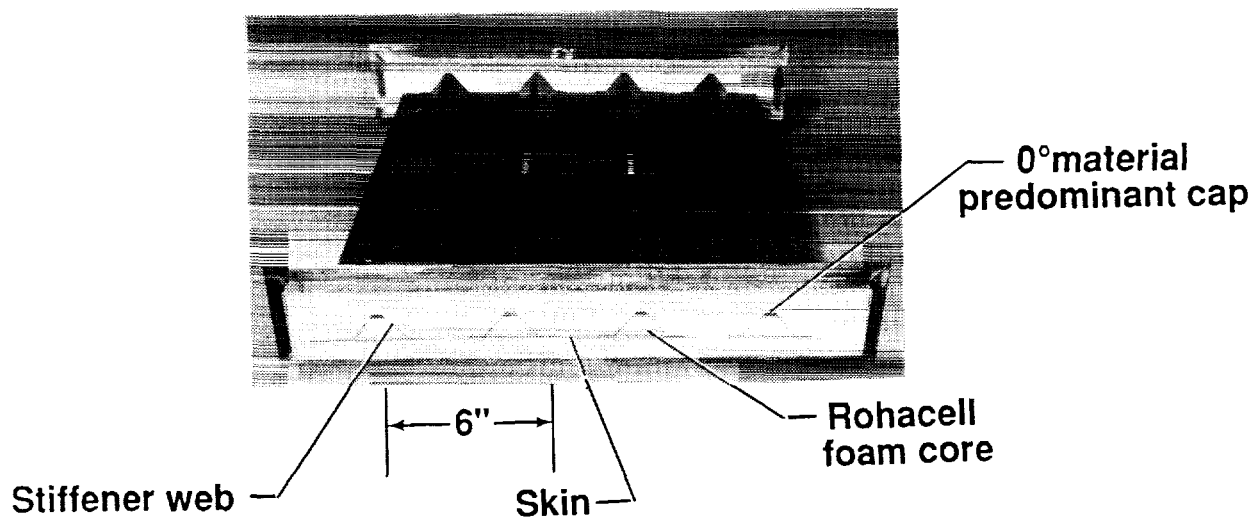


Figure 2. Structural efficiency of foam-filled stiffener panel concepts.

FOAM-FILLED HAT-STIFFENED PANEL SPECIMEN

A photograph of the foam-filled hat-stiffened panel is shown in Figure 3. The ends of the panel were potted, and machined flat and parallel to introduce load. The sides of the panel were simply-supported using knife edges. The ply layup for the skin, stiffener cap, and stiffener web are provided in this figure. The plies in all structural elements are oriented in at least three directions for laminate stability.



● Ply layup

- Skin: $(\pm 45/\mp 45/\pm 45/\mp 45/0)_s$
- Stiffener cap: $(\pm 45/0_5/-45/0_5/45/0_5/\bar{90})_s$
- Stiffener web: $(\pm 45/\mp 45/\bar{90})_s$

Figure 3. Laminate details of foam-filled hat-stiffened panel.

FAILURE MODE OF ELEMENT SPECIMEN WITHOUT DAMAGE

The element specimen is a single stiffener structure which was tested as a wide column. For this test, strain gages were placed at the mid-length of the specimen on the stiffener cap, skin, and skin-stiffener flange locations. Displacement transducers were used to monitor specimen end-shortening and out-of-plane displacements and shadow moire interferometry was used to obtain a field view of the out-of-plane displacement contours.

As the specimen was loaded, the skin buckled first at about 33,500 lb and further loading of the element specimen resulted in failure at 36,080 lb. The out-of-plane displacement contour of the specimen is shown on the left of Figure 4. At the instance of failure, the skin had seven half-waves along the length of the specimen. The failure appeared to initiate along the nodal line slightly below the mid-length of the specimen due to high interlaminar stresses and propagated across the width of the specimen as shown on the right of the figure. The failure is characterized by a clean break of the foam-filled stiffener.

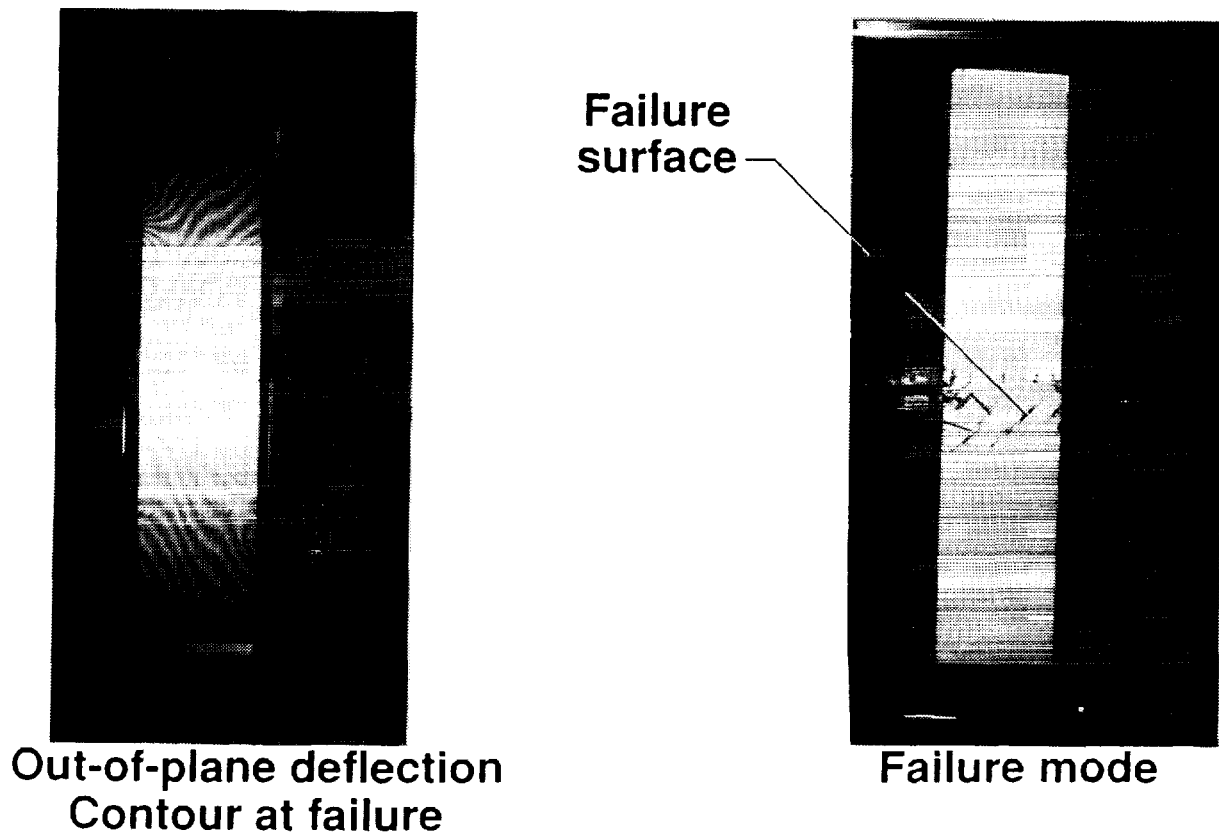


Figure 4. Failure mode of undamaged element specimen.

FAILURE MODE OF ELEMENT SPECIMEN WITH DAMAGE AT STIFFENER CAP

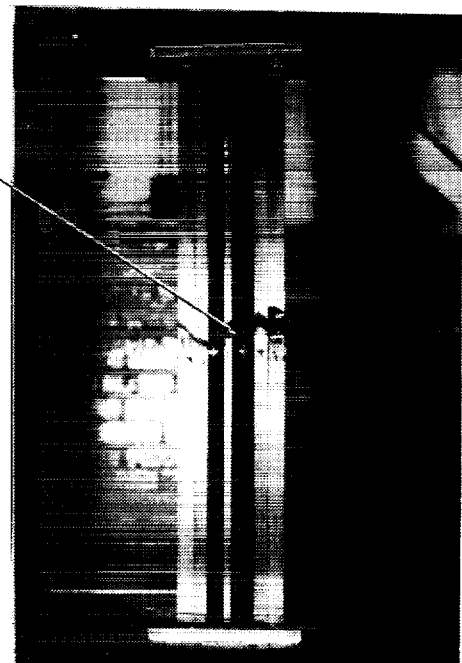
The element specimen was impact damaged by dropping a weight on the stiffener cap. This test was intended to simulate impact to the interior of the structure by dropped tools during manufacturing and servicing. Several impact tests were performed on additional specimens at increasing energy levels to determine the magnitude of the energy that caused barely visible damage to occur. This threshold level was determined to be 15 ft-lb for the stiffener cap. The rationale is that if the damage is visible the structure will be repaired or replaced before flying the aircraft.

The location of impact is at mid-length of the specimen as shown in Figure 5. An impact energy level of 20 ft-lb was chosen as an upper bound for impact. As the specimen was loaded with the damage resulting from this impact, the specimen skin buckled at approximately 33,500 lb and the final failure of the specimen occurred at 35,552 lb. The failure mode was very similar to the element specimen without impact damage. This result suggests that the imposed damage scenario of 20 ft-lb on the stiffener cap does not result in any reduction in residual strength.



**Out-of-plane deflection
Contour at failure**

**Dropped
weight
impact at
20 ft-lb**



Failure mode

Figure 5. Failure mode of element specimen subjected to dropped-weight impact.

FAILURE MODE OF ELEMENT SPECIMEN WITH DAMAGE AT SKIN-STIFFENER FLANGE INTERFACE LOCATION

An element specimen was subjected to damage on the skin side of the specimen by an airgun-propelled impactor. This damage was intended to simulate impact to the exterior of the structure due to runway debris and hailstones. A barely visible damage criterion was also used in this case. Several impact tests were performed on additional specimens at increasing levels of airgun impact velocity to determine the threshold velocities for both skin and skin-stiffener flange interface locations. The velocities corresponding to barely visible damage are 125 ft/sec and 150 ft/sec for the skin and skin-stiffener flange interface locations, respectively. The actual impact velocities selected were 150 ft/sec for the skin and 175 ft/sec for the skin-stiffener interface locations. Since the skin-stiffener interface location is more critical, the element specimen was impacted at the skin-stiffener interface location. The location of impact is shown in Figure 6.

Failure initiated from the impact damaged skin-stiffener flange interface location and propagated across the width of the specimen before skin could buckle and propagated across the width of the specimen in a catastrophic manner. The specimen failed at 31,304 lb which is 15 percent lower than the undamaged element specimen failure load. The failure mode is shown on the right of the figure.

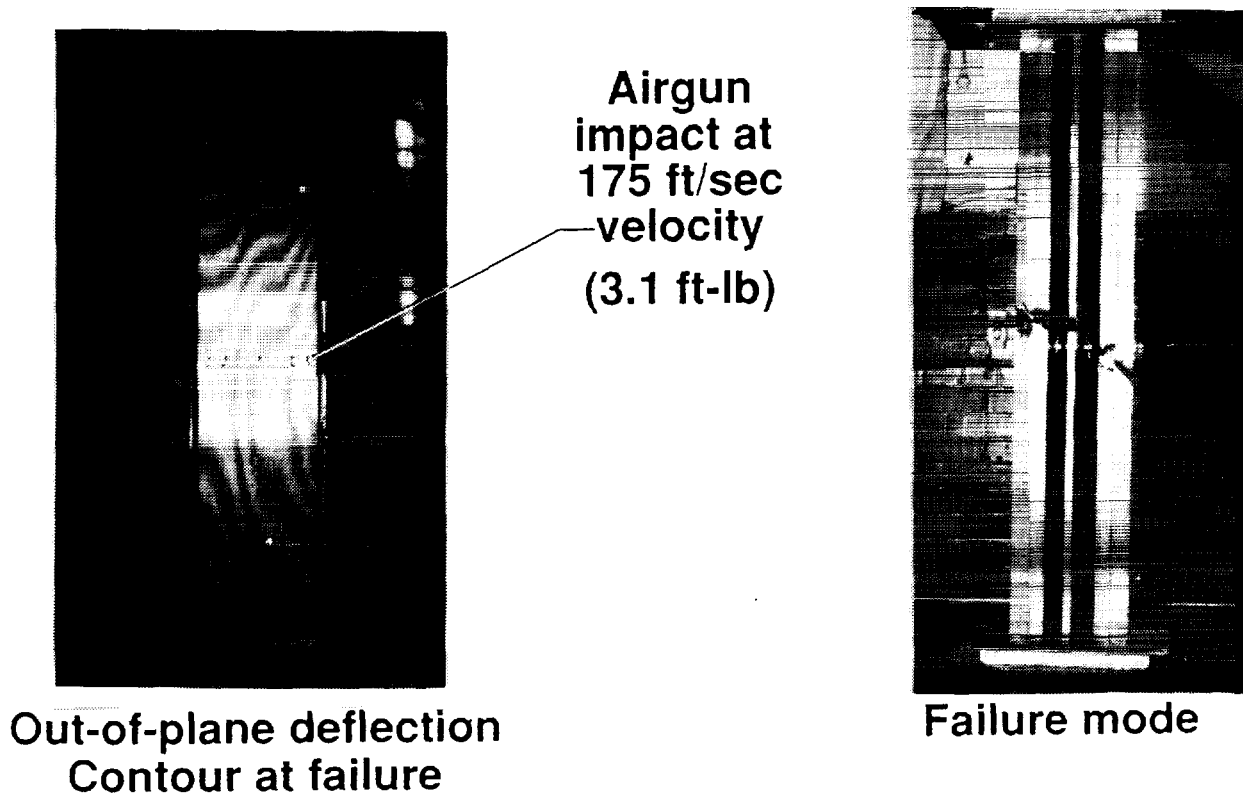


Figure 6. Failure mode of element specimen subjected to airgun impact.

END-SHORTENING RESPONSE FOR ELEMENT TEST SPECIMENS

The end-shortening results for the element test specimens are summarized in Figure 7. In this figure, end-shortening results are normalized by the overall length of the specimen and then plotted against the total applied load normalized by the axial stiffness of the specimen. Thus, the numbers along the axes represent global axial strains. The open circles, squares, and triangles represent data for specimens without damage, with airgun impact damage, and with dropped-weight impact damage, respectively. The solid symbols represent the corresponding failure events. All specimens exhibit nonlinear behavior beyond approximately 33,000 lb, which is the load at which skin buckling occurred. The specimens without damage and dropped-weight impact damage failed at an axial strain of $7,500\mu$ in./in. while the specimen with airgun impact damage at the skin-stiffener flange interface location failed at $6,000\mu$ in./in.

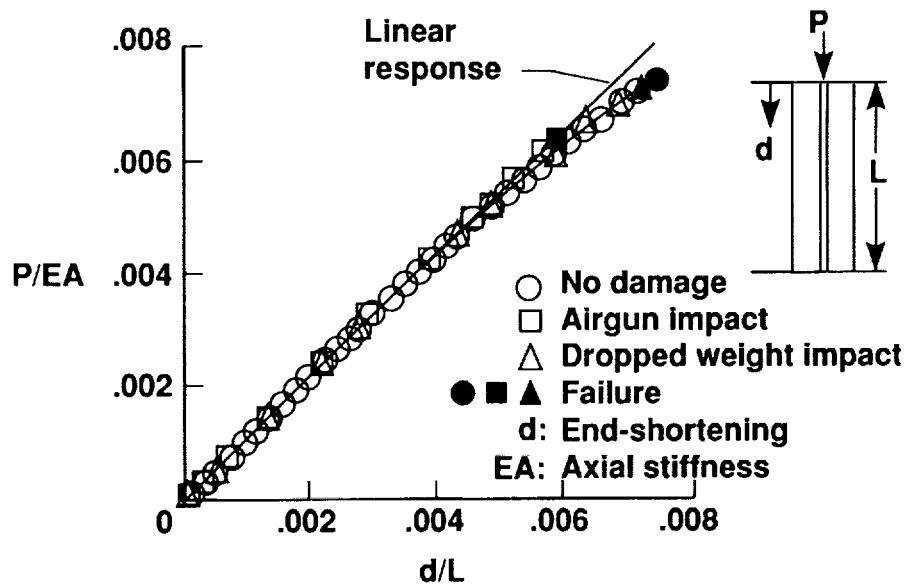


Figure 7. Summary of load versus end-shortening results for element test specimens.

STRAIN RESULTS FOR ELEMENT TEST SPECIMEN WITHOUT DAMAGE

The strain results for the undamaged element specimen are plotted in Figure 8. The strain gages are mounted across the specimen at mid-length. All gages except gage 2 indicate a similar global bending trend which is nonlinear beyond approximately 15,000 lb. The initial response of gage 2 suggests local bending of the skin element under the stiffener and strain reversal at about 33,000 lb indicates local buckling of skin. The maximum value of the local strains at failure is approximately $7,500\mu$ in./in.

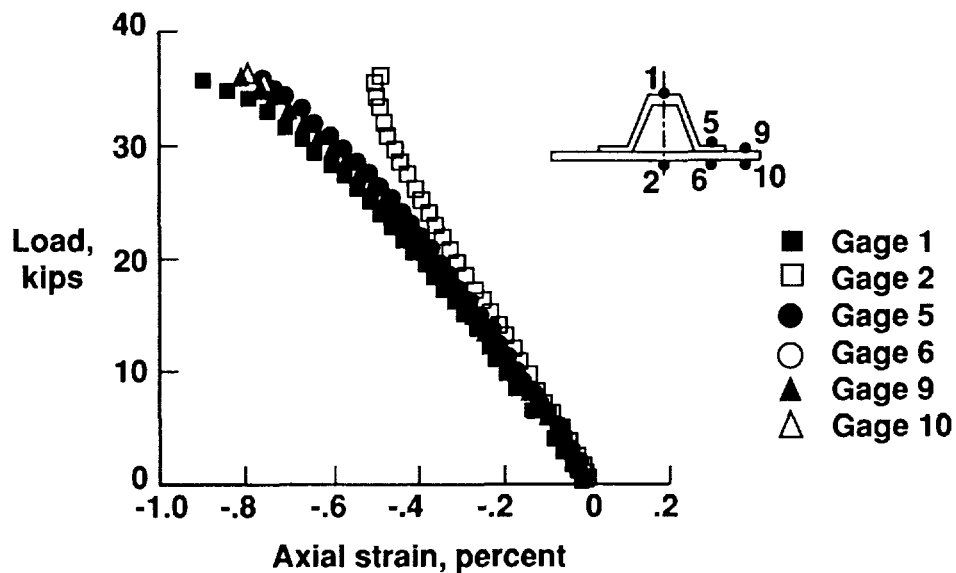
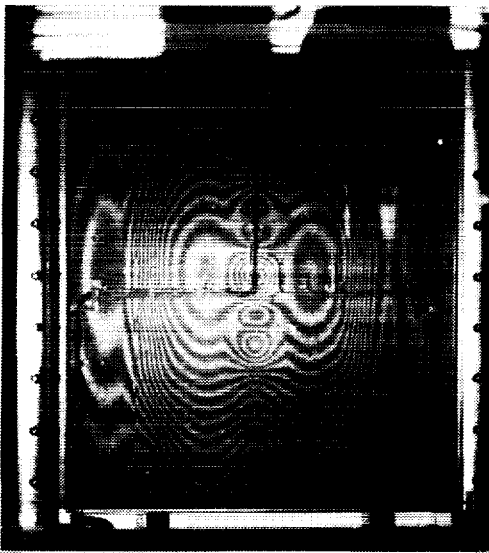


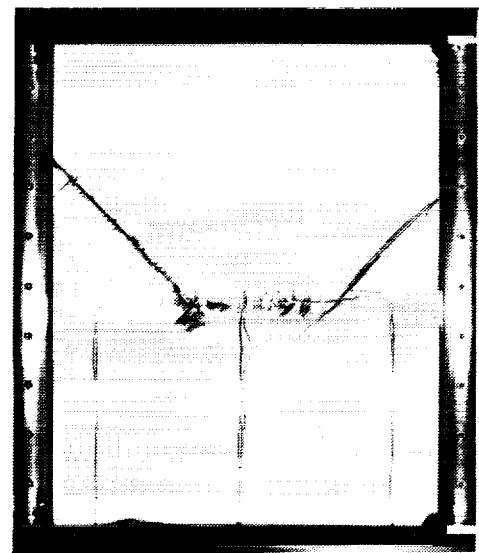
Figure 8. Axial strain results for undamaged element test specimen.

FAILURE MODE OF PANEL SPECIMEN WITHOUT DAMAGE

The panel test specimens were instrumented with strain gages, displacement transducers, and shadow moire interferometry to monitor local strains, out-of-plane and end-shortening displacements. As this undamaged panel specimen was loaded, it exhibited observable out-of-plane displacement at about 50,000 lb in the form of two lobes that were observed at the left and right of the specimen as shown in Figure 9. As the loading was increased, the skin in the central bay of the specimen buckled at approximately 125,000 lb with further loading resulting in failure of the specimen at 133,828 lb. The out-of-plane displacement contour at failure is shown on the left of the figure. The failure appears to have originated along the skin buckle nodal line below the mid-length of the specimen. The failure propagated catastrophically following the nodal line direction to the boundaries. The failure surface of the specimen is shown on the right of the figure.



**Out-of-plane displacement
Contour at failure**



**Failure mode
Skin side**

Figure 9. Failure mode of undamaged panel specimen.

FAILURE MODE OF PANEL SPECIMEN WITH AIRGUN IMPACT DAMAGE

In this experiment, the panel was subjected to airgun impact damage at three locations on the skin side of the panel to assess the criticality of damage location on the residual strength and failure mode. A 0.5-in.-diameter aluminum ball was used to impact the specimen with a velocity of 175 ft/sec at the skin-stiffener flange interface location and 150 ft/sec at two skin locations. One skin location was in the mid-bay of the panel approximately 8 inches below the top potted end and the other location was in the side bay approximately 8 inches above the bottom potted end. The locations of the impact damage are shown in Figure 10. The skin impact in the mid-bay is considered more critical due to the skin local buckling in this region that precedes failure. As the specimen was loaded, failure initiated at the skin-stiffener flange interface location before skin buckling could occur and damage propagated catastrophically across the width of the panel. The failure surface is shown on the right of the figure. The failure load was 118,477 lb which is 13 percent lower than the failure load of the undamaged panel.

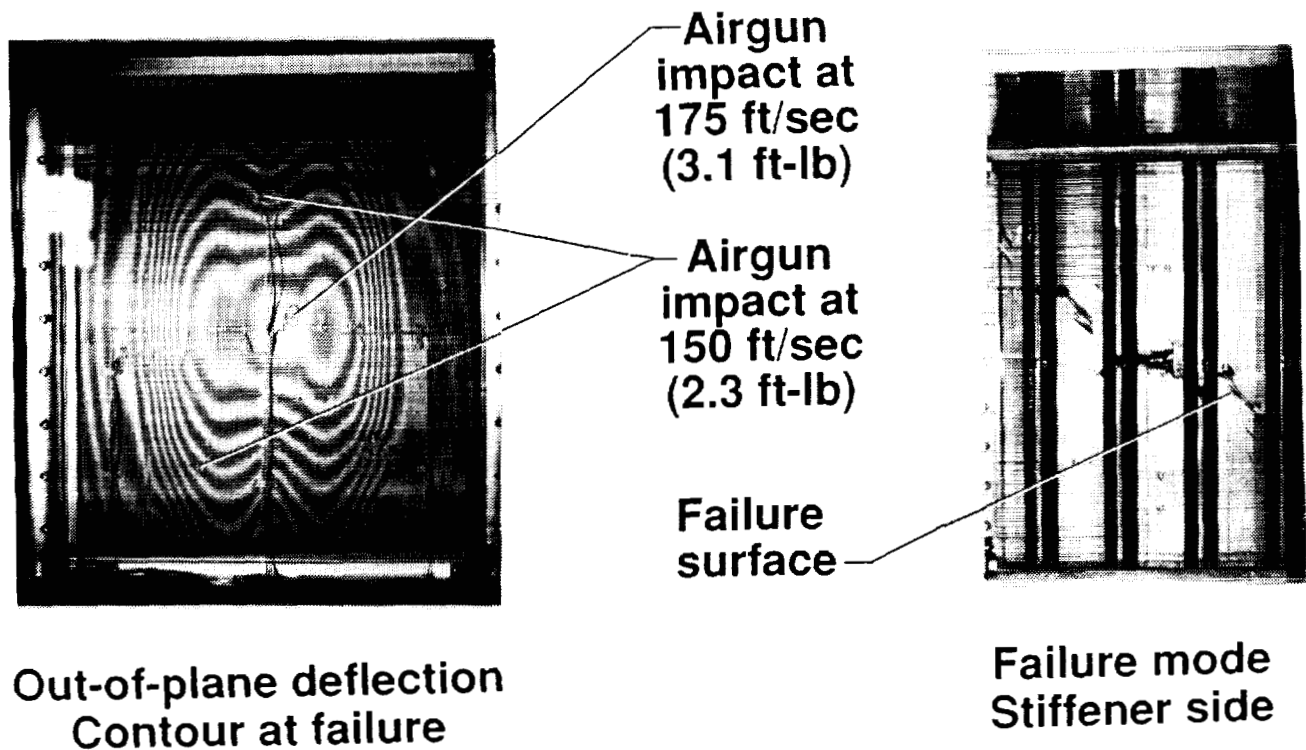


Figure 10. Failure mode of panel specimen subjected to airgun impact.

FAILURE MODE OF PANEL SPECIMEN WITH AIRGUN AND DROPPED-WEIGHT IMPACT DAMAGE

A panel was subjected to a combination of airgun and dropped-weight impact damage and loaded to failure in this experiment. The airgun impact was at 150 ft/sec at the same two skin locations described in the previous test whereas the dropped-weight impact was on the stiffener cap. The stiffener to the left of the center line shown in Figure 11 was impacted at a 15 ft-lb energy level first and then the specimen was loaded to 2/3 of the undamaged failure load for the panel. The panel specimen was then unloaded and the stiffener to the right of the center line of the panel was impacted at a 20 ft-lb energy level before reloading it to failure. When loaded, failure initiated at the skin impact location in the mid-bay and propagated across the width of the specimen. The failure load was 118,887 lb. Considering that the element specimen subjected to a 20 ft-lb dropped-weight impact energy had no degradation in behavior, it appears that damage to the skin is the more critical damage for this foam-filled stiffener concept.

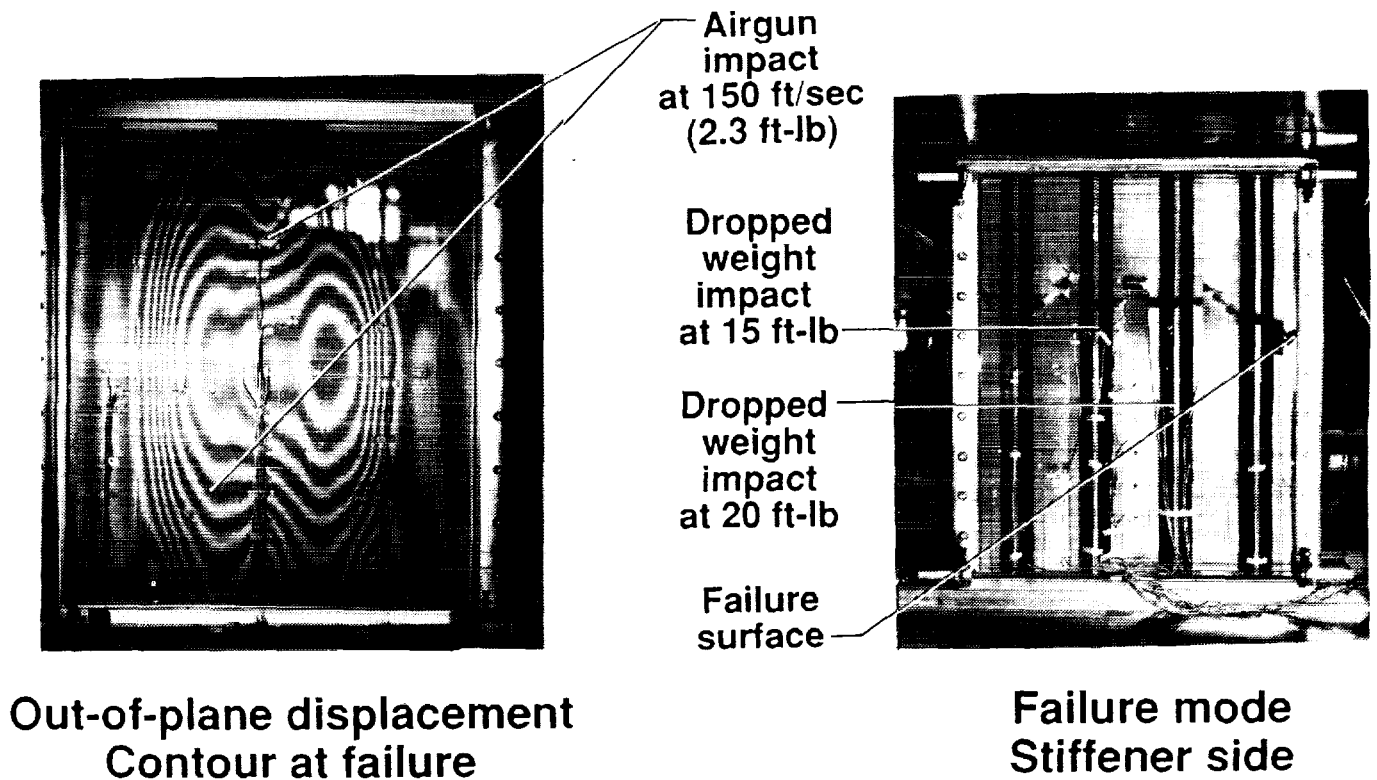


Figure 11. Failure mode of panel specimen subjected to airgun and dropped-weight impact.

END-SHORTENING RESPONSE FOR PANEL TEST SPECIMENS

The panel specimen end-shortening results are summarized in Figure 12. The out-of-plane displacement results normalized by the length of the specimen are plotted as a function of the total applied load normalized by the axial stiffness. The responses of all the panel specimens tested are nonlinear. Compared to the undamaged panel results, both damaged panels exhibit degradation of 13 percent in load carrying ability. The response of the panel subjected to a 15 ft-lb dropped-weight impact falls on top of the response of the panel with a 20 ft-lb impact suggesting that damage due to the 15 ft-lb impact did not result in a stiffness degradation. For all the three panel specimens tested to failure, the global strain at failure is approximately $5,500\mu$ in./in.

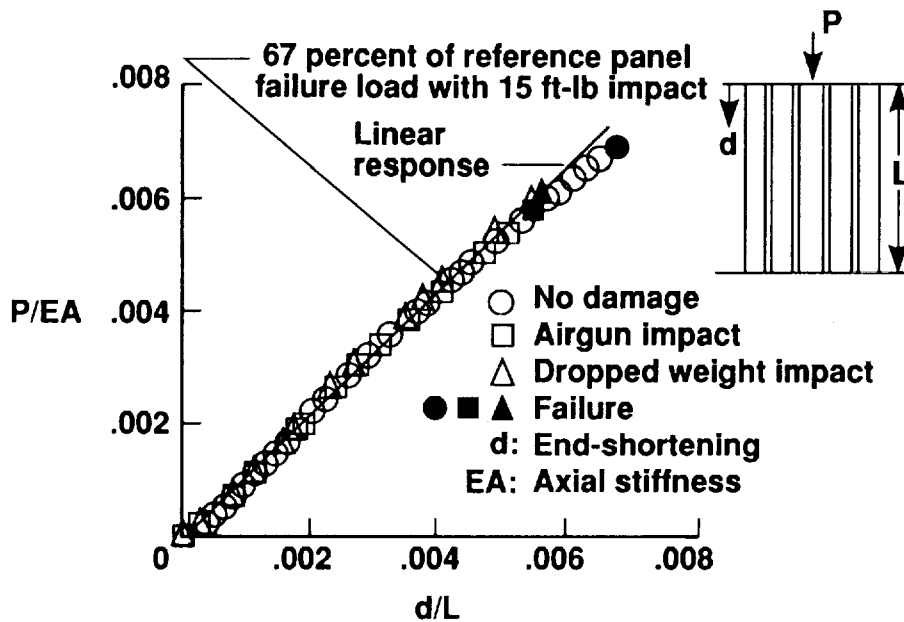


Figure 12. Summary of load versus end-shortening results for panel test specimens.

TYPICAL STRAIN RESULTS FOR PANEL TEST SPECIMENS

The strain results in the skin at mid-length for the panel test specimens are presented in Figure 13. The specimens behaved well and exhibited consistent response in all cases. In the case of the undamaged panel, the skin buckles at approximately 125,000 lb as indicated by the strain reversal in one of the back-to-back gages. The out-of-plane displacement contours obtained from moire interferometry confirmed local skin buckling in the mid-bay of the panel at this load value. The strain levels in the skin of the damaged specimens corresponding to the failure event are approximately $7,000\mu$ in./in.

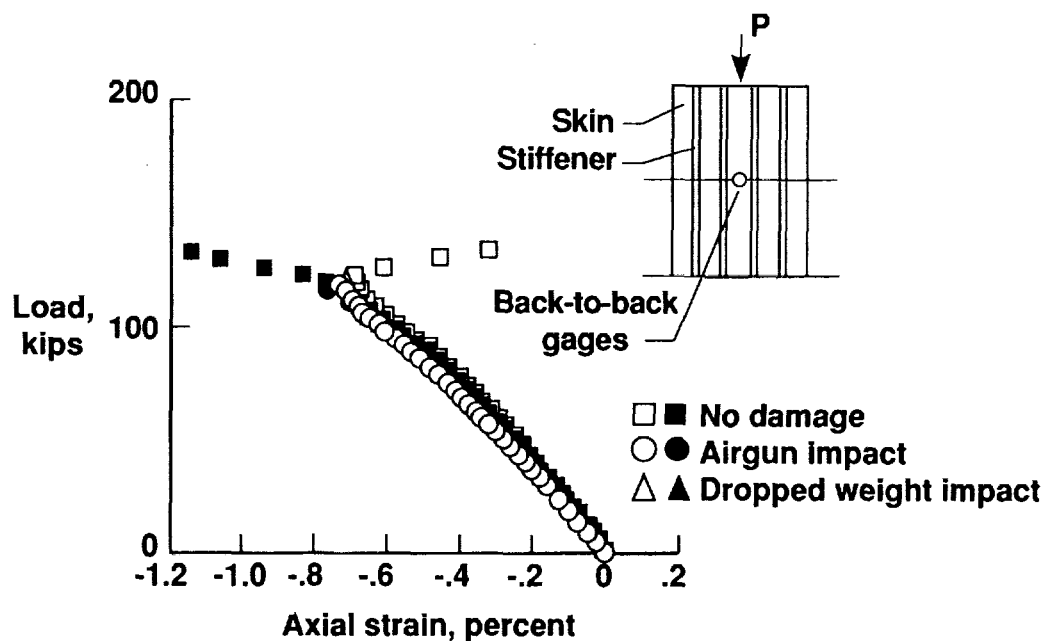


Figure 13. Strain results for panel test specimens at a skin location.

CORRELATION OF ANALYTICAL AND EXPERIMENTAL RESULTS FOR ELEMENT SPECIMEN

The experimental end-shortening results for the element specimen are compared with analytical results in Figure 14. Although linear static and bifurcation buckling analyses for the specimen were performed prior to testing to make instrumentation and loading decisions, geometrically nonlinear static analysis was performed after the test to correlate the displacement and strain results. The DIAL finite element code (Ref. 4) was used to perform buckling and nonlinear static analyses. The analysis results obtained by using the modified Newton-Raphson method are presented as a solid line in the figure. The experimental results are presented as open circles with the failure event indicated by a filled circle. The correlation between the results is good.

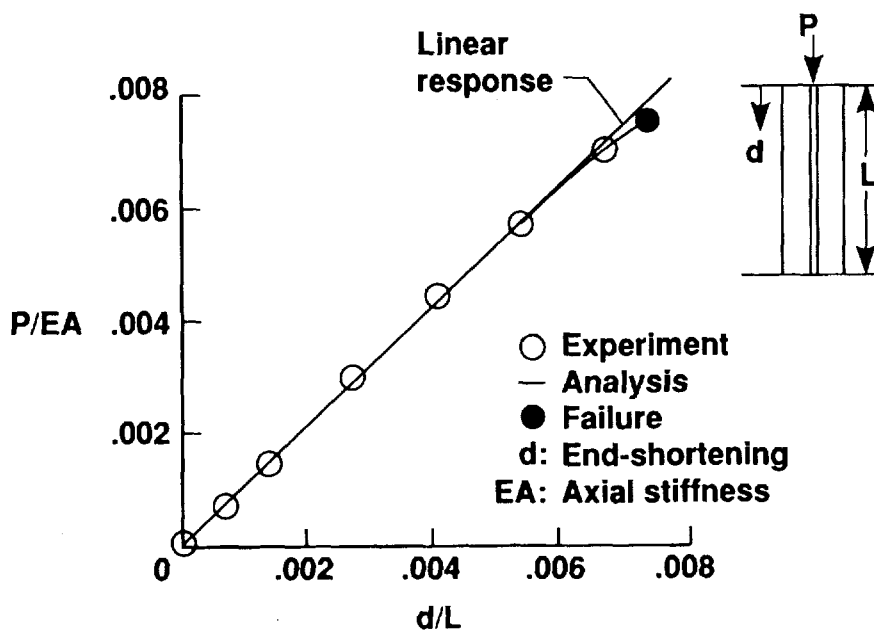


Figure 14. Correlation of element specimen end-shortening results.

CORRELATION OF ELEMENT TEST SPECIMEN BUCKLING RESPONSE

Experimental buckling response of the element test specimen is compared with the finite element analysis result in Figure 15. From moire interferometry and strain results it appears that the element specimen skin buckled into a six half-wave pattern at approximately 33,625 lb. The analysis predicts this first buckling mode at 34,502 lb with the same number of half-waves.

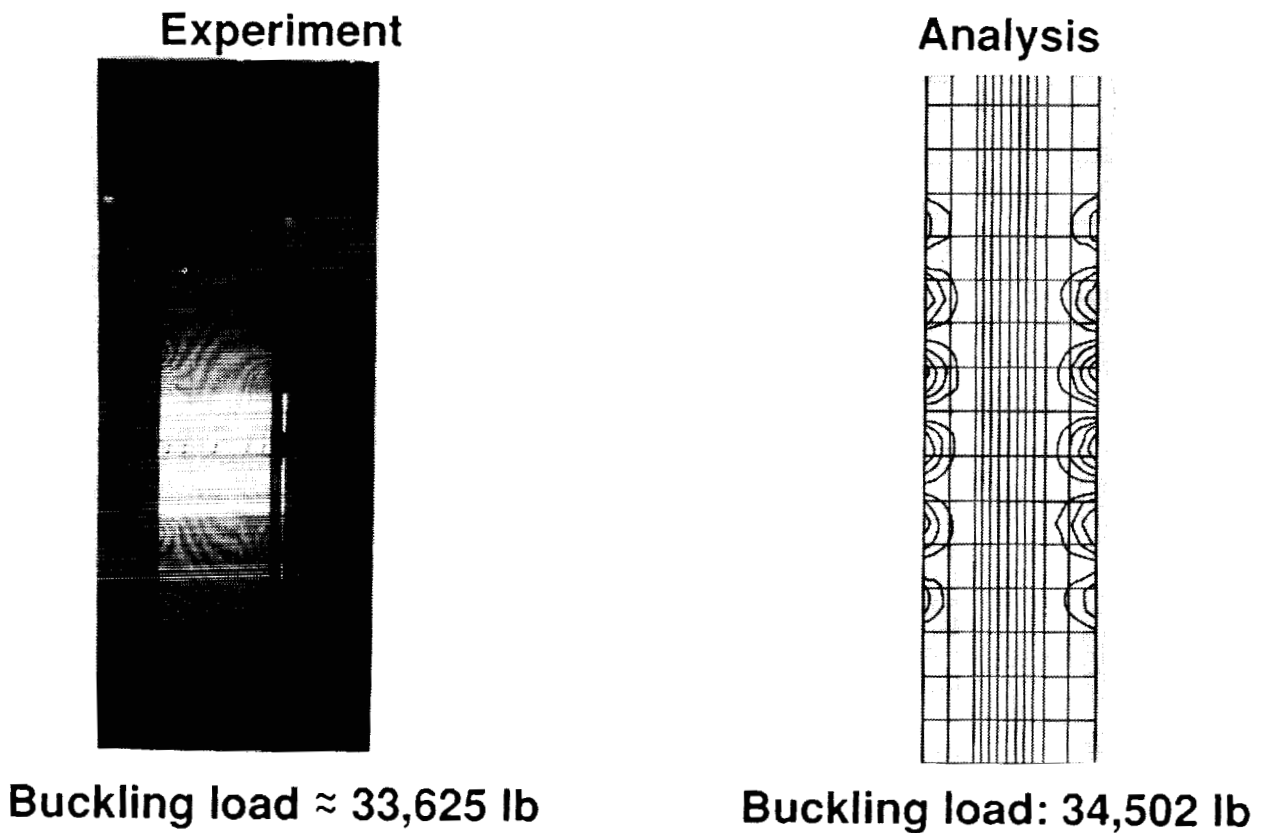


Figure 15. Element test specimen buckling response.

CORRELATION OF ANALYTICAL AND EXPERIMENTAL RESULTS FOR PANEL SPECIMEN

Nonlinear analysis of the panel specimen was performed using the DIAL finite element code and the end-shortening results are compared with experimental results in Figure 16. The finite element model was generated using shear deformable plate elements resulting in a 16,500 degree-of-freedom model when appropriate boundary conditions were imposed. The analytical results are represented in the figure by a solid line and the experimental results are represented by open squares with the filled square representing the failure event. The specimen nonlinear response compares well with the analytical results.

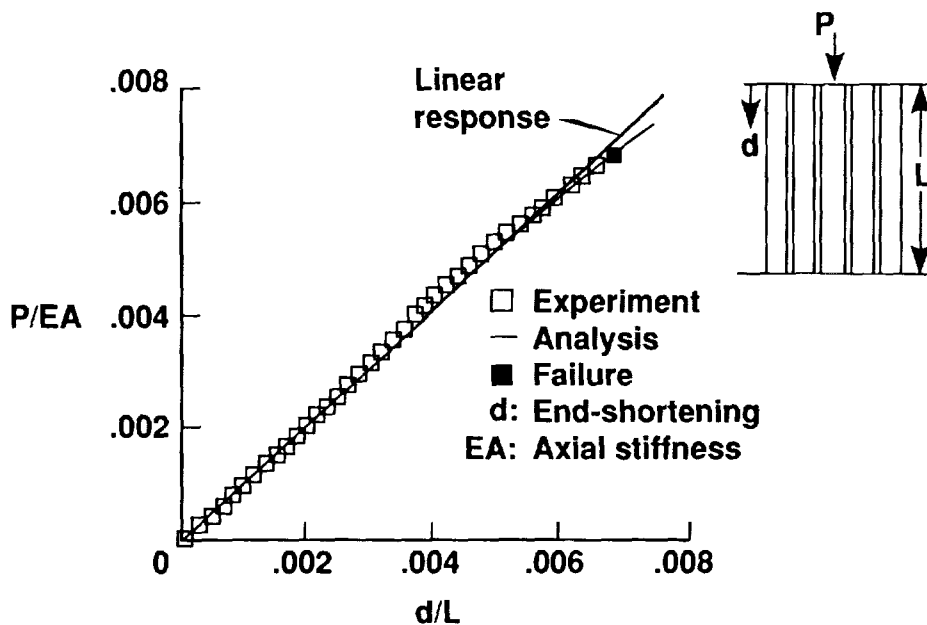


Figure 16. Correlation of panel specimen end-shortening results.

COMPARISON OF PANEL SPECIMEN STATIC RESPONSE AT 75,000 LB

The analytical results for panel static response are compared with the experimental results in Figure 17. As described earlier, the panel exhibited observable out-of-plane displacement beyond 50,000 lb in the form of two lobes at the central stiffener locations. The nonlinear analysis results are compared with the experimental results at 75,000 lb in the figure. The comparison between the analytical and experimental out-of-plane displacement shape and location is good.

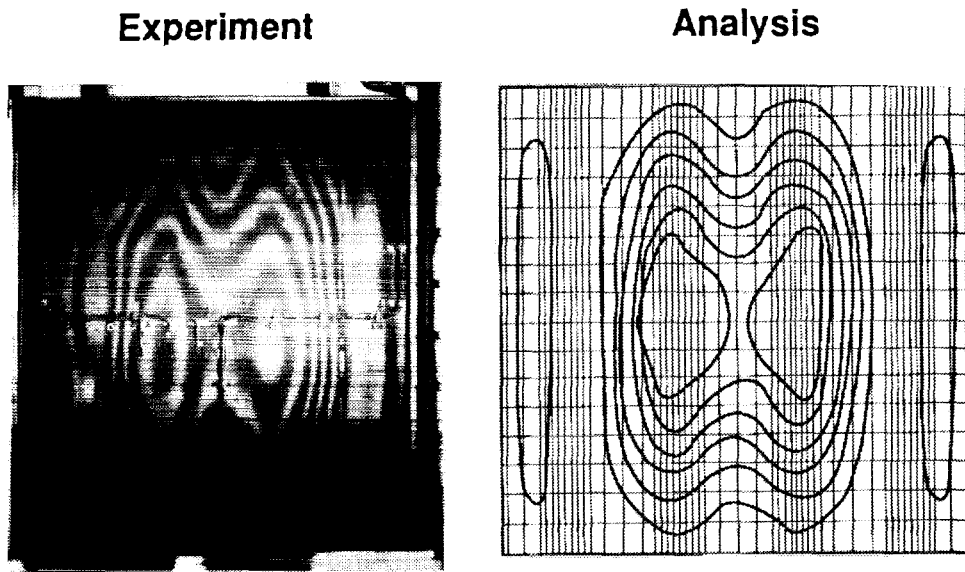


Figure 17. Out-of-plane displacement results for panel specimen at 75,000 lb.

CONCLUDING REMARKS

Design, analysis, and experimental studies have been conducted to evaluate a foam-filled hat-stiffened panel concept. Design studies suggest that using this new concept could result in 6 to 10 percent improvement in structural efficiency compared to the more conventional hat-stiffened panel. The foam-filled hat-stiffened concept is amenable to automated manufacturing processes that are suitable for solid-blade-stiffener geodesic structures and are 20 percent lighter than the solid-blade-stiffener panels in the 3,000 to 20,000 lb/in. load range.

Element specimen results indicate that a 20 ft-lb dropped-weight impact damage to the stiffener cap does not result in significant degradation of performance. Panel test results suggest that airgun impact damage to skin or skin-stiffener flange interface results in the most reduction in residual strength. This reduction in load carrying ability is estimated to be 13 percent which is not very significant. From the tests conducted it appears that the foam-filled hat structural concept is tolerant to the type of damage considered. For all test specimens with and without damage, the global failure strain was above $5,500\mu$ in./in. The analysis results for buckling and nonlinear response compared well with the experimental results.

REFERENCES

1. Reddy, A. D.; Rehfield, L. W.; Haag, R. S.; and Wideman, C. B.: Compressive Buckling Behavior of Graphite/Epoxy Isogrid Wide Columns with Progressive Damage. *Compression Testing of Homogeneous Materials and Composites*, ASTM STP 808, edited by R. Chair and R. Paperino, 1983, pp. 187-199.
2. Ambur, D. R.; and Rehfield, L. W.: Effect of Stiffness Characteristics on the Response of Composite Grid-stiffened Structures. AIAA Paper No. 91-1087, Proceedings of the 32nd Structures, Structural Dynamics, and Materials Conference, April 8-10, 1991, Part 2, pp. 1349-1356.
3. Stroud, W. J.; and Anderson, M. S.: PASCO: Structural Panel Analysis and Sizing Code, Capability and Analytical Foundations, NASA TM-80181, November 1981.
4. Anon.: DIAL Finite Element Analysis System - Version L3D2. Lockheed Missiles and Space Company, July 1987.

A STUDY OF STRUCTURALLY EFFICIENT GRAPHITE-THERMOPLASTIC
TRAPEZOIDAL-CORRUGATION SANDWICH AND SEMI-SANDWICH PANELS

Dawn C. Jegley
NASA Langley Research Center
Hampton, VA

519-24
51419

ABSTRACT

The structural efficiency of compression-loaded trapezoidal-corrugation sandwich and semi-sandwich composite panels is studied to determine their weight savings potential. Sandwich panels with two identical face sheets and a trapezoidal corrugated core between them, and semi-sandwich panels with a corrugation attached to a single skin are considered. An optimization code is used to find the minimum weight designs for critical compressive load levels ranging from 3,000 to 24,000 lb/in. Graphite-thermoplastic panels based on the optimal minimum weight designs were fabricated and tested. A finite-element analysis of several test specimens was also conducted. The results of the optimization study, the finite-element analysis, and the experiments are presented.

INTRODUCTION

The high stiffness, high strength, low density, and tailorability of composite materials has greatly increased the potential for designing structures which are more efficient than metallic structures. An important consideration in designing these structures is the cost involved in their manufacturing. To make composite structures a viable replacement for metallic structures, composite structures must be designed to take advantage of cost-effective manufacturing techniques in order to minimize their cost.

A cost-effective manufacturing technique that is receiving attention is thermoforming. A structural concept that can exploit thermoforming is a panel with one or two face sheets and a trapezoidal-shaped corrugated core. This structural concept is attractive since the trapezoidal corrugation can be thermoformed from one continuous constant-thickness graphite-thermoplastic sheet of material and consolidated into a sandwich panel with two face sheets or a semi-sandwich panel with one face sheet. The manufacturing process involves thermoforming these large sheets of composite material with metal tools after the sheets have been laid up in the appropriate stacking sequence. Since the corrugated sheet is initially a continuous flat sheet, it is relatively easy to fabricate these panel elements into the desired shape. The corrugations require no additional cutting or aligning, thereby requiring less effort to construct than discrete stiffeners. However, one drawback to this technique is that thermoforming can impose restrictions on the design if a constant thickness corrugation is required.

For panels of this type to be used in aircraft structures, they must be structurally efficient, easily manufacturable, and their behavior must be predictable. The present study focuses on examining the response of thermoformed sandwich and semi-sandwich panels with a trapezoidal corrugation. An analytical

optimization study was conducted to identify structurally efficient designs for panels subjected to compressive loads. Results of this study are presented herein. Based on optimal designs, representative panels were fabricated and tested. The results of these tests and of a corresponding finite-element analysis are presented in the present paper.

PANEL CONFIGURATIONS AND STRUCTURAL EFFICIENCY CALCULATIONS

Two panel configurations were considered in this study. The first configuration is a semi-sandwich panel with a trapezoidal-shaped continuous corrugation attached to a single face sheet. A cross-section of a semi-sandwich panel is shown in figure 1(a). The second configuration is a sandwich panel with a trapezoidal-shaped continuous corrugation attached to two identical face sheets. A cross-section of a sandwich panel is shown in figure 1(b).

Structurally efficient designs were determined for sandwich and semi-sandwich panels with trapezoidal corrugations. The optimal (minimum weight) configurations were determined and evaluated using the computer code PASCO (ref. 1). The design variables were ply thicknesses and corrugation dimensions (see figure 1). Optimum panels for each configuration were designed to support axial compressive loads corresponding to N_x/L (where N_x is the axial stress resultant and L is the panel length) of 100, 250, 500 and 800 lb/in². No lateral or shear loading was considered.

Allowable stacking sequences contained only $\pm 45^\circ$, 0° and 90° -degree plies. Design constraints are given in table I and include maximum allowable strains and minimum ply thicknesses on the outermost $+45^\circ$ -degree and -45° -degree plies. The angle between the skin and the sides of the corrugation (see figure 1) was required to be 45 degrees and the skin was assumed to be flat. For the optimization process, all panels were designed to be 30 inches long and 24 inches wide and the material properties for a typical graphite-thermoplastic material given in table II were used. These properties accurately represent the experimentally determined properties of flat graphite-thermoplastic panels as shown in reference 2. Initially, no restrictions were placed on corrugation width (shown as b in figure 1). Minimum overall extensional and shear stiffness constraints, as given in reference 3, were also included. All panels were designed to be buckling critical; however, the buckling loads determined by PASCO are based on the assumption that no out-of-plane prebuckling deformations are present.

SPECIMENS, APPARATUS AND TESTS

Panel Configurations

Six panels were fabricated from Hercules AS4 graphite fiber and ICI PEEK thermoplastic resin, and are described in table III. In each panel, the $\pm 45^\circ$ -degree plies were made with woven fabric and all other plies were made from unidirectional tape. Four types of semi-sandwich panels and two types of sandwich panels were constructed. The panel designs were based on the PASCO optimization results but significant changes were made to the optimum designs to provide a more realistic design. Changes to the PASCO designs included increasing layer thickness to obtain an integral number of plies (i.e., fractions of plies were rounded up or down), forcing all laminates to

be balanced (PASCO requires symmetric laminates) and requiring at least one 90-degree ply in each laminate. The stacking sequences and dimensions of each fabricated panel are shown in table III. Semi-sandwich panels are identified as panels A, B, C, and D. Sandwich panels are identified as panels E and F.

The semi-sandwich panels were constructed with one flat skin and a corrugation and were placed in the autoclave for consolidation. However, when the panels cooled to room temperature, the skin of the semi-sandwich panels deformed out-of-plane into a cylindrical surface. A photograph of the cross-section of panel A is shown in figure 2(a). The amount of curvature of the skin was measured for each panel prior to testing. The variation of the skin from a flat surface (designated as h in figure 2) was .85, .42, .48 and .22 inches for panels A, B, C, and D, respectively. The maximum curvature was in panel A and this curvature corresponds to an equivalent cylinder with radius of curvature of the skin of 91 inches. The sandwich panels did not deform out-of-plane during the fabrication or cooling processes and were essentially flat. A photograph of the cross-section of panel E is shown in figure 2(b).

Prior to compression testing, one inch of each end of each panel was potted in an epoxy compound and the potted ends were ground flat and parallel. The semi-sandwich panels were not flattened to remove the curvature prior to potting the ends. Strain gages were bonded to each panel. The semi-sandwich panels had strain gages on the skin and corrugations while the sandwich panels only had gages on the skins since the corrugation was not accessible for gage application. The skin of each semi-sandwich panel and one skin of each sandwich panel was painted white to produce a reflective surface so moiré interferometry could be used to monitor out-of-plane deformations during the test.

Panel Properties

Two flat coupons 1.5 inches wide, 2 inches long and approximately 0.2 inches thick were cut from sandwich panel E after the panel was tested. The coupons were cut from a section of the panel where the corrugation was attached to the skin and where post-failure ultrasonic C-scan inspection indicated that no damage was present. These coupons were loaded in axial compression while the end-shortening displacement was recorded to determine the stiffness of the coupon. Flat coupons could not be cut from the semi-sandwich panels so coupons cut from panel E are assumed to be representative of all panels tested. Stiffnesses of these coupons were calculated based on load-end-shortening results from the compression tests. Stiffness predictions were also calculated using laminate theory and finite-element analysis with the typical graphite-thermoplastic material properties given in table II. A comparison of the assumed and experimentally determined stiffnesses indicates that the assumed material properties for typical graphite-thermoplastic materials were approximately 25% too high to accurately represent the coupons and the panels tested. Therefore, the experimentally determined stiffness values were used for the finite-element analysis of the test specimens. Equivalent lamina properties corresponding to these stiffnesses are shown in table II. No allowance is made for the fact that all ± 45 degree plies were made from woven fabric in all panels tested. These layers are assumed to be tape layers in the analysis (i.e., no fiber undulations were considered). Each flat coupon was measured and weighed prior to testing to determine the density. The assumed density was accurate.

Apparatus and Testing

All panels were slowly loaded to failure in axial compression in a 1.2 Mlb-capacity hydraulic testing machine. Unloaded edges were unsupported. Strain gage data and out-of-plane deformations at selected locations and panel end-shortening displacements were recorded during the test. Moiré fringe patterns were photographed and video taped during the test.

FINITE-ELEMENT ANALYSIS

A nonlinear finite-element analysis of each panel was conducted using the STAGS computer code (ref. 4). Actual stacking sequences, measured thicknesses and corrugation dimensions were used for the analytical model. All plies within a laminate were assumed to be the same thickness, with a woven ± 45 layer assumed to be the thickness of two plies. All corrugations were assumed to be identical within a given panel. The entire panel was modeled and the overall panel curvature was included as an initial geometric imperfection. The section of each panel in the potting compound was included in the analytical model and no out-of-plane or lateral deformations were permitted in this region. The unloaded edges of the panel were unrestrained. Four-noded quadrilateral elements were used to model the panels. A uniform grid was implemented along the length of the panel with each element being one inch long for panels A, B, C, D and F. Elements which were 0.5 inches long were used to model panel E. These models involved 6,000 to 10,000 degrees of freedom, depending upon panel geometry. The element width varied depending on panel configuration. The boundary conditions for a semi-sandwich panel are shown in figure 3.

One semi-sandwich panel was modeled with 1-inch-long elements and with .5-inch-long elements to determine if a converged solution had been obtained. Less than one percent difference was found in the end-shortening, prebuckling and postbuckling out-of-plane displacements or eigenvalues from the analyses based on 1-inch-long elements and on 0.5-inch-long elements.

The prebuckling stiffness, prebuckling out-of-plane deformation shape and buckling load were determined for each panel based on a nonlinear prebuckling stress state. For panels A and E the analysis was continued for loading beyond the buckling load. Nonlinear analysis for the postbuckling response was conducted using the eigenvector corresponding to the lowest eigenvalue to represent an initial geometric imperfection and to initiate the analysis to determine postbuckling deformation shape and postbuckling stiffness.

RESULTS AND DISCUSSION

Optimized Panel Designs

Optimum designs for semi-sandwich and sandwich panels are presented in this section for a variety of design constraints. In all cases, all four edges of the panel were assumed to be simply supported (PASCO requires simply supported loaded edges) and all corrugations within a panel were assumed to be identical. The initial design imposed no restrictions on the number of corrugations across the panel width

of approximately 24 inches. However, in each case, the optimum design resulted in five corrugations. Since final optimal designs required exactly a 24-inch width, five 4.8-inch-wide corrugations were required. The skin of the panel was assumed to be flat prior to loading for all designs.

The structural efficiency of optimal panel designs were determined assuming the typical material properties of graphite-thermoplastic material shown in table II. The structural efficiency results are shown in figure 4 in the form of a weight index W/AL (where W is the panel weight, A is the panel planform area and L is the panel length) versus a load index N_x/L . Results are presented in this manner for ease of comparison with results presented in the literature such as in references 3 and 5. The solid lines represent optimum semi-sandwich panels and the dashed lines represent optimum sandwich panels. The most structurally efficient configurations are those represented by the lowest curves on the plot, which are those designs with the lowest weight index for a specified load index. The lowest dashed and solid curves on the plot were determined using the constraints listed in table I. Laminate thicknesses and corrugation width of optimum panel designs found by using the constraints in table I are given in table IV.

Practical designs would include additional restrictions not included in table I. Examples of such restrictions would be an additional requirement of one 90-degree ply in each laminate and requiring an integral number of plies of each orientation. These additional restrictions were imposed on the designs and the results are also shown in figure 4. These additional requirements increased the weight of each designed panel by 4 to 13 percent above the optimum weight when these additional constraints were not included. Also shown on the figure is the structural efficiency of typical aluminum aircraft panels, represented by the shaded region. The results indicate that the graphite-thermoplastic panels are significantly more structurally efficient than the aluminum panels for all load levels considered. The results also indicate that there is little difference between the structural efficiency of the semi-sandwich and sandwich panels. The results also indicate that additional constraints which might be required to make the panel designs more practical, such as including a minimum number of 90-degree plies and an integral number of plies, do not significantly reduce the panel's structural efficiency.

Critical constraints of optimum-design panels are dependent upon design load level and are given in table IV. Extensional stiffness is a critical constraint in all panels except the most heavily loaded semi-sandwich panel. Shear stiffness is critical in all semi-sandwich panels. PASCO cannot calculate an overall shear stiffness for sandwich panels so no overall shear stiffness requirement was imposed on the sandwich panel design, hence, overall shear stiffness could not be critical. At least one buckling mode is also critical for each panel. Allowable inplane shear strain is a critical constraint for the most heavily loaded semi-sandwich panel. Optimum corrugation width decreases and height increases as load level increases. The optimal thickness of the ± 45 - and 0-degree plies depends on load level. The lightest weight panel designs have no 90-degree plies. For the lowest load level considered, the thickness of the ± 45 -degree plies is the minimum thickness allowed.

The structural efficiency of optimal panel designs in which the constraints in table I were used are shown again in figure 5. The structural efficiency of optimal panel designs that include all constraints in table I except those on minimum overall stiffnesses and minimum thickness of exterior ± 45 -degree plies are also shown in figure 5. Removing these constraints reduces the weight of the lightly-loaded semi-sandwich panels significantly and has a small effect on the sandwich panel weights.

The minimum thickness constraint has little effect on the heavily-loaded panels so there is little difference between the heavily-loaded semi-sandwich panels and there is no difference between the heavily-loaded sandwich panels. Sandwich panels are not as structurally efficient as semi-sandwich panels in some cases because both skins in each sandwich panel were required to be identical, resulting in increased weight.

A comparison between the PASCO and finite-element models and results was conducted for a heavily-loaded semi-sandwich panel by comparing the critical buckling loads predicted by PASCO and by STAGS using the method described in reference 6. This comparison is only used for model verifications since the allowable boundary conditions in PASCO do not accurately reflect test conditions, since PASCO does not allow for any prebuckling deformations, and since panel skin curvature is not included in the PASCO analysis. Buckling loads predicted by PASCO and by STAGS for this case differ by less than 5 percent.

Fabricated Panels

The panels described in table III and figures 1 and 2 were loaded to failure in axial compression. A comparison of the test and finite-element results of the panels is presented in this section. A comparison of W/A and N_x of tested panels indicates that the graphite-thermoplastic panels weigh approximately half the weight of aluminum panels designed to support the same load.

The test specimens described in this section exhibit nonlinear prebuckling deformations. This result is substantiated by the presence of moiré fringe patterns at low load levels that indicate out-of-plane deformations in the specimen skins. Moreover, the semi-sandwich specimens inherently have load path eccentricity. When these deformation characteristics are present, the onset of buckling is difficult to identify experimentally. Therefore, experimental buckling loads are not presented herein. Analytical buckling loads for the test specimens were obtained using finite-element analysis. The results are used in the present study to provide insight into the test results. For example, results are presented in figure 6 that show the values of the axial stress resultant N_x in the specimens at failure, represented by bars in the figure. Analytical predictions of buckling are also shown, represented by symbols. These results suggest that panels B and D failed prior to buckling and that the remaining panels supported load into the postbuckling region. To gain further insight into panel behavior, selected postbuckling analyses were conducted. A discussion of the test results for each of the panels is presented subsequently.

Semi-sandwich Panels

The semi-sandwich specimens exhibited noticeable out-of-plane deformation at low load levels. These deformations were detected using moiré interferometry. However, the load versus end-shortening curves were linear over most of the load range prior to failure, and gave no indication of a stiffness change associated with an overall general instability type of buckling response. To gain insight into panel response, buckling and postbuckling finite-element analyses were conducted. The presence of out-of-plane deformations in the test specimens at low load levels motivated the use of buckling analyses that include nonlinear prebuckling deformations.

For panel A, the global axial stiffness predicted by finite-element analysis is 3 percent less than that of the test specimen. The buckling analysis predicted a localized mode with out-of-plane deformations only in one corner of the panel. Postbuckling analysis indicated a change in the global axial stiffness of less than

one percent, which is consistent with the experimental data, and the presence of local regions of out-of-plane deformation. A contour plot of the predicted nonlinear out-of-plane prebuckling deformation pattern at a load of 97 percent of the predicted buckling load is shown in figure 7(a). A similar plot of the postbuckling deformation pattern at a load of 169 percent of the predicted buckling load is shown in figure 7(b). These results indicate that the nonlinear prebuckling deformation and postbuckling deformation patterns are very similar in shape and that the bending gradients are much more pronounced in the postbuckling range. The center of the panel has an out-of-plane deformation of .06 in. at $P/P_{cr}=0.97$ and .078 in. at $P/P_{cr}=1.69$, which is just before failure. Both of these deformations are larger than the skin thickness and indicate the presence of large nonlinear bending gradients. Photographs of the panel, showing moiré patterns of out-of-plane deformations, are shown in figures 8(a) and 8(b) for load levels approximately 95 percent and 170 percent of the predicted buckling load, respectively. These moiré patterns agree with the analytically determined patterns. Out-of-plane deformations in panel A are generally confined to regions of the skin where it is not attached to the corrugation and regions near the free edge.

Maximum strains occur in the skin under the corrugation nearest each free edge. The maximum axial and lateral strains occur near the horizontal center of the panel and have values of -.0055 and .0032 in./in., respectively. Maximum shear strains occur at the edge of the potting and have values of ± 0.0022 in./in. Separation at the interface between the skin and corrugation caused the failure of panel A. As the amplitude of the out-of-plane deformation grew, high strains developed in the skin (at the center of the panel, strain gages indicated the axial strain was -.0055 in./in. and the lateral strain was .0070 in./in. at failure) and deformations caused separation at points where the corrugation meets the skin. A sketch of the initial and deformed cross-section of panel A is shown in figure 9 (with the magnitude of the deformations amplified). Separation occurred at points labeled A on the sketch. The largest deformations are located in the regions of the skin not attached to the corrugation. Also influencing strains in the panel is the difference in Poisson's ratios between the skin and corrugation. This difference can be expressed as a ratio of the values of the Poisson's ratios in the skin to the value of the Poisson's ratios in the corrugation, as calculated using laminate analysis. In panel A these ratios are $\nu_{xy}(\text{skin})/\nu_{xy}(\text{corrugation})=1.3$ and $\nu_{yx}(\text{skin})/\nu_{yx}(\text{corrugation})=6.4$. The further these ratios are from 1 (which would represent two laminates with the same Poisson's ratios), the larger the mismatch in properties and the larger the interlaminar stresses which develop during loading. This mismatch causes the skin and corrugation to try to deform different amounts even though they are bonded together and must maintain deformation compatibility. These resulting high interlaminar stresses eventually result in separation between the skin and the corrugation. A photograph of panel A after failure is shown in figure 10.

To examine the local deformations under the corrugation, a finite-element analysis of a panel with only one corrugation was conducted. Since the panel skin is less than .05 inches thick and contains only one 90-degree ply, little lateral load is required to induce out-of-plane deformations in the thin skin. Analysis indicates that, away from the clamped edges, an applied compressive axial stress resultant induces a tensile lateral stress resultant which is 10 percent of the magnitude of the axial stress resultant. However, near the clamped edges the applied compressive axial stress resultant induces a compressive lateral stress resultant 60 percent as large as the axial stress resultant. This compressive lateral stress causes local out-of-plane deformations at the clamped ends, as seen in the tested panel.

Panel B also exhibited out-of-plane deformations at very low load levels, but the deformation pattern was different from that in panel A. Prebuckling stiffness predicted by analysis is 3 percent higher than the stiffness found from experiment. The finite-element prediction of prebuckling deformation at $P/P_{cr}=.75$ is shown in figure 11, where P_{cr} is the buckling load predicted by finite-element analysis. No local deformations or high bending gradients of the type seen in panel A are present. Axial strain gages indicated strains of $-.0056$ in./in. at failure. Finite-element analysis also indicates high axial strain levels at the failure load. Initial failure appears to cause a sudden increase in strain in the corrugation leading to separation between the corrugation and skin. A photograph of panel B after failure is shown in figure 11(b). The skin and corrugation have separated over a large section of the panel. The difference in Poisson's ratios between the skin and corrugation is less than in panel A. The ratios of the Poisson's ratios are $\nu_{xy}(\text{skin})/\nu_{xy}(\text{corrugation})=.91$ and $\nu_{yx}(\text{skin})/\nu_{yx}(\text{corrugation})=.21$, in panel B. The panel failed at $P/P_{cr}=.88$.

Out-of-plane deformations at very low load levels also occurred in panels C and D. Analytically determined prebuckling deformations at $P/P_{cr}=.95$ in panel C and at $P/P_{cr}=.88$ in panel D are shown in figures 12 and 13, respectively. A deformation shape resembling one half-wave in each direction occurred in panel C just prior to failure. A deformation shape resembling that found in panel B occurred in panel D, with the out-of-plane deformation at the unsupported edges opposite in sign from the deformation at the center of the panel. Deformations in panels B and D were not limited to the thin section of skin between the corrugations.

The strain gages at the horizontal centerline of panel C indicated a maximum axial strain of approximately $-.0055$ in./in. prior to failure. Strain gages on panel D indicated a maximum failure strain of $-.0048$ in./in. at the panel horizontal centerline on the corrugation. Panels C and D failed across the corrugation midlength and the corrugation separated from the skin but little damage in the skin due to panel failure could be seen. The separation between the corrugation and the skin was only at the corrugation-skin interface in panel C. However, plies from the skin stuck to the corrugation and vice versa in panel D. Little damage to the skin could be seen after loading was removed from panels C and D. The ratio the skin and corrugation Poisson's ratios is $\nu_{xy}(\text{skin})/\nu_{xy}(\text{corrugation})=1.87$ and $\nu_{yx}(\text{skin})/\nu_{yx}(\text{corrugation})=5.6$, in panel C and 1.41 and 2.21, respectively, in panel D.

Sandwich Panels

Panels E and F also exhibited out-of-plane deformation at very low load levels, however, the magnitude of this deformation remained quite small throughout loading. Predicted and experimental prebuckling stiffnesses differ by less than one percent in panel E but differ by 12 percent in panel F. Predicted and experimental postbuckling stiffnesses differ by 4 percent in panel E.

According to the analysis of panel E, the sections of skin not attached to the corrugations deform prior to buckling, as shown in the contour plot of out-of-plane deformation in figure 14(a). The prebuckling deformation pattern resembles one axial half-wave under each center corrugation. However, the maximum magnitude of the prebuckling deformations is less than one ply thickness. The deformations shown correspond to 94 percent of the predicted buckling load. Moiré patterns indicate that the center sections of thin skin in panel E deform into a pattern resembling two axial half-waves. However, the skin of the panel was only .05 inches thick and the

predicted deformation in this region is so small that any imperfection in this section of skin could cause an unexpected deformation shape.

Predicted postbuckling deformations are shown in figure 14(b) for 161 percent of the predicted buckling load. This load corresponds to a value just below that of test specimen failure. Loading was stopped when the attempt to increase load resulted in increased end-shortening and a reduction in load carrying capability. The failure load was defined as the maximum load level reached. Strains in the panel skins were calculated for this load level. At the maximum load, large deformations occur near the free edges of both skins. The magnitude of the deformations are indicated on the figure. The maximum axial and shear strains, $-.0050$ and $-.0025$ in./in., respectively, occur near the corners of one skin of the panel. Panel E was ultrasonically inspected by C-scan after testing to determine where damage had occurred since no damage was visible after the panel was removed from the test machine. C-scan inspection indicated that the only damaged region of the panel is a separation between the skin and corrugation at the location of maximum axial and shear strains. The mismatched Poisson ratios between the skin and corrugation can be expressed as $\nu_{xy}(\text{skin})/\nu_{xy}(\text{corrugation})=1.11$ and $\nu_{yx}(\text{skin})/\nu_{yx}(\text{corrugation})=7.79$ in panel E. According to the analysis, when panel E reaches a load of $P/P_{cr}=1.8$, the end-shortening rapidly grows with slight increases in load, indicating that panel failure would occur.

Panel F behaved in a manner similar to panel E; however, each thin section of skin initially deformed into two axial half-waves and then the entire panel buckled into a one axial half-wave. The deformation patterns predicted by analysis indicate out-of-plane prebuckling deformations of $.07$ inches at the free edges and $.045$ inches in the skin at the center of the panel at a load of 95 percent of the buckling load. The value of $.045$ inches agrees with the experimentally measured value but no measurements were recorded during testing at the panel's unsupported edges. This maximum deformation prior to buckling is larger than the skin thickness. This panel failed by shortening rapidly without additional increase in load, but with no visible damage after loading reached a maximum value. C-scan inspection indicated extensive damage near one potted end in a region several inches long and about ten inches wide. When panel F reaches $P/P_{cr}=.99$, the end-shortening rapidly grows and the panel fails. The Poisson's ratios in panel F are the same as those in panel E since the only difference between the panels is length.

CONCLUDING REMARKS

The potential of structurally efficient graphite-thermoplastic panels for aircraft components that were fabricated using the thermoforming technique was examined. Thermoforming can be used to fabricate trapezoidal-corrugation sandwich and semi-sandwich panels which consist of a continuous corrugation and two or one face sheets, respectively. An optimization study indicates that minimum-weight trapezoidal-corrugation sandwich and semi-sandwich composite panels are more structurally efficient than current aluminum wing compression panels used on aircraft today. However, semi-sandwich panels are likely to deform out-of-plane during the fabrication process, which must be taken into account in any design. Testing of semi-sandwich panels identified a nonlinear displacement behavior, so a finite-element analysis based on a nonlinear prebuckling stress state was conducted. This analysis accurately predicts panel deformations and strains caused by axial compressive loading. Analysis indicates that significant prebuckling out-of-plane

deformations occurred in all semi-sandwich panels, as shown by moiré patterns of test specimens under load. Sandwich panels did not deform out-of-plane during fabrication and did not display as much nonlinear behavior as the semi-sandwich panels. Failure of each panel involved separation of the corrugation from the skin either near the clamped edge or midlength but always across the entire panel width.

This study indicates that the thermoforming technique can be used to build structurally efficient graphite-thermoplastic panels and that the prebuckling and postbuckling behavior of these panels can be accurately predicted. Thermoforming is a viable manufacturing technique worthy of further consideration.

REFERENCES

1. Anderson, Melvin S.; and Stroud, W. Jefferson: A General Panel Sizing Computer Code and Its Applications to Composite Structural Panels. AIAA Journal, Vol. 17., No. 8, August 1979, pp. 892-897.
2. Jegley, Dawn C.: Compression Behavior of Graphite-Thermoplastic and Graphite-Epoxy Panels with Circular Holes or Impact Damage. NASA TP-3071, March 1991.
3. Williams, J. G.; Anderson, M. S.; Rhodes, M. D.; Starnes, J. H., Jr.; and Stroud, W. J.: Recent Developments in the Design, Testing, and Impact-Damage Tolerance of Stiffened Composite Panels, Fibrous Composites in Structural Design (Proceedings of Fourth Conference on Fibrous Composites in Structural Design), Plenum Press, New York, 1980, pp. 259-291.
4. Almroth, B. O.; and Brogan, F. A.: The STAGS Computer Code. NASA CR-2950, 1980.
5. Williams, Jerry G.; and Mikulas, Martin M., Jr.: Analytical and Experimental Study of Structurally-Efficient Composite Hat-Stiffened Panels Loaded in Axial Compression. NASA TM X-72813, 1976.
6. Stroud, W. Jefferson; Greene, William H.; and Anderson, Melvin S.: Buckling Loads of Stiffened Panels Subjected to Combined Longitudinal Compression and Shear: Results Obtained with PASCO, EAL, and STAGS Computer Programs. NASA TP-2215, January 1984.

Table I. Design Constraints

Constraint	Requirement
panel length	30 in.
panel width	24 in.
buckling	panel does not buckle below design load
minimum thickness of outer ± 45 -degree plies	.0055 in.
maximum compressive or tensile strain	.006 in./in.
maximum shear strain	$\pm .01$ in./in.
minimum global axial stiffness	dependent upon design load (see ref. 3)
minimum global shear stiffness	dependent upon design load (see ref. 3)
corrugation angle, α (see fig. 1)	45 degrees
corrugation width, b (see fig. 1)	same for top and bottom
skins	same stacking sequence for top and bottom skins of sandwich panel

Table II. Material Properties

Material property	typical graphite- thermoplastic material	coupons and fabricated panels
Longitudinal Young's modulus, Msi	19.4	14.5
Transverse Young's modulus, Msi	1.29	.97
Shear modulus, Msi	.74	.55
Major Poisson's ratio	.38	.38
Specific Weight, lb/in. ³	.057	.057

Table III. Test Specimens

Specimen Designation	Skin Stacking Sequence	Corrugation Stacking Sequence	Corrugation Width, ^a in.	Panel Length, in.
Semi-Sandwich Panels				
A	$[(\pm 45)_2/\overline{90}]_s$	$[\pm 45/0_5/90/0_4/\pm 45]_s$	2.03	12.
B	$[(\pm 45)_2/0_4/90/\pm 45/0_2/90]_s$	$[\pm 45/0_6/\overline{90}]_s$	1.64	12.
C	$[(\pm 45)_3/0_2/90/(\pm 45)_2/0/\overline{90}]_s$	$[\pm 45/0_6/90/0_4/\overline{90}]_s$	1.54	24.
D	$[(\pm 45)_3/0_6/90_2/\pm 45/0_6/\pm 45]_s$	$[\pm 45/0_5/90/0_3]_s$	1.32	24.
Sandwich Panels				
E	$[(\pm 45)_2/\overline{90}]_s$	$[\pm 45/0_6/\pm 45/0_6/90]_s$	2.00	12.
F	$[(\pm 45)_2/\overline{90}]_s$	$[\pm 45/0_6/\pm 45/0_6/90]_s$	2.00	24.

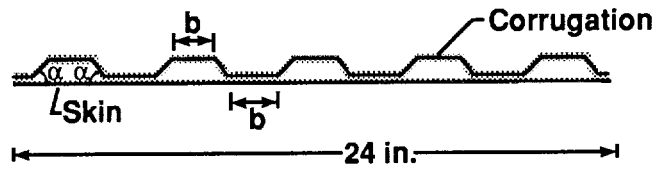
^a Corrugation width is b in figure 1.

Table IV. Optimum panels

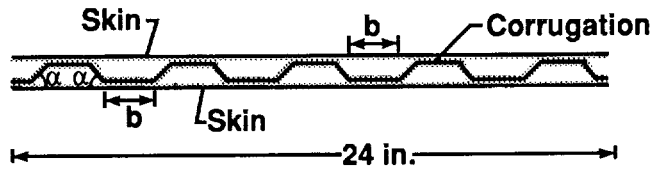
N_x/L , lb/in. ²	critical constraints ^a	corrugation width ^b , in.	skin thickness, in.	corrugation thickness, in.
Semi-Sandwich				
100	E, G, λ_{30}	1.82	.060	.112
250	E, G, λ_{30}	1.42	.145	.080
500	E, G, λ_1, λ_{15}	.98	.192	.084
800	G, $\lambda_1, \lambda_9, \lambda_{10}, \gamma$.77	.203	.125
Sandwich				
100	E, $\lambda_1, \lambda_{12}, \lambda_{13}$	1.88	.060	.049
250	E, $\lambda_1, \lambda_{15}, \lambda_{16}$	1.68	.041	.138
500	E, λ_1, λ_{15}	1.56	.056	.164
800	E, $\lambda_1, \lambda_{12}, \lambda_{13}, \lambda_{14}$	1.21	.077	.166

^a E is the extensional stiffness, G is the inplane shear stiffness, λ_i is the buckling mode with i axial half-waves, and γ is the inplane shear strain.

^b Corrugation width is b in figure 1.



a) Semi-sandwich panel



b) Sandwich panel

Figure 1. Panel design configurations.



a) Cross-section of panel A



b) Cross-section of panel E

Figure 2. Test specimens.

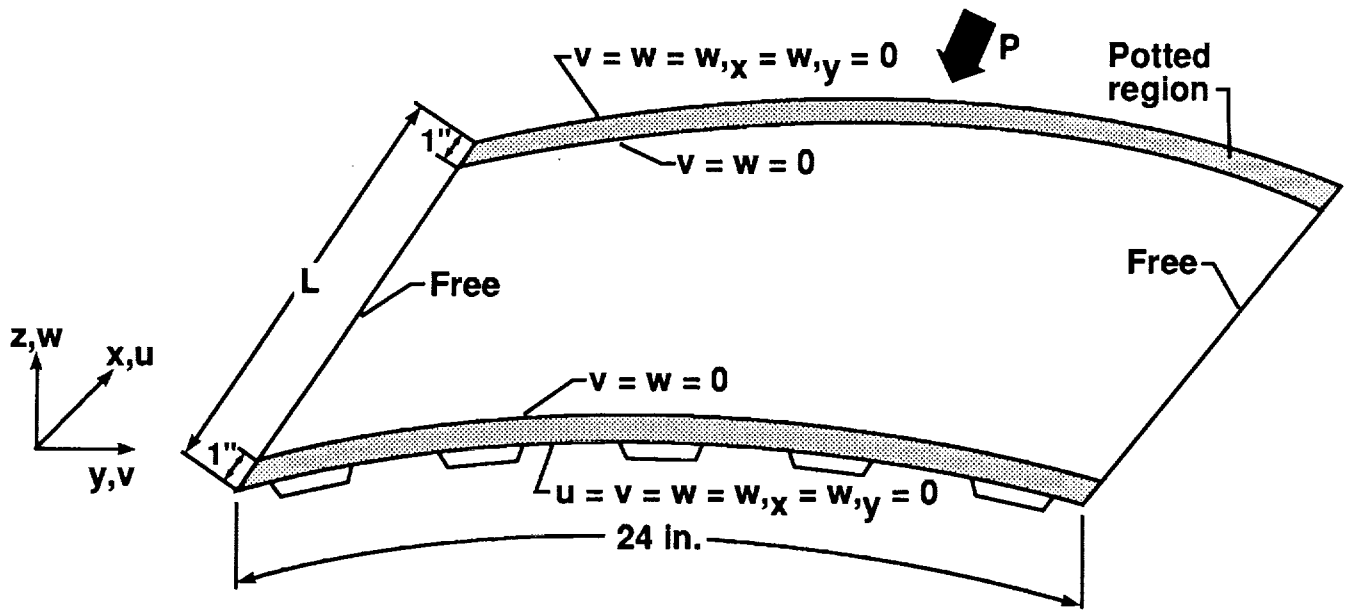


Figure 3. Finite element boundary conditions.

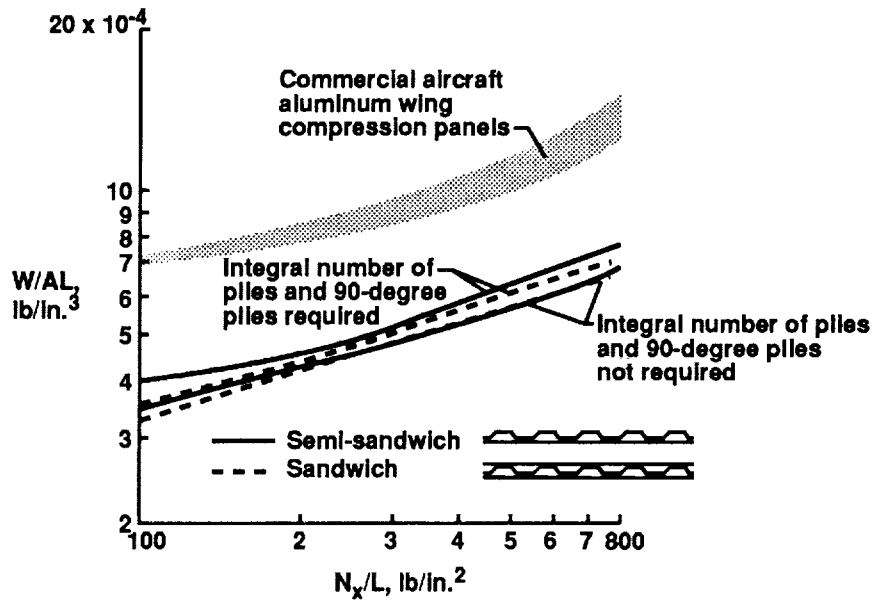


Figure 4. Structural efficiency of graphite-thermoplastic panels.

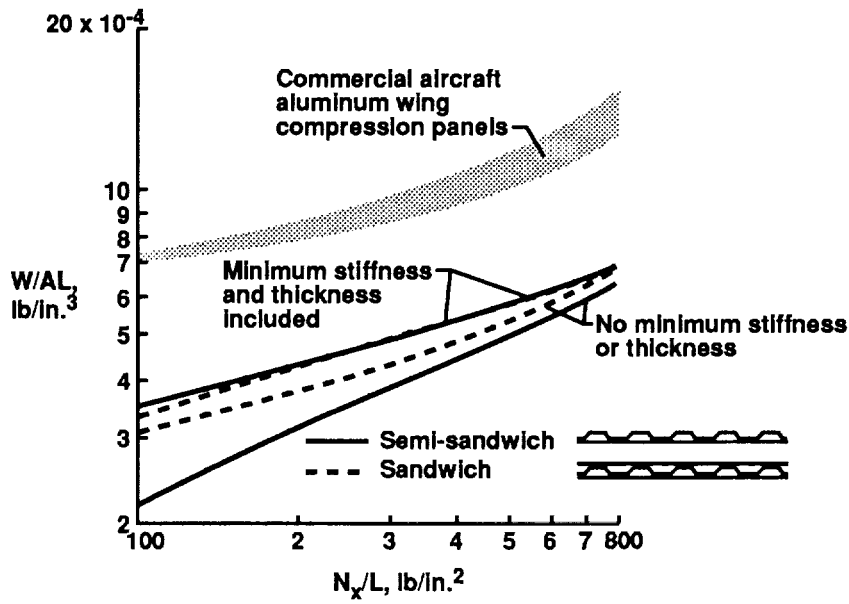


Figure 5. Effect of thickness and stiffness constraints on structural efficiency.

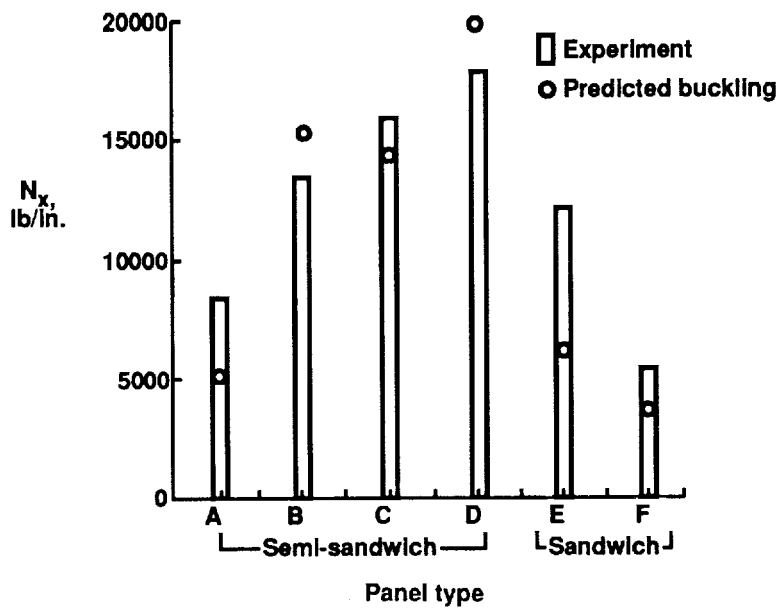


Figure 6. Stress resultants of control panels.

C-5

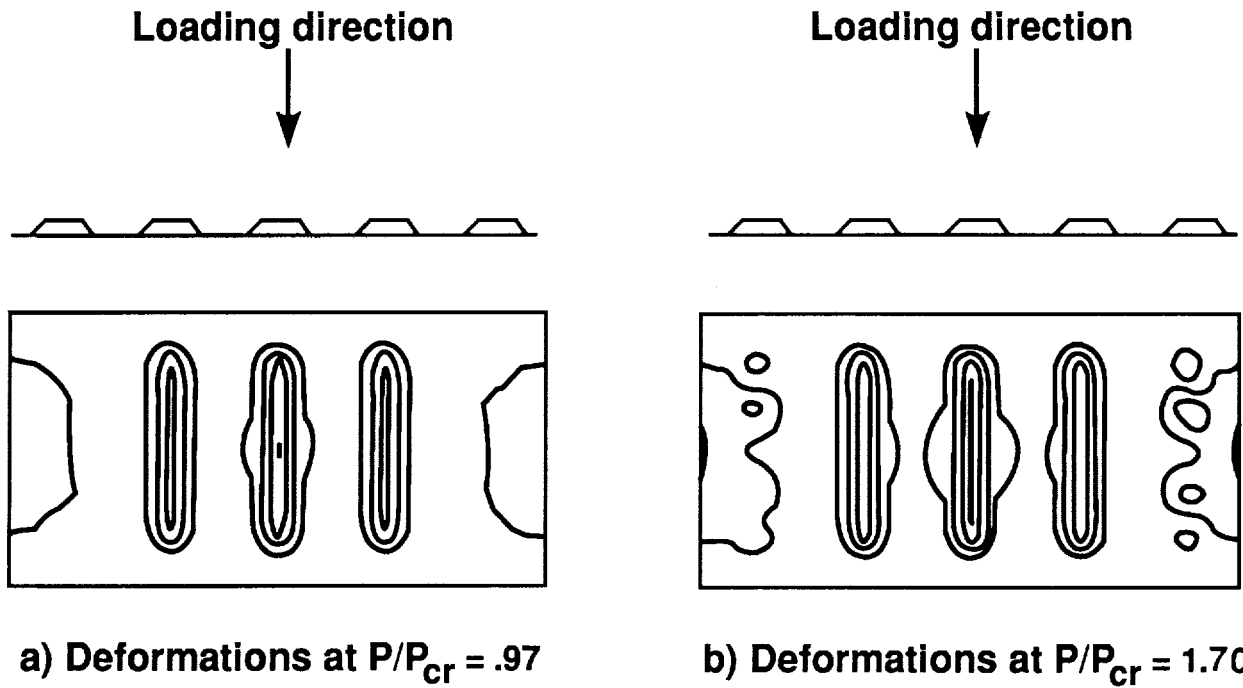


Figure 7. Analytically determined out-of-plane deformation of the skin of panel A.

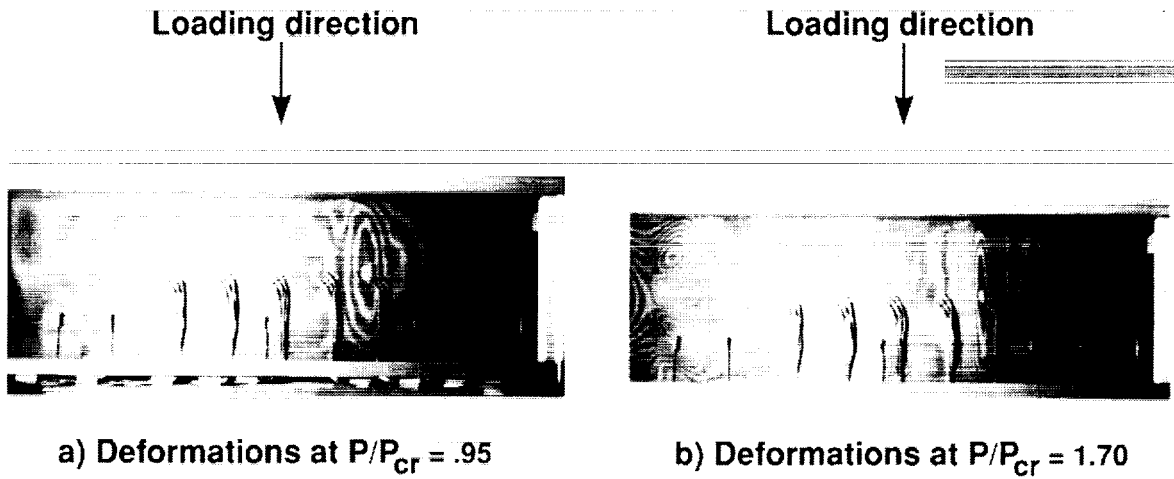


Figure 8. Moiré patterns of out-of-plane deformations of the skin of panel A.

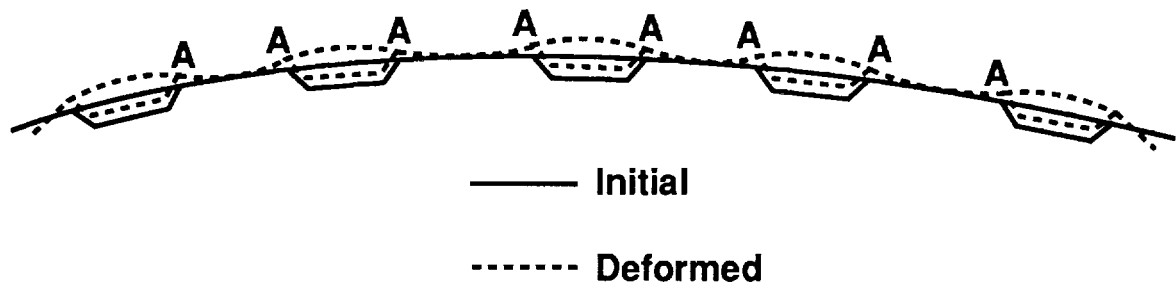


Figure 9. Sketch of deformation shape of semi-sandwich panel.

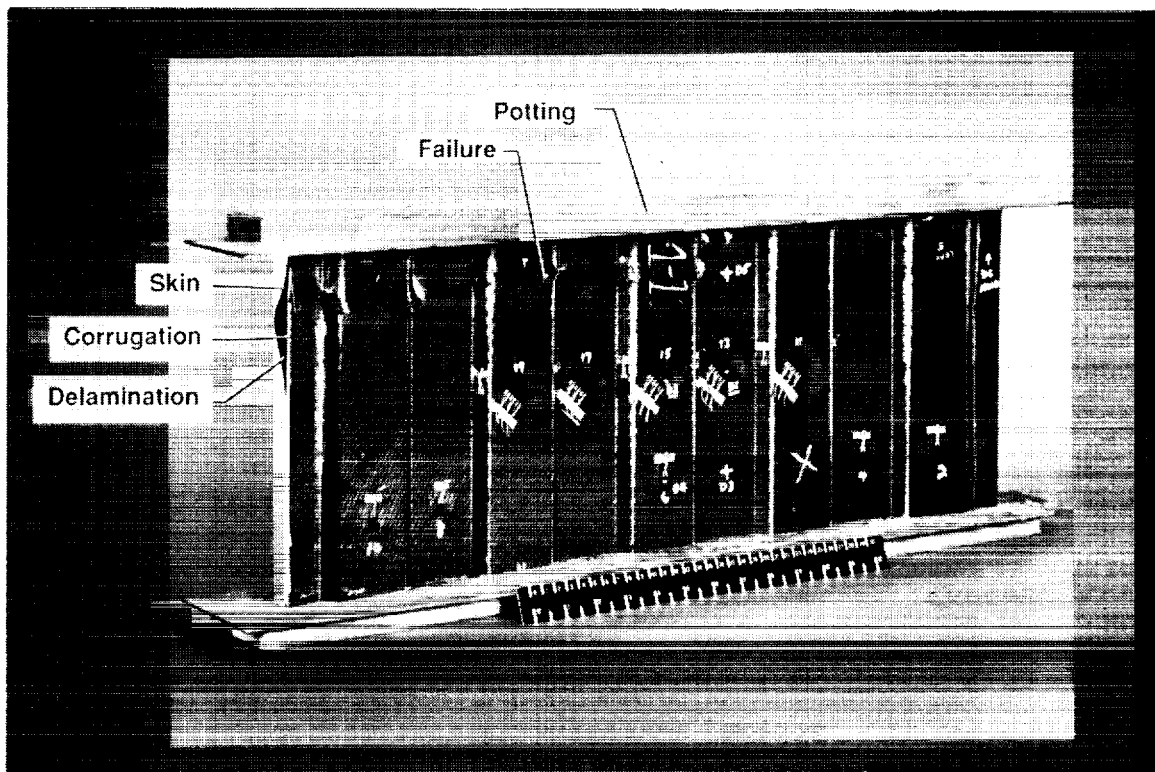


Figure 10. Panel A after failure.

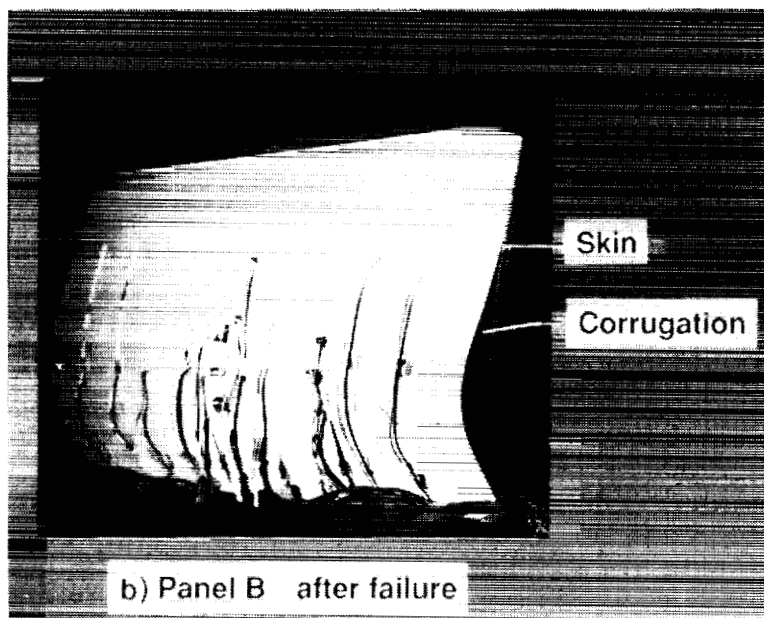
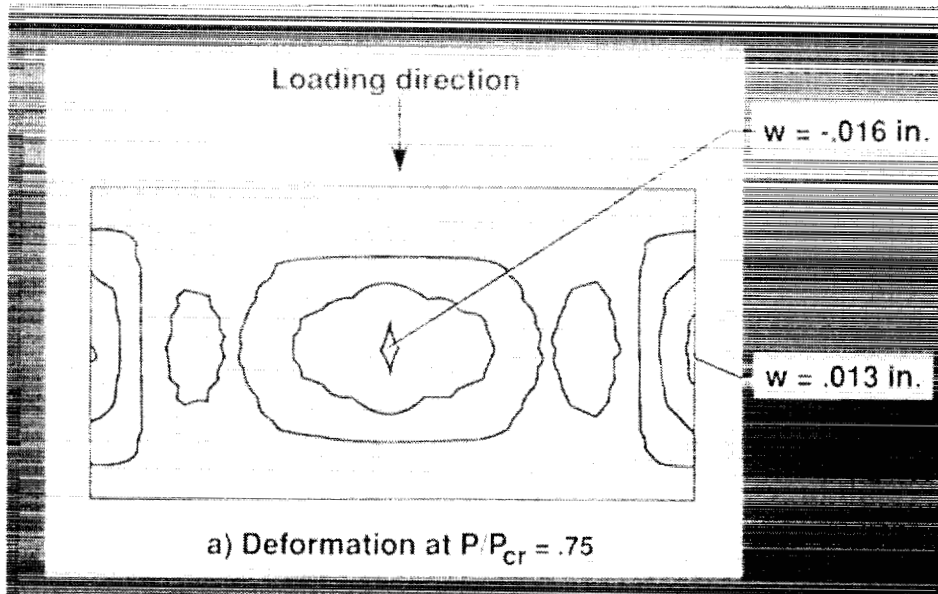


Figure 11. Deformations in panel B during and after loading.

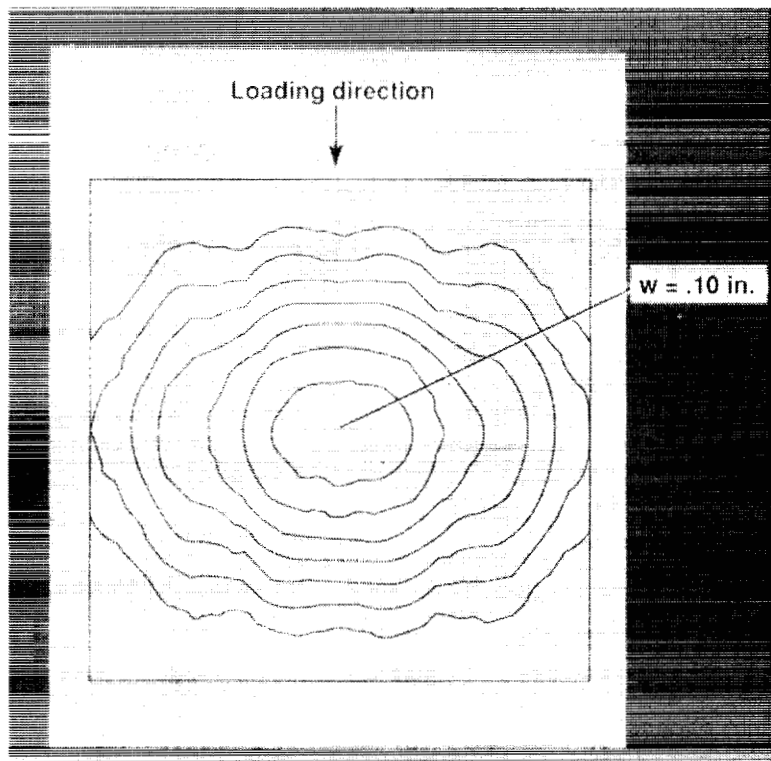


Figure 12. Deformations in panel C at $P/P_{cr} = .95$.

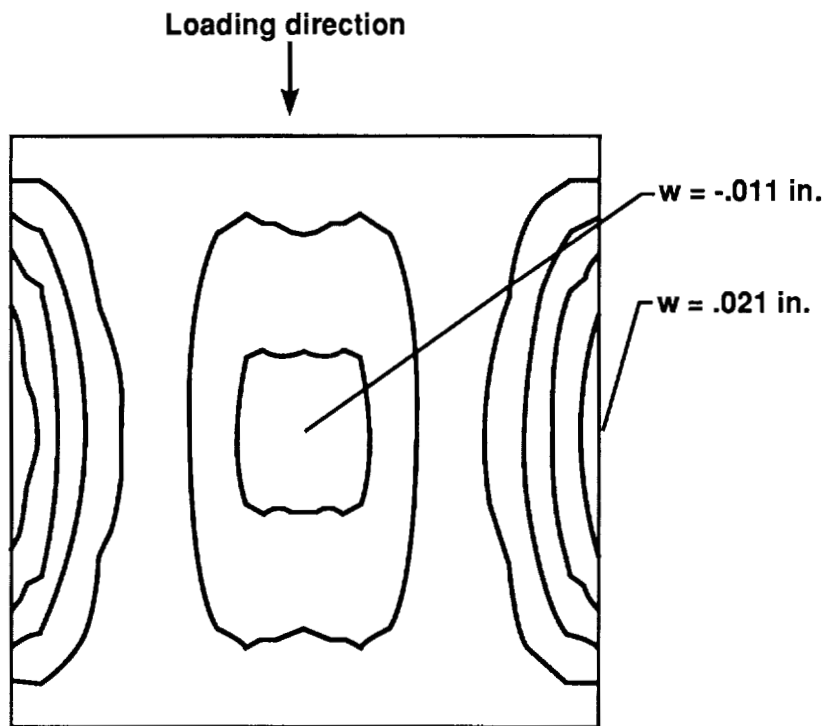
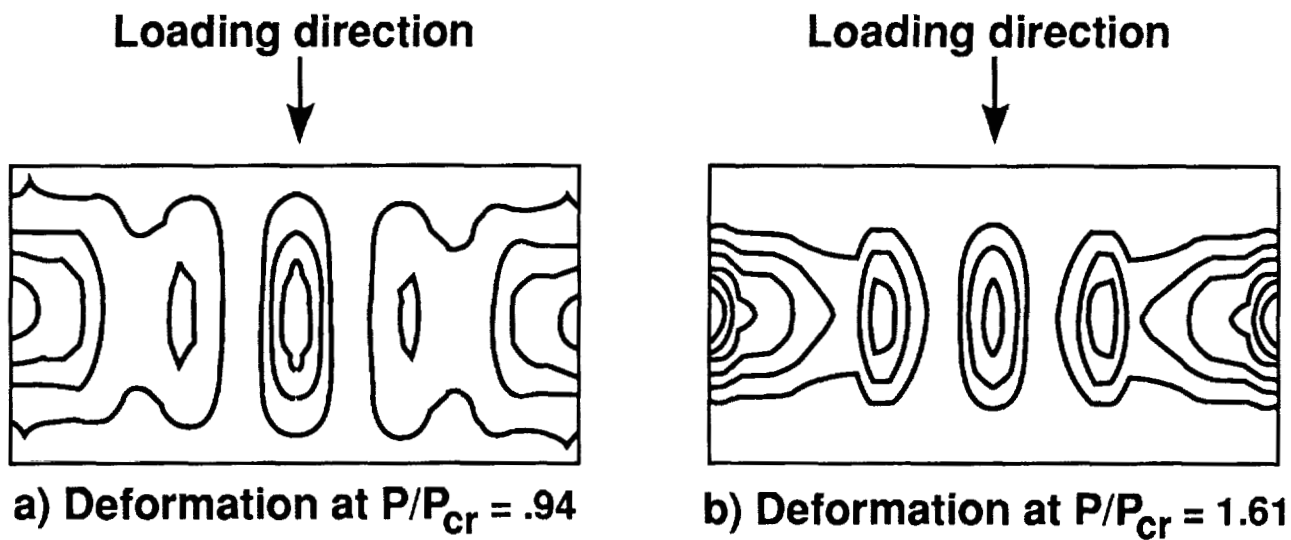


Figure 13. Deformations in panel D at $P/P_{cr} = .88$.



P/P_{cr}	w	
	edge, in.	center, in.
.94	.007	.004
1.61	.120	.060

Figure 14. Deformations of one skin of panel E during loading.

A WEIGHT-EFFICIENT DESIGN STRATEGY FOR
CUTOUTS IN COMPOSITE TRANSPORT STRUCTURES*S. G. Russell
J. Hangen
T. E. Palm520-24
51420Northrop Corporation
Aircraft Division
Hawthorne, California

ABSTRACT

Two design procedures for composite panels with cutouts are described and illustrated by example applications. One of these procedures uses a specialized cutout analysis code to obtain preliminary sizing information for the panel laminate, cutout padup, and cutout stiffener reinforcements. The other procedure uses a finite element based structural optimization code to develop a minimum weight panel design. The best features of both procedures form the basis of a design strategy for weight-efficient cutout panels.

INTRODUCTION

Composite structural concepts for commercial transport aircraft must possess significantly reduced weight relative to conventional metallic designs to be economically viable over the life of the aircraft. This need for weight savings has motivated substantial interest in the development of efficient design procedures and tailoring methods for composite aircraft structures. Cutout panels are one class of structural elements where these methods can be profitably applied to realize weight savings while satisfying strength requirements.

Numerous design and analysis procedures have been devised for composite structural elements containing cutouts. A number of the more commonly used procedures are discussed in Reference 1, which also introduces a new methodology for sizing composite panels subjected to prescribed loads. This methodology, which was developed at Northrop under NASA Contract NAS1-18842, contains procedures for sizing the cutout panel base laminate as well as the padups and stiffener reinforcements required to ensure that the panel meets strength requirements. Recently, an alternative approach using the finite element based design optimization code ASTROS (Reference 2) has also been applied to the cutout design problem. This procedure is attractive from the structural efficiency standpoint because it generates a minimum weight design for the cutout panel.

* This work was performed under NASA/Northrop Contract NAS1-18842 entitled "Innovative Structural Concepts for Supersonic Transports."

The purpose of this paper is to describe how the NASA/Northrop cutout design methodology (Reference 1) and the ASTROS optimal design methodology (Reference 2) can be used to provide a weight-efficient design strategy for cutouts in composite transport structures. To this end, both procedures are described and illustrated by examples. The weight savings potential associated with optimal design is illustrated for an application involving a highly loaded wing skin with access cutout. The roles of the NASA/Northrop and ASTROS design procedures in cutout applications are discussed. Finally, the best features of both techniques are combined to suggest a basic approach to weight efficient design of composite cutout panels. This approach is illustrated by revisiting the lower wing skin access cutout design used in the discussion of the optimal design methodology.

NASA/NORTHROP CUTOUT DESIGN METHODOLOGY

Under NASA contract, Northrop has developed a systematic preliminary design methodology for composite panels containing cutouts. The procedure uses modified Boeing design guidelines (Reference 3) to place bounds on the panel sizing problem. Base laminate, padup, and reinforcing stiffener sizing equations are then used to develop a panel design that satisfies the design guidelines and strength requirements. The NASA/Northrop procedure assumes a constant thickness base laminate, a fixed padup geometry, and a conventional picture-frame cutout stiffener arrangement.

The NASA/Northrop cutout design methodology requires an analysis procedure to predict panel strains and generate panel strength predictions. A specialized analysis code named RARICOM (Reference 4) was developed for this purpose. RARICOM uses the Rayleigh-Ritz method to perform stress analysis of stiffened panels with elliptical cutouts and padups under generalized in-plane loading conditions. The ratio of major to minor cutout dimensions must be less than 2. Panel strength predictions are generated using a generalized version of the average stress criterion (Reference 5).

The following paragraphs summarize design guidelines and sizing procedures for rectangular panels containing cutouts with padups. To permit application of the RARICOM code, elliptical cutout and padup geometries are assumed; however, the design methodology can be generalized to other cutout and padup geometries provided that suitable stress analysis techniques are available. An example involving design of a spar shear web containing an access cutout is provided to illustrate the methodology.

Design Guidelines

Consider a cutout panel with an integral padup reinforcement, as shown in Figure 1. In the thickness direction, the padup is assumed to be symmetric with respect to the mid-plane of the base laminate. The following guidelines are used for the sizing of the panel:

- (i) The panel is sized with the notched allowable design strains used for the design of panels without cutouts.
- (ii) The panel contains a minimum of 12.5 percent 0° plies, 25 percent ±45° plies, and 12.5 percent 90° plies.
- (iii) Cutout dimensions and panel dimensions as defined in Figure 1 satisfy the relations $a/S < 0.67$, $b/H < 0.5$.
- (iv) Reinforcing plies in the integral padup are placed so that the base laminate and padup region elastic constants are approximately equal.
- (v) The padup area dimensions defined in Figure 1 satisfy the relations $a_1 \geq 2a$, $b_1 \geq 2b$. The padup thickness dimension satisfies the relation $t_p \leq 3t$, where t_p is the padup thickness and t is the base laminate thickness.
- (vi) Ply dropoff rates from the padup region to the base laminate are $\leq 5^\circ$. A drop off rate of 2° is preferred if the panel can accommodate it.

These design guidelines provide bounds for the base laminate and padup sizing operations.

Base Laminate Sizing

Let N_x , N_y , N_{xy} be the panel design loads expressed as laminate stress resultants. The following equations determine the number of plies required for each major ply orientation in the base laminate:

$$\# \ 0^\circ \text{ plies} = \frac{2N_x}{E_1^t \epsilon_n^t t \text{ ply}}$$

$$\# \ 45^\circ \text{ plies} = \frac{2N_{xy}}{E_1^t \epsilon_n^t t \text{ ply}}$$

$$\# \ -45^\circ \text{ plies} = \frac{-2N_{xy}}{E_1^c \epsilon_n^c t \text{ ply}}$$

(1)

$$\# \text{ } 90^\circ \text{ plies} = \frac{2N_y}{E_1^t \epsilon_n^t t_{\text{ply}}}$$

where E_1^t , E_1^c are the ply elastic moduli in the fiber direction; ϵ_n^t , ϵ_n^c are notched tension and compression design allowable strains, and t_{ply} is the ply thickness. The factor of 2 in these equations is intended to reduce the amount of reinforcing material required in padups. This minimizes the thickness discontinuity caused by the padup and makes it easier for padup designs to satisfy the thickness dimension guideline introduced previously.

The results of Equation (1) can be used to establish a practical layup for the cutout panel base laminate. Strength analysis by RARICOM or other suitable procedures then provides a margin of safety MS for the unreinforced cutout panel. If $MS > 0$, the panel is adequately sized and there is no need for panel reinforcement. If $MS < 0$, a padup design can be generated.

Padup Sizing

Padups are required when the margin of safety MS for strength failure of the unreinforced cutout panel is less than zero. The padup sizing can be performed by the following steps:

- (i) Let MS be the margin of safety from the strength analysis of the unreinforced panel ($MS < 0$). An initial estimate for the padup region layup can be obtained by multiplying the base laminate ply requirements from Equation (1) by the factor $1/(1+MS)$. Padup area dimensions a_1 and b_1 are set at their minimum permissible values, $a_1 = 2a$ and $b_1 = 2b$. The padup area dimensions a_2 and b_2 are calculated to satisfy the ply dropoff guideline quoted previously. For the initial padup design, RARICOM can be used to determine an updated margin of safety. Let this result be $MS^{(1)}$.
- (ii) If $MS^{(1)} < 0$, repeat Step (i) using $MS^{(1)}$ in place of MS. Let the updated margin of safety be $MS^{(2)}$.
- (iii) If $MS^{(2)} < 0$, additional updated estimates for the padup thickness can be generated from the previous two estimates by the Secant Method:

$$t_p^{(i)} = t_p^{(i-1)} - \frac{MS^{(i-1)}[t_p^{(i-1)} - t_p^{(i-2)}]}{MS^{(i-1)} - MS^{(i-2)}} \quad (2)$$

where i is the iteration number, $i \geq 3$. It will be necessary to specify a padup layup and calculate new padup elastic constants for each padup thickness t_p calculated in this manner.

The padup sizing procedure terminates when a positive margin of safety is obtained.

For highly loaded panels, it is often impossible to specify a padup that satisfies the guidelines for thickness, areal dimensions, and ply dropoffs. In these cases, the cutout panel with a permissible padup design can be further reinforced by picture frame stiffeners surrounding the cutout. The logic of the stiffener sizing procedure, discussed in References 1 and 4, is similar to the padup sizing procedure except that stiffener axial stiffness is used as the design variable in the iterations. Alternately, the base laminate can be thickened and the padup sizing procedure repeated.

Example: Spar Shear Web With Cutout

To illustrate the NASA/Northrop design methodology, consider a 20 inch by 20 inch spar shear web with a 6 inch diameter central circular cutout, as shown in Figure 2(a). The shear web is fabricated from AS/3501-6 graphite/epoxy material. The ply properties and notched allowable design strains for 250°F/wet conditions are

$$\begin{array}{lll}
 E_1^t = 18.7 \text{ Msi} & \nu_{12} = 0.30 & \epsilon_n^t = 4550\mu \\
 E_1^c = 17.3 \text{ Msi} & G_{12} = 0.42 \text{ Msi} & \epsilon_n^c = -4550\mu \\
 E_2^t = 1.74 \text{ Msi} & t_{\text{ply}} = 0.0052 \text{ in} & \\
 E_2^c = 0.91 \text{ Msi} & &
 \end{array}$$

The design loads for the shear web are $N_x = N_y = 0$, $N_{xy} = 1500 \text{ lb/in}$.

Following base laminate sizing by Equation (1), a (14/72/14) layup, i.e. 14 percent 0° plies, 72 percent $\pm 45^\circ$ plies, and 14 percent 90° plies, was selected. The resulting base laminate thickness was $t = 0.1456 \text{ in}$, with 4 0° plies, 10 $\pm 45^\circ$ ply sets, and 4 90° plies. A RARICOM strength analysis for the unreinforced cutout panel gave $MS = -0.412$. Figure 3 shows the critical strain distribution for this case, which occurs along the x' axis oriented 45° counterclockwise with respect to the x axis.

To alleviate the strain concentration around the padup, the padup sizing feature of the NASA/Northrop design methodology was applied. With $1/(1+MS) = 1.7 \approx 2$, the initial padup region thickness was $t_p = 0.2912 \text{ in}$, which is twice the thickness of the base laminate. Setting $a_1 = 2a = 6 \text{ in}$, $b_1 = 2b = 6 \text{ in}$ and using a 2° ply dropoff angle, the outer padup dimensions were found to be $a_2 = b_2 = 8.1 \text{ in}$. Laminate elastic constants for the padup and base laminate regions were taken to be equal. A schematic of the padup reinforced panel design is shown in Figure 2(b).

Execution of the RARICOM strength analysis for the initial padup design yielded $MS = 0.086$, which is satisfactory for design purposes. Figure 3 shows the critical strain distribution for the padup-reinforced panel.

OPTIMAL DESIGN METHODOLOGY

For highly loaded structure, substantial amounts of material are often required to attain acceptable margins of safety. Significant weight savings can be realized by using a minimum weight structural optimization procedure in place of conventional approaches in this class of design problems. Cutout design problems in highly loaded structure are good candidates for optimal design since substantial ply buildups or padups are usually placed around the periphery of the cutout to meet strength requirements.

Under NASA/Northrop Contract NAS1-18842, minimum weight designs for cutout panels have been obtained using ASTROS, a finite element based structural optimization code developed at Northrop under Air Force contract (Reference 2). ASTROS is a multidisciplinary optimization tool capable of generating minimum weight structural designs based on strength, aeroelastic, buckling, and flutter constraints. The present paper considers only minimum weight cutout panel designs based on strength constraints.

Finite element modeling of flat composite panels with cutouts can be accomplished using triangular membrane, isoparametric quadrilateral membrane or quadrilateral shell elements available in the ASTROS element library. The membrane elements lump all plies of common orientation in the laminate into a layer. The thicknesses of these layers are design variables in the optimization process. The shell element, which models both membrane and bending deformation, possesses the general capability to treat individual plies of a laminate as separate design variables.

In principle, the layer thickness variables for every element in a structural model could be used as independent variables in the optimization process. This practice, however, would make the optimization process very unwieldy. To reduce the optimization problem to a tractable level, ASTROS offers an option called shape function linking. Shape function linking allows the user to define element layer thicknesses over a specified region of the structure by means of a polynomial shape function. The shape function is of the form

$$t(\xi, \eta) = \sum_{i=1}^3 \sum_{j=1}^3 a_{ij} \xi^{i-1} \eta^{j-1} \quad (3)$$

where t is the layer thickness variable, and ξ and η are local coordinates spanning the specified region of the structure. Equation (3) defines local design variables, or element layer thicknesses, as the weighted sum of several global design variables, the coefficients a_{ij} . The global variables a_{ij} are then adjusted during the optimization process.

The minimum weight design of cutout panels is carried out by constraining fiber direction strains in 0°, +45°, -45°, and 90° layers of composite shell elements to lie within a specified range defined by tension and compression allowable strains. Additional constraints on percentage of plies with a particular orientation can also be used. These constraints allow the user to satisfy minimum gage requirements as well as practical ply distribution guidelines for composite laminates.

The ASTROS code uses a mathematical programming procedure based on the MICRO-DOT algorithm to obtain the minimum weight design. The MICRO-DOT algorithm (References 6 and 7) is a direct optimization method that uses constraint information directly in the optimization process. It combines features from feasible directions (Reference 8) and generalized reduced gradient (Reference 9) algorithms to provide an efficient search procedure. ASTROS terminates the optimization procedure when the structural weight change following a redesign operation differs by less than 0.5 percent from the previous iteration.

Example: Lower Wing Skin With Access Cutout

Consider a 90 in by 30 in rectangular lower wing skin panel with an 18 in by 10 in elliptical access cutout as shown in Figure 4. The panel is fabricated from IM7/5260 composite material. The ply properties and allowable design strains are

$$\begin{array}{lll}
 \begin{array}{l} t \\ E_1 = 22.0 \text{ Msi} \end{array} & \begin{array}{l} \nu_{12} = 0.32 \end{array} & \begin{array}{l} t \\ \epsilon_n = 7350\mu \end{array} \\
 \\
 \begin{array}{l} c \\ E_1 = 22.0 \text{ Msi} \end{array} & \begin{array}{l} G_{12} = 0.86 \text{ Msi} \end{array} & \begin{array}{l} c \\ \epsilon_n = -4600\mu \end{array} \\
 \\
 \begin{array}{l} t \\ E_2 = 1.4 \text{ Msi} \end{array} & \begin{array}{l} t \\ = 0.0052 \text{ in} \\ \text{ply} \end{array} & \\
 \\
 \begin{array}{l} c \\ E_2 = 1.4 \text{ Msi} \end{array} & &
 \end{array}$$

The design loads for the panel are $N_x = 30,000 \text{ lb/in}$, $N_y = N_{xy} = 0$.

The ASTROS finite element mesh for minimum weight design of the panel is shown in Figure 5. Due to the symmetry of the deformation and loading, the model was restricted to a single panel quadrant. Thirty-seven QUAD4 shell elements were used to discretize the panel quadrant.

The shape function linking option in ASTROS was used to formulate the panel sizing optimization problem. For this purpose, nine thickness shape function variables spanning various regions of the panel were defined. The shape function variables allow for constant or linear layer thickness variation over all or part of the panels, as defined by the shaded regions shown in Figure 6. As discussed previously, the shape function variables are adjusted in the optimization procedure to obtain the minimum weight panel design.

For modeling of the composite skin laminate, the QUAD4 elements were divided into 0°, 45°, -45°, and 90° layers. The following constraints were imposed:

- (i) layer thickness of no less than 10 percent of the total panel thickness
- (ii) 0° layer thickness of no more than 60 percent of the total panel thickness
- (iii) minimum layer thickness of 0.10 inch, leading to a minimum laminate thickness of eight plies
- (iv) equal 45° and -45° layer thicknesses

Subject to these restrictions, the layer thicknesses were each allowed to vary as defined by the shape functions shown in Figure 6.

A schematic of the minimum weight wing skin panel design is shown in Figure 7. Thickness contours are shown to illustrate the distribution of material in the minimum weight solution. Outside the immediate vicinity of the cutout, the laminate ply mix varies little from a (60/30/10) arrangement. Along the cutout periphery, the laminate ply mix varies from (60/20/20) at the point of maximum tensile stress concentration, at the intersection with the ellipse minor axis, to (10/66/24) at the point of maximum compressive stress concentration, at the intersection with the ellipse major axis. The maximum laminate thickness of 0.913 inch occurs along the cutout periphery in the region of maximum tensile stress concentration.

In the ASTROS design, the thickness is reinforced along the longitudinal edges of the panel to divert load away from the cutout region. The overall design suggests longitudinal stiffening for cutout load relief, and a localized padup to relieve stress and strain concentration effects adjacent to the hole.

DISCUSSION OF PANEL DESIGN APPROACHES

The two design approaches discussed in previous sections can be used to formulate a weight efficient strategy for design of cutout panels in composite aircraft structures. The key to this strategy is an understanding of the strengths and weaknesses of each methodology, and an appreciation of the appropriate role of each technique in the design process. By exploiting the strengths of each approach, a realistic, weight-efficient panel design can be obtained.

The NASA/Northrop design methodology, and its counterpart analysis code RARICOM, are most effective when used in the preliminary stages of the cutout design process. Preliminary design requires iterative use of stress and strength analysis procedures to establish initial sizing information for the panel base laminate and conventional reinforcement details, such as padups and stiffener frames around the cutout. The RARICOM code is well-suited for this

purpose, since these characteristics of the design can be varied and re-evaluated with minimal effort. RARICOM is also useful for evaluation of localized cutout effects, such as the influence of panel reinforcement details on stress and strain gradients at the periphery of the hole.

With its foundation in modified Boeing cutout design guidelines (Reference 3), the NASA/Northrop procedure produces conservative panel designs that converge rapidly to satisfy panel strength requirements. The panel base laminate is designed to two times the prescribed load level so that reinforcement details can be sized to satisfy design guidelines. Failure assessment is based upon notched strain allowables for the composite material system. The simplicity of the reinforcement details considered in the NASA/Northrop methodology makes these designs relatively simple to manufacture.

The ASTROS code provides an optimal design methodology that can be used to obtain minimum weight designs for cutout panels. ASTROS designs satisfy strength requirements, based on an evaluation of the maximum strain failure criterion in each element. Rod elements with negligible stiffness connect the nodes along the cutout periphery to facilitate evaluation of the failure criterion in regions of maximum stress and strain concentration. Finite element mesh refinement around the cutout is necessary to accurately model stress and strain gradients at the periphery of the hole.

Some ASTROS designs may be difficult to manufacture, particularly if a large number of shape functions are used in the optimization process. Despite this shortcoming, the ASTROS design is extremely valuable for identifying material distribution trends for weight-efficient design. An example of this type of trend was shown in Figure 7, where ply buildups were placed along the longitudinal edges of the panel to channel load away from the cutout region. This feature of the ASTROS solution could be easily implemented to obtain weight savings in the final panel design.

WEIGHT EFFICIENT DESIGN STRATEGY

The strengths of the two design approaches discussed in this paper can be exploited to develop a weight efficient design strategy for composite cutout panels in transport aircraft structures. This strategy consists of four steps: conventional and optimal sizing, design revision, and final analysis.

Step 1: Conventional Sizing

Conventional sizing consists of sizing the base laminate, padup, and stiffener reinforcements for the prescribed design loads. The NASA/Northrop design methodology and RARICOM analysis code are useful for this purpose, since they provide a systematic approach for evaluating these features of the panel. Results of the conventional sizing step can be viewed as a first attempt at the panel design.

Step 2: Optimal Sizing

Optimal sizing of the cutout panel can be accomplished using the ASTROS computer code. As a first step, the results of the conventional sizing are converted into a finite element model. After an ASTROS solution is obtained, weight savings associated with the minimum weight design can be evaluated by comparison with the conventional design in Step 1. If the weight savings prove to be minimal, the conventional design can be prepared for manufacturing implementation.

Step 3: Design Revision

Weight savings associated with the optimal design may indicate a number of improvements that can be made to the conventional design. In these cases, general material distribution trends from the optimal design can be assessed to reveal base laminate and padup design features that can be made more weight efficient.

In the design revision process, panel design features must be modified with manufacturing producibility in mind. Simple spanwise and chordwise ply buildups and dropoffs can be used to tailor the base laminate. Care must be taken to ensure that ply buildups and dropoffs are sufficiently gradual to facilitate smooth load transfer throughout the panel. Otherwise, structural discontinuity effects could induce out-of-plane failure of the panel.

ASTROS designs for the localized padup around the cutout must be examined with care. The optimal solution tends toward a variable thickness padup with variable fiber orientation around the periphery of the hole. This design is difficult to manufacture and may not reflect the influence of localized stress and strain gradients immediately adjacent to the hole. The padup configuration used in the NASA/Northrop design methodology, which features a constant thickness padup surrounding the hole and a linear ply dropoff between the padup and base laminate, is more appropriate for the final design.

Step 4: Final Analysis

After the revised panel design is obtained, the structural model of the conventional panel design must be modified to incorporate design changes. This model can be used to establish final safety margins for the cutout panel.

Example: Lower Wing Skin Access Cutout Revisited

To illustrate the application of the weight efficient design strategy, consider the lower wing skin access cutout design used in the discussion of the optimal design methodology. The first step in the strategy involves conventional sizing with the NASA/Northrop design methodology and RARICOM analysis code. Using the panel design data given previously, the preliminary cutout panel design is shown in Figure 8. The base laminate contains a (61/25/14) ply mix with total thickness of 0.6136 inch. An elliptical padup with identical ply mix is used to reinforce the cutout.

The elliptical padup in the preliminary design attains a maximum thickness of 1.0296 inch at the cutout boundary and is blended into the base laminate by a linearly tapered ply dropoff region. Referring to Figure 1, the

padup areal dimensions are $a_1 = 10$ in, $b_1 = 6$ in, $a_2 = 12.5$ in, $b_2 = 8.5$ in. Picture frame stiffeners with axial stiffness $EA = 22 \times 10^6$ lb are required to eliminate negative strength margins in the compressive stress concentration regions at the ends of the major axis of the elliptical cutout. The stiffener length and width as defined in Figure 1 are $L_{st} = 26$ in and $W_{st} = 18$ in. Using a material density of 0.057 lb/in³ for IM7/5260, the preliminary panel design weighs 97 lb.

The minimum weight optimal design for the lower wing skin access cutout has been discussed and is shown in Figure 7. This design weighs 46.5 lb, which is substantially less than the weight of the preliminary design. Examination of the minimum weight solution reveals the following features:

- (i) the base laminate thickness away from the immediate cutout region is less than half the base laminate thickness used in the preliminary design
- (ii) the variable thickness padup surrounding the cutout is rich in $\pm 45^\circ$ and 90° plies away from the small region of maximum tensile stress concentration
- (iii) the ply buildup region along the longitudinal edges of the panel extends across approximately one quarter of the panel width, with an average thickness of about 0.35 inch and a ply mix of roughly (60/30/10)

These material distribution trends provide insight into the modifications required for weight savings in the preliminary panel design.

A modified conventional design that satisfies panel strength requirements is shown in Figure 9. The base laminate has a (60/27/13) ply mix and 0.312 inch thickness obtained by sizing the unnotched panel to the given design load (as opposed to twice the design load in the preliminary design). The padup contains a (25/29/46) ply mix with a maximum thickness of 1.04 inch adjacent to the cutout. The padup areal dimensions are the same as in the preliminary design. Finally, a (60/27/13) ply buildup with total width of 7.5 inch and maximum thickness of 0.352 inch is present along the longitudinal edges of the panel. The final strength check on the modified conventional design was performed with the RARICOM code. The ply buildup along the longitudinal edges of the panel was treated as an equivalent axial stiffener located at the centroid of the ply build-up.

The weight of the modified conventional panel design is 53 lb, only 6.5 lb more than the optimal design. In this example, substantial weight savings have been obtained by modifying the preliminary panel design to include weight saving features identified in the minimum weight optimal design.

SUMMARY

Two design procedures for composite panels with cutouts have been reviewed and illustrated by examples. The first procedure, developed at Northrop under NASA contract, is appropriate for preliminary sizing of the

panel base laminate and simple reinforcement features, such as padups and stiffener frames surrounding the hole. The second procedure uses a finite element based structural optimization code to obtain a minimum weight cutout panel design. Material distribution trends suggested by the optimal solution can be used to modify the NASA/Northrop panel design for improved weight efficiency.

REFERENCES

1. Russell, Steven G., "A Rayleigh-Ritz Design Methodology for Cutouts in Composite Structures," Proceedings of the 33rd AIAA/ASME/ASCE/AHS/ASC Structures, Structural Dynamics, and Materials Conference, April 1992, pp. 181-189.
2. Johnson, E. H. and Venkayya, V. B., "Automated Structural Optimization System (ASTROS), Volume I - Theoretical Manual," USAF Contract Report AFWAL-TR-88-3028, Volume I, December 1988.
3. Advanced Composites Design Handbook, Book 1, REV E, Boeing Commercial Airplane Company, October 1986.
4. Russell, Steven G., "A Rayleigh-Ritz Analysis Methodology for Cutouts in Composite Structures," First NASA Advanced Composites Technology Conference, NASA CP 3104, Part 2, 1991, pp. 901-920.
5. Whitney, J. M. and Nuismer, R. J., "Stress Fracture Criteria for Laminated Composites Containing Stress Concentrations," Journal of Composite Materials, Volume 8, 1974, pp. 253-265.
6. Vanderplaats, G. N., "An Efficient Feasible Directions Algorithm for Design Synthesis," AIAA Journal, Vol. 22, No. 11, November 1984, pp. 1633-1640.
7. MICRO-DOT User's Manual, Version 1.0, Engineering Design Optimization, Inc., Santa Barbara, California, 1985.
8. Vanderplaats, G. N. and Moses, F., "Structural Optimization By Methods of Feasible Directions," Journal of Computers and Structures, Vol. 3, July 1973, pp. 739-755.
9. Gabriele, G. A. and Ragsdell, K. M., "Large Scale Nonlinear Programming Using the Generalized Reduced Gradient Method," Journal of Mechanical Design, Vol. 102, No. 3, July 1980, pp. 566-573.

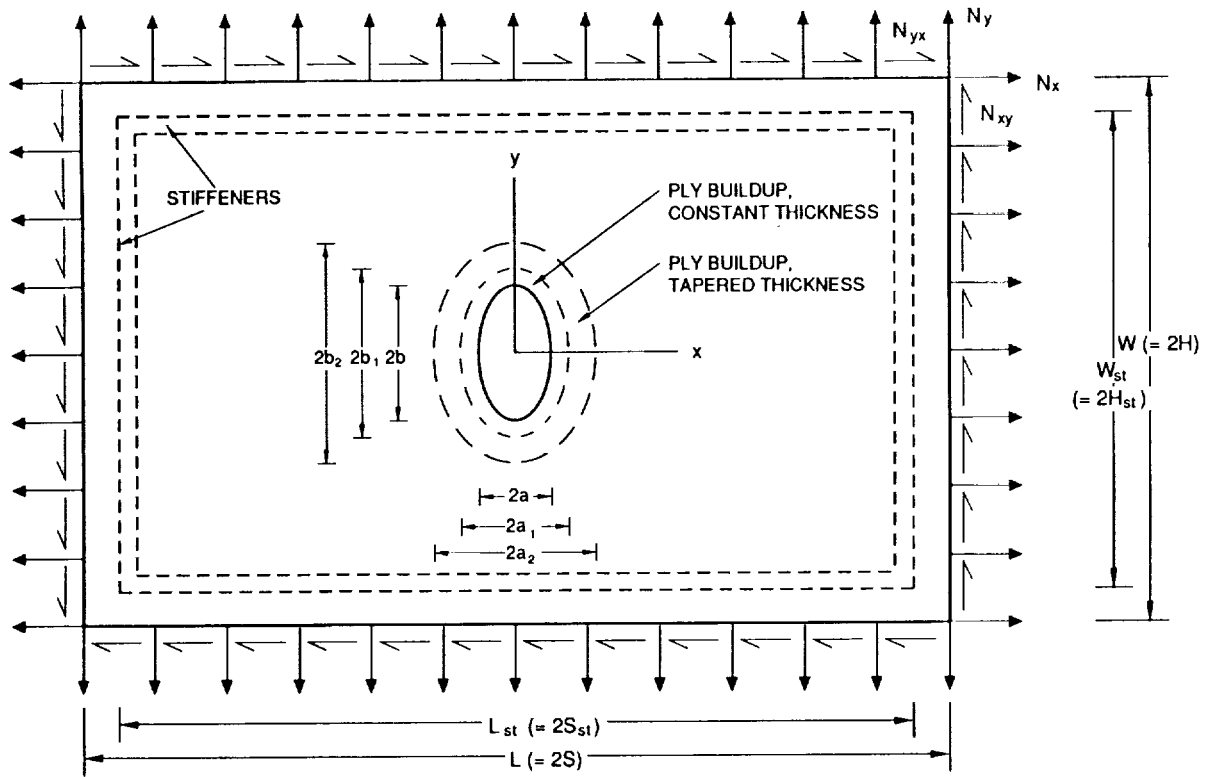


Figure 1. Elliptical Cutout in a Reinforced Panel Under Generalized In-Plane Loading.

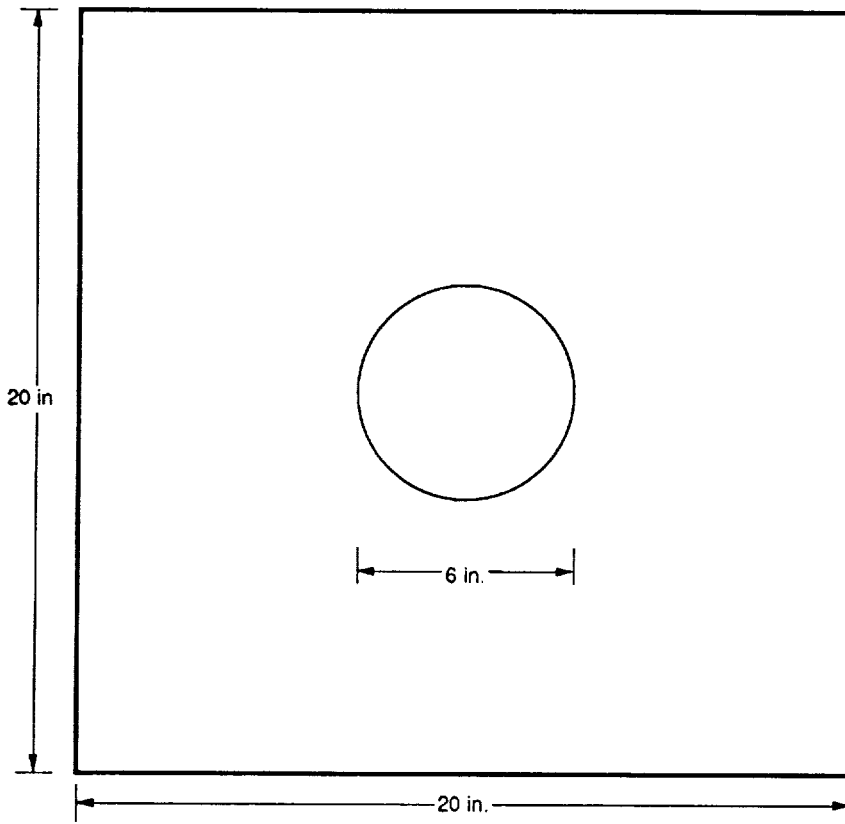


Figure 2(a). Spar Shear Web With Circular Cutout.

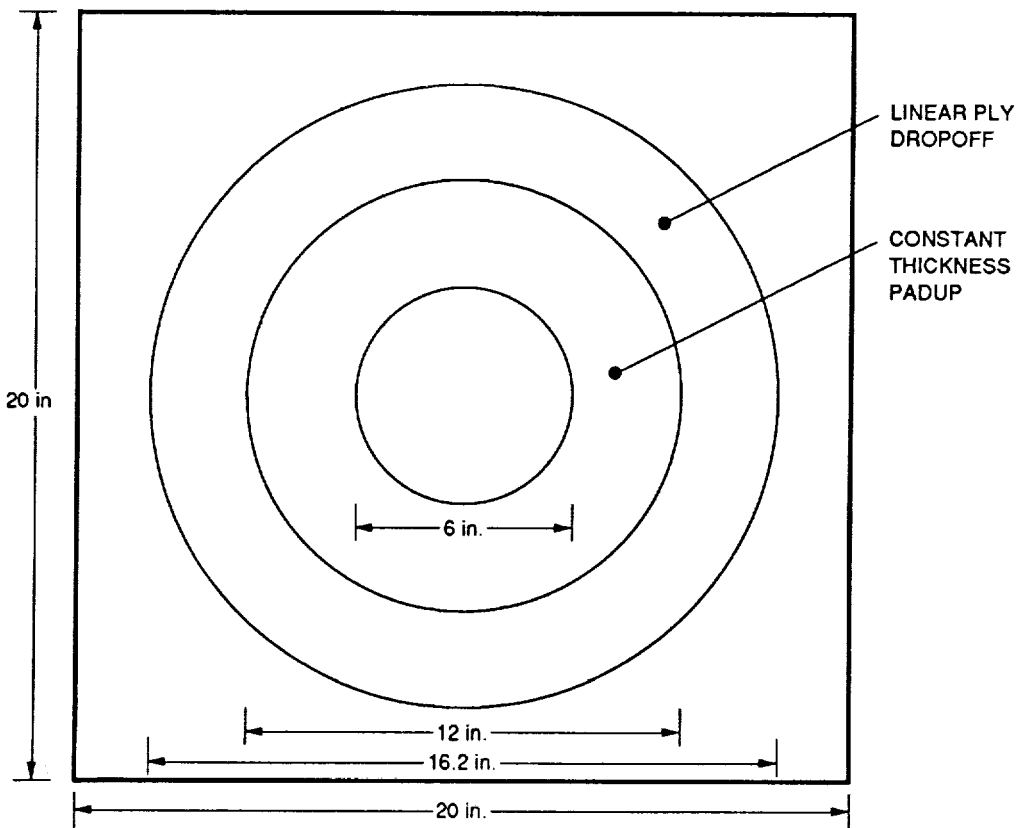


Figure 2(b). Padup for Spar Shear Web Cutout.

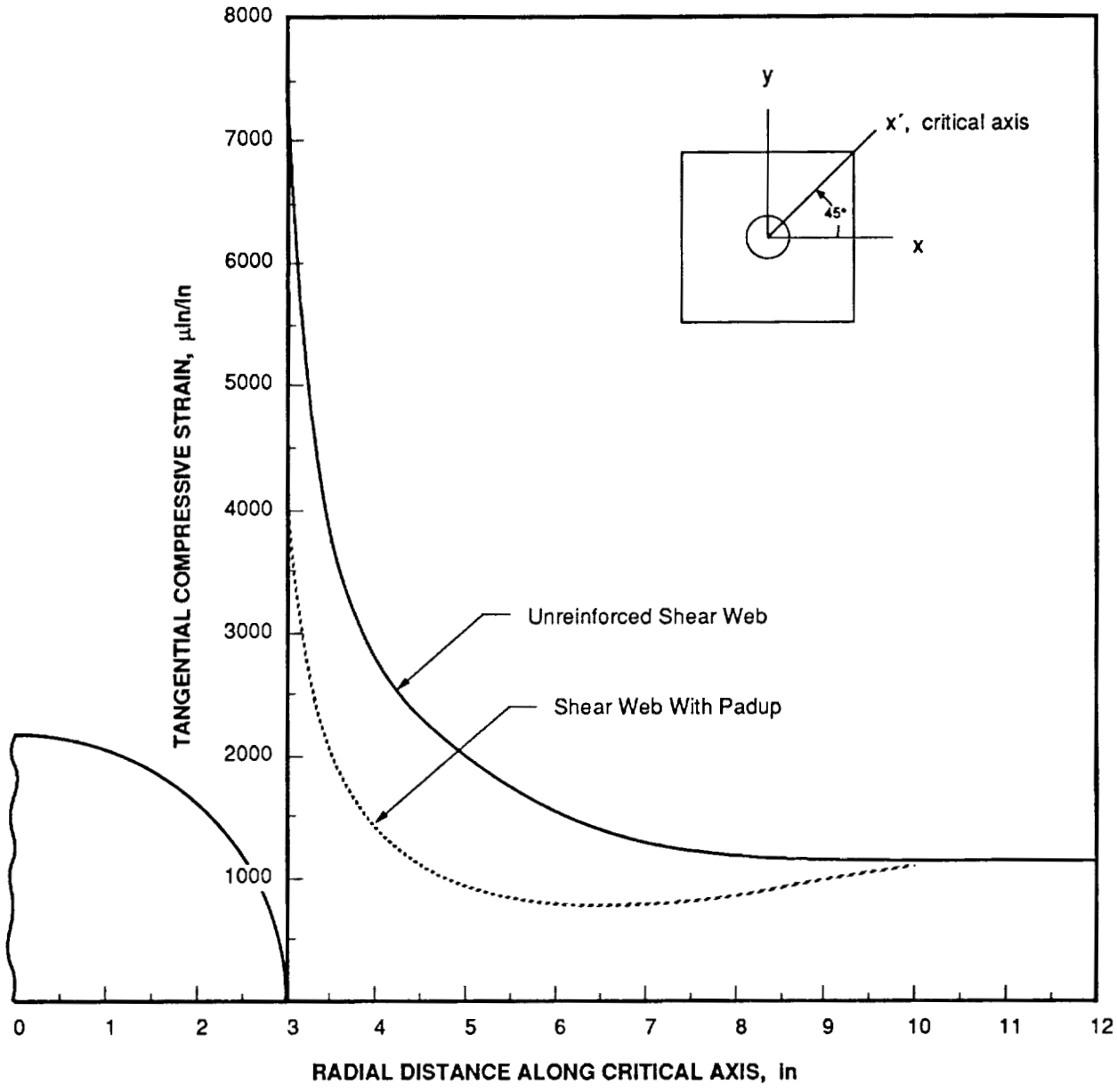


Figure 3. Critical Strain Distributions in Spar Shear Web Design.

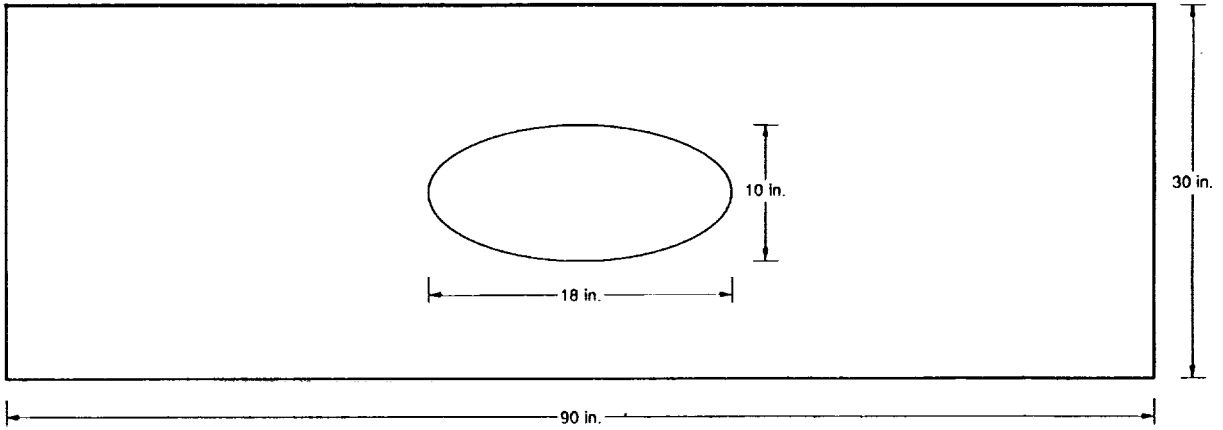


Figure 4. Lower Wing Skin With Access Cutout.

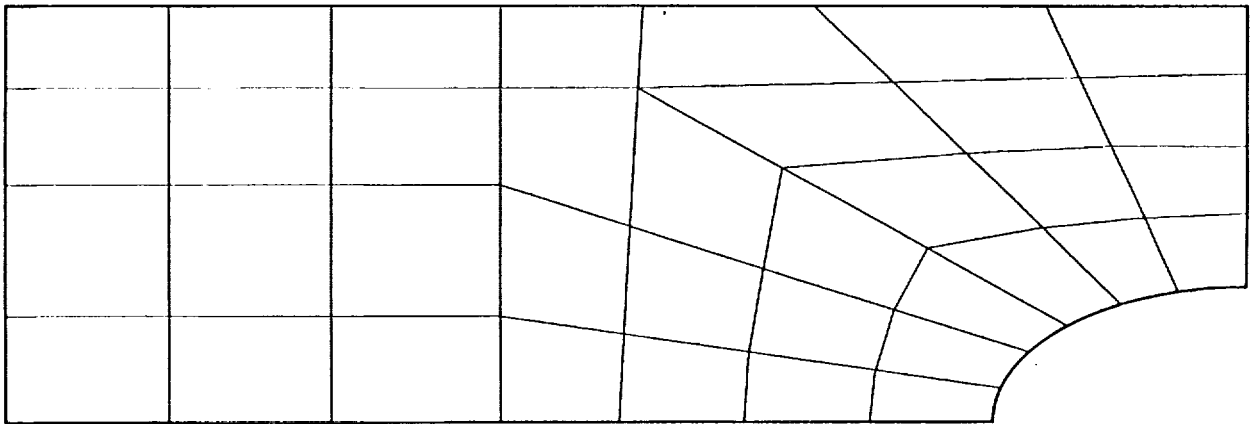
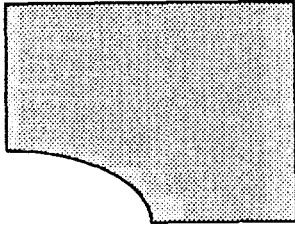
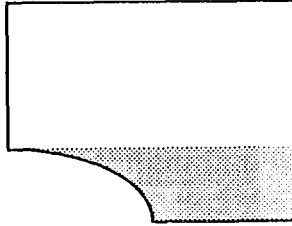


Figure 5. ASTROS Finite Element Mesh for Lower Wing Skin Panel.

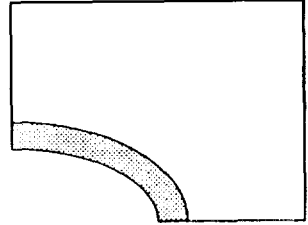
SHAPE 1: CONSTANT PANEL



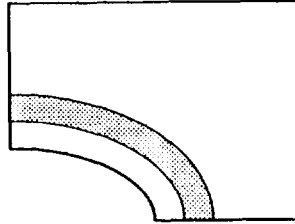
SHAPE 2: CONSTANT STRIP



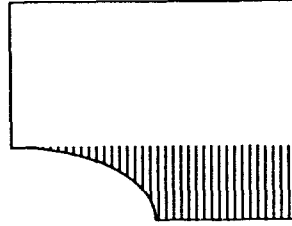
SHAPE 3: CONSTANT INNER PADUP



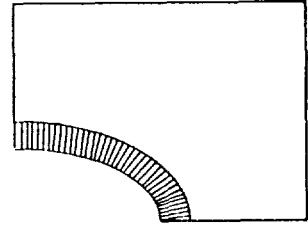
SHAPE 4: CONSTANT OUTER PADUP



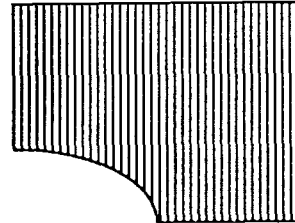
SHAPE 5: LINEAR SPANWISE STRIP



SHAPE 6: LINEAR INNER PADUP



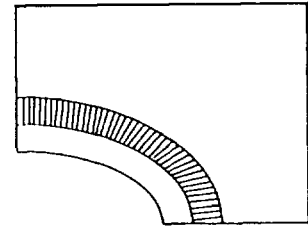
SHAPE 7: LINEAR SPANWISE PANEL



SHAPE 8: LINEAR CHORDWISE PANEL



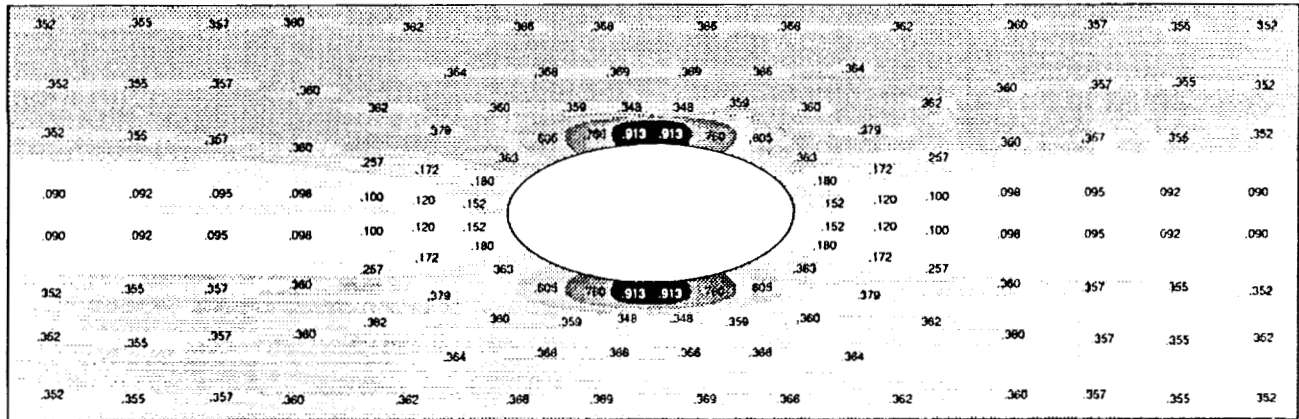
SHAPE 9: LINEAR OUTER PADUP



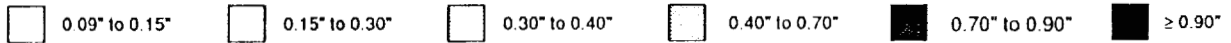
PANEL LOADS: $N_x = 30,000 \text{ lb/in}$, $N_{xy} = 0 \text{ lb/in}$

Figure 6. Shape Function Definitions for ASTROS Design.

ASTROS 60% 0° Fiber Orientation Solution



LAMINATE THICKNESS RANGES



PANEL WEIGHT = 46.5 lb

Figure 7. Thickness Contours from ASTROS Panel Design.

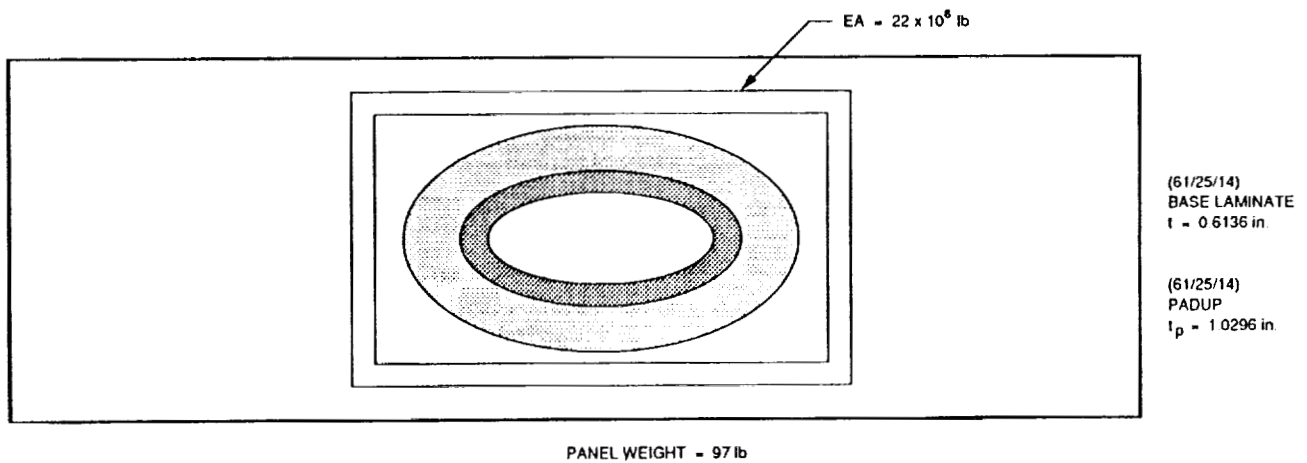


Figure 8. Preliminary Design for Lower Wing Skin Access Panel.

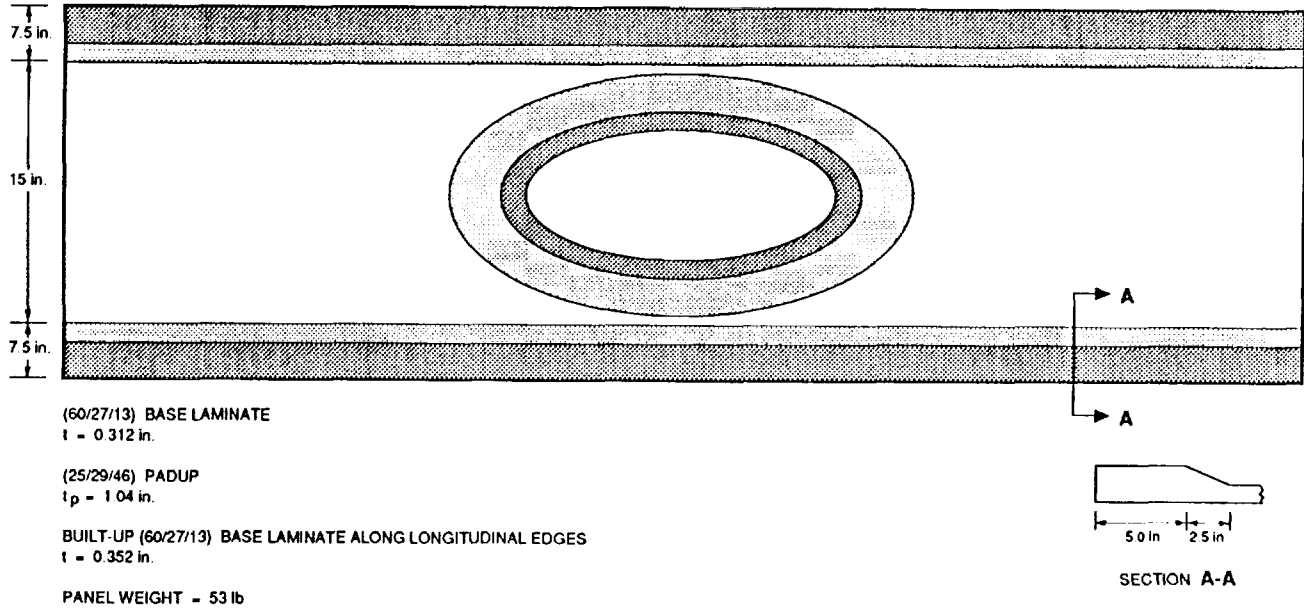


Figure 9. Modified Design for Lower Wing Skin Access Panel.

**EFFECTS OF CUTOUTS ON THE BEHAVIOR OF SYMMETRIC COMPOSITE
LAMINATES SUBJECTED TO BENDING AND TWISTING LOADS**

C. B. Prasad
Analytical Services and Materials, Inc.
Hampton, Virginia 23666

M. J. Stuart, N. J. Bains, and M. Rouse
NASA Langley Research Center
Hampton, Virginia 23665

51-34

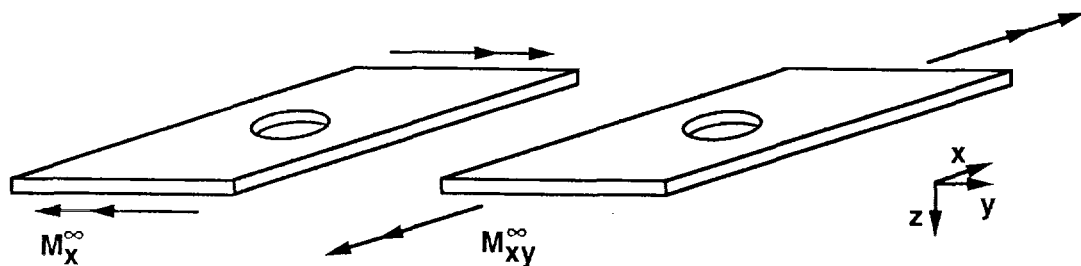
51421

Introduction

Composite structures are used for a wide variety of aerospace applications. Practical structures contain cutouts and these structures are subjected to inplane and out-of-plane loading conditions. Structurally efficient designs for composite structures require a thorough understanding of the effects of cutouts on the response of composite plates subjected to inplane or out-of-plane loadings. Most investigations of the behavior of composite plates with cutouts have considered inplane loadings only. Out-of-plane loadings such as bending or twisting have received very limited attention. The response of homogeneous plates (e.g., isotropic or orthotropic plates) subjected to bending or twisting moments has been studied analytically [1, 2]. These analyses are for infinite plates and neglect finite-plate effects. Recently, analytical and experimental studies were conducted to determine the effects of cutouts on the response of laminated composite plates subjected to bending moments [3, 4]. No analytical or experimental results are currently available for the effects of cutouts on the response of composite laminates subjected to twisting moments.

Objective

The objective of this paper is to determine the effects of cutouts on the response of finite-size symmetric composite laminates subjected to bending or twisting moments as illustrated in figure 1. Results for a combined analytical and experimental investigation are presented. Analytical results were obtained using the STAGS finite element computer program [5]. Predicted stress distributions for the outer-most plies are presented. Experimental results are presented for $[+45/0/-45/90]_6s$ quasi-isotropic and $[\pm 45/\mp 45]_6s$ IM7/5260 graphite-bismaleimide laminates with circular cutouts. The response of laminates subjected to bending are compared to the response of laminates subjected to twisting. The failure modes for laminates subjected to bending or twisting loads are discussed. Failure strain results for each laminate are presented as a function of normalized hole diameter for each loading condition.



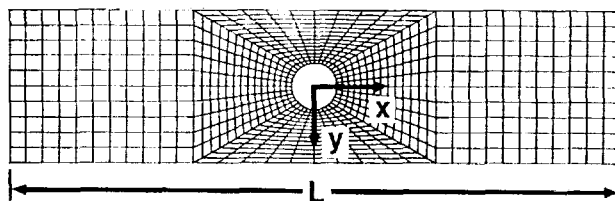
Bending and twisting are fundamental loading conditions

- Analytical results
- Experimental results

Figure 1

STAGS Analysis

The STAGS finite element computer program [5] was used in this study, and a typical model is shown in figure 2. The model has 23,304 degrees-of-freedom and is composed of transverse-shear deformable plate elements. Previous studies [3, 6] have suggested that transverse shearing effects must be included to obtain accurate results for laminates like those in the present study. A linear stress analysis was conducted for plates with centrally located, circular cutouts and subjected to bending or twisting loads. Displacement boundary conditions were used to simulate the loadings. These boundary conditions are described on the right side of the figure.



- Linear analysis, 23,304 DOFs
- Transverse shear deformation

Loading, boundary conditions

- Inplane
 $u=0$ along $x=0$
 $v=0$ along $y=0$
- Bending ($L= 20.0$ in.)



$w=0.01$ in. along $x=\pm 4.0$ in.
 $w=0$ along $x=\pm 8.0$ in.

- Twisting ($L= 15.0$ in.)



$w=0$ along $x=+7.5$ in.
 $-0.01 \leq w \leq 0.01$ in.
 along $x=-7.5$ in.

Figure 2

Analytical Axial Strain Contours for $[+45/0/-45/90]_6s$ Laminates Subjected to Bending

Predicted strain contours for quasi-isotropic laminates subjected to bending are shown in figure 3. Axial surface strain ϵ_x results are shown for a laminate with a 0.5-in.-diameter hole and for a laminate with a 1.5-in.-diameter hole. The hole-diameter-to-plate-width ratio d/w for each laminate is also shown on the figure. The highest strains occur at the edge of each hole, and the strain gradients extend to the long edges of the laminates. These results are reasonable for these laminates.

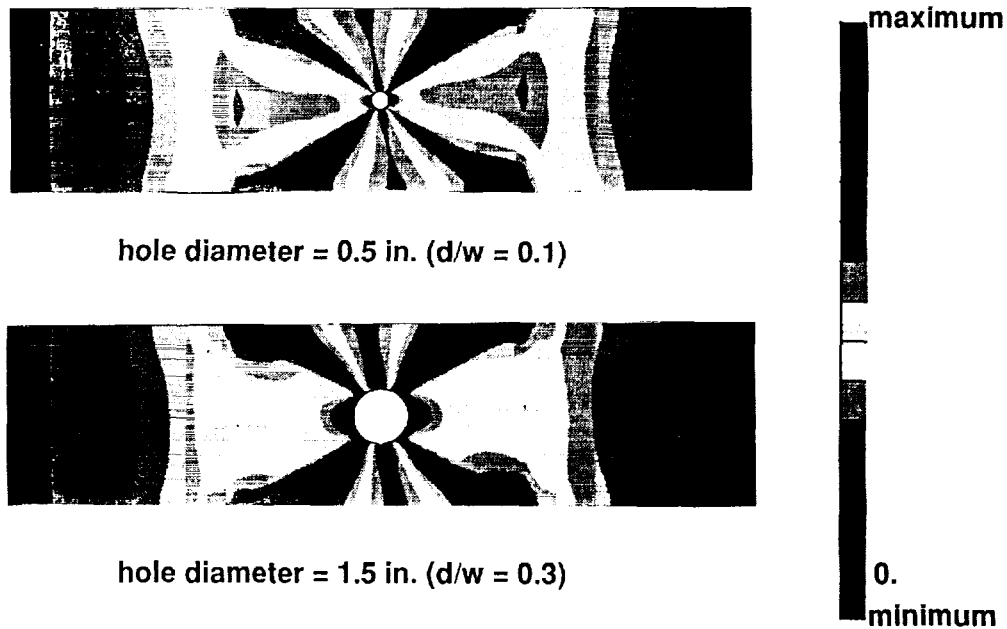


Figure 3

Analytical Axial Strain Contours for $[\pm 45/\mp 45]_6$ Laminates Subjected to Bending

Predicted strain contours for $[\pm 45/\mp 45]_6$ laminates subjected to bending are shown in figure 4. Axial surface strain ϵ_x results are shown for a laminate with a 0.5-in.-diameter hole and for a laminate with a 1.5-in.-diameter hole. The hole-diameter-to-plate-width ratio d/w for each laminate is also shown on the figure. The highest strains occur at the edge of each hole, and the strain gradients extend to the long edges of the laminates. These results are reasonable for these laminates.

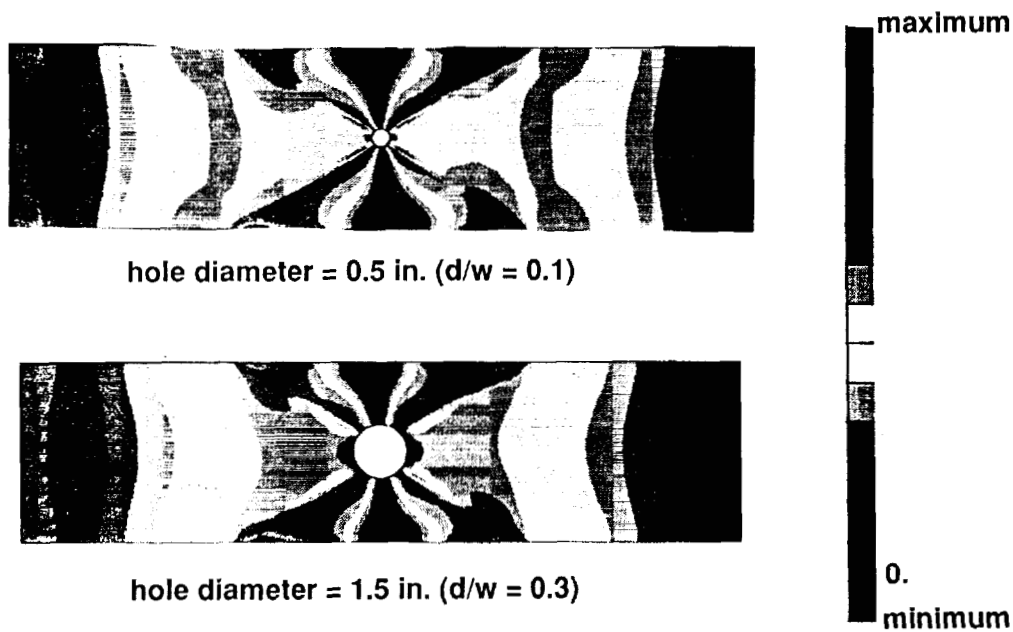


Figure 4

Analytical Shear Strain Contours for $[+45/0/-45/90]_6s$ Laminates Subjected to Twisting

Predicted strain contours for quasi-isotropic laminates subjected to twisting are shown in figure 5. Shear surface strain γ_{xy} results are shown for a laminate with a 0.5-in.-diameter hole and for a laminate with a 1.5-in.-diameter hole. The hole-diameter-to-plate-width ratio d/w for each laminate is also shown on the figure. The highest strains occur at the edge of each hole, and the strain gradients extend to the long edges of the laminates. These results are reasonable for these laminates.

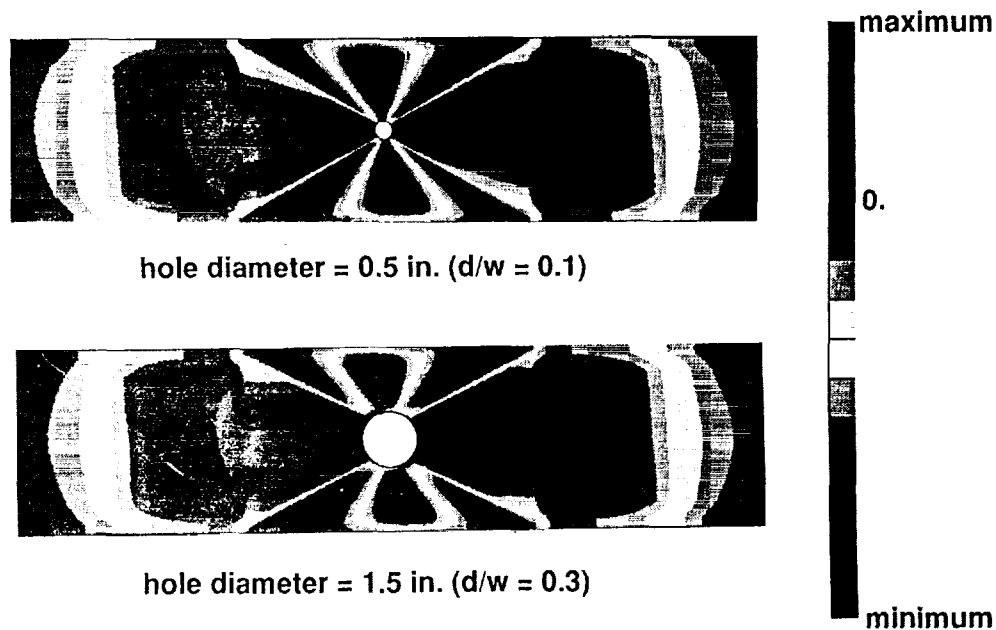


Figure 5

Analytical Shear Strain Contours for $[\pm 45/\mp 45]_6$ s Laminates Subjected to Twisting

Predicted strain contours for $[\pm 45/\mp 45]_6$ s laminates subjected to twisting are shown in figure 6. Shear surface strain γ_{xy} results are shown for a laminate with a 0.5-in.-diameter hole and for a laminate with a 1.5-in.-diameter hole. The hole-diameter-to-plate-width ratio d/w for each laminate is also shown on the figure. The highest strains occur at the edge of each hole, and the strain gradients extend to the long edges of the laminates. These results are reasonable for these laminates.

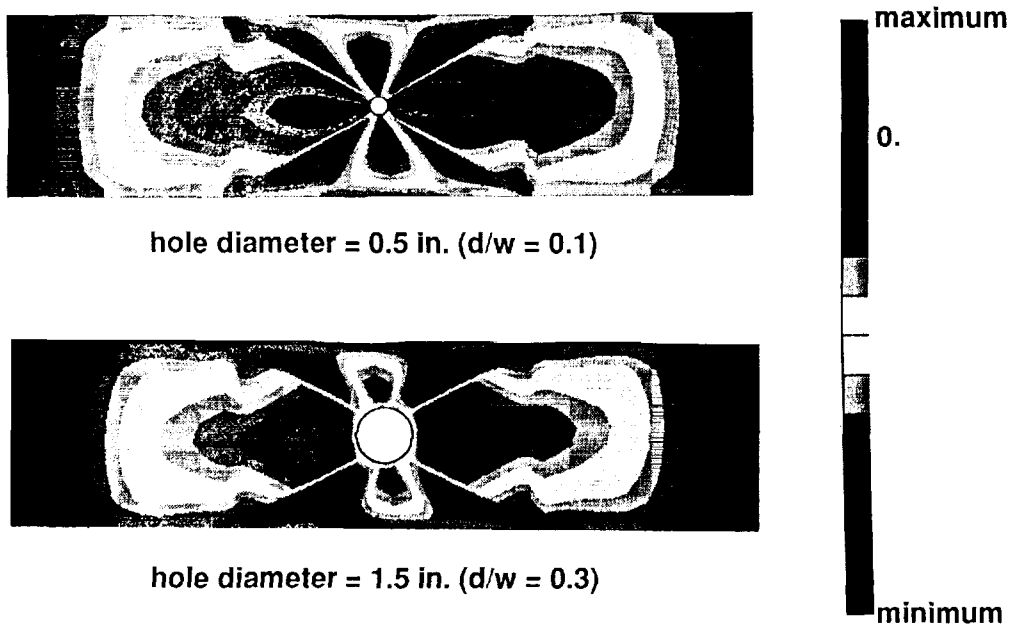


Figure 6

Test Specimens

The graphite-bismaleimide composite specimens tested in this investigation were fabricated from unidirectional Hercules IM7 graphite fiber tapes preimpregnated with 424°F cure Narmco 5260 bismaleimide resin. The tapes were laid-up to form 48-ply $[+45/0/-45/90]_{6S}$ quasi-isotropic and $[\pm 45/\mp 45]_{6S}$ laminates that were approximately 0.70 in. thick. The laminates were cured in an autoclave using the manufacturer's recommended procedure. Following cure, the laminates were ultrasonically C-scanned to establish specimen quality and then cut into test specimens. All specimens were 5 in. wide. The bending specimens were 20 in. long, and the twisting specimens were 15 in. long. Centrally located circular holes were machined with diamond impregnated core drills. The hole diameters ranged from 0.25 in. to 3.00 in. These diameters resulted in hole-diameter-to-plate-width ratios d/w ranging from 0.05 to 0.60. Control specimens (specimens without holes) were also included in the investigation. A total of 33 specimens were fabricated for testing. The specimen material, stacking sequences, and geometries are summarized in figure 7.

- IM7/5260 graphite-bismaleimide composite material
- $[+45/0/-45/90]_{6S}$ and $[+45/+45]_{6S}$
 - Bending: 20 in. by 5 in.
 - Twisting: 15 in. by 5 in.
- Hole diameters, normalized hole diameters:

<u>d, in.</u>	<u>d/w</u>	<u>d, in.</u>	<u>d/w</u>
0.	0.	1.5	0.3
0.25	0.05	2.0	0.4
0.50	0.10	2.5	0.5
0.75	0.15	3.0	0.6
1.00	0.20		

Figure 7

Test Set-Up

The test specimens were subjected to bending or twisting loading as shown in the top half and bottom half, respectively, of figure 8. The bending specimens were loaded in 4-point bending to simulate a cylindrical bending condition (i.e., $M_x^\infty \neq 0$, $M_y^\infty = M_{xy}^\infty = 0$). The loading rollers were located 8 in. apart, and the support roller at each end was typically located 4 in. from the nearest loading roller. The twisting specimens were clamped in steel grips at each end of the specimen. One grip remained fixed during testing, and the other grip was rotated to apply the twisting load. All bending and twisting specimens were tested to failure by slowly applying the load to simulate a static loading condition. Electrical resistance strain gages were used to monitor strains. Electrical signals from the instrumentation and the corresponding applied loads were recorded at regular time intervals during the test.

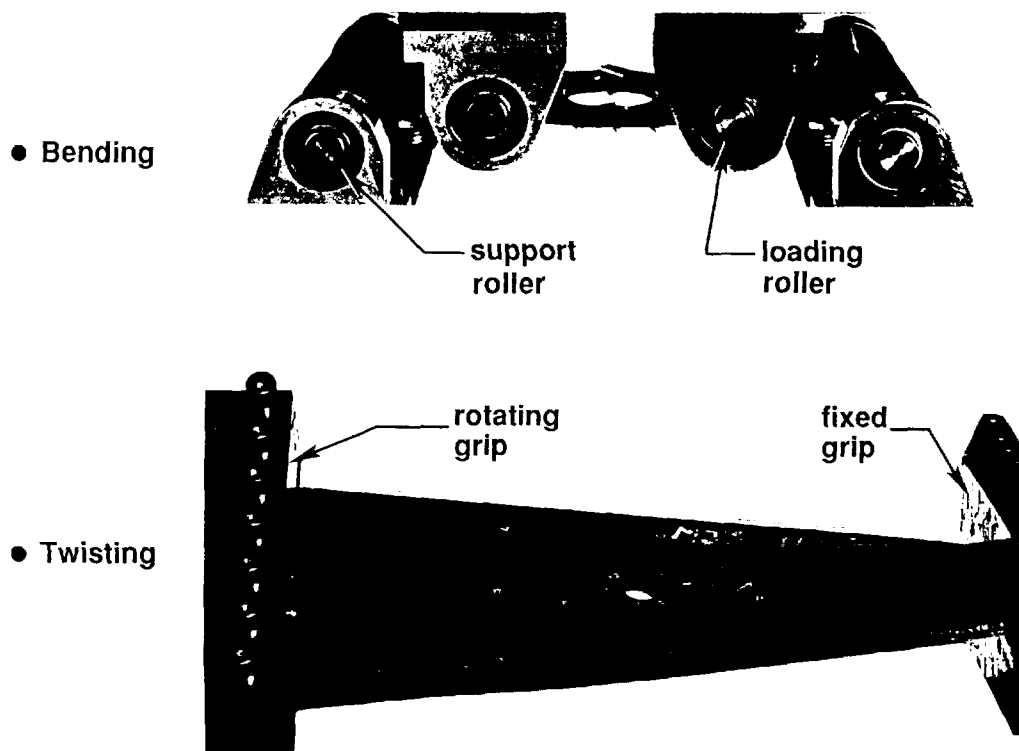


Figure 8

Response of [+45/0/-45/90]_{6s} Laminates Subjected to Bending

Far-field moment M_x^∞ as a function of axial strain is shown in figure 9 for quasi-isotropic laminates subjected to bending. Results are presented for far-field strains and for local strains near the hole boundary at $\eta = 0.03$ in. where η is identified in the figure. Generally, the far-field moment versus far-field strain response for these laminates is nonlinear and approximately the same. The far-field strain at failure decreases with increasing hole diameter for the laminates. This decrease is significant between the control specimen with $d/w = 0$ and the specimen with a small hole with $d/w = 0.1$. The far-field moment versus local strain behavior for the specimens is slightly nonlinear, and specimen stiffness, as measured by the slope of this curve, decreases with increasing hole diameter. The specimens fail at approximately the same strain level.

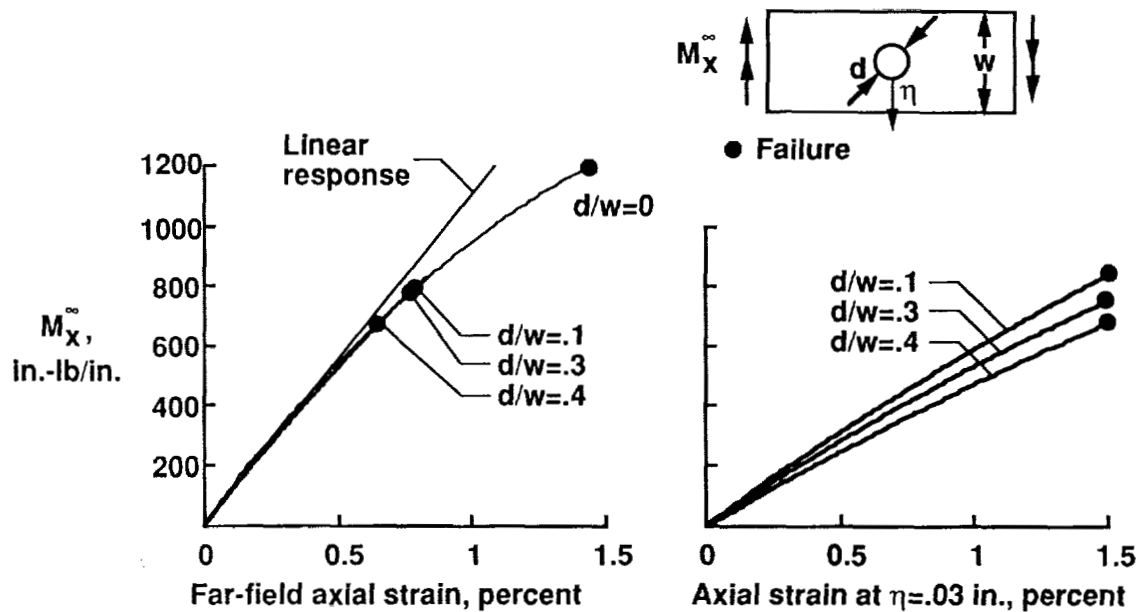


Figure 9

Failed [+45/0/-45/90]_{6s} Bending Specimens

Typical failed quasi-isotropic bending specimens are shown in figure 10. Failure always initiated at the hole boundary on the compression-loaded side of the specimen and propagated along a line across the width of the specimen that is located at the specimen mid-length. The outer-most 0° ply for the compression side of the specimen appears to fail across the specimen width first. This failure is followed by failure of the next outer-most 0° ply for the compression side of the specimen. The failure visibly progresses through the laminate thickness to successive next outer-most 0° plies until a catastrophic specimen failure occurs that includes failure of the outer-most 0° ply on the tension side of the laminate. The brooming failure mode exhibited on the compression side of these specimens is similar to the failure mode for uniaxial compression-loaded unidirectional specimens [7].

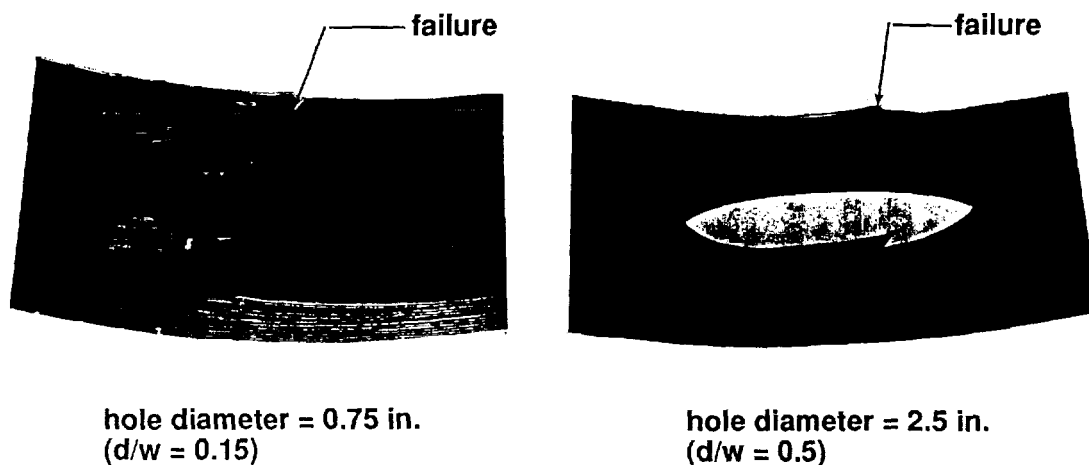


Figure 10

Response of $[\pm 45/\mp 45]_6s$ Laminates Subjected to Bending

Far-field moment M_x^∞ as a function of axial strain is shown in figure 11 for $[\pm 45/\mp 45]_6s$ laminates subjected to bending. Results are presented for far-field strains and for local strains near the hole boundary at $\eta = 0.03$ in. where η is identified in the figure. The far-field moment versus far-field strain response for these laminates is nonlinear. Anticlastic curvature was observed during the test of these specimens. The far-field strain at failure decreases with increasing hole diameter for the laminates with holes. The $d/w = 0$ control specimen test was stopped prior to catastrophic failure since large out-of-plane displacements caused the specimen to contact the test machine load platen. The far-field moment versus local strain behavior for the specimens is also nonlinear. The large local strains at failure are illustrated by the $d/w = 0.3$ and $d/w = 0.4$ specimens having a failure strain of approximately 2 percent and the $d/w = 0.1$ specimen having a failure strain approaching 3 percent.

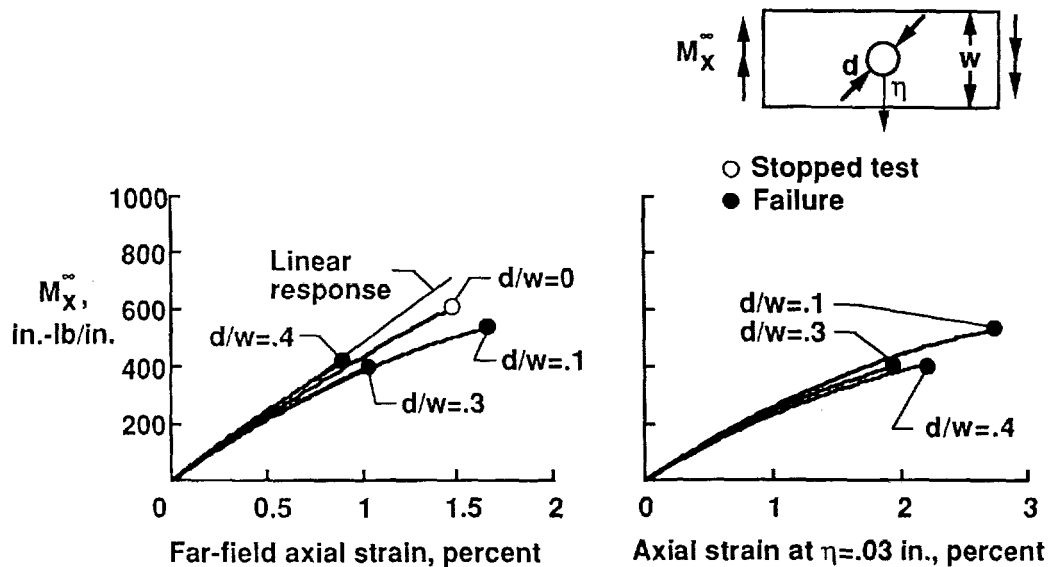
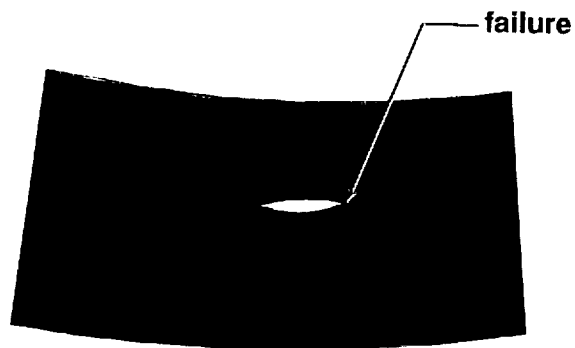


Figure 11

Failed $[\pm 45/\mp 45]_6$ s Bending Specimen

A typical failed $[\pm 45/\mp 45]_6$ s bending specimen is shown in figure 12. Failure always initiated at the hole boundary on the compression-loaded side of the specimen and propagated along radial lines oriented at $\pm 60^\circ$ to the mid-length centerline of the specimen. The failure appeared to initiate in the outer-most plies and progress through the thickness of the specimen. The observed failure mode exhibited on the compression side of these specimens is similar to the matrix-shearing failure mode for uniaxial compression-loaded $[\pm 45]_S$ -class specimens [7].



hole diameter = 1.0 in.
($d/w = 0.2$)

Figure 12

Effect of Cutouts on Compressive Strain at Failure for Laminates Subjected to Bending

The effect of cutout size on the far-field failure strain for quasi-isotropic and $[\pm 45/\mp 45]_6s$ bending specimens is shown in figure 13. Results for the quasi-isotropic and the $[\pm 45/\mp 45]_6s$ laminates are plotted as circular and square symbols, respectively, on the figure. The results for the quasi-isotropic laminates with a hole show a sudden decrease followed by a gradual decrease in failure strain with increasing hole diameter suggesting a notch sensitive behavior for this laminate. The failure strain for a $[\pm 45/\mp 45]_6s$ specimen is greater than the failure strain for a quasi-isotropic specimen for a given hole diameter. The failure strain for the $[\pm 45/\mp 45]_6s$ specimens decreases almost linearly with increasing hole diameter suggesting a notch insensitive behavior for this laminate.

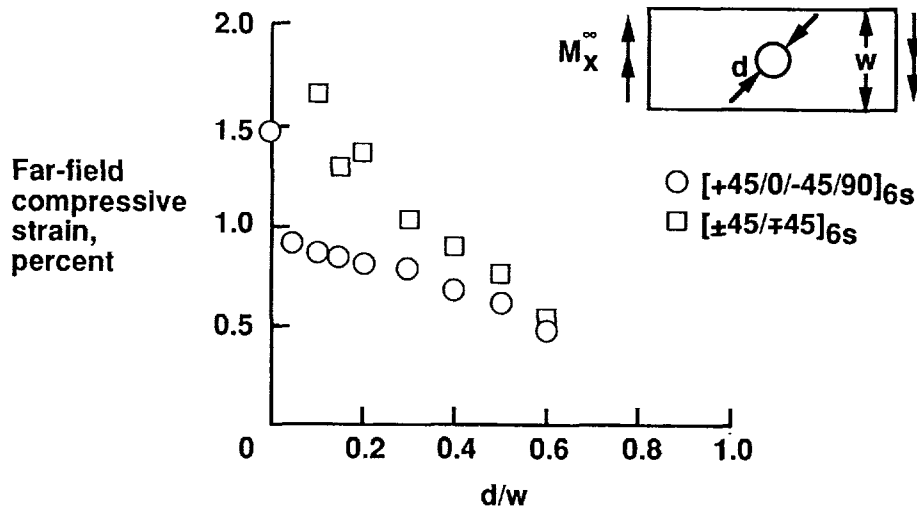


Figure 13

Response of [+45/0/-45/90]_{6s} Laminates Subjected to Twisting

Far-field moment M_{xy}^{∞} as a function of shear strain is shown in figure 14 for quasi-isotropic laminates subjected to twisting. Results are presented for far-field shear strains and for local shear strains near the hole boundary at $\eta = 0.08$ in. where η is identified in the figure. Generally, the far-field moment versus far-field strain response for these laminates is very nonlinear. The specimen stiffness, as measured by the slope of the far-field-moment–far-field-shear-strain curve, increases with increasing load. The far-field moment versus local strain behavior for the specimens is also very nonlinear and is characterized by increasing stiffness with increasing load.

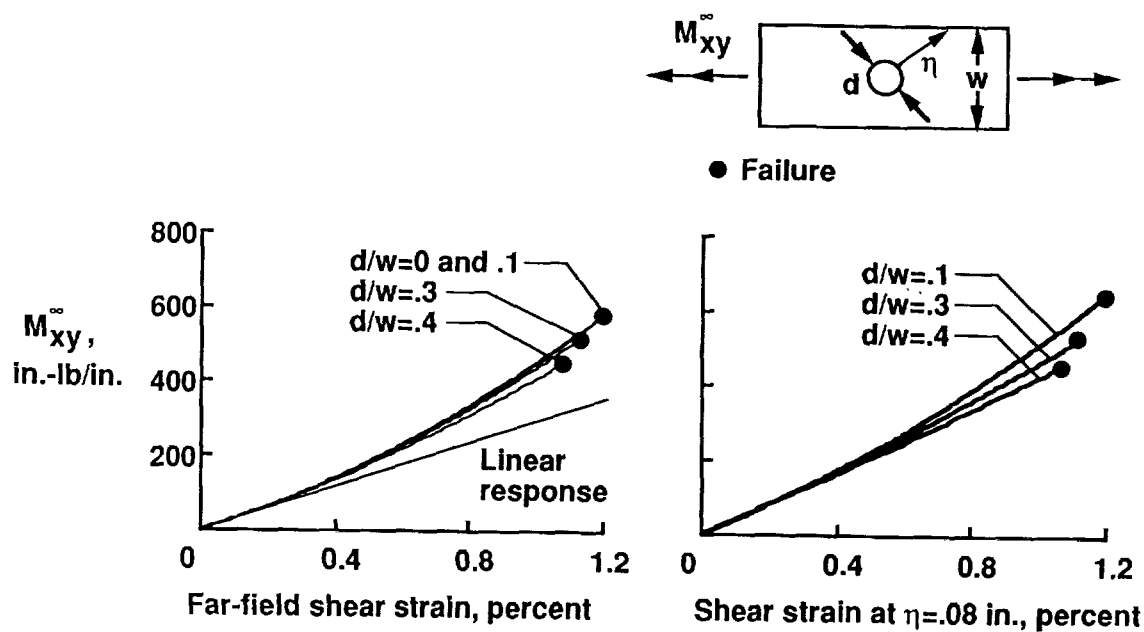


Figure 14

Failed [+45/0/-45/90]_{6s} Twisting Specimen

A typical failed quasi-isotropic twisting specimen is shown in figure 15. The failure of these twisting specimens was catastrophic. The failure surface is a plane located near the middle surface of the laminate. The failure surface extends from end to end and from side to side for this laminate.

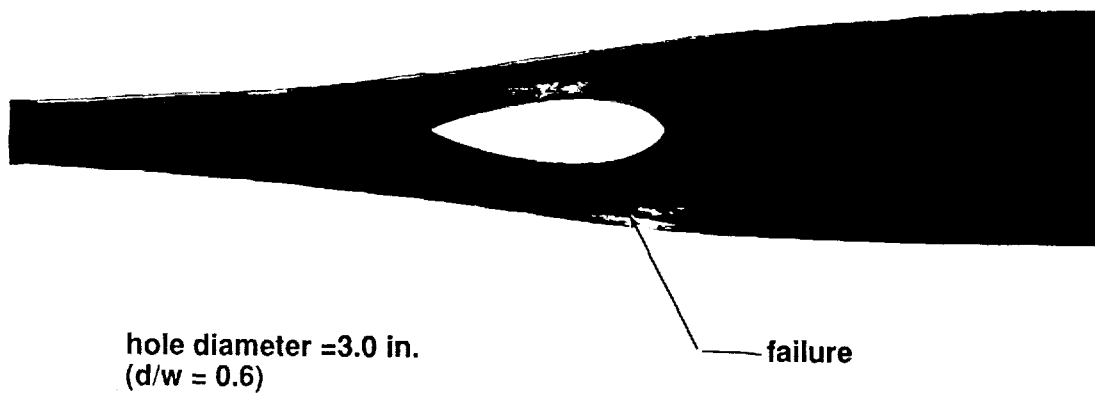


Figure 15

Response of $[\pm 45/\mp 45]_6$ s Laminates Subjected to Twisting

Far-field moment M_{xy}^{∞} as a function of shear strain is shown in figure 16 for $[\pm 45/\mp 45]_6$ s laminates subjected to twisting. Results are presented for far-field shear strains and for local shear strains near the hole boundary at $\eta = 0.08$ in. where η is identified in the figure. Generally, the far-field moment versus far-field strain response for these laminates is nonlinear and approximately the same. The specimen stiffness, as measured by the slope of the far-field-moment–far-field-shear-strain curve, increases with increasing load. The far-field strain at failure decreases with increasing hole diameter. The far-field moment versus local strain behavior for the specimens is also nonlinear and is characterized by increasing stiffness with increasing load. The local failure strain for the $d/w = .4$ specimen is greater than the failure strain for the $d/w = .3$ specimen.

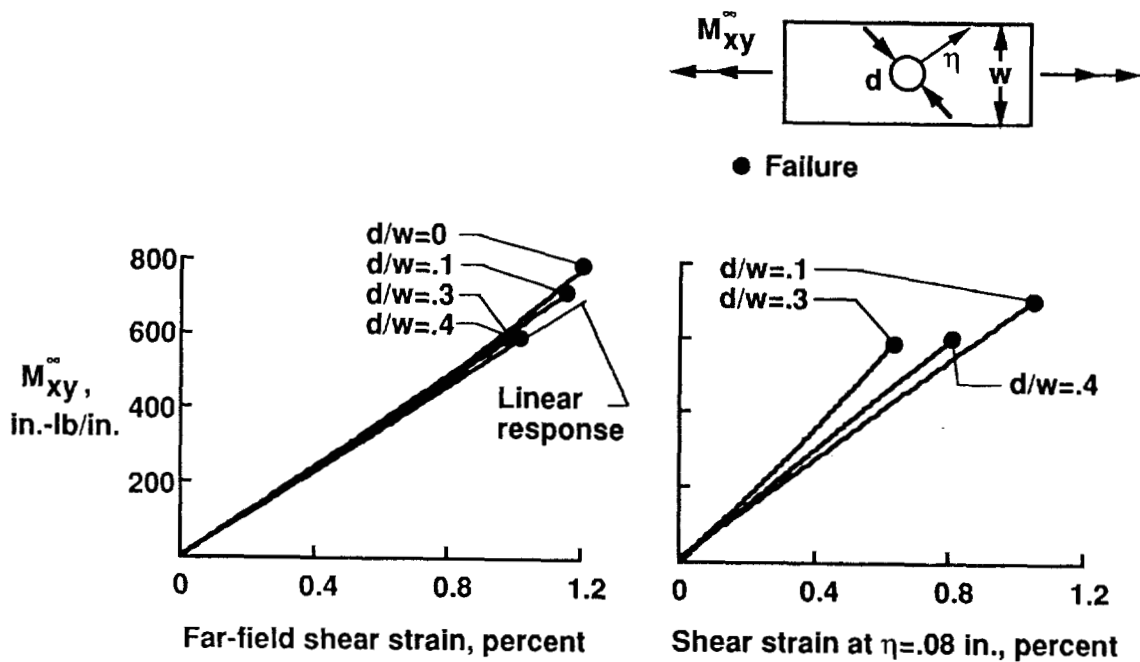


Figure 16

Failed $[\pm 45/\mp 45]_6$ s Twisting Specimens

Typical failed $[\pm 45/\mp 45]_6$ s twisting specimens are shown in figure 17. The failure surface is a plane located near the middle surface of the laminate. The failure of these twisting specimens was catastrophic. The failure surface extends from end to end and from side to side for specimens with small holes (e.g., the $d/w = 0.1$ specimen shown in the figure) but only extends across the width and partially along the length for specimens with large holes (e.g., the $d/w = 0.6$ specimen shown in the figure).

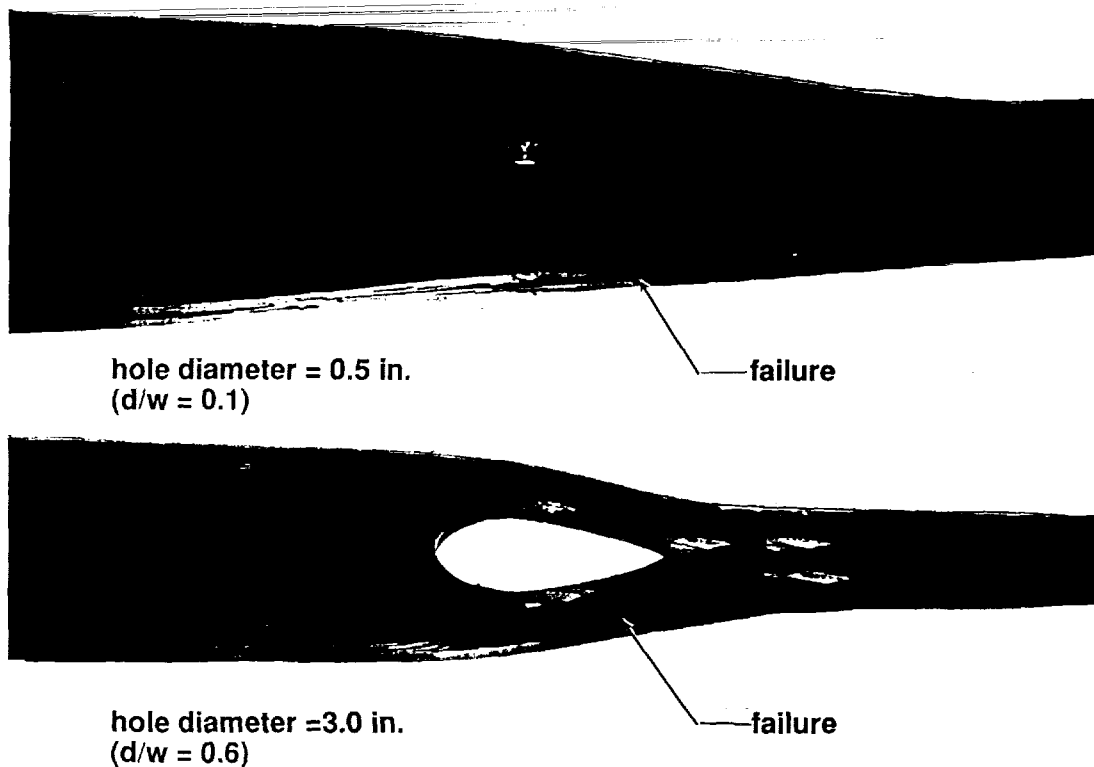


Figure 17

Effect of Cutouts on Shear Strain at Failure for Laminates Subjected to Twisting

The effect of cutout size on the far-field shear failure strain for quasi-isotropic and $[\pm 45/\mp 45]_6S$ twisting specimens is shown in figure 18. Results for the quasi-isotropic and the $[\pm 45/\mp 45]_6S$ laminates are plotted as circular and square symbols, respectively, on the figure. The results for both types of laminates with a hole show that the failure strain decreases almost linearly with increasing hole diameter suggesting a notch insensitive behavior for these laminates. The failure strain for a $[\pm 45/\mp 45]_6S$ specimen is less than the failure strain for a quasi-isotropic specimen for a given hole diameter. The failure strain for the $[\pm 45/\mp 45]_6S$ control specimen is greater than the failure strain for the quasi-isotropic control specimen.

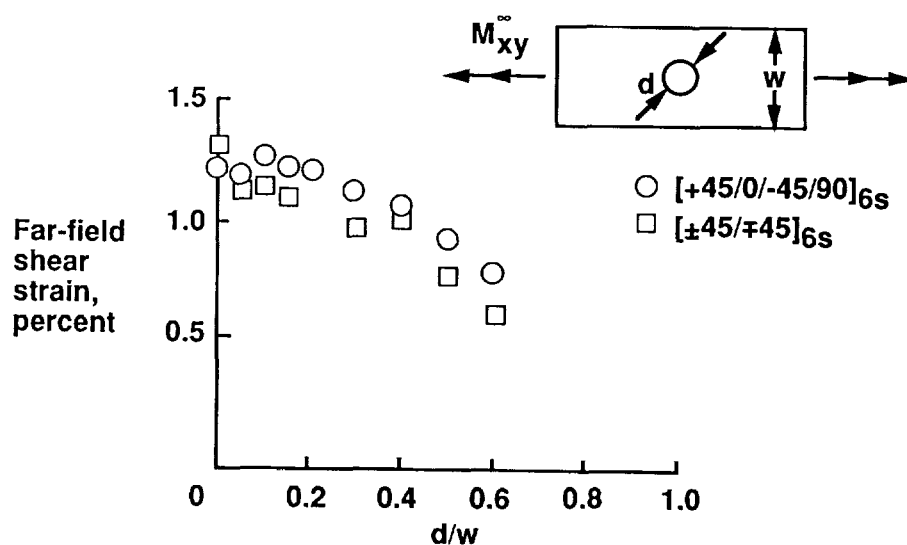


Figure 18

Concluding Remarks

Results have been presented for the effects of circular cutouts on the behavior of $[+45/0/-45/90]_{6S}$ quasi-isotropic and $[\pm 45/\mp 45]_{6S}$ graphite-bismaleimide laminates loaded by bending or twisting. The bending specimens had a nonlinear response and a failure mode that initiated on the compression-loaded side of the laminate and progressed through the laminate thickness. The observed ply-level failure mechanisms for the bending specimens were similar to the ply-level mechanisms observed for uniaxially loaded compression specimens. Bending specimen results were presented for axial failure strain as a function of normalized hole diameter. The $[+45/0/-45/90]_{6S}$ bending specimens exhibited a notch sensitive response, and the $[\pm 45/\mp 45]_{6S}$ bending specimens exhibited a notch insensitive response. The twisting specimens also had a nonlinear response, but the specimen failure was catastrophic. The failure surface for these specimens was near the laminate middle surface. Twisting specimen results were presented for shear failure strain as a function of normalized hole diameter. Both the $[+45/0/-45/90]_{6S}$ and $[\pm 45/\mp 45]_{6S}$ twisting specimens exhibited a notch insensitive response.

References

1. Lekhnitskii, S. G.: Anisotropic Plates. Gordon and Breach Science Publishers, 1968.
2. Savin, G. N.: Stress Concentrations Around Holes. Pergamon Press, 1961.
3. Prasad, C. B.; and Shuart, M. J.: Moment Distribution Around Holes in Symmetric Composite Laminates Subjected to Bending Moments. AIAA Journal, Vol. 28, No. 5, May 1990, pp. 877-882.
4. Shuart, M. J.; and Prasad, C. B.: Analysis and Experiments for Composite Laminates with Holes and Subjected to 4-Point Bending. AIAA Paper No. 90-0961, 1990.
5. Almroth, B. O.; and Brogan, F. A.: The STAGS Computer Code. NASA CR-2950, 1980.
6. Kurtz, R. D.; and Whitney, J. M.: Torsion of Laminates Containing Orthotropic Layers. Proceedings of the American Society for Composites, Third Technical Conference, September 25-29, 1988, Technomic Publishing Co., Inc., Lancaster, PA, 1988, pp. 115-124.
7. Shuart, M. J.: Failure of Compression-Loaded Multidirectional Composite Laminates. AIAA Journal, Vol. 27, No. 9, September 1989, pp. 1274-1279.

Buckling Analysis of Curved Composite Sandwich Panels Subjected to Inplane Loadings

Juan R. Cruz
NASA Langley Research Center
Hampton, Virginia 23681

522-24
51422

Introduction

Composite sandwich structures are being considered for primary structure in aircraft such as subsonic and high speed civil transports. The response of sandwich structures must be understood and predictable to use such structures effectively. Buckling is one of the most important response mechanisms of sandwich structures. In reference 1, a simple buckling analysis is derived for sandwich structures. This analysis is limited to flat, rectangular sandwich panels loaded by uniaxial compression (N_x) and having simply supported edges. In most aerospace applications, however, the structure's geometry, boundary conditions, and loading are usually very complex. Thus, a general capability for analyzing the buckling behavior of sandwich structures is needed.

The present paper describes and evaluates an improved buckling analysis for cylindrically curved composite sandwich panels. This analysis includes orthotropic facesheets and first-order transverse shearing effects. Both simple support and clamped boundary conditions are also included in the analysis. The panels can be subjected to linearly varying normal loads N_x and N_y in addition to a constant shear load N_{xy} . The analysis is based on the modified Donnell's equations for shallow shells [2]. The governing equations are solved by direct application of Galerkin's method. The accuracy of the present analysis is verified by comparing results with those obtained from finite element analysis for a variety of geometries, loads, and boundary conditions. The limitations of the present analysis are investigated, in particular those related to the shallow shell assumptions in the governing equations. Finally, the computational efficiency of the present analysis is considered.

Panel Geometry

The geometry of the composite panel analyzed in this study is shown in figure 1. This panel is rectangular, of length a and width b . The panel is cylindrically curved with radius of curvature R . The panel as a whole, and the individual facesheets, are symmetrically laminated. In addition, the facesheets are considered to be specially orthotropic plates ($A_{16} = A_{26} = 0$, $D_{16} = D_{26} = 0$). The principal directions of the core material are assumed to coincide with the x and y coordinate directions. The core possesses only shear stiffness and is also considered to be specially orthotropic. Only two constants, G_{xz} and G_{yz} , are needed to define the core shear stiffness. Monolithic panels are a special case of the composite sandwich panel shown in figure 1. For monolithic panels the core thickness is zero and the total panel thickness is denoted by t_0 . The transverse shear moduli G_{xz} and G_{yz} are those of the panel material.

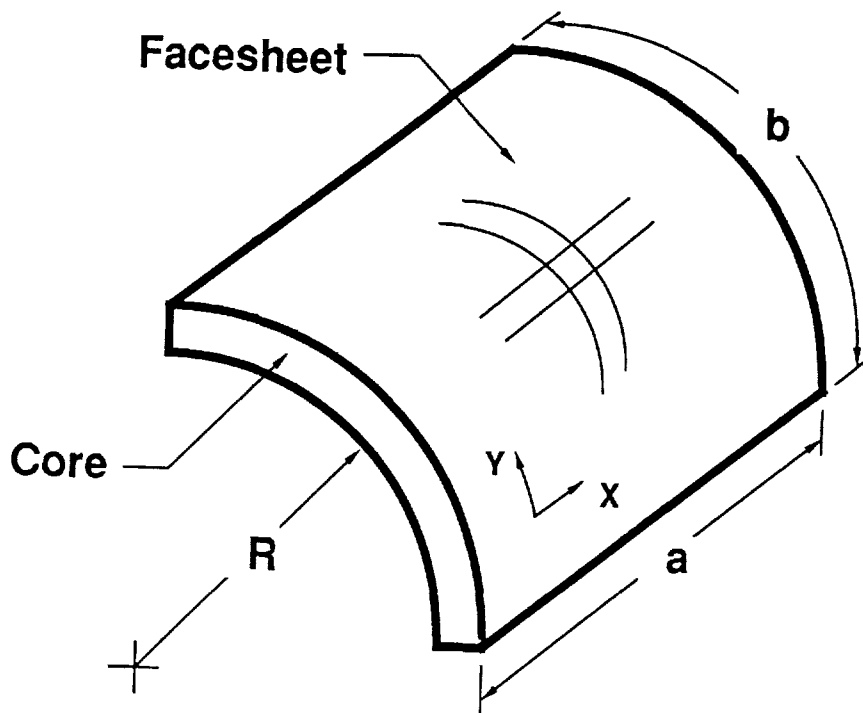


Figure 1

Panel Loading and Boundary Conditions

General inplane loadings, N_x , N_y , and N_{xy} are considered for the sandwich panels in this study. In the present study the panel can be subjected to linearly varying N_x and N_y loads, in addition to a constant N_{xy} load. An example loading is shown in figure 2. All four edges of the panel must have the same boundary condition and may be either simply supported or clamped.

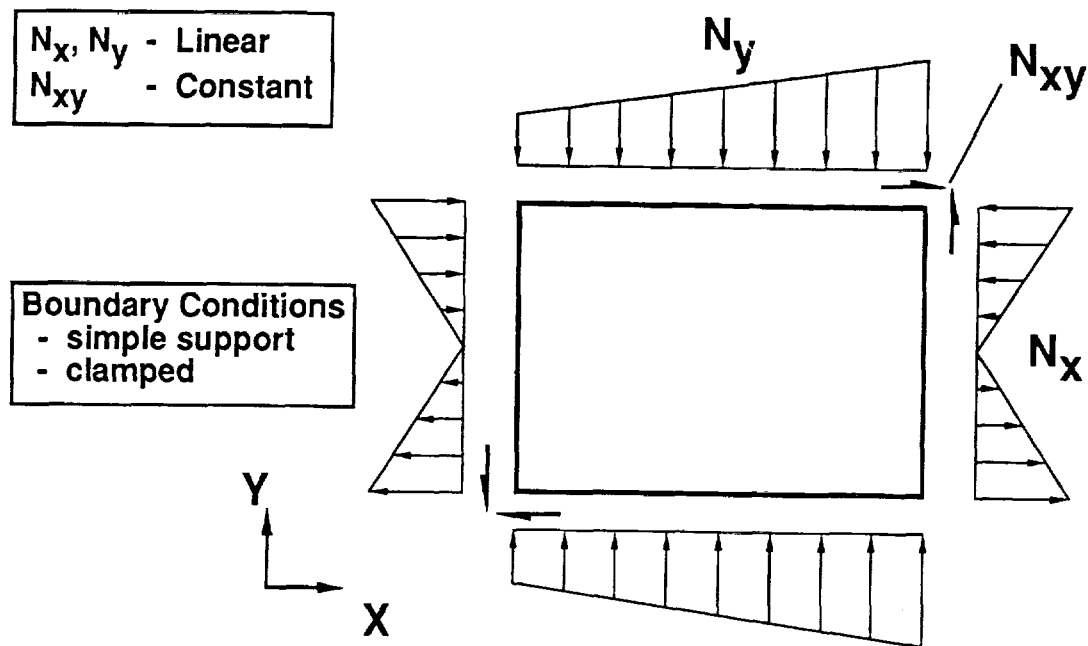


Figure 2

Governing Partial Differential Equations

The governing differential equations for buckling used in this study were derived in reference 2. These equations are three, coupled equations in the unknowns w , Q_x , and Q_y , the out-of-plane displacement and the transverse shear stress resultants, respectively. These equations form a set of Donnell's equations modified to include first order transverse shear effects.

An inverse differential operator is used with the governing equations to avoid escalating the partial differential equation. As shown in reference 3, escalating differential equations may lead to incorrect solutions. The inverse differential operator results when the inplane displacements u and v are removed as independent variables in the governing equations. A drawback of using this inverse differential operator is that boundary conditions cannot be specified for u and v ; these boundary conditions are implied in the assumed solution for w .

The governing equations used in the present study define a simple shell theory. The shell curvature, R , appears only in one term of the governing equations. In addition, an important simplifying assumption in the derivation of these equations is that the pre-buckling out-of-plane displacement w_0 can be ignored. These assumptions limit the application of these equations to shallow shells.

Assumed Series Solutions

The governing equations are solved using assumed trigonometric series for the independent variables w , Q_x , and Q_y . Two sets of series solutions corresponding to the simple support and the clamped boundary conditions are shown in figure 3. These series solutions must satisfy all boundary conditions. The series solution for w implies specific boundary conditions for u and v since an inverse differential operator is used to remove u and v as independent variables. Different boundary conditions for u and v than those implied by the series solution may result in significantly different buckling loads and mode shapes.

SIMPLY SUPPORTED SOLUTION

$$w = \sum_{m=1}^{\infty} \sum_{n=1}^{\infty} a_{mn} \sin\left(\frac{m\pi x}{a}\right) \sin\left(\frac{n\pi y}{b}\right)$$

$$Q_x = \sum_{m=1}^{\infty} \sum_{n=1}^{\infty} b_{mn} \cos\left(\frac{m\pi x}{a}\right) \sin\left(\frac{n\pi y}{b}\right)$$

$$Q_y = \sum_{m=1}^{\infty} \sum_{n=1}^{\infty} c_{mn} \sin\left(\frac{m\pi x}{a}\right) \cos\left(\frac{n\pi y}{b}\right)$$

CLAMPED SOLUTION

$$w = \sum_{m=1}^{\infty} \sum_{n=1}^{\infty} a_{mn} \left[\cos\left(m-1\right)\left(\frac{\pi x}{a}\right) - \cos\left(m+1\right)\left(\frac{\pi x}{a}\right) \right] \left[\cos\left(n-1\right)\left(\frac{\pi y}{b}\right) - \cos\left(n+1\right)\left(\frac{\pi y}{b}\right) \right]$$

$$Q_x = \sum_{m=1}^{\infty} \sum_{n=1}^{\infty} b_{mn} \left[\sin\left(m-1\right)\left(\frac{\pi x}{a}\right) - \sin\left(m+1\right)\left(\frac{\pi x}{a}\right) \right] \left[\cos\left(n-1\right)\left(\frac{\pi y}{b}\right) - \cos\left(n+1\right)\left(\frac{\pi y}{b}\right) \right]$$

$$Q_y = \sum_{m=1}^{\infty} \sum_{n=1}^{\infty} c_{mn} \left[\cos\left(m-1\right)\left(\frac{\pi x}{a}\right) - \cos\left(m+1\right)\left(\frac{\pi x}{a}\right) \right] \left[\sin\left(n-1\right)\left(\frac{\pi y}{b}\right) - \sin\left(n+1\right)\left(\frac{\pi y}{b}\right) \right]$$

Figure 3

Solution Approach

The governing equations are solved by Galerkin's method. Applying Galerkin's method as illustrated in figure 4 yields a set of equations which constitute a symmetric algebraic eigenvalue problem. Solving the eigenvalue problem yields the buckling loads and mode shapes.

Galerkin's Method

$$\int_0^a \int_0^b L_1(w, Q_x, Q_y) \left(\frac{\partial w}{\partial a_{mn}} \right) dy dx = 0$$

$$\int_0^a \int_0^b L_2(w, Q_x, Q_y) \left(\frac{\partial Q_x}{\partial b_{mn}} \right) dy dx = 0$$

$$\int_0^a \int_0^b L_3(w, Q_x, Q_y) \left(\frac{\partial Q_y}{\partial c_{mn}} \right) dy dx = 0$$

Figure 4

Analysis Verification

The present analysis has been implemented in two FORTRAN computer programs corresponding to the simple support and the clamped boundary conditions. The present analysis was verified and evaluated as outlined in figure 5. To verify the accuracy of the present analysis, comparisons are made with results obtained from a finite element analysis. In addition, the number of terms required in the solution series to achieve convergence is evaluated. Since the analysis is limited to shallow shells, the analysis accuracy is also assessed as a function of the panel curvature. Finally, the computational expense (as measured in CPU seconds) of the present method is compared to an equivalent solution obtained by a finite element analysis to assess the present method's computational efficiency.

- **Comparison with Finite Element results**
- **Convergence rate**
- **Limitations of shallow shell theory**
- **Computational efficiency**

Figure 5

Verification Test Cases

A set of 48 test cases has been defined and are described in figure 6. These test cases include a variety of geometries, materials, and loadings. For computational convenience, all test cases consist of monolithic panels. Transverse shear effects are introduced in some cases by setting low values for G_{xz} and G_{yz} . All panels are assumed to be made out of a typical graphite-epoxy composite material. The laminates are assumed to be homogeneous and to have either a unidirectional, with the 0° direction along the x axis, or a quasi-isotropic stacking sequence. Three sets of load conditions are considered: uniaxial compression only, shear only, and combined inplane bending and shear. All 48 test cases are evaluated for both simple support and clamped boundary conditions.

Wide range of test cases:

- **Geometry: length, width, radius of curvature**
- **Layup: isotropic, unidirectional**
- **Transverse shear stiffness: infinite, finite**
- **Loading: compression, shear, combined load**

Total load cases: 48

All test cases applied to both simply supported and clamped panels

Figure 6

Simply Supported Panels

Results for the buckling load ratio, R_s , as a function of the number of terms in the series solution are shown in figure 7 for plates with simple support boundary conditions. The buckling load ratio is defined as the ratio of the present analysis solution to the converged finite element solution. The finite element solution is assumed to be exact. Buckling load ratio results for the case with the worst convergence rate are shown by the solid line on the figure. Even for this worst case, ten terms for the assumed series solution were sufficient to obtain a converged R_s within one percent of the exact solution. Most other cases had converged results with much fewer terms for the assumed series solution. All 48 test cases converged to within ± 1 percent of the exact solution as illustrated by the dotted lines on the figure. These results illustrate that for panels consistent with the assumptions of the present analysis, accurate response can be predicted for a wide variety of structural parameters (e.g., high aspect ratio, high degree of orthotropy).

Convergence Rate and Comparison with FE Results

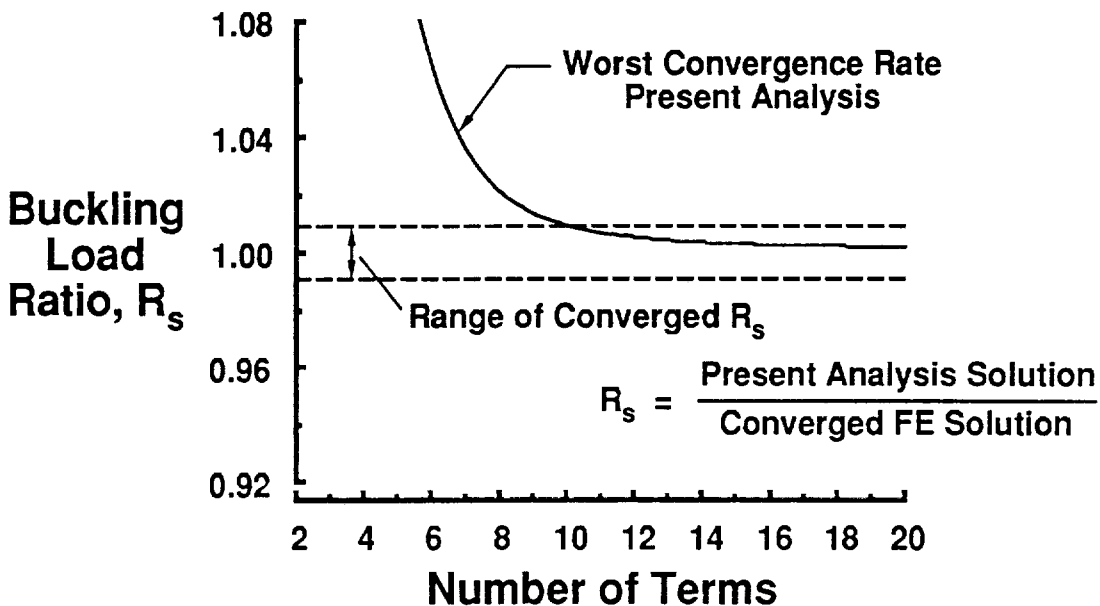


Figure 7

Clamped Panels

Results for the buckling load ratio, R_s , as a function of the number of terms in series solution are shown in figure 8 for plates with clamped boundary conditions. The buckling load ratio is defined as the ratio of the present analysis solution to the converged finite element solution. The finite element solution is assumed to be exact. Buckling load results for the case with the worst convergence rate are shown by the solid line on the figure. For this case, twelve terms for the assumed series solution were required to obtain a converged R_s within eight percent of the exact solution. Most other cases had converged results with much fewer terms for the assumed series solution. All 48 test cases converged to within plus eight to minus three percent of the exact solution. The reason for the slower convergence as compared to the simple support results is that the assumed series for clamped boundaries does not capture the buckling behavior as rapidly as the assumed series for simple support boundaries. The range of converged results for panels with clamped boundaries is wider than the converged results for panels with simple support boundaries. This difference is due to the limitations of the present analysis.

Convergence Rate and Comparison with FE Results

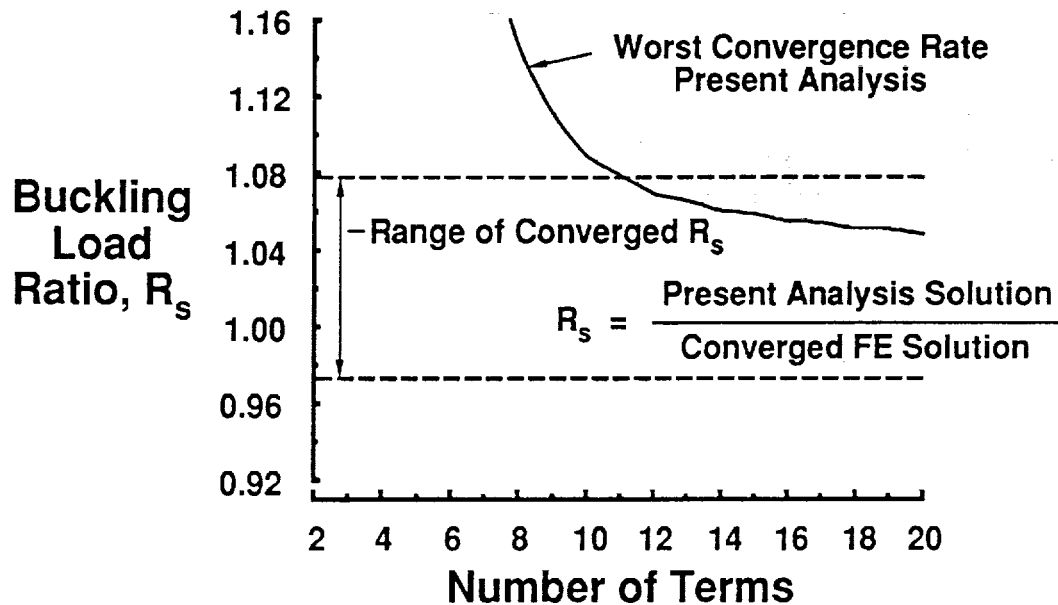


Figure 8

Limitations of Shallow Shell Theory

The theory used in the present work is limited to shallow shells. Results for the buckling load ratio, R_s , as a function of the width-to-radius-of-curvature ratio, b/R , are shown in figure 9. The ratio, b/R , is a measure of the curvature of the shell, e.g., for $b/R = 0$, the panel is a flat plate. Results are shown on the figure for a clamped panel subjected to three types of loading: shear only, compression and shear, and compression only. The material, stacking sequence, and geometry (except for the radius of curvature R) for the panel remain constant. The results on the figure show that the accuracy of R_s decreases as the shell curvature, b/R increases. However, this decrease in accuracy depends on the panel loading. When the panel is loaded in shear only, the accuracy of R_s decreases very slowly as b/R increases. For the case of compression only loading, however, the accuracy of R_s decreases rapidly as b/R increases. The results for combined compression and shear loading are between those for compression only loading and for shear only loading. An example of the application of the present analysis for the conservative case of compression only loading is as follows: a 5 percent error ($R_s = 0.95$) results for a panel with $b/R = 0.22$. This example suggests that the present theory may be used for panels with $b/R < 0.22$ if a 5 percent error is allowable. The results on the figure are typical for the present analysis.

Clamped Panel Example - Comparison with FE Results

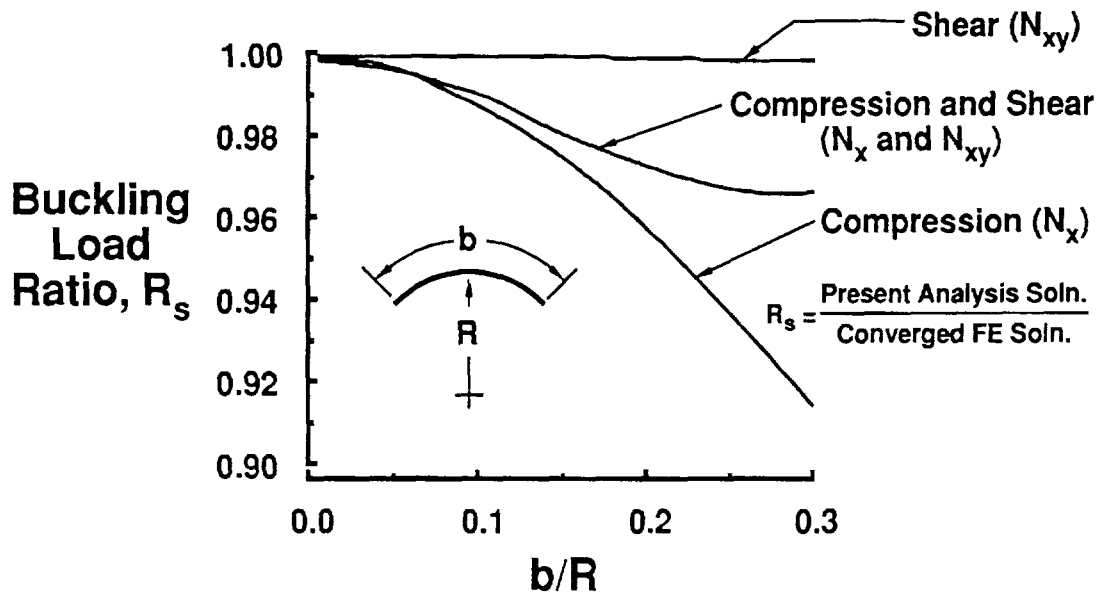


Figure 9

Computational Efficiency

A significant advantage of the present analysis is its computational efficiency. In an optimization program the analysis portion may be performed hundreds or even thousands of times. Thus, the analysis must be as computationally efficient as possible in terms of CPU time. The results presented herein were obtained using a Convex C-240 computer for both the present analysis and the finite element analysis. The FORTRAN programs for the present analysis used the vectorizing option in the compiler. The finite element results were generated with the COMET finite element computer program [4]. The computational efficiency of the present analysis is outlined in figure 10. The present analysis was 340 to 420 times faster and 50 to 80 times faster than the corresponding finite element analysis for panels with simple support boundary conditions or with clamped boundary conditions, respectively. The times required for completing the present analysis suggest that this analysis is well suited for optimization.

- **Simply Supported Analysis**

- **340 to 420 times faster than finite element analysis**
- **Ten term solution requires \approx 0.5 to 0.8 CPU seconds**

- **Clamped Analysis**

- **50 to 80 times faster than finite element analysis**
- **Ten term solution requires \approx 3.7 to 4.0 CPU seconds**

Present analysis well suited for optimization

Figure 10

Concluding Remarks

A buckling analysis for cylindrically curved composite sandwich panels has been derived and implemented. This analysis is capable of analyzing panels with orthotropic facesheets and first-order transverse shear effects. The panels can be subjected to linearly varying N_x and N_y loads, in addition to a constant N_{xy} load. Both simple support and clamped boundary conditions are included in the analysis.

The governing equations for the analysis are a set of modified Donnell's equations in the unknowns w , Q_x , and Q_y . These equations use inverse differential operators to avoid escalating the partial differential equations. Series solutions which satisfy all boundary conditions are assumed for w , Q_x , and Q_y . A direct application of Galerkin's method is then used to solve the governing equations. Because of assumptions made during the derivation, this analysis is only valid for shallow shells.

To verify the accuracy of the analysis, comparisons were made with results obtained from a finite element analysis. For simply supported panels, the present analysis buckling load is usually within ± 1 percent of the finite element results for shallow shells. For clamped panels the present analysis yields less accurate, but still acceptable, results; the buckling load is within -4 to +8 percent of the finite element results for shallow shells. As the curvature of the panels is increased, and the shell becomes less shallow, the accuracy of the present analysis decreases. The degree to which the accuracy decreases with increasing curvature is a strong function of the loading. Within the context of the shallow shell assumptions, the present analysis provides useful results for a wide variety of structures.

References

1. Cruz, Juan R.: Optimization of Composite Sandwich Cover Panels Subjected to Compressive Loadings. NASA TP-3173, 1991.
2. Stein, Manuel; and Mayers, J.: A Small-Deflection Theory for Curved Sandwich Plates. NACA Report 1008, 1951.
3. Batdorf, S. B.: On the Application of Inverse Differential Operators to the Solution of Cylinder Buckling and Other Problems. Proceedings of the AIAA/ASME 10th Structures, Structural Dynamics and Materials Conference, New Orleans, Louisiana, April 14-16, 1969, pp. 386-391.
4. Lotts, C. G.; Greene, W. H.; McCleary, S. L.; Knight, N. F.; Paulson, S. S.; and Gillian, R. E.: Introduction to the Computational Mechanics Testbed. NASA TM 89096, 1987.

ISPAN
INTERACTIVE STIFFENED PANEL ANALYSIS
A TOOL FOR
QUICK CONCEPT EVALUATION AND DESIGN TRADE STUDIES

John W. Hairr, William J. Dorris, J. Edward Ingram, and Bharat M. Shah*

Lockheed Aeronautical Systems Company

Marietta, Georgia 30063

523-24

51423

ABSTRACT

Interactive Stiffened Panel Analysis (ISPAN) modules, written in FORTRAN, were developed to provide an easy to use tool for creating finite element models of composite material stiffened panels. The modules allow the user to interactively construct, solve and post-process finite element models of four general types of structural panel configurations using only the panel dimensions and properties as input data. Linear, buckling and post-buckling solution capability is provided. This interactive input allows rapid model generation and solution by non finite element users. The results of a parametric study of a blade stiffened panel are presented to demonstrate the usefulness of the ISPAN modules. Also, a non-linear analysis of a test panel was conducted and the results compared to measured data and previous correlation analysis.

INTRODUCTION

Stiffened panel analysis computer programs have been in existence for many years. Typically, they are based on a combination of closed form solutions and a large data base of metallic stiffened panel test results. Developing a similar analysis capability for composite materials would be a formidable task due to the the lack of a complete composite stiffened panel test data base and due to the complex failure modes resulting from material anisotropy and variations in design/fabrication techniques. Closed-form solutions for the complex failure modes and out-of-plane response characteristics of the composite materials

are being developed; but so far, have not demonstrated sufficient applicability and accuracy. As finite element programs, and in particular, the pre- and post-processing programs have matured, it has become apparent that a more practical alternative to the closed-form solutions would be a non-linear finite element-based program which is user friendly. That alternative is envisioned here as an interactive input module which functions as an interface between the structures engineer and the finite element program (see Figure 1). The modules developed jointly at Lockheed Missiles and Space Company (LMSC) and at Lockheed Aeronautical Systems Company (LASC) are referred to as ISPAN, for Interactive Stiffened Panel Analysis.

Four user input/interface modules were developed; one each for flat and curved stiffened panels, truss-core panels and geodesic stiffened panels. Each module prompts the user for panel dimensions, properties, loads, boundary conditions and solution type (linear, buckling or post-buckling). The data supplied are then used to automatically prepare the finite element model. No knowledge of the finite element program commands or data format is required of the user. A typical stiffened panel geometry and solution procedure can be generated in a few minutes; solution time will obviously depend on the computer. Once a panel problem has been defined, the data are saved to a file, so that any changes to geometry, mechanical properties or loads may be accomplished by updating this database file with the data only requiring the changes. This allows the data for successive analyses be created in a fraction of the time required for the initial problem definition. This operational efficiency is valuable in the trade study.

The functioning of ISPAN modules, as illustrated in Figure 2, is analogous to a command module. In addition to interactively developing DIAL compatible geometry and materials files from the user supplied data, it also establishes procedures to communicate with the DIAL pre-processor, the solver, and post-processor. Thus it allows the user a direct control over the overall problem solving.

The Lockheed developed DIAL finite element code was selected for use in ISPAN because of its versatile non-linear and collapse analyses capability. DIAL also has very powerful pre- and post-processors requiring a relatively few number of commands. While the model generation data needed for DIAL is very concise, it is not intuitively obvious to an analyst not already familiar with the DIAL code which commands and which options should be used. Thus, if the structure to be analyzed is confined to a certain type, such as a stiffened panel, DIAL lends itself well to an interface procedure such as ISPAN. The

DIAL code also features a capability called syntactic input, which is a FORTRAN-like language that allows variable names for model data, and subroutines which use these variables to construct model generation commands. Finally, DIAL maintains a database, which contains model data, output data (internal loads, stresses, deflections, etc) and information generated during a post-processing session.

PROGRAM CAPABILITIES AND LIMITATIONS

The ISPAN modules are presently capable of analyzing the panel types and general cross-sections shown in Figure 3. The following list describes the options available to the user in the four modules

- | | |
|-----------|--|
| Stiffener | <ul style="list-style-type: none">- cross-section type- number of stiffeners- spacing (may be irregular)- flange widths, thickness- materials , ply orientation |
| Skin | <ul style="list-style-type: none">- width, length and thickness- materials , ply orientations |
| Loading | <ul style="list-style-type: none">- axial end load, N_x (tension or compression)- lateral load perpendicular to the stiffener direction) N_y- in-plane edge shear, N_{xy}- normal pressure |

Boundary Conditions	<ul style="list-style-type: none"> - Each of the four panel edges may be specified separately as free, simply-supported or clamped. - Vertical translations and/or rotations may also be specified across the width of the panel to simulate the rib/frame supports.
Solutions	<ul style="list-style-type: none"> - linear static - bifurcation (buckling) - post-buckling (arc length method)

DIAL Shell Element

All components of the stiffened panel models are constructed using a modified thick shell element as shown in Figure 4. This element is an eight node, super-parametric, doubly-curved thick shell element. The element was modified by separating the membrane, bending and transverse shear responses, thus allowing the adequate representation of both the laminate and the sandwich type structures. Linear, parabolic and cubic versions of this element are available in DIAL. The parabolic and cubic shell elements are vastly superior to the linear elements in terms of accuracy and are generally recommended. The parabolic elements were selected for use in ISPAN to provide optimum accuracy for a given level of complexity. An example of a typical flat, hat-stiffened panel model generated by ISPAN is shown in Figure 5.

Although the stiffener elements are generally distinct from the skin elements, it should be noted that the stiffener attach flanges are assumed to be included in the skin. Therefore, elements in the stiffener attach flange region should be given thickness and orientations which reflect the sum of the flange and skin in this region as indicated by the shaded area in Figure 6.

The ribs (frames) are not modeled with structural elements in this analysis. However, they are represented by constraints on the degrees of freedom at the rib locations. The details of this are discussed in the sub-section on boundary conditions.

Loads

In-plane axial (N_x), lateral (N_y) and shear loads (N_{xy} , N_{yx}) as well as normal pressure (P) may be applied to the model. Figure 7 shows the definition and sign convention of these load components.

The axial loads on the panel ends (N_x) are applied in such a way as to produce uniform strain, (ϵ_x). That is, the total applied load is effectively distributed to the base panel and the stiffeners according to their relative stiffnesses. This is accomplished in DIAL by forcing a set of edge "slave" nodes to displace as the weighted average of the displacements of the two "master" nodes at the panel corners as shown in Figure 8. The weights used are inversely proportional to the distances of the slave nodes to the master nodes. This method of applying axial loads simulates the loading produced by the surrounding wing or fuselage structure as well as in most stiffened panel test set-ups.

Boundary Conditions

Each edge (boundary) of the panel may be independently specified to be free, simply-supported or clamped. The simple supports are simulated constraining only the out-of-plane (normal to panel) degree of freedom at each node. Clamped conditions are simulated by constraining both normal translations and rotations along the edge. In addition to the constraints used to simulate the structural support provided by the adjacent structure, kinematic constraints are specified to prevent rigid body motions as shown in Figure 9. These kinematic constraints are generated automatically by the ISPAN modules. Under normal circumstances, the kinematic constraints will produce no internal loading in the panel. If a pressure load were inadvertently specified without the balancing normal or hoop loads on the panel edges, then the kinematic constraints would provide the balancing loads. This undesirable condition would become obvious to the user once the deflected shape and/or stress contours are examined.

The option exists in ISPAN modules to provide out-of-plane support at specified locations on the stiffened panel in such a way as to simulate a rib or circumferential frame. The support is modeled by constraining the out-of-plane displacement normal to the panel at user specified locations. The inherent assumption in this modeling technique is that the rib or frame has sufficient stiffness to enforce a node in the buckled mode shape of the panel. The rotations about the y-axis at the rib locations may also be constrained in order to simulate a very rigid support such as a main frame. In most applications (intermediate frames or ribs), constraining these rotations will be unconservative.

Solutions

Three solution procedures, linear static, bifurcation (initial buckling) and post-buckling, are presently available in ISPAN. The linear static solution is straightforward and needs no explanation.

The initial buckling solution is an analysis to determine the multiplier on the applied load (eigenvalue) at which any part of the structure first becomes unstable. No knockdown factors nor initial imperfections are accounted for in this bifurcation analysis.

A post-buckling solution allows the user to determine the ultimate load capability of a structure. Some flight vehicle structures are permitted to buckle locally at load levels below ultimate, provided they retain the capability to carry the ultimate load without complete collapse. This loading condition can be analyzed using the post-buckling solution in DIAL, which enables an investigation of the integrity of the structure after initial buckling, to establish the ultimate allowable load based on strain cutoff, strain interaction or general instability /total collapse. The DIAL program uses the Arc-Length method, described in reference 2, to perform the non-linear analysis. This method requires the user to select a target point in the form of either load factor or a maximum displacement at a certain location (grid point). Since strength, rather than displacement is the criterion most often used for structural design, the load factor option is recommended for this type of analysis.

The solution procedure for conducting the non-linear analysis performs an initial buckling calculation first, and uses the resulting load and mode shape as the starting point for the non-linear post-buckling analysis. ISPAN multiplies the first eigenvector by 2%

(.02) to establish the shape of the imperfect panel at the zero load state. This procedure not only facilitates the non-linear solution procedure, but provides a more realistic analysis of actual structures; a feature in this analysis that is normally handled by knock-down factors in other solution techniques.

ANALYSIS-TEST COMPARISON OF POST-BUCKLED RESPONSE

The ISPAN module was used to analyze a composite flat stiffened panel for which test and previous analysis work already exists (ref 1). The purpose of this analysis was to verify the accuracy of the post-buckled analysis solution in DIAL. The panel in this case is an "I" stiffened panel 81.3 cm long (parallel to stiffeners) and 61.0 cm wide with four stiffeners spaced at 17.8 cm. The panel was loaded in pure compression.

The model geometry generated by ISPAN is shown in Figure 10. As in all ISPAN modules, modified thick shell elements were used for all components. The deflected shape of the panel at a load of 92.7 kips is shown in Figure 11. This shape, which consists of five half-waves, is identical to that observed in the test panel and in the STAGS analysis of ref. 1.

The comparisons of the DIAL analysis with the results from ref. 1 in terms of load vs. end shortening and load vs. strain curves are presented in Figures 12 and 13 respectively, and show reasonably good agreement. ISPAN presently does not include the capability to generate tapered elements such as the attach flanges in the test panel. This difference is thought to be responsible for the disagreement between test results and the ISPAN-generated DIAL model results. Plans for future enhancements to the ISPAN program may include incorporation of the interface element, which can be used to simulate the bond between the stiffener and the skin panel. This interface element allows the determination of the longitudinal and transverse shear and normal stresses (and strains) at each load step in the non-linear solution; and thus can be used to predict stiffener interface failure such as the one observed in the ref. 1 test.

PARAMETRIC STUDY

A trade study was conducted to illustrate one of the uses of ISPAN. A 24 in. by 24 in. blade-stiffened panel was analyzed with varying stiffener heights and spacings. The loading for the study was uniform compression and the boundaries were simply supported. Figure 14 shows an example of one of the blade stiffened panel model geometries generated with ISPAN, in which the stiffener height was 2.0 in., and the spacing was 4.0 in. The combinations of height and spacing considered in this study are shown in Figure 15 along with the critical loads resulting from the linear and non-linear solutions. Both the applied load at the strain cutoff value and the critical or collapse load are included in Figure 15. These results are presented in graphical form in Figure 16, in which it may be seen that for a given load, there is an optimum combination of height and spacing. In this limited study, the skin and stiffener thickness and laminate descriptions were not allowed to vary; and obviously a comprehensive analysis to determine the optimum panel for a given application would involve not only variations in thickness and properties, but panel length, stiffener type and many other variables.

CONCLUSION

The ISPAN interface modules allow both experts and non-users of finite element codes access to a powerful non-linear analysis procedure to enhance their efficiency and analysis accuracy. The interface module procedure fills a void in the available methods of analysis for anisotropic stiffened panel analysis. The expected benefit from this program is the ability to consider a broad range of stiffened panel geometries and materials for multi-axial loads application during the trade study phase of a new design also accounting for the critical failure modes .

The analysis of an I-stiffened test panel shows that the accuracy of the ISPAN non-linear analysis procedure compares favorably with test data and with other finite element analyses.

Plans for future enhancements to ISPAN include incorporation of the existing DIAL skin-stiffener interface element into the automatic mesh generation . The interface element

is used to represent the stiffness of the bond between the stiffener (s) and the skin. The output stresses and strains for the interface element will allow bond failure modes to be included in the analysis.

ACKNOWLEDGMENT

The authors wish to thank Messrs. Wayne Brown, Tony Wei and Dr. Norm Cyr, of Lockheed Missiles and Space Company for their work in the development of the ISPAN program(s). The authors also thank Dr. Randall Davis (NASA/LaRC) for his review and comments.

REFERENCES

1. Starnes, James H., Jr., Knight, Norman F., Jr., and Rouse, Marshall
"Postbuckling Behavior of Selected Flat Stiffened Graphite-Epoxy Panels
Loaded in Compression," AIAA Paper No. 81-0543, 1982.
2. Anon., "DIAL Structural Analysis System User's Manual", Version L3D3,
August 1,1991, Lockheed Missiles and Space Company, Sunnyvale California.

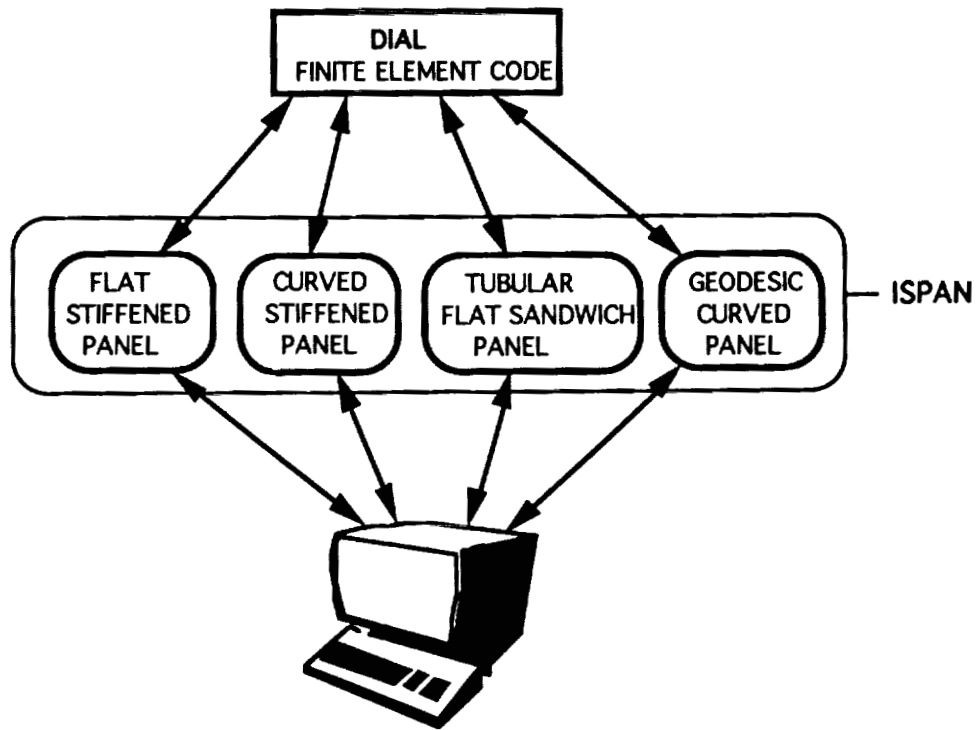


Figure 1 ISPAN - The Interface Between the Non-Finite Element Users and DIAL

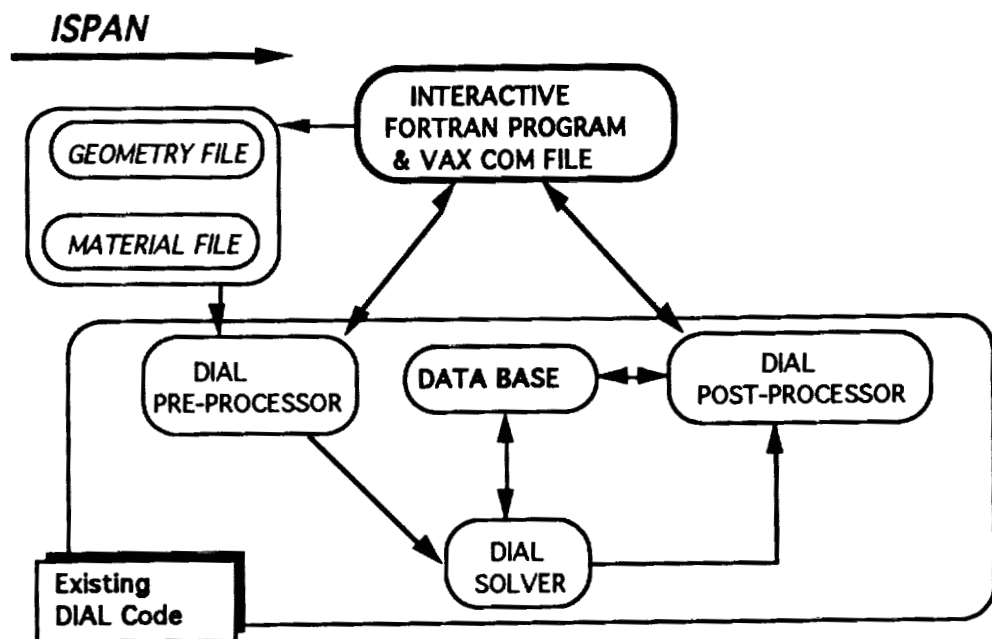


Figure 2 ISPAN Module Functional Flow

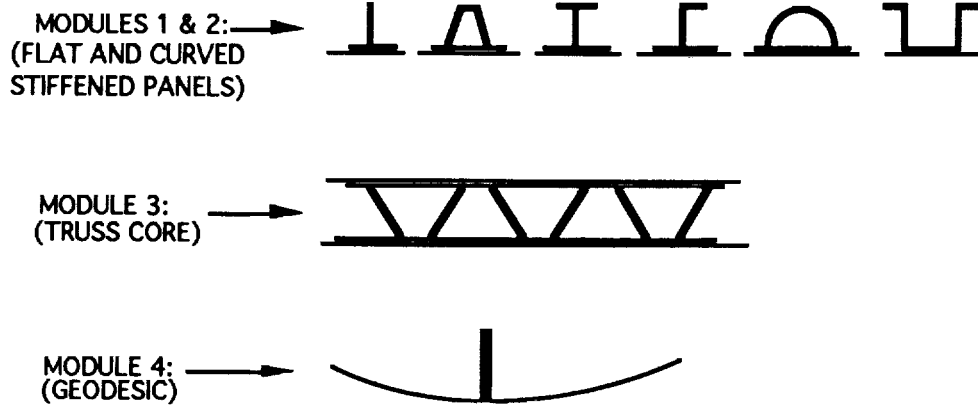


Figure 3 Stiffener Cross Sections Available in ISPAN

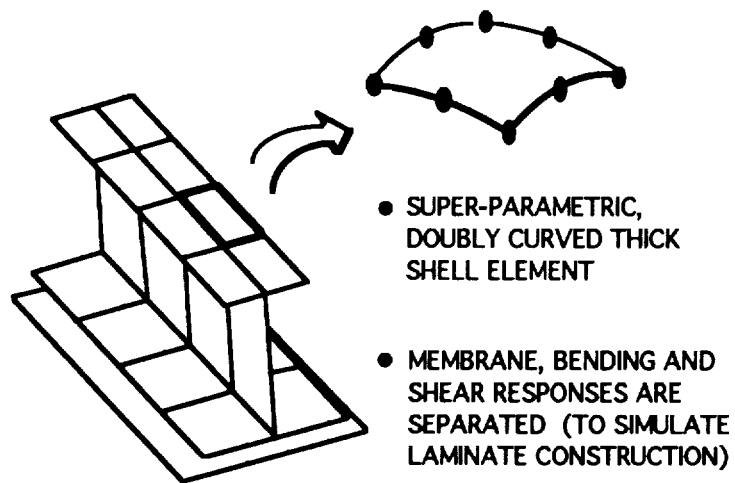


Figure 4 Shell Element Type Used in ISPAN

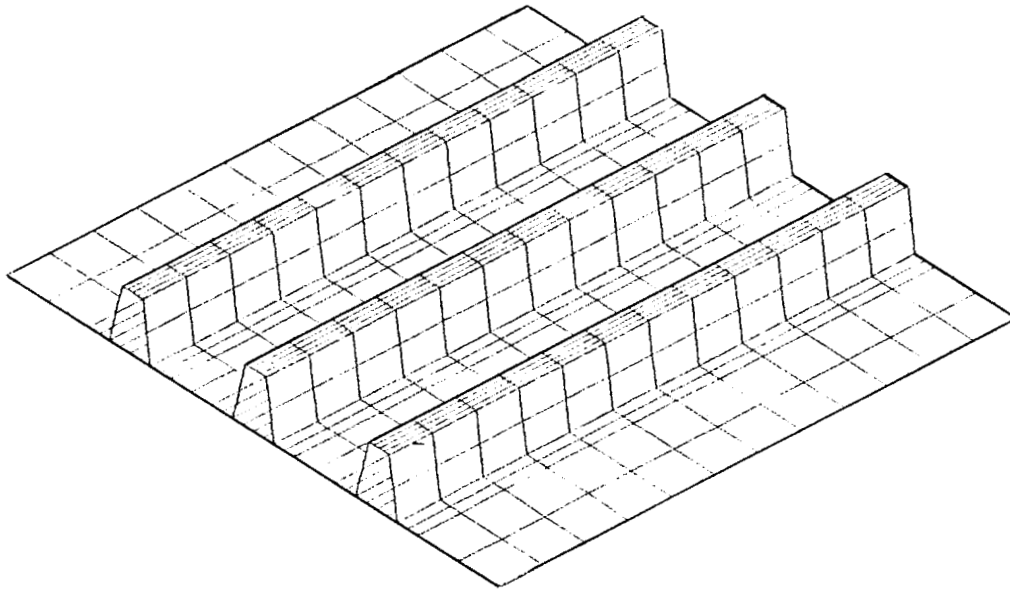


Figure 5 Hat Stiffened Panel Model Generated by ISPAN

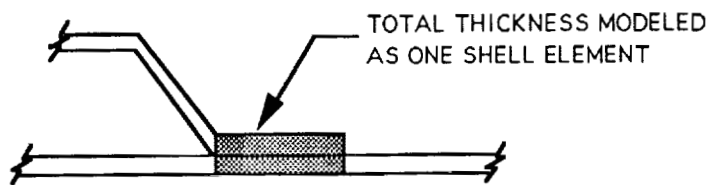


Figure 6 Attach Flanges of Stiffeners and Skin Elements are Modeled as One Shell Element

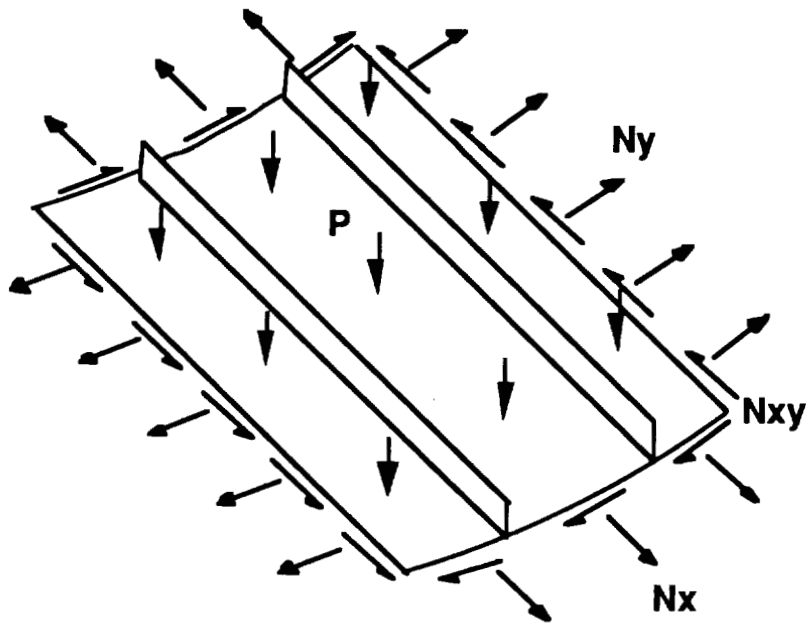


Figure 7 Applied Loads Definition

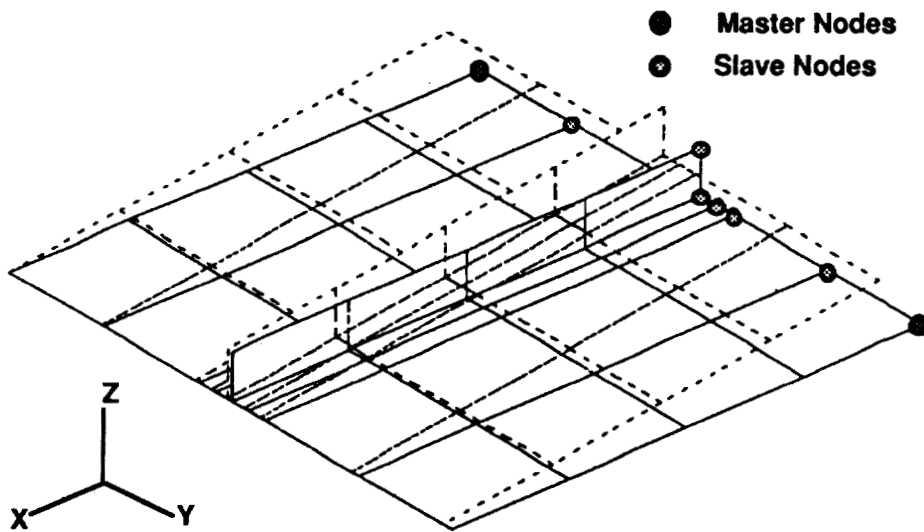


Figure 8 Master and Slave Nodes in CONODE Command

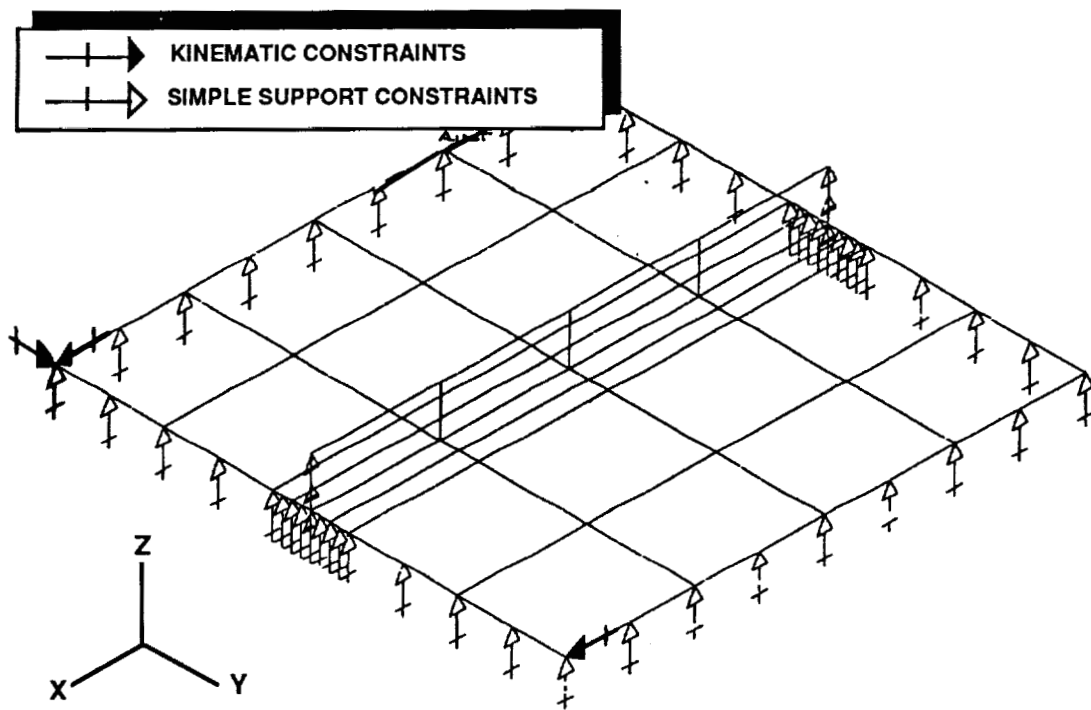


Figure 9 Typical Constraint Vectors for Flat Panel

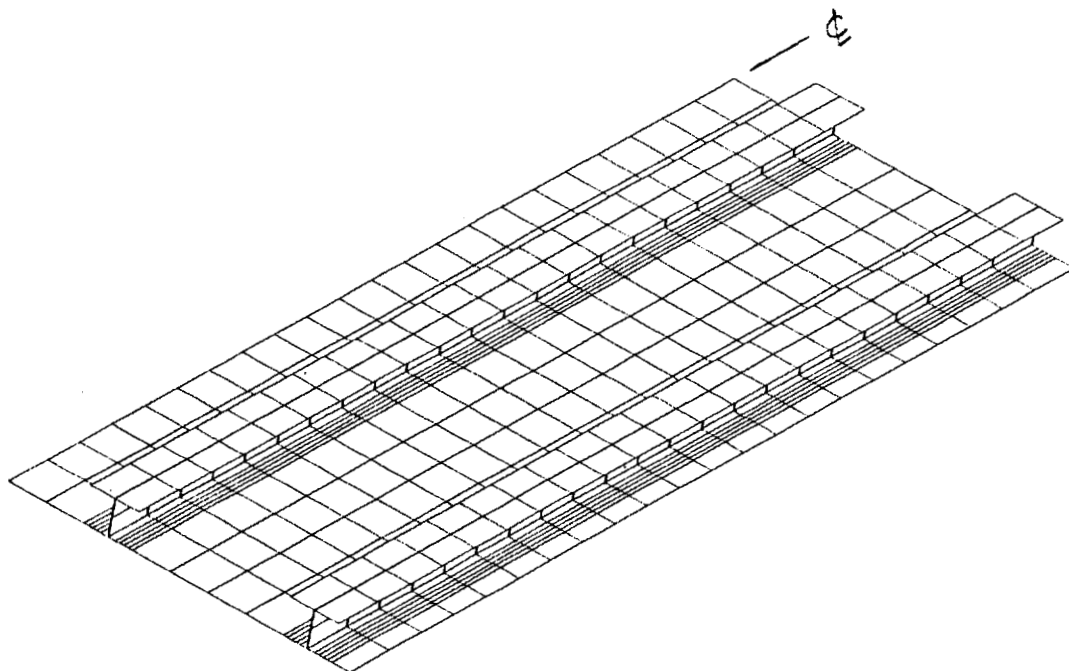


Figure 10 DIAL Model Geometry of Test Panel From Reference 1.

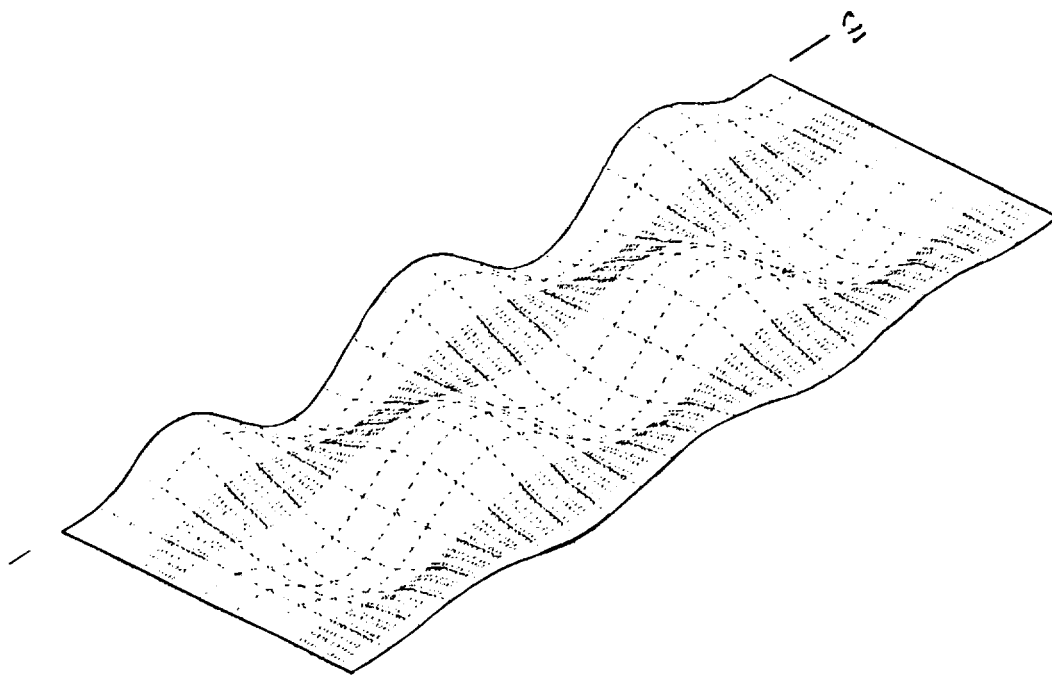


Figure 11 Deflected Shape of DIAL Test Panel Model at Final Load Step

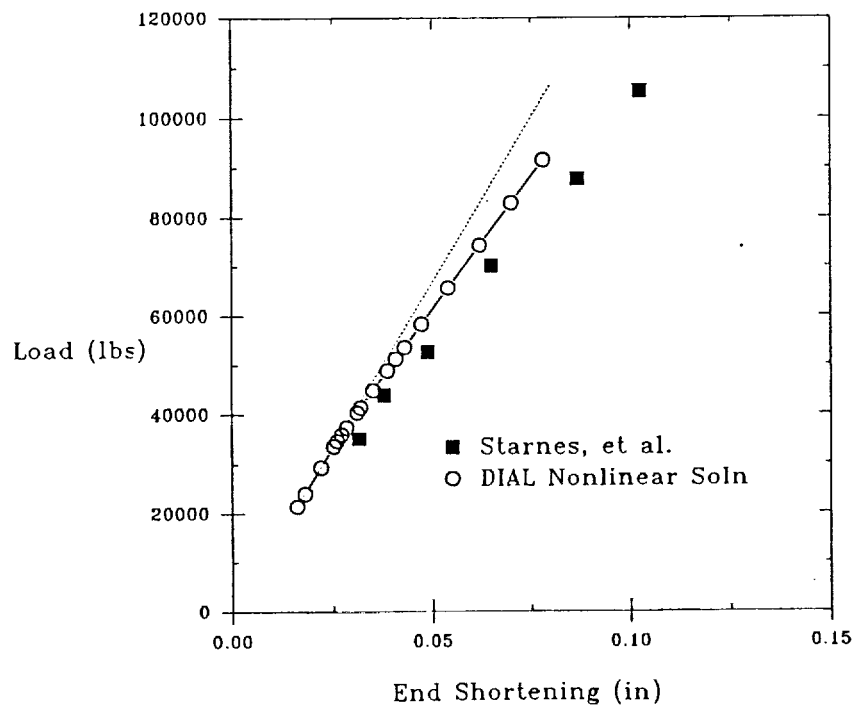


Figure 12 Comparison of Load-Displacement Results from DIAL and from Ref. 1 Test and Analysis

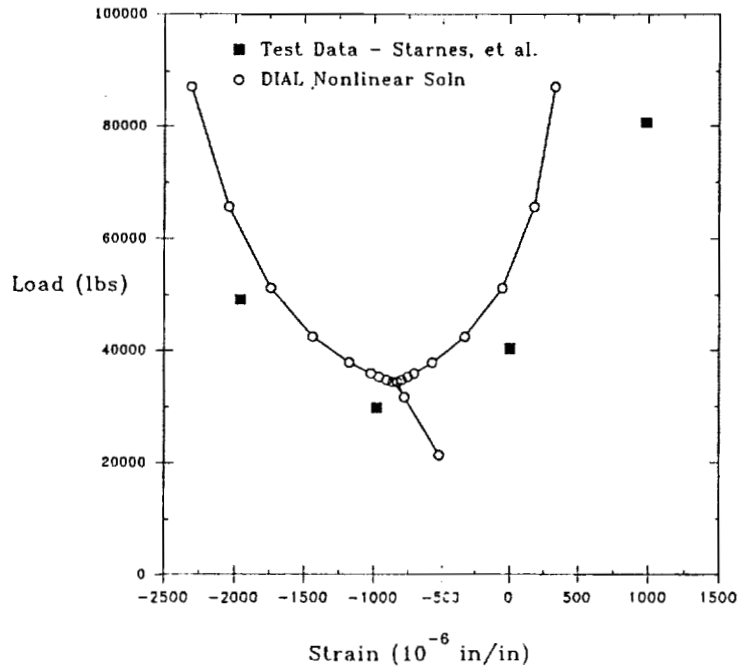


Figure 13 Comparison of Load-Strain Results from DIAL with Test Data (ref. 1)

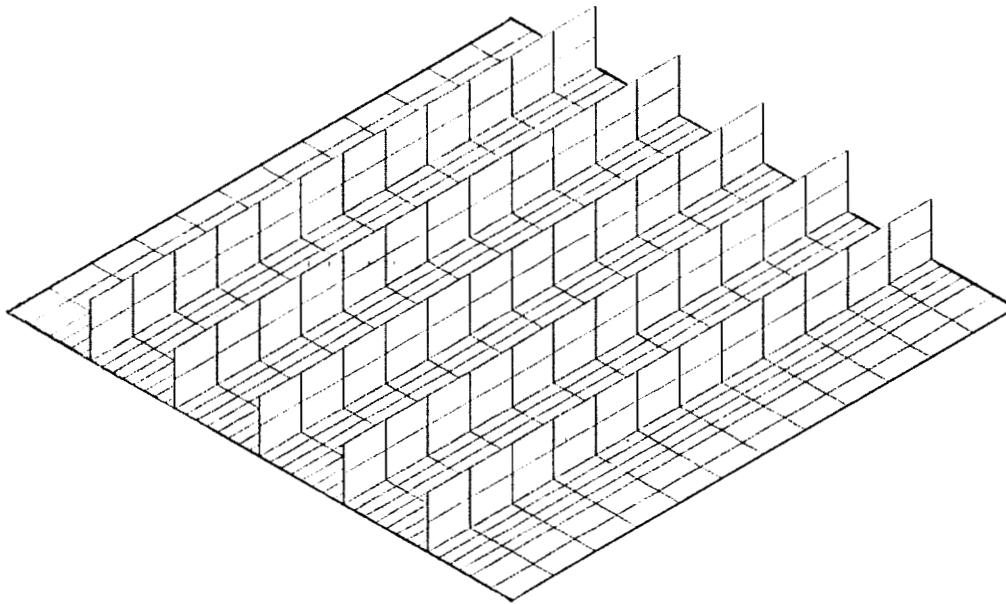


Figure 14 Typical Blade Stiffened Panel Model Geometry from Parametric Study

Number of Stiffeners	SPACING b (in)	HEIGHT h (in)	t bar (in)	N _x co (lb/in)	N _x cr (lb/in)
5	4.0	0.75	.0988	-3019.8	-2789.4
5	4.0	1.00	.1050	-3357.7	-3340.5
5	4.0	1.50	.1175	-4033.3	-5475.0
5	4.0	2.00	.1300	-4708.9	-3897.9
5	4.0	2.25	.1362	-5046.7	-3871.8
3	6.0	0.75	.0913	-2614.5	-1616.7
3	6.0	1.00	.0950	-2817.2	-2175.0
3	6.0	1.50	.1025	-3222.5	-3015.3
3	6.0	1.75	.1063	-3425.2	-3174.0
3	6.0	2.25	.1138	-3830.6	-2417.1
2	8.0	1.50	.0950	-2817.2	-1146.7
2	8.0	2.00	.1000	-3087.4	-2827.1
2	8.0	2.25	.1025	-3222.5	-2982.3

Figure 15 Stiffened Panel Parametric Study Dimensions And Results

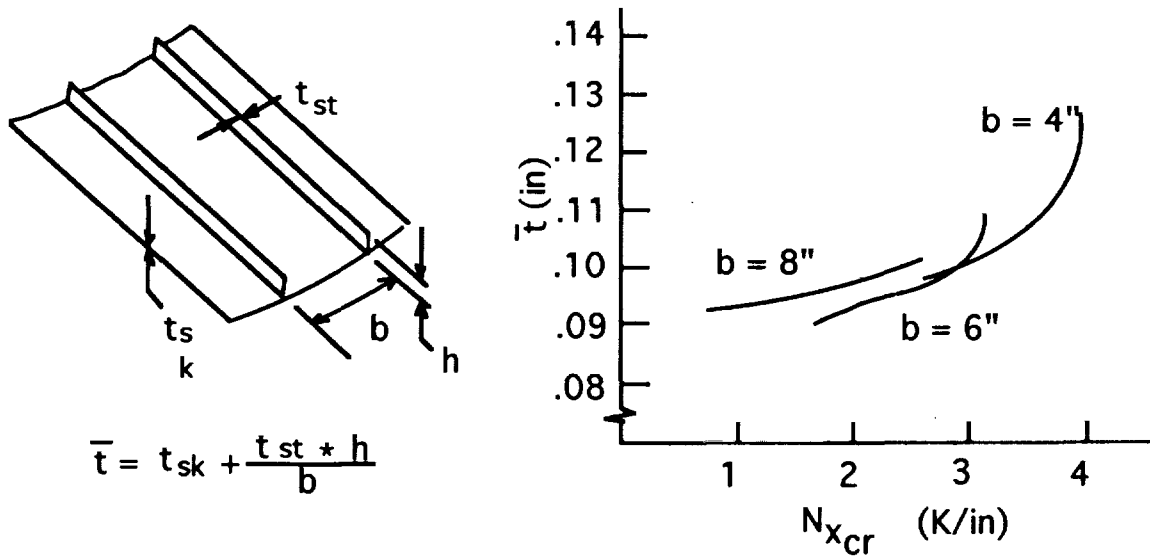


Figure 16 Results of Parametric Analysis of Blade Stiffened Panel

Technology Integration Box Beam Failure Study

M. J. Shuart, D. R. Ambur, D. D. Davis, Jr.,
R. C. Davis, G. L. Farley, C. G. Lotts, and J. T. Wang

NASA Langley Research Center
Hampton, Virginia 23665

524-39
51424

Introduction

Composite structures have the potential to be cost-effective, structurally efficient primary aircraft structures. The Advanced Composites Technology (ACT) Program has the goal to develop the technology to exploit this potential for heavily loaded aircraft structures. As part of the ACT Program, Lockheed Aeronautical Systems Company completed the design and fabrication of the Technology Integration Box Beam (TIBB). The TIBB is an advanced composite prototype structure for the center wing section of the C-130 aircraft and is illustrated in figure 1. Lockheed subjected the TIBB to downbending, upbending, torsion and combined upbending and torsion load conditions to verify the design. The TIBB failed at 83 percent of design ultimate load for the combined upbending and torsion load condition.

The objective of this paper is to describe the mechanisms that led to the failure of the TIBB. The results of a comprehensive analytical and experimental study are presented. Analytical results include strain and deflection results from both a global analysis of the TIBB and a local analysis of the failure region. These analytical results are validated by experimental results from the TIBB tests. The analytical and experimental results from the TIBB tests are used to determine a sequence of events that resulted in failure of the TIBB. A potential cause of failure is high stresses in a stiffener runout region. Analytical and experimental results are also presented for a stiffener runout specimen that was used to simulate the TIBB failure mechanisms.

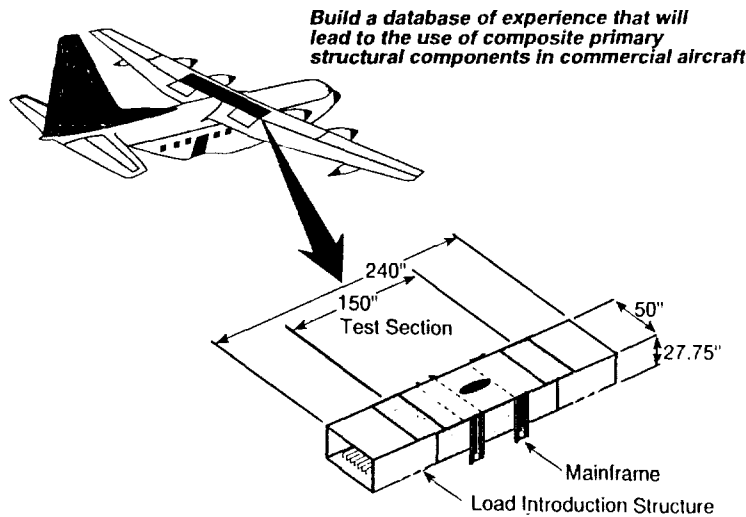
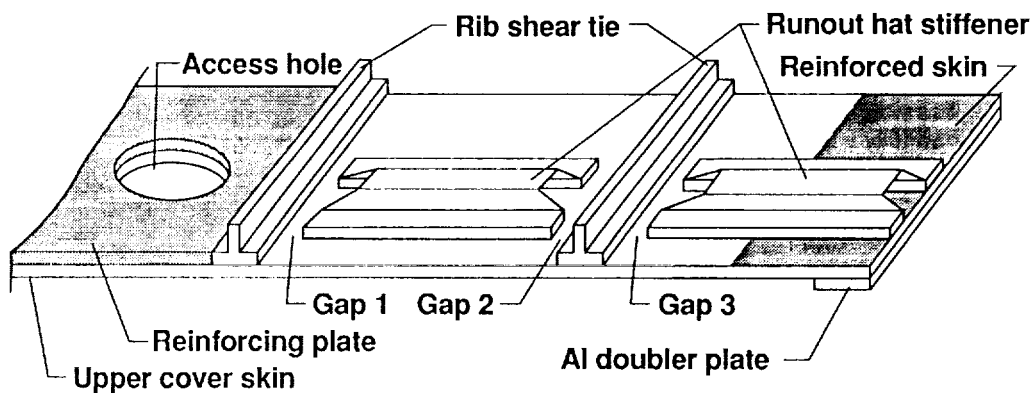


Figure 1

Geometrical Features Contributing to TIBB Failure

Key details of the TIBB geometry are shown in figure 2 to assist in understanding the TIBB response. Discontinuous (or runout) hat stiffeners extend spanwise along the TIBB upper cover panel and are located near the mid-chord of the panel. These stiffeners were included in the design to prevent local buckling and are mechanically fastened and bonded to the upper cover panel skin. The ends of the runout hat stiffeners do not abut against the rib shear ties. Small unstiffened regions of the upper cover panel, or gaps, exist between the flanges of the runout hat stiffeners and the flanges of the rib shear ties. The gap at the end of the hat stiffener closest to the access hole is referred to as Gap 1 and is shown on the figure. The gap at the other end of this hat stiffener is referred to as Gap 2. Gap 2 and Gap 3 are separated by a rib shear tie as shown on the figure. Reinforcing and doubler plates were used in selected regions to add stiffness to the upper cover panel and are also shown on the figure.

The details of the TIBB geometry described above significantly affected the TIBB response. Since the hat stiffener is discontinuous, the location of the neutral axis for the upper cover panel cross-section changes as a function of the spanwise coordinate. The compressive load in the upper cover panel and changing location of the neutral axis cause local bending moments at the ends of the runout hat stiffeners and in the gaps. The gaps do not have reinforcing or doubler plates, and the relatively thin skin in the gaps is subjected to severe bending and compressive strains. The magnitude of the strains in the gaps appears to be a function of both the size of the gap as well as the gap location. The gap strains will be described subsequently in this paper.



- Load path eccentricities are present at hat stiffener discontinuities
- Stiffened regions adjacent to the gaps channel load into the gaps
- Strain magnitude in a gap is a function of gap size and the proximity of the gap to the stiffened region

Figure 2

Understanding the Response of TIBB

An outline of details needed to understand the TIBB response is given in figure 3. The TIBB was tested in a self-equilibrating test fixture. The ends of the TIBB were loaded by hydraulic actuators, and the loads were reacted at mainframe attachments located near the center of the TIBB. The loads applied to the TIBB were substantial and caused significant deformations to occur in the test fixture itself. These deformations were not measured during the test but contributed to an unsymmetric loading of the TIBB as evidenced by the experimental results (ref. 1). The deformations of the TIBB were measured with respect to the floor of the testing laboratory, and these TIBB deformations were used in the analysis to model the loading condition created by the test fixture.

A global/local approach was used to analyze the TIBB. The TIBB deformations were applied as boundary conditions to a global model of the TIBB. Deformations from the global model were used as input boundary conditions to a local model of a portion of the TIBB including the failure region. Results from the global and local analyses were compared to experimental results to validate these analytical models.

- **Test fixture response led to unquantified rigid body motions and unsymmetric loading of TIBB.**
- **Hydraulic actuator displacements and mainframe displacements at the slot and pin locations used as boundary conditions to the TIBB analysis.**
- **Experimental and analytical results used to develop the failure scenario.**
- **Global/local analysis approach was used to understand TIBB response mechanisms.**

Figure 3

Axial Surface Strain for Failure Load Case From Linear Global Analysis

Axial surface strain distributions obtained from an MSC/NASTRAN (ref. 2) global model of the TIBB are shown in figure 4. These strains correspond to the TIBB loading at failure, and this loading is referred to herein as the failure load case. The model used for the present analysis was based on a model developed by Lockheed for the TIBB and has been modified to update laminate stacking sequences and stiffener geometry. This model contains 3,885 quadrilateral, triangular, and bar elements and has 2,763 nodes. The total number of unconstrained degrees of freedom is 16,578.

The exterior surface strain distribution is shown on the TIBB global model in the upper half of the figure. These results do not indicate any unusually high exterior surface strains. A portion of the interior surface strain distribution is shown in the lower half of the figure. The interior surface strain distribution is presented for the upper cover panel region near the observed failure. These results show strains for the skin of the upper cover panel that are greater than -0.01 in./in. in the gap region. The high skin strains are caused by the flange termination and an eccentric load path that induces local bending. The observed TIBB failure extends through the gap region.

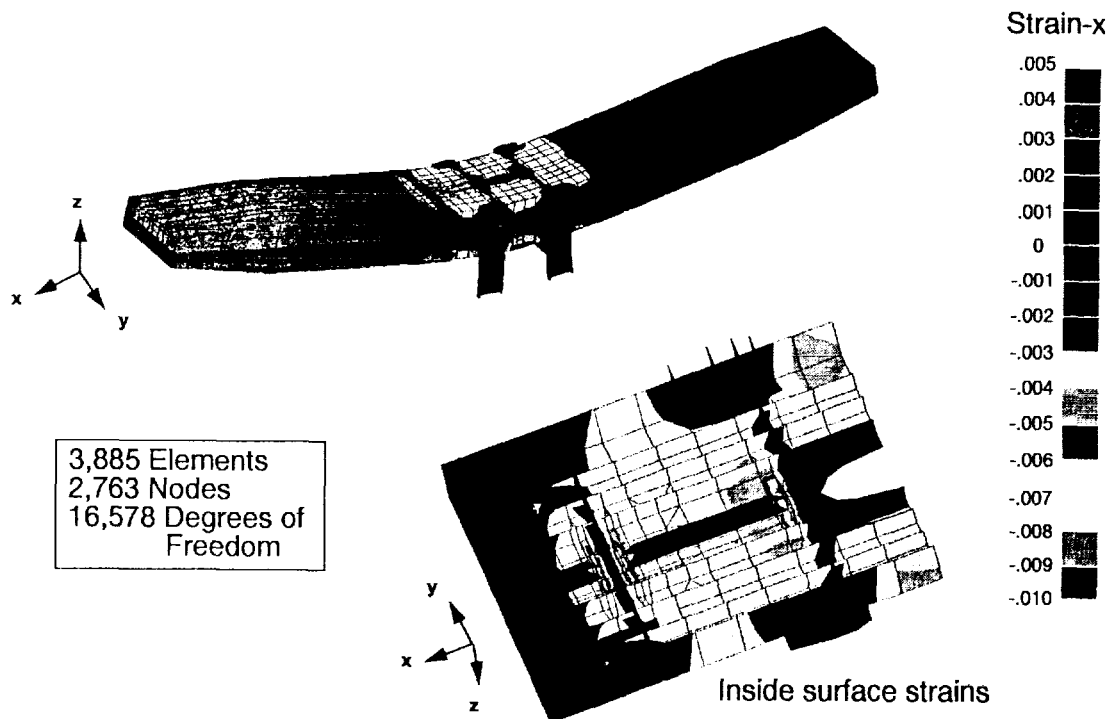


Figure 4

Finite Element Model for Local Analysis

A detailed local finite element model for half of the upper cover panel was developed to understand better the strains at the hat stiffener terminations where failure of the TIBB occurred. The local model is shown in figure 5 and consists of 4338 9-noded Assumed Natural-Coordinate Strain elements (ref. 3) resulting in approximately 88,000 degrees-of-freedom. Displacements from the global analysis were applied to all four edges of the local model as well as at the skin where the rib shear ties attached to the upper cover panel. The local analysis was performed using the COmputational MEchanics Testbed (COMET, ref. 4).

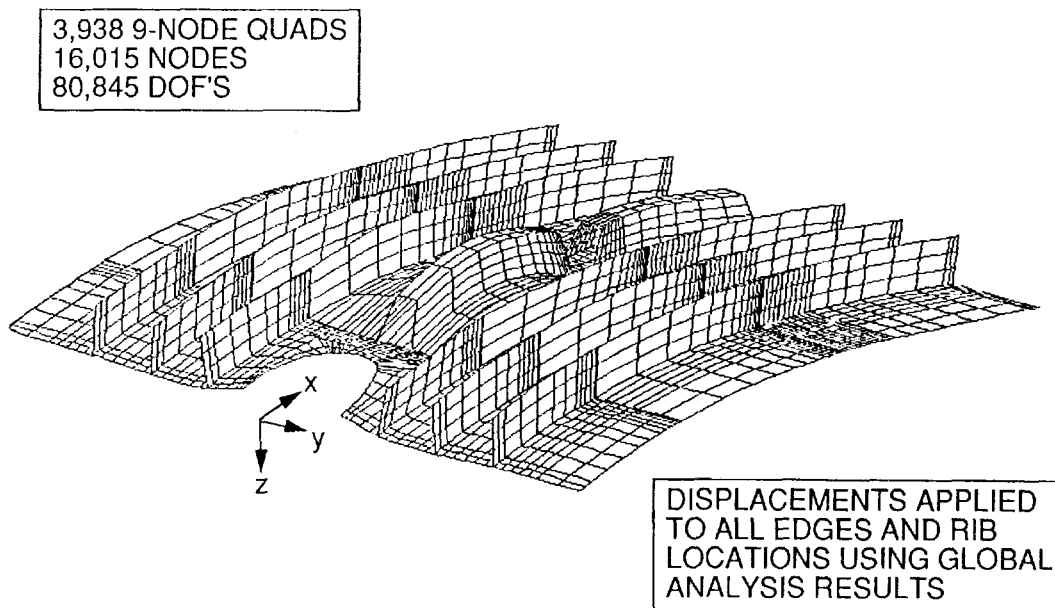


Figure 5

Axial Strains for TIBB Specimen

Axial strains for the TIBB specimen from analyses and test are presented in figure 6 for the failure load case. Three sets of analytical results are presented including local linear analysis, local nonlinear analysis, and global nonlinear analysis. The MSC/NASTRAN computer program (solution 106, V67) was used for the global nonlinear analysis. Strain results for Gages 24 and 25 are shown as open symbols on the figure. These back-to-back gages are located midway between Gap 1 and Gap 2 (see Figure 1) on the top of the hat stiffener. The strains measured by Gage 24 show that the exterior surface of the skin is in compression. The strains measured by Gage 25 show that this region of the hat stiffener is loaded in tension due to the severe bending that results when the TIBB is subjected to upbending load. As mentioned previously, the severe bending is due to the changing location of the cross-section neutral axis along the TIBB span.

The results from the local nonlinear and global nonlinear analyses agree very well with the experimental results. Nonlinear bending was predicted by both analyses. The linear analysis results underestimated the strains at Gage 25 significantly. The strain curve for Gage 25 is highly nonlinear, while the strain curve for Gage 24 is linear. This behavior is due to the fact that the neutral surface for the panel cross-section is much closer to Gage 24 than to Gage 25.

Comparisons of analytical and experimental results were made for other regions of the TIBB and for other load cases using the linear global and nonlinear local analytical models. Generally, good agreement was observed between the analytical and experimental results thereby verifying the analytical models.

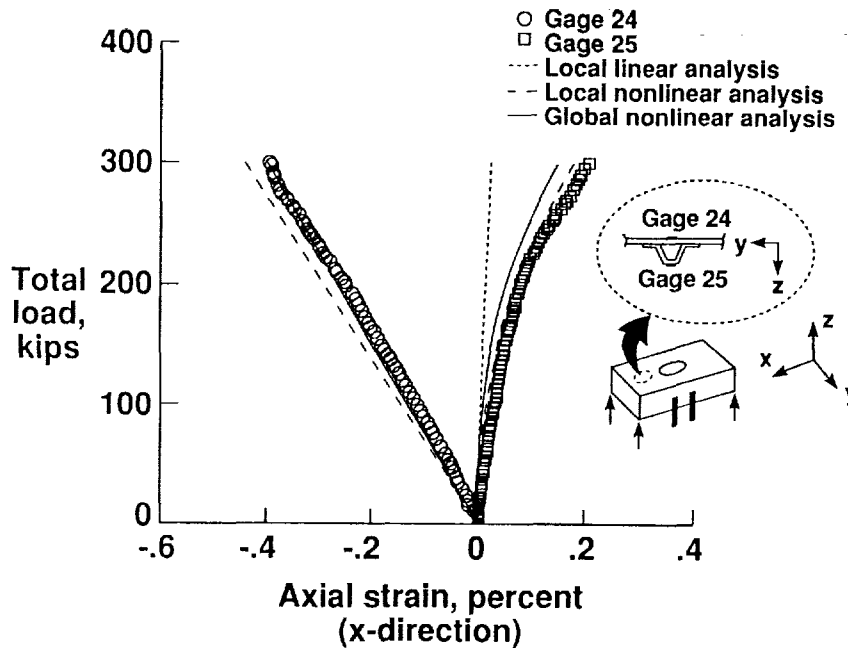
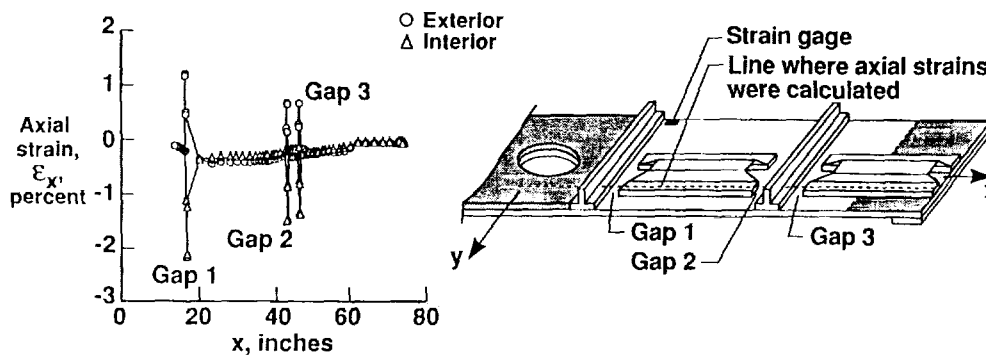


Figure 6

Failure Scenario of TIBB

The failure scenario of TIBB was developed based on the analytical results and available test results. Because the TIBB failure was catastrophic and instrumentation in the failure region was insufficient, the failure sequence could not be determined solely from the test data. The results shown on figure 7 illustrate how experimental observations were used with the verified analytical models to develop the TIBB failure scenario. Strain results along the center line of the runout hat stiffener flange from a local nonlinear analysis are plotted in the left half of the figure. This center line is shown as a dashed line on the TIBB sketch in the right half of the figure. Very high strains are found at each gap. The highest strain calculated by the analysis is found at Gap 1. The gap exterior skin surfaces are subjected to tension, and the gap interior skin surfaces are subjected to compression. These strain results indicate that the skin in the gap regions is subjected to severe bending which may cause compression or interlaminar shear failure in the laminate.

Test results for strain gages located near Gap 1 showed a significant strain change at 287 kips test load when a loud noise was heard. The TIBB was visually inspected while the load was held constant. However, no damage was observed. These observations combined with the analytical results suggest that failure initiated at Gap 1. The damage at Gap 1 may not have been detected during inspection since this gap region was not identified as a critical region for the TIBB. After inspection, the test was continued and the TIBB ultimately failed at 300 kips at Gap 2 which is also predicted to be a high stress region. Load redistribution subsequent to the failure in Gap 1 may have caused Gap 2 to become the critical stress region leading to the observed failure in Gap 2.



- Gap 1 is suspected to be the critical gap prior to the initial failure event
- A load noise was heard at 287 kips prior to ultimate failure. Load was held constant while the TIBB was inspected. No damage was observed.
- Based upon strain data from a gage near gap 1 the noise may have been associated with a local failure in or near gap 1. The load redistributed making gap 2 critical.
- When loading continued the TIBB ultimately failed at 300 kips in gap 2

Figure 7

Selection of Stiffener Runout Test Specimen

A Stiffener Runout Test Specimen (SRTS) was defined to simulate the response of the TIBB in the region of failure and to validate the TIBB failure scenario. The SRTS was cut from an undamaged region of the TIBB as indicated by the dashed rectangle on the illustration in figure 8. The SRTS contained gaps and similar design details as those contained in the TIBB failure region (see detail A-A). The SRTS was approximately 60 in. long and 33 in. wide and was tested in uniaxial compression.

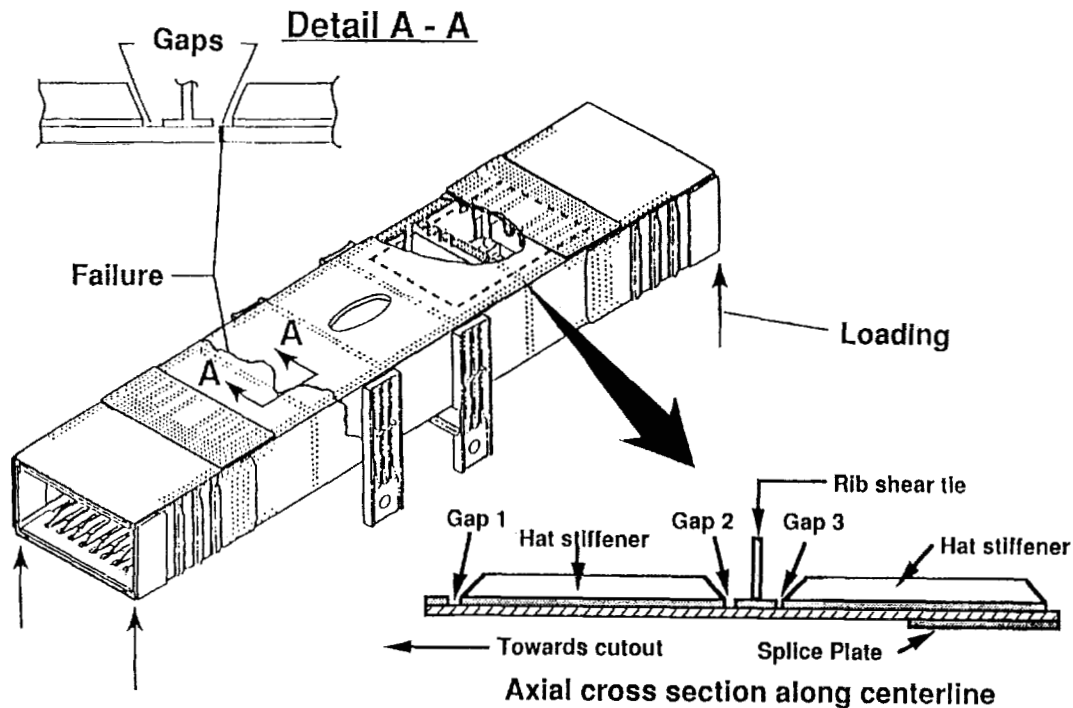


Figure 8

SRTS Specimen Deformed Geometry Axial Compression Load = 430 kips

An extensive parametric study was performed to determine the proper test specimen geometry, loading, and boundary conditions to best simulate the response of the TIBB upper cover at failure. A half model of the SRTS was developed with approximately 32,000 degrees of freedom and is shown in figure 9. The analyses indicated that continuous knife-edge supports were required along both sides of the panel during testing and that the cap of the hat stiffener should not be loaded directly in compression. The deformed model is shown in the figure and illustrates the bending of the hat stiffener that is characteristic of the TIBB failure mode. Axial strain contours are superimposed on the deformed model, and they indicate high stresses in the gap regions.

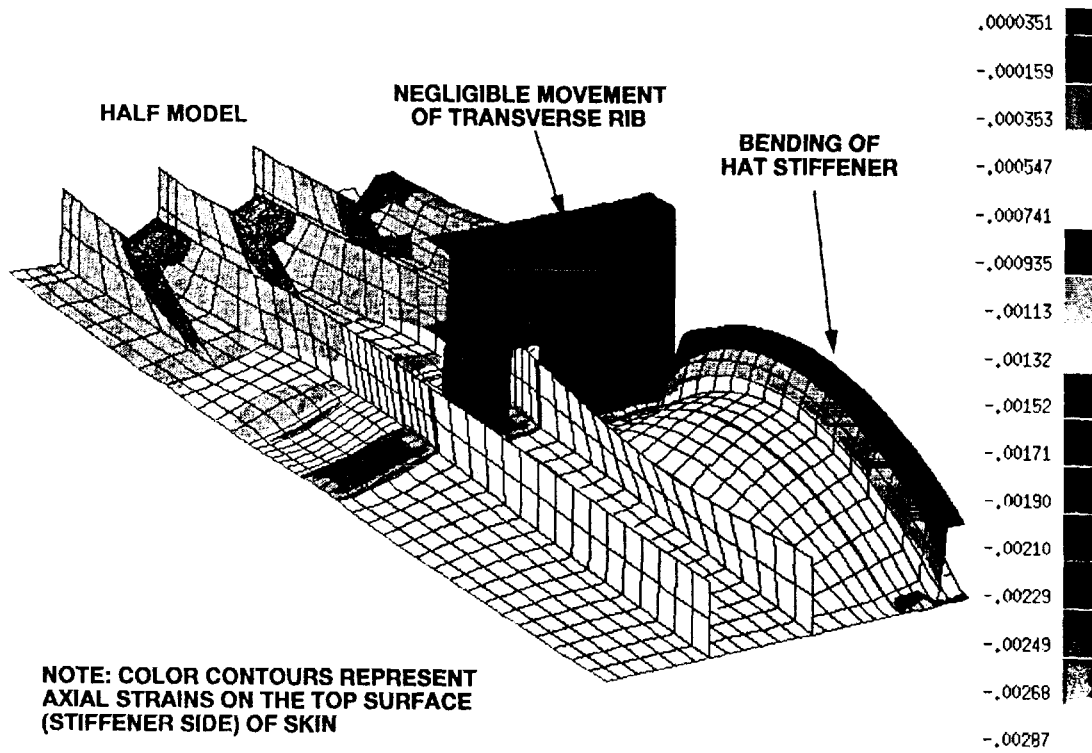


Figure 9

Test Objectives and Program for SRTS

The test objectives and program for the SRTS are outlined in figure 10. The SRTS test program was designed to correlate the response and failure mechanisms predicted by the finite element analysis with the experimental response. Preloading tests at approximately 20 to 50 percent of the predicted initial failure loads were conducted first to obtain experimental results for validating the predicted response of the SRTS and to make necessary modifications to the test setup, if needed. The specimen initial failure was predicted to occur in Gap 3 at a total load of 460 kips. After processing this information and ensuring that the response was as predicted, the SRTS was loaded to failure. Although the TIBB failed through Gap 2, the predicted SRTS failure in Gap 3 still would confirm both the severe bending failure mechanism as well as the sensitivity of stresses in a gap to the gap geometry.

- **Test Objectives**
 - **Simulate TIBB response and failure mechanisms**
 - **Correlate response and failure mechanisms with predictions**

- **Test Program**
 - **Apply 100- and 250-kip uniaxial compression load to SRTS to understand response mechanisms and validate analysis**
 - **Apply uniaxial compressive load to SRTS until failure; failure predicted at 460 kips gap 3**

Figure 10

Axial Displacement of the SRTS

Experimental results and a photograph of the SRTS are shown in figure 11. A comparison between experiment and analysis of the end shortening and axial rib displacement of the SRTS was performed. An LVDT displacement transducer was attached to the upper load platen of the test machine to measure the overall shortening of the panel as a function of applied load. Another LVDT was attached to the rib along the longitudinal centerline of the panel and at the most out-of-plane part of the rib. The measured displacement of the LVDT on the rib consists of both axial panel shortening and rib rolling.

The experimentally measured and analytically predicted end shortening of the SRTS was nearly linear to failure. The predicted end shortening was less than the measured end shortening for a given load level which implies that the predicted panel membrane stiffness was greater than the corresponding measured stiffness. The difference in panel stiffness is attributed to the coarse level of finite element discretization used in this region resulting in a stiffer structure and to the nonuniform thickness distribution along the longitudinal axis of the panel.

The experimentally measured axial rib displacement was nearly linear until approximately 500 kips of load was applied which resulted in large displacements. However, the predicted response was nearly linear to failure. The highly nonlinear response of the rib is due to the rolling of the rib. During the linear portion of the load-deflection response, the good agreement between experimental and analytical results is attributed to the high level of discretization and the uniform thickness along the length of the SRTS. However, the mechanisms that produced rib rolling were not adequately represented by the analysis.

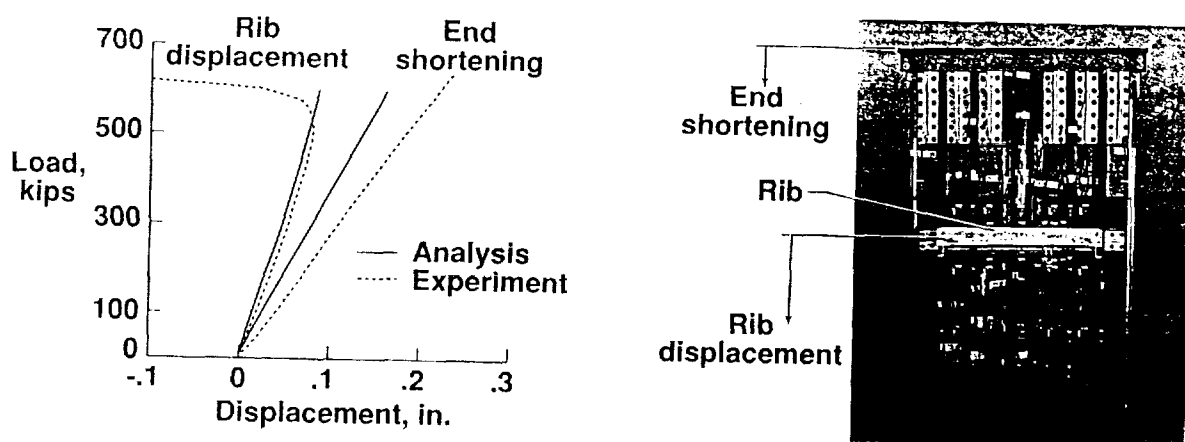


Figure 11

Global Strain Response for the SRTS

Far-field (or global) strain results are presented in figure 12. Over 190 strain gages were mounted to the SRTS to measure global strain response and the strain response in the gap and near the rib. The strain gages away from rib provide an indication of the global response of the panel and determine whether the load is evenly distributed in the panel. A comparison is made between the predicted and measured global strains. Strain gages used in this comparison were located on (A) the hat stiffener above the rib (upper hat stiffener), (B) the center of the hat stiffener below the rib (lower hat stiffener), and (C) a blade stiffener midway between the rib and the potted end. Gages were located on both the stiffener and skin sides of the SRTS to quantify any local bending.

In general, good agreement was achieved between all measured and predicted global strains. The strains below the rib (e.g., locations B and C) were more accurately predicted than strains above the rib. Considerable bending of the lower hat stiffener occurred producing a localized nonlinear response. A similar response occurred in the TIBB. The strains on the blade stiffeners were linear to failure with little or no blade stiffener bending occurring. The hat stiffener above the rib exhibited a nearly linear response to failure with little bending. The differences in response of the hat stiffeners are attributed to the local reinforcement of the skin around the upper hat stiffener.

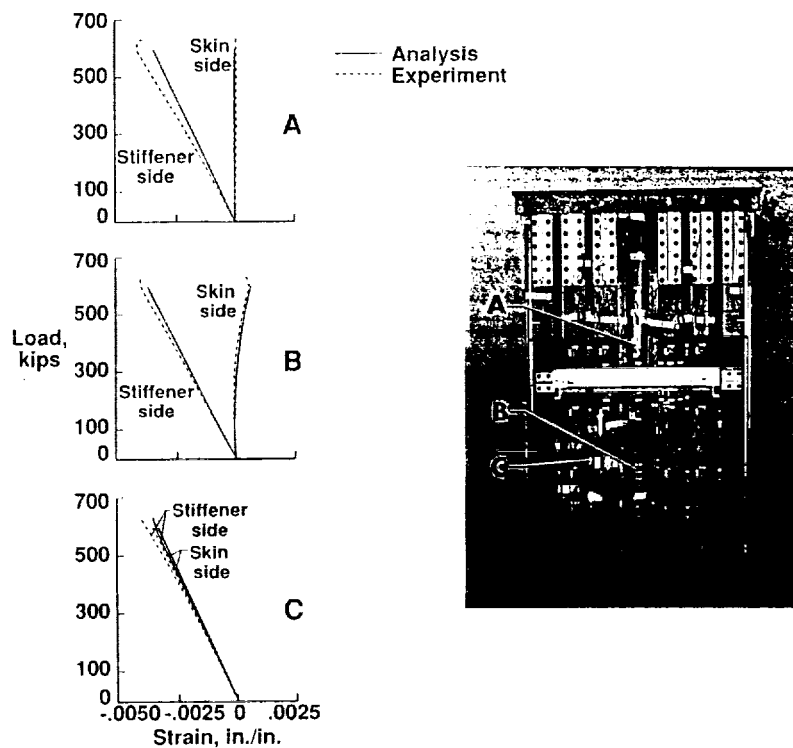


Figure 12

Strains in and Near Gaps 2 and 3

Strain results near Gaps 2 and 3 are shown in figure 13. Back-to-back strain gages were mounted on the SRTS in Gap 2, location (A), and on both sides of the rib outside of the gaps, locations (B) and (C). The purpose of these gages was to quantify the magnitude of the strains in the gap, to determine the extent of bending that occurred in the gap, and to compare these results with predictions.

Surface strains in Gap 2 did not exceed -0.8 percent. A considerable amount of bending occurred as indicated by the strain reversal occurring at approximately 500 kips. The strain outside of Gap 2, such as at locations (B) and (C), was nearly linear until the rib began to roll at approximately 500 kips. The maximum measured strain occurred at location (C) and was approximately -0.9 percent. The agreement between predicted and measured strain in the gap was poor. The poor agreement is attributed to the finite element modeling assumptions of the elements in the gap and the use of strain gages to measure strain in a region of high strain gradients. Reasonable agreement, prior to rolling of the rib, was achieved between experiment and analysis for skin side strains near the rib, however poor agreement occurred on the stiffener side.

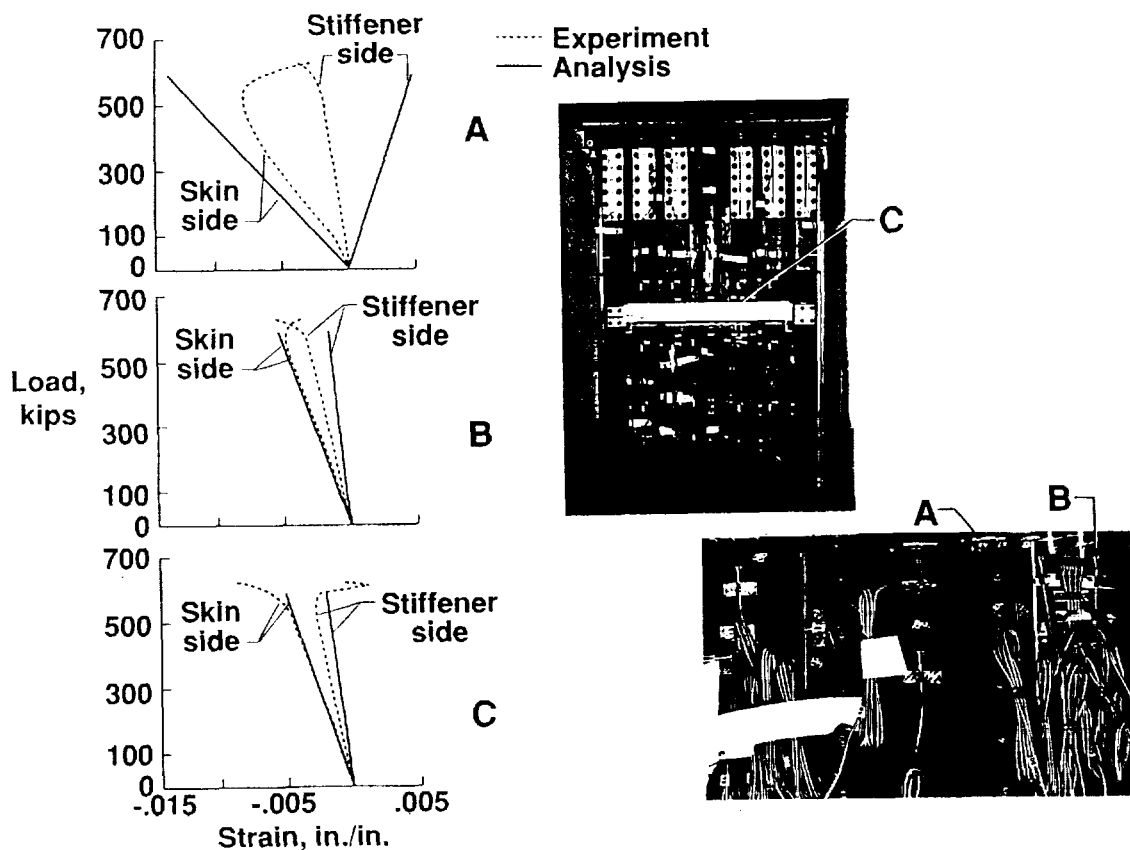
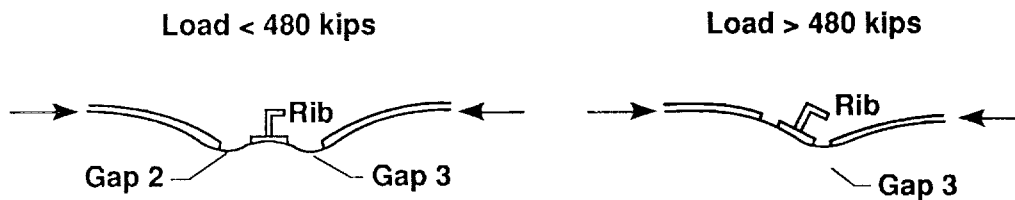


Figure 13

SRTS FAILURE SCENARIO

The SRTS failure scenario is outlined in figure 14. The response of the SRTS resembled the response of the TIBB's upper cover panel at loads below 350 kips. Due to the load path eccentricities in the SRTS, the skin in Gaps 2 and 3 formed "bucket-like" regions in Gaps 2 and 3. For loads above 350 kips the rib began to roll towards Gap 3. As the rib rolled, the "bucket" in Gap 2 began to flatten, thus relieving the stresses in Gap 2 but creating a hinge at Gap 3. Significant audible sounds were recorded at 467 and 474 kips that suggested that a local failure event had occurred. At approximately 500 kips, the rib response became nonlinear, possibly due to the local failure events and the increased bending of the hat stiffener. As loading continued, high stresses in Gap 3 precipitated final failure of SRTS at 625 kips.



- SRTS response resembled TIBB upper cover panel response. SRTS response beyond 350-kip load involved significant bending of the hat stiffener and rolling of the rib.
- SRTS response relieved stresses in gap 2 but created a hinge at gap 3.
- Significant audible sounds were registered at 467- and 474-kip loads that suggested local failure events.
- As loading continued, high stresses in gap 3 precipitated final failure of SRTS at 625 kips.

Figure 14

Concluding Remarks

A thorough analytical and experimental study has been completed for the failure of the Technology Integration Box Beam (TIBB). Nonlinear finite element analyses were used to predict accurately the TIBB response and were verified by experimental results. Experimental and analytical results indicate that the TIBB failure initiated in Gap 1 between a rib and a terminated stiffener and that subsequent load redistribution resulted in the observed failure in Gap 2 between a rib and a terminated stiffener. A Stiffener Runout Test Specimen (SRTS) was defined to simulate the TIBB response in the failure region and to validate the TIBB failure scenario. A detailed parametric study of the SRTS was conducted prior to testing to determine the specimen geometry and boundary conditions needed to simulate the TIBB failure and to predict the SRTS response. The SRTS response and failure was observed to resemble the TIBB response and failure. The predicted SRTS response correlated reasonably well with the experimental results up to initial failure. The predicted failure mode and location for the SRTS agreed with the observations.

References

1. Shuart, M. J.; Ambur, D. R.; Davis, D. D., Jr.; Davis, R. C.; Farley, G. L.; Lotts, C. G.; and Wang, J. T.: Technology Integration Box Beam Failure Study: Status Report. Proceedings of the Second NASA Advanced Composites Technology Conference, Lake Tahoe, NV, November 4-7, 1991, NASA CP 3154, pp. 99-111.
2. Anon: MSC/NASTRAN User's Manual, Version 65, Vols. 1 and 2. MacNeal-Schwendler Corporation.
3. Park, K. C.; and Stanley, G. M.: A Curved C^0 Shell Element Based on Assumed Natural-Coordinate Strains. Journal of Applied Mechanics, vol. 108, 1986, pp. 278-290.
4. Knight, N. F., Jr.; and Stroud, W. J.: Computational Structural Mechanics: A New Activity at the NASA Langley Research Center. NASA TM 87612, 1985.
5. Lotts, C. G.; Greene, W. H.; McCleary, S. L.; Knight, N. F.; Paulson, S. S.; and Gillian, R. E.: Introduction to the Computational Structural Mechanics Testbed. NASA TM 89096, 1987.



**A GLOBAL/LOCAL ANALYSIS METHOD FOR
TREATING DETAILS IN STRUCTURAL DESIGN**

Mohammad A. Aminpour*

Analytical Services and Materials, Inc.

Susan L. McCleary**

Lockheed Engineering and Sciences Company

Jonathan B. Ransom†

NASA Langley Research Center

525-39
51425

Abstract

A method for analyzing global/local behavior of plate and shell structures is described. In this approach, a detailed finite element model of the local region is incorporated within a coarser global finite element model. The local model need not be nodally compatible (i.e., need not have a one-to-one nodal correspondence) with the global model at their common boundary; therefore, the two models may be constructed independently. The nodal incompatibility of the models is accounted for by introducing appropriate constraint conditions into the potential energy in a hybrid variational formulation. The primary advantage of this method is that the need for transition modeling between global and local models is eliminated. Eliminating transition modeling has two benefits. First, modeling efforts are reduced since tedious and complex transitioning need not be performed. Second, errors due to the mesh distortion, often unavoidable in mesh transitioning, are minimized by avoiding distorted elements beyond what is needed to represent the geometry of the component. The method is applied herein to a plate loaded in tension and transverse bending. The plate has a central hole, and various hole sizes and shapes are studied. The method is also applied to a composite laminated fuselage panel with a crack emanating from a window in the panel. While this method is applied herein to global/local problems, it is also applicable to the coupled analysis of independently modeled components as well as adaptive refinement.

Nomenclature

a minor axis of ellipse
b major axis of ellipse
E Young's modulus

* Research Scientist, 107 Research Drive, Hampton, VA, 23666.

** Senior Engineer, 144 Research Drive, Hampton, VA, 23666.

† Aerospace Engineer, Mail Stop 240, Hampton, VA, 23665.

\mathbf{f} generalized force vector
 i superscript associated with interface nodes
 j subscript associated with subdomains
 k subscript associated with interface segment
 L length
 \mathbf{K} stiffness matrix
 K_t stress concentration factor
 M_x moment resultant in x-direction
 $(M_x)_0$ applied far field moment resultant in x-direction
 m number of interface nodes for subdomains
 \mathbf{N} generalized displacement shape function matrix
 N_x stress resultant in the x-direction
 $(N_x)_0$ applied far field stress resultant in x-direction
 \mathbf{n} outward unit normal to subdomain interface
 n number of pseudo-nodes on interface
 o superscript associated with non-interface nodes
 p number of degrees of freedom per node
 \mathbf{q} generalized displacement vector
 \mathbf{R} interpolation matrix for Lagrange multipliers
 S interface path
 \mathbf{T} interpolation matrix for interface displacements
 τ superscript indicating transpose of a matrix
 t thickness
 \mathbf{u} displacement vector along the interface for subdomains
 \mathbf{v} displacement vector on the interface, S
 W width
 α vector of unknown coefficients for Lagrange multipliers
 δ variational operator
 λ vector of Lagrange multipliers
 ν Poisson's ratio
 σ stress tensor
 σ_z normal stress component in z-direction
 Π total potential energy
 Ω domain of discretization

Introduction

The finite element method is the most widely used structural analysis tool mainly due to its flexibility in modeling complicated geometries. While the finite element method can be used to make accurate calculations of detailed stresses, the method is not generally efficient for the design phase because it requires extensive modeling and is computationally expensive. However, with increased utilization of composite materials in aerospace structures, there is a need for detailed modeling at material or geometric discontinuities (e.g., ply dropoffs, cutouts, and stiffener runouts) in order to predict accurately the strength and failure modes of these structures early in the design process. Analytical methods which reduce modeling time while providing the necessary detailed stress and strain states are therefore needed. Global/local analysis is often used to reduce modeling complexities and to predict detailed stress and strain states in structural components.

The global/local analysis of plate and shell structures has, in the past, primarily been accomplished using one of two approaches. The first approach is usually used when the region of interest is not known prior to an analysis^{1,2}. In this approach, results from a global analysis are interpolated and applied as boundary conditions on an independent detailed local model. While this approach leads to a smaller overall problem size and simplified modeling, methods developed using the approach usually provide no interaction between the local and global models. To overcome this problem, an iterative global/local method³ has recently been proposed that provides for this interaction. This method, however, has been applied only to mesh discretizations with a one-to-one nodal correspondence across the boundary between subdomains. Finite element meshes which preserve this one-to-one nodal correspondence across the boundary between subdomains will hereafter be referred to as nodally compatible.

The second approach, usually used when the region of interest is known *a priori*, typically involves a single finite element analysis with the finite element mesh highly refined in the known region of interest⁴⁻⁶. This approach may, however, lead to highly complex modeling because mesh transitioning between the local region and the rest of the model is essential to obtain a solution to the problem in a timely and cost effective manner.

Recently, a third approach, which combines the desirable features of the first two approaches, has been the subject of research. The methods developed using this approach provide modeling flexibility (i.e., they permit independent modeling of global and local subdomains) as well as a coupling of the global and local analyses (i.e., they provide the necessary interaction between the global and local models). Some of these methods have concentrated on the development of techniques for parallel computers⁷⁻⁸ while others have used some form of multi-point constraints along the common subdomain boundaries⁹⁻¹⁰. In reference 11, three formulations for coupling the independently modeled regions were developed and studied. The hybrid variational formulation was shown to be the most robust and accurate of the three examined.

The purpose of this paper is to describe a coupled global/local analysis method developed using the third approach. This method couples global and local subdomains using an independent function along the interface between the subdomains¹¹. The nodal compatibility of the models is accounted for by introducing appropriate constraint conditions into the total potential energy functional.

The description of the coupled global/local analysis method is presented, followed by two applications of the method to plate and shell structures. The first application is a plate loaded in tension and transverse bending. The plate has a central hole, and various hole sizes and shapes are studied. In these analyses, the region in the vicinity of the hole is taken to be the local region; the remainder of the panel is taken to be the global region, and the two regions are modeled independently. The second application is a composite laminated fuselage panel with a crack emanating from a window in the panel. In this analysis, the region in the immediate vicinity of the crack is taken to be the local region and

the remainder of the panel is taken to be the global region. While these demonstration problems are typical global/local problems, the present coupled analysis method is also applicable to the analysis of independently modeled components and may be used to perform adaptive refinement.

Description of Coupled Global/Local Analysis Method

The coupled analysis method presented herein allows the independent modeling of different regions or components without concern for the nodal compatibility between the finite element models. Transition modeling between a region with a fine mesh and a region with a coarse mesh is no longer necessary. This approach prevents changes in the modeling of the local region from affecting the modeling in the global region. For example, with a judiciously chosen local model, an analyst may perform a geometrically parametric study of hole size and shape by changing the mesh in the immediate vicinity of the hole, without having to change the modeling of the global region.

This method does not improve the performance of the finite elements used in the analysis and therefore does not improve the quality of the results attainable by a particular element. However, by eliminating or reducing transition modeling, the introduction of distorted elements into the finite element model is limited to what is necessary to represent the geometry of the component. Therefore, no additional errors associated with mesh distortion are introduced. The elimination of unnecessary element distortion errors allows the use of coarser meshes, and, therefore, the same qualitative results may be obtained with a smaller number of degrees of freedom.

The method described herein may generally be applied to connect an arbitrary number of independently modeled subdomains. However, in the following discussion, the mathematical formulation will be described in terms of two subdomains and a single, multi-segmented interface. Consider a two-dimensional domain, Ω , that is modeled as two independently discretized subdomains, Ω_1 and Ω_2 , as shown in Figure 1. The interface, S , is modeled as two semi-independent line segments. Each segment of the interface, S , is discretized with evenly spaced "pseudo-nodes" (open circles in Figure 1) which need not conform to the discretization of either of the subdomains. An interface such as that shown in Figure 1 is considered to be a single, two-segmented interface (segments AB and BC in Figure 1). At the corner (point B in Figure 1), a pseudo-node must exist.

The displacement vector along each interface segment, k , may be written as

$$\mathbf{v} = \mathbf{T}\mathbf{q}_k, \quad (1)$$

where \mathbf{T} is a $p \times pn_k$ matrix of interpolating functions, and \mathbf{q}_k is a vector of pn_k generalized displacements associated with the n_k interface pseudo-nodes each having p degrees of freedom. The specific form of the matrix \mathbf{T} depends on the type of function chosen and the number of evenly spaced pseudo-nodes, n_k , selected along segment k of the interface, S . As in reference 11, cubic splines are used to describe the

displacement field vector, \mathbf{v} , along each segment of the interface, S . Equation 1 is assumed to be valid along each segment (segments AB and BC in Figure 1); at the interface corner (point B in Figure 1), the values from each interface segment are constrained to be the same.

In the hybrid variational formulation, the total potential energy equation is modified to include an integral form for the compatibility between the interface and the subdomains and is given by

$$\Pi = \Pi_{\Omega_1} + \Pi_{\Omega_2} + \int_S \lambda_1^T (\mathbf{v} - \mathbf{u}_1) ds + \int_S \lambda_2^T (\mathbf{v} - \mathbf{u}_2) ds \quad (2)$$

where Π_{Ω_j} is the total potential energy, λ_j is a vector of Lagrange multipliers, and \mathbf{u}_j is the displacement field vector along the interface for subdomain j . The constraint integrals are added to the functional to enforce the continuity, in the variational sense, of displacements across the interface. Equation 2 corresponds to the "double layer interface" or "frame" method of the hybrid variational principle¹² and has in the past been used primarily to enforce compatibility between adjacent elements that have incompatible assumed displacement shape functions within the context of a nodally compatible finite element model¹³⁻¹⁶. Herein, however, the variational statement in equation 2 is utilized to enforce compatibility between nodally incompatible finite element models.

Assuming that the displacement boundary conditions are satisfied, the stationary condition for the modified total potential energy for arbitrary \mathbf{u}_j in the subdomains, arbitrary \mathbf{v} on the interface, S , and arbitrary λ_j on the interface parts of the subdomains, results in the following Euler equations

$$\delta\Pi = 0 \Rightarrow \begin{cases} \lambda_j = (\sigma\mathbf{n})_j; & j = 1, 2 \\ \lambda_1 + \lambda_2 = \mathbf{0} \\ \mathbf{u}_j = \mathbf{v}; & j = 1, 2 \end{cases} \quad \text{on } S. \quad (3)$$

These equations are in addition to the usual Euler equations which satisfy the equilibrium equations and traction boundary conditions. In equation 3, σ is the stress tensor and \mathbf{n} is the outward unit normal to the subdomain interface. Thus, equation 3 states that λ_j represent the tractions on the interface for subdomain j and that the sum of the tractions across the interface is zero (i.e., equilibrium is maintained, in the variational sense, across the interface). Equation 3 also states that the displacement field on the interface for subdomain j is equal to the assumed displacement field, \mathbf{v} , along the interface (i.e., displacement continuity is maintained, in the variational sense, across the interface).

In the finite element discretization, the displacements, \mathbf{u}_j , and the Lagrange multipliers, λ_j , are independently approximated for each element along the interface, and the displacement field, \mathbf{v} , is approximated on the interface, S , as discussed previously. The displacements, \mathbf{u}_j , along the interface are expressed in terms of unknown nodal displacements, \mathbf{q}_j^i , as $\mathbf{u}_j = \mathbf{N}_j \mathbf{q}_j^i$, and the Lagrange multipliers, λ_j , are expressed in terms of unknown coefficients, α_j , as $\lambda_j = \mathbf{R}_j \alpha_j$, where \mathbf{N}_j and \mathbf{R}_j are matrices of interpolating functions. The interpolating functions in the matrix, \mathbf{R}_j , are taken to be constant parameters for linear elements and linear functions for quadratic elements. With these assumptions,

equation 2 may be rewritten as

$$\Pi = \Pi_{\Omega_1} + \Pi_{\Omega_2} + \alpha_1^T M_1^T q_1^i + \alpha_2^T M_2^T q_2^i + \alpha_1^T G_1^T q_s + \alpha_2^T G_2^T q_s \quad (4)$$

where M_j and G_j are integrals on the interface defined in terms of R_j , N_j , and T as

$$M_j = - \int_S N_j^T R_j ds \quad \text{and} \quad G_j = \int_S T^T R_j ds \quad ; \quad j = 1, 2 \quad (5)$$

Taking the first variation of the modified total potential energy with respect to the independent variables (q_j^i , q_j^o , q_s , α_j , $j = 1, 2$) and setting it to zero yields the system of equations

$$\begin{bmatrix} K_1^{ii} & K_1^{io} & 0 & 0 & 0 & M_1 & 0 \\ K_1^{oi} & K_1^{oo} & 0 & 0 & 0 & 0 & 0 \\ 0 & 0 & K_2^{ii} & K_2^{io} & 0 & 0 & M_2 \\ 0 & 0 & K_2^{oi} & K_2^{oo} & 0 & 0 & 0 \\ 0 & 0 & 0 & 0 & 0 & G_1 & G_2 \\ M_1^T & 0 & 0 & 0 & G_1^T & 0 & 0 \\ 0 & 0 & M_2^T & 0 & G_2^T & 0 & 0 \end{bmatrix} \begin{bmatrix} q_1^i \\ q_1^o \\ q_2^i \\ q_2^o \\ q_s \\ \alpha_1 \\ \alpha_2 \end{bmatrix} = \begin{bmatrix} f_1^i \\ f_1^o \\ f_2^i \\ f_2^o \\ 0 \\ 0 \\ 0 \end{bmatrix} \quad (6)$$

where q_j is the generalized displacement vector, f_j is the external force vector, and K_j is the stiffness matrix associated with subdomain j . The system of equations given by equation 6 is symmetric, not banded and not positive definite. Thus, a general solver which uses Gaussian elimination and operates on a dense matrix is used in this case. Therefore, modeling efficiency has been achieved at the expense of possible additional computer time required to solve the system of equations. The above system of equations may also be partially solved first (e.g., using a singular value decomposition algorithm two times) to obtain a smaller, symmetric, and positive definite system of equations which may be solved by conventional solvers. It is also believed that current and future fast parallel and serial computers and new solution algorithms will address the problem of computational efficiency and that this problem should not be considered a serious drawback for the present method described herein.

Applications

The coupled analysis approach described in this paper and validated in reference 11 has been utilized to analyze representative global/local examples. An isotropic plate subjected to tension and transverse bending is first analyzed. The plate has a central hole, and various hole shapes and sizes are studied. This example demonstrates the use of the coupled analysis method in studying the effect of details in structural design, such as hole configuration. The effectiveness of the method is then demonstrated on a more complicated example. In this example, a representative composite laminate fuselage panel with simulated stringers and frames and with a crack emanating from a window in the panel is analyzed. A nine-node assumed natural-coordinate strain (ANS) element¹⁷ is used in the problems discussed in this paper. This element has five degrees of freedom at each node (i.e., three displacements and two bending rotations) and uses a strain field approximation (equivalent to a selective directionally reduced order of integration) to calculate the element stiffness matrix.

Plate with a Central Hole

An isotropic plate with a central hole (shown in Figure 2) is an ideal structure to verify the global/local capability of the method since solutions are available in the literature. In addition, geometrically parametric studies may be performed to demonstrate the added modeling flexibility provided by the method. Tension and transverse bending loads are applied to the plate, and various hole sizes and shapes are studied.

Taking advantage of symmetry, only a quarter of the plate is modeled in the coupled analysis. The region in the vicinity of the hole is taken to be the local region and the remainder is taken to be the global region. The hole size and shape are varied by changing the finite element model of the local region, while the model of the global region remains unchanged. The finite element meshes for the global model and four typical local models with different hole configurations are shown in Figure 3.

The stress concentration factor, K_t , for an infinite plate in tension which has a central circular hole is defined as the ratio of the maximum longitudinal stress resultant, $(N_x)_{max}$, to the far field longitudinal stress resultant, $(N_x)_0$. The exact value of K_t is 3 for an infinite isotropic plate¹⁸. For a finite-width plate loaded in tension with a half-width, w , and with a central circular hole of radius a the stress concentration factor, K_t , may be defined as the ratio of the maximum longitudinal stress resultant, $(N_x)_{max}$, to the nominal longitudinal stress resultant, $(N_x)_{nom}$, where

$$(N_x)_{nom} = \frac{(N_x)_0}{\left(1 - \frac{a}{w}\right)}$$

The finite-width effects on the stress concentration factors for an isotropic plate loaded in tension and having a circular hole have been obtained numerically by Howland¹⁹, using successive approximations, and reproduced by Peterson²⁰. Figure 4 shows the stress concentration factor as a function of the hole radius to plate half-width ratio, $\frac{a}{w}$. The coupled analysis solution is seen to be in excellent agreement with the solution by Howland.

The stress concentration factor, K_t , for an infinite plate subjected to transverse bending and having a central circular hole is defined as the ratio of the maximum longitudinal moment resultant, $(M_x)_{max}$, to the far field longitudinal moment resultant, $(M_x)_0$. The exact solution for the stress concentration factor for an infinite plate subjected to transverse bending and having a circular hole has been obtained by Goodier²¹ and Reissner²² and reproduced by Peterson²⁰. The exact solution for the stress concentration factor along with the results obtained by the coupled method are shown in Figure 5 as a function of the hole diameter to plate thickness ratio, $\frac{2a}{t}$. The coupled analysis solution is in excellent agreement with the exact solution.

The effect of the hole shape on the stress concentration factor for an infinite plate subjected to tension and transverse bending is shown in Figures 6 and 7, respectively. The exact solution for the

stress concentration factor for an infinite plate subjected to tension load has been obtained by Kolosoff²³ and Inglis²⁴, and reproduced by Peterson²⁰. The stress concentration factor for an infinite plate subjected to a pure transverse bending load has been obtained by Goodier²¹ and reproduced by Peterson²⁰. The stress concentration factor for each load case is shown as a function of the ratio of the hole axes, $\frac{a}{b}$. The coupled analysis is in excellent agreement with the exact solution for each loading condition.

Composite Fuselage Panel

In the second application, the coupled analysis method is applied to a composite fuselage panel shown in Figure 8. It should be emphasized that the purpose of this example is not to perform a comprehensive detailed analysis of a complicated panel, but rather to demonstrate that the method described herein may be utilized to perform such analyses. The panel is made of a 16 ply composite laminate ($\pm 45/0_2/\pm 45/90_2$)_s. Stringer and frame actions are simulated by constraining appropriate motions of the panel along the stringer and frame paths as shown in Figure 8. A hole is introduced at the center of the panel to simulate a window. The square window has rounded corners, and there is a crack emanating from one of the corners. The loading on this panel is composed of a uniform pressure load on the concave side of the panel and uniform displacements applied on the curved edges of the panel in the longitudinal direction in order to simulate typical loads experienced by a panel in a fuselage under hydrostatic pressure. To simulate the presence of glass in the window, an equivalent approximate load is applied to the edges of the hole. This load is calculated by integrating the constant pressure over the surface of the window and distributing the result uniformly around the edge of the hole. The region in the immediate vicinity of the crack is taken to be the local region. The rest of the panel is taken to be the global region, and the two regions are modeled independently (see Figure 9). For this example, the interface between the local and global regions has a slightly curved geometry (which is due to the curvature of the panel) and is composed of four segments (which are shown as four straight line segments in Figure 9c forming the boundaries of the local model). The model for the coupled analysis has 4591 active degrees of freedom.

Since there are no theoretical solutions for this example, a reference solution is obtained using a finite element model of the panel (shown in Figure 10) which does not have an interface. This finite element model has the same refinement in the region around the crack-tip as the local model used in the coupled analysis. In order to avoid transition modeling, this high level of discretization is extended around the entire hole. The reference solution model is also more refined in the region away from the window than the global model used in the coupled analysis due to the propagation of the local discretization. The model for the reference solution has 11876 active degrees of freedom, which is nearly 2.6 times as many degrees of freedom as the model in the coupled analysis. Although there are many ways to model this panel, (e.g., the region around the hole and away from the crack-tip need not be

as fine in the reference model), this reference model was selected because of ease of modeling and to minimize transition modeling.

The deformation patterns for global/local analysis and the reference solution are shown in Figure 11. The distribution of axial stress, σ_x , from the coupled analysis and the reference solution are shown in Figure 12. A comparison of the results shown in Figures 11 and 12 reveals that the coupled analysis correlates well with the reference solution. In fact, the maximum value of the normal displacement obtained from the coupled analysis is within 0.08% of the reference solution. Moreover, the maximum value of the stresses obtained from the coupled analysis is within 1% of the reference solution. Therefore, quantities such as stress intensity factors and the strain energy release rates will also be nearly identical. Thus, one may obtain quantities such as critical crack length (which indicates the onset of unstable crack growth) by incrementally extending the crack length and repeating the coupled analysis until the critical stress intensity factors and critical strain energy release rates are obtained. A comparison of the stress distribution between the coupled analysis and the reference solution demonstrates the robustness of the method.

Concluding Remarks

A coupled analysis method for analyzing plate and shell structures composed of two or more independently modeled finite element subdomains has been described and applied herein to selected global/local examples. The method allows the analyst to incorporate a detailed model of the local subdomain within the global model. The local model need not be nodally compatible with the global model. Thus, the need for tedious transition modeling is eliminated. A hybrid variational formulation was utilized to achieve compatibility, in a variational sense, between the nodally incompatible models.

The coupled analysis method described herein was applied to two demonstration problems: (1) an isotropic plate which is loaded in tension and transverse bending and which has a central hole of various sizes and shapes, and (2) a composite fuselage panel with a crack emanating from a window cutout. Excellent agreement was obtained between the coupled analysis solutions and the reference solutions in each case. The capability of the method for treating details in structural design was demonstrated by the parametric study of the hole configuration in the isotropic plate example. The potential of the method for the detailed analysis of complicated shell structures was demonstrated by the coupled analysis of a composite fuselage panel with a crack emanating from a window cutout.

The coupled analysis method presented herein provides a technique for predicting local, detailed stress states for plate and shell structures. The simplified modeling provided by the coupled analysis method should enhance efficiency of analysis methods and provide the modeling flexibility needed to address local details. Such enhancements should lead to a means of integrating detailed analysis into the design process.

Acknowledgements

This work was performed at NASA Langley Research Center under NASA Contracts NAS1-19317 and NAS1-19000.

References

1. Jara-Almonte, C.C., and Knight, C. E., "The Specified Boundary Stiffness/Force SBSF Method for Finite Element Subregion Analysis," *International Journal for Numerical Methods in Engineering*, Vol. 26, 1988, pp. 1567-1578.
2. Ransom, J.B., and Knight, N.F., Jr., "Global/Local Stress Analysis of Composite Panels," *Computers and Structures*, Vol. 37, No. 4, 1990, pp. 375-395.
3. Whitcomb, J.D., "Iterative Global/Local Finite Element Analysis," *Computers and Structures*, Vol. 40, No. 4, 1991, pp. 1027-1031.
4. Hirai, I., Wang, B. P., and Pilkey, W. D., "An Efficient Zooming Method for Finite Element Analysis," *International Journal for Numerical Methods in Engineering*, Vol. 20, 1984, pp. 1671-1683.
5. Hirai, I., Wang, B. P., and Pilkey, W. D., "An Exact Zooming Method," *Finite Element Analysis and Design*, Vol. 1, No. 1, April 1985, pp. 61-68.
6. *ANSYS User's Manual*, Swanson Analysis Systems, Inc., Houston, PA, 1979.
7. Farhat, C., "A Method of Finite Element Tearing and Interconnecting and its Parallel Solution Algorithm," *International Journal for Numerical Methods in Engineering*, Vol. 32, No. 6, 1991, pp. 1205-1228.
8. Maday, Y., Mavriplis, D., and Patera, A., "Nonconforming Mortar Element Methods: Application to Spectral Discretizations," NASA CR-181729, ICASE Report No. 88-59, October 1988.
9. Shaeffer, H.G., *MSC/NASTRAN Primer, Static and Normal Modes Analysis*, Shaeffer Analysis, Inc., Mont Vernon, New Hampshire 1979, pp. 262-265.
10. Krishnamurthy, T., and Raju, I. S., "An Independent Refinement and Integration Procedure in Multiregion Finite Element Analysis," *Proceedings of the 33rd AIAA/ASME/ASCE/AHS/ASC Structures, Structural Dynamics and Materials Conference*, Part 1, April 13-15, 1992, Dallas, TX, pp. 302-312.
11. Aminpour, M.A., Ransom, J.B., and McCleary, S.L., "Coupled Analysis of Independently Modeled Finite Element Subdomains," *Proceedings of the 33rd AIAA/ASME/ASCE/AHS/ASC*

- Structures, Structural Dynamics and Materials Conference*, Part 1, April 13-15, 1992, Dallas, TX, pp. 109-120.
12. Zienkiewicz, O.C., *The Finite Element Method*. Third Edition, McGraw-Hill Book Company, UK, 1977, pp. 304-328.
 13. Atluri, S.N., Nishioka, T., and Nakagaki, M., "Numerical Modeling of Dynamic and Nonlinear Crack Propagation in Finite Bodies by Moving Singular Elements," *Nonlinear and Dynamic Fracture Mechanics*, (Edited by N. Perrone and S.N. Atluri, AMD), Vol. 35, ASME 1979, pp. 37-66.
 14. Gunther, C.K., Holsapple, K.A., and Kobayashi, A.S., "Finite Element Analysis of Cracking Bodies," *AIAA J.* 19, 1981, pp. 789-795.
 15. Aminpour, M.A., and Holsapple, K.A., "Finite Element Solutions for Propagating Interface Cracks with Singularity Elements," *Engineering Fracture Mechanics*, Vol. 39, No. 3, 1991, pp. 451-468.
 16. Jinping, Z., and Huizu, S., "Stress Analysis Around Holes in Orthotropic Plates by the Subregion Mixed Finite Element Method," *Computers and Structures*, Vol. 41, No. 1, 1991, pp. 105-108.
 17. Park, K.C.; Stanley, G.M., "A Curved C^0 Shell Element Based on Assumed Natural-Coordinate Strains," *ASME Journal of Applied Mechanics*, Vol. 108, 1986, 278-290.
 18. Timoshenko, S.P., and Goodier, J.N., *Theory of Elasticity*. Third Edition, McGraw-Hill Book Company, New York, 1970, pp. 90-97.
 19. Howland, R.C., "On the Stresses in the Neighborhood of a Circular Hole in a Strip under Tension," *Phil. Trans. Roy. Soc. (London) A*, Vol. 229, 1929-30.
 20. Peterson, R.E., *Stress Concentration Design Factors*, Wiley-International, New York, 1953.
 21. Goodier, J.N., "Influence of Circular and Elliptical Holes on Transverse Flexure of Elastic Plates," *Phil. Mag.*, Vol. 22, 1936.
 22. Reissner, E., "The Effect of Transverse Shear Deformation on the Bending of Elastic Plates," *Trans. ASME*, Vol. 67, 1945.
 23. Kolosoff, G., Dissertation, St. Petersburg, 1910.
 24. Inglis, C.E., "Stresses in a Plate due to the Presence of Cracks and Sharp Corners," *Engineering (London)*, Vol. 95, 1913.

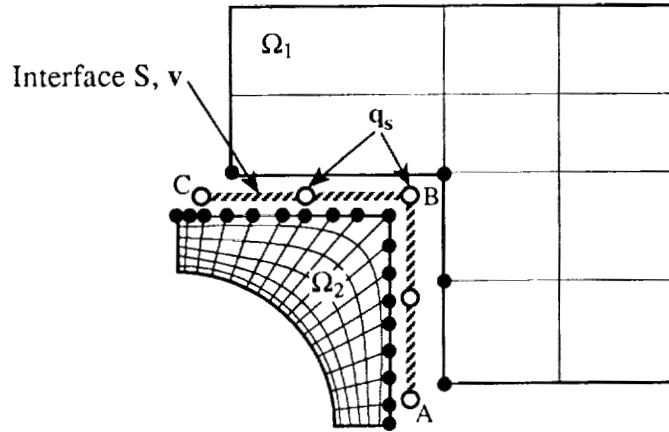


Figure 1. Interface definition for coupled analysis

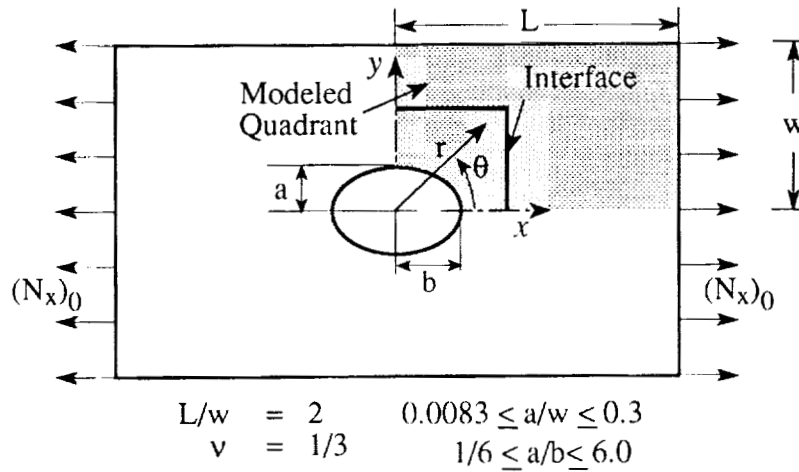


Figure 2. Plate with central hole

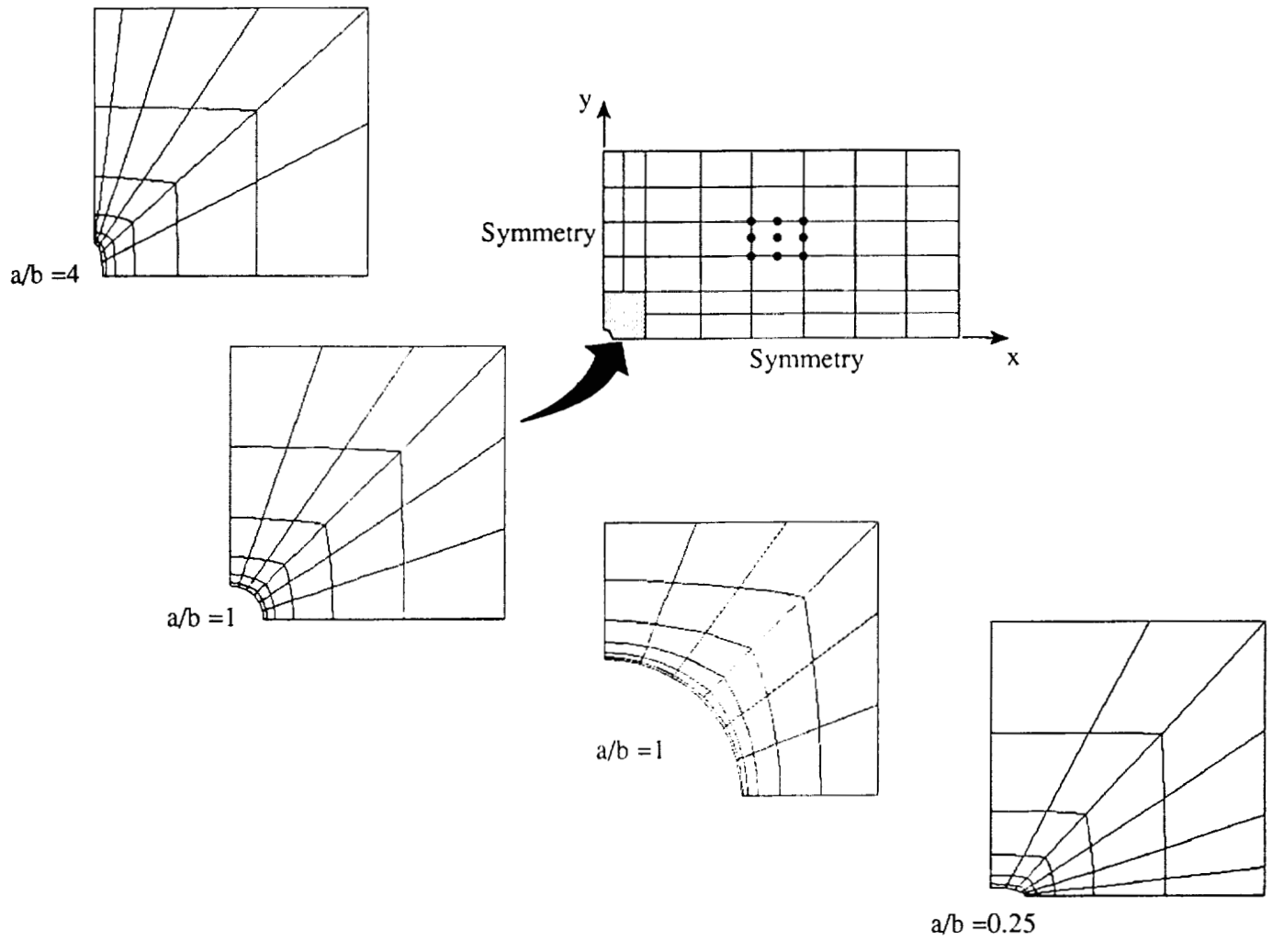


Figure 3. Finite element models for local and global regions of plate with hole

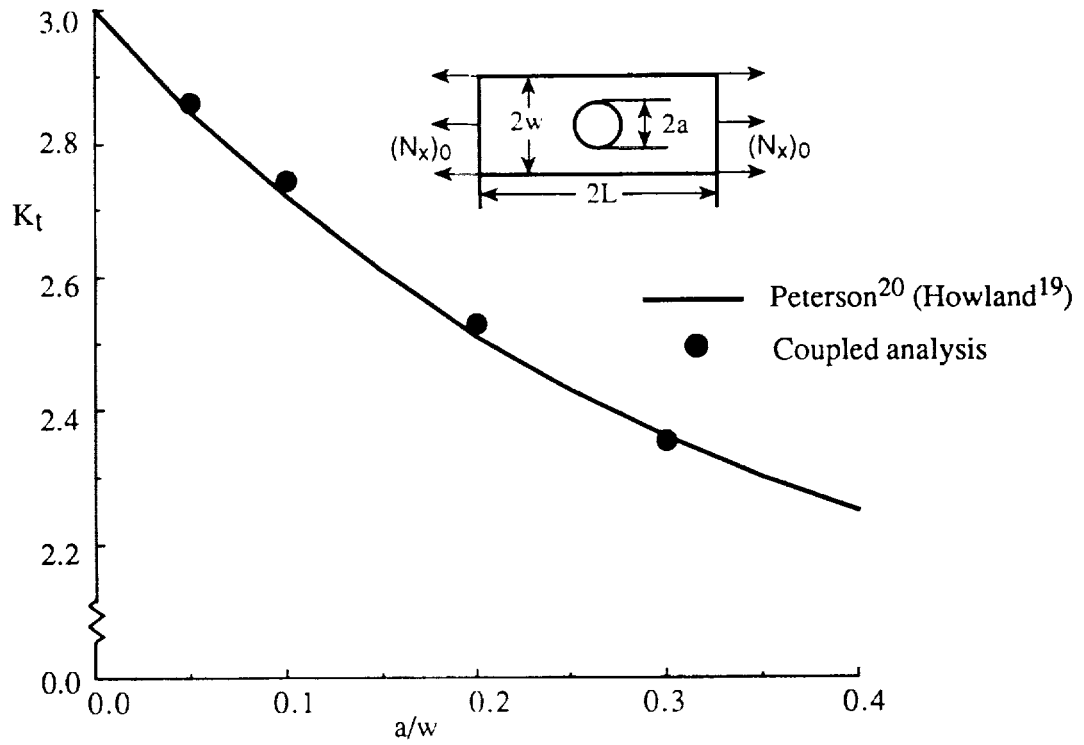


Figure 4. Stress concentration factor, K_t , of finite-width plate subjected to inplane tension

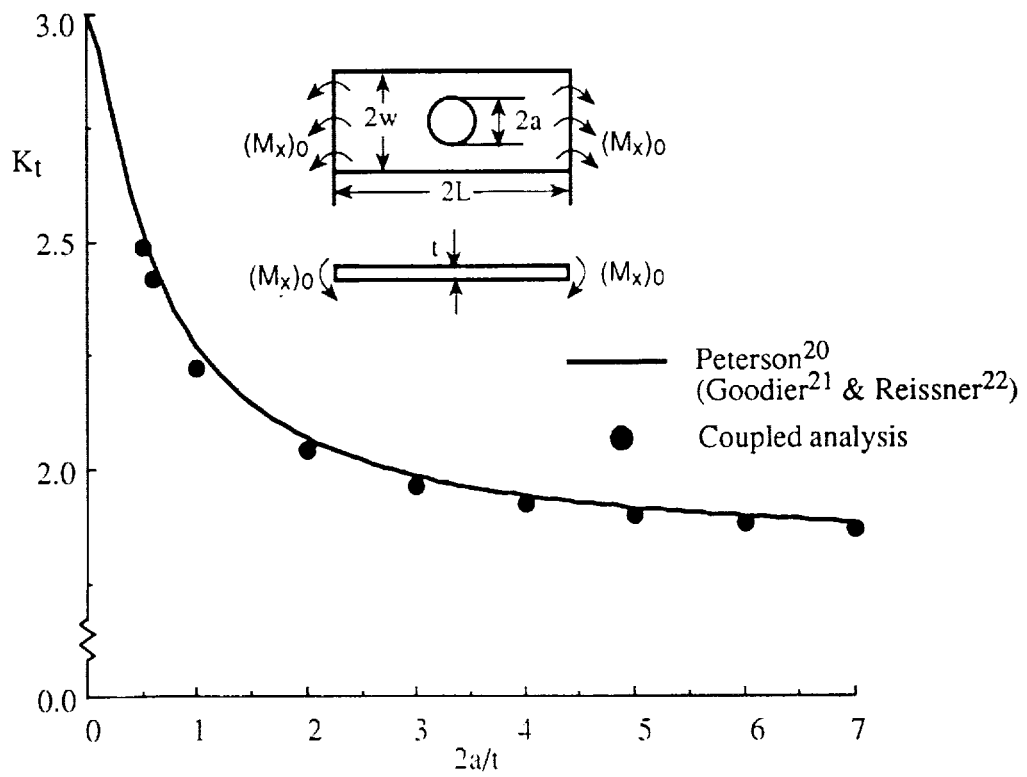


Figure 5. Stress concentration factor, K_t , of infinite plate subjected to transverse bending

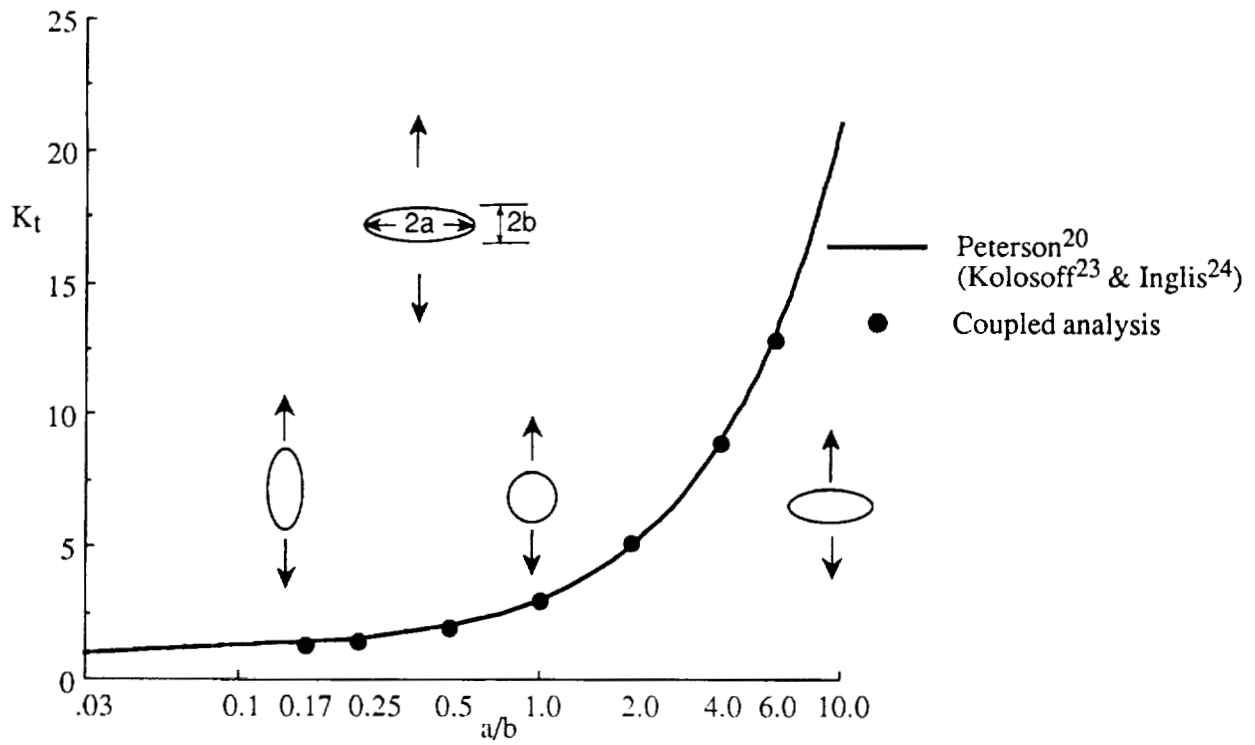


Figure 6. Effect of hole configuration on stress concentration factor, K_t , of infinite plate subjected to inplane tension

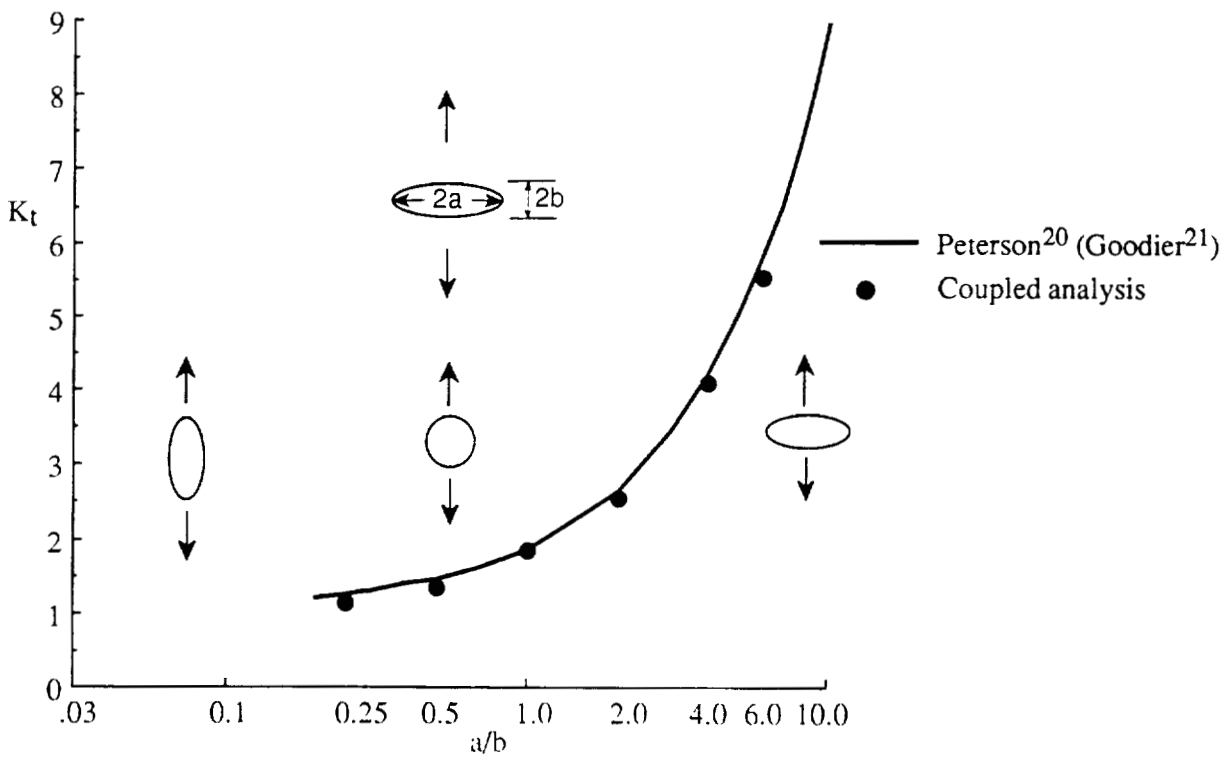
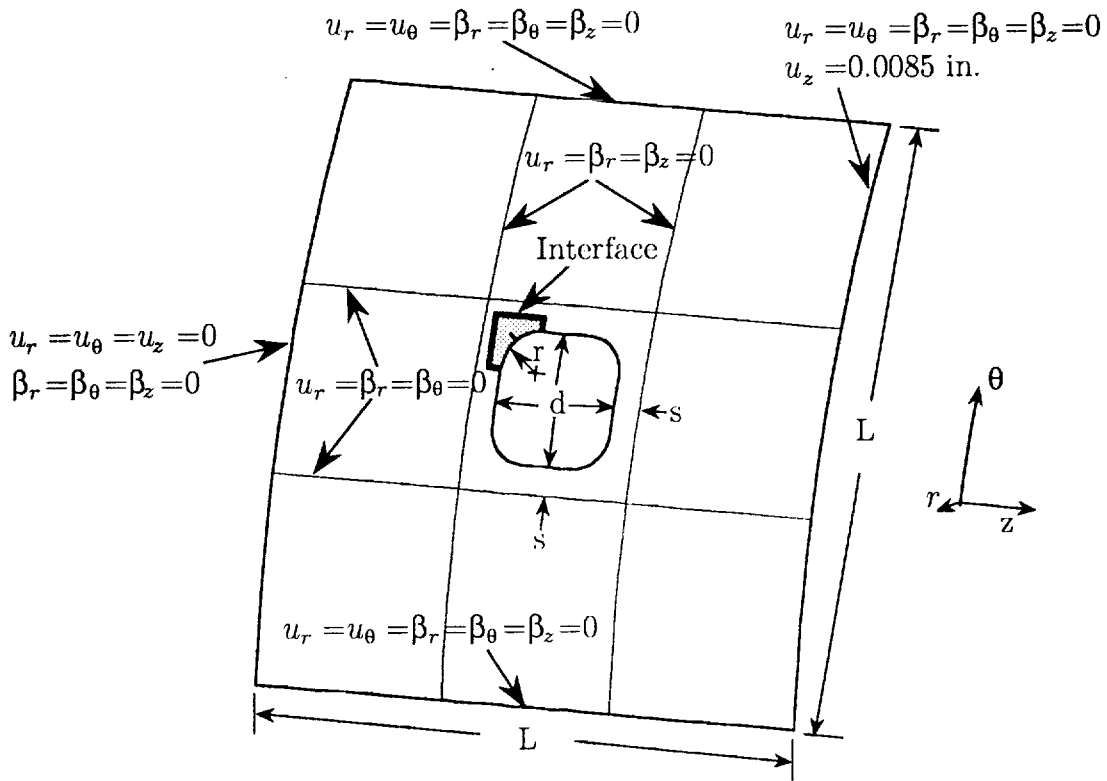
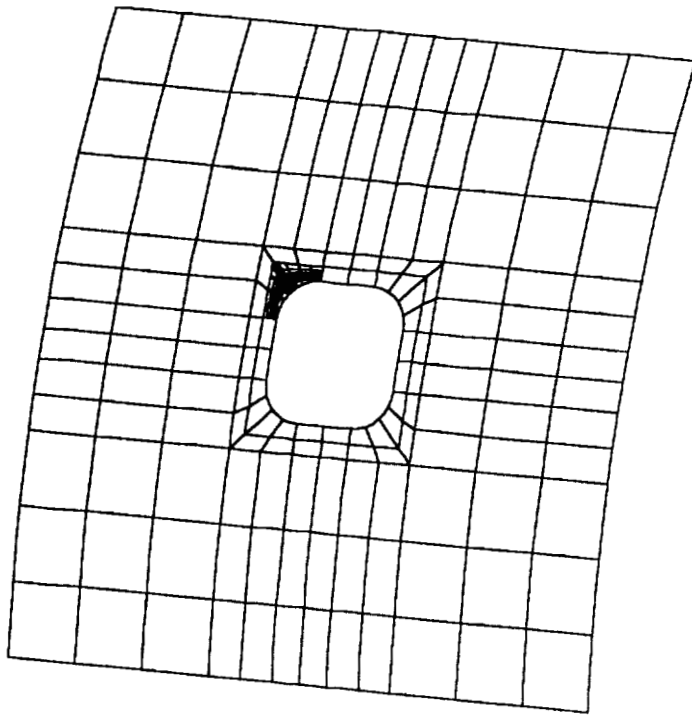


Figure 7. Effect of hole configuration on stress concentration factor, K_t , of infinite plate subjected to transverse bending

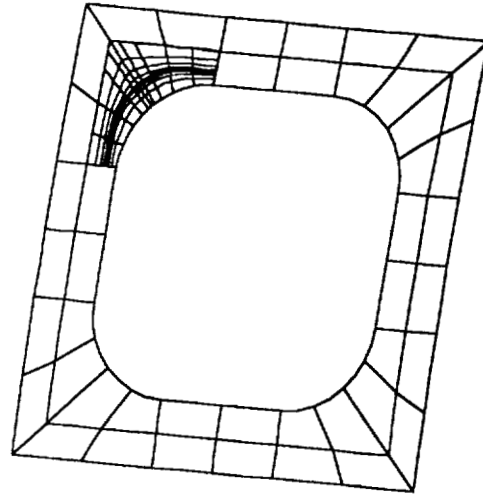


$E_1 = 18500 \text{ ksi}$	$s = 1.5 \text{ in.}$
$E_2 = 1890 \text{ ksi}$	$d = 7.0 \text{ in.}$
$\nu_{12} = 0.38$	$r = 2.0 \text{ in.}$
$t_{\text{ply}} = 0.0056 \text{ in.}$	$L = 32.0 \text{ in.}$
$t_{\text{lam}} = 0.3136 \text{ in.}$	$R = 85.0 \text{ in (panel radius)}$
$p = 10.0 \text{ psi}$	panel arc is 21.6 degrees

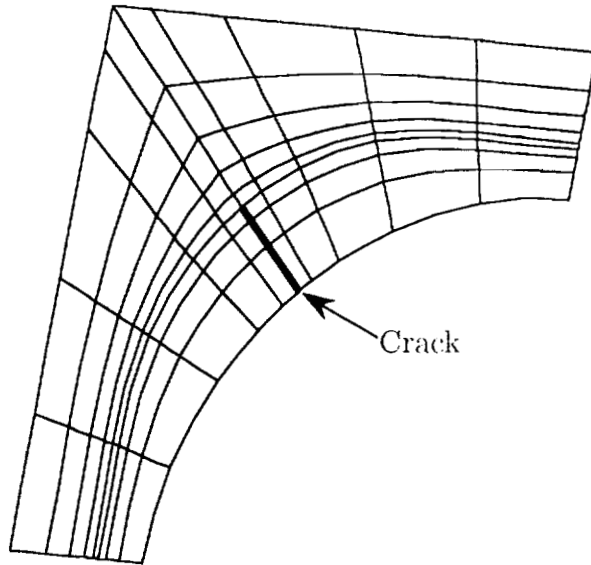
Figure 8. Cracked fuselage panel



a. Global model

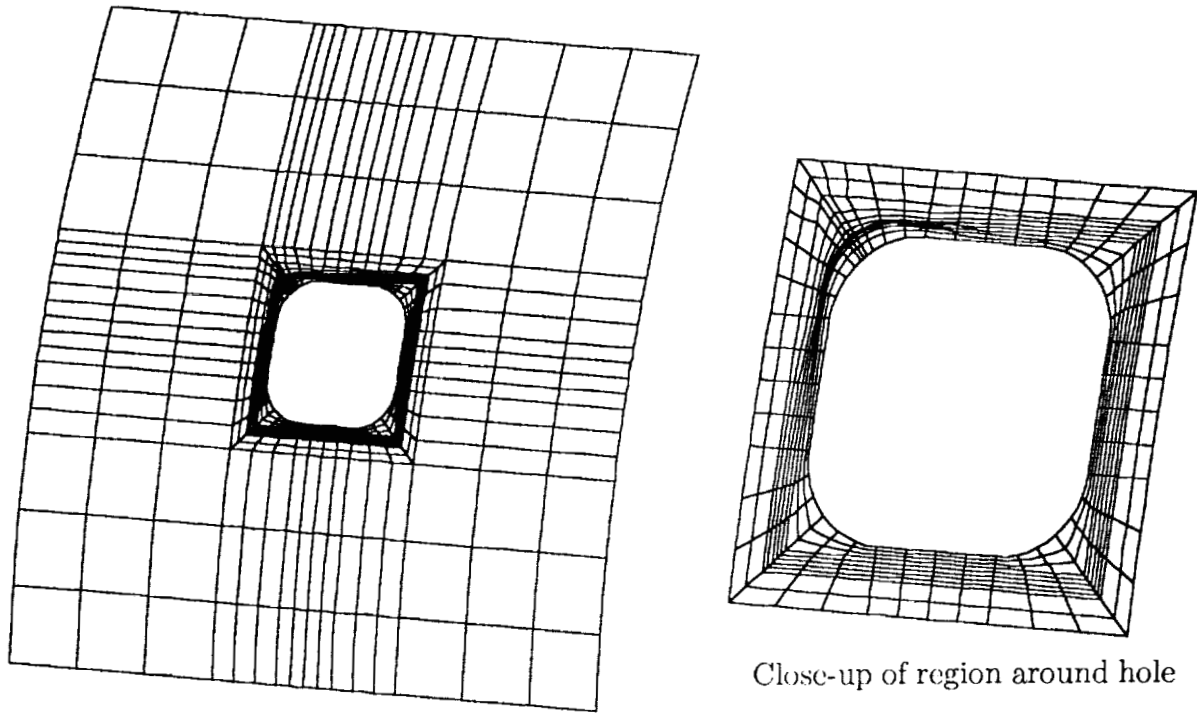


b. Close-up of region around hole



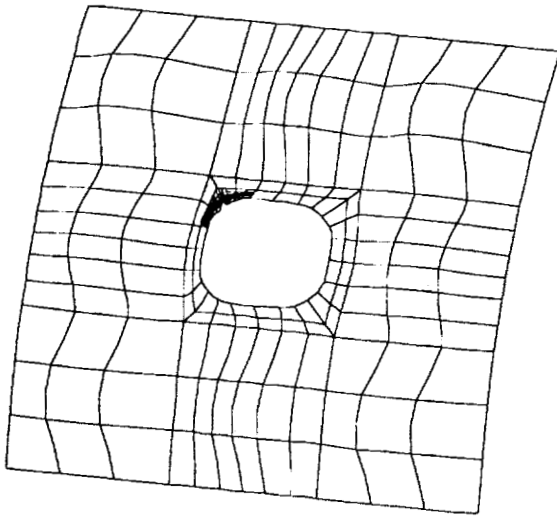
c. Local Model

Figure 9. Finite element models for coupled analysis

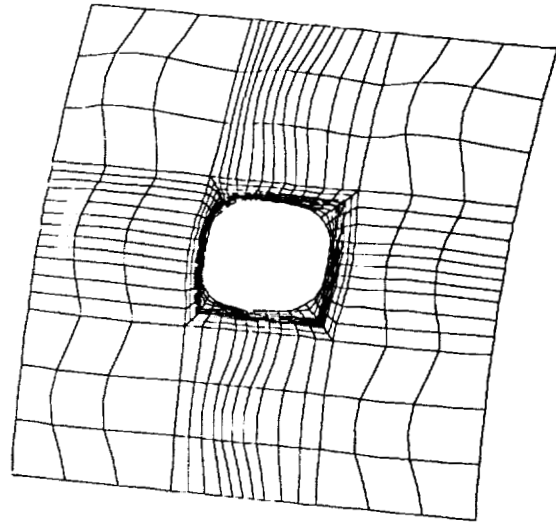


Close-up of region around hole

Figure 10. Finite element model for reference solution

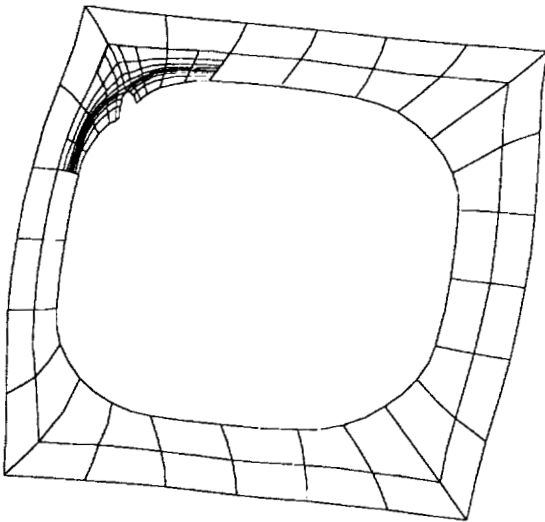


Coupled analysis solution

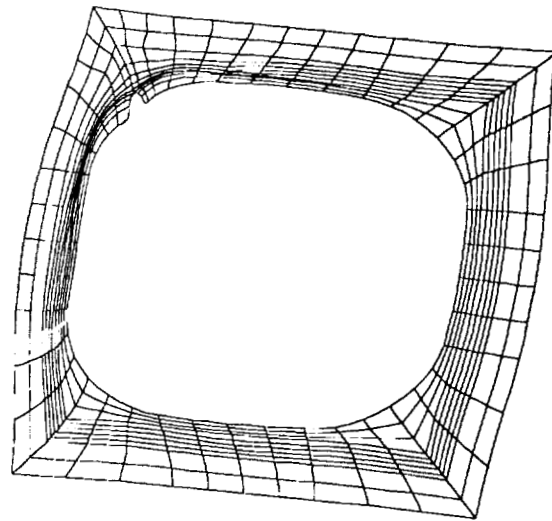


Reference solution

a. Global perspective



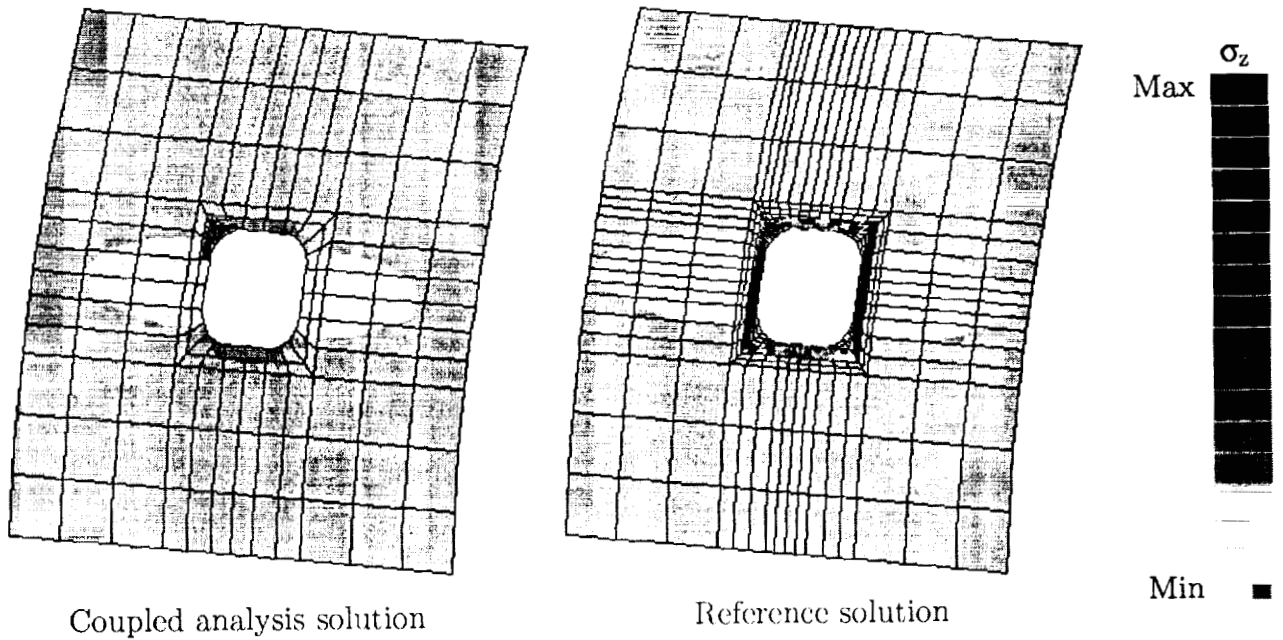
Coupled analysis solution



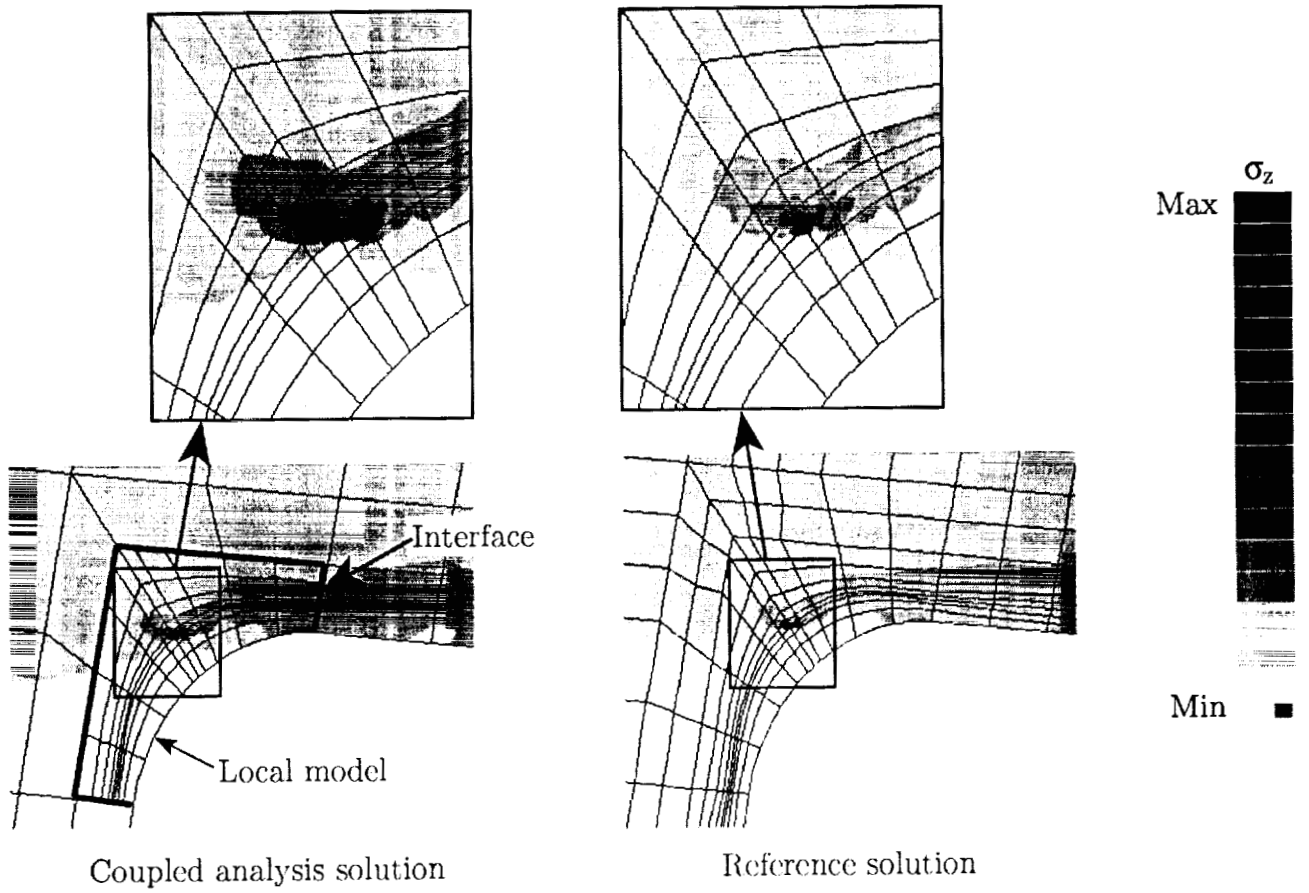
Reference solution

b. Local perspective

Figure 11. Deformed geometry



a. Global perspective



b. Local perspective

Figure 12. Axial stress, σ_z , distribution

IPACS - INTEGRATED PROBABILISTIC ASSESSMENT
OF COMPOSITE STRUCTURES:
CODE DEVELOPMENT AND APPLICATIONS

C. C. Chamis
NASA Lewis Research Center
Cleveland, OH 44135

526-39
58426


Michael C. Shiao
Sverdrup Technology, Inc.
Lewis Research Center Group
Brook Park, Ohio

SUMMARY

A methodology and attendant computer code have been developed and are described to computationally simulate the uncertain behavior of composite structures. The uncertain behavior includes buckling loads, stress concentration factors, displacements, stress/strain etc., which are the consequences of the inherent uncertainties (scatter) in the primitive (independent random) variables (constituent, ply, laminate and structural) that describe the composite structures. The computer code is IPACS (Integrated Probabilistic Assessment of Composite Structures). IPACS can handle both composite mechanics and composite structures. Application to probabilistic composite mechanics is illustrated by its uses to evaluate the uncertainties in the major Poisson's ratio and in laminate stiffness and strength. IPACS application to probabilistic structural analysis is illustrated by its use to evaluate the uncertainties in the buckling of a composite plate, in the stress concentration factor in a composite panel and in the vertical displacement and ply stress in a composite aircraft wing segment.

INTRODUCTION

Probabilistic composite mechanics and probabilistic composite structural analysis are formal methods which are used to quantify the scatter that is observed in composite material properties and structural response. The observed scatter in composite material properties is the range of measured values in modulus, strength, thermal expansion coefficient, etc., while that in structural response is the range of measured values for displacement, frequency, buckling load, etc. The formal methods relate the scatter in the observed values to the corresponding scatter in the physical parameters which make up the composite and/or the composite structure. For example, these parameters include constituent material properties, fabrication process variables, structural component geometry, and any other variables which contribute to the composite behavior and/or structural response.



The development of these types of formal methods has been the subject of considerable research at NASA Lewis Research Center. This research has led to computational simulation methods and attendant computer codes for relating the scatter (uncertainties) in the composite properties or composite structural response to the corresponding uncertainties in the respective parameters (primitive variables) which are used to describe the composite in all its inherent scales: micro, macro, laminate and structural. A more recent continuing development is the computer code IPACS (Integrated Probabilistic Assessment of Composite Structures). The objective of this paper is to summarize the status of the IPACS and to present results of select examples to illustrate its application to evaluate the uncertainties in composites and in composite structures. The fundamental concepts driving the methodology are briefly described for completeness. The significance and/or relevance of the results obtained to actual design problems are noted.

FUNDAMENTAL CONCEPTS

The fundamental concepts/assumptions in the probabilistic composite mechanics described herein are (1) the scatter in all the primitive variables, which describe the composite, can be represented by well known probabilistic distribution, (2) the values for the primitive variables can be randomly selected from the known distributions for a specific composite, (3) these values can be used in composite mechanics to predict composite behavior, and (4) the whole process can be repeated many times to obtain sufficient information to develop the distribution of the ply properties, composite properties, or structural responses. These concepts are analogous to making and testing composites. The probabilistic distributions represent available materials that the composite can be made from. The composite mechanics represent the physical experiment and the process repetition represents several experiments. Subsequent statistical analysis of the data is the same for both approaches.

The primitive variables which describe the composite are identified by examining the fabrication process. A schematic depicting the fabrication process for an aircraft wing top cover is shown in Figure 1. The formal procedure is summarized in the schematic in Figure 2.

PROBABILISTIC COMPOSITE MECHANICS

Probabilistic composite mechanics is key to probabilistic structural analysis. Probabilistic composite mechanics from micromechanics to laminate theory is described in Reference 1. Representative results from ref. 2 for composite micromechanics are shown in Figure 3 for the major ply Poisson's ratio. It is interesting to observe from the sensitivity analysis results that: (1) the fiber misalignment (THETA 1) has the greatest effect on the Poisson's ratio followed by the in situ matrix Poisson's ratio and then by the fiber Poisson's ratio; (2) the fiber volume ratio has comparatively negligible effect; (3) the single experimental point is near the mean (50 percent probability); and (4) the level of probability does not affect the magnitude of the sensitivities.

Representative results of probabilistic laminate behavior simulation are summarized in Table 1 for three different laminates. Scanning the ranges in this table, it can be observed that the experimental data is within the simulated scatter for all the values except one Poisson's ratio and two shear models, both of which are sensitive to the boundary and loading conditions. The simulation scatter can be modified to include these data points by modeling the specimen in its entirety.

PROBABILISTIC STRUCTURAL ANALYSIS

Probabilistic structural analysis is performed by using IPACS (Integrated Probabilistic Assessment of Composite Structures). A schematic of the physics integrated into IPACS is shown in Figure 4 while a block diagram of its constituent modules is shown in Figure 5. As can be seen in Figure 4, IPACS consists of a combination of two major modules: (1) NESSUS for probabilistic structural analysis and (2) PICAN for probabilistic composite mechanics. IPACS is used to evaluate the scatter in several structures as is described below. Additional discussions on IPACS are found in Reference 3.

Composite Plate Buckling

Representative results from applying IPACS to simulate buckling of composite plates are shown in Figure 6. The most significant point to observe in this Figure is that the plates with the asterisk required probabilistic simulation of the support fixity to increase the simulated results upper bound in order to include the experimental values. The fixity of the supports was simulated by assuming a ten percent moment and a five percent scatter about this ten percent fixity. The conclusion is that experimental results can be bounded by including uncertainties in all the variables that describe the composite structure.

Stress Concentration Factor

An interesting problem in composite structures is stress concentration factors in open holes. IPACS was used to evaluate the scatter in the Stress Concentration Factor (SCF) in a composite panel with a center hold, shown in Figure 7. Results obtained for the SCF are shown in Figure 8. These results were obtained by assuming two and five percent scatter in the participating (primitive) variables that describe the physics of the problem (Fig. 4). In Figure 8, results are also shown for comparison with experimental data, an independent source (independent source same as experimental data) and from a close form solution. It is worthy of note that the IPACS results with two percent scatter in the primitive-variables bound the data and that the results from the close form solution over-predict the stress concentration factor. It is not know what scatter was used to obtain the independent source results.

The important point to be made is that the IPACS results are obtained by using the whole panel while those for the close form solution are only at a point. In a limited way these results underline the importance of modeling the whole structure rather than evaluating responses by considering only a local region which is the traditional approach. Cumulative distribution function comparisons are shown in Figure 9 for 1.5 percent scatter. The comparisons are very good, if not excellent, and lend credence to the simulation capability in IPACS.

The corresponding sensitivity factors for the two percent scatter are shown in Figure 10. Only four of the forty factors used have significant effect on the stress concentration factor. All four of these contribute to the stiffness of the panel. The important observation is that IPACS can handle composite scatter with numerous primitive variables such as fiber composites.

COMPOSITE WING SECTION

Aircraft wings are current candidates for composites application. The uncertainties in an assumed wing segment shown in Figure 11 were simulated by using IPACS. This section consisted of composite skins with 3-internal spars and 3-internal frames as shown by the interrupted lines in the plan view. The composite system, wing geometry, loading conditions and uncertainties assumed are summarized in Figure 11. The IPACS finite element model consisted of 840 nodes and 908 quadrilateral elements.

The range of uncertainty predicted by IPACS is shown in Figure 12, for the transverse (vertical) displacement where a computer plot of the finite element model is also shown. As can be seen, three times out of 10,000 the displacement will be less than four inches while three times out of 10,000 it will be greater than seven inches. The bounded range is very useful for the following important reasons: (1) static tests for qualifying the wing segment will produce results in this range and will be consistent with the uncertainties in the primitive variables and, (2) the seven inch dimension is critical in sizing actuators to prevent displacements from growing beyond this range.

The sensitivity factors for the transverse displacement are shown in Figure 13. Several factors influence the lower bound of the displacement while the pressure is the most dominant factor for the upper bound. This is a very interesting and perhaps expected result: "The upper bounds of the scatter are mainly influenced by uncertainties in the loading conditions."

Corresponding results for the highest longitudinal ply stress are shown in Figure 14 for the range of the scatter in terms of cumulative distribution function. Only about three times out of 10,000 will the stress be less than about 30 ksi or greater than about 55 ksi. The sensitivity factors for the ply longitudinal stress are shown in Figure 15. The stringer misalignment influences the lower bound of the stress scatter. This factor did not influence the displacement. Only the pressure influences the upper bound of the stress scatter. It is doubtful that this would be an expected result. It demonstrates the wealth of information

provided by the probabilistic structural analysis or, more generally, the computational simulation of probabilistic structural behavior.

The three different and important structural examples previously described demonstrate the breadth and depth of the IPACS computer code to probabilistically assess inherent uncertainties in composite structures. The results from these three examples are evidence of the maturity of the methodology, the status of the IPACS computer code and in a limited way, the effectiveness of IPACS for: (1) application to the design of composite structures and, (2) assessment of their reliability.

CONCLUSIONS

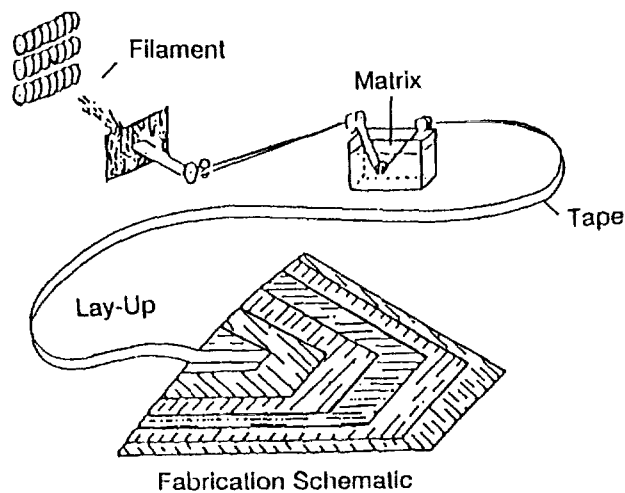
Formal methods and a computer code IPACS for integrated probabilistic assessment of composite structures were described. Select examples for probabilistic composite mechanics and probabilistic structural analysis were presented to demonstrate the status of the development of the code and its applications. Results from these examples (composite plate buckling, stress concentration factors and structural response of an aircraft/segment wing) illustrate that IPACS can be used to quantify the uncertainties in composite structural behavior from the inherent uncertainties in the various parameters that define the composite structure. In addition, the methodology can be used to evaluate sensitivity factors which influence composite structural response. Boundary conditions are important in composite plates with certain laminate configurations. Parameters contributing to stiffness are important in stress concentration factors. While several factors influence the lower bounds of the vertical displacement and ply stress of an aircraft wing segment, only the pressure dominates the upper bounds of the scatter. Collectively, the results demonstrate that the IPACS computer code has matured to the point that it can be very useful for the design and reliability assessment of composite structures.

REFERENCES

1. C. C. Chamis and P.L.N. Murthy: Probabilistic Composite Analysis. NASA CP 3104, Part 2, 1991, pp. 891-900.
2. G. T. Mase, P.L.N. Murthy and C. C. Chamis: Probabilistic Micromechanics and Macromechanics of Polymer Matrix Composites. NASA TM 103669, January 1991.
3. M. C. Shiao and C. C. Chamis: Probabilistic Evaluation of Fuselage-Type Composite Structures. NASA TM 105881, 1992.

Table 1 - Pican Verification for Laminate Stiffness

Laminate	Lower bound (95% confidence)	Mean	Experimental value	Upper bound (95% confidence)
$[0/\pm 45_2/0/\pm 45]_s$ Long. modulus (MSI) Trans. modulus (MSI) Shear modulus (MSI) Major Poisson's ratio	5.48 2.76 3.34 0.771	6.31 3.16 3.85 0.792	6.30 3.08 3.21 0.803	7.12 3.54 4.38 0.813
$[0_2/\pm 45/0_2/90/0]_s$ Long. modulus (MSI) Trans. modulus (MSI) Shear modulus (MSI) Major Poisson's ratio	11.49 3.85 1.42 0.305	13.27 4.40 1.63 0.312	13.00 4.20 1.50 0.325	15.08 4.93 1.84 0.318
$[(0/\pm 45/90)_2]_s$ Long. modulus (MSI) Trans. modulus (MSI) Shear modulus (MSI) Major Poisson's ratio	6.27 6.27 2.38 0.310	7.22 7.22 2.74 0.315	6.68 6.62 2.34 0.350	8.16 8.16 3.10 0.320



- o Constituents
- o Fiber Misalignment
- o Fiber Volume Ratio
- o Void Volume Ratio
- o Ply Orientation Angle
- o Ply Thickness

Figure 1 - Sources of Scatter - Fabrication Process

- o Assume statistical distributions of scatter in all primitive variables.
- o Probabilistically select values from these distributions.
- o Enter these values in ICAN to calculate composite properties.
- o Repeat process until sufficient values have been obtained to develop statistical distributions for the desired composite properties/structural response.
- o Evaluate sensitivities.

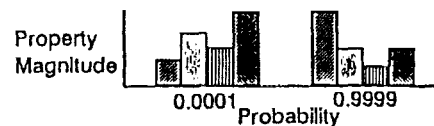
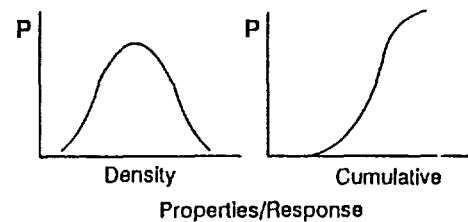
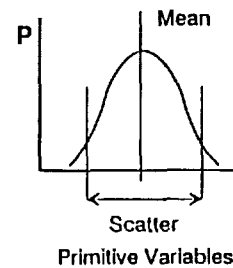


Figure 2 - Probabilistic Simulation

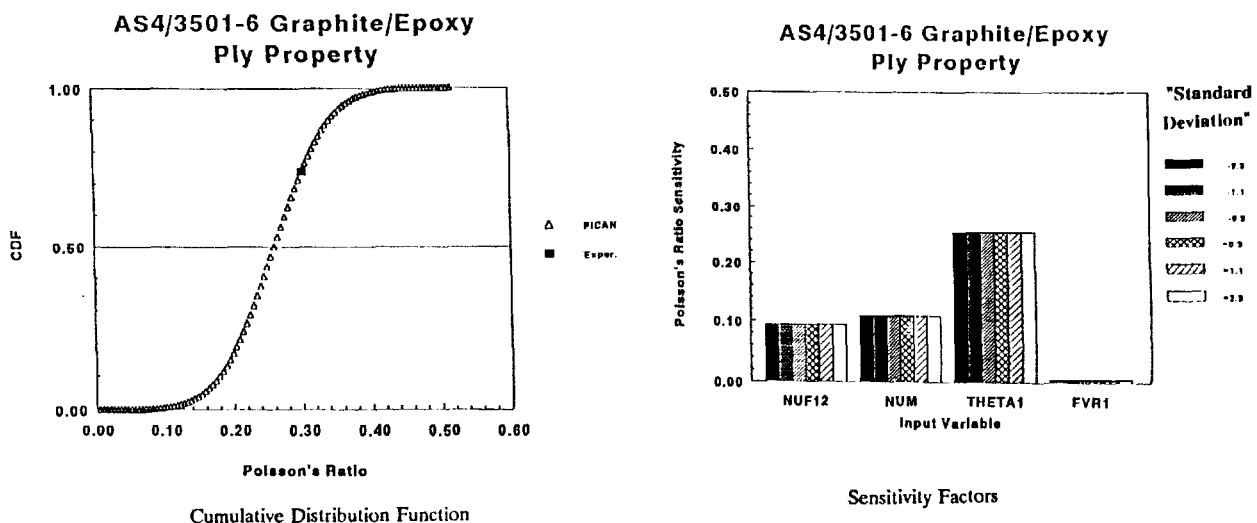


Figure 3 - Probabilistic Composite Micromechanics Simulation Results - Major Poisson's Ratio (AS4/3501-6 Graphite/Epoxy)

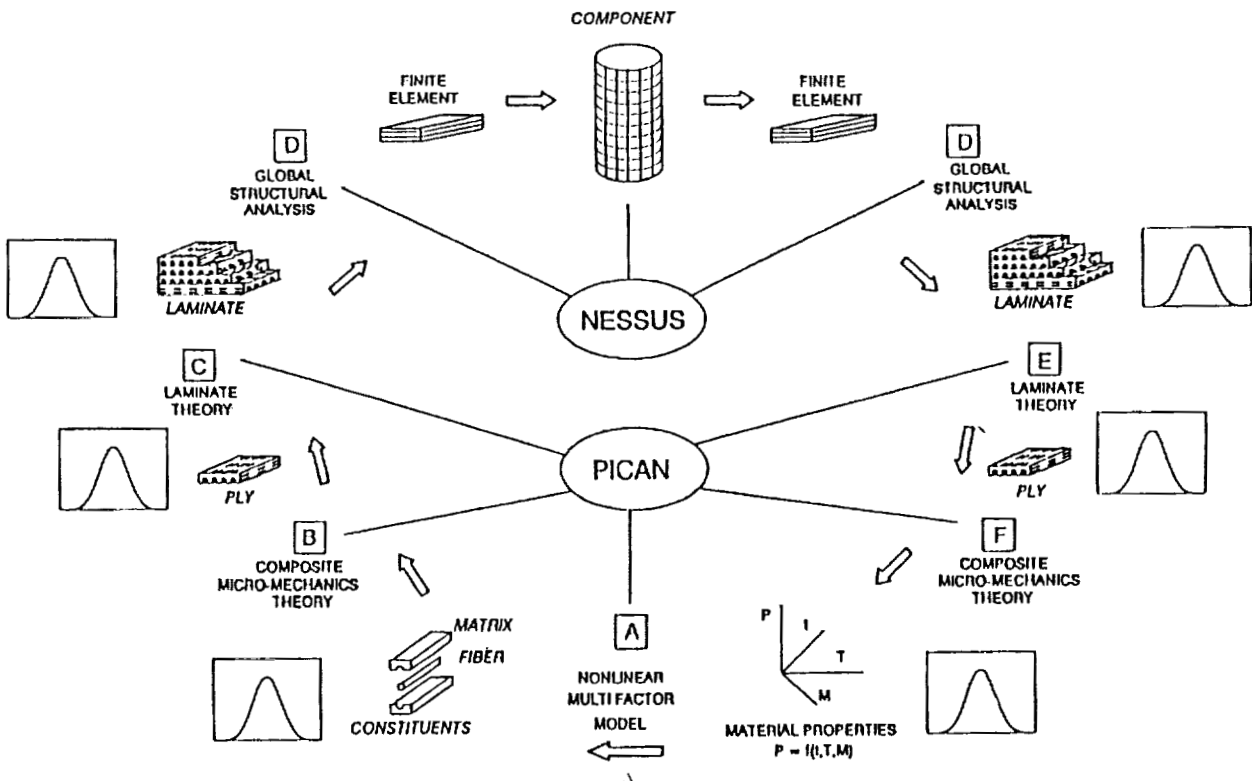


Figure 4 - IPACS: Integrated Probabilistic Assessment of Composite Structures

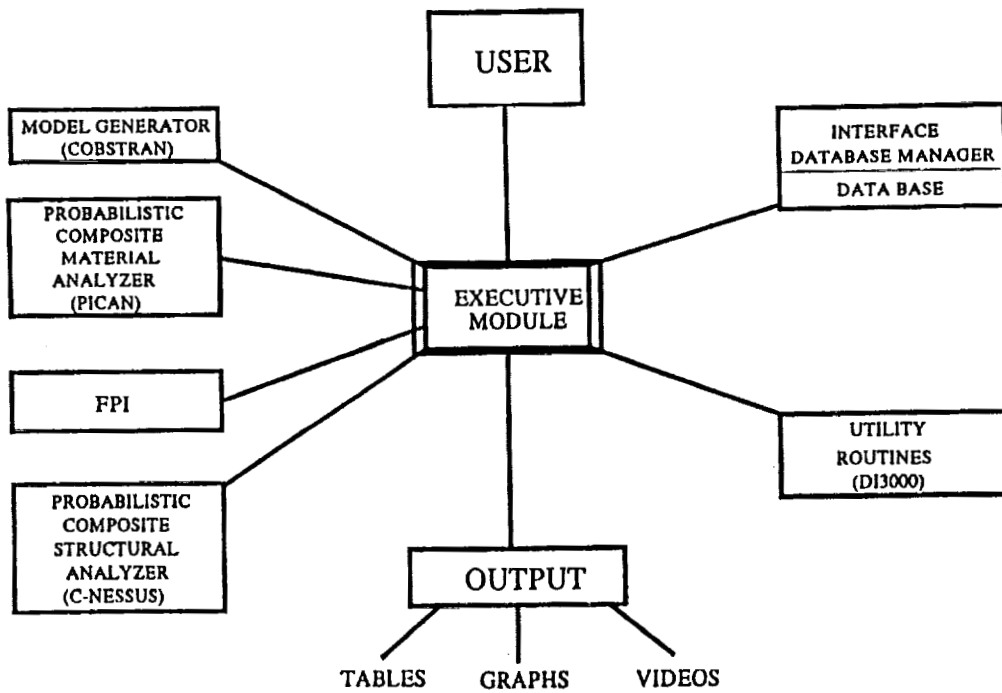


Figure 5 - Integrated Probabilistic Assessment of Composite Structures (IPACS) Architecture of Software System

GEOMETRY OF THE PLATE

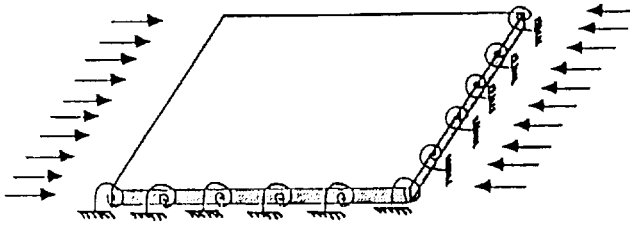


Plate Geometry

IPACS VERIFICATION FOR BUCKLING LOADS

Laminate	lower bound (mean-2σ)	mean	experimental value	upper bound (mean+2σ)
20[0]20 buckling load	247	284	271	322
20[90]20 * buckling load	173	195	251	293
10[±30]5S, 10[∓30] * buckling load	513	567	662	688
10[±45]5S, 10[∓45] buckling load	555	609	592	663
10[±60]5S, 10[∓60] buckling load	562	623	661	684

*with uncertainties in the boundary conditions

Buckling Loads Summary

Figure 6 - Probabilistically Simulated Buckling Loads of Boron/Epoxy Composite Plates

FINITE ELEMENT MODELING:

For Coarse Mesh:
 No. of Nodes = 180
 No. of Elements = 160

For Fine Mesh:
 No. of Nodes = 680
 No. of Elements = 640

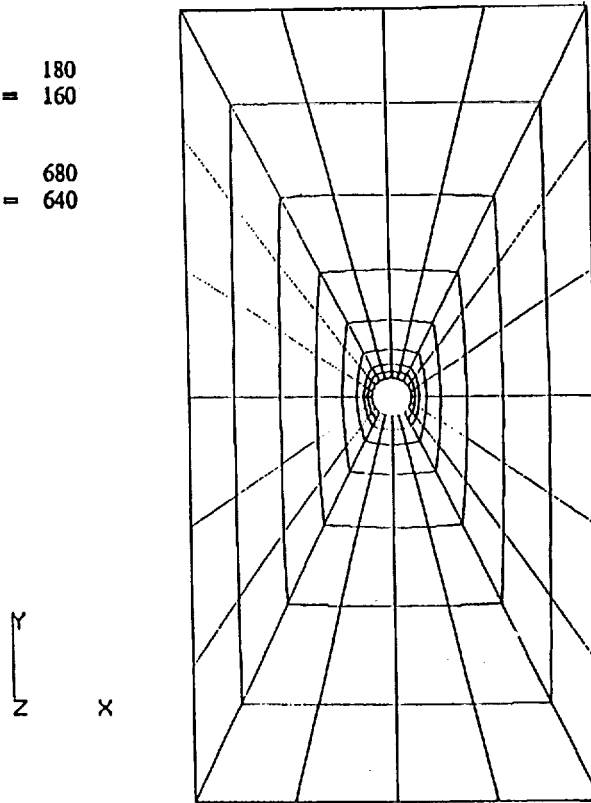


Figure 7 - Composite Panel with Center Hole

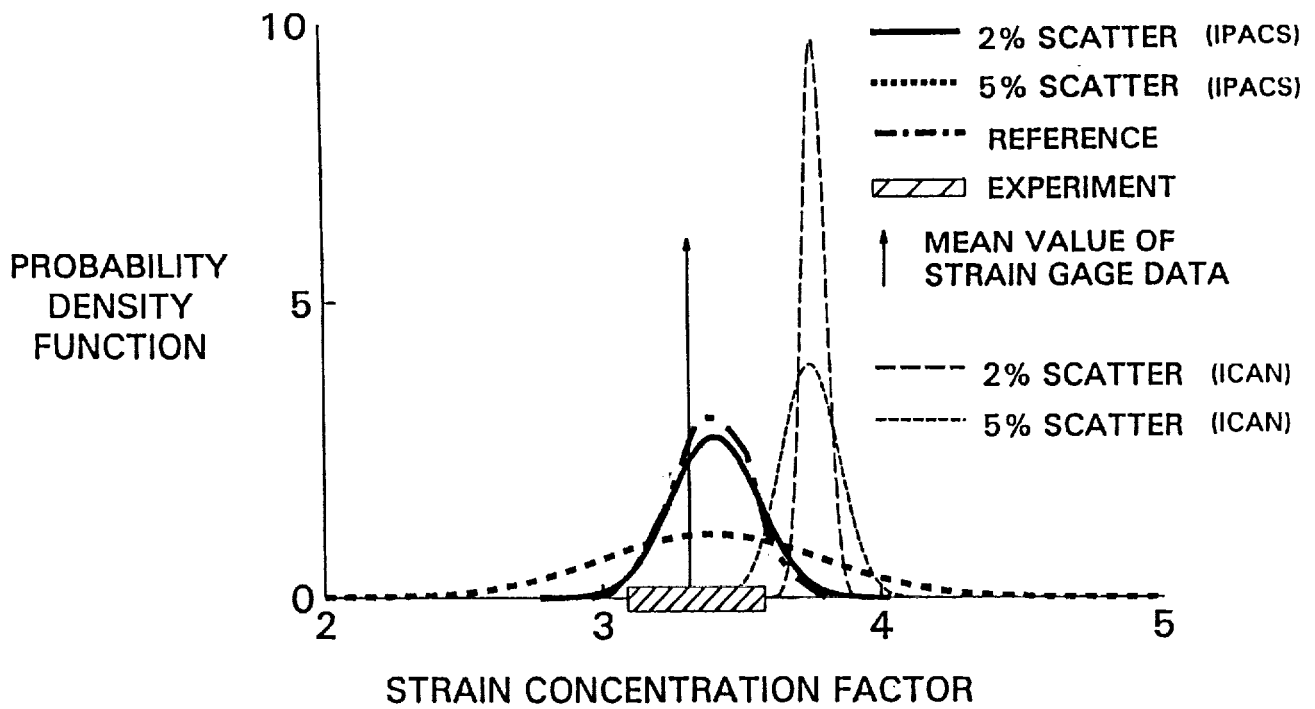


Figure 8 - Probabilistic Strain Concentration Factor of a (0/45/-45/0/90)s Laminate Plate (Boron/Epoxy)

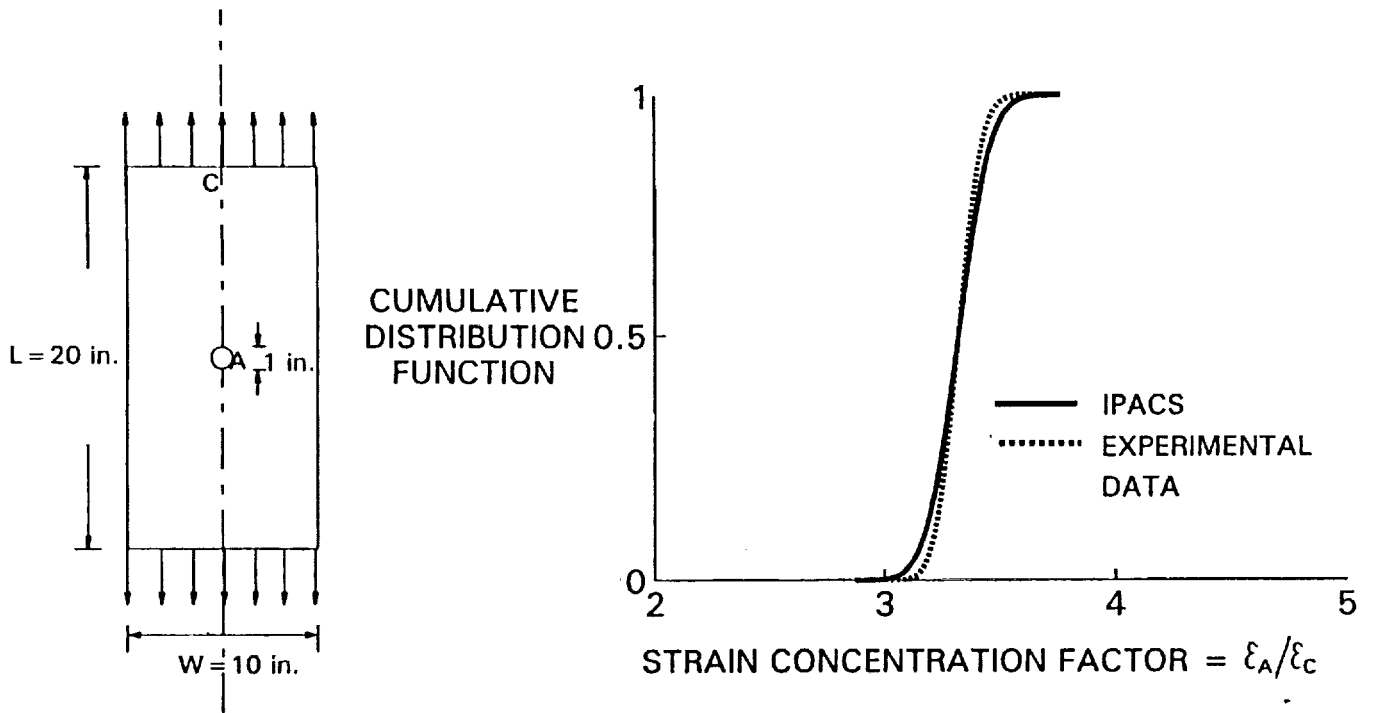


Figure 9 - Probabilistic Strain Concentration Factor of a (0/45/-45/0/90)s Laminate Plate (Boron/Epoxy with 1.5% Scatter)

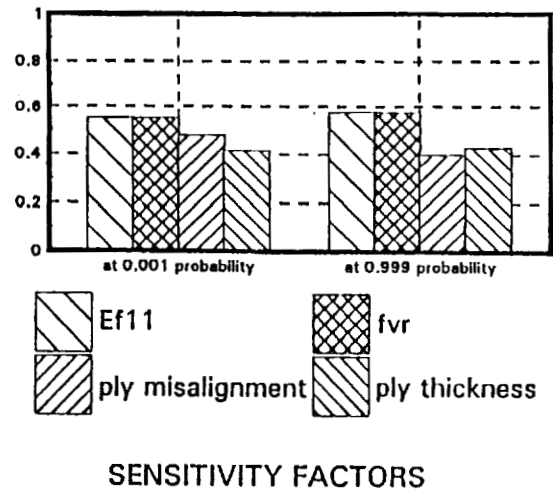
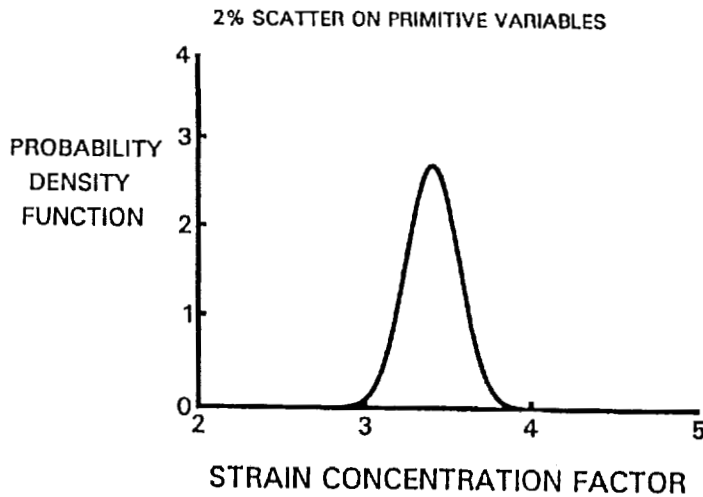


Figure 10 - Probability Density Function of the Strain Concentration Factor (SCF) and the Sensitivity of Each Primitive Variable to the Probabilistic SCF of a Boron/Epoxy Laminate Plate is Simulated by IPACS

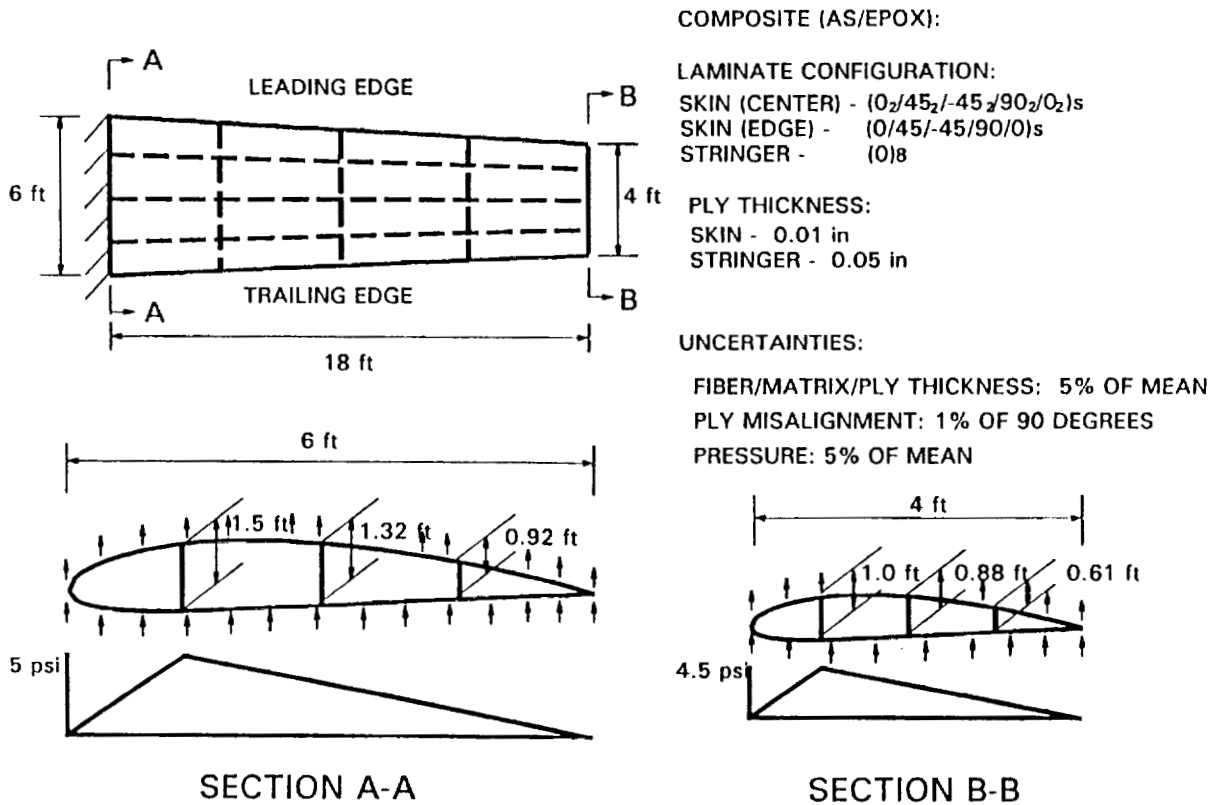


Figure 11 - Geometry and Loading for a Composite Wing

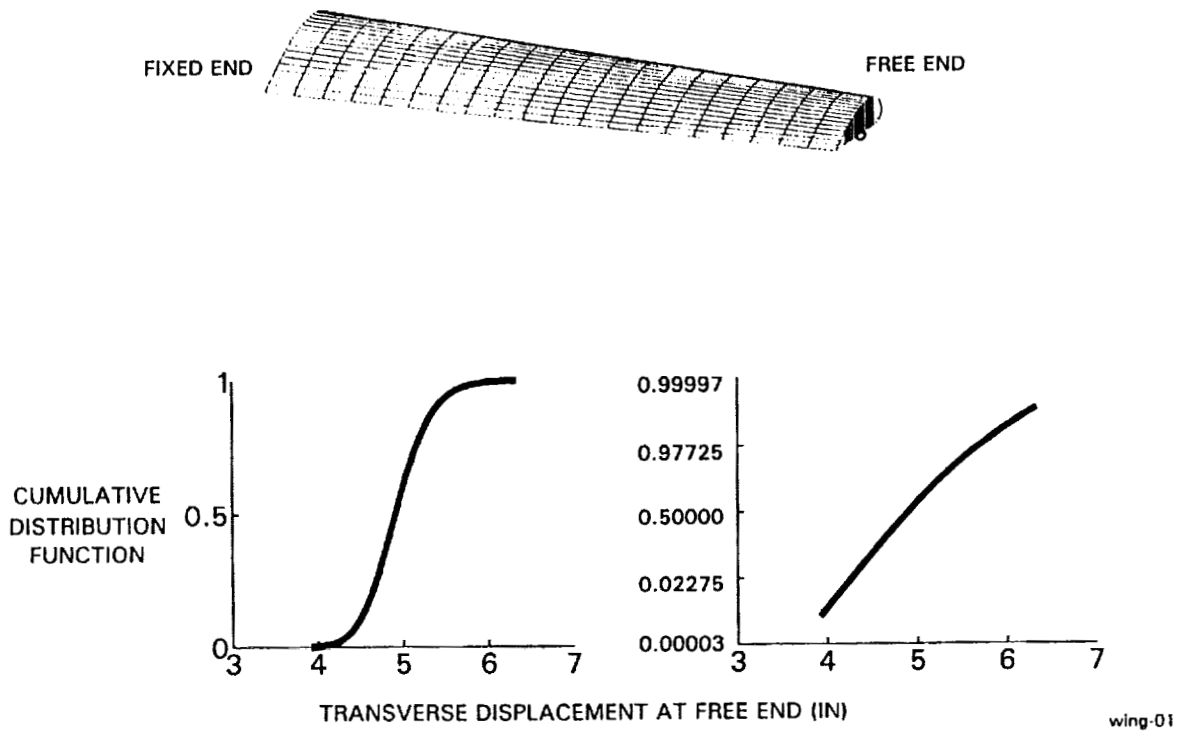


Figure 12 - Probabilistic Transverse Displacement of a Composite Wing

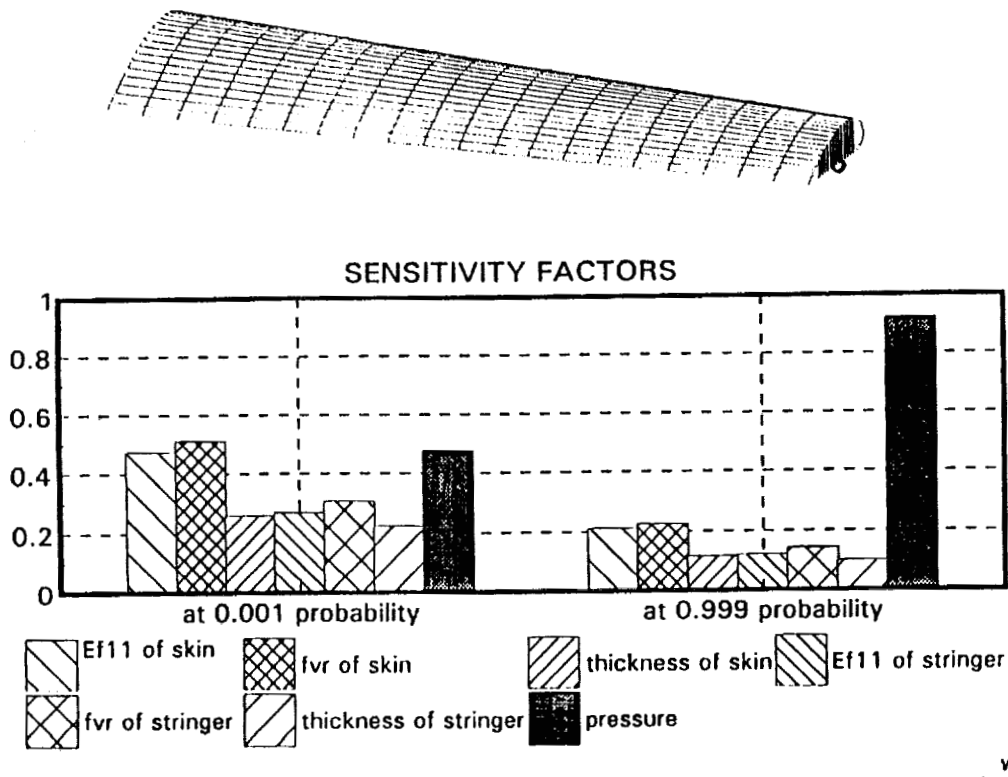


Figure 13 - Sensitivity Analysis of Probabilistic Transverse Displacement of the Composite Wing

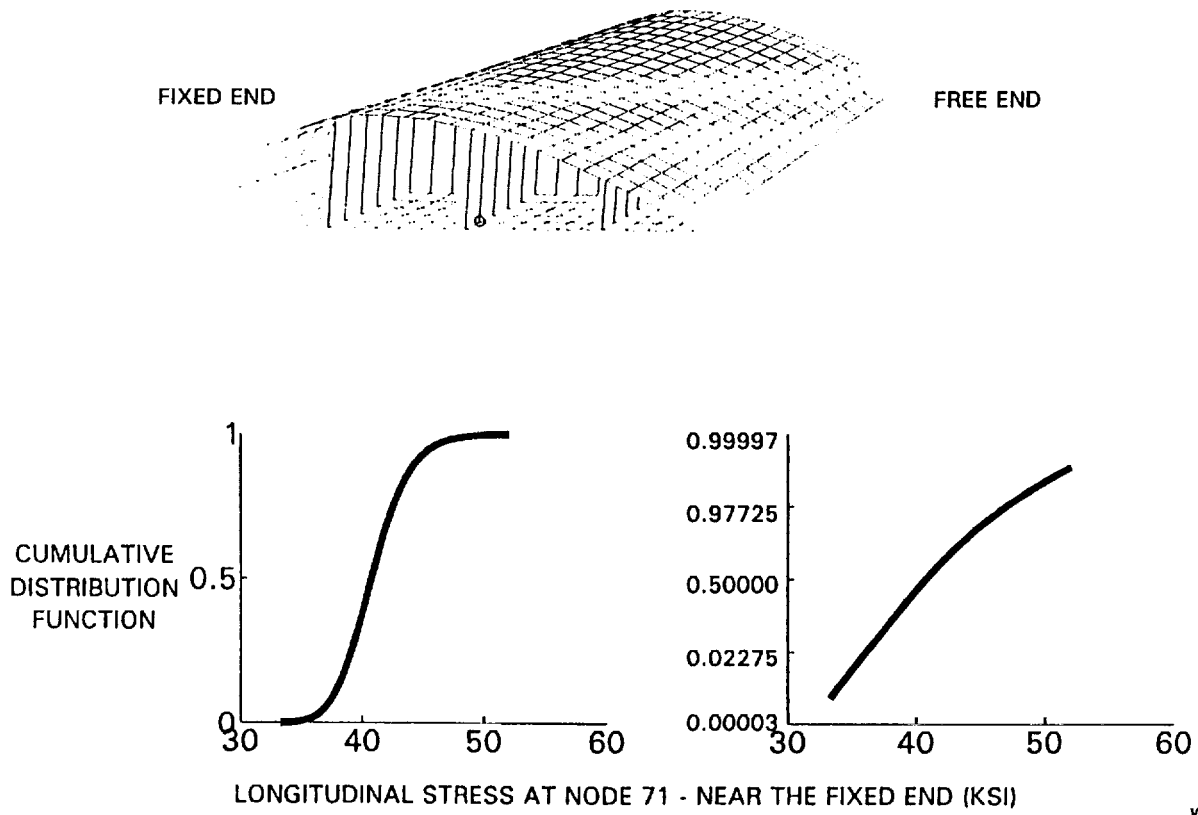


Figure 14 - Probabilistic Longitudinal Stress of a Composite Wing

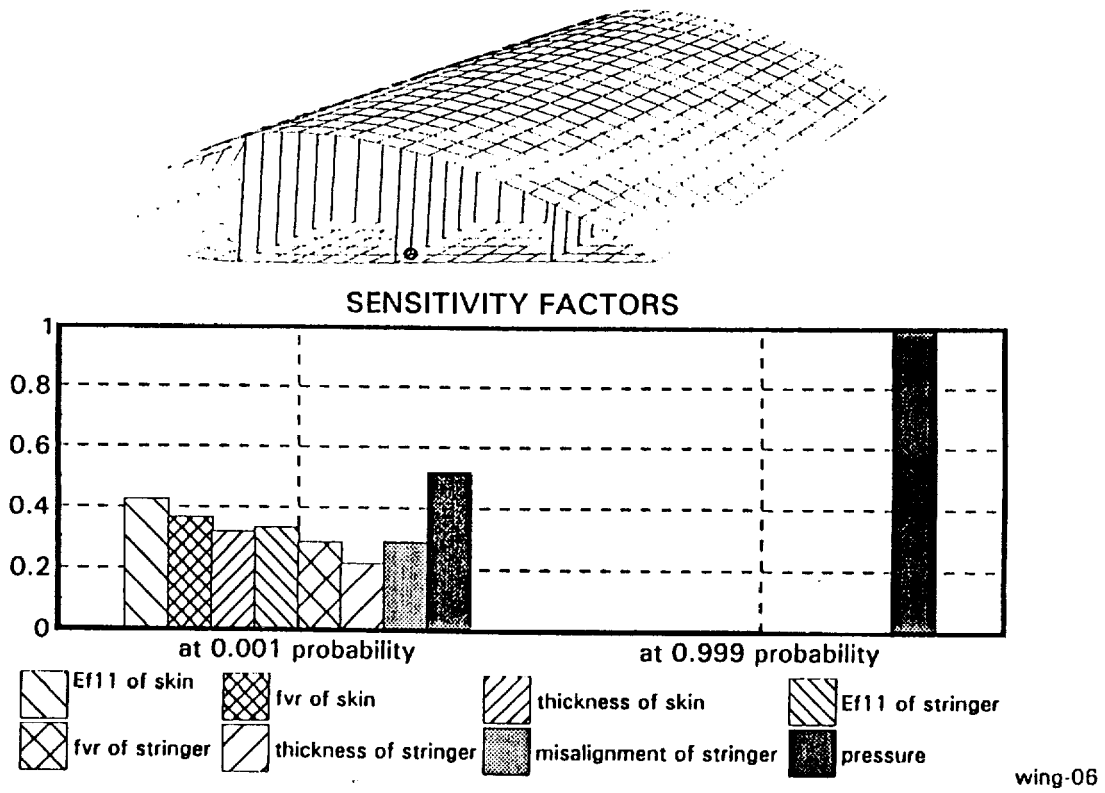


Figure 15 - Sensitivity Analysis of Probabilistic Longitudinal Stress of the Composite Wing

REPORT DOCUMENTATION PAGE			Form Approved OMB No. 0704-0188	
Public reporting burden for this collection of information is estimated to average 1 hour per response, including the time for reviewing instructions, searching existing data sources, gathering and maintaining the data needed, and completing and reviewing the collection of information. Send comments regarding this burden estimate or any other aspect of this collection of information, including suggestions for reducing this burden, to Washington Headquarters Services, Directorate for Information Operations and Reports, 1215 Jefferson Davis Highway, Suite 1204, Arlington, VA 22202-4302, and to the Office of Management and Budget, Paperwork Reduction Project (0704-0188), Washington, DC 20503.				
1. AGENCY USE ONLY (Leave blank)	2. REPORT DATE January 1993	3. REPORT TYPE AND DATES COVERED Conference Publication		
4. TITLE AND SUBTITLE Third NASA Advanced Composites Technology Conference Volume I, Part 2			5. FUNDING NUMBERS 510-02-13-01	
6. AUTHOR(S) John G. Davis, Jr., and Herman L. Bohon (Compilers)				
7. PERFORMING ORGANIZATION NAME(S) AND ADDRESS(ES) NASA Langley Research Center Hampton, VA 23681-0001			8. PERFORMING ORGANIZATION REPORT NUMBER L-17167B	
9. SPONSORING/MONITORING AGENCY NAME(S) AND ADDRESS(ES) National Aeronautics and Space Administration Washington, DC 20546-0001 Department of Defense Washington, DC 20301			10. SPONSORING/MONITORING AGENCY REPORT NUMBER NASA CP-3178, Part 2	
11. SUPPLEMENTARY NOTES				
12a. DISTRIBUTION/AVAILABILITY STATEMENT Review for general release November 1994 Subject Category 24			12b. DISTRIBUTION CODE	
13. ABSTRACT (Maximum 200 words) This document is a compilation of papers presented at the Third NASA Advanced Composites Technology (ACT) Conference held at Long Beach, California, June 8-11, 1992. The ACT Program is a major multi-year research initiative to achieve a national goal of technology readiness before the end of the decade. Conference papers recorded results of research in the ACT Program in the specific areas of automated fiber placement, resin transfer molding, textile preforms, and stitching as these processes influence design, performance, and cost of composites in aircraft structures. Papers sponsored by the Department of Defense on the Design and Manufacturing of Low Cost Composites (DMLCC) are also included in Volume II of this document.				
14. SUBJECT TERMS Thermosets; Graphite fibers; Composite design; Stitching; Preforms; Manufacturing; Processing; Analysis			15. NUMBER OF PAGES 504	
			16. PRICE CODE A22	
17. SECURITY CLASSIFICATION OF REPORT Unclassified	18. SECURITY CLASSIFICATION OF THIS PAGE Unclassified	19. SECURITY CLASSIFICATION OF ABSTRACT Unclassified	20. LIMITATION OF ABSTRACT	

NSN 7540-01-280-5500

Standard Form 298 (Rev. 2-89)
Prescribed by ANSI Std. Z39-18
298-102

NASA-Langley, 1992

PRECEDING PAGE BLANK NOT FILMED